

**Atmospheric Nanoaerosols:
from Instrumentation to Organic New Particle Formation**

Dissertation
zur Erlangung des Doktorgrades
der Naturwissenschaften

vorgelegt beim Fachbereich 11
der Johann Wolfgang Goethe - Universität
in Frankfurt am Main

von
Andrea Christine Wagner
aus Siegburg

Frankfurt 2018

vom Fachbereich 11 Geowissenschaften / Geographie der
Johann Wolfgang Goethe - Universität als Dissertation angenommen.

Dekan: Prof. Dr. Georg Rümpker

Gutachter : Prof. Dr. Joachim Curtius
Prof. Dr. Paul Winkler

Datum der Disputation :

Table of Contents

Abstract	1
1 Aerosols, Health and Climate	3
1.1 Atmospheric Aerosols	3
1.2 Health Effects of Atmospheric Aerosols	3
1.3 Climate Impacts of Atmospheric Aerosols	4
1.4 Instrumentation for Aerosol Research	5
1.4.1 Particle Number Concentration	5
1.4.2 Size-Resolved Particle Number Concentration	6
1.4.3 Molecules and Ions	7
1.5 New Particle Formation	8
1.6 The CLOUD Experiment	10
2 Introduction to the Projects	11
2.1 Size-resolved online chemical analysis of nanoaerosol particles: a thermal desorption differential mobility analyzer coupled to a chemical ionization time-of-flight mass spectrometer (Wagner et al. (2018))	11
2.1.1 Development Details	12
2.1.2 Characterization	16
2.1.3 Analysis of Organic Nanoparticles	18
2.2 Characterization of Aerosol Particles Produced by a Skyscraper by Blasting (Wagner et al. (2017))	20
2.3 Observation of new particle formation and measurement of sul- furic acid, ammonia, amines and highly oxidized organic molecules at a rural site in central Germany (Kürten et al. (2016)))	22
2.4 Characterization of the mass-dependent transmission efficiency of a CIMS (Heinritzi et al. (2016))	24
2.5 Ion-induced nucleation of pure biogenic particles (Kirkby et al. (2016))	26
2.6 The role of low-volatility organic compounds in initial particle growth in the atmosphere (Tröstl et al. (2016))	28
2.7 Rapid growth of organic aerosol nanoparticles over a wide tro- pospheric temperature range (Stolzenburg et al. (2018))	30

2.8	Molecular understanding of the suppression of new-particle formation by isoprene (Heinritzi et al. (2018))	32
3	Personal Contribution to the Projects	35
4	Publications	39
4.1	Size-resolved online chemical analysis of nanoaerosol particles: a thermal desorption differential mobility analyzer coupled to a chemical ionization time-of-flight mass spectrometer (Wagner et al. (2018))	39
4.2	Characterization of Aerosol Particles Produced by a Skyscraper by Blasting (Wagner et al. (2017))	58
4.3	Observation of new particle formation and measurement of sulfuric acid, ammonia, amines and highly oxidized organic molecules at a rural site in central Germany (Kürten et al. (2016))	73
4.4	Characterization of the mass-dependent transmission efficiency of a CIMS (Heinritzi et al. (2016))	95
4.5	Ion-induced nucleation of pure biogenic particles (Kirkby et al. (2016))	108
4.6	The role of low-volatility organic compounds in initial particle growth in the atmosphere (Tröstl et al. (2016))	129
4.7	Rapid growth of organic aerosol nanoparticles over a wide tropospheric temperature range (Stolzenburg et al. (2018))	150
4.8	Molecular understanding of the suppression of new-particle formation by isoprene (Heinritzi et al. (2018))	171
5	Summary and Outlook	207
6	Zusammenfassung	211
	Glossary	219
	References	221
	Curriculum Vitae	235

Abstract

Atmospheric nanoaerosols have extensive effects on the Earth's climate and human health. This cumulative work focuses on the development and characterization of instrumentation for measuring various parameters of atmospheric nanoaerosols, and its use to understand new particle formation from organic precursors. The principal research question is, how the chemical composition of nanoaerosol particles can be measured and how atmospheric chemistry influences aerosol processes, especially new particle formation and growth. Therefore, nanoaerosols are investigated under various aspects. More specifically, an instrument is developed to analyze nanoparticles, and field as well as chamber studies are conducted.

The main project is the instrument development of the Thermal Desorption Differential Mobility Analyzer (TD-DMA, project 1, Wagner et al. (2018)). This instrument analyzes the chemical composition of small aerosol particles. By characterization and testing in chamber experiments, it is proven to be suitable for the analysis of freshly nucleated particles.

The second project (Wagner et al. (2017)) applies a broad spectrum of aerosol measurement instruments for the characterization of aerosol particles produced by a skyscraper blasting. A comprehensive picture of the particle population emitted by the demolition is obtained.

Project 3 (Kürten et al. (2016)) is also an ambient aerosol measurement, focusing on new particle formation in a rural area in central Germany, and the ability of a negative nitrate CI-APi-TOF to detect various substances in atmosphere. Project 4 (Heinritzi et al. (2016)) is a characterization of the negative nitrate CI-APi-TOF used in projects 1, 3, 5, 6, 7 and 8. The following projects focus on understanding new particle formation from atmospherically abundant organic precursors. Key instruments comprise the negative nitrate CI-APi-TOF for gas-phase measurements of the nucleating species, and various sizing and counting instruments for quantifying the particle formation and growth. Project 5 (Kirkby et al. (2016)) shows that biogenic organic compounds formed from alpha-pinene can nucleate on their own without the influence of e.g. sulfuric acid. Project 6 (Tröstl et al. (2016)) describe the subsequent growth of these particles. Project 7 (Stolzenburg et al. (2018)) covers the temperature dependence of this growth and in project 8 (Heinritzi et al. (2018)), the suppressing influence of isoprene on the new particle formation is assessed.

1 | Aerosols, Health and Climate

1.1 Atmospheric Aerosols

Aerosols are defined as the entity of a gas and solid or liquid particles dispersed therein. The particles are referred to as aerosol particles. In the lower atmosphere, aerosol particles are omnipresent, although their number concentration can vary by orders of magnitude. It can range from less than 10^3 cm^{-3} in the free troposphere, over $10^3 - 10^4 \text{ cm}^{-3}$ in rural areas up to $10^4 - 10^6 \text{ cm}^{-3}$ and more in cities. The particle sizes range from a few nanometers to several hundred micrometers (Seinfeld and Pandis (2006)).

Aerosol particles in the atmosphere can originate from direct emission of solids or liquids (primary particles), such as pollen, soot, bacteria, sea salt or mineral dust. But around 50% of the particles are formed in the atmosphere from the gas-phase (secondary particles) (Merikanto et al. (2009), Dunne et al. (2016)). This process is called new particle formation (see also section 1.5).

1.2 Health Effects of Atmospheric Aerosols

Aerosol particles pose adverse effects on human health. In this context they are known as “fine dust”.

Fine particles can reach deep into the lungs, can even penetrate to the bloodstream and are found in the lymph nodes, kidney and liver (Choi et al. (2010)). Insoluble fibrous particles like asbestos can lead to lung inflammation and mesothelioma tumors (Donaldson et al. (2010)). Furthermore, Li et al. (2003) observed damage on the mitochondria of human cells due to exposure to aerosol particles.

From the statistical point of view, an enhanced occurrence of lung cancer and cardiovascular diseases can be linked to an exposure to high concentrations of fine particles (Brook et al. (2010), Anderson et al. (2012)). Also a connection between particles smaller than $2.5 \mu\text{m}$ and ischemic stroke is drawn (Wellenius et al. (2012)). In total, Lelieveld et al. (2015) estimated that fine dust is responsible for 3.3 million premature deaths per year worldwide.

1.3 Climate Impacts of Atmospheric Aerosols

Another strong motivation to understand atmospheric aerosols is their extensive effect on the Earth's climate.

Aerosol particles which can act as cloud condensation nuclei (CCN, typically $> 50 \mu\text{m}$) are the necessary starter to form droplets, and thus clouds. Although clouds mainly consist of water, its supersaturation in the atmosphere is not high enough to homogeneously condense and form droplets on its own. An aerosol particle is needed as a nucleus for the water to condense on. Without aerosol particles, there would be no clouds and no rain. Therefore, the concentration of CCN affects also the properties of clouds. A higher number of particles means more and smaller droplets (for the same amount of water), the cloud being brighter (higher *albedo*) and reflecting more sunlight back into space. This has a cooling effect on the climate. Also, the presence of more particles leads to an enhanced number of droplets and a higher capability to hold water, which extends the clouds *lifetime* and has influence on both the reflection of solar radiation and the Earth's water cycle (Lohmann and Feichter (2005), Forster et al. (2007)).

Aerosol particles that have grown to larger sizes can interact with the solar radiation and thus have also a direct effect on the radiative balance of the Earth. *Reflection* leads to a cooling effect as a fraction of the solar radiation is inhibited from reaching the Earth's surface. In contrary, the low-frequency radiation emitted from the Earth can mostly pass. *Absorption* of radiation by particles can have a positive, warming effect on the radiative balance, e.g. over light surfaces as deserts, snow, ice and clouds. Over dark surfaces as oceans and forests it can have a negative, cooling effect. This is because not only the direct solar radiation can be absorbed, but also the sunlight reflected by the Earth's surface that otherwise would be emitted to space. Radiation directly from the sun is partially absorbed so that the surface is initially cooled, but the atmospheric layers where the absorbing particles are located are heated. Low-frequency radiation from the Earth can also be absorbed but this is only relevant for the radiation budget in the special case of very high particle concentrations at high altitudes. Furthermore, absorption of low-frequency radiation in the troposphere can lead to a local warming, decrease of relative humidity, thermodynamic instability and thus influence on clouds and precipitation (Forster et al. (2007)).

In total, these processes are estimated to have a negative, cooling effect on the

radiative budget (Forster et al. (2007), Boucher et al. (2013)). To quantify the effects of aerosol particles on the radiation budget and clouds, as well as to predict them for the present, past and future atmosphere, the understanding of aerosol formation processes is crucial.

1.4 Instrumentation for Aerosol Research

To understand atmospheric aerosols, it is inevitable to measure them. A number of techniques are used in atmospheric science to measure the different parameters of the aerosol, and over time, more and more capable instruments are developed.

In this section, some key instruments that form the base of this work, are introduced.

1.4.1 Particle Number Concentration

A important parameter that characterizes an aerosol particle population, is their number per volume.

Charged particles can be detected by electrometers, which count the number of elementary charges. However, for a more sensitive detection, optical techniques are favored (McMurry (2000)). While particles larger than ≈ 70 nm can be directly optically detected, smaller particles need to be enlarged to interact with light to a sufficient extent. Therefore, Condensation Particle Counters (CPCs) ((Aitken (1890), Hermann et al. (2007)) are used to measure the number concentration of small aerosol particles. A liquid, usually butanol or water, is condensed onto the particles before optical detection. There are also two-step systems like Particle Size Magnifiers (PSMs, Vanhanen et al. (2011)). They first use a liquid of very low volatility (e.g. diethylene-glycol, Iida et al. (2009)) that can condense on the smallest particles. In a second step, another condensation liquid (e.g. butanol) is used, which is more volatile and can be brought to the gas-phase in sufficient amounts to grow the small droplets enough for optical detection. With these instruments, particles as small as ≈ 2.5 nm (one-step system, Hermann et al. (2007)) or even ≈ 1 nm (two step system, Jiang et al. (2011), Vanhanen et al. (2011)) can be detected. The diameter at which 50% of the particles can be activated and detected, is called the *cut-off diameter*, and is a an important characteristic of a CPC. As information about the particle number concentration is a crucial parameter, counters were used in all the projects of the current work.

1.4.2 Size-Resolved Particle Number Concentration

Not only the total number concentration, but also the particle size are important information.

Aerodynamic Particle Sizers (APS, Peters et al. (2006)) use the inertia of particles to select them according to their size. The incoming aerosol is accelerated and while small particles travel with a similar speed as the gas, larger particles are slower due to their inertia and reach the optical detection later. Optical Particles Counters (OPC, e.g. Hinds (1999)) use the light scattered by particles to determine their size, but also estimate other properties like refraction index and shape. These methods, however, can only target larger particles of several hundred nanometers as the interaction cross section of smaller particles with light is too low. These instruments were used in project 2 (Wagner et al. (2017)) and project 4 (Kürten et al. (2016)). As these projects were ambient measurements, particles of all sizes could be present and the APS and OPC were used to monitor the particle population at larger sizes.

For smaller sizes, Differential Mobility Analyzers (DMAs) are the instruments of choice. They select a particle size and are combined with a particle detector, e.g. a CPC. A fraction of the particles are charged and introduced to a selection area, where they are exposed to both a laminar gas flow dragging them to one direction and an electric field dragging them orthogonal to it. Depending on their so called electrical mobility, which is a parameter depending on their number of elementary charges and size, particles are either reaching the outlet or impacting on the wall. By variation of the voltage determining the electric field, different sizes can be selected one after the other. This principle is also used in Scanning Mobility Particle Sizers (SMPS, Wang and Flagan (1990)), where the voltage and thus selected size is varied continuously in order to measure the number size distribution. The DMA-train (Stolzenburg et al. (2017)) used in projects 7 and 8 (Stolzenburg et al. (2018), Heinritzi et al. (2018)), follows a different principle to measure several particle sizes. Here, a set of six DMAs is each set to a constant diameter, so that a high time-resolution is achieved, which is very beneficial for new particle formation measurements. DMAs and SMPS were also used in all projects of the current work.

Depending on the needs, DMAs come in all shapes and sizes. For example, when larger particles should be measured, the selection area should be longer, whereas for small particle sizes a short selection area is beneficial. A low sheath flow leads to a high sensitivity but less accurate size-selection, as for example in project 1, the TD-DMA (Wagner et al. (2018)). A high sheath flow, in

the contrary, compromises on sensitivity and leads to a high size resolution. In High Resolution Differential Mobility Analyzers (HR-DMA, Steiner et al. (2010), Fernández de la Mora and Kozlowski (2013)), as used in project 4 (Heinritzi et al. (2016)), the resolution is so high that even molecular clusters can be separated from one another. These are then detected by electrometers or mass spectrometers as they are too small for CPCs.

Another approach to gain some information about particle sizes is to use several CPCs with different cut-off diameters and compare the measured concentrations. This gives a sparse size-resolution, but high sensitivity and time-resolution. For example when observing the formation of new particles in presence of larger background particles, a CPC with cut-off diameter 2.5 nm and a CPC with cut-off diameter 10 nm can be used to determine the number of freshly formed particles between 2.5 and 10 nm.

1.4.3 Molecules and Ions

To detect molecules and ions, mass spectrometry is a versatile tool (Maher et al. (2015)). Mass spectrometers measure the mass to charge ratio (m/z) of ions. If the detection of neutral molecules is intended, they need to be charged beforehand in a so-called ion source, e.g. by chemical ionization or by electrospray ionization. There are different principles on how to separate the masses, but all involve applying electromagnetic forces to the ions. The ions are then detected by a detector, e.g. a channeltron (Allen (1939)) or an assembly of many channeltrons, a microchannel plate (Wiza (1979)).

While mass spectrometers have an extremely broad range of applications, they are also used in atmospheric science for the detection of various gaseous compounds (Laskin et al. (2018)). Time-of-flight mass spectrometers have a high mass resolution, which allows an identification of isobaric species even in the complex atmospheric systems. Atmospheric Pressure Interface Time-of-Flight Mass Spectrometers (APi-TOFs) are used to measure naturally occurring ions and charged clusters. As instrument development proceeds, particle counters can activate and detect smaller and smaller particles. Conversely, the APi-TOF can detect large clusters, so that the nucleating gases, clusters and particles can now be counted at every stage of the formation process (Schobesberger et al. (2013)).

Chemical Ionization Atmospheric Pressure Interface Time-of-Flight Mass Spectrometers (CI-APi-TOFs) are used for the detection of neutral molecules, which are charged by chemical ionization before entering the mass spectrom-

eter (Kürten et al. (2014), Jokinen et al. (2012)). Depending on the target analyte, the reaction ion for the chemical ionization is chosen. For example, volatile organic compounds such as alpha-pinene or isoprene are targeted by the proton transfer reaction (PTR) technique using hydronium ions (Hansel et al. (1995), Graus et al. (2010), Breitenlechner et al. (2017)). A key instrument in this work is the negative nitrate CI-API-TOF, which is capable of measuring sulfuric acid, organic molecules of high oxygen content and many more species (Eisele and Tanner (1993), Kürten et al. (2012), Simon et al. (2016)). Both these techniques measure organic molecules relevant for new particle formation (see section 1.5). They are thus used in projects 3, 5, 6, 7 and 8, which are focusing on new particle formation. The PTR is most sensitive for volatile and semi-volatile organic compounds with lower oxygen content (precursors) while the negative nitrate CI is suited for the detection of highly oxygenated organic molecules formed thereof. In project 7, they are combined to obtain information about organic compounds of all oxidation states. The negative nitrate CI-API-TOF was chosen as a detector for the TD-DMA in project 1, and it was characterized in project 4.

Also the molecular composition of particles is assessed by mass spectrometry. For particles of larger size, the Aerosol Mass Spectrometer (AMS, Jayne et al. (2000), Zhang et al. (2011)) and single particle mass spectrometry (Noble and Prather (2000), Bzdek et al. (2012)) are used. Targeting small particles below 30 nm is very challenging because of their very low mass, and few instruments are capable of such an analysis (for more detail see the overview in Wagner et al. (2018)). This was however one of the motivations to develop a dedicated instrument for this size range: In project 1, the TD-DMA was developed to prepare small particles between 10 and 30 nm for mass spectrometric analysis.

1.5 New Particle Formation

A large fraction of atmospheric aerosol particles are secondary aerosol particles, formed from the gas-phase (Merikanto et al. (2009), Dunne et al. (2016)). When two gas molecules collide and stick together, it is called a *cluster*. More and more molecules can stick to it, and at a point where this cluster is large enough to be thermodynamically stable, it is called an aerosol particle. Depending on the conditions, this is typically at a size between 1 and 2 nm. The freshly nucleated particles can grow as more molecules condense on them, or two particles collide and form a single bigger particle (*coagulation*). The

condensation of molecules on a particle is determined by their vapor pressure for the given circumstances. When particles are large enough that water can condense on them, they can act as cloud condensation nuclei (see section 1.3). In all sizes, particles can be lost by processes like evaporation or coagulation, but in the small size range, the losses are highest. The full process of aerosol nucleation and early growth is called *new particle formation*. It is observed in a wide range of environments, from rural to urban areas, from boreal forests to coastal areas, from tropical to polar regions and from ground level to the free troposphere (Kulmala et al. (2004), Kerminen et al. (2018)).

A parameter to quantify the nucleation is the *nucleation rate* J , the number of particles produced per volume and time ($\text{cm}^{-3}\text{s}^{-1}$). This number is calculated for a specific particle size, usually 1.7 nm or 2.5 nm (as these are the cut-off diameters of state-of-the-art counters), and considers also the losses of particles in the process to reach that diameter. The growth is quantified by the *growth rate* GR , the increase of diameter per time (nm h^{-1}). In the atmosphere, nucleation rates range up to $10^4 \text{ cm}^{-3}\text{s}^{-1}$, and growth rates of usually up to 15 nm h^{-1} , but in some cases even up to 200 nm h^{-1} are observed (Kulmala et al. (2004)).

Sulfuric acid was for a long time thought to be the key substance for nucleation (Curtius (2006), Kuang et al. (2008), Kulmala et al. (2013)), as it strongly correlates with it and has a low vapor pressure in the presence of water. However, it can not explain nucleation rates observed in the atmosphere on its own. Laboratory measurements using only sulfuric acid and water yield nucleation rates that are much lower than those observed in the ambient (Weber et al. (1996)). When a base is present, nucleation is observed to increase as the cluster evaporation is suppressed by acid-base-stabilization. This is for example the case for ammonia (Weber et al. (1996), Kirkby et al. (2011)) and amines (Almeida et al. (2013), Kürten et al. (2014)). Another binding agent that stabilizes clusters and thus enhances nucleation, is charge: Although later in the growth process, the charged clusters recombine to neutral particles, the charge helps clusters to survive the crucial size range in which they are very prone to re-evaporation. This mechanism of charge stabilization is especially efficient when there is no other stabilization mechanism: It has a significant effect on the system of sulfuric acid with water as well as the sulfuric acid-ammonia-water system, whereas clusters from sulfuric acid and amines are so strongly bound on their own that the charge effect is less pronounced (Lovejoy et al. (2004), Kirkby et al. (2011), Almeida et al. (2013)).

Organics play an important role in new particle formation: *Volatile organic compounds* (VOCs) are emitted by plants (Guenther et al. (2012)), and even as they are too volatile to form particles themselves, they undergo chemical reactions in the atmosphere (Atkinson and Arey (2003)). From the various reaction pathways, some produce *highly oxygenated organic molecules* (HOMs). These substances can have, depending on the conditions, a low or very low vapor pressure, and are thus called *low volatile organic compounds* (LVOCs) or *extremely low volatile organic compounds* (ELVOCs, Ehn et al. (2014)). The volatility of a molecule in a given condition (temperature, presence of other molecules) determines if they can nucleate or at which stage of the growth they start to contribute. These processes of new particle formation from organic precursors were observed in the ambient in project 3 and studied in detail in projects 5, 6, 7 and 8. In project 5, it is shown that HOMs produced from alpha-pinene can nucleate on their own, and charge is the binding agent of the clusters. In projects 6 and 7, the consecutive growth of this organic system is studied and in project 8, the influence of an additional organic precursor, isoprene, is explored.

1.6 The CLOUD Experiment

The Cosmics Leaving Outdoor Droplets experiment (CLOUD) aims to understand new particle formation, cloud droplets and ice particles. The nucleation and growth experiments for project 5-8 as well as the test measurement for project 1 were conducted with CLOUD.

The CLOUD chamber is a 26.1 m³ stainless steel reactor (Kirkby et al. (2011)), in which an artificial atmosphere is created. All parameters can be precisely controlled, including the temperature, relative humidity, UV light to simulate the sun, and the level of different trace gases. It has a special cleaning system where the chamber can be rinsed with ultrapure water and heated. Careful preparation of the incoming gases is realized by using nitrogen and oxygen from cryogenic tanks. This system ensures the ability to investigate specific chemical systems with extremely low levels of contamination, which is a special feature of the CLOUD chamber. To investigate ion effects and to simulate processes at high atmospheric levels (where ion concentrations are higher) CLOUD has the ability to remove ions by an electric field cage, but also to add ions by using pions from a secondary beam of the proton synchrotron accelerator of CERN.

A suite of instruments sample from the chamber to analyze the aerosol. Over the past years, this has grown to a very diverse composition of state-of-the-art instruments that enables to measure most of the relevant parameters. The instruments include several particle sizing and counting instruments such as CPCs, PSMs, the DMA-train and SMPSs, as well as different mass spectrometers like the negative nitrate CI-API-TOF, PTR-MS, API-TOF, and more. This allows understanding different chemical systems including sulfuric acid, ammonia, amines and lately the biogenic organics that are a focus of this work.

2 | Introduction to the Projects

2.1 Size-resolved online chemical analysis of nanoaerosol particles: a thermal desorption differential mobility analyzer coupled to a chemical ionization time-of-flight mass spectrometer (Wagner et al. (2018))

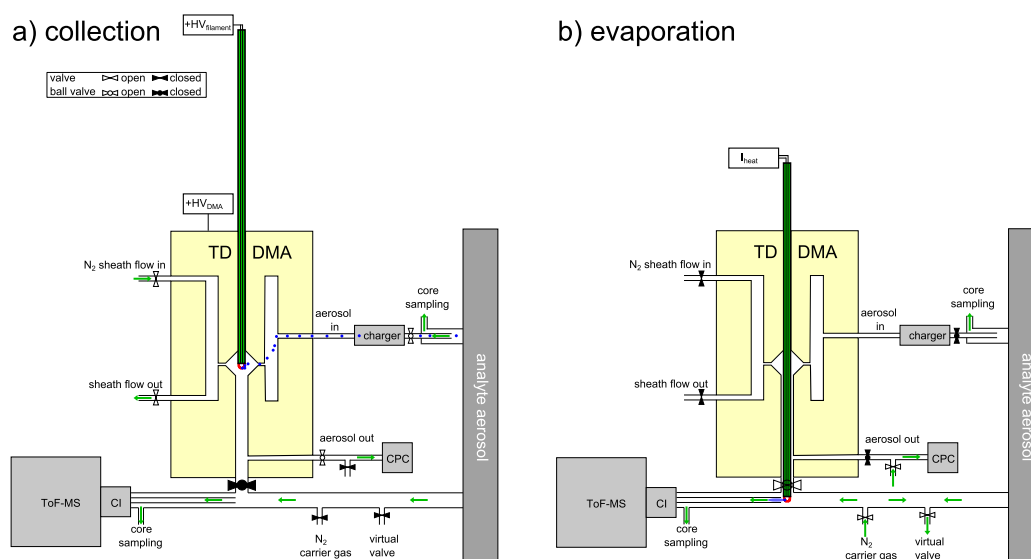


Figure 2.1: Measurement setup of the TD-DMA with step (a) particle collection, and (b) evaporation.

For investigating new particle formation, the speciation of condensing vapors is highly important. For gas-phase molecules and molecular clusters, e.g. the CI-APi-TOF (Kürten et al. (2014), Jokinen et al. (2012)) is used, and for particles that have already grown to larger sizes, the AMS (Jayne et al. (2000), Zhang et al. (2011)) is most commonly deployed. The chemical analysis of

small particles below 30 nm, however, is very challenging due to the minute mass contained in the particles, so there are very few instruments that are capable of such measurements at all.

We therefore developed the TD-DMA (Thermal Desorption Differential Mobility Analyzer). This instrument prepares small particles for the chemical analysis with e.g. a mass spectrometer. The particles are charged and a specific size is selected in a DMA. Inside the DMA, the particles are electrostatically precipitated on a filament. Once enough mass is collected, the filament is moved to the inlet line of a mass spectrometer and thermally desorbed in a clean carrier gas. Like this, the particle-phase is separated from the gas-phase and the concentration is enhanced to meet the detection limit of the mass spectrometer. The advantages of this measurement principle are as follows: I) The *size-selective mode* allows it to compare the chemical composition of particles at different stages of the growth process and therefore to determine the relative contribution of different vapors as a function of particle size. II) An *integral mode* also allows to collect all particle sizes, which maximizes the collected mass and makes measurement also possible for very weak particle concentrations. III) The TD-DMA is modular and compact. Up to now it was combined with a negative nitrate CI-API-TOF, but it can in principle also be combined with any other gas-phase analyzer. IV) While the collection takes place, the detector can still be used to analyze the gas-phase. Therefore the costs for an additional analyzer are saved and both phases can be directly compared.

The newly developed TD-DMA is suitable for the chemical analysis of small aerosol particles in the nucleation and Aitken mode ($< \approx 10$ nm and $< \approx 50$ nm). The sensitivity allows measuring at atmospherically relevant aerosol mass concentrations in the pg m^{-3} -range. The characterization of the instrument shows reproducible results and the capability to measure freshly nucleated particles as small as 15 nm was proven in chamber experiments.

2.1.1 Development Details

Some additional information, which is not included in the publication (Wagner et al. (2018)), shall be given here. The full setup of the TD-DMA coupled to a mass spectrometer is shown in figure 2.7, and the graphical user interface of the LabVIEW control software as well as the electronic control unit can be seen in figures 2.2 and 2.3. A detailed technical description of the instrument can be found in Bergen (2016) and Brilke (2016).

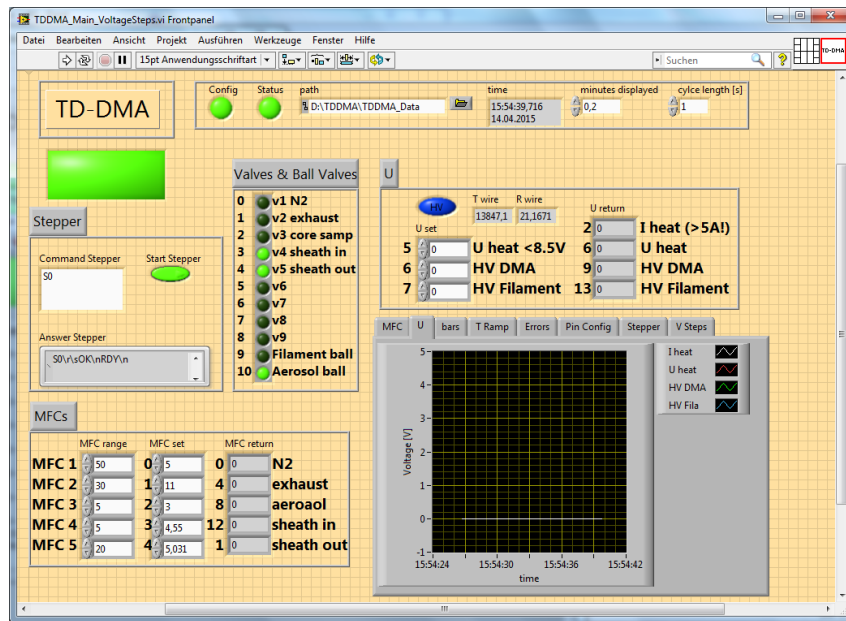


Figure 2.2: The graphical user interface of the LabVIEW control software.

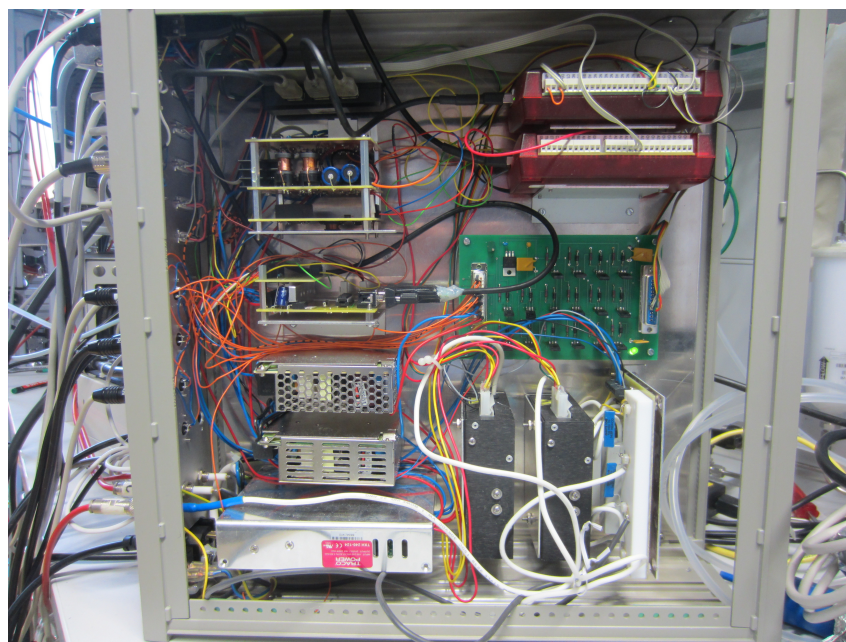


Figure 2.3: View into the electronic control unit.

DMA Unit

In the TD-DMA's DMA unit, charged particles are classified by their electrical mobility (see section 1.4). The DMA measurement principle is based on having a sheath flow that is laminar and evenly distributed around the electrode. We tested different possibilities to achieve this, including a plate with regularly distributed boreholes and grid plates. Best results were achieved by introducing the sheath flow via a circular cavity with 16 drilled holes for distribution of the sheath flow, and by including an evenly webbed tissue for laminarization of the flow.

The first DMA unit showed transmission efficiency versus diameter curves that were not Gaussian, but had a tailing towards larger diameters. As the particle mass is proportional to the cubic diameter, larger particles were strongly overrepresented in samples from this DMA. This was most likely due to imprecisions in the alignment of the central electrode. In the next DMA prototype (figure 2.4), the design ensured that this could not happen and the transmission curves were Gaussian. Additionally, due to some modifications of inlet and outlet, a higher transmission efficiency could be achieved.

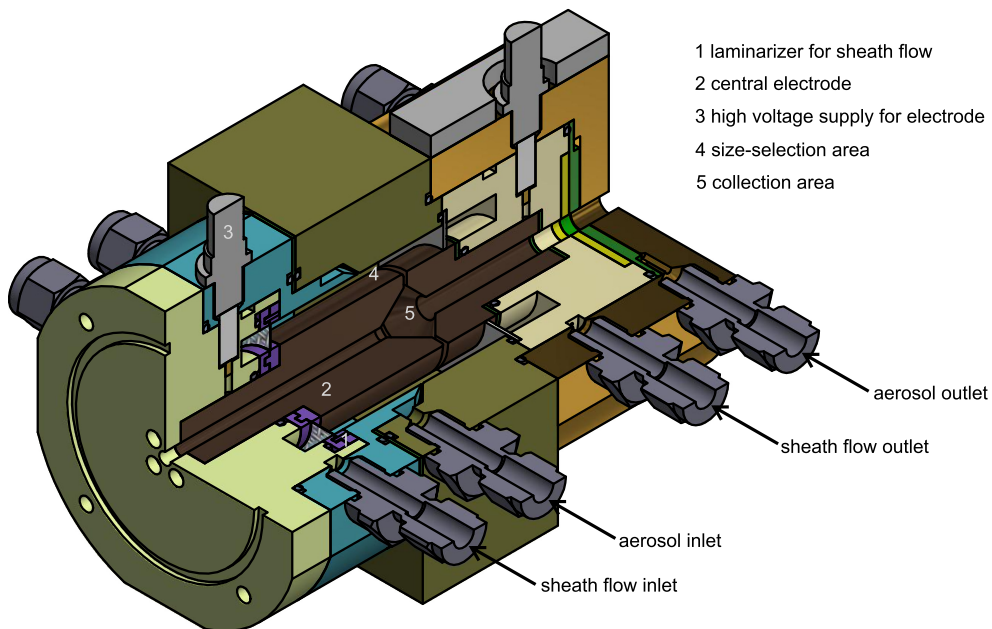


Figure 2.4: Quarter section of the TD-DMA's DMA unit.

Filament

The filament (figure 2.5) is the part on which the particles are electrostatically collected and from which they are thermally desorbed in order to reach the mass spectrometer. To ensure that the measured signal represents the chemical composition of the particle-phase and for a direct comparison of both phases, it is important not to alter the substances during the measurement process. The heating used to transfer the collected material to the gas-phase, might lead to fragmentation or chemical modification of the original molecules. We investigated this by applying a defined amount of malonic acid on the filament and desorbing it. Additionally, we investigated measurements of freshly nucleated particles. We found that the filament material and the way it is fabricated has a strong influence. Best results were obtained with an annealed alloy of platinum and rhodium. Also the rate at which the filament is heated has an influence: A steep heating curve could fragment the substances, whereas a slower heating seems to lead to a more controlled desorption. With our optimized parameters, fragmentation could be kept low and we did not observe any peaks in the spectra that would point to a complete degeneration of substances. It is even possible to desorb organosulfates, which are very fragile, in a nondestructive way. Figure 2.6 shows an example of an organosulfate measured with the TD-DMA, sulfoacetic acid hydrate ($C_2H_6O_6S$).

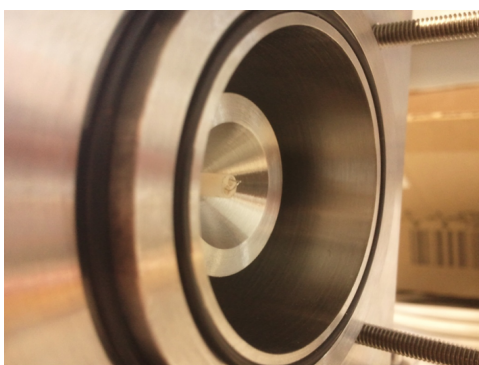


Figure 2.5: Look inside the DMA unit with the filament on which particles are collected (photographed by Anton Bergen).

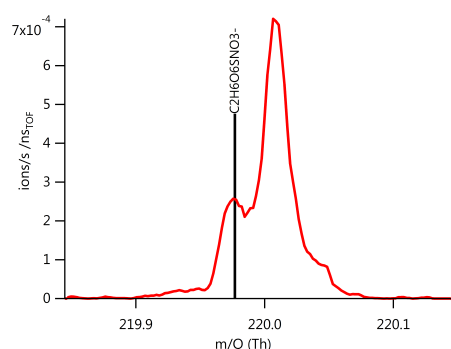


Figure 2.6: Example of an organosulfate measured by TD-DMA.

Coupling to a Mass Spectrometer

The coupling of the TD-DMA to the mass spectrometer is realized by moving the filament with the particle sample into a core sampling probe in front of the mass spectrometer's ion source (see schematic figure 2.1 and figure 2.7). The line is flushed with clean nitrogen and the excess is removed through an outlet towards the analyte aerosol reservoir (e.g. an aerosol chamber or the ambient air). This virtual valve excludes contamination of the analyte aerosol. The exact geometry of the coupling has a huge influence on the detection limit. The distance from the place of evaporation to the inlet line of the ion source, as well as the flows of the core sampling, carrier gas and virtual valve are crucial. In the first test, the lowest detectable mass was 1 ng of sulfuric acid. By optimizing the coupling and flows, the sensitivity could be enhanced so that already a mass of 0.01 ng could be detected.

2.1.2 Characterization

We characterized all steps of the measurement process in order to allow quantification of the signal. The DMA unit is optimized for a high transmission at a coarse resolution in order to collect a sufficient amount of particle mass. It was tested for six diameters between 7.5 and 30 nm. The transmission efficiency versus diameter shows good agreement with Gaussian fits and the maximum transmission efficiency for 15 nm particles is above 50%. The size resolution is with 1.19 rather coarse, so that a high amount of mass is collected while still allowing size selection. The collection efficiency of particles on the filament is 100% below 15 nm and then decreases due to the decreasing electrical mobility of the particles. The particle mass collected on the filament is related to the mass spectrometer signal by the sample mass calibration, where defined amounts of a substance are placed on the filament and subsequently desorbed. This calibration is depending on the inlet system and mass spectrometer that the TD-DMA is deployed with, in this case the factor is $42.95 \text{ ng ncps}^{-1} \cdot \text{s}^{-1}$ for sulfuric acid, for other substances their ionization efficiencies have to be taken into account.

Combining these characterizations, the signal in the mass spectrometer can be linked quantitatively to the analyte aerosol population.

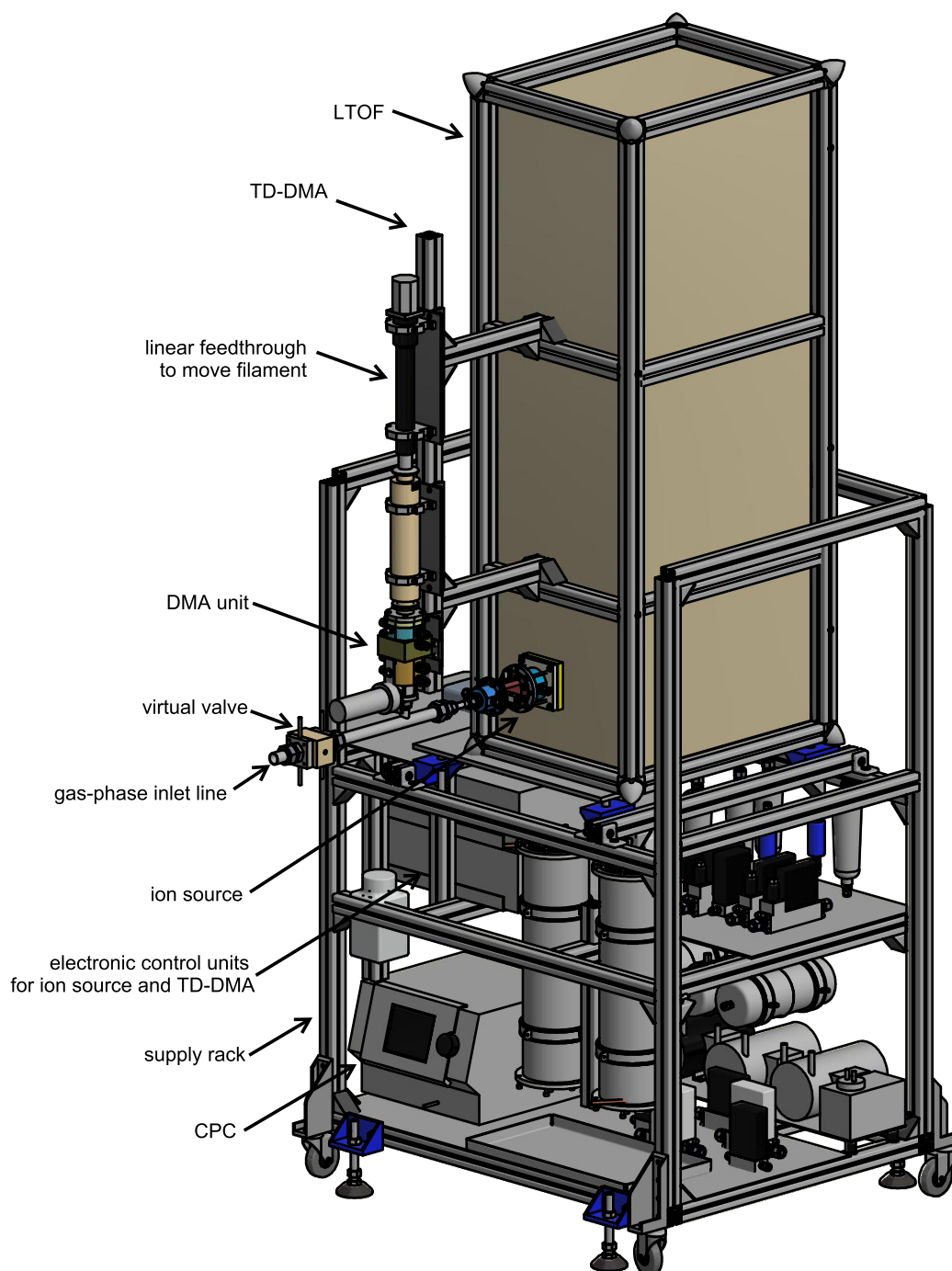


Figure 2.7: The TD-DMA coupled to a CI-API-TOF. (Technical drawing of multiple authors: Supply rack with contents: Laurin Merkel. Ion source and ion precipitator: Andreas Kürten. TD-DMA, inlet system, mass spectrometer rack and assembly: Andrea Wagner)

2.1.3 Analysis of Organic Nanoparticles

The TD-DMA was deployed at the CLOUD chamber. In these experiments, the effect of the relative humidity on the growth of organic particles from isoprene was investigated. Unfortunately, the source of isoprene that we used was contaminated with monoterpenes that could have affected strongly the nucleation and growth process. We executed two experiments with the same conditions and varied only the relative humidity (35% and 85%, see figure 2.8). The TD-DMA measurements are corrected with the mass spectrometer's transmission efficiency and normalized to the isoprene concentration present in the gas-phase (measured by PTR-MS) as well as the sampling time to ensure comparability. Figure 2.9 is a comparison of the spectra obtained for both conditions. The spectra show a strong pattern that is similar for low and high humidity. The overall intensity is higher for the high RH case, this could be confirmed by an SMPS, which shows slightly higher particle concentrations for the high humidity experiment. When viewing the ratio of low RH and high RH spectra (2.10, an increase with mass to charge ratio can be seen. This means that the presence of water shifts the chemical composition of the particle-phase slightly to lower masses.

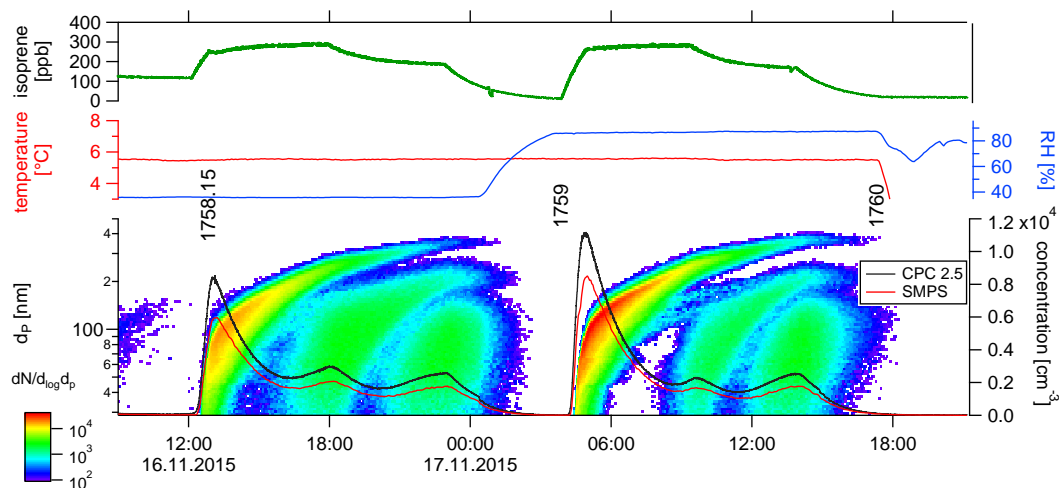


Figure 2.8: Overview over experiments for investigating new particle formation from isoprene.

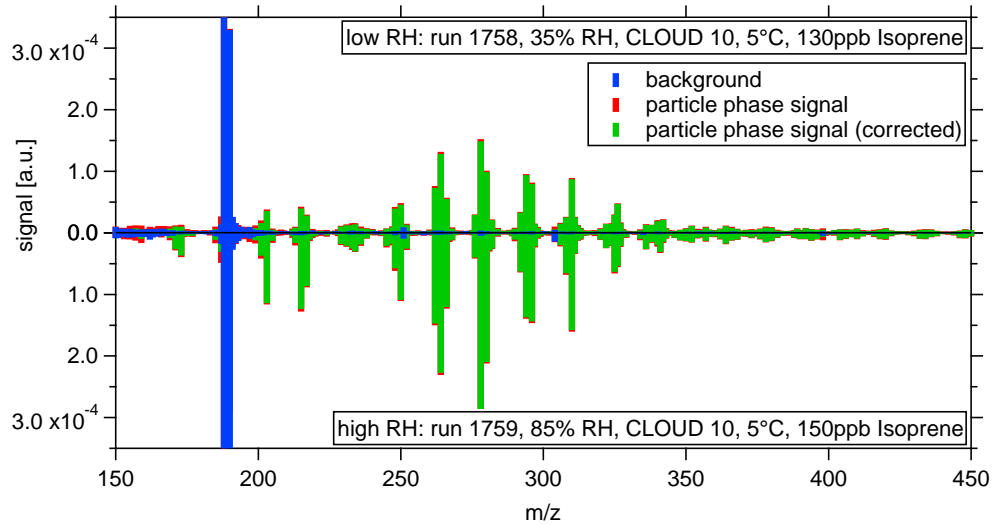


Figure 2.9: Comparison of particle-phase spectra for low and high humidity obtained by the TD-DMA.

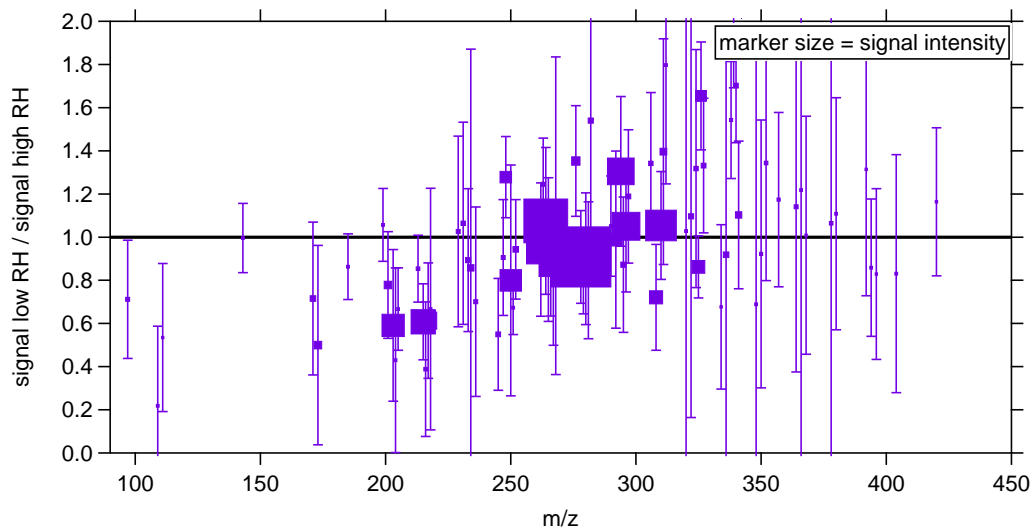


Figure 2.10: Ratio of particle-phase signals in low and high humidity conditions: The presence of water shifts the chemical composition slightly to lower masses.

2.2 Characterization of Aerosol Particles Produced by a Skyscraper by Blasting (Wagner et al. (2017))

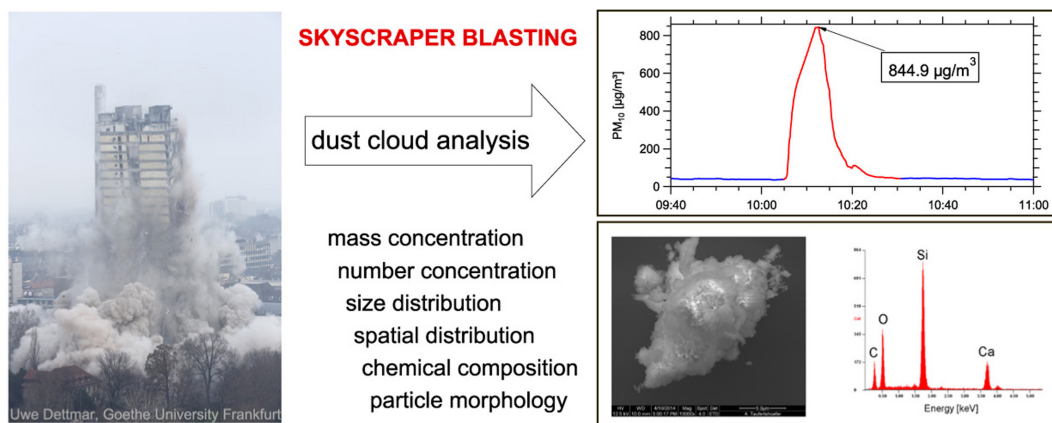


Figure 2.11: Highlights of the skyscraper blasting analysis: Strong increase in mass concentration (upper right), and exemplary SEM/EDX analysis of a single particle (lower right).

In February 2014, a skyscraper was blasted in Frankfurt to avoid lengthy deconstruction work. Such a detonation inevitably produces aerosol particles, which is a potential health hazard. Concerns were raised by the residents and our working group had the expertise as well as the instruments to characterize these particle emissions, so we used the opportunity to analyze the emissions and estimate the hazard. Usually deployed for our research on secondary aerosols, we applied the same instruments for characterizing the population of primary aerosols. Additionally, we collaborated with other institutes to complete the set of instruments.

The instruments were positioned 350 m downwind of the tower and measurements were performed for two days around the event. A Condensation Particle Counter (CPC, TSI Model 3776, TSI Incorporated (2007), Hermann et al. (2007)) measured the total number concentration starting at a cut-off diameter of 2.5 nm. The size-resolved number concentration (Baron and Willeke (2001)) was determined by three instruments with overlapping size ranges: A Scanning Mobility Particle Sizer (SMPS, TSI Model 3080, TSI Incorporated (2001), Wang and Flagan (1990)), an Optical Particle Counter (OPC, TSI Model 3330, TSI Incorporated (2012b)) and an Aerodynamic Particle

Sizer (APS, TSI Model 3321, TSI Incorporated (2012a), Peters et al. (2006)) ranging from 0.0146 to 0.6612 μm , 0.337 to 9.016 μm and 0.542 to 19.81 μm , respectively. We used a Synchronized Hybrid Ambient Real Time Particulate Monitor (SHARP, Thermo Scientific Model 5030i, Thermo Fisher Scientific Inc. Air Quality Instruments (2007)) to measure the mass concentration of particulate matter below 10 μm (PM_{10}). Additionally, dust samples were collected on silicon wafers and analyzed by Scanning Electron Microscopy (SEM) with Energy Dispersive X-Ray Spectroscopy (EDX) (Goldstein et al. (2012)) to obtain images and the chemical composition of the particles. A portable weather station (Vaisala Model WXT520) recorded meteorological parameters (temperature, pressure, humidity, wind speed and direction). While these instruments gave broad information on the particle population at this position, Bergerhoff glass collection vessels were distributed around the site to obtain a rough spatial distribution of the sedimented aerosol mass and additionally were used for metal analysis.

We found that the blasting produced a single mode of ultrafine particles with a mode diameter of 93 nm. As the number concentration was dominated by particles that were even smaller, it rose only by a factor of 3.8 over background to $6.9 \cdot 10^4 \text{ cm}^{-3}$, whereas the mass concentration rose by a factor of 30.7 to $844.9 \mu\text{g m}^{-3}$. The spatial distribution showed the dust cloud to be pushed along the street canyon in wind direction decreasing with distance. At the main measurement site, the event passed within only 15 minutes. Therefore, the 24h mean of PM_{10} mass concentrations did not exceed the EU maximum permissive value. The particles consisted mainly of the building's concrete, that is 60% calcium carbonates, 19% calcium sulfates, 19% silicates and 2% steel from the grinders. They were not fibrous and did not have an enhanced level of heavy metals in them.

We thus conclude that the skyscraper blasting led to a short-termed, yet high strain with ultrafine particles. However, particles were not fibrous (like e.g. asbestos, which had been removed from the building prior to the blasting) or contaminated with heavy metals. There is no such thing as a lower limit of particle mass or concentration regarding adverse health effects, but in comparison to other, longer lasting demolition activities and with respect to the short exposure duration, the event did not pose an excessively high risk to the spectators.

The observations from the blasting in Frankfurt are an important data point to add to the very sparse statistics on particle emissions from building blastings.

This helps to identify sources of fine dust in urban environments and might help with a decision whether to blast or conventionally demolish a building. More important, we could address the concerns of the residents exposed to the visible dust cloud as we distributed information about the scientific side of the event via media.

2.3 Observation of new particle formation and measurement of sulfuric acid, ammonia, amines and highly oxidized organic molecules at a rural site in central Germany (Kürten et al. (2016))

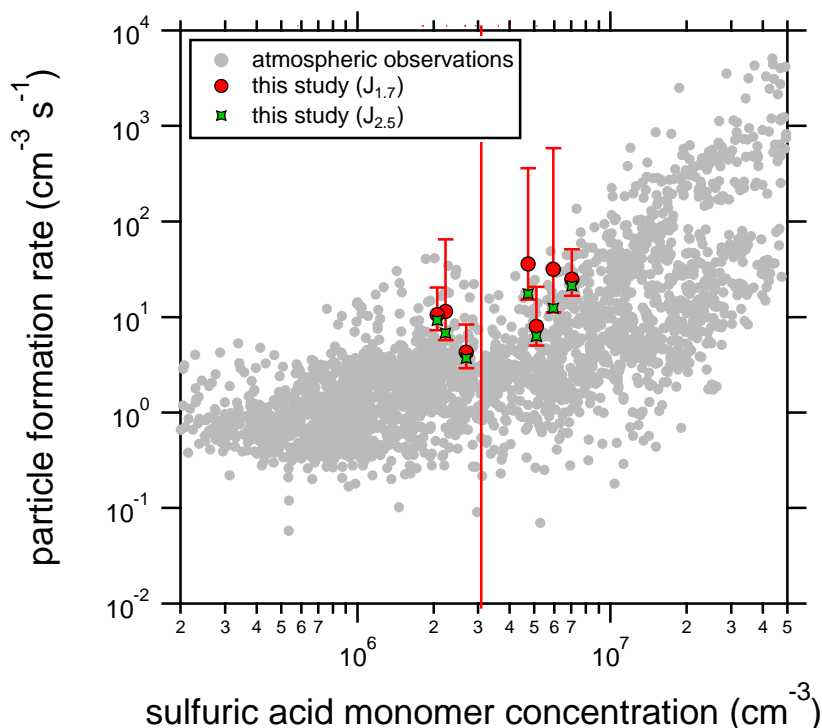


Figure 2.12: Particle formation rates observed in Vielbrunn compared to a dataset of other atmospheric observations.

Ambient measurements were conducted to investigate new particle formation in a central European rural agricultural area. The measurement site Vielbrunn in the Odenwald was in close proximity to three dairy farms which are a potential source for ammonia and amines, and surrounded by forests as a potential source for biogenic HOMs.

In chamber experiments, ammonia and amines were found to nucleate efficiently in combination with sulfuric acid via acid-base-stabilization (Kirkby et al. (2011), Kürten et al. (2014)), and cattle are a known source of ammonia (Behera et al. (2013)). Apart from that, biogenic organic substances have the ability to nucleate and grow particles (see also project 5 and 6). We also wanted to test our instrument's ability to conduct field measurements and were curious if there would be any substances detected apart from what was expected. We used our CI-APi-TOF with negative nitrate primary ions (Kürten et al. (2014)), a PTR-MS, a set of particle counting instruments including CPCs, a nDMA, an SMPS and OPC. Trace gas detectors for O₃, SO₂, NO and NO₂ were installed and meteorological parameters were obtained by a weather station of the German Weather Service DWD.

Several new particle formation events were observed, with formation rates ($J_{1.7}$ and $J_{2.5}$) of about 5 to 200 cm⁻³s⁻¹, which is rather high for a rural area. Still as to the variety of parameters, not one single source for the new particle formation could be stated. The negative nitrate CI-APi-TOF showed its capability for sensitive ambient measurements of sulfuric acid, HOMs and amines. For the first time also iodic acid, nitrosamine and ammonia could be detected by this instrument. It therefore proved to be even more versatile than previously known.

This measurement campaign adds data points to the set of ambient observations. The observation of iodic acid in this area was unexpected and raises new research question as to its source and transport.

2.4 Characterization of the mass-dependent transmission efficiency of a CIMS (Heinritzi et al. (2016))

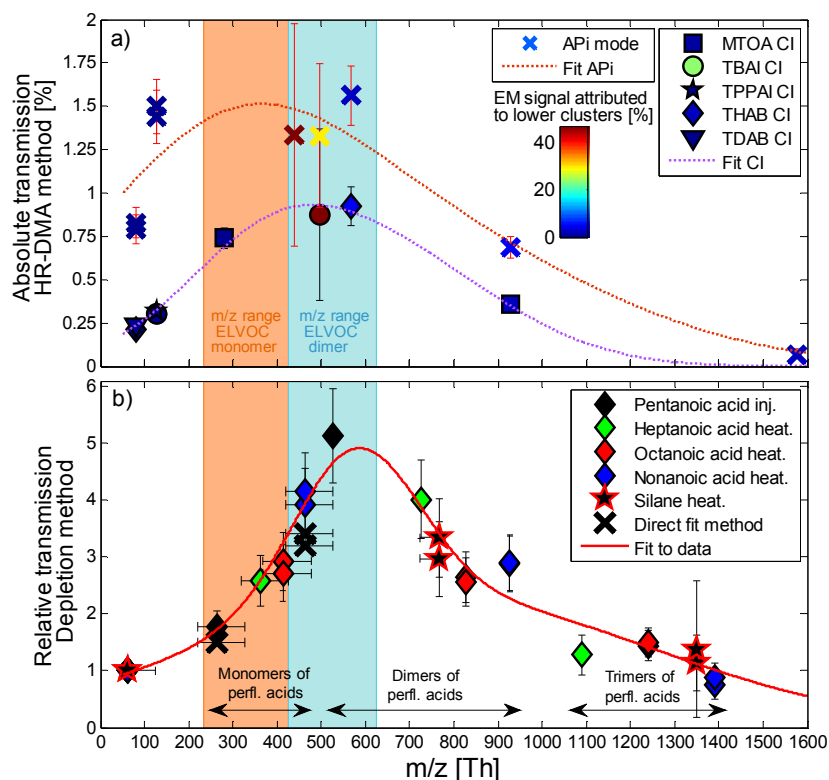


Figure 2.13: Transmission efficiency dependant on the mass to charge ratio (a) absolute transmission obtained by HR-DMA method and (b) relative transmission efficiency obtained by the depletion method.

The CI-API-TOF is a very capable tool not only for atmospheric science, and scientific analysis very much depends on knowing the instrument's behavior in order to quantify the measured signals. Ideally, target substances are calibrated for, but there remains a huge variety of other substances where this can not be done directly. The quantification of these depends on a) their ionization efficiency in the ion source, and b) the fraction of ions that reach the detector in the mass spectrometer itself. The latter phenomenon is targeted in this study. In our case, the negative nitrate CI-API-TOF used in our group is calibrated for sulfuric acid (Kürten et al. (2012)), and it can be assumed

that the target substance class of HOMs with six or more oxygen atoms have a similar ionization efficiency (Ehn et al. (2014)). Thus, knowing the difference in transmission efficiency between calibrated substance and target substance allows better quantification of the HOMs.

We compared two methods to characterize the mass discrimination effects in our mass spectrometer. I) An absolute method using a HR-DMA (Steiner et al. (2010), Fernández de la Mora and Kozłowski (2013)). Here, a known concentration of ions of a certain m/z ratio is introduced to the mass spectrometer and related to the detected signal. An electrospray source produces the ion clusters, a HR-DMA selects different sizes in the desired mass range in succession. Then the flow is split towards an electrometer as reference counter and towards the mass spectrometer. The ratio of the signals in the mass spectrometer and the electrometer gives the absolute transmission for the mass range in question. This method is performed with and without the mass spectrometer's ion source. II) A relative method using depletion of the primary ions. A substance is introduced into the CI-APi-TOF in an excessive amount so that the primary ions are significantly depleted. The charge provided by the primary ions is thus shifted to the m/z region of the substance's product ions. As the total amount of charge is constant in the ion source, comparison of the change in primary ion signals to product ion signals yields their relative transmission efficiency. By using several substances, the whole desired m/z range can be covered. A similar approach was used for PTR-MS before, but for the CI-APi-TOF the suitable substances cluster and are detected on more than one m/z peak, which is addressed by a statistical analysis.

The first method has the advantage that it characterizes the absolute transmission efficiency and thus can also be used to optimize the sensitivity by varying the mass spectrometer's voltage settings. The second method however, is quick and easy to perform as it has a simple setup in which no further instrumentation is needed. More important, the CI-APi-TOF including its ion source is characterized in the same setting as when used for the analyte: By using neutral substances and charging them in the ion source.

We obtained the relative transmission efficiency function and found that it changes significantly over the m/z range. Especially in the range up to 500 Th, where many HOMs are detected, it increases by a factor of 5, followed by a less steep decrease towards higher masses. The curve produced by the absolute method, which has a maximum of 1.5%, shows a different shape and a shift of the maximum position towards lower m/z . This suggests that not only

the mass spectrometer itself has mass dependent transmission efficiency, but also the ion source has non-negligible mass discrimination effects. Therefore the depletion method for obtaining the relative transmission efficiency is more suitable for this purpose.

This study provides an easy way to estimate the mass dependent transmission efficiency of a CIMS and thus improves the quantification of substances that can not be directly calibrated for. The method can not only be applied to negative nitrate CI-API-TOFs, but also to instruments with different reagent ions by selecting appropriate depleting substances.

2.5 Ion-induced nucleation of pure biogenic particles (Kirkby et al. (2016))

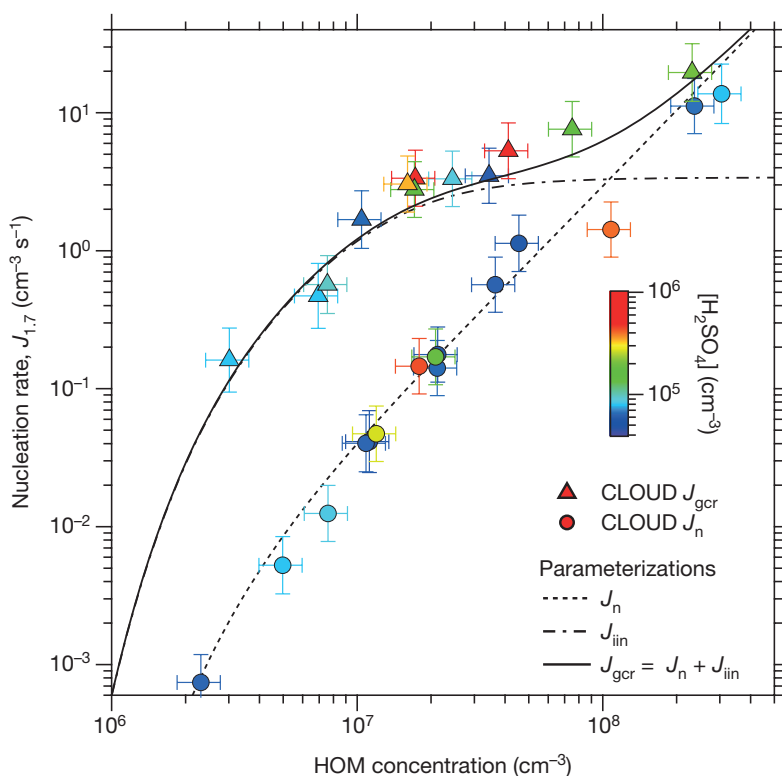


Figure 2.14: Pure biogenic formation rates versus HOM concentration. For low HOM concentrations, the charge significantly enhances the new particle formation (natural charge by galactic cosmic rays=GCR in comparison to neutral=n), whereas for high HOM concentrations, the formation rates converge.

It was previously thought that sulfuric acid is the necessary key compound for new particle formation. For pristine environments and the preindustrial climate, there is little sulfuric acid pollution but potentially more biogenic organic substances emitted from plants. The question arises if these organic compounds or their reaction products are also able to nucleate on their own without the presence of sulfuric acid.

The CLOUD collaboration for the first time had the possibility to investigate this, as on the one hand the chamber was very clean and on the other hand we had instruments that are sensitive enough to exclude contamination with e.g. sulfuric acid.

We introduced alpha-pinene and ozone into the CLOUD chamber with and without the presence of ions, and in different concentrations. HOMs were formed by alpha-pinene ozonolysis. A set of instruments measured the relevant parameters, e.g. sulfuric acid and HOMs were measured with a negative nitrate CI-APi-TOF, alpha-pinene was measured by a PTR-MS and the particle population was characterized by a set of counters.

We found that HOMs can indeed nucleate on their own and that the binding agent is charge. An atmospherically relevant HOM concentration range of $10^6 - 10^8 \text{ cm}^{-3}$ was spanned, resulting in nucleation rates of $10^{-1} - 10^1 \text{ cm}^{-3}\text{s}^{-1}$, which are comparable to atmospheric occurrences. At lower concentrations, the nucleating rate depends strongly on the presence of ions, e.g. for $\text{HOM} = 10^7 \text{ cm}^{-3}$, it differs by two orders of magnitude. The reason for this is the stabilization of clusters by charge. In the contrary, for higher HOM concentrations, the nucleation rates for neutral and charged conditions almost converge, as the number of ions is limited by the incoming galactic cosmic rays producing them. Thus the number of charge-stabilized clusters is not any more limited by the HOM concentration, but by the availability of charge. These results were also verified by quantum chemical calculations of the cluster binding energies. The discovery of the ion-induced pure biogenic nucleation is a significant improvement in the understanding of new particle formation processes. The results of this project and the follow-up project 6 (Tröstl et al. (2016)), could directly be implemented in the global aerosol model GLOMAP (Gordon et al. (2016), Mann et al. (2010)) and are helping to estimate the particle concentrations in pristine environments and in the preindustrial climate. The GLOMAP model reveals that the additional new particle formation process impacts especially our understanding of the preindustrial period, where measurements are not possible any more and it needs to be relied on models. The model

including pure biogenic nucleation shows higher preindustrial particle concentrations and thus in combination with a given temperature difference between then and the present helps to reduce uncertainty on other climate parameters as for example greenhouse gases.

2.6 The role of low-volatility organic compounds in initial particle growth in the atmosphere (Tröstl et al. (2016))

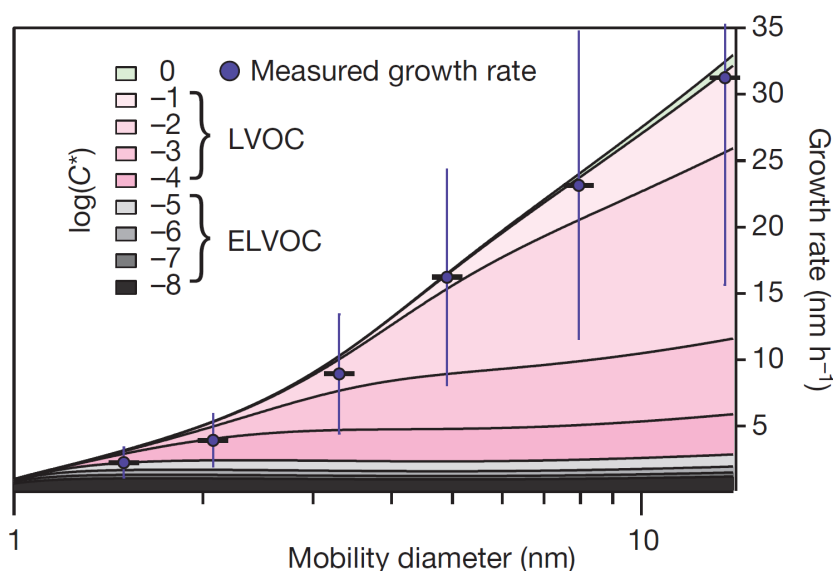


Figure 2.15: Growth rates as a function of diameter. Calculated volatilities ($\log(C^*)$) of the measured HOMs show that with increasing size, more and more substances contribute to particle growth.

Following up on project 5 (Kirkby et al. (2016)), the next step from freshly nucleated particles to CCN is growth in the small size range. Atmospheric observations show that the growth accelerates significantly between 1 – 10 nm (Kulmala et al. (2013), Kuang et al. (2012)), but it can not be explained by sulfuric acid alone. Also, in this size range, the losses due to coagulation with larger particles are highest, so that a high growth rate is necessary to get a significant fraction of particles to reach CCN size (Lehtinen et al. (2007)). The question arises in how far organic substances are able to grow new particles

and at which sizes which kind of substances can condense and thus drive the growth. We used the same experiments as in project 5, with products from alpha-pinene ozonolysis as biogenic organic substances. The SIMPOL model (Pankow and Asher (2008)) was used to estimate the volatility of the substances from their atomic composition and assumed structure.

We found that the biogenic vapors are indeed able to grow the particles significantly. At low sizes, substances of extremely low volatility (ELVOCs) with saturation concentrations lower than $10^{-4.5} \mu\text{g cm}^{-3}$ condense and as the particles grow, the Kelvin effect allows more and more volatile substances to contribute (LVOCs, $10^{-4.5} - 10^{-0.5} \mu\text{g cm}^{-3}$). Also, in this chemical system, low volatile organic compounds (LVOCs) are more abundant than ELVOCs, as 60% of HOMs are LVOCs whereas only 36% are ELVOCs. The contribution of LVOCs to growth leads to an increase of the growth rate with size. Considering these findings in the global aerosol model GLOMAP (Mann et al. (2010)) leads to a substantial change in CCN concentration. Compared to not considering organics, our parametrization yields up to 50% increase in CCN concentration, depending on the region. Conversely, assuming all organics would contribute to the growth from the start gives 50% higher CCN concentrations than our parametrization. Therefore our new findings have a significant positive impact on the quality of global aerosol modeling.

2.7 Rapid growth of organic aerosol nanoparticles over a wide tropospheric temperature range (Stolzenburg et al. (2018))

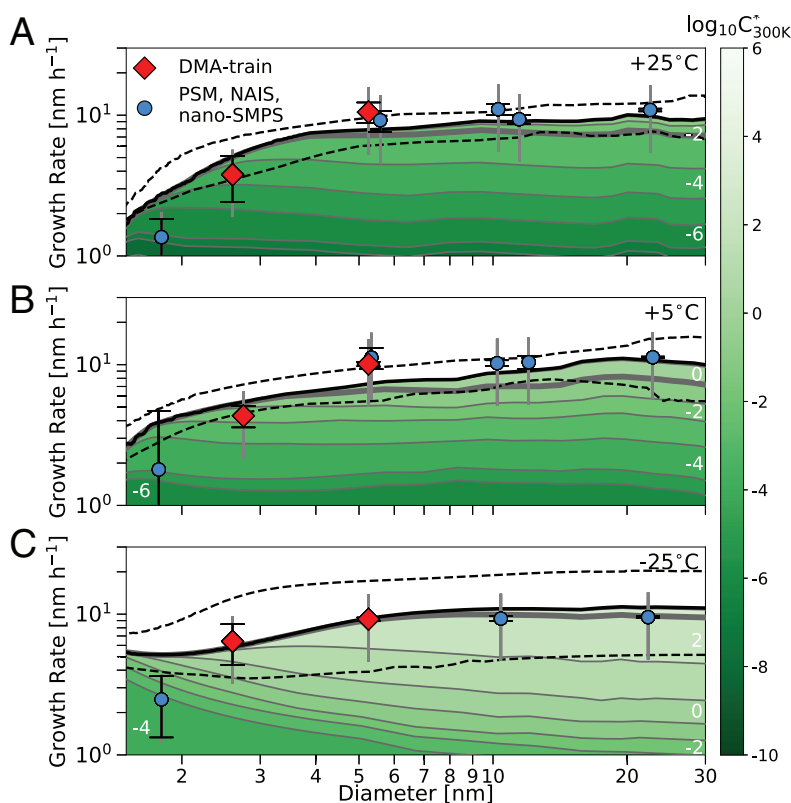


Figure 2.16: Growth rates as a function of diameter for three different temperatures. For this comparison, volatilities $\log(C^*)$ are calculated for a constant temperature so that a given molecule is attributed one volatility. With increasing temperature, the formation of higher oxidized molecules (dark green) is favored. With decreasing temperature, also less oxidized HOMs (light green) are capable to grow the small particles, so that the observed growth rates are almost constant over temperature.

The ability of biogenic organic molecules to grow particles in the low size range was shown in project 6 (Tröstl et al. (2016)). However, these experiments were all conducted at the temperature of +5 °C. In the current project, we studied the temperature dependence of that growth. We assessed the change in

growth rate and which substances contribute to growth over a broad range of tropospheric temperatures ($-25\text{ }^{\circ}\text{C}$, $+5\text{ }^{\circ}\text{C}$ and $+25\text{ }^{\circ}\text{C}$).

We once more conducted experiments of alpha-pinene ozonolysis in the CLOUD chamber, but with an upgraded set of instrumentation and analysis methods compared to projects 5 and 6. An advanced set of size-resolved counting instruments was combined to provide a particle number size distribution from 1.8 to 65 nm. In the range of special interest (1.8 to 8 nm), where the growth rate changes rapidly, a DMA train (Stolzenburg et al. (2017)) performed precision measurements on multiple channels. For the gas-phase measurements of HOMs, we combined a PTR-MS and a negative nitrate CI-APi-TOF to cover a broad range of oxidation states and thus volatilities, as the sensitivity of the PTR is highest for lower oxidation states whereas the negative nitrate chemical ionization is optimized for higher oxidation states. We were thus able to measure biogenic organics with saturation vapor pressures from 10^{-10} to $10^{+4}\text{ }\mu\text{g cm}^{-3}$. Additionally, we were able to analyze the chemical composition of the particle-phase with a negative iodide FIGAERO (Lopez-Hilfiker et al. (2014)).

We found the growth driven by biogenic organics to be very efficient over the whole temperature range. There are two opposing effects: On the one hand, with increasing temperature, the formation of higher oxidized molecules is favored. These higher oxidation states lead to a lower volatility and thus increased ability to condense on smaller particles. On the other hand, with decreasing temperature, the volatility of a given substance decreases, so that also less oxidized molecules are capable to grow the small particles. The combination of these two effects leads to almost constant growth rates over temperature. As in Tröstl et al. (2016), we also found the growth rate to increase steeply in the size range from 1 to 10 nm. The measured growth rates could be reproduced by a model. This project completes what we started in project 5 (Kirkby et al. (2016)) and project 6 (Tröstl et al. (2016)), as it explains the accelerated growth of particles from 1 to 10 nm despite the coagulation sink, and enables global models to parametrize the growth of freshly nucleated particles by biogenic vapors over a wide temperature range.

2.8 Molecular understanding of the suppression of new-particle formation by isoprene (Heinritzi et al. (2018))

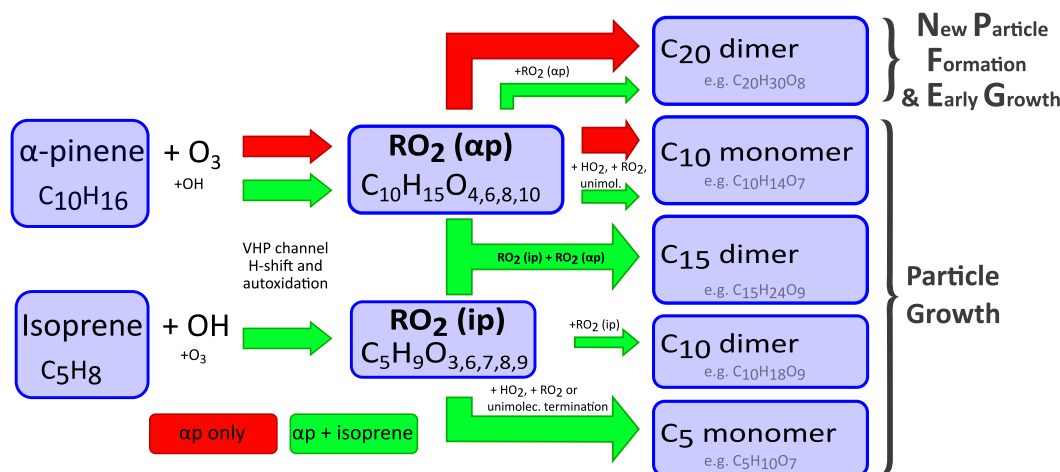


Figure 2.17: Proposed mechanism for the interference of isoprene in alpha-pinene oxidation chemistry. The peroxy-radicals (RO₂) of both isoprene and alpha-pinene compete for reaction partners. Thus, in the presence of isoprene, smaller HOMs are formed, which are too volatile to contribute to the very first steps of nucleation and growth.

After exploring the chemical system of alpha-pinene, we investigated the effect of adding isoprene. Isoprene has the highest global emissions of all biogenic vapors and was observed to suppress new particle formation, yet the mechanism behind that remained unclear. We used the CLOUD chamber to perform new particle formation experiments with alpha-pinene and ozone with and without isoprene. Two different temperatures in the atmospherically relevant range were used (+5 °C and +25 °C). We detected the HOMs with our negative nitrate CI-APi-TOF. A set of size-resolved counting instruments, including PSMs and the DMA-train (see also project 7) were used to determine the nucleation and growth rates.

We found the mechanism how isoprene suppresses new particle formation from alpha-pinene to be in the competition of oxidation products: Both alpha-pinene (a C₁₀ molecule), and isoprene (a C₅ molecule), form peroxy-radicals (RO₂), that then terminate to HOMs. For alpha-pinene alone, C₁₀ monomers

and C₂₀ dimers are formed. When isoprene is added, it forms its C₅ monomers and C₁₀ dimers. But additionally, the isoprene-related peroxy-radicals react with the alpha-pinene related peroxy-radicals to C₁₅ HOMs. This additional termination channel reduces the availability of alpha-pinene related peroxy-radicals for the formation of C₂₀. There is thus a competition that reduces the amount of C₂₀ produced. In the HOM spectrum, we observed that the addition of isoprene leads to the appearance of C₁₅ molecules and reduction of C₂₀ molecules.

At the same time, we observed the nucleation and early growth below ≈ 3.2 nm to decrease significantly in the presence of isoprene. We thus find that it is the C₂₀ HOMs that are needed for the first steps of nucleation and growth. The C₁₅ HOMs, as the C₁₀ and C₅, do contribute to growth from 3.2 nm, but not to the initial nucleation. This confirms their higher vapor pressure compared to the C₂₀.

The presence of isoprene leads to a reduction of formation and growth rate both at 5 °C and +25 °C. At warmer temperature of +25 °C, the growth rate reduction is more pronounced, as the vapor pressure increases with temperature, thus the absolute value of growth rates are lower, the particles remain longer in the crucial size range and thus the process is more prone to losses. Additionally, we found a dependance on UV light. The peroxy-radicals from alpha-pinene and isoprene are formed both by ozonolysis and by OH radicals. While ozonolysis is the predominant channel for peroxy-radical formation from alpha-pinene, reaction with OH is favoured for isoprene. UV light supplies more OH, which benefits the formation of isoprene related peroxy-radicals more than the alpha-pinene related. Therefore the competing situation is more favored towards the isoprene products which enhances the suppression effect of isoprene on new particle formation.

3 | Personal Contribution to the Projects

All my projects were to some extent a team effort. This section outlines which role I had in each project and what my personal contribution was.

Project 1 is the development of the TD-DMA. This was my main project. I was the project leader and main developer. I was planning and executing the development and supervised the development team. At different times, the multidisciplinary team consisted of master students, bachelor students, student assistants, electrical engineering technicians and precision mechanics. I designed the instrument and made the technical drawings. I wrote the control software and together with our electronic workshop designed the electronic control unit. Together with my students I assembled the instrument, tested it and performed the characterization measurements. All development was in several iterations. I co-planned an instrument test campaign at the CLOUD chamber. Together with my team I performed measurements at the chamber. I analyzed the data, made the figures and wrote the manuscript.

Project 2 is the characterization of aerosol emitted by a skyscraper blasting. I led this project. I organized the measurement weekend, personnel and instrument set. Together with my team I set up the instruments and took the data. I analyzed the data of the CPC, SMPS, OPC, APS and weather station. The sediment samples were analyzed by an external company and the SEM and EDX analysis by a collaborating institute. I put these measurement in context and combined the data from all instruments to an integral analysis. I interpreted the data and led the discussion with my coauthors. I made all figures and wrote the manuscript. I helped to inform the public about the scientific side of the event by giving interviews to several journalists.

Project 3 was an ambient measurement campaign in a rural central European area. I was responsible for the particle instruments. I set up the sizing and counting instruments and maintained them. After the campaign I planned and supervised the calibration of the nDMA. Together with the team I set up the negative nitrate CI-APi-TOF. I was involved in the discussion of the results and commented on the manuscript.

Project 4 is the characterization of the mass dependent transmission efficiency of a CIMS. It is one of the key areas of expertise of our group to have our instruments well-calibrated. I was involved in the development of the measurement method and of the technical execution. I contributed to the discussion of the data and to writing the manuscript.

Projects 5 and **6** describe for the first time new particle formation from purely biogenic precursors. Project 5 is about the initial nucleation and project 6 about the subsequent growth, and they are based on the same measurements. These big projects only became possible as a highly collaborative effort from several institutes. In a small team I set up, characterized and ran the negative nitrate CI-APi-TOF, which provided the key measurements of sulfuric acid and HOMs for both publications. I contributed to executing the experiments and was involved in the discussion of the data during and after the campaign. I contributed to the quantification of HOM data and commented on the manuscript.

Project 7 is about the temperature dependence of particle growth from biogenic organics. My contribution was mainly on the mass spectrometric side: I prepared the negative nitrate CI-APi-TOF, conducted measurements and discussed the HOM gas-phase data. Furthermore, I deployed the TD-DMA (project 1) to measure the chemical composition of the particle-phase. I analyzed this data, although it was not included in the manuscript in the end it supported and confirmed the understanding of the particle-phase composition. I was closely involved in the discussion on the particle-phase mass spectrometer data. I commented on the manuscript.

Project 8 is about how isoprene suppresses biogenic organic new particle formation. I was in the core planning team (three members in total) of the isoprene experiments in CLOUD10 and executed them. These measurements

could not be used due to contamination issues but were necessary to achieve good data quality in the following campaigns, which are the database for this project. I set up and maintained the key instrument of this project, the negative nitrate CI-API-TOF, in a small team. I conveyed the analysis of the data and contributed to the discussion and development of the story. I contributed to writing the manuscript.

4 | Publications

- 4.1 Size-resolved online chemical analysis of nanoaerosol particles: a thermal desorption differential mobility analyzer coupled to a chemical ionization time-of-flight mass spectrometer
(Wagner et al. (2018))

Atmos. Meas. Tech., 11, 5489–5506, 2018
https://doi.org/10.5194/amt-11-5489-2018
© Author(s) 2018. This work is distributed under
the Creative Commons Attribution 4.0 License.



Atmospheric
Measurement
Techniques
Open Access
EGU

Size-resolved online chemical analysis of nanoaerosol particles: a thermal desorption differential mobility analyzer coupled to a chemical ionization time-of-flight mass spectrometer

Andrea C. Wagner¹, Anton Bergen¹, Sophia Brilke^{1,2}, Claudia Fuchs^{1,3}, Markus Ernst¹, Jesica Hoker¹, Martin Heinritzi¹, Mario Simon¹, Bertram Bühner¹, Joachim Curtius¹, and Andreas Kürten¹

¹Institute for Atmospheric and Environmental Sciences, Goethe University Frankfurt, Frankfurt, 60438, Germany

²Aerosol Physics and Environmental Physics, University of Vienna, Vienna, 1090, Austria

³Laboratory of Atmospheric Chemistry, Paul Scherrer Institute, Villigen, 5232, Switzerland

Correspondence: Andrea C. Wagner (acwagner@iau.uni-frankfurt.de)

Received: 13 April 2018 – Discussion started: 28 May 2018

Revised: 30 August 2018 – Accepted: 3 September 2018 – Published: 8 October 2018

Abstract. A new method for size-resolved chemical analysis of nucleation mode aerosol particles (size range from ~ 10 to ~ 30 nm) is presented. The Thermal Desorption Differential Mobility Analyzer (TD-DMA) uses an online, discontinuous principle. The particles are charged, a specific size is selected by differential mobility analysis and they are collected on a filament by electrostatic precipitation. Subsequently, the sampled mass is evaporated in a clean carrier gas and analyzed by a chemical ionization mass spectrometer. Gas-phase measurements are performed with the same mass spectrometer during the sampling of particles. The characterization shows reproducible results, with a particle size resolution of 1.19 and the transmission efficiency for 15 nm particles being slightly above 50 %. The signal from the evaporation of a test substance can be detected starting from 0.01 ng and shows a linear response in the mass spectrometer. Instrument operation in the range of pg m^{-3} is demonstrated by an example measurement of 15 nm particles produced by nucleation from dimethylamine, sulfuric acid and water.

1 Introduction

Aerosol particles play an important role in the earth's climate. They influence the radiative budget directly by scattering and absorbing solar radiation, and indirectly by changing cloud properties such as albedo and lifetime. In climate models, these interactions are still the largest source

of uncertainty (Core Writing Team et al., 2007; Fuzzi et al., 2015). Aerosol particles also affect air quality and human health. Depending on their size and shape, they can protrude deep into the lungs (Kreyling et al., 2006) and even enter the bloodstream (Nel, 2005), causing problems such as ischemic stroke (Wellenius et al., 2012), premature mortality (Lelieveld et al., 2015) and many others (e.g., Pope and Dockery, 2006; Donaldson and Borm, 2006).

A large fraction of atmospheric aerosol particles originates from new particle formation (Merikanto et al., 2009; Dunne et al., 2016). Several major formation mechanisms have already been subject of intense research (Hallquist et al., 2009; Zhang et al., 2012; Kulmala et al., 2014; Kirkby et al., 2016), yet various reaction pathways and processes remain unknown. The newly formed particles need to grow to a certain size (~ 50 – 100 nm) to act as cloud condensation nuclei (e.g., Hallquist et al., 2009; Riccobono et al., 2012; Vehkamäki and Riipinen, 2012; Tröstl et al., 2016; Lehtipalo et al., 2016). In order to better understand the nucleation and subsequent growth to cloud condensation nuclei (CCN), the condensing vapors, the freshly nucleated small particles, as well as the larger particles need to be chemically speciated and quantified.

For the analysis of atmospherically relevant nucleation precursors, chemical ionization mass spectrometry is quite commonly used. Depending on the target analyte, the primary ion is chosen. Prominent examples include the proton transfer reaction technique using hydronium ions (Hansel et al., 1995; Graus et al., 2010; Breitenlechner et al., 2017),

successfully targeting volatile organic compounds or negatively charged nitrate ions for the detection of sulfuric acid (Eisele and Tanner, 1993; Kürten et al., 2011; Jokinen et al., 2012), the class of extremely low volatile organic compounds (ELVOCs) (Ehn et al., 2014) and clusters of sulfuric acid and dimethylamine (Kürten et al., 2014).

Particles that have already grown to larger sizes are frequently analyzed by the well-established technologies of the aerosol mass spectrometer (AMS) (Jayne et al., 2000; Zhang et al., 2011) and single particle mass spectrometry (Noble and Prather, 2000; Bzdek et al., 2012). The chemical composition of particles, however, changes with size, and obtaining detailed chemical information about smaller particles is very challenging as they have an extremely low mass.

To close the gap between the measurement of gas-phase and larger particles, a number of interesting techniques have emerged in the past few years. Only a few instruments are capable of analyzing sub-30 nm particles. They can be distinguished based on the following main criteria (see Table 1): (1) a discontinuous principle to enrich the analyte vs. continuous measurements, (2) size-resolved methods vs. integral sampling methods, (3) particle evaporation method, e.g., by thermal desorption or laser evaporation, and (4) ability to analyze gas and particle phase vs. only particle phase.

The nanoaerosol mass spectrometer (NAMS) (Wang et al., 2006) is a single particle mass spectrometer for small particles and uses a continuous principle. It consists of an aerodynamic lens, ion guide and quadrupole ion trap with laser evaporation. The Volatile Aerosol Component Analyzer (VACA) (Curtius et al., 1998; Arnold et al., 1998; Curtius and Arnold, 2001) is able to continuously measure sulfuric acid in sub-30 nm particles in aircraft plumes, where gas-phase concentrations are much lower than particle-phase concentrations. The thermal desorption chemical ionization mass spectrometer (TDCIMS) (Voisin et al., 2003; Smith et al., 2004; McMurry et al., 2009) is a size-resolved method collecting particles electrostatically and using thermal desorption to measure the particle-phase composition. It has provided important insights to several chemical systems including aerosol from marine environments (Lawler et al., 2014), and has even been able to perform size-resolved measurements for extremely small particle sizes of 8–10 nm (Smith et al., 2010). The aerosol mass spectrometer from Laitinen et al. (2009) precipitates particles on a platinum surface and emits them by laser ablation. It has been used for organic compounds in the size range of 10 to 50 nm (Laitinen et al., 2011). Two other size selective techniques using thermal desorption are the devices by Phares and Collier (2010) and the CaCHUP by Gonser and Held (2013). The Filter Inlet for Gases and AEROSols (FIGAERO) (Lopez-Hilfiker et al., 2014) is a bulk-phase filter sampler using thermal desorption. Although it does not provide size-resolved information, it is able to measure both gas and particle phase and thus to investigate partitioning effects (Lopez-Hilfiker et al., 2015). A new technique for the discontinuous particle-phase analysis

is the Electrostatic Precipitation Electrospray Mass Spectrometer (EP-ESI-MS) from He et al. (2015). Particles are charged and electrostatically collected. Thereafter, the material is brought to the gas phase and softly ionized at the same time by using the collection surface as an electrospray tip. The Droplet Assisted Inlet Ionization (DAII) (Horan et al., 2017) condenses water on particles and rapidly evaporates them in a heated inlet. It is a continuous method and has proven the ability to measure test particles as small as 13 nm. A more detailed discussion is given in Sect. 6.2.

In this study, we present our novel device for the online chemical analysis of nucleation and Aitken mode particles. The Thermal Desorption – Differential Mobility Analyzer (TD-DMA) is capable of measuring in a size-resolved and integral setting. It allows taking gas-phase measurements with the same mass spectrometer. As a mobile interface, it can be combined with different mass spectrometers or other real-time gas-phase analyzers.

Here, the instrument is described (Sect. 2), followed by a detailed characterization (Sect. 3) comprising the DMA unit's transmission efficiency, the particle collection efficiency, the filament temperature and the reproducibility of the evaporation process. The measurement procedure (Sect. 4) is specified, including determination of the background and an exemplary measurement of 15 nm particles. Lastly, the signal is quantified (Sect. 5) and the results are discussed (Sect. 6), closing with a short summary (Sect. 7).

2 Instrument description

The TD-DMA is designed for size-resolved chemical analysis of nanometer sized aerosol particles. The particles are charged, a specific size is selected and they are electrostatically collected on a filament. Subsequently, the sampled mass is evaporated in a clean carrier gas to be analyzed by a detector, e.g., a mass spectrometer. In this way, the particle phase is efficiently separated from the gas phase and the concentration is enhanced to meet the detection limit of the analyzer. The coupling between TD-DMA and detector allows for gas-phase measurements during particle sample collection periods. This enables an existing gas-phase analyzer to measure the particle phase as well without the requirements of cost and space for a second analyzer. Only a small fraction of the gas-phase measurement time is lost when it is interrupted by the short evaporation period for the particles. The chemical composition of gas and particle phase can be compared directly without the need to consider instrumental differences in, e.g., ionization and characteristics of the mass spectrometer, as would be the case when using two separate instruments. This modular concept allows obtaining a broad picture of both particle and gas-phase chemical composition and to observe the condensation, reactive uptake and partitioning of the analyzed substances.

Table 1. Instruments capable of chemical analysis of sub-30 nm particles. For interpretation of the parameters, see the discussion Sect. 6.2, and for references to later work on the individual instruments, see the introduction Sect. 1.

Method	First reference	Size selective	Continuous or discontinuous	Evaporation method	Phase(s) measured	Minimum mass concentration analyte aerosol [pg m^{-3}]	Minimum detectable mass [pg]	Smallest detected particle size
VACA	Curtius et al. (1998)	no	continuous	thermal desorption	gas & particle ^a	$\sim 3.3 \times 10^5 \text{ pg m}^{-3}$ sulfuric acid	n/a	n/a
TDCIMS	Voisin et al. (2003)	yes	discontinuous	thermal desorption	particle	n/a	e.g., 1–5 pg ammonium sulfate	8–10 nm
NAMS	Wang et al. (2006)	yes	continuous	laser ablation	particle	n/a	n/a	~ 7 –10 nm
Aerosol MS	Laitinen et al. (2009)	yes	discontinuous	laser ablation	particle	n/a	n/a	10 nm
Aerosol inlet	Phares and Collier (2010)	yes	discontinuous	thermal desorption	particle	n/a	n/a	n/a
CACHUP	Gonser and Held (2013)	yes	discontinuous	thermal desorption	particle	n/a	0.5 – 5×10^3 pg camphene	25 nm
FIGAERO	Lopez-Hilfiker et al. (2014)	no	discontinuous	thermal desorption	gas & particle	e.g., 5 ^b 60 ^c pg m^{-3} $\text{C}_{10}\text{H}_{14}\text{O}_8$ 1690 ^b 900 ^c pg m^{-3} $\text{C}_9\text{H}_{14}\text{O}_4$	e.g., 1 ^b 40 ^c pg $\text{C}_{10}\text{H}_{14}\text{O}_8$ 170 ^b 630 ^c pg $\text{C}_9\text{H}_{14}\text{O}_4$	n/a
EP-ESI-MS	He et al. (2015)	no	discontinuous	electrospray	particle	10^5 pg m^{-3}	$\sim 2 \times 10^3$ pg cesium iodide $\sim 2 \times 10^4$ pg levoglucosan	n/a
DAII	Horan et al. (2017)	no	continuous	heating	particle	10^5 pg m^{-3} polypropylene glycol	n/a	13 nm
TD-DMA	this work	yes	discontinuous	thermal desorption	gas & particle	27 pg m^{-3} for all sizes 811 pg m^{-3} for 15 nm sulfuric acid	10 pg sulfuric acid	15 nm

^a Not separated, ^b chamber study, ^c ambient study; n/a: not applicable or not specified.

The TD-DMA is a stand-alone instrument that can be attached to any existing technique suitable for real-time chemical analysis of gas-phase compounds. In this case, individual compounds relevant for nucleation and early growth of atmospheric nanoaerosol particles should be measured. For this we used a chemical ionization atmospheric pressure interface time-of-flight (CI-API-TOF) mass spectrometer with negative nitrate primary ions generated by a corona ion source (Kürten et al., 2011). This technique is specialized for the detection of sulfuric acid, amines and highly oxygenated organic molecules (HOMs) (Kürten et al., 2014; Simon et al., 2016; Kirkby et al., 2016), and calibrated for its internal transmission efficiency (Heinritzi et al., 2016) as well as for its detection efficiency regarding the sulfuric acid concentration (Kürten et al., 2012). For the gas-phase measurement, the removal of aerosol particles by, e.g., a filter is not required. As the inlet line and ion source are at the same temperature as the analyte aerosol, and the gas composition surrounding the particles is unchanged, the particles do not evaporate significantly on their way to the mass spectrom-

eter and thus are not detected during gas-phase measurements. On the contrary, applying a particle filter would influence the gas-phase measurement negatively as a significant fraction of the gas-phase analyte, especially sulfuric acid or highly oxygenated organics of low volatility, would adsorb on the filter.

2.1 Setup and measurement procedure

Before a more detailed technical description of the TD-DMA is given (Sect. 2.2), an overview of the measurement procedure shall be provided. The measurement procedure is discontinuous and is performed in two steps as follows: the first step is the collection of particles (see Fig. 1a). The analyte aerosol passes through a charger, where a charge equilibrium is established. A core sampling system, where the analyte is isokinetically sampled from the center of a larger tube, is used to reduce losses in the inlet line (e.g., Wimmer et al., 2015). The aerosol then enters the DMA unit of the TD-DMA. The gas phase of the analyte aerosol is removed by

5492

A. C. Wagner et al.: Size-resolved online chemical analysis of nanoaerosol particles

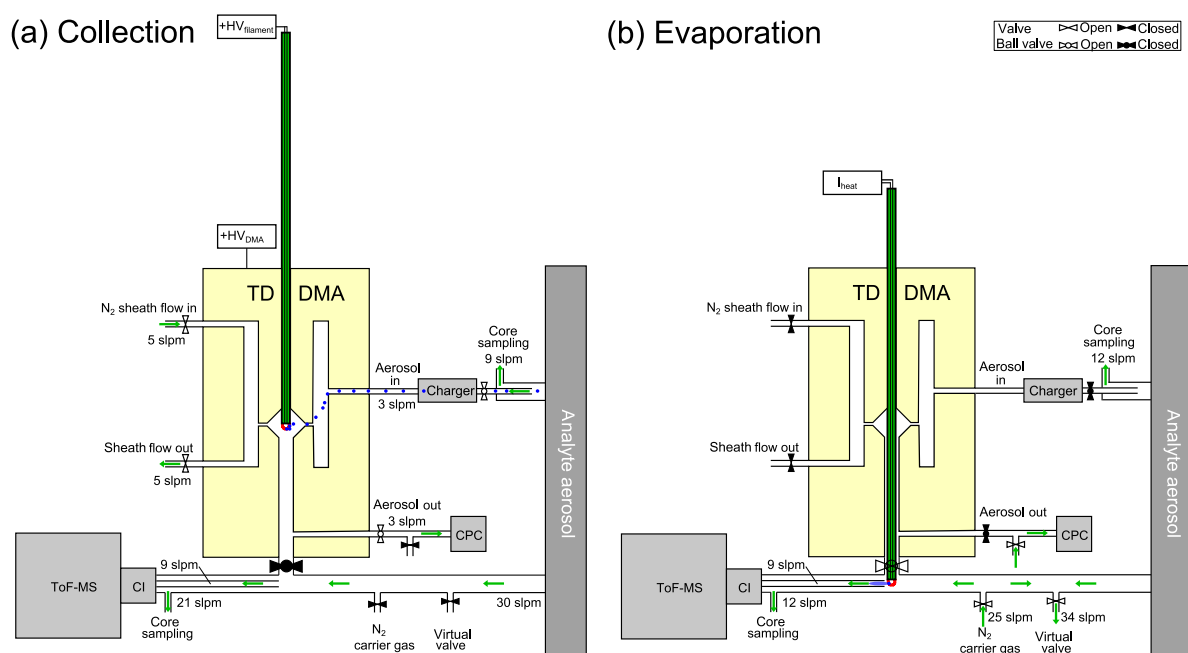


Figure 1. Measurement setup of the TD-DMA with step (a) collection, and (b) evaporation. Filled valves correspond to closed, unfilled ones to open. In step (a), particles (blue) from the aerosol sample are charged, size selected and collected on a filament (red) inside the DMA unit (yellow). In step (b), the filament is moved in front of a mass spectrometer and the collected material is evaporated and analyzed.

the pure nitrogen sheath gas, which is controlled in a non-recirculating way. Charged particles are attracted towards the central electrode and a well-defined size enters the selection slit. A platinum filament is placed inside the central electrode. It is only exposed to pure nitrogen from the sheath gas and samples the preselected particles by electrostatic precipitation. The position of the filament inside the central electrode implements the collection of particles directly after classification and thereby minimizes losses. While the sampling takes place, the mass spectrometer is used to measure the gas-phase chemical composition of the analyte aerosol through a separate sampling line. It is also possible to collect the whole size distribution by turning off the DMA's sheath flow (see also Sects. 4 and 6).

Once enough particle mass is collected on the filament, the second step begins (see Fig. 1b). The inlet line of the mass spectrometer is flushed with ultrapure nitrogen. Another outlet in the inlet line works as a virtual valve that flushes out the excess nitrogen added to the sampling line while maintaining a flow of air into the sampling line. This prevents contamination of the reservoir where the sample gas is taken from and also keeps the sample gas flow rate constant, which is important for chamber or flow tube experiments. The filament is then moved into the mass spectrometer's inlet line. An electrical current is sent through the filament, which is thereby

heated. The sampled particles evaporate and the vapor is analyzed by the mass spectrometer.

2.2 Instrument details

The main part of the TD-DMA system is the in-house developed DMA unit, where the particle size selection and collection takes place. The charger is a soft X-ray diffusion charger (TSI 3088; Tigges et al., 2015). A linear feedthrough (MDC vacuum, 152.4 mm maximum travel distance) and a stepper motor are used to translate a ceramic rod with the collection filament from its collection position to its evaporation position and back. An in-house built electronic control unit allows the precise control of all parameters, i.e., flow rates, valve positions, high voltages and the heating current for the filament. In the collection mode, the unit supplies the DMA central electrode and filament with the required positive high voltages via safe high-voltage (SHV) connectors and cables. In the evaporation mode, the filament is operated with a defined heating current that can be ramped as a function of time to increase the evaporation temperature stepwise (up to about 600 °C). The mass flow controllers and magnetic valves enable software controlled adjustment of the flows for the aerosol, sheath gas, carrier gas and virtual valve. Further magnetic valves are used to completely shut-off or redirect flows when necessary, e.g., during the evaporation. Two automated ball valves (Grotec OSE-M) allow for separation of

the TD-DMA from the gas-phase measurement during sampling mode as well as closing the aerosol inlet during evaporation mode (Fig. 1). The stepper motor moving the linear feedthrough and filament is also controlled by the electronic unit. PC control of the electronics is realized by means of USB data acquisition boards (Meilhaus 1608 and 3103) and a LabVIEW software program.

The DMA unit (see Fig. 2) is designed to collect a maximum amount of particulate mass for a defined diameter. Its characteristics are determined by the dimensions as well as the sheath and aerosol flow rates. The amount of collected particles is maximized when the transmission efficiency is high. Also, increasing the aerosol flow rate leads to an increase in collected mass for constant transmission efficiency. Therefore, we chose the maximum possible aerosol flow rate for the dimensions of the DMA unit, 3 standard liters per minute (slpm). As the overall number of selected particles is higher when the size resolution of the DMA is low, a low size resolution and thus low sheath flow rate is beneficial in this case. However, the size resolution still needs to be high enough to warrant size selection and at values of the sheath flow rate that are too low, the DMA will not work anymore. With a sheath flow of 5 slpm, as much particle mass as possible is collected while still allowing sufficient size selection. The DMA has a cylindrical geometry (Reischl et al., 1997; Chen et al., 1998) with a positive high voltage on the central electrode (1) and ground potential on the outer electrode. The DMA's inner radius is 15 mm, the outer radius is 20 mm and the classification length is 15 mm. The collection of particles on the filament takes place inside the central electrode (2). In this way, losses are minimized as the transfer lines are very short and the particles do not need to overcome an additional voltage step (from high voltage to ground potential) because they do not need to leave the DMA (Franchin et al., 2016). In order to position the filament, the central electrode has a through-hole in its center (3, 4) through which a ceramic rod is inserted. The rod carries two thick copper wires with a short piece of platinum wire spot-welded to both of their ends. The electrical resistance of the thin platinum wire is high compared to that of the remaining system. Thus, when a current is applied, a voltage drop occurs mainly across the filament. The deposited energy leads to heating and desorption of the particle material. Electronic relays suitable for high-voltage operation are used to disconnect the wires from the current source during collection mode; in this mode a third relay is used to apply a positive high voltage to the wires for electrostatic particle collection. While the opening in the first part (3, towards the linear feedthrough) of the central electrode is just large enough to center the ceramic rod while allowing for its axial movement, the through-hole in the second part (4, towards the DMA exit) is larger to allow moving the filament smoothly towards the sampling line of the mass spectrometer. The outlet is closed by a ball valve during collection mode and is only opened when the filament is positioned in the CI-APi-TOF sampling line. In this mode,

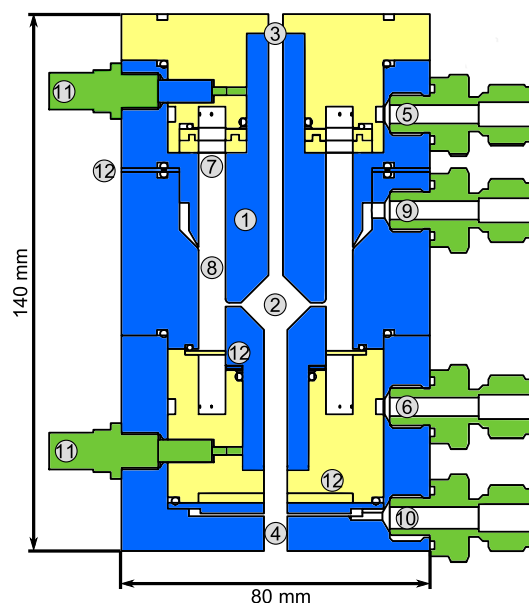


Figure 2. Schematic quarter section of the DMA unit of the TD-DMA with (1) central electrode, (2) collection area, (3) inlet for the filament, (4) outlet for the filament, (5) sheath flow inlet, (6) sheath flow outlet, (7) tissue for laminarizing the sheath flow, (8) selection area, (9) aerosol inlet, (10) aerosol outlet, (11) SHV supplies and (12) spacer plates. Conductive stainless steel parts are shown in blue, isolating PEEK parts in yellow.

all other valves connected to the DMA are closed to avoid gas leaking from the DMA into the sampling line or vice versa. The shape of the collection area (2) is an attempt to keep potential disturbances in the air flow small, while maximizing the distance between the filament and electrode to avoid flashovers and leakage currents due to the electric field. However, leakage currents could not be fully avoided (see Sect. 3.2).

The DMA sheath flow is distributed in azimuthal direction by introducing a pressure drop at the inlet (5) and outlet (6) using a circular cavity and a total of 16 small drilled holes. To achieve a laminar sheath flow, which is crucial for accurate size selection, an evenly webbed tissue (7) is placed 20 mm upstream of the selection area (8). The aerosol flow is introduced into the selection area through a narrow slit (9) with a design as recommended by Chen et al. (1998). The aerosol outlet (10) has to be at the side and cannot be on the central axis as this is used for moving the filament to its evaporation position. In order to achieve an evenly distributed sample and outlet flow over the whole cross section of the inner part of the central electrode, a small slit introducing a pressure drop and two outlet connectors (separated by 180°) are used. The losses in this slit do not matter as the particles are sampled upstream. However, the characterization of

the DMA unit (see Sect. 3.1) is performed at the side outlets to ensure the flow conditions are the same as for the actual measurements. Therefore, note that the actual transmission efficiencies at the filament position (i.e., the fraction of particles that reach the filament) are likely higher than determined by the characterization measurements.

A positive high voltage is applied to the central electrode by two SHV connectors (11) as this electrode is split into two parts. Small spacers (12) allow changing the width of the aerosol inlet, the selection slit and the outlet, respectively. These spacers proved to be helpful for finding suitable distances for an appropriate transmission efficiency, resolution and sizing accuracy when first testing the DMA design. The material of the DMA is stainless steel for the conductive parts (blue) and PEEK (polyether ether ketone) for the insulating parts (yellow), as these materials are considered to be chemically inert to the substances present in the aerosol sample. The full instrument (Fig. 10) measures $12\text{ cm} \times 12\text{ cm} \times 95\text{ cm}$ and weighs 13 kg.

3 Characterization

In this section, the general performance of the TD-DMA is described based on characterization experiments in the laboratory. These measurements are used to derive the sizing accuracy, the DMA's resolution as well as its transmission and collection efficiency. Furthermore, application of defined amounts of sulfuric acid on the filament yields information on the detection limit of the TD-DMA in combination with the CI-API-TOF and on the linearity between signal and collected mass.

3.1 DMA unit

The DMA unit is characterized in a tandem DMA setup (Fig. 3). Ammonium nitrate particles are produced in a nebulizer followed by a diffusion dryer. The particles are brought into charge equilibrium by using a soft X-ray charger (TSI model 3088, Tigges et al., 2015). A first DMA (Grimm Aerosol Technik GmbH model 55-100, Jiang et al., 2011) then selects particles of a defined electrical mobility and thus corresponding size (if all particles are singly charged, which is a valid assumption for sub-30 nm particles). This quasi-monodisperse aerosol flow is subsequently split into two flows. One flow enters the TD-DMA, after which a CPC (TSI model 3776, Hermann et al., 2007) measures the number concentration N_1 , while the filament is removed. The other flow is directly led into a CPC which serves as a reference and measures the concentration N_2 . This method is based on having identical counting efficiencies for both CPCs. Therefore, the CPCs are characterized against each other for each diameter using the same setup but without the TD-DMA, and a corresponding correction factor is applied. The ratio of the two measured concentrations yields the TD-DMA's transmis-

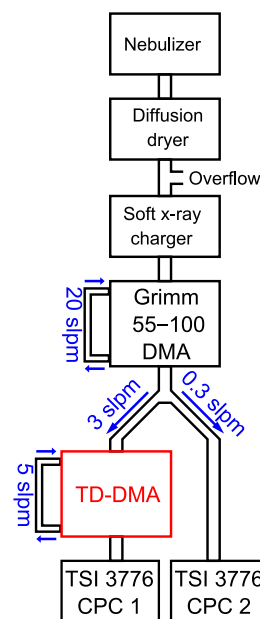


Figure 3. Tandem DMA setup for the characterization of the TD-DMA's DMA unit.

sion efficiency τ :

$$\tau(d_p) = \frac{N_1}{N_2}. \quad (1)$$

Note that the aerosol coming from the first DMA is not strictly monodisperse; instead the DMA provides a Gaussian-shaped size distribution. As in this case, the resolution of the first DMA is much higher than that of the second DMA, Eq. (1) introduces only a small error; using the methods by Stolzenburg and McMurry (2008) this can be demonstrated for the relevant sizes of the TD-DMA. At a fixed diameter selected for the first DMA, the TD-DMA voltage is varied. This method is repeated for six particle diameters d_p , ranging from 7.5 to 30 nm. These measurements yield the transmission efficiency curves (Fig. 4). The error bars for the transmission efficiency are calculated using the statistical error of all individual measurements of the CPCs as well as assuming systematic errors of 10 % as suggested by the manufacturer (TSI Incorporated, 2007). The errors of the voltage set by the TD-DMA control box originate from the high voltage module and are assumed to be 5 %. As the selection slit of the TD-DMA has a non-infinitesimal width, the resulting distribution is not singular but triangular to a first approximation. Particle diffusion distorts it further and results in a Gaussian shaped curve (Stolzenburg and McMurry, 2008). The experimental data points are fit by the Gaussian function

$$\tau(U) = \tau_{\max} \cdot \exp\left(-\left(\frac{U - U_{\text{center}}}{\text{HWHM}}\right)^2\right), \quad (2)$$

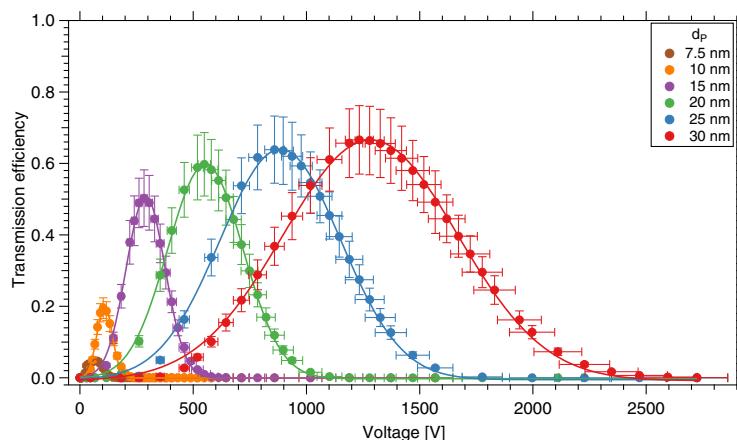


Figure 4. Transmission efficiency of the TD-DMA for different diameters. The DMA unit is characterized in a tandem DMA setup.

where τ_{\max} is the maximum transmission efficiency for each diameter, HWHM is the half width at the half maximum of the curve, and U_{center} is the voltage applied to the central electrode to select the given particle size. In Fig. 5a, the fitted voltage values from the measurement are displayed as a function of the mobility diameter. The theoretical curve is calculated from the dimensions of the DMA according to Stolzenburg and McMurry (2008) and Wang and Flagan (1990). The curve fits best when corrected by a factor of 0.81. The reason for this is unclear, but the factor is constant for all measurements. The maximum transmission efficiency τ_{\max} for each diameter is shown in Fig. 5b. For 15 nm particles, it is slightly above 50%. These values are used to estimate the collected mass when sampling.

The resolution R is defined as the ratio of the electrical mobility Z to the width of the transmission curve at half maximum with respect to electrical mobility (Zhang and Flagan, 1996; Flagan, 2008):

$$R = \frac{Z}{2 \cdot \text{HWHM}_Z}. \quad (3)$$

Deriving the electrical mobility from the diameter (Stolzenburg and McMurry, 2008; Hinds, 1999),

$$Z(d_p) = \frac{q \cdot C_C(d_p)}{3\pi\eta \cdot d_p}, \quad (4)$$

the abscissa can be transformed into mobility values, using q the particle charge (for singly charged particles, q equals one elementary charge), C_C the Cunningham slip correction factor and η the viscosity of the fluid. The resolution can then be derived using the fitted HWHM of the Gaussian curves. The resolution vs. the diameter is displayed in Fig. 5, lower panel, which shows a maximum value of 1.19.

With a resolution of 1.19 and a transmission efficiency above 50% at 15 nm particle size, the performance of

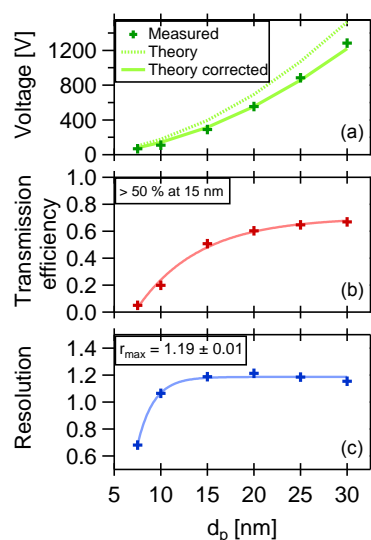


Figure 5. Summary of DMA performance parameters. The DMA is optimized for a coarse resolution and high transmission in order to collect a maximum amount of particle mass while still allowing size selection.

the TD-DMA is suitable for atmospheric field studies and aerosol chamber investigations.

5496

A. C. Wagner et al.: Size-resolved online chemical analysis of nanoaerosol particles

3.2 Collection efficiency

The same tandem DMA setup as in Sect. 3.1 is also used to characterize the collection efficiency of the filament as a function of the particle diameter. For these measurements, the first DMA and the TD-DMA are set to select the same particle size. The filament voltage is increased to the maximum possible value without influencing the voltage on the central electrode, which is also monitored continuously. Unfortunately, it is technically not possible to set the filament voltage high enough to collect 100 % of the particles for all tested particle sizes. The reason for this is most likely a leak current along the surface of the ceramic rod and thus a transfer of charge from filament to central electrode. Therefore, the filament voltage is set as high as possible with some margin to avoid an influence on the DMA high voltage.

The ratio of the two measured concentrations corrected with the DMA transmission efficiency equals the fraction of particles that are not collected on the filament. The collection efficiency is thus defined as

$$\eta(d_p) = 1 - \frac{N_1}{N_2} \cdot \frac{1}{\tau(d_p)}, \quad (5)$$

with $\tau(d_p)$ being the transmission efficiency from Sect. 3.1. The results are displayed in Fig. 6. The efficiency at which the selected particles are collected on the filament decreases with increasing size. As the flow velocity and the distance between electrode and filament remain constant during the sampling, the collection efficiency depends only on the particle electrical mobility for a given potential difference between filament and central electrode. However, the collection efficiency is close to unity for all sizes up to 15 nm and above 50 % for sizes up to 30 nm, which can be regarded as the current upper size limit of the TD-DMA. Therefore, it can be claimed that the collection efficiency is sufficiently high for the size range up to 30 nm, and the results can be corrected with the experimentally determined values (see Sect. 5.1, Eq. 11).

3.3 Filament temperature

In order to evaporate the sample in front of the mass spectrometer, the filament is heated. This is achieved by sending an electric current through the wire. Due to the rather high resistance of the filament, power is released and the filament temperature increases. Also, the platinum changes its resistance (R_{Filament}) due to the heating. This feature can be used to estimate the filament temperature in a similar way as in platinum thermometers such as Pt100. Here, it is not crucial to know the temperature with high precision, nevertheless it can be beneficial to determine it, e.g., in order to gain information about the volatilities of substances in an aerosol sample.

The control unit of the TD-DMA monitors the voltage U and current I across the filament. However, the circuit in the

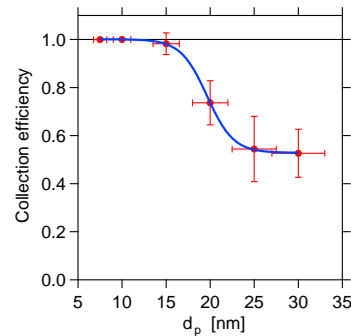


Figure 6. Collection efficiency depending on the particle size. Due to the decreased electrical mobility, the required collection voltage increases with particle size, which currently limits the collection efficiency at larger sizes.

electronic control unit as well as the wires connecting the filament also add to the total resistance:

$$\frac{U}{I} = R_{\text{Filament}}(T) + R_{\text{System}}. \quad (6)$$

The filament resistance at room temperature (20 °C) is 0.4 Ω . Using this number together with the temperature dependent resistance of platinum,

$$R_{\text{Filament}}(T) = R(0^\circ\text{C}) \cdot (1 + aT + bT^2), \quad (7)$$

with $a = 3.9083 \times 10^{-3} \Omega \text{K}^{-1}$ and $b = -5.775 \times 10^{-7} \Omega \text{K}^{-2}$ (International Electrotechnical Commission, 2008), $R(0^\circ\text{C})$ can be derived. Then, by applying very small currents that hardly warm the filament and measuring the magnetic field resulting thereof with a current clamp, one can estimate the resistance of the system as $R_{\text{system}} = (0.1 \pm 0.1) \Omega$. With this information we can derive the temperature T during all times of the evaporation process by using the feedback voltage U and current I :

$$T(U, I) = \quad (8)$$

$$-\frac{a}{2b} - \sqrt{\left(\frac{a}{2b}\right)^2 - \frac{1}{b} - \frac{R_{\text{system}}}{b \cdot R(0^\circ\text{C})} + \frac{U}{I \cdot R(0^\circ\text{C}) \cdot b}}.$$

During standard operation, the filament is heated up to 350 °C for evaporating the sample and up to 600 °C for cleaning.

3.4 Sample mass calibration and reproducibility

Sample mass calibration tests relate evaporated mass to mass spectrometer response. This method is used to test the evaporation method regarding its reproducibility and is required for the signal quantification (see Sect. 5.2) and determination of the detection limit. When installing the TD-DMA at the

mass spectrometer, e.g., after transport, they are also used to find the optimum filament position in front of the mass spectrometers ion source.

For the sample mass calibration experiments, a defined amount of a test substance is deposited on the filament and evaporated in front of the mass spectrometer. In this case, a solution of sulfuric acid (H_2SO_4) in water is used. After reaction with the nitrate primary ions, this substance produces different ion signals (peaks) with the main contribution coming from clusters of sulfuric acid with the primary ion monomer ($\text{H}_2\text{SO}_4\text{NO}_3^-$) and bisulfate ions (HSO_4^-). Sulfuric acid dimers ($\text{H}_2\text{SO}_4\text{HSO}_4^-$) as well as clusters of sulfuric acid with the primary ion dimer ($\text{H}_2\text{SO}_4\text{HNO}_3\text{NO}_3^-$) are also detected, but with a much lower intensity than the former, so that clusters with the primary ion trimer and higher are negligible.

However, for measuring internally or externally mixed particles, it should be noted that these consist of more than one substance; therefore, the signals are spread over many m/z peaks, which will require more total particle mass to overcome the detection limit. In addition, the ionization efficiency of a compound will affect its detection limit in the same way as in gas-phase measurements.

Figure 7a shows the typical shape of the signals resulting from the desorption process. It shows a sharp increase when a certain temperature is reached followed by an exponential decay reaching background levels within less than 30 s. This indicates that the substance desorbs from the filament within a narrow temperature range and that the temperature distribution of the filament is fairly homogeneous, otherwise the signal would be smeared out more strongly.

For signal analysis, the full spectrum is corrected with the relative transmission efficiency (Heinritzi et al., 2016), which takes into account that the detection efficiency inside the mass spectrometer is a function of ion mass. The individual signals S_j are then normalized by the primary ions' count rates, in this case NO_3^- (m/z 62), $(\text{HNO}_3)\text{NO}_3^-$ (m/z 125) and $(\text{HNO}_3)_2\text{NO}_3^-$ (m/z 188). Subsequently, the signal is integrated over the evaporation time in order to obtain the total signal resulting of a substance i from the evaporation. Finally, the signals of all relevant peaks j are summed up.

$$\tilde{S}_i = \sum_{\substack{\text{contributing} \\ \text{peaks } j}} \int_{t=t_{\text{start}}}^{t=t_{\text{end}}} S_j(t) \ln \left(1 + \frac{S_j(t)}{S_{\text{NO}_3^-}(t) + S_{\text{HNO}_3\text{NO}_3^-}(t) + S_{\text{(HNO}_3)_2\text{NO}_3^-}(t)} \right) dt \quad (9)$$

These time integrated signals are displayed in Fig. 7b and c. All data points are corrected with blank measurements obtained by evaporating only the solvent (water), without the test substance. Reproducible results are obtained for a sample mass as small as 0.01 ng. Additionally, the filament is

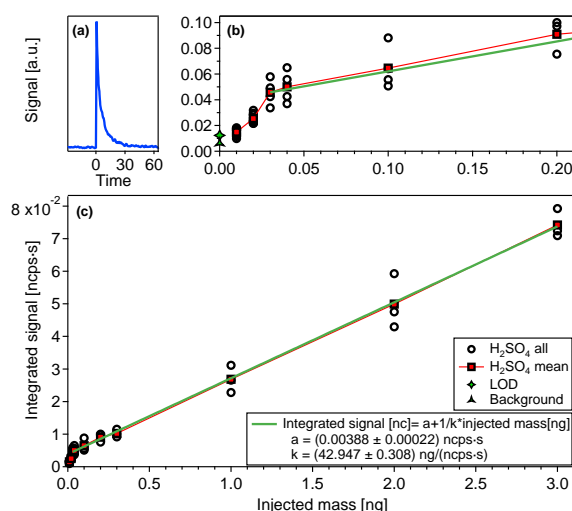


Figure 7. Sample mass calibration with (a) typical desorption shape of signals, (c) integrated signal vs. injected mass, and (b) zoom on lower masses with detection limits.

heated without any sample or solvent on it to obtain a zero measurement (see also Sect. 4.1, heating background). This zero measurement plus 3 times its standard deviation defines the lower detection limit. The zero measurement and the measurement points below 0.03 ng, although they show a good reproducibility, are systematically lower than the signals when larger masses are applied, which is not yet understood.

Starting from a deposited mass of 0.03 ng, the data indicates very good linearity, which is an important feature of the TD-DMA combined with a CI-APi-TOF. Furthermore, we can now relate the mass spectrometer signal to a sample mass. For the component used here, the conversion factor k is $42.95 \text{ ng} (\text{ncps s})^{-1}$. For other substances, their individual ionization efficiencies relative to that of the test substance need to be taken into account (relative ionization efficiency RIE_i , see also Sect. 5.2) and a mass spectrometer signal S_i relates to a mass of

$$m_i = k \cdot \text{RIE}_i \cdot \tilde{S}_i. \quad (10)$$

In conclusion, the reproducibility and linearity of the evaporation process can be clearly stated.

4 Measurement procedure

For measuring a nucleation event, the following procedure is desirable: at the beginning of the event, the integral measurement mode is used to analyze the freshly nucleated, smallest particles. When the mode diameter of the particle size distribution reaches around 10 nm, several size-resolved measurements are performed. The sampling time is adjusted so

that enough mass is collected for a given particle size and concentration in the aerosol sample. However, due to the minute mass contained in the nanoparticles, such a procedure is not always possible, especially for short or weak nucleation events. In the future, we thus aim to improve the sensitivity, as suggested in Sect. 6. For now, in case of short nucleation events or those with low concentrations, one can choose one size and sample for the whole event or use the integral mode. In either case, different kinds of background measurements are important and thus the different steps during a full measurement cycle are described in the following.

4.1 Background measurements and signal correction

To verify measurements and to distinguish the signal arising from particles from possible other sources, background measurements need to be taken regularly.

1. *Mass spectrometer background.* To determine this background contribution, the nitrogen carrier gas (the flow applied to the sampling line of the mass spectrometer during the evaporation of particles) is applied to the mass spectrometers sampling line without positioning the filament inside it (Fig. 1a). This measurement accounts for the instrumental backgrounds of the CI-APi-TOF (ion source and detector) and is taken shortly before and after every evaporation. It is also used to correct the gas-phase measurements of the CI-APi-TOF.
2. *Heating background.* The filament is placed at its evaporation position and heated, but without an aerosol sample. As the evaporation takes place in the inlet line that is also used for the gas-phase measurements, the walls contain adsorbed material, which could re-enter into the gas phase due to the heating. The core sampling system, in which the filament is placed (see Fig. 2b), prevents most of the gas flow directly in contact with the walls from entering the ion source of the mass spectrometer. However, the inlet line downstream of the core sampling probe has been in contact with the gas phase. In the chemical settings tested, it has been observed that for filament temperatures lower than 400 °C, the signal from this process is negligible. This is the temperature range where most of the particle-phase sample desorbs. For higher temperatures, the background signals increase. When observing individual ion signals as a function of time during heating, the background contribution from the sampling line walls also shows a different shape compared to the particle-phase signal (Fig. 8). The signals from particles on the filament show distinct spikes with a fast increase and a rapid exponential decay, while the wall background results in slowly rising signals, which do not show a pronounced decay.
3. *Gas-phase adsorption background.* The gas-phase adsorption on the filament is corrected for by placing the

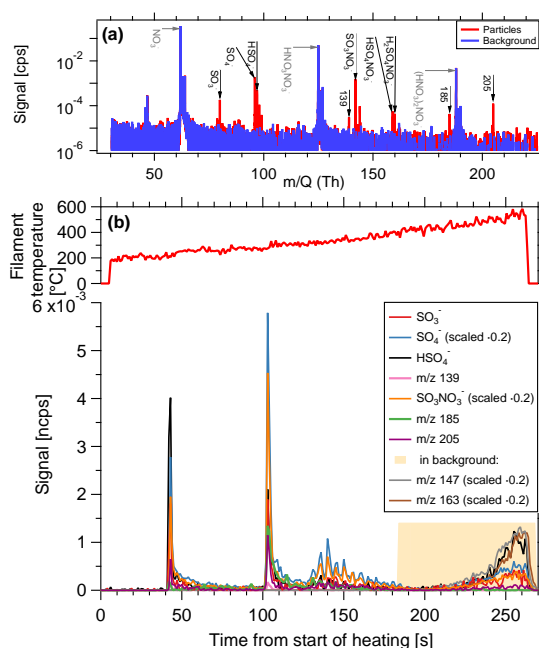


Figure 8. Composition measurement of 15 nm particles generated from dimethylamine, sulfur dioxide and ozone in presence of UV light. (a) Spectrum of particle phase compared to the background. Prominent particle-phase peaks in black, primary ions in grey. (b) Time series of evaporation. As filament temperature increases, substances desorb from the filament and are depleted rapidly. At high temperatures, signals originating from the inlet line appear.

filament in the sampling position inside the TD-DMA and performing the measurement in the same way as regular sampling, the only difference being that the filament is set to the same potential as the central electrode; thus, no particles are sampled. When the nitrogen sheath flow is used, as in the size-resolved measurements, the filament is only exposed to nitrogen and there is hardly any relevant gas-phase adsorption. However, for the integral mode, the sheath flow is turned off and the filament is thus exposed to the gas phase of the aerosol sample. When heating the filament, the signals show the same shape as for the particle measurements, as they are originating from the filament itself. This background measurement is taken for every major change in gas-phase chemistry. For most of our tested systems, this background was comparably low and mostly negligible.

4.2 Example measurement

The instrument was tested during the CLOUD10T campaign at the Cosmics Leaving Outdoor Droplets (CLOUD) chamber at the European Organization for Nuclear Research

(CERN). CLOUD is a 26 m³ stainless steel chamber used for investigating nucleation and growth of aerosol particles under atmospherically relevant and precisely controlled conditions (Kirkby et al., 2011). Figure 8 shows a measurement of size selected 15 nm particles generated from 119 ppt_v of dimethylamine, 4.3 × 10⁶ cm⁻³ sulfuric acid, at a temperature of 4.8 °C and relative humidity of 40.2 %. The total particle number concentration (> 2.5 nm) is approximately 1.7 × 10⁵ cm⁻³ and the TD-DMA collected its analyte particles for a duration of 60 min. While the filament is gradually heated, substances desorb and are subsequently ionized by the negative nitrate primary ions and detected by the mass spectrometer. The example substances shown here desorb at different temperatures. The signal shape for a given ion signal as a function of time is the same as for the sample mass calibration (Sect. 3.4, Fig. 7); a sharp increase is followed by an exponential decrease, as the material on the filament is depleted. At filament temperatures beyond 350 to 400 °C, signals of different shapes appear (in this case, e.g., *m/z* 147 and *m/z* 163). These signals are also found in the heating background measurements and do not originate from the collected analyte particles. Instead, they are caused by desorption of substances from the inlet line due to the increased temperature of the carrier gas. The fact that the inlet line is a much larger reservoir than the filament explains why the shape of these background signals is different and why they do not decrease within a few seconds. The temperature range where valid measurements are taken is thus up to ~ 350 °C. Nevertheless, the filament is heated up to 600 °C in order to ensure that all particulate material evaporates and memory effects are avoided.

Some substances seem to desorb at two different temperatures. This can happen for two reasons: (1) the filament might be heated unevenly, but this would also result in less pronounced peaks instead of two sharp peaks. (2) Different chemical species that do not possess the same evaporation temperature, can result in the same product ions. In the example shown here, it is not exactly clear whether sulfuric acid belongs to dimethylammonium-bisulfate or dimethylammonium-sulfate, and what influence potential contaminants such as ammonia can have on the evaporation temperature (Lawler et al., 2016). (3) The signal appearing first originates from desorption of the molecule with this given mass to charge ratio, whereas the second appearance could be due to the fragmentation of a larger molecule. Some amount of the larger molecules seem to fragment and these fragments are then detected at higher temperatures than expected for a desorption (see also Sect. 6). In the chemical system of dimethylamine and sulfuric acid, one can also observe the selectivity of the ionization by nitrate ions. Sulfuric acid, for example, has a lower detection limit of 5 × 10⁴ cm⁻³ (~ 0.00185 ppt_v) (Kirkby et al., 2016), whereas for dimethylamine the lower detection limit of 1.7 ppt_v (Simon et al., 2016) is almost a factor of 10³ higher. Therefore, the signals

related to sulfuric acid are very strong whereas DMA related signals mostly do not reach the detection limit.

5 Signal quantification

5.1 Collected particle mass during a measurement

The collected mass on the filament is calculated in order to quantify the measured signals. Additionally, it is estimated before the measurement from the present particle size distribution and the selected particle diameter so that the collected particle mass exceeds the detection limit.

As a DMA cannot provide an absolute monodisperse aerosol (see Sect. 3.1), the incoming number size distribution dn/dd_p of the sample in combination with the transmission efficiency $\tau(d_p)$, collection efficiency $\eta(d_p)$ and charge fraction $x(d_p)$ is needed to calculate the collected mass precisely. The transmission and collection efficiency are retrieved from the TD-DMA characterization (Sect. 3, Figs. 4, 5, and 6) and the incoming size distribution can be provided by an SMPS or other instrument measuring the number size distribution of the analyte aerosol in the applicable size range. Thus, the collected mass on the filament can be calculated according to the following equation:

$$m_{\text{coll}}(d'_p) = Q_{\text{aerosol}} \cdot \rho \cdot \frac{\pi}{6} \cdot \int_{t=t_0}^{t_{\text{coll}}} \int_{d_p=0}^{d_{p,\text{max}}} d_p^3 \cdot \frac{dn(d_p, t)}{dd_p} \cdot x(d_p) \cdot \eta(d_p) \cdot \tau_{d'_p}(d_p) \cdot dd_p \cdot dt, \quad (11)$$

with Q_{aerosol} the aerosol flow rate through the TD-DMA, ρ the particle density and d'_p the selected diameter. The amount of mass collected per time thus depends both on the selected diameter and on the size distribution of the aerosol analyte. In addition, as for any DMA, the effective diameter collected varies with the size distribution of the background aerosol. To get an impression of the amount of mass that can be collected under certain conditions, we look at the aerosol size distribution of the example event described in Sect. 4.2 (see Fig. 9). The lower panel displays the number size distribution and median diameter (black line), as well as the time period of collection (pink line). The upper panel shows the particle mass collected by the TD-DMA per unit time when the instrument is set to collect a certain diameter; it ranges between 10⁻⁵ and 10⁻³ ng s⁻¹. Integration over time yields the total mass collected as described by Eq. (11).

The minimum mass concentration in the analyte aerosol where measurements with the TD-DMA are possible, depends not only on size distribution and selected size but also on sampling time and analyte aerosol composition. For example, the lower limit for sulfuric acid particles with a sampling time of 2 h is 27 pg m⁻³. Measuring in size-resolved mode from monodisperse 15 nm particles, 811 pg m⁻³ are needed. Assuming the number size distribution from the example nucleation event (Fig. 8) and measuring all sizes, the

5500

A. C. Wagner et al.: Size-resolved online chemical analysis of nanoaerosol particles

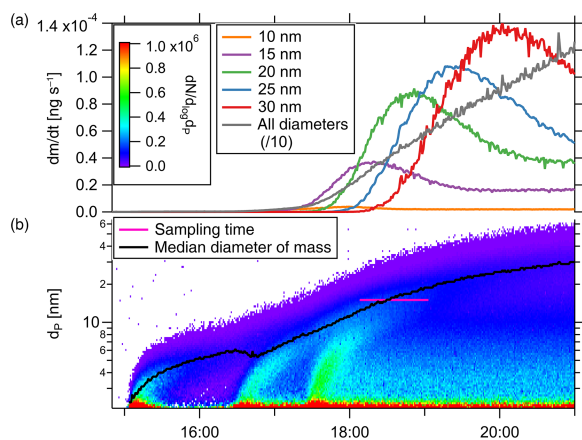


Figure 9. Particle mass collected by the TD-DMA per unit time when the instrument is set to collect a certain diameter (a), for a given size distribution (b).

mass concentration should be higher than 385 pg m^{-3} . The TD-DMA's sensitivity is thus comparable to other instruments operating in this size range (see Sect. 6.2).

5.2 Mass fraction of individual substances from time integrated signals

The fraction of a substance in the aerosol sample shall be determined. Like this, the relative contribution of an individual substance or a group of substances (e.g., all organic compounds) to nucleation can be investigated, e.g., for the same size under different conditions or with increasing size under constant conditions.

The calculation requires the collected mass from Sect. 5.1 and the conversion factor from the sample mass calibration in Sect. 3.4. The fraction f_i of an individual substance in the aerosol sample is thus

$$f_i = \frac{m_i}{m_{\text{coll}}} \quad (12)$$

Note that the collected mass calculated from the SMPS data should be used instead of the sum of all identified components, $\sum_i m_i$. Using the latter would be based on the assumption that all compounds of the aerosol could be charged, detected, identified and quantified. As we know from gas-phase measurements, this is usually not the case for the chemically complex atmospheric aerosols. Chemical ionization, especially the negative nitrate ionization used here, is a selective technique. A substance needs to react with the primary ions to be charged and detected in the mass spectrometer. This can either be the transfer of a positively charged hydrogen atom from the substance to the primary ion, or clustering with the primary ion (Hytinen et al., 2017). For the same reason, the signal of each substance also needs to be corrected with its

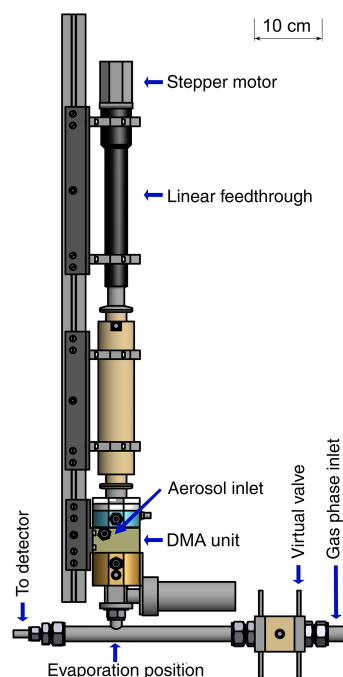


Figure 10. The TD-DMA coupled to a gas-phase detector inlet line.

ionization efficiency (see Sect. 3.4) and this property is not known for all substances. That circumstance can also be bypassed by comparing the contribution of compounds under different conditions rather than providing an absolute concentration.

6 Discussion

6.1 Discussion on the newly developed TD-DMA

The detection limit and sensitivity are a limit to the parameters particle size, number concentration of the analyte aerosol, ionization efficiency, complexity of the spectrum and time resolution. A major challenge is the fact that small particles have an extremely low mass. For example, a particle of half the diameter contains less mass by a factor of 8. In addition, charging probability decreases with size. At 15 nm, the fraction of singly negatively charged particles is less than 0.07 (Fuchs, 1963; Tigges et al., 2015) for the soft X-ray charger used here. For an aerosol of multi component composition, it applies that the more particle mass is collected, the more substances overcome the lower detection limit and the more detailed the observed mass spectrum will be. The TD-DMA is thus designed for high transmission at a coarse resolution. In this way, a size selection is possible but still a sufficient amount of mass is collected. In case of very low particle

concentrations or when a high time resolution is needed, it is also possible to sample all particle sizes in an integral mode by turning off the sheath flow. The low mass concentration of the particulate matter is also the reason why a discontinuous system with consecutive collection and evaporation is chosen. Conversely, the probability for multiple charging increases with particle diameter, so that particles larger than the target size can contaminate the sample. This can be corrected for when counting, but not in the chemical analysis. Within the size range of 10 to 30 nm that the TD-DMA is specialized for, multiple charging does not play a significant role. A typical particle size selected with the TD-DMA is 15 nm. Doubly charged particles of the same electrical mobility have a diameter of 21 nm (Stolzenburg and McMurry, 2008; Hinds, 1999). Considering the charging probabilities of the used soft X-ray charger (Tigges et al., 2015), a fraction of 7.6×10^{-2} of the 15 nm particles carry one charge, whereas just a fraction of 2.6×10^{-4} of the 21 nm particles carry two charges. With the particle mass being proportional to their cubic diameter, the contribution of 21 nm particles to a 15 nm sample would be $2.6 \times 10^{-4} \times (21 \text{ nm})^3 / (7.6 \times 10^{-2} \times (15 \text{ nm})^3 + 2.6 \times 10^{-4} \times (21 \text{ nm})^3)$. Thus, at the maximum only a fraction of 0.009 of the particle mass in the sample would originate from doubly charged larger particles. This assumes a uniform particle number size distribution. As for new particle formation events, the smallest particles have the highest number concentration, this estimate calculation gives an upper limit. In case of very large background particles in the accumulation mode size range, as, for example, in field use, an impactor should be used.

The soft X-ray charger was chosen for that reason and due to the fact that it does not change the chemistry much, compared to, e.g., a corona charger. Nevertheless, it would be beneficial to find a charger which offers a higher charging probability for small particles while still fulfilling the above criteria.

For optimizing the collection process, it would be beneficial to enhance the collection efficiency (see Sect. 3.2) also for larger sizes. Applying a larger collection voltage to the filament increases the collection efficiency, which is currently limited by leak currents occurring between filament and central electrode when the potential difference is too high. It is also a possibility to prepare the DMA for a higher flow of the analyte aerosol in order to collect more mass.

The exact position of the filament, in combination with the flow profiles at the place of evaporation, is crucial and optimization of these features has a high impact on the sensitivity. Also, the high temperature gradient when heating the filament releases the analyte in a very compact way, which benefits the lower detection limit. This method of direct heating ensures a homogeneous and precisely controlled temperature for the desorption of the substances. Currently we have a discrepancy between the TD-DMA's sample mass calibration and the gas-phase calibration of sulfuric acid (Kürten et al., 2012). This can be explained by losses in the transition

from filament to mass spectrometer due to condensation on the mass spectrometer's inlet line. There have also been tests to evaporate the sample directly inside the ion source, but for the presently used ion source (Kürten et al., 2011) this was not expedient. Nevertheless, these losses are unsatisfactory and possibilities for further improvements are being investigated.

As discussed in Sect. 4.2, the filament material might be problematic in terms of influencing the analyte. Heating, especially from metallic surfaces, might lead to fragmentation or other chemical modification of the original molecules. We tested different filaments and saw that not only the material but also the way the wire is manufactured strongly influences this process and thus the suitability of the filament. Also, it was found that a careful heating procedure seems to reduce these effects. This was investigated by using the sample mass calibration method (see Sect. 3.4) with different substances and by careful examination of the spectra from nucleation events. Some fraction of the larger molecules (for example of the HOMs) seem to fragment and these fragments are then detected at higher temperatures than molecules that have the same elemental composition. A detailed analysis of this issue will be the subject of future studies. A complete degeneration of substances is hardly observed for the relevant temperature range, only very small peaks that might originate from such reactions are present in the spectra at higher temperatures. Nevertheless, it cannot be excluded that some material breaks up into substances that are not ionized by the negative nitrate CI-API-TOF and are thus not visible in the spectra. By coating the filament with a thin layer of a chemically inert material, this could be reduced.

The ionization with negative nitrate primary ions is a selective technique. To target more substances like, e.g., amines and ammonia, different primary ions can be chosen (Lawler et al., 2016). To distinguish the aerosol sample from potential gas-phase adsorption, a sheath flow of pure nitrogen surrounds the filament in the size selective mode. In the integral mode, the filament is also exposed to the gas phase of the analyte and a gas-phase background measurement is advised (see Sect. 4.1).

Up to now, the TD-DMA has been used in chamber experiments with timed nucleation events, but it is also intended for field use in the future. Here, the size selective mode is especially useful because the larger background particles would otherwise dominate the mass concentration. Also, background measurements, as suggested in Sect. 4.1 (3) are not straightforward when chemical conditions change over time. To look further into the chemistry of aerosol growth, it will be interesting to perform measurements at a flow tube, where a steady state production of the analyte aerosol is possible. When not being limited by the time resolution or small number concentrations, one can analyze particles starting at small sizes with a high size resolution, which is variable in this method, and thus gain a very detailed picture of the growth process.

6.2 Comparison of instruments capable of chemical analysis of sub-30 nm particles

The new instrument TD-DMA shall be placed in the context of existing techniques for the online chemical analysis of sub-30 nm aerosol particles. When comparing the different nanoparticle instruments, one has to focus on a selection of criteria as the instruments strongly differ from one another and have their individual functional principles and thus strengths and weaknesses.

To give an overview regarding the functional principle of the devices (see Table 1), we introduced the following criteria: (1) continuous vs. discontinuous, (2) size-selective vs. non-size-selective, (3) how the particulate material is evaporated and (4) whether the gas phase can be measured simultaneously.

One of the most important criteria is the sensitivity of the instruments, but the question arises of which is the appropriate parameter to describe this. Especially the fact that the cited studies do not all refer to the same parameter when discussing the sensitivities of their instruments, makes a comparison difficult.

One option for a meaningful number is the minimum mass concentration of the analyte aerosol (pg m^{-3}) which is needed to perform measurements. However, this is not a constant number for each instrument but depends strongly on the number size distribution, target substances, chemical composition of the analyte aerosol, collection time and other factors. For example, an instrument specialized for size selective analysis of small particles will profit more from a mode of smaller particles, whereas an approach sampling all sizes will benefit more from a mode of larger particles as they contain more mass. Thus for small particles, the first instrument will have a higher sensitivity, and for larger particles, the second one. For the TD-DMA, we thus derived the sensitivity towards sulfuric acid for three different circumstances: measuring all particles (27 pg m^{-3}), selecting 15 nm particles from a monodisperse mode (811 pg m^{-3}) and a non-size-resolved measurement assuming the number size distribution of an example nucleation event (385 pg m^{-3} , see also Sect. 5.1). Lopez-Hilfiker et al. (2014) compared their sensitivities between a chamber study and an ambient study with different background aerosol conditions, temperature, gas-phase concentrations and sample volume. Although their target molecules were all oxygenated organics, the resulting detection limits in pg m^{-3} span a range of two orders of magnitude. The minimum detectable mass (pg) would be another option, but this parameter is only meaningful in combination with the information how much mass can be sampled from the analyte aerosol. In addition, most techniques use chemical ionization to charge the sample after it is transferred to the gas phase. This is a selective technique and depending on the primary ion chosen, different target substances will result in different sensitivities. Horan et al. (2017) report a seemingly rather high lower detection limit of 10^5 pg m^{-3} ,

but the instrument has nevertheless proven the ability to analyze particles as small as 13 nm. Therefore, a higher number in pg m^{-3} does not necessarily mean that an instrument is less suitable for analyzing small particles. However, the smallest detectable particle size certainly depends on parameters like the mass concentration of the analyte aerosol and collection time. Table 1 contains a selection of parameters considering the sensitivity. However, we emphasize that this table represents only an overview on the available techniques and care has to be taken for the exact interpretation due to the sensitivity's dependence on other parameters.

Apart from the sensitivity of a technique, other criteria are also relevant. An important example is in how far the aerosol components fragment when they are transferred to the gas phase, or in how far the instrument can detect semi stable reaction products from particle-phase reactions. These questions are not discussed in this short overview as it is beyond the scope of the present manuscript. Ultimately, it would be beneficial to have several instruments measure the same sub-30 nm aerosol particle population during an intercomparison campaign.

7 Summary

The TD-DMA is suitable for measuring nucleation and Aitken mode particles and is successfully analyzing aerosol mass concentrations in the pg m^{-3} range. The DMA unit is optimized for a high transmission at a coarse resolution to collect a sufficient amount of mass. The characterization of the DMA unit and the evaporation of a test substance show to be reproducible. The instrument's ability to measure freshly nucleated particles was proven in chamber experiments.

The advantages of the instrument are as follows: (a) the TD-DMA allows for size selection, thus the chemical composition of different particle sizes can be compared in order to determine the relative importance of different vapors for particle growth as a function of size. (b) An integral, non-size-selective mode of operation is possible in order to maximize the mass of collected particles. (c) The TD-DMA is a modular and compact unit that can in principle be used with different mass spectrometers or other gas analyzers. (d) During the particle collection process, the gas phase can be analyzed. For this reason, the same mass spectrometer can be used for particle as well as gas-phase measurements and both phases can be directly compared. With this instrument, the processes affecting particle composition and growth can be investigated in detail.

Data availability. The research data can be accessed from <https://doi.org/10.5281/zenodo.1443176> (Wagner et al., 2018).

A. C. Wagner et al.: Size-resolved online chemical analysis of nanoaerosol particles

5503

Author contributions. The instrument was mainly developed by ACW and AK, with major contributions from JC, AB, SB, CF, ME and JH. ACW, AB and SB carried out the measurements and analyzed the data. ACW wrote the manuscript. All authors contributed to the scientific discussion and commented on the manuscript.

Competing interests. The authors declare that they have no conflict of interest.

Acknowledgements. We thank the workshop team of our institute for manufacturing the components and for technical support. We appreciate the useful discussion with Jim Smith from University of California, Irvine, USA, and Alexander Vogel, Institute for Atmospheric and Environmental Science, Frankfurt, Germany. We also thank Jasmin Tröstl and Urs Baltensperger from Paul Scherrer Institute, Villigen, Switzerland, for providing a nSMPS and the whole CLOUD team for support during the CLOUD10T measurement campaign.

This research was supported by the German Federal Ministry of Education and Research (project “CLOUD-12” 01LK1222A and “CLOUD-16” 01LK1601A) as well as the EC Seventh Framework Programme (MC-ITN “CLOUD-TRAIN” 316662).

Edited by: Johannes Schneider

Reviewed by: two anonymous referees

References

- Arnold, F., Curtius, J., Spreng, S., and Deshler, T.: Stratospheric aerosol sulfuric acid: First direct in situ measurements using a novel balloon-based mass spectrometer apparatus, *J. Atmos. Chem.*, 30, 3–10, <https://doi.org/10.1023/A:1006067511568>, 1998.
- Breitenlechner, M., Fischer, L., Hainer, M., Heinritzi, M., Curtius, J., and Hansel, A.: PTR3: An Instrument for Studying the Lifecycle of Reactive Organic Carbon in the Atmosphere, *Anal. Chem.*, 89, 5824–5831, <https://doi.org/10.1021/acs.analchem.6b05110>, 2017.
- Bzdek, B. R., Pennington, M. R., and Johnston, M. V.: Single particle chemical analysis of ambient ultrafine aerosol: A review, *J. Aerosol Sci.*, 52, 109–120, <https://doi.org/10.1016/j.jaerosci.2012.05.001>, 2012.
- Chen, D. R., Pui, D. Y. H., Hummes, D., Fissan, H., Quant, F. R., and Sem, G. J.: Design and evaluation of a nanometer aerosol differential mobility analyzer (Nano-DMA), *J. Aerosol Sci.*, 29, 497–509, [https://doi.org/10.1016/S0021-8502\(97\)10018-0](https://doi.org/10.1016/S0021-8502(97)10018-0), 1998.
- Core Writing Team, Pachauri, R. K., and Reisinger, A. (Eds.): Climate Change 2007: Synthesis Report. Contribution of Working Groups I, II and III to the Fourth Assessment Report of the Intergovernmental Panel on Climate Change, IPCC, Geneva, Switzerland, 2007.
- Curtius, J. and Arnold, F.: Measurement of aerosol sulfuric acid: 1. Experimental setup, characterization, and calibration of a novel mass spectrometric system, *J. Geophys. Res.-Atmos.*, 106, 31965–31974, <https://doi.org/10.1029/2001JD000604>, 2001.
- Curtius, J., Sierau, B., Arnold, F., Baumann, R., Busen, R., Schulte, P., and Schumann, U.: First direct sulfuric acid detection in the exhaust plume of a jet aircraft in flight, *Geophys. Res. Lett.*, 25, 923–926, <https://doi.org/10.1029/98GL00512>, 1998.
- Donaldson, K. and Borm, P.: Particle Toxicology, CRC Press, Boca Raton, Florida, USA, ISBN: 1420003143, 2006.
- Dunne, E. M., Gordon, H., Kürten, A., Almeida, J., Duplissy, J., Williamson, C., Ortega, I. K., Pringle, K. J., Adamov, A., Baltensperger, U., Barmet, P., Benduhn, F., Bianchi, F., Breitenlechner, M., Clarke, A., Curtius, J., Dommen, J., Donahue, N. M., Ehrhart, S., Flagan, R. C., Franchin, A., Guida, R., Hakala, J., Hansel, A., Heinritzi, M., Jokinen, T., Kangasluoma, J., Kirkby, J., Kulmala, M., Kupc, A., Lawler, M. J., Lehtipalo, K., Makhmutov, V., Mann, G., Mathot, S., Merikanto, J., Miettinen, P., Nenes, A., Onnela, A., Rap, A., Reddington, C. L. S., Riccobono, F., Richards, N. A. D., Rissanen, M. P., Rondo, L., Sarnela, N., Schobesberger, S., Sengupta, K., Simon, M., Sipilä, M., Smith, J. N., Stozhkov, Y., Tomé, A., Tröstl, J., Wagner, P. E., Wimmer, D., Winkler, P. M., Worsnop, D. R., and Carslaw, K. S.: Global atmospheric particle formation from CERN CLOUD measurements, *Science*, 354, 1119, <https://doi.org/10.1126/science.aaf2649>, 2016.
- Ehn, M., Thornton, J. A., Kleist, E., Sipilä, M., Junninen, H., Pullinen, I., Springer, M., Rubach, F., Tillmann, R., Lee, B., Lopez-Hilfiker, F., Andres, S., Acir, I.-H., Rissanen, M., Jokinen, T., Schobesberger, S., Kangasluoma, J., Kontkanen, J., Nieminen, T., Kurtén, T., Nielsen, L. B., Jørgensen, S., Kjaergaard, H. G., Canagaratna, M., Maso, M. D., Berndt, T., Petäjä, T., Wahner, A., Kerminen, V.-M., Kulmala, M., Worsnop, D. R., Wildt, J., and Mentel, T. F.: A large source of low-volatility secondary organic aerosol, *Nature*, 506, 476, <https://doi.org/10.1038/nature13032>, 2014.
- Eisele, F. L. and Tanner, D. J.: Measurement of the gas phase concentration of H₂SO₄ and methane sulfonic acid and estimates of H₂SO₄ production and loss in the atmosphere, *J. Geophys. Res.-Atmos.*, 98, 9001–9010, <https://doi.org/10.1029/93JD00031>, 1993.
- Flagan, R. C.: Differential Mobility Analysis of Aerosols: A Tutorial, *KONA Powder Part. J.*, 26, 254–268, <https://doi.org/10.14356/kona.2008023>, 2008.
- Franchin, A., Downard, A., Kangasluoma, J., Nieminen, T., Lehtipalo, K., Steiner, G., Manninen, H. E., Petäjä, T., Flagan, R. C., and Kulmala, M.: A new high-transmission inlet for the Caltech nano-RDMA for size distribution measurements of sub-3 nm ions at ambient concentrations, *Atmos. Meas. Tech.*, 9, 2709–2720, <https://doi.org/10.5194/amt-9-2709-2016>, 2016.
- Fuchs, N. A.: On the stationary charge distribution on aerosol particles in a bipolar ionic atmosphere, *Geofisica pura e applicata*, 56, 185–193, <https://doi.org/10.1007/BF01993343>, 1963.
- Fuzzi, S., Baltensperger, U., Carslaw, K., Decesari, S., Denier van der Gon, H., Facchini, M. C., Fowler, D., Koren, I., Langford, B., Lohmann, U., Nemitz, E., Pandis, S., Riipinen, I., Rudich, Y., Schaap, M., Slowik, J. G., Spracklen, D. V., Vignati, E., Wild, M., Williams, M., and Gilardoni, S.: Particulate matter, air quality and climate: lessons learned and future needs, *Atmos. Chem. Phys.*, 15, 8217–8299, <https://doi.org/10.5194/acp-15-8217-2015>, 2015.

- Gonser, S. G. and Held, A.: A chemical analyzer for charged ultrafine particles, *Atmos. Meas. Tech.*, 6, 2339–2348, <https://doi.org/10.5194/amt-6-2339-2013>, 2013.
- Graus, M., Müller, M., and Hansel, A.: High Resolution PTR-TOF: Quantification and Formula Confirmation of VOC in Real Time, *J. Am. Soc. Mass Spectr.*, 21, 1037–1044, <https://doi.org/10.1016/j.jasms.2010.02.006>, 2010.
- Hallquist, M., Wenger, J. C., Baltensperger, U., Rudich, Y., Simpson, D., Claeys, M., Dommen, J., Donahue, N. M., George, C., Goldstein, A. H., Hamilton, J. F., Herrmann, H., Hoffmann, T., Iinuma, Y., Jang, M., Jenkin, M. E., Jimenez, J. L., Kiendler-Scharr, A., Maenhaut, W., McFiggans, G., Mentel, Th. F., Monod, A., Prévôt, A. S. H., Seinfeld, J. H., Surratt, J. D., Szmigielski, R., and Wildt, J.: The formation, properties and impact of secondary organic aerosol: current and emerging issues, *Atmos. Chem. Phys.*, 9, 5155–5236, <https://doi.org/10.5194/acp-9-5155-2009>, 2009.
- Hansel, A., Jordan, A., Holzinger, R., Prazeller, P., Vogel, W., and Lindinger, W.: Proton transfer reaction mass spectrometry: on-line trace gas analysis at the ppb level, *Int. J. Mass Spectrom.*, 149–150, 609–619, [https://doi.org/10.1016/0168-1176\(95\)04294-U](https://doi.org/10.1016/0168-1176(95)04294-U), 1995.
- He, S., Li, L., Duan, H., Naqwi, A., and Hogan, C. J.: Aerosol Analysis via Electrostatic Precipitation-Electrospray Ionization Mass Spectrometry, *Anal. Chem.*, 87, 6752–6760, <https://doi.org/10.1021/acs.analchem.5b01183>, 2015.
- Heinritzi, M., Simon, M., Steiner, G., Wagner, A. C., Kürten, A., Hansel, A., and Curtius, J.: Characterization of the mass-dependent transmission efficiency of a CIMS, *Atmos. Meas. Tech.*, 9, 1449–1460, <https://doi.org/10.5194/amt-9-1449-2016>, 2016.
- Hermann, M., Wehner, B., Bischof, O., Han, H. S., Krinke, T., Liu, W., Zerrath, A., and Wiedensohler, A.: Particle counting efficiencies of new TSI condensation particle counters, *J. Aerosol Sci.*, 38, 674–682, <https://doi.org/10.1016/j.jaerosci.2007.05.001>, 2007.
- Hinds, W. C.: *Aerosol Technology*, 2nd ed., Wiley Interscience, ISBN: 978-0-471-19410-1, 1999.
- Horan, A. J., Apsokardu, M. J., and Johnston, M. V.: Droplet Assisted Inlet Ionization for Online Analysis of Airborne Nanoparticles, *Anal. Chem.*, 89, 1059–1062, <https://doi.org/10.1021/acs.analchem.6b04718>, 2017.
- Hyttinen, N., Otkjær, R. V., Iyer, S., Kjaergaard, H. G., Rissanen, M. P., Wennberg, P. O., and Kurtén, T.: Computational Comparison of Different Reagent Ions in the Chemical Ionization of Oxidized Multifunctional Compounds, *J. Phys. Chem. A*, 122, 269–279, <https://doi.org/10.1021/acs.jpca.7b10015>, 2017.
- International Electrotechnical Commission: IEC 60751 – Industrial platinum resistance thermometers and platinum temperature sensors, Geneva, Switzerland, ISBN: 2-8318-9849-8, 2008.
- Jayne, J. T., Leard, D. C., Zhang, X., Davidovits, P., Smith, K. A., Kolb, C. E., and Worsnop, D. R.: Development of an Aerosol Mass Spectrometer for Size and Composition Analysis of Submicron Particles, *Aerosol Sci. Tech.*, 33, 49–70, <https://doi.org/10.1080/027868200410840>, 2000.
- Jiang, J., Attoui, M., Heim, M., Brunelli, N. A., McMurry, P. H., Kasper, G., Flagan, R. C., Giapis, K., and Mouret, G.: Transfer Functions and Penetrations of Five Differential Mobility Analyzers for Sub-2 nm Particle Classification, *Aerosol Sci. Tech.*, 45, 480–492, <https://doi.org/10.1080/02786826.2010.546819>, 2011.
- Jokinen, T., Sipilä, M., Junninen, H., Ehn, M., Lönn, G., Hakala, J., Petäjä, T., Mauldin III, R. L., Kulmala, M., and Worsnop, D. R.: Atmospheric sulphuric acid and neutral cluster measurements using CI-API-TOF, *Atmos. Chem. Phys.*, 12, 4117–4125, <https://doi.org/10.5194/acp-12-4117-2012>, 2012.
- Kirkby, J., Curtius, J., Almeida, J., Dunne, E., Duplissy, J., Ehrhart, S., Franchin, A., Gagne, S., Ickes, L., Kurten, A., Kupc, A., Metzger, A., Riccobono, F., Rondo, L., Schobesberger, S., Tsagko-georgas, G., Wimmer, D., Amorim, A., Bianchi, F., Breitenlechner, M., David, A., Dommen, J., Downard, A., Ehn, M., Flagan, R. C., Haider, S., Hansel, A., Hausser, D., Jud, W., Junninen, H., Kreissl, F., Kvashin, A., Laaksonen, A., Lehtipalo, K., Lima, J., Lovejoy, E. R., Makhmutov, V., Mathot, S., Mikkilä, J., Minginette, P., Mogo, S., Nieminen, T., Onnela, A., Pereira, P., Petaja, T., Schnitzhofer, R., Seinfeld, J. H., Sipilä, M., Stozhkov, Y., Stratmann, F., Tome, A., Vanhanen, J., Viisanen, Y., Virtala, A., Wagner, P. E., Walther, H., Weingartner, E., Wex, H., Winkler, P. M., Carslaw, K. S., Worsnop, D. R., Baltensperger, U., and Kulmala, M.: Role of sulphuric acid, ammonia and galactic cosmic rays in atmospheric aerosol nucleation, *Nature*, 476, 429–433, <https://doi.org/10.1038/nature10343>, 2011.
- Kirkby, J., Duplissy, J., Sengupta, K., Frege, C., Gordon, H., Williamson, C., Heinritzi, M., Simon, M., Yan, C., Almeida, J., Tröstl, J., Nieminen, T., Ortega, I. K., Wagner, R., Adamov, A., Amorim, A., Bernhammer, A.-K., Bianchi, F., Breitenlechner, M., Brilke, S., Chen, X., Craven, J., Dias, A., Ehrhart, S., Flagan, R. C., Franchin, A., Fuchs, C., Guida, R., Hakala, J., Hoyle, C. R., Jokinen, T., Junninen, H., Kangasluoma, J., Kim, J., Krapf, M., Kürten, A., Laaksonen, A., Lehtipalo, K., Makhmutov, V., Mathot, S., Molteni, U., Onnela, A., Peräkylä, O., Piel, F., Petäjä, T., Praplan, A. P., Pringle, K., Rap, A., Richards, N. A. D., Riipinen, I., Rissanen, M. P., Rondo, L., Sarnela, N., Schobesberger, S., Scott, C. E., Seinfeld, J. H., Sipilä, M., Steiner, G., Stozhkov, Y., Stratmann, F., Tomé, A., Virtanen, A., Vogel, A. L., Wagner, A. C., Wagner, P. E., Weingartner, E., Wimmer, D., Winkler, P. M., Ye, P., Zhang, X., Hansel, A., Dommen, J., Donahue, N. M., Worsnop, D. R., Baltensperger, U., Kulmala, M., Carslaw, K. S., and Curtius, J.: Ion-induced nucleation of pure biogenic particles, *Nature*, 533, 521, <https://doi.org/10.1038/nature17953>, 2016.
- Kreyling, W. G., Möller, W., Semmler-Behnke, M., Oberdörster, G., Donaldson, K., and Borm, P.: Particle dosimetry: deposition and clearance from the respiratory tract and translocation towards extrapulmonary sites, in: *Particle toxicology*, edited by: Donaldson, K. and Borm, P., CRC Press, Boca Raton, FL, USA, 46–69, 2006.
- Kulmala, M., Petäjä, T., Ehn, M., Thornton, J., Sipilä, M., Worsnop, D. R., and Kerminen, V.-M.: Chemistry of Atmospheric Nucleation: On the Recent Advances on Precursor Characterization and Atmospheric Cluster Composition in Connection with Atmospheric New Particle Formation, *Annu. Rev. Phys. Chem.*, 65, 21–37, <https://doi.org/10.1146/annurev-physchem-040412-110014>, 2014.
- Kürten, A., Rondo, L., Ehrhart, S., and Curtius, J.: Performance of a corona ion source for measurement of sulfuric acid by chemical ionization mass spectrometry, *Atmos. Meas. Tech.*, 4, 437–443, <https://doi.org/10.5194/amt-4-437-2011>, 2011.

- Kürten, A., Rondo, L., Ehrhart, S., and Curtius, J.: Calibration of a Chemical Ionization Mass Spectrometer for the Measurement of Gaseous Sulfuric Acid, *J. Phys. Chem. A*, 116, 6375–6386, <https://doi.org/10.1021/jp212123n>, 2012.
- Kürten, A., Jokinen, T., Simon, M., Sipilä, M., Sarnela, N., Junninen, H., Adamov, A., Almeida, J., Amorim, A., Bianchi, F., Breitenlechner, M., Dommen, J., Donahue, N. M., Duplissy, J., Ehrhart, S., Flagan, R. C., Franchin, A., Hakala, J., Hansel, A., Heinritzi, M., Hutterli, M., Kangasluoma, J., Kirkby, J., Laaksonen, A., Lehtipalo, K., Leiminger, M., Makhmutov, V., Mathot, S., Onnela, A., Petäjä, T., Praplan, A. P., Riccobono, F., Rissanen, M. P., Rondo, L., Schobesberger, S., Seinfeld, J. H., Steiner, G., Tomé, A., Tröstl, J., Winkler, P. M., Williamson, C., Wimmer, D., Ye, P., Baltensperger, U., Carslaw, K. S., Kulmala, M., Worsnop, D. R., and Curtius, J.: Neutral molecular cluster formation of sulfuric acid–dimethylamine observed in real time under atmospheric conditions, *P. Natl. Acad. Sci. USA*, 111, 15019–15024, <https://doi.org/10.1073/pnas.1404853111>, 2014.
- Laitinen, T., Hartonen, K., Kulmala, M., and Riekkola, M.-L.: Aerosol time-of-flight mass spectrometer for measuring ultrafine aerosol particles, *Boreal Environ. Res.*, 14, 539–549, 2009.
- Laitinen, T., Ehn, M., Junninen, H., Ruiz-Jimenez, J., Parshintsev, J., Hartonen, K., Riekkola, M.-L., Worsnop, D. R., and Kulmala, M.: Characterization of organic compounds in 10- to 50-nm aerosol particles in boreal forest with laser desorption-ionization aerosol mass spectrometer and comparison with other techniques, *Atmos. Environ.*, 45, 3711–3719, <https://doi.org/10.1016/j.atmosenv.2011.04.023>, 2011.
- Lawler, M. J., Whitehead, J., O'Dowd, C., Monahan, C., McFiggans, G., and Smith, J. N.: Composition of 15–85 nm particles in marine air, *Atmos. Chem. Phys.*, 14, 11557–11569, <https://doi.org/10.5194/acp-14-11557-2014>, 2014.
- Lawler, M. J., Winkler, P. M., Kim, J., Ahlm, L., Tröstl, J., Praplan, A. P., Schobesberger, S., Kürten, A., Kirkby, J., Bianchi, F., Duplissy, J., Hansel, A., Jokinen, T., Keskinen, H., Lehtipalo, K., Leiminger, M., Petäjä, T., Rissanen, M., Rondo, L., Simon, M., Sipilä, M., Williamson, C., Wimmer, D., Riipinen, I., Virtanen, A., and Smith, J. N.: Unexpectedly acidic nanoparticles formed in dimethylamine–ammonia–sulfuric–acid nucleation experiments at CLOUD, *Atmos. Chem. Phys.*, 16, 13601–13618, <https://doi.org/10.5194/acp-16-13601-2016>, 2016.
- Lehtipalo, K., Rondo, L., Kontkanen, J., Schobesberger, S., Jokinen, T., Sarnela, N., Kürten, A., Ehrhart, S., Franchin, A., Nieminen, T., Riccobono, F., Sipilä, M., Yli-Juuti, T., Duplissy, J., Adamov, A., Ahlm, L., Almeida, J., Amorim, A., Bianchi, F., Breitenlechner, M., Dommen, J., Downard, A. J., Dunne, E. M., Flagan, R. C., Guida, R., Hakala, J., Hansel, A., Jud, W., Kangasluoma, J., Kerminen, V.-M., Keskinen, H., Kim, J., Kirkby, J., Kupc, A., Kupiainen-Määttä, O., Laaksonen, A., Lawler, M. J., Leiminger, M., Mathot, S., Olenius, T., Ortega, I. K., Onnela, A., Petäjä, T., Praplan, A., Rissanen, M. P., Ruuskanen, T., Santos, F. D., Schallhart, S., Schnitzhofer, R., Simon, M., Smith, J. N., Tröstl, J., Tsagkogeorgas, G., Tomé, A., Vaattovaara, P., Vehkamäki, H., Vrtala, A. E., Wagner, P. E., Williamson, C., Wimmer, D., Winkler, P. M., Virtanen, A., Donahue, N. M., Carslaw, K. S., Baltensperger, U., Riipinen, I., Curtius, J., Worsnop, D. R., and Kulmala, M.: The effect of acid–base clustering and ions on the growth of atmospheric nano-particles, *Nat. Commun.*, 7, 11594, <https://doi.org/10.1038/ncomms11594>, 2016.
- Lelieveld, J., Evans, J. S., Fnais, M., Giannadaki, D., and Pozzer, A.: The contribution of outdoor air pollution sources to premature mortality on a global scale, *Nature*, 525, 367–371, <https://doi.org/10.1038/nature15371>, 2015.
- Lopez-Hilfiker, F. D., Mohr, C., Ehn, M., Rubach, F., Kleist, E., Wildt, J., Mentel, Th. F., Lutz, A., Hallquist, M., Worsnop, D., and Thornton, J. A.: A novel method for online analysis of gas and particle composition: description and evaluation of a Filter Inlet for Gases and AEROSols (FIGAERO), *Atmos. Meas. Tech.*, 7, 983–1001, <https://doi.org/10.5194/amt-7-983-2014>, 2014.
- Lopez-Hilfiker, F. D., Mohr, C., Ehn, M., Rubach, F., Kleist, E., Wildt, J., Mentel, Th. F., Carrasquillo, A. J., Daumit, K. E., Hunter, J. F., Kroll, J. H., Worsnop, D. R., and Thornton, J. A.: Phase partitioning and volatility of secondary organic aerosol components formed from α -pinene ozonolysis and OH oxidation: the importance of accretion products and other low volatility compounds, *Atmos. Chem. Phys.*, 15, 7765–7776, <https://doi.org/10.5194/acp-15-7765-2015>, 2015.
- McMurry, P. H., Ghimire, A., Ahn, H.-K., Sakurai, H., Moore, K., Stolzenburg, M., and Smith, J. N.: Sampling Nanoparticles for Chemical Analysis by Low Resolution Electrical Mobility Classification, *Environ. Sci. Technol.*, 43, 4653–4658, <https://doi.org/10.1021/es8029335>, 2009.
- Merikanto, J., Spracklen, D. V., Mann, G. W., Pickering, S. J., and Carslaw, K. S.: Impact of nucleation on global CCN, *Atmos. Chem. Phys.*, 9, 8601–8616, <https://doi.org/10.5194/acp-9-8601-2009>, 2009.
- Nel, A.: Air pollution-related illness: effects of particles, *Science*, 308, 804–806, <https://doi.org/10.1126/science.1108752>, 2005.
- Noble, C. A. and Prather, K. A.: Real-time single particle mass spectrometry: A historical review of a quarter century of the chemical analysis of aerosols, *Mass Spectrom. Rev.*, 19, 248–274, [https://doi.org/10.1002/1098-2787\(200007\)19:4<248::AID-MAS3>3.0.CO;2-I](https://doi.org/10.1002/1098-2787(200007)19:4<248::AID-MAS3>3.0.CO;2-I), 2000.
- Phares, D. J. and Collier, S.: Direct Collection of Aerosols by Electrostatic Classification for Size-Resolved Chemical Analysis, *Aerosol Sci. Tech.*, 44, 173–181, <https://doi.org/10.1080/02786820903482914>, 2010.
- Pope III, C. A. and Dockery, D. W.: Health effects of fine particulate air pollution: lines that connect, *J. Air Waste Manage.*, 56, 709–742, <https://doi.org/10.1080/10473289.2006.10464485>, 2006.
- Reischl, G. P., Mäkelä, J. M., and Necid, J.: Performance of Vienna Type Differential Mobility Analyzer at 1.2–20 Nanometer, *Aerosol Sci. Tech.*, 27, 651–672, <https://doi.org/10.1080/02786829708965503>, 1997.
- Riccobono, F., Rondo, L., Sipilä, M., Barmet, P., Curtius, J., Dommen, J., Ehn, M., Ehrhart, S., Kulmala, M., Kürten, A., Mikkilä, J., Paasonen, P., Petäjä, T., Weingartner, E., and Baltensperger, U.: Contribution of sulfuric acid and oxidized organic compounds to particle formation and growth, *Atmos. Chem. Phys.*, 12, 9427–9439, <https://doi.org/10.5194/acp-12-9427-2012>, 2012.
- Simon, M., Heinritzi, M., Herzog, S., Leiminger, M., Bianchi, F., Praplan, A., Dommen, J., Curtius, J., and Kürten, A.: Detection of dimethylamine in the low pptv range using nitrate chemical ionization atmospheric pressure interface time-of-flight (CI-API-TOF) mass spectrometry, *Atmos. Meas. Tech.*, 9, 2135–2145, <https://doi.org/10.5194/amt-9-2135-2016>, 2016.

- Smith, J. N., Moore, K. F., McMurry, P. H., and Eisele, F. L.: Atmospheric Measurements of Sub-20 nm Diameter Particle Chemical Composition by Thermal Desorption Chemical Ionization Mass Spectrometry, *Aerosol Sci. Tech.*, 38, 100–110, <https://doi.org/10.1080/02786820490249036>, 2004.
- Smith, J. N., Barsanti, K. C., Friedli, H. R., Ehn, M., Kulmala, M., Collins, D. R., Scheckman, J. H., Williams, B. J., and McMurry, P. H.: Observations of ammonium salts in atmospheric nanoparticles and possible climatic implications, *P. Natl. Acad. Sci. USA*, 107, 6634–6639, <https://doi.org/10.1073/pnas.0912127107>, 2010.
- Stolzenburg, M. R. and McMurry, P. H.: Equations Governing Single and Tandem DMA Configurations and a New Lognormal Approximation to the Transfer Function, *Aerosol Sci. Tech.*, 42, 421–432, <https://doi.org/10.1080/02786820802157823>, 2008.
- Tigges, L., Wiedensohler, A., Weinhold, K., Gandhi, J., and Schmid, H. J.: Bipolar charge distribution of a soft X-ray diffusion charger, *J. Aerosol Sci.*, 90, 77–86, <https://doi.org/10.1016/j.jaerosci.2015.07.002>, 2015.
- Tröstl, J., Chuang, W. K., Gordon, H., Heinritzi, M., Yan, C., Molteni, U., Ahlm, L., Frege, C., Bianchi, F., Wagner, R., Simon, M., Lehtipalo, K., Williamson, C., Craven, J. S., Duplissy, J., Adamov, A., Almeida, J., Bernhammer, A.-K., Breitenlechner, M., Brilke, S., Dias, A., Ehrhart, S., Flagan, R. C., Franchin, A., Fuchs, C., Guida, R., Gysel, M., Hansel, A., Hoyle, C. R., Jokinen, T., Junninen, H., Kangasluoma, J., Keskinen, H., Kim, J., Krapf, M., Kürten, A., Laaksonen, A., Lawler, M., Leiminger, M., Mathot, S., Möhler, O., Nieminen, T., Onnela, A., Petäjä, T., Piel, F. M., Miettinen, P., Rissanen, M. P., Rondo, L., Sarnela, N., Schobesberger, S., Sengupta, K., Sipilä, M., Smith, J. N., Steiner, G., Tomè, A., Virtanen, A., Wagner, A. C., Weingartner, E., Wimmer, D., Winkler, P. M., Ye, P., Carslaw, K. S., Curtius, J., Dommen, J., Kirkby, J., Kulmala, M., Riipinen, I., Worsnop, D. R., Donahue, N. M., and Baltensperger, U.: The role of low-volatility organic compounds in initial particle growth in the atmosphere, *Nature*, 533, 527, <https://doi.org/10.1038/nature18271>, 2016.
- TSI Incorporated: Ultrafine Condensation Particle Counter Model 3776, Instruction Manual, Shoreview, MN, USA, 2007.
- Vehkamäki, H. and Riipinen, I.: Thermodynamics and kinetics of atmospheric aerosol particle formation and growth, *Chem. Soc. Rev.*, 41, 5160–5173, <https://doi.org/10.1039/C2CS00002D>, 2012.
- Voisin, D., Smith, J. N., Sakurai, H., McMurry, P. H., and Eisele, F. L.: Thermal Desorption Chemical Ionization Mass Spectrometer for Ultrafine Particle Chemical Composition, *Aerosol Sci. Tech.*, 37, 471–475, <https://doi.org/10.1080/02786820300959>, 2003.
- Wagner, A. C., Bergen, A., Brilke, S., Fuchs, C., Ernst, M., Hoker, J., Heinritzi, M., Simon, M., Bühner, B., Curtius, J., and Kürten, A.: Dataset for 10.5194/amt-11-1-2018, <https://doi.org/10.5281/zenodo.1443176>, 2018.
- Wang, S., Zordan, C. A., and Johnston, M. V.: Chemical Characterization of Individual, Airborne Sub-10-nm Particles and Molecules, *Anal. Chem.*, 78, 1750–1754, <https://doi.org/10.1021/ac052243i>, 2006.
- Wang, S. C. and Flagan, R. C.: Scanning Electrical Mobility Spectrometer, *Aerosol Sci. Tech.*, 13, 230–240, <https://doi.org/10.1080/02786829008959441>, 1990.
- Wellenius, G. A., Burger, M. R., Coull, B. A., Schwartz, J., Suh, H. H., Koutrakis, P., Schlaug, G., Gold, D. R., and Mittleman, M. A.: Ambient air pollution and the risk of acute ischemic stroke, *Arch. Intern. Med.*, 172, 229–234, <https://doi.org/10.1001/archinternmed.2011.732>, 2012.
- Wimmer, D., Lehtipalo, K., Nieminen, T., Duplissy, J., Ehrhart, S., Almeida, J., Rondo, L., Franchin, A., Kreissl, F., Bianchi, F., Manninen, H. E., Kulmala, M., Curtius, J., and Petäjä, T.: Technical Note: Using DEG-CPCs at upper tropospheric temperatures, *Atmos. Chem. Phys.*, 15, 7547–7555, <https://doi.org/10.5194/acp-15-7547-2015>, 2015.
- Zhang, Q., Jimenez, J. L., Canagaratna, M. R., Ulbrich, I. M., Ng, N. L., Worsnop, D. R., and Sun, Y.: Understanding atmospheric organic aerosols via factor analysis of aerosol mass spectrometry: a review, *Anal. Bioanal. Chem.*, 401, 3045–3067, <https://doi.org/10.1007/s00216-011-5355-y>, 2011.
- Zhang, R., Khalizov, A., Wang, L., Hu, M., and Xu, W.: Nucleation and Growth of Nanoparticles in the Atmosphere, *Chem. Rev.*, 112, 1957–2011, <https://doi.org/10.1021/cr2001756>, 2012.
- Zhang, S.-H. and Flagan, R. C.: Resolution of the radial differential mobility analyzer for ultrafine particles, *J. Aerosol Sci.*, 27, 1179–1200, [https://doi.org/10.1016/0021-8502\(96\)00036-5](https://doi.org/10.1016/0021-8502(96)00036-5), 1996.

4.2 Characterization of Aerosol Particles Produced by a Skyscraper by Blasting (Wagner et al. (2017))



Contents lists available at ScienceDirect

Journal of Aerosol Science

journal homepage: www.elsevier.com/locate/jaerosci

Characterization of Aerosol Particles Produced by a Skyscraper Demolition by Blasting



Andrea C. Wagner^{a,*}, Anton Bergen^a, Sophia Brilke^a, Bertram Bühner^a, Martin Ebert^c, Werner Haunold^{a,1}, Martin Heinritzi^a, Stephan Herzog^a, Stefan Jacobi^b, Andreas Kürten^a, Felix Piel^a, Alfons Ramme^b, Daniel Weber^a, Stephan Weinbruch^c, Joachim Curtius^a

^a Institute for Atmospheric and Environmental Sciences, Goethe University Frankfurt, Frankfurt am Main, Germany

^b Hessian Agency for the Environment and Geology, Wiesbaden, Germany

^c Institute for Applied Geosciences, Technical University of Darmstadt, Darmstadt, Germany

ARTICLE INFO

Keywords:

Demolition emissions
Urban aerosol
Ultrafine particles
PM₁₀
Chemical composition
Size distribution

ABSTRACT

We present a study characterizing aerosol particles resulting from a skyscraper blasting. High PM₁₀ mass concentrations with a maximum of 844.9 $\mu\text{g m}^{-3}$ were present for a short time period of approximately 15 minutes. They result in a day mean of 32.6 $\mu\text{g m}^{-3}$ compared to a 27.6 $\mu\text{g m}^{-3}$ background not exceeding the 50 $\mu\text{g m}^{-3}$ EU maximum permissible value. The increase in particle number concentration was less pronounced with a maximum concentration of $6.9 \cdot 10^4 \text{ cm}^{-3}$ compared to the local background value of $1.8 \cdot 10^4 \text{ cm}^{-3}$. The size-resolved number concentration shows a single mode of ultrafine particles at approximately 93 nm. The spatial distribution of deposited dust was investigated with Bergerhoff glass collection vessels, showing a decrease with distance. In the deposited dust samples the concentrations of twelve metals was determined, none of them exceeded the regional background concentrations significantly. The chemical composition of individual particles emitted by the demolition was studied by Scanning Electron Microscopy. They were mainly concrete and steel particles, with 60% calcium carbonates, 19% calcium sulfates, 19% silicates and 2% steel. In energy-dispersive X-Ray Spectroscopy, no fibers like asbestos were observed. Using a broad spectrum of instruments and methods, we obtain comprehensive characterization of the particles emitted by the demolition.

1. Introduction

Exposure to airborne particles is associated with a number of adverse health effects including cardiovascular and respiratory diseases as well as premature death (e.g. Pope & Dockery, 1999, 2006; WHO, 2006). Although biologically plausible mechanisms have been proposed, there is still considerable uncertainty about the exact pathways linking particle exposure and the observed health effects (e.g. WHO, 2006; Donaldson & Borm, 2006).

The major anthropogenic sources contributing to ambient particulate matter are traffic, power generation, industrial and waste combustion, metallurgy, domestic heating, agriculture and biomass burning (Holman, 1999; WHO, 2006; Lelieveld et al., 2015; Viana et al., 2008). On a local scale, demolition and blasting of buildings may also contribute significantly to the particle burden. For

* Corresponding author.

E-mail address: acwagner@iau.uni-frankfurt.de (A.C. Wagner).

¹ deceased.

example, it was estimated by Fuller & Green (2004) that fugitive emissions from building and road works may have been responsible for exceedance of the twenty four hours limit value of PM_{10} ($50 \mu\text{g m}^{-3}$) at 25% of the monitoring sites in and around London.

Although blasting of large buildings is taking place regularly (e.g., 23 buildings in the US in the year 2000; Beck et al., 2003), it is from a public health perspective a very rare event. However, due to the potentially high particle concentrations (despite short exposure time) and the possible release of hazardous materials (e.g., asbestos fibers, lead), blasting of large buildings is often of public concern. In addition to the direct short-term exposure to airborne particulates, longer-term exposure to the deposited dust may occur due to inhalation after re-suspension or ingestion after hand-to-mouth activities (Liroy et al., 2002; Beck et al., 2003). As a large number of people including vulnerable groups (children, the elderly, the sick) may be affected, characterization of emissions of building detonations is highly desirable. However, despite their potential adverse impacts, the data base on particulate emissions during blastings of large buildings is sparse (Beck et al., 2003; Stefani et al., 2005). The aerosol emitted after the collapse of the World Trade Center (Liroy et al., 2002; Gavett, 2006) cannot be compared directly to the former, as the blasting of buildings mostly takes place after careful removal of hazardous materials. Building demolition by mechanical disruption and the particle burden resulting thereof were recently investigated by Azarmi & Kumar (2016), Azarmi et al. (2016), Dorevitch et al. (2006) and Hansen et al. (2008).

Most studies on adverse health effects of ambient particles focus on PM_{10} or $PM_{2.5}$, because both are often measured and regulations are based on these size fractions. Ultrafine particles (diameter $< 100 \text{ nm}$) became of prime importance after it was recognized that these particles can cross the air blood barrier of the lung (e.g., Kreyling et al., 2007). Recently, the need to quantify the emission of ultrafine particles from building activities, including demolition, was emphasized by Kumar et al. (2012).

In the present contribution, a detailed characterization of the aerosol emitted from the detonation of a 116 m-high building (Afe tower) in Frankfurt am Main (Germany) on February 2nd, 2014 is presented. The Afe ("Abteilung für Erziehungswissenschaften") tower is the highest building blasted in Europe to date. About 40 000 spectators followed the event in close proximity (distance between 250 and 500 m) and thus were exposed to the large dust cloud resulting therefrom. To characterize the particles produced by the detonation, the event is assessed by different approaches. This includes measuring the size-resolved number concentration of particles as well as the mass concentration before, during and after the event. A rough spatial distribution as well as maximum spread of the pollution due to the demolition is estimated. Dust samples are analyzed for the chemical composition of individual particles as well as bulk concentration of a number of different metals. This thorough approach is expected to contribute to a better assessment of potential adverse health effects of particle exposure from the blasting of buildings.

2. Material and methods

A suite of instruments were positioned at N50.11936 E8.65316, 350 m downwind of the tower (Fig. 1), with their sampling ports

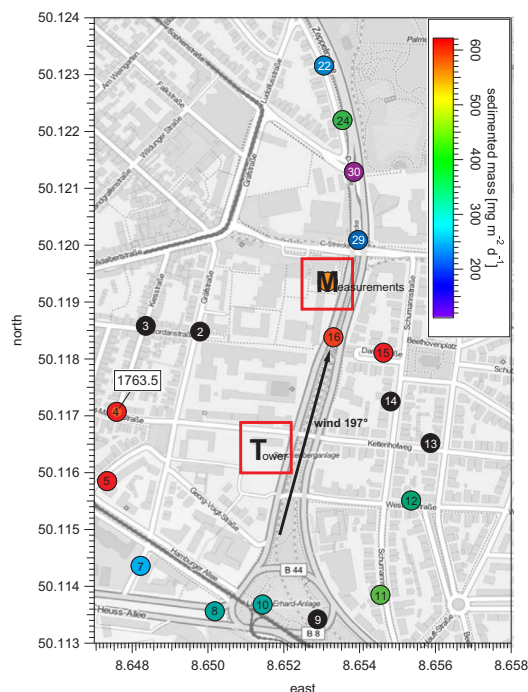


Fig. 1. Location of the blasted tower (T) at N50.11640 E8.65133 and main measurement site (M) at N50.11936 E8.65316. Circles are the positions of the Bergerhoff glass vessels as discussed in Section 3.4. The measurement of the sedimented mass is indicated by a color-code. Map: ©OpenStreetMap contributors.

2.5 to 3 m above ground. Measurements were performed for two days around the event. A Condensation Particle Counter (CPC, TSI Model 3776, TSI Incorporated, 2007; Hermann et al., 2007) measured the total number concentration starting at a cut-off diameter of 0.0025 μm . The size-resolved number concentration (Baron & Willeke, 2001) was determined by three instruments with overlapping size ranges: A Scanning Mobility Particle Sizer (SMPS, TSI Model 3080, TSI Incorporated, 2001; Wang & Flagan, 1990), an Optical Particle Counter (OPC, TSI Model 3330, TSI Incorporated, 2012b) and an Aerodynamic Particle Sizer (APS, TSI Model 3321, TSI Incorporated, 2012a; Peters et al., 2006) ranging from 0.0146 to 0.6612 μm , 0.337 to 9.016 μm and 0.542 to 19.81 μm , respectively. The mass concentration of particulate matter with an aerodynamic diameter less than 10 μm (PM_{10}) was measured by a Synchronized Hybrid Ambient Real Time Particulate Monitor (SHARP, Thermo Scientific Model 5030i, Thermo Fisher Scientific Inc. Air Quality Instruments, 2007). Furthermore, dust samples were collected on silicon wafers and analyzed by Scanning Electron Microscopy (SEM) with Energy Dispersive X-Ray Spectroscopy (EDX) (Goldstein et al., 2012) to obtain images and the chemical composition of the particles. A portable weather station (Vaisala Model WXT520) recorded meteorological parameters such as temperature, pressure, humidity, wind speed and direction. While these measurements give broad information on the particle population at this position, the spatial distribution was targeted by distributing Bergerhoff glass collection vessels around the site (Fig. 1). This method allowed obtaining a rough spatial distribution of the sedimented aerosol mass according to VDI guideline 4320 (The Association of German Engineers) and additionally was used for further chemical analyses corresponding to VDI guideline 2267.

3. Results and discussion

3.1. Overview: Total number and mass concentration

A time series of the total number concentration and the mass concentration of PM_{10} is shown in Fig. 2. The measurements were started half a day before and ended on the day after the blasting. The average background of the PM_{10} mass concentration is $27.5 \mu\text{g m}^{-3}$. The demolition event produces a high peak in the mass concentration for a short period of time. Shortly after the blasting, it rises by a factor of 30.7 and reaches a maximum value of $844.9 \mu\text{g m}^{-3}$. After 25 minutes, the mass concentration has decreased back to the background value. Note that the decrease is not primarily triggered by processes of removing particles from the atmosphere but mostly by the wind transporting the dust away from the sampling site. However, the total particle number concentration, measured by the CPC, rises only by a factor of 3.8 over the local and 2.9 over the full background. The local background is here taken as the mean concentration measured during 50 minutes before and after the blasting, excluding the peak, the full background is calculated over the full time range recorded. The highest number concentration measured while the dust cloud was present is $6.9 \cdot 10^4 \text{ cm}^{-3}$. Also, we see several short spikes in the number concentration which are higher than the increase caused by the demolition event. These are assumed to originate most likely from local traffic, e.g. diesel trucks without diesel particle filters which pass by close to the measurement site. These particles must be small in size, as they do not influence the mass concentration. Therefore, the peak from the blasting is not as prominent in the number concentration as it is in the mass concentration. This observation can be explained by the number concentration being dominated by small particles. The demolition event, however, produces comparatively fewer but larger particles (see also Section 3.2, Fig. 3), which then dominate the mass concentration.

For air quality statements, a 24-h mean is usually applied. The World Health Organization (WHO, 2000) suggests the 24-h mean of PM_{10} mass concentration not to exceed $50 \mu\text{g m}^{-3}$, which is also stated by the European Union as a maximum permissible value that should not be exceeded on more than 35 days per year (EU, 2008). As the high concentrations caused by the demolition only occurred for a very short time, they disappear in the daily mean. With $32.6 \mu\text{g m}^{-3}$ on the day of the demolition, the maximum permissible value of the EU was not exceeded.

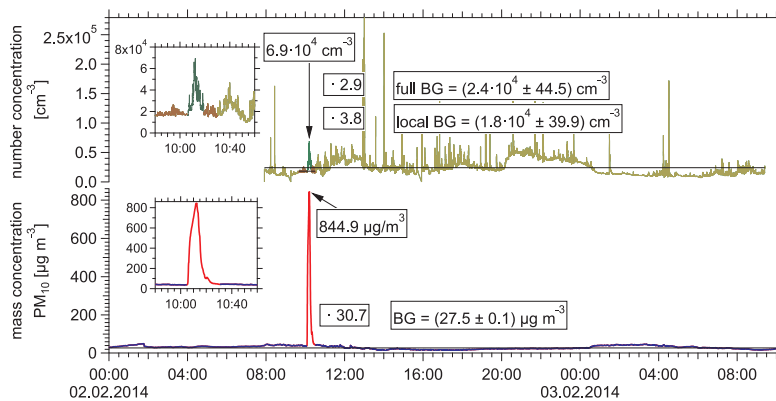


Fig. 2. Rise in number concentration (green) and mass concentration (red) occurring due to the particles from the demolition. The local and full backgrounds of the number concentration are shown in brown and light brown, the background of the mass concentration is shown in blue. The rise due to the event can clearly be seen in the mass concentration but is less pronounced in the number concentration, as number concentration is dominated by small particles which is also influenced by numerous spikes from local traffic. The blasting event however produces numerous larger particles, dominating the mass concentration.

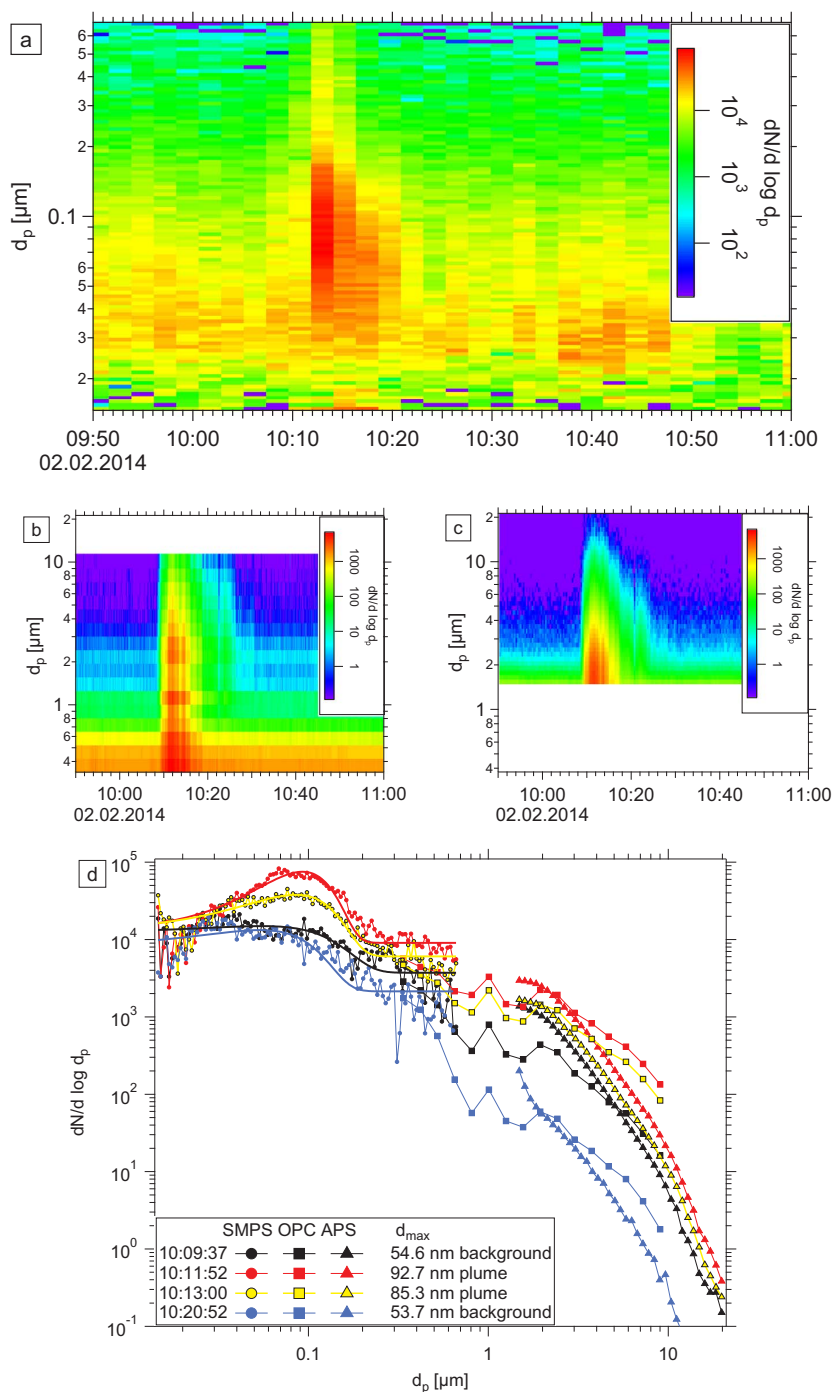


Fig. 3. Size-resolved number concentration measured by the a) SMPS, b) OPC and c) APS as time series and d) for different times around the moment of blasting. A substantial increase in particles is observed for all sizes > 40 nm. During the plume event, the number size distribution peaks at around 93 nm. Fluctuations in the OPC data are an artifact of the devices internal calculation procedure. For comparability, OPC and APS data in b) and c) are shown on equal scales.

3.2. Typical size of produced particles

The size-resolved number concentration was measured to get precise information about the particle size distribution of the aerosol produced by the demolition. Fig. 3 shows the combined size distribution measurement by the SMPS, OPC and APS instruments for different time intervals around the detonation time. The instruments show reasonable agreement in the size regions where the instrument ranges overlap. Some fluctuations of the OPC data (small peak of the concentration at 1 μm size) are most likely due to the automated method by which the device derives the concentration from the measured Mie scattering of light by the particles. Note that the aerosol sizes measured by the different techniques are not identical. While the SMPS measures the electrical mobility diameter, the size classification of the OPC relies on the optical properties of the aerosol, assuming, for example, a certain refractive index and shape. The APS measures the aerodynamic size, which depends on shape and density. Therefore, the derived sizes are strictly speaking not directly comparable without more detailed knowledge about the density, shape factor, and the optical properties of the aerosol. None of these properties is well known and therefore particle size corrections are not straightforward and have not been attempted. However, we have some information about the particle shape from the EDX (see Section 3.6) and know that they are not fibrous, which would be relevant for the sizing technique of the APS. Keeping in mind these different sizing techniques, the size distributions shown in Fig. 3 should not be interpreted as a homogeneous size distribution measurement over the entire size range, and differences in the overlapping regions may also be caused by these methodological differences.

The black symbols show the data measured at 10:10 h just before the dust cloud passes the measurement site, the red line represents maximum plume exposure and the following lines show the decrease until particle concentrations reach background level again. The size distribution of the background can be represented by a log-normal distribution with a geometric mode diameter of 54 nm. The plume then produces a log-normal mode with mode diameter of around 93 nm. Within only 10 minutes, the particles from the plume are no longer detected at the measurement site and the 50 nm mode dominates the size distribution again.

Compared to the maximum diameter occurring in the $\text{PM}_{2.5}$ range, which is by definition 2500 nm, these particles below 100 nm are very small.

3.3. Comparison of number concentrations

To cross-check the performance of the devices, size-resolved number concentrations measured by SMPS, OPC and APS are integrated and compared to the total number concentration measured by the CPC. Fig. 4 presents these concentrations for a 70 minutes time interval around the blasting. In general, the measurements show a good agreement. The CPC concentrations are systematically slightly higher. This difference can potentially be explained by the presence of ultrafine particles with sizes between 2.5 and 15 nm which are counted by the CPC (cut-off diameter of 2.5 nm) but not detected by the SMPS (smallest particles detected at 15 nm), or it is due to unaccounted losses in the SMPS system. Also, the difference is smaller at the blasting peak, which is consistent with the observation that the particles originating from the explosion are small, but yet larger than the background.

3.4. Spatial distribution

Bergerhoff glass collection vessels were distributed around the site as a low-cost method for getting a rough spatial distribution of the sedimented mass. Fig. 1 shows the measurement site with the position of tower (T) and the collection sites of the Bergerhoff vessels (circles). All other measurements took place at the point indicated with M. The vessels were positioned around the tower at a distance of approximately 300 m and along a street canyon approximately in line with the downwind direction with different distances from the site.

Comparison of the PM_{10} mass concentration with measurements from the regular air quality monitoring stations of HLUG (Hessian Agency for the Environment and Geology) allows to refine the maximum spread of the plume to less than 3.1 km in north-eastern direction and 7.9 km in western direction (see appendix C). Unfortunately, vessels 2, 3, 9, 13 and 14 had to be removed from the

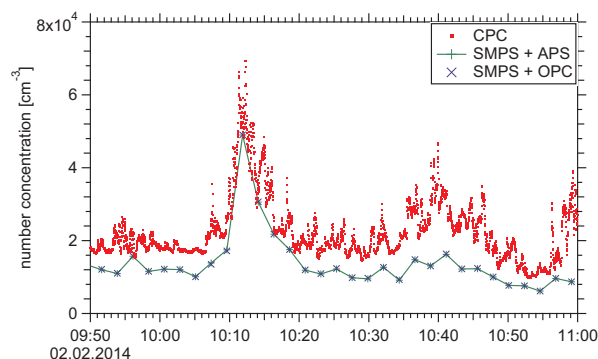


Fig. 4. Total number concentrations derived from SMPS, OPC and APS compared to CPC. They agree well regarding the lower cut-off diameter of the CPC.

Table 1

Summary statistics of chemical composition of deposition samples in which N=number of samples, LOD=limit of detection, LOQ=limit of quantification and Regional background = mean value of Frankfurt from January to June 2014.

Element	Lower quartile [$\mu\text{g g}^{-1}$]	Median [$\mu\text{g g}^{-1}$]	Upper quartile [$\mu\text{g g}^{-1}$]	N ($\leq\text{LOD}$)	N ($>\text{LOD}$, $\leq\text{LOQ}$)	N ($>\text{LOQ}$)	Regional background [$\mu\text{g g}^{-1}$]
Sb	<dl	<dl	<dl	14	0	0	14.5
As	4.7–4.9	4.7–4.9	11.4	5	8	1	5.9
Pb	53.8	67.4	80.9	0	0	14	60.7
Cd	0.81	0.81	1.76–2.27	4	9	1	0.7
Cr	70.4	108.8	155.8	0	1	13	90.6
Fe	2790	6432	10300	0	0	14	16800.4
Cu	181.4	217.4	278.4	0	0	14	207.0
Ni	41.2–45.5	58.2	67	0	7	7	42.8
Tl	0–1.6	0–1.6	1.9–4.5	13	1	0	0.3
V	5.5	14.6	30.3	3	4	7	32.3
Mn	59.8	143.1	278	0	5	9	368.8
Co	6.1	6.5	10.8	2	6	6	8.0

analysis due to breakage or contamination.

The local wind direction of 197° and wind speed of 0.74 ms^{-1} measured at point M shows that the dust cloud moved slowly along the street Senckenberganlage, which was visually observed after the detonation as well. The samples taken along that street canyon show a decrease of the mass of the settled dust as a function of distance from the demolition site as the largest particles settle closest to the demolition site. However, the locally measured wind direction is expected to be strongly influenced by the surrounding buildings. Meteorological data show the average wind direction at the time of explosion to be around 135° (south-east) which is consistent with the highest sedimented mass in vessels located to the north-west of the tower.

For a detailed interpretation of the results from the Bergerhoff vessels the exact position of the vessels must be taken into account, as small scale differences in wind speed and direction can effect sedimentation and the distribution of the dust. For example, vessel 29 was placed at a crossing with prevailing wind direction from the East, whereas vessel 24 was located in a more protected spot closer to the buildings and thus shows a higher value in comparison to vessel 29. Vessel 4 shows an extremely high sedimented mass of $1763.5 \text{ mg m}^{-2} \text{ d}^{-1}$ and was placed downwind at an exposed position in a street directly leading to the tower. The vessel M positioned directly at the main measurement site showed a sedimented mass of $564.3 \text{ mg m}^{-2} \text{ d}^{-1}$. This needs to be taken into account when interpreting the other measurements taken there: They represent the particle burden at this place, and the pollution might have been higher at other places, especially those directly in line of sight with the tower.

3.5. Chemical composition - Metals

The sediment samples from the Bergerhoff glass collection vessels were used to test for contamination with metals by chemical precipitation according to VDI guideline 2267. Table 1 shows the resulting mass fractions of different metals in the samples taken during the event and the mean of the surrounding area for January to June 2014. As a significant fraction of the deposition samples investigated contained values below detection limit or between detection limit and quantitation limit, the statistical analysis follows the recommendations given by Helsel (2011) for censored data. Summary statistics for elements with censored data was computed using nonparametric survival analysis methods. As the data set consists of interval censored data, the nonparametric maximum likelihood estimate of Turnbull (1976) was used to calculate a survival function and to determine quantiles. For the elements Pb, Fe, and Cu with all measurements above the quantitation limit (uncensored data), quantiles were determined in the conventional way. All statistical calculations were performed with R version 3.0.3 (R Core Team, 2012) and using the package “interval” (Fay & Shaw, 2010).

Compared to the surrounding area, which can be used as background, the median value of each metal shows only slightly or not enhanced mass fraction. We conclude that there are no significantly enhanced concentration of hazardous substances like arsenic or thallium in the analyzed samples.

3.6. Chemical composition and particle morphology

Dust samples from the demolition collected on silicon wafers were analyzed by Scanning Electron Microscopy (SEM) with Energy Dispersive X-Ray Spectroscopy (EDX). Out of 1330 particles, 60% were identified as calcium carbonates, 19% as calcium sulfates, 19% as silicates and 2% as steel (see exemplary images and spectra in Fig. 5). The calcium carbonate and calcium sulfate particles might also contain silicates as there is always a Si-peak in the spectrum due to the silicon wafer material and a contribution from the sample could be hidden therein. The steel material is most likely from the buildings girders. The main purpose of this analysis, however, was to determine whether or not there was an enhanced concentration of fibers in the dust from the demolition. Some fibers, such as asbestos, are known to be especially hazardous to human health (Donaldson et al., 2010). The building did contain asbestos originally, which was removed prior to the demolition. According to the World Health Organization (WHO) fibers are

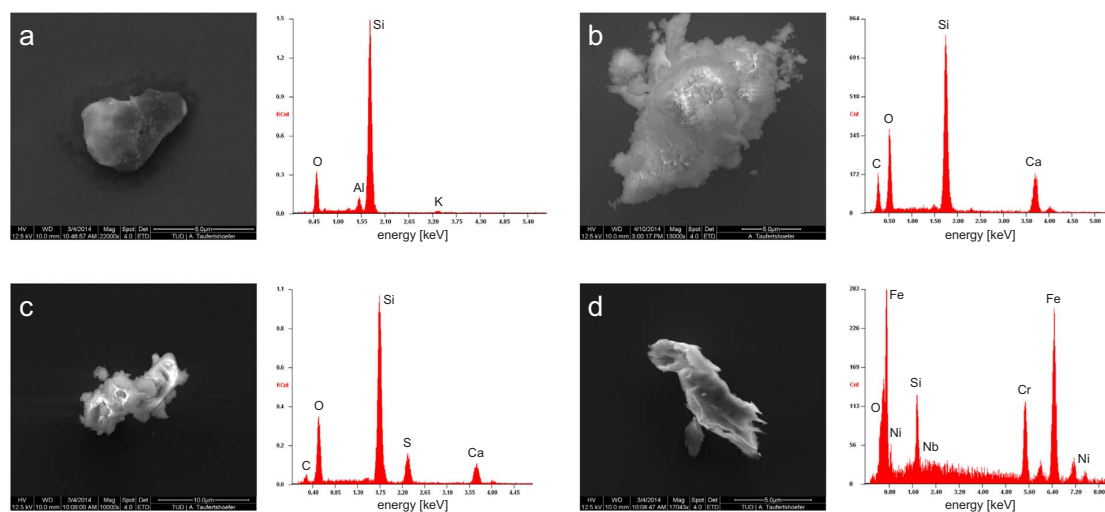


Fig. 5. Secondary electron images and corresponding energy dispersive X-ray spectra of the most abundant particle types collected on a silicon wafer during the plume at the measurement site: a) Silicate; b) Calcium carbonate (+ silicate); c) Calcium sulfate (+ silicate); and d) steel abrasion particle.

defined as particles longer than 5 μm , no thicker than 3 μm and with a length-to-width-ratio larger than 3. Two wafers from the blasting (sampled volume 2 and 6 l) as well as two wafers from the background measurement (sampled volume 10 l each) were searched, but not a single fiber was found. Thus it can be assumed that the demolition did not lead to an enhanced concentration of fibers.

4. Conclusion

We characterized particle emissions originating from a skyscraper blasting. Regarding all aspects, it can be concluded that the demolition event itself did not pose a special long-term risk.

Nevertheless, there is no lower limit of particle mass or number concentration regarding adverse health effects, thus we can only compare the particle burden to the urban background and conclude that the enhanced concentrations only strained the public for a time period shorter than 15 minutes.

Although there was a significant increase of ultrafine particles, number concentrations were not much different from other peaks in regular urban environment. Both number and mass concentrations decreased to background levels within short time. Furthermore, there was no enhancement of components with particular toxicological relevance. Heavy metals were not enriched in the deposition samples compared to regional background, so re-suspension of the deposited particles, which may occur on a longer time scale of weeks or months, did not lead to higher exposure to toxic compounds. Considering the large amounts of asbestos installed during construction of the building and the absence of fibers in our samples, the removal of this material prior to the demolition proved to be very effective. The high relative humidity on that day as well as the large water reservoirs installed in the tower for the blasting may also have helped to reduce the particle burden.

However, spectators and vulnerable people living close to the demolition site may still have experienced acute effects (e.g., irritation of the airways, triggering of asthma attacks). In addition, cleanup and transport of the debris may have lead to enhanced particle exposure as it is the case in conventional demolition work. However, this aspect is beyond the scope of the present paper.

Combining a broad spectrum of instruments and methods, we obtained a comprehensive characterization of the emitted particles, including number size distribution and chemical composition. The measurements can serve as a basis for comparison of particle emissions from continuous demolition work to those from blastings. In this way, the overall particle exposure of the public due to building demolition work can be minimized.

Acknowledgements

Funded by: German Federal Ministry of Education and Research (no. 01LK1222A), Marie Curie Initial Training Network "CLOUD-TRAIN" (no. 316662).

Appendix A–E. Supplementary data

Supplementary data associated with this article can be found in the online version at <http://dx.doi.org/10.1016/j.jaerosci.2017.06.007>.

References

- Azarmi, F., & Kumar, P. (2016). Ambient exposure to coarse and fine particle emissions from building demolition. *Atmospheric Environment*, 137, 62–79. <http://dx.doi.org/10.1016/j.atmosenv.2016.04.029>.
- Azarmi, F., Kumar, P., Marsh, D., & Fuller, G. (2016). Assessment of the long-term impacts of PM₁₀ and PM_{2.5} particles from construction works on surrounding areas. *Environmental Science: Processes & Impacts*, 18(2), 208–221. <http://dx.doi.org/10.1039/C5EM00549C>.
- Baron, P. A., & Willeke, K. (2001). *Aerosol measurement - Principles, techniques and applications*. Wiley Interscience.
- Beck, C. M., Geyh, A., Srinivasan, A., Breyse, P. N., Eggleston, P. A., & Buckley, T. J. (2003). The impact of a building implosion on airborne particulate matter in an urban community. *Journal of the Air & Waste Management Association*, 53(10), 1256–1264. <http://dx.doi.org/10.1080/10473289.2003.10466275>.
- Donaldson, K., & Borm, P. (2006). *Particle toxicology*. CRC Press.
- Donaldson, K., Murphy, F. A., Duffin, R., & Poland, C. A. (2010). Asbestos carbon nanotubes and the pleural mesothelium: A review of the hypothesis regarding the role of long fibre retention in the parietal pleura, inflammation and mesothelioma. *Part Fibre Toxicol*, 7(5), 5. <http://dx.doi.org/10.1186/1743-8977-7-5>.
- Dorevitch, S., Demirtas, H., Perksy, V. W., Erdal, S., Conroy, L., Schoonover, T., & Scheff, P. A. (2006). Demolition of high-rise public housing increases particulate matter air pollution in communities of high-risk asthmatics. *Journal of the Air & Waste Management Association*, 56(7), 1022–1032. <http://dx.doi.org/10.1080/10473289.2006.10464504>.
- EU. Directive 2008/50/ec of the european parliament and of the council of 21 may 2008 on ambient air quality and cleaner air for europe. *Official Journal of the European Union* 2008.
- Fay, M. P., & Shaw, P. A. (2010). Exact and asymptotic weighted logrank tests for interval censored data: The interval R package. *Journal of Statistical Software*, 36, 2.
- Fuller, G. W., & Green, D. (2004). The impact of local fugitive from building works and road works on the assessment of the european union limit value. *Atmospheric Environment*, 38(30), 4993–5002. <http://dx.doi.org/10.1016/j.atmosenv.2004.06.024>.
- Gavett, S. H. (2006). Physical characteristics and health effects of aerosols from collapsed buildings. *Journal of Aerosol Medicine*, 19(1), 84–91. <http://dx.doi.org/10.1089/jam.2006.19.84>.
- Goldstein J., Newbury D., Echlin P., Joy D., Romig A., Lyman C., Fiori C., Lifshin E. (2012). Scanning Electron Microscopy and X-Ray Microanalysis: A Text for Biologists, Materials Scientists, and Geologists. Springer US, volume 2.
- Hansen, D., Blahout, B., Benner, D., & Popp, W. (2008). Environmental sampling of particulate matter and fungal spores during demolition of a building on a hospital area. *Journal of Hospital Infection*, 70(3), 259–264. <http://dx.doi.org/10.1016/j.jhin.2008.07.010>.
- Helsel D.R. (2011). Statistics for censored environmental data using Minitab and R. John Wiley & Sons, volume 77.
- Hermann, M., Wehner, B., Bischof, O., Han, H. S., Krinke, T., Liu, W., Zerrath, A., & Wiedensohler, A. (2007). Particle counting efficiencies of new TSI condensation particle counters. *Journal of Aerosol Science*, 38(6), 674–682. <http://dx.doi.org/10.1016/j.jaerosci.2007.05.001>.
- Holman, C. (1999). Sources of air pollution. *Air Pollution and Health*, 116, 148.
- Kreyling W.G., Möller W., Semmler-Behnke M., Oberdörster G., Donaldson K., Borm P. (2007). Particle dosimetry: deposition and clearance from the respiratory tract and translocation towards extrapulmonary sites. *Particle toxicology*.
- Kumar, P., Mulheron, M., Fisher, B., & Harrison, R. M. (2012). New directions: Airborne ultrafine particle dust from building activities—a source in need of quantification. *Atmospheric Environment*, 56, 262–264. <http://dx.doi.org/10.1016/j.atmosenv.2012.04.028>.
- Lelieveld, J., Evans, J., Fnais, M., Giannadaki, D., & Pozzer, A. (2015). The contribution of outdoor air pollution sources to premature mortality on a global scale. *Nature*, 525(7569), 367–371. <http://dx.doi.org/10.1038/nature15371>.
- Lioy P.J., Weisel C.P., Millette J.R., Eisenreich S., Vallero D., Offenber J., Buckley B., Turpin B., Zhong M., Cohen M.D. (2002). Characterization of the dust/smoke aerosol that settled east of the World Trade Center (WTC) in lower manhattan after the collapse of the WTC 11 september 2001. *Environmental Health Perspectives* 110(7) (p. 703).
- Peters, T. M., Ott, D., & O’Shaughnessy, P. T. (2006). Comparison of the grimm 1.108 and 1.109 portable aerosol spectrometer to the TSI 3321 aerodynamic particle sizer for dry particles. *Annals of Occupational Hygiene*, 50(8), 843–850. <http://dx.doi.org/10.1093/annhyg/mel067>.
- Pope, C., III, & Dockery, D. (1999). Epidemiology of particle effects. *Air Pollution and Health*, 31, 673–705.
- Pope, C. A., III, & Dockery, D. W. (2006). Health effects of fine particulate air pollution: Lines that connect. *Journal of the Air & Waste Management Association*, 56(6), 709–742. <http://dx.doi.org/10.1080/10473289.2006.10464485>.
- R Core Team. R: A language and environment for statistical computing. R Foundation for Statistical Computing, Vienna, Austria, 2012, 2014.
- Stefani, D., Wardman, D., & Lambert, T. (2005). The implosion of the calgary general hospital: Ambient air quality issues. *Journal of the Air & Waste Management Association*, 55(1), 52–59. <http://dx.doi.org/10.1080/10473289.2005.10464605>.
- Thermo Fisher Scientific Inc., Air Quality Instruments. *Model 5030 synchronized hybrid ambient real-time particulate monitor*. 2007.
- TSI Incorporated. Model 3080-series electrostatic classifiers. 2001.
- TSI Incorporated. Model 3776 ultrafine condensation particle counter. 2007.
- TSI Incorporated. Aerodynamic particle sizer model 3321. 2012a.
- TSI Incorporated. Optical particle sizer model 3330. 2012b.
- Turnbull, B. W. (1976). The empirical distribution function with arbitrarily grouped, censored and truncated data. *Journal of the Royal Statistical Society Series B (Methodological)*, 290–295.
- VDI guideline 2267. VDI Verein Deutscher Ingenieure 2267: VDI/DIN-Handbuch Reinhaltung der Luft, Band 4: Analysen- und Messverfahren, Blatt 14/Part 14.
- VDI guideline 4320. VDI Verein Deutscher Ingenieure 4320: VDI/DIN-Handbuch Reinhaltung der Luft, Band 4: Analysen- und Messverfahren, Blatt 2/Part 2.
- Viana, M., Kuhlbusch, T., Querol, X., Alastuey, A., Harrison, R., Hopke, P., Winiwarer, W., Vallius, M., Szidat, S., & Prevot, A. (2008). Source apportionment of particulate matter in Europe: A review of methods and results. *Journal of Aerosol Science*, 39(10), 827–849. <http://dx.doi.org/10.1016/j.jaerosci.2008.05.007>.
- Wang, S. C., & Flagan, R. C. (1990). Scanning electrical mobility spectrometer. *Aerosol Science and Technology*, 13(2), 230–240. <http://dx.doi.org/10.1080/02786829008959441>.
- WHO. Air Quality Guidelines - Second Edition, Chapter 8.2. Man-made vitreous fibres. World Health Organization, 2000.
- WHO. Air quality guidelines: global update 2005: particulate matter, ozone, nitrogen dioxide, and sulfur dioxide. WHO Regional Office for Europe, Copenhagen, Denmark: World Health Organization, 2006.

Characterization of Aerosol Particles
Produced by a Skyscraper Demolition by Blasting

-

Supplementary Information

Andrea C. Wagner^{1,a}, Anton Bergen^a, Sophia Brilke^a, Bertram Bühner^a,
Martin Ebert^c, Werner Haunold^{†a}, Martin Heinritzi^a, Stephan Herzog^a, Stefan
Jacobi^b, Andreas Kürten^a, Felix Piel^a, Alfons Ramme^b, Daniel Weber^a,
Stephan Weinbruch^c, Joachim Curtius^a

^a*Institute for Atmospheric and Environmental Sciences,
Goethe University Frankfurt, Frankfurt am Main, Germany*

^b*Hessian Agency for the Environment and Geology, Wiesbaden, Germany*

^c*Institute for Applied Geosciences,
Technical University of Darmstadt, Darmstadt, Germany*

1 To support the data and conclusions of the main paper, the complete dataset is
2 shown here, including Appendix A, meteorological data taken by the portable
3 weather station and Appendix B, the size-resolved number concentration mea-
4 sured by SMPS, OPC and APS. Supplementary information Appendix C is an
5 estimation of the maximum spread of the plume, Appendix D is the chemical
6 analysis of the sediment samples and Appendix E an Ice Nuclei analysis.

¹Corresponding author. E-mail: acwagner@iau.uni-frankfurt.de

²†deceased

7 Appendix A. Meteorological Data

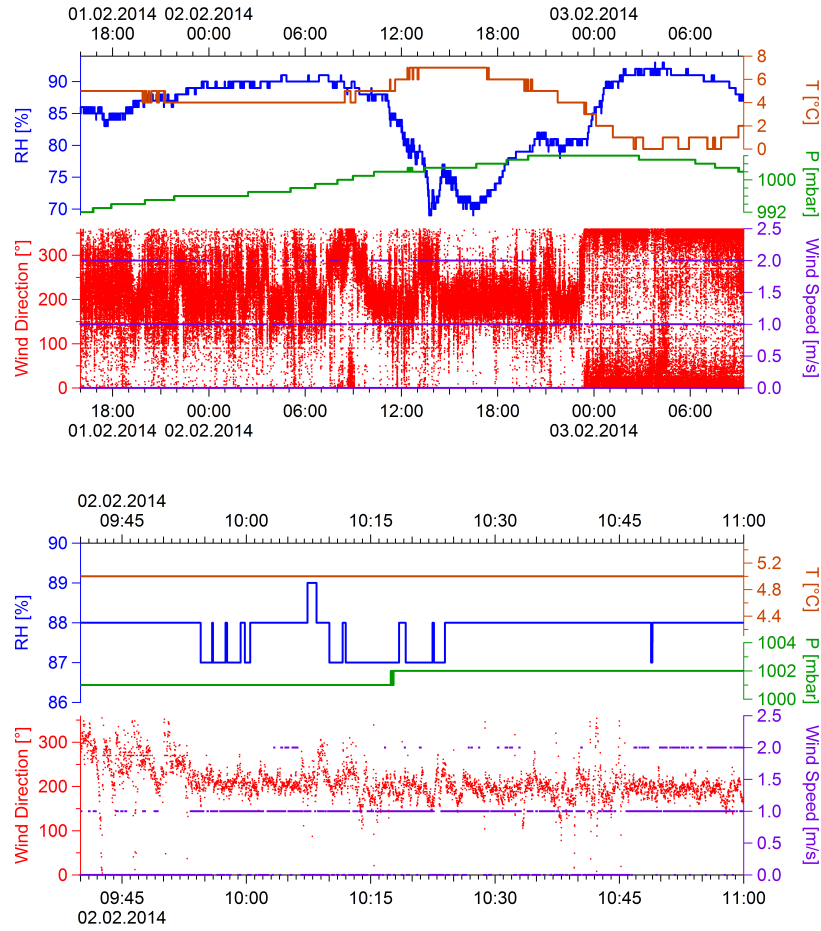


Figure A.1: Meteorological data from the day of the blasting. Shortly after the blasting, the local wind direction (red) was 197° with a wind speed (purple) of 0.74 m s^{-1} . The relative humidity (blue) was 87%, the temperature (brown) about 5° and the pressure (green) 1001.7 mbar.

8 Appendix B. Size-Resolved Number Concentration

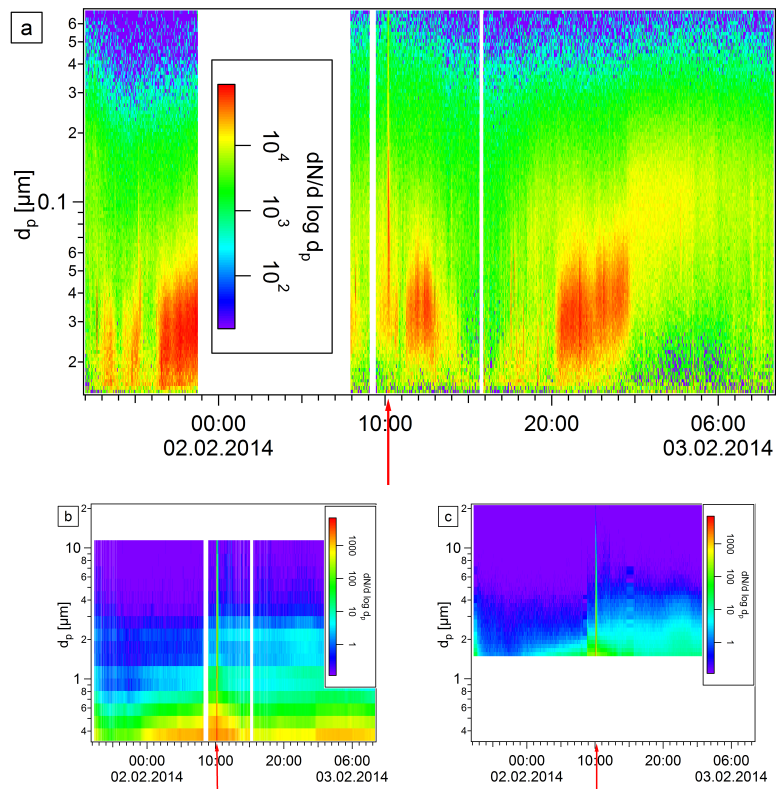


Figure B.1: Size-resolved number concentration measured by a) SMPS b) OPC and c) APS. For larger particle diameters (OPC and APS), the blasting is dominant, whereas the smaller sizes (SMPS) have a higher background. For comparability, OPC and APS data are shown on equal scales.

9 Appendix C. Maximum Spread

10 The PM_{10} mass concentration data taken at the measurement site near the
 11 tower were compared to data from regular air quality monitoring stations of
 12 HLUG (Hessian Agency for the Environment and Geology) in Frankfurt. The
 13 stations “Friedberger Landstraße” (50.125656 8.693006, northeast of the tower),
 14 “Höchst” (50.102906 8.542172, west) and “Ost” (50.126914 8.748594, east),
 15 which are 3.148 km, 7.936 km and 7.040 km linear distance from the tower,
 16 respectively, show a similar diurnal variation, but the blasting cannot be seen.
 17 Thus, this can be used to estimate a maximum spread of the particles from
 18 the blasting. The enhanced concentrations spread no further than 3.148 km
 19 north-east direction and 7.936 km in west direction.

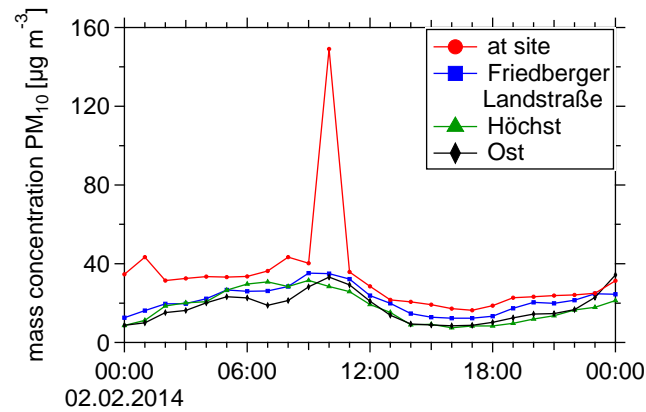


Figure C.1: PM_{10} mass concentrations at the measurement site near the tower (red), compared to “Friedberger Landstraße” (blue), “Höchst” (green) and “Ost” (black) in 30 minute time resolution. The stations further away from the tower show no detectable enhancement in concentration due to the blasting.

20 Appendix D. Chemical Composition - Metals

Element	Sample M	Sample 4	Sample 5	Sample 7	Sample 8	Sample 10	Sample 11
Sb	12.5	4.0	11.4	25.0	20.8	20.8	16.1
As	9.1	11.4	9.1	10.0	9.1	8.3	6.5
Pb	81.4	71.2	84.4	79.1	54.0	51.9	46.8
Cd	0.9	0.8	0.7	1.5	1.6	1.2	1.1
Cr	66.2	131.5	88.9	108.8	68.6	171.6	314.9
Fe	8018.8	16928.0	10489.0	4192.6	3330.2	2610.4	2280.6
Cu	207.7	89.9	101.7	390.3	224.7	178.5	458.9
Ni	50.8	61.6	37.7	87.4	48.1	88.2	161.3
Tl	5.0	1.6	4.5	10.0	8.3	8.3	6.5
V	14.6	32.7	21.7	10.0	12.4	9.4	6.5
Mn	205.6	406.0	278.0	85.2	81.2	66.6	50.6
Co	6.1	15.9	11.2	3.5	4.2	3.2	3.0
total mass	564.3	1763.5	620.8	282.2	338.6	338.6	437.4

Element	Sample 12	Sample 15	Sample 16	Sample 22	Sample 24	Sample 29	Sample 30
Sb	19.2	11.4	11.6	20.8	29.4	4.9	16.7
As	7.7	7.6	10.8	12.4	18.2	4.3	6.7
Pb	53.7	61.0	79.3	117.8	138.1	28.8	63.6
Cd	1.2	0.8	0.8	1.6	2.7	1.0	3.3
Cr	130.0	70.4	89.7	155.8	165.3	31.6	115.8
Fe	2594.2	9715.9	15680.0	9744.8	19676.0	2393.5	4844.2
Cu	229.7	261.4	190.2	210.2	409.4	77.2	284.1
Ni	74.1	42.5	58.2	73.3	109.3	21.8	67.0
Tl	7.7	4.5	4.7	8.3	11.8	3.7	6.7
V	7.7	47.9	30.3	20.2	41.6	5.5	8.9
Mn	43.8	253.0	433.0	229.9	555.0	59.8	143.1
Co	2.7	6.5	10.8	5.6	12.2	1.6	5.2
total mass	366.8	620.8	606.7	239.8	423.3	211.6	183.4

Table D.1: Chemical composition of deposition samples. Mass fractions of elements in $\mu\text{g g}^{-1}$. Total mass in $\text{mg m}^{-2} \text{d}^{-1}$. Sample M was taken directly at the main measurement site.

21 Appendix E. Ice Nuclei

22 The ice nuclei counter FRIDGE (Klein et al. (2010)) was used to study the
 23 particles ice nucleation ability in deposition mode. Therefore, aerosol particles
 24 were collected on silicon wafers before, during and after the skyscraper blasting
 25 (wafers 1 + 2, 3 + 4 and 5, respectively). Afterwards the sample was analyzed
 26 in the FRIDGE chamber, where it was exposed to a temperature of -18°C and
 27 a stepwise increased relative humidity of 111% - 118% with respect to ice. The
 28 absolute number of activated ice nuclei as well as the ice nuclei concentration
 29 were not significantly increased in the samples from the blasting (fig. E.1). The
 30 measurement suggests that the particles from the blasting do not generate ice
 31 nucleation under the analyzed conditions, thus the blasting apparently did not
 32 affect the ice nuclei concentration.

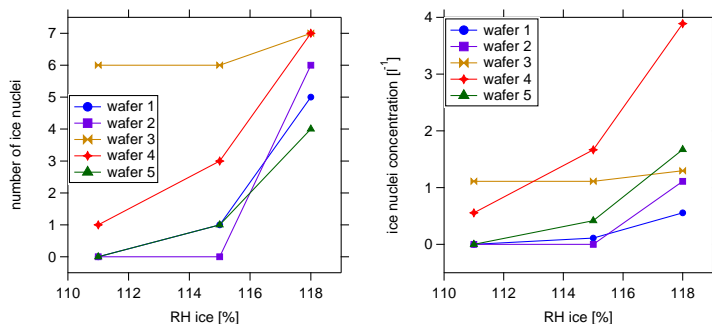


Figure E.1: Number of ice nuclei per sample and ice nuclei concentration under different relative humidities with respect to ice. Wafers 1, 2 and 5 are samples with background aerosol, wafers 3 and 4 contain aerosol from the blasting. The samples taken during the blasting do not show significantly enhanced ice nuclei concentration compared to background.

33 References

34 Klein H, Haunold W, Bundke U, Nillius B, Wetter T, Schallenberg S, Bingemer
 35 H. A new method for sampling of atmospheric ice nuclei with subsequent
 36 analysis in a static diffusion chamber. *Atmospheric Research* 2010;96(23):218–
 37 24.

4.3 Observation of new particle formation and measurement of sulfuric acid, ammonia, amines and highly oxidized organic molecules at a rural site in central Germany (Kürten et al. (2016))

Atmos. Chem. Phys., 16, 12793–12813, 2016
www.atmos-chem-phys.net/16/12793/2016/
doi:10.5194/acp-16-12793-2016
© Author(s) 2016. CC Attribution 3.0 License.



Atmospheric
Chemistry
and Physics
Open Access
EGU

Observation of new particle formation and measurement of sulfuric acid, ammonia, amines and highly oxidized organic molecules at a rural site in central Germany

Andreas Kürten, Anton Bergen, Martin Heinritzi, Markus Leiminger, Verena Lorenz, Felix Piel, Mario Simon, Robert Sitals, Andrea C. Wagner, and Joachim Curtius

Institute for Atmospheric and Environmental Sciences, Goethe University Frankfurt, Frankfurt am Main, Germany

Correspondence to: Andreas Kürten (kuernten@iau.uni-frankfurt.de)

Received: 5 April 2016 – Published in Atmos. Chem. Phys. Discuss.: 6 June 2016

Revised: 26 September 2016 – Accepted: 27 September 2016 – Published: 14 October 2016

Abstract. The exact mechanisms for new particle formation (NPF) under different boundary layer conditions are not known yet. One important question is whether amines and sulfuric acid lead to efficient NPF in the atmosphere. Furthermore, it is not clear to what extent highly oxidized organic molecules (HOMs) are involved in NPF. We conducted field measurements at a rural site in central Germany in the proximity of three larger dairy farms to investigate whether there is a connection between NPF and the presence of amines and/or ammonia due to the local emissions from the farms. Comprehensive measurements using a nitrate chemical ionization–atmospheric pressure interface time-of-flight (CI-API-TOF) mass spectrometer, a proton-transfer-reaction mass spectrometer (PTR-MS), particle counters and differential mobility analyzers (DMAs), as well as measurements of trace gases and meteorological parameters, were performed. We demonstrate here that the nitrate CI-API-TOF is suitable for sensitive measurements of sulfuric acid, amines, a nitrosamine, ammonia, iodic acid and HOMs. NPF was found to correlate with sulfuric acid, while an anti-correlation with RH, amines and ammonia is observed. The anti-correlation between NPF and amines could be due to the efficient uptake of these compounds by nucleating clusters and small particles. Much higher HOM dimer (C_{19}/C_{20} compounds) concentrations during the night than during the day indicate that these HOMs do not efficiently self-nucleate as no nighttime NPF is observed. Observed iodic acid probably originates from an iodine-containing reservoir substance, but the iodine signals are very likely too low to have a significant effect on NPF.

1 Introduction

The formation of new particles from gaseous compounds (nucleation) produces a large fraction of atmospheric aerosol particles (Zhang et al., 2012). While the newly formed particles have diameters between 1 and 2 nm, they can grow and reach larger sizes, which enables them to act as cloud condensation nuclei (CCN, ~ 50 nm in diameter or larger). Removal processes such as coagulation scavenging due to larger pre-existing particles can be important if the growth rates (GR) for the newly formed particles are slow and/or if the coagulation sink (CS) is high. The climatic effect of nucleation depends strongly on the survival probability of the newly formed particles, i.e., if they reach CCN size or not. Model calculations indicate that nucleation can account for ca. 50 % of the CCN population globally (Merikanto et al., 2009). In addition to their climatic effect, secondary particles can also influence human health (Nel, 2005) or reduce visibility, e.g., in megacities (Chang et al., 2009).

New particle formation (NPF) is a global phenomenon and has been observed in many different environments (Kulmala et al., 2004). In most cases a positive correlation with the concentration of gaseous sulfuric acid has been observed (Sihto et al., 2006; Kuang et al., 2008). However, other trace gases besides H_2SO_4 and H_2O need to be involved in the formation of clusters, as otherwise the high particle formation rates measured in the boundary layer cannot be explained (Weber et al., 1997; Kirkby et al., 2011). One ternary compound which enhances the binary nucleation of sulfuric acid and water significantly is ammonia. However, at the relatively warm temperatures of the boundary layer the presence

12794

of ammonia is probably not sufficient for reaching the observed NPF rates when acting together with sulfuric acid and water (Kirkby et al., 2011; Kürten et al., 2016). The same applies for ion-induced nucleation (IIN); the observed IIN rates for the binary and ternary system including ammonia are not high enough to explain the observations (Kirkby et al., 2011). Therefore, recent nucleation experiments have focused on organic compounds acting as a ternary compound (besides H_2SO_4 and H_2O). Many studies indicate that amines have a very strong enhancing effect on nucleation (Kurtén et al., 2008; Chen et al., 2012; Glasoe et al., 2015). Indeed, a chamber experiment was able to show that the nucleation of sulfuric acid, water and dimethylamine (DMA) at 5 °C and 38 % RH produced particles at a rate which is compatible with atmospheric observations in the boundary layer over a relatively wide range of sulfuric acid concentrations (Almeida et al., 2013). For sulfuric acid concentrations $< 10^7$ molecules cm^{-3} , which is typical for the boundary layer, and dimethylamine mixing ratios of $> \sim 10$ pptv, nucleation was found to proceed at or close to the kinetic limit. This means that every collision between sulfuric acid molecules and clusters associated with DMA leads to a larger cluster which does not evaporate significantly (Kürten et al., 2014).

In principle, mass spectrometry using nitrate chemical ionization could be used to detect neutral clusters consisting of sulfuric acid and bases in the atmosphere. However, only a few studies indicate that neutral nucleating atmospheric clusters consist of sulfuric acid and ammonia or amines (Zhao et al., 2011; Jiang et al., 2011), while other studies could not identify such clusters (Jokinen et al., 2012; Sarnela et al., 2015). A further outstanding issue is the question about the magnitude of the atmospheric amine mixing ratios at different locations. In the past several years, experimental tools for sensitive online measurement of amines in the pptv range have become available (Hanson et al., 2011; Yu and Lee, 2012). The reported amine levels reach from up to tens of pptv (Hanson et al., 2011; Freshour et al., 2014; You et al., 2014; Hellén et al., 2014) to < 0.1 pptv (Sipilä et al., 2015). An important question is therefore whether some of the reported mixing ratios could be biased high or low due to instrumental issues, or whether the natural variability in the amine mixing ratios due to different source strengths can explain the differences.

Other possible contributors to particle formation are highly oxidized organic compounds (HOMs) originating, for example, from the reaction of monoterpenes with atmospheric oxidants (Zhao et al., 2013; Ehn et al., 2014; Riccobono et al., 2014; Jokinen et al., 2015; Kirkby et al., 2016; Bianchi et al., 2016). From this perspective it seems likely that different nucleation pathways are possible and may dominate at different sites depending, for example, on the concentration of sulfuric acid, amines, oxidized organic compounds and other parameters such as temperature and relative humidity. Synergistic effects are also possible; for example, it

A. Kürten et al.: Observation of new particle formation

has been demonstrated that the combined effect of ammonia and amines can lead to more efficient particle formation with sulfuric acid and water than for a case where ammonia is not present (Glasoe et al., 2015). Due to the manifold possibilities for nucleation and the low concentrations of the growing clusters, it is challenging to identify the dominant particle formation pathway from field measurements in an environment where many possible ingredients for nucleation are present at the same time. However, such measurements are necessary and previous measurements from Hyytiälä, Finland, underscored the importance of sulfuric acid, organic compounds and amines regarding NPF (Kulmala et al., 2013).

In this study, we have chosen to conduct measurements with an emphasis on the observation of NPF at a rural site in central Germany. The goal of this field campaign was to measure NPF in an amine-rich environment in the vicinity of dairy farms, as cows are known to emit a variety of different amines as well as ammonia (Schade and Crutzen, 1995; Ge et al., 2011; Sintermann et al., 2014). The measurements were performed using different particle counters and particle size analyzers as well as trace gas (O_3 , SO_2 and NO_x) monitors. A proton-transfer-reaction mass spectrometer (PTR-MS) is used to determine the gas-phase concentration of monoterpenes and isoprene, whereas a chemical ionization time-of-flight mass spectrometer using nitrate primary ions (Jokinen et al., 2012; Kürten et al., 2014) is used for the measurement of sulfuric acid, amines, ammonia and highly oxidized organics.

2 Methods and measurement site description

2.1 Measurement site description

The measurement site is located right next to a meteorological weather station operated by the German Weather Service (DWD measurement station Michelstadt-Vielbrunn/Odenwald; 49°43′04.4″ N, 09°05′58.9″ E; 452 m a.s.l.). The village of Vielbrunn has a total of ~ 1300 inhabitants and is surrounded by fields and forests. The next larger cities are Darmstadt (~ 35 km to the WNW) and Frankfurt am Main (~ 50 km to the NNW). The site was chosen for several reasons: (i) three larger dairy farms are close by, which should possibly enable us to study the effect of amines on NPF; (ii) it can be regarded as typical for a rural or agricultural area in central Europe; (iii) the site is not too far away from the University of Frankfurt, which allowed for the station to be visited for instrument maintenance on a daily basis; and (iv) since we could measure right next to a meteorological station, infrastructure and meteorological data from the DWD could be used.

In terms of studying the effect of amines on NPF, we were expecting to see a direct effect due to the local emissions from the dairy farms. Each of these farms keeps a few hun-

A. Kürten et al.: Observation of new particle formation

12795

dred cows in shelters, which essentially consist of only a roof and a fence, such that the wind can easily carry away the emissions. As mentioned in the introduction, livestock are known to emit a variety of amines as well as ammonia (Schade and Crutzen, 1995; Sintermann et al., 2014), both of which should have an influence on NPF and growth (Almeida et al., 2013; Lehtipalo et al., 2016). The farms are located in the west (~ 450 m distance), south-southwest (~ 1100 m distance) and southeast (~ 750 m distance) of the station.

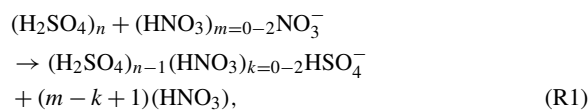
One further aspect that should be considered is the fact that the site is also surrounded by forests (mixed type of coniferous and deciduous trees, at least 1 km away). Consequently, emissions of, for example, monoterpenes ($C_{10}H_{16}$ compounds) can also potentially influence NPF as recent studies indicate that their oxidation products can contribute to NPF and particle growth (Schobesberger et al., 2013; Riccobono et al., 2014; Ehn et al., 2014; Kirkby et al., 2016).

2.2 CI-APi-TOF

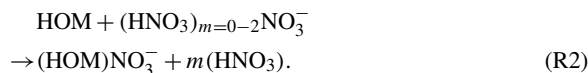
The key instrument for the data discussed in this study is the chemical ionization–atmospheric pressure interface time-of-flight mass spectrometer (CI-APi-TOF). The instrument was first introduced by Jokinen et al. (2012), and the one used in the present study is described by Kürten et al. (2014). The CI-APi-TOF draws a sample flow of 8.5 slm (standard liters per minute), which interacts with nitrate primary ions ($(HNO_3)_{0-2}NO_3^-$) within an ion reaction zone at ambient pressure (~ 50 ms reaction time). The primary ions are generated from the interaction of HNO_3 in a sheath gas and a negative corona discharge (Kürten et al., 2011). The ion source is based on the design by Eisele and Tanner (1993) for the measurement of sulfuric acid. The primary and product ions are drawn into the first stage of a vacuum chamber through a pinhole (~ 350 μ m diameter). Quadrupoles in the first and a second stage of the chamber, operated in rf-only mode, are used to guide the ions. A lens stack in a third stage focuses and prepares the ions energetically before they enter the time-of-flight mass spectrometer (Aerodyne Research Inc., USA, and Tofwerk AG, Switzerland). This mass spectrometer has a mass resolving power of ~ 4000 Th/Th and a mass accuracy of better than 10 ppm. These characteristics allow the elemental identification of unknown ions – i.e., different species with the same nominal (integer) m/z ratio can be separated due to their mass defect. Using isotopic patterns for an expected ion composition supports the ion identification. For the data analysis the software tofTools (Junninen et al., 2010) is used within the Matlab environment.

Previous work has shown that the CI-APi-TOF can be used for highly sensitive measurements of sulfuric acid (Jokinen et al., 2012), clusters of sulfuric acid and dimethylamine (Kürten et al., 2014), organic compounds with very low volatility (Ehn et al., 2014) and dimethylamine (Simon et al., 2016). Sulfuric acid and its clusters can be detected after do-

nating a proton to the primary ions, i.e.,



whereas the low-volatility organic compounds (HOMs) are detected after clustering with NO_3^- , i.e.,



In both Reactions (R1) and (R2) the presence of water has been neglected for simplicity. The measurement of amines is possible because they can be associated with nitrate cluster ions (Sect. 3.6). Generally, the quantification of a substance is derived with the following equation:

$$\text{concentration} = C \cdot \ln \left(1 + \frac{\sum \text{product ion count rates}}{\sum \text{primary ion count rates}} \right). \quad (1)$$

Equation (1) relates the sum of the product ion count rates to the sum of the primary ion count rates. Using a calibration constant C , the concentration of a neutral substance can be determined. In the case of the sulfuric acid concentration ($[H_2SO_4]$) the product ion count rates are due to HSO_4^- and $(HNO_3)HSO_4^-$, while the primary ion count rates include NO_3^- , $(HNO_3)NO_3^-$ and $(HNO_3)_2NO_3^-$. The calibration constant has been determined as 6×10^9 molecules cm^{-3} (Kürten et al., 2012).

The same calibration constant has also been used for the quantification of HOMs. However, in this case the mass dependent transmission of the CI-APi-TOF was taken into account by the method of Heinritzi et al. (2016). This requires an additional correction factor in Eq. (1), which is around 0.4 for the m/z range 300 to 400 Th and 0.22 for the range 500 to 650 Th; these factors take into account only the transmission as a function of the m/z value, while assuming the same ionization efficiency as for sulfuric acid, which has been shown to be a valid assumption by Ehn et al. (2014). The quantification of amines will be detailed in Sect. 3.6. Table 1 gives an overview of the identified ion signals used in the further analysis evaluating sulfuric acid monomer and dimer concentrations as well as amine, nitrosamine, ammonia and iodic acid signals (further explanations will be given in the following sections).

Regarding the loss of sample molecules within the inlet line of the CI-APi-TOF, we expect only a minor effect. As the sample line has a total length around 1 m, a very high flow rate was applied over most of the inlet length (Berresheim et al., 2000). Only for the last ~ 15 cm was the flow of 8.5 slm applied when taking the sample from the central part of the first inlet stage, where the inlet has a significantly larger diameter (5 cm instead of 1 cm for the last part) to avoid wall contact of the relevant portion of the sampled air.

12796

A. Kürten et al.: Observation of new particle formation

Table 1. List of ions used in the identification of sulfuric acid (monomer and dimer), iodic acid, ammonia, amines (C₁, C₂, C₃, C₄ and C₆) and dimethylnitrosamine. Cattle farms in the vicinity of the measurement site are expected to be a source for the listed amines (Ge et al., 2011).

Ion	Exact mass	Neutral compound
HSO ₄ ⁻ , (HNO ₃)HSO ₄ ⁻	96.9601, 159.9557	sulfuric acid monomer
(H ₂ SO ₄)HSO ₄ ⁻ , (HNO ₃)(H ₂ SO ₄)HSO ₄ ⁻	194.9275, 257.9231	sulfuric acid dimer
IO ₃ ⁻ , (H ₂ O)IO ₃ ⁻ , (HNO ₃)IO ₃ ⁻	174.8898, 192.9003, 237.8854	iodic acid
(NH ₃)(HNO ₃) _{1,2} NO ₃ ⁻	142.0106, 205.0062	ammonia
(CH ₅ N)(HNO ₃) _{1,2} NO ₃ ⁻	156.0262, 219.0219	C ₁ amines (e.g., methylamine)
(C ₂ H ₇ N)(HNO ₃) _{1,2} NO ₃ ⁻	170.0419, 233.0375	C ₂ amines (e.g., ethylamine, dimethylamine)
(C ₃ H ₉ N)(HNO ₃) _{1,2} NO ₃ ⁻	184.0575, 247.0532	C ₃ amines (e.g., trimethylamine, propylamine)
(C ₄ H ₁₁ N)(HNO ₃) _{1,2} NO ₃ ⁻	198.0732, 261.0688	C ₄ amines (e.g., diethylamine, butylamine)
(C ₆ H ₁₅ N)(HNO ₃) _{1,2} NO ₃ ⁻	226.1045, 289.1001	C ₆ amines (e.g., triethylamine)
(C ₂ H ₆ N ₂ O)(HNO ₃) _{1,2} NO ₃ ⁻	199.0320, 262.0277	dimethylnitrosamine

2.3 PTR-MS

Volatile organic compounds (VOCs) were measured with a calibrated proton-transfer-reaction mass spectrometer (PTR-MS) using a quadrupole mass spectrometer, IONICON GmbH, Innsbruck, Austria). The instrument inlet was heated to 60 °C and the same temperature was applied to the ion drift tube. The drift tube was operated at an E/N of 126 Td in order to minimize the formation of protonated water clusters while maintaining a high sensitivity (E/N is the ratio between the electric field strength E in $V\text{ cm}^{-1}$ and the number density N of gas molecules in cm^{-3} ; see Blake et al., 2009).

A calibration of the instrument was performed prior to the campaign with a gas mixture containing several VOCs at a known volume mixing ratio (Ionimed VOC standard, Innsbruck, Austria), including isoprene, α -pinene, and acetone, amongst others. The calibration was performed for a relative humidity range of 0 to 100 % (steps of 20 %) at room temperature. However, especially for α -pinene (measured at 81 and 137 Th), the sensitivity of the PTR-MS operating at the rather high E/N was not depending on relative humidity. For isoprene (measured at 41 and 69 Th), a higher RH led to lower fragmentation inside the instrument, but this did not affect the overall sensitivity much (<5 % decrease from 20 to 100 %).

The PTR-MS cannot readily distinguish between different monoterpenes as all have the same molecular weight, so

only the sum of monoterpenes could be measured. However, since α -pinene is often the most abundant monoterpene in continental midlatitudes (Geron et al., 2000; Janson and de Serves, 2001) and the reaction rate constants for different monoterpenes are rather similar (Tani et al., 2003; Cappellin et al., 2012), our estimation of total monoterpene concentration should not be affected by large errors.

2.4 Other instrumentation

Trace gas monitors were used to measure the mixing ratios of sulfur dioxide (model 43i TLE trace level SO₂ analyzer, Thermo Scientific), ozone (model 400 ozone monitor, Teledyne API) and nitrogen oxides (NO_x, APNA-360 ambient NO_x monitor, Horiba). These instruments were calibrated once before the campaign with known amounts of trace gases and dry zero air was applied on a daily basis for a duration of at least half an hour in order to take instrument drifts into account. The detection limits of the gas monitors are 0.05 ppbv for the SO₂ monitor (for a 5 min integration time), approximately 0.5 ppbv for the NO_x monitor and 0.5 to 1 ppbv for the O₃ monitor.

Further instruments used include condensation particle counters (CPCs) and differential mobility analyzers (DMAs). Model 3025A and 3010 CPCs (TSI, Inc.) were used to determine the total particle concentration above their cut-off sizes of 2.5 and 10 nm, respectively. A scanning mobility parti-

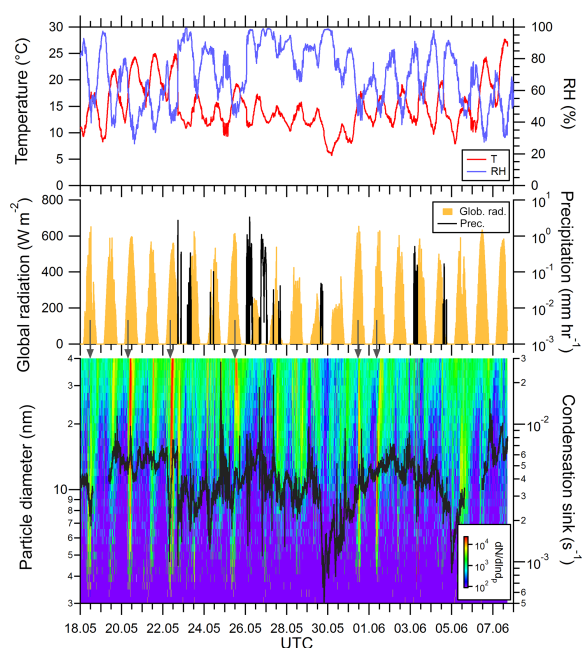


Figure 1. Overview of the different parameters measured between 18 May and 8 June 2014. Temperature (T) and relative humidity (RH) are shown in the upper panel, the center panel shows the global radiation and precipitation, and the bottom panel shows the number size distribution measured by the nano-DMA together with the condensation sink (black line). Gray arrows above the bottom panel indicate days when significant NPF was observed.

cle sizer (SMPS) from TSI (model 3081 long DMA with a model 3776 CPC) determined the particle size distribution between 16 and 600 nm. The smaller size range was covered by a nDMA (Grimm Aerosol Technik, Germany) and a TSI model 3776 CPC for diameters between 3 and 40 nm. The combined size distribution can be used to calculate the condensation/coagulation sink towards certain trace gases (e.g., sulfuric acid) or particle diameters.

Meteorological parameters were both obtained from our own measurements with a Vaisala sonde (model WXT 520), which yielded the temperature, RH, wind speed and direction, and the amount of precipitation. The same parameters are also available for the Vielbrunn meteorological station from the DWD; additionally, values for the global radiation were provided by the DWD.

3 Results

3.1 Meteorological conditions and overview

The intensive phase of the campaign was from 18 May to 7 June 2014 (21 campaign days). Figure 1 shows an overview

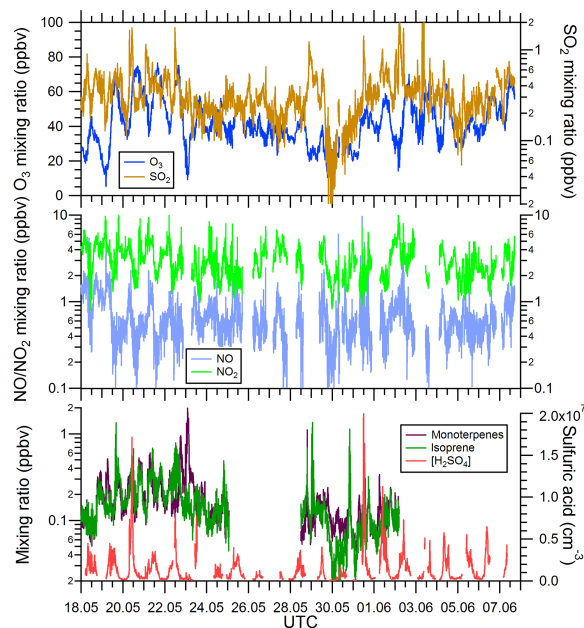


Figure 2. Overview of the trace gas measurements between 18 May and 8 June 2014. The SO_2 and O_3 mixing ratios are shown in the upper panel, the NO and NO_2 mixing ratios are shown in the center panel, and the bottom panel shows the sulfuric acid monomer concentration ($[\text{H}_2\text{SO}_4]$) together with the isoprene and monoterpene mixing ratios.

of the meteorological conditions, i.e., temperature, relative humidity, global radiation and precipitation. The size distribution of small particles (Fig. 1, bottom panel) was measured by the nDMA. In addition, the condensation sink calculated for the loss of sulfuric acid on aerosol particles is also shown taking into account the full size distribution (up to 600 nm).

The first part of the campaign (including 22 May) was characterized by warm temperatures and sunny weather without precipitation. Between 22/23 and 31 May the weather conditions were less stable with colder temperatures and some precipitation events. Especially on 29 May, a strong drop in temperature and the condensation sink was observed, due to a cold front followed by the passage of relatively clean air. From 31 May onward, temperatures increased again and it was mostly sunny, with only two rain events on 3 and 4 June.

Elevated concentrations of small particles could be observed on almost every day. However, NPF from the smallest sizes (around 3 nm) followed by clear growth were seen only on 6 days out of 21 (i.e., 29%). These events, which were also used for the calculation of NPF rates (Sect. 3.9), are highlighted in the bottom panel of Fig. 1 by the dark-gray arrows. The presence of small particles was also observed on

12798

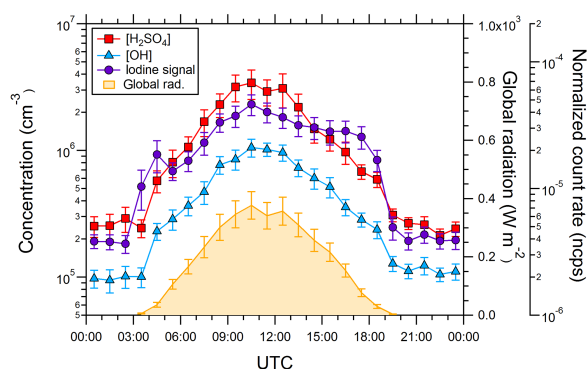


Figure 3. Diurnal averages for the sulfuric acid ($\text{[H}_2\text{SO}_4\text{]}$) and the calculated hydroxyl radical ([OH]) concentrations (axis on the left). The iodine signal is not converted into a concentration; instead, the normalized count rates per second (ncps) are shown (axis on the right). A value of 5×10^{-5} ncps for iodine would correspond to a concentration of 3×10^5 molecules cm^{-3} when applying the same conversion factor for iodic acid as for sulfuric acid. The global radiation indicates that all signals are related to photochemistry. Error bars indicate 1 standard deviation for the 30 min averaged values.

several other days; however, the events were either relatively weak or no clear particle growth was observable.

3.2 Trace gas measurements

The trace gas measurements are shown in Fig. 2. Typical maximum daytime ozone mixing ratios ranged from ~ 40 to 75 ppbv (Fig. 2, upper panel). The sulfur dioxide levels were between 0.05 and a maximum of 2 ppbv, with average values around 0.3 ppbv (Fig. 2, upper panel). Especially during the passage of clean air on 29 and 30 May, the SO_2 levels were quite low. NO_2 mixing ratios showed a distinct diurnal pattern with a minimum in the late afternoon and an average mixing ratio around 3 ppbv (Fig. 2, middle panel; see also Fig. 8). The NO mixing ratios were about a factor of 5 lower compared to NO_2 on average (Fig. 2, middle panel; see also Fig. 8); similar values were reported for another rural site in Germany (Mutzel et al., 2015). The maximum sulfuric acid concentrations were reached around noon and ranged between $\sim 1 \times 10^6$ and 2×10^7 molecules cm^{-3} (Fig. 2, lower panel; see also Fig. 3), which is comparable to other sites (Fiedler et al., 2005; Petäjä et al., 2009). The total monoterpene and isoprene mixing ratios measured by the PTR-MS were similar to each other with values between ~ 0.03 and 1 ppbv (Fig. 2, lower panel). Mixing ratios in the same range have also been reported for the boreal forest (Rantala et al., 2014).

3.3 H_2SO_4 measurement and calculation from proxies

Figure 3 shows the average diurnal sulfuric acid concentration along with other data, which will be discussed in later

A. Kürten et al.: Observation of new particle formation

sections. The maximum average $\text{[H}_2\text{SO}_4\text{]}$ around noon was $\sim 3 \times 10^6$ molecules cm^{-3} ; the error bars represent 1 standard deviation.

Recently, Mikkonen et al. (2011) introduced approximations to calculate sulfuric acid as a function of different proxies. Since the relevant parameters (sulfur dioxide mixing ratio, global radiation, relative humidity and condensation sink) are available, we have used the following formula to approximate the sulfuric acid concentration (Mikkonen et al., 2011):

$$[\text{H}_2\text{SO}_4]_{\text{proxy}} = a \cdot k(T, p) \cdot [\text{SO}_2]^b \cdot \text{Rad}^c \cdot \text{RH}^d \cdot \text{CS}^e. \quad (2)$$

The $[\text{H}_2\text{SO}_4]$ (expressed in molecules cm^{-3}) is calculated as a function of the SO_2 mixing ratio (in ppbv), the global radiation Rad (in W m^{-2}), the relative humidity RH (in %), the condensation sink CS (in s^{-1}), a rate constant k , which depends on ambient pressure p and temperature T (see definition for k by Mikkonen et al., 2011) and a scaling factor a . A least-squares fit made with the software IGOR yields the coefficients $a = 1.321 \times 10^{15}$, $b = 0.913$, $c = 0.990$, $d = -0.217$ and $e = -0.526$ (linear correlation coefficient, Pearson's r , is 0.87). Following the recommendations given by Mikkonen et al. (2011) we restricted the data used in the derivation of the parameters to conditions where the global radiation was equal or larger than 50 W m^{-2} . In addition, a simpler formulation was also tested, which neglects the dependence on RH and CS:

$$[\text{H}_2\text{SO}_4]_{\text{proxy}} = a' \cdot k(T, p) \cdot [\text{SO}_2]^{b'} \cdot \text{Rad}^{c'}. \quad (3)$$

Here, the coefficients $a' = 1.343 \times 10^{16}$, $b' = 0.786$ and $c' = 0.941$ yield good agreement (linear correlation coefficient, Pearson's r , is 0.85) between calculated and measured $[\text{H}_2\text{SO}_4]$. Figure 4 shows a comparison between the two approximation methods and the measured sulfuric acid for the full campaign (when $\text{Rad} \geq 50 \text{ W m}^{-2}$). In almost all cases the predicted 5 min averages are within a factor of 3 of the measured values for both methods. This indicates that even the simpler method (Eq. 3) can yield relatively accurate results for the conditions of this study. This is probably due to the fact that RH and CS show only relatively small variations over the duration of the campaign and it would therefore not be absolutely necessary to include these factors in the sulfuric acid calculation. Nevertheless, whenever the data are available, we recommend using the more detailed parameterization (Eq. 2) as it treats the sulfuric acid concentration calculation more rigorously. The parameters found are in good agreement with the ones reported by Mikkonen et al. (2011) for different sites.

3.4 Calculated OH

For further data evaluation, knowledge of the OH concentrations is useful. In this study the hydroxyl radical concentration is required to derive an estimated concentration of the

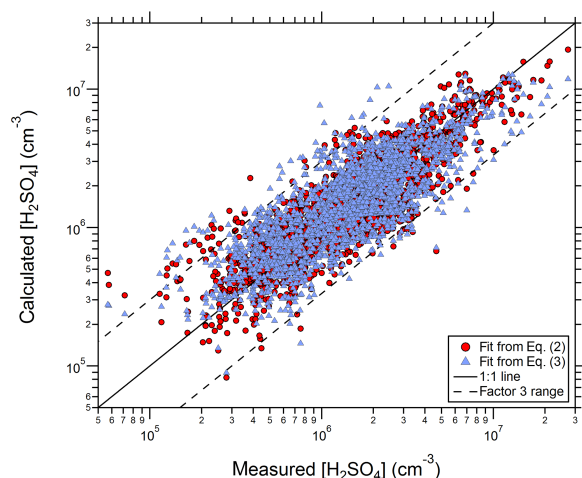


Figure 4. Calculated $[\text{H}_2\text{SO}_4]$ as a function of the measured concentrations. Only data points where the global radiation exceeded 50 W m^{-2} were considered in deriving the fit parameters for Eqs. (2) and (3). The red circles take into account SO_2 , global radiation (Rad), condensation sink (CS) and relative humidity (RH) to calculate the $[\text{H}_2\text{SO}_4]$, whereas only SO_2 and global radiation are used for the blue triangles.

iodine species OIO (Sect. 3.5) and for a comparison of conditions during nucleation and no-nucleation days (Sect. 4). Since there was no direct measurement of the hydroxyl radical available, only an estimation based on other measured parameters can be made. This estimation is based on the assumption that most of the sulfuric acid is produced from the reaction between SO_2 and OH. Using the condensation sink CS the balance equation between production and loss at steady state can be used to derive the OH:

$$[\text{OH}] = \frac{\text{CS} \cdot [\text{H}_2\text{SO}_4] - k_{X+\text{SO}_2} \cdot [X] \cdot [\text{SO}_2]}{k_{\text{OH}+\text{SO}_2} \cdot [\text{SO}_2]} \approx \frac{\text{CS} \cdot [\text{H}_2\text{SO}_4]}{k_{\text{OH}+\text{SO}_2} \cdot [\text{SO}_2]} \quad (4)$$

Recently, it was discovered that there are also other species capable of oxidizing SO_2 to SO_3 (which lead to subsequent production of H_2SO_4 due to further reactions with O_2 and H_2O ; Mauldin et al., 2012). Those species X , e.g., stabilized Criegee intermediates (sCI), can be formed via the ozonolysis of alkenes (e.g., isoprene, α -pinene, limonene; Mauldin et al., 2012; Berndt et al., 2014). Therefore, if some H_2SO_4 is generated from sCI reactions with SO_2 , then the calculated OH is an upper estimate. During the day this effect should be relatively small, i.e., $< 50\%$ (Boy et al., 2013; Sarwar et al., 2013), although Berndt et al. (2014) state that no final answer can be given regarding the effect of the sCI on the sulfuric acid formation because it depends strongly on the sCI structure and competitive reactions between sCI and water vapor. However, it should also be noted that the reaction

between alkenes and ozone generates not only sCI but also OH at significant yields (e.g., the OH yield for the reaction of α -pinene and O_3 is ca. 0.77; Forester and Wells, 2011) and that the OH produced via this mechanism is taken into account by Eq. (4). Data from Sipilä et al. (2014) further suggest that the production of sulfuric acid from sCI oxidation of SO_2 is probably minor compared to that from OH and SO_2 . For these reasons we have decided to calculate the [OH] not only for the daytime but for the full day. The derived diurnal pattern of [OH] is shown in Fig. 3 with a maximum concentration of 1×10^6 molecules cm^{-3} around noon, which is in good agreement with other studies where OH was measured directly (Berresheim et al., 2000; Rohrer and Berresheim, 2006; Petäjä et al., 2009).

3.5 Iodic acid (HIO_3) and OIO

The high-resolution CI-API-TOF mass spectra revealed the presence of iodine containing substances. It can be ruled out that these signals result from instrument contamination as our CI-API-TOF had never been in contact with iodine (i.e., no nucleation experiments with iodine have yet been performed and no iodide primary ions have been used). The observed signals could be assigned to IO_3^- , $(\text{H}_2\text{O})\text{IO}_3^-$ and $(\text{HNO}_3)\text{IO}_3^-$ (Table 1). To our knowledge the identification of iodine-related peaks has not been reported from measurements with a nitrate chemical ionization mass spectrometer (CIMS). However, Berresheim et al. (2000) reported the presence of a peak at m/z 175 in the spectrum for the marine environment, which was not identified previously but, in the light of this study, can almost certainly be attributed to IO_3^- .

The diurnal pattern of IO_3^- and the related iodine peaks show a distinct pattern with a maximum around noon following the diurnal pattern of sulfuric acid almost perfectly (Fig. 3). This may not be surprising since the formation of HIO_3 is due to reaction between OIO and OH (Saiz-Lopez et al., 2012); therefore, the iodic acid concentration is connected to the OH chemistry. After normalization of the iodic acid signals with the nitrate primary ion count rates, a concentration of the neutral compound HIO_3 can be obtained by tentatively adopting the same calibration constant for iodic acid as for sulfuric acid. Thereby a maximum average daytime concentration of $\sim 3 \times 10^5$ molecules cm^{-3} can be found. Further, using the derived OH concentrations from the H_2SO_4 and CS measurements (Sect. 3.4), the derived $[\text{HIO}_3]$ can be used to estimate the concentration of OIO (Saiz-Lopez et al., 2012):

$$[\text{OIO}] = \frac{\text{CS} \cdot [\text{HIO}_3]}{k_{\text{OH}+\text{OIO}} \cdot [\text{OH}]} \quad (5)$$

Equation (5) assumes that the only production channel of HIO_3 is the reaction between OH and OIO and the only loss mechanism of HIO_3 is the uptake on aerosol. The reaction rate $k_{\text{OH}+\text{OIO}}$ can be taken from the literature (Plane et al., 2006). In this way the concentration of OIO can be estimated

12800

to a typical value of 5×10^6 molecules cm^{-3} , which is much lower than the values reported for the marine environment (3 to 27 pptv, i.e., 7.5×10^7 to 6.8×10^8 molecules cm^{-3} ; see Saiz-Lopez et al., 2012).

The relatively low values of [HIO₃] and [OIO] probably indicate that iodine chemistry is not very important in terms of NPF at this site. This is supported by the fact that we could not observe any clusters containing, for example, sulfuric acid and iodic acid or clusters containing more than one iodine molecule. However, it is surprising that iodine can be detected more than 400 km away from the nearest coast line. On the other hand, HYSPLIT back-trajectory calculations (Stein et al., 2015) reveal that in most cases the air was arriving from westerly directions and therefore had contact with the ocean within the last 48 h before arriving at the station. During the measurement period there was unfortunately never a day where the air was clearly coming from easterly directions and had not been in contact with the Atlantic Ocean or Mediterranean Sea within the previous days. Therefore, we could not check whether this would result in lower iodine signals. Despite the marine origin of the air masses observed, it is not clear how the iodine is transported over relatively large distances without being lost on aerosol particles. If iodic acid is irreversibly lost on aerosol (similar to sulfuric acid) its lifetime should only be on the order of several minutes at typical boundary layer conditions. Therefore, the presence of iodine indicates either a local iodine source or its transport from marine environments in the form of a reservoir substance, e.g., CH₃I (the lifetime of CH₃I is in the order of 1 week; see Saiz-Lopez et al., 2015), and subsequent release due to photolysis.

Regarding the sensitivity of the CI-APi-TOF it can be said that iodic acid (and, if present, probably also its clusters) can be detected with high sensitivity. One aspect that helps in unambiguously identifying iodic acid is the high negative mass defect of the iodine atom ($\Delta m \approx -0.1$ Th). Furthermore, this also contributes to the low detection limit for this compound because generally there will not be any overlapping signals from other substances with the same integer mass (mass resolving power of the instrument is ~ 4000 Th/Th – i.e., at m/z 175 the peak width at half maximum is ~ 0.04 Th). The method introduced here therefore allows high-sensitivity measurement of [HIO₃] as well as the estimation of [OIO] with the help of Eq. (5) in future studies. The lowest detectable concentrations should be around 3×10^4 molecules cm^{-3} , or better, for [HIO₃] and 5×10^5 molecules cm^{-3} (ca. 0.02 pptv) for [OIO] when assuming the same calibration constant for HIO₃ as for H₂SO₄ and considering the lowest iodine signal from Fig. 3.

3.6 Amine, nitrosamine and ammonia measurements

The detection of dimethylamine (DMA, (CH₃)₂NH) by means of nitrate chemical ionization with a CI-APi-TOF has been described previously (Simon et al., 2016). The clus-

A. Kürten et al.: Observation of new particle formation

tering between diethylamine (DEA) and nitrate ion clusters has also been reported by Luts et al. (2011). The amines detected in the present study include CH₅N (monomethylamine), C₂H₇N (dimethylamine, DMA, or ethylamine, EA), C₃H₉N (trimethylamine, TMA, or propylamine, PA), C₄H₁₁N (diethylamine, DEA) and C₆H₁₅N (triethylamine, TEA). All of these amines are identified as clusters in the CI-APi-TOF spectra where the amines are associated with both the nitrate dimer ((amine)(HNO₃)NO₃⁻) and the trimer ((amine)(HNO₃)₂NO₃⁻).

The high mass resolving power of the CI-APi-TOF allowed the identification of five different amines (C₁, C₂, C₃, C₄ and C₆ amines; see above). Since the amines are all identified at two different masses each (with either the nitrate dimer or the nitrate trimer), plotting the time series of each pair of signals allows further verification of the amine signals since a different time trend would reveal that another ion would interfere with the amine signal. This was sometimes the case when the relative humidity was high and clusters of water and nitrate appeared with high water numbers. The cluster of NO₃⁻ and 6 water molecules has a mass of 170.0518 Th and the C₂ amine cluster (C₂H₇N)(HNO₃)NO₃⁻ (170.0419 Th) cannot be separated from this primary ion cluster. Therefore, if large nitrate plus water clusters were observed in the spectra, no C₂ amine signal could be evaluated.

The same ion cluster chemistry applies for ammonia, which can also bind with the nitrate cluster ions. Consequently, ammonia is detected as (NH₃)(HNO₃)NO₃⁻ and (NH₃)(HNO₃)₂NO₃⁻ (Table 1). To our knowledge the existence of these cluster ions has not been reported previously.

In accordance with Simon et al. (2016), the cluster ion signals have been normalized by the following relationship:

$$\text{amine}_{\text{neps}} = \ln \left(1 + \frac{\{(\text{amine})(\text{HNO}_3)\text{NO}_3^-\} + \{(\text{amine})(\text{HNO}_3)_2\text{NO}_3^-\}}{\{(\text{HNO}_3)_2\text{NO}_3^-\}} \right). \quad (6)$$

where the curly brackets denote the count rates of the different ion clusters and the same formula can be used when “amine” is replaced by NH₃ to obtain the normalized ammonia signal. The normalization with the nitrate trimer has been chosen because we think that this is the dominant nitrate ion cluster the amines (and ammonia) can bind to within the CI-APi-TOF ion reaction zone (Simon et al., 2016). Partial evaporation of one HNO₃ from the resulting amine nitrate cluster within the CI-APi-TOF vacuum chamber leads to the spread of the signal over the related masses separated by 62.9956 Th (HNO₃).

In addition to the five amines mentioned before, we were able to identify dimethylnitrosamine (NDMA, (CH₃)₂NNO) from its clusters ((CH₃)₂NNO)(HNO₃)NO₃⁻ and ((CH₃)₂NNO)(HNO₃)₂NO₃⁻ (Table 1). The signals from NDMA show a clear diurnal pattern on some days, which can be up to about 2 orders of magnitude higher during the night compared to the day. This is in agreement with the formation mechanism of NDMA via the reaction of DMA

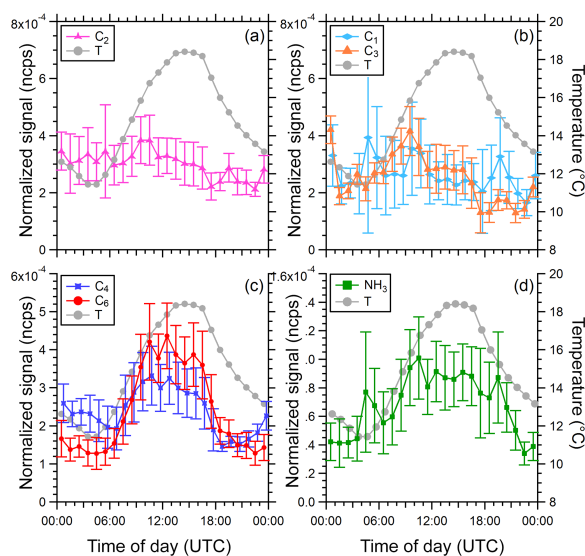


Figure 5. Diurnal averages for different amines (C_1 , C_2 , C_3 , C_4 and C_6) and ammonia. The temperature profile is shown in addition. Error bars represent 1 standard deviation of the 30 min averages. The lower detection limits for the different compounds are not well defined. However, the lowest measured signals during some periods were 0.3×10^{-4} ncps for C_1 ; $\sim 0.5 \times 10^{-4}$ ncps for C_2 , C_3 , C_4 and C_6 ; and 0.1×10^{-4} ncps for ammonia. For most of the time (and for all averaged values shown) the signals were clearly above these “background” levels.

with OH and NO (Nielsen et al., 2012). The lower concentrations during the day can be explained by the rapid photolysis rate of NDMA (Nielsen et al., 2012). Since only C_2 amines are capable of forming nitrosamines, no further nitrosamine could be identified from the mass spectra. Only a rough estimation of the mixing ratio can be provided by using the calibration constant from Simon et al. (2016) which was derived for DMA. Using this calibration constant the maximum mixing ratio of NDMA would be ~ 100 pptv (or 2.5×10^9 molecules cm^{-3}). However, this value has a high uncertainty because no direct calibration with NDMA was performed.

The average diurnal patterns of the four amines and ammonia are shown in Fig. 5. The data are an average over 21 measurement days and the error bars represent 1 standard deviation. The temperature profile is shown along with the CI-API-TOF signals. The C_4 and C_6 amines and ammonia show a distinct diurnal profile which follows the temperature profile closely. The temperature-dependent signal intensity could be due to partial re-evaporation of amines from the particulate phase. No correlation with temperature is seen for the C_1 , C_2 and C_3 amines, which could indicate efficient stabilization of these amines in the particulate phase due to acid–base reactions (Kirkby et al., 2011; Almeida et al., 2013).

No direct calibration for amines, NDMA and ammonia was performed during the campaign. Therefore, only a rough estimation of the mixing ratios can be made. Using the calibration curve for DMA by Simon et al. (2016), 1×10^{-4} ncps (normalized counts per second) corresponds to ~ 1 pptv of DMA. With this conversion the average mixing ratios are between about 1 and 5 pptv for the amines. The mixing ratios from this study are in a similar range to those reported from measurements in a southeastern US forest (You et al., 2014) but generally lower than those from three different sites in the USA (Freshour et al., 2014).

The ncps for ammonia are lower than for the amines, which should not be the case if the sensitivity towards ammonia and amines were the same because the ammonia mixing ratios are almost certainly higher than the ones for the amines in this environment. The ammonia mixing ratio can be above several ppbv in rural areas (von Bobruzki et al., 2010). Therefore, the sensitivity of the nitrate CI-API-TOF towards ammonia seems to be significantly lower than for amines. This is reasonable since other studies have found that acid–base clusters between sulfuric acid (including the bisulfate ion) and amines are much more stable compared to sulfuric acid ammonia clusters (Kirkby et al., 2011; Almeida et al., 2013). Therefore, the acid–base clustering between nitric acid (including the nitrate ion) and ammonia or amines could follow a similar rule, which would lead to faster evaporation of the ammonia nitrate clusters. For this reason, only the relative signals for ammonia can be used at the moment without providing estimated mixing ratios.

Recently, it was suggested that diamines could play an important role in ambient NPF (Jen et al., 2016a); however, we could not identify diamines from the high-resolution mass spectra.

3.7 Sulfuric acid dimer

Occasionally, the CI-API-TOF sulfuric acid dimer signal was above background levels. The dimer ($(\text{H}_2\text{SO}_4)\text{HSO}_4^-$) was identified from the high-resolution spectra on nine campaign days. The measured sulfuric acid dimer concentrations are shown as a function of the sulfuric acid monomer concentrations in Fig. 6. For comparison, CLOUD chamber data from nucleation experiments in the ternary sulfuric acid–water–dimethylamine system are included (red circles in Fig. 6; Kürten et al., 2014). In addition, the lower dashed line shows the expected dimer formation due to ion-induced clustering (IIC) of sulfuric acid monomers in the CI-API-TOF ion reaction zone (Hanson and Eisele, 2002; Zhao et al., 2010).

The data indicate that the measured dimer concentrations are clearly above the background level set by ion-induced clustering. On the other hand, the concentrations are lower than what has been measured in CLOUD for kinetic nucleation in the sulfuric acid–water–dimethylamine system at 5°C and 38 % RH (Almeida et al., 2013; Kürten et al., 2014). Clearly, the neutral sulfuric acid dimers were stabilized by a

12802

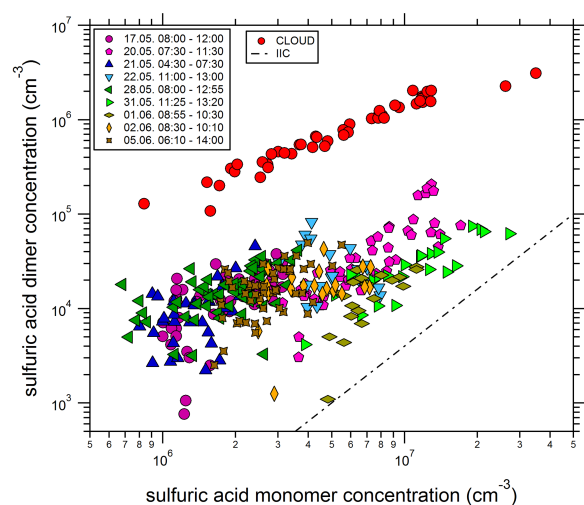


Figure 6. Sulfuric acid dimer concentrations as a function of the sulfuric acid monomer concentrations. The legend on the left lists the periods when high dimer signals were observed. In addition, data from CLOUD chamber experiments with at least 10 pptv of dimethylamine are shown; under these conditions dimer formation proceeds at or close to the kinetic limit (Kürten et al., 2014). The dashed-dotted line indicates the lower detection limit for neutral dimers set by ion-induced clustering (IIC) within the CI-API-TOF ion reaction zone.

ternary compound, as otherwise their concentrations would not have been measurable at these relatively warm conditions because the dimer (without a ternary compound) evaporation rate is quite high ($> 10^5 \text{ s}^{-1}$ at 290 K; Hanson and Lovejoy, 2006; Kürten et al., 2015). On the other hand, the ternary stabilizing agent evaporates after charging of the sulfuric acid dimers because no cluster between the sulfuric acid dimer and another compound (besides HNO_3 from the ion source) could be identified. This means that although the dimers contained at least one additional molecule in the neutral state, the ionized dimer will be detected as $(\text{H}_2\text{SO}_4)\text{HSO}_4^-$ (Ortega et al., 2014; Jen et al., 2014), which makes it impossible to identify the stabilizing agent. Only when larger clusters of sulfuric acid are present (trimer and larger) can stabilizing agents like ammonia or amines stay in the cluster after charging with the nitrate ion (Zhao et al., 2011; Kirkby et al., 2011; Ortega et al., 2014; Kürten et al., 2014). Unfortunately, no large sulfuric acid clusters (trimer and larger) were measurable during the campaign, probably because their concentrations were too low. Therefore, only speculations about the stabilizing agent responsible for the high dimer concentrations can be made. It is quite unlikely that ammonia would be the only stabilizing compound for the dimers since previous studies have shown that the relatively high dimer concentration measured at rather low sulfuric acid monomer concentrations ($< 2 \times 10^7 \text{ molecules cm}^{-3}$) cannot be explained by sulfuric

A. Kürten et al.: Observation of new particle formation

acid–ammonia–water nucleation (Hanson and Eisele, 2002; Jen et al., 2014). In addition, efficient clustering between sulfuric acid and iodic acid can probably be ruled out (provided that these compounds would be capable of producing a cluster with a low evaporation rate) as the concentrations of iodic acid are quite low ($\sim 3 \times 10^5 \text{ molecules cm}^{-3}$ at maximum; see Sect. 5). This means that the arrival rate of iodic acid on a sulfuric acid dimer is on the order of 10^{-4} s^{-1} (using a collision rate of $5 \times 10^{-10} \text{ cm}^3 \text{ molecules}^{-1} \text{ s}^{-1}$). Due to the high evaporation rate of the pure sulfuric acid dimer, no significant dimer stabilization by iodic acid can be expected.

Whether amines are responsible for the dimer formation in the present study cannot be concluded. If they were, the lower dimer concentrations compared to the CLOUD chamber results (Kürten et al., 2014) could be attributed to the higher temperatures in the present study, which result in faster evaporation rates. Another explanation would be the lower amine mixing ratios. In the CLOUD study, dimethylamine was present at 10 pptv or higher. In addition, it cannot be concluded that, for example, the measured C_2 amines are all dimethylamine; if a significant fraction of them were, for example, ethylamine, its stabilizing effect could be significantly lower. This remains somewhat speculative as no data regarding NPF from ethylamine and sulfuric acid were found; however, triethylamine was reported to have a relatively weak effect on nucleation compared to DMA or TMA (Glasoe et al., 2015). Other compounds which are present and have been shown to form new particles are HOMs (Schobesberger et al., 2013; Ehn et al., 2014; Riccobono et al., 2014), although their stabilizing effect on neutral sulfuric acid dimers remains to be elucidated.

Regarding the observations shown in Fig. 6, it should be noted that no ion filter (high-voltage electric field in the CI-API-TOF inlet to remove ambient ions) was used in the present study. This could in principle lead to the detection of ambient ions and clusters, which did not undergo charging in the CI-API-TOF ion reaction zone. If this were the case, no representative concentrations of the corresponding neutral sulfuric acid dimer would be derived. CLOUD studies reported that charged sulfuric acid monomers (HSO_4^-) and dimers ($(\text{H}_2\text{SO}_4)\text{HSO}_4^-$) could be observed with a different nitrate CIMS under some conditions (Rondo et al., 2014; Kürten et al., 2015). However, for ambient measurements, no significant effect could be observed for sulfuric acid monomers (Rondo et al., 2014). In principle, the sulfuric acid dimer could be more strongly affected by the detection of ambient ions since the neutral dimer concentration is much lower than the sulfuric acid monomer, while the negative ambient ion spectrum can be dominated by the charged sulfuric acid dimer (Eisele et al., 2006). Therefore, we cannot entirely rule out that ambient ions had some effect on the data shown in Fig. 6. However, the ambient ions would need to overcome an electric field before they could enter the ion reaction zone (Kürten et al., 2011; Rondo et al.,

A. Kürten et al.: Observation of new particle formation

12803

2014). In the CIMS and the CI-API-TOF a negative voltage is used to focus the primary ions to the center of the reaction zone, while the sample line is electrically grounded. This means negative ambient ions would need to overcome a repulsing electric field which acts as a barrier. Light ions will be efficiently deflected due to their high mobility, but heavier ions can in principle penetrate more easily. Consequently, CIMS measurements at the CLOUD chamber showed that the apparent dimer signal measured by the CIMS correlated with large ion clusters (pentamer, i.e., $(\text{H}_2\text{SO}_4)_4\text{HSO}_4^-$, and larger, which underwent subsequent fragmentation) but not with the $(\text{H}_2\text{SO}_4)\text{HSO}_4^-$ signal; the charged clusters were measured simultaneously with an API-TOF (Junninen et al., 2010; Kürten et al., 2015). The CI-API-TOF used in this study utilized a higher voltage for the ion focusing compared to the CIMS (ca. -500 V instead of -220 V in the CIMS) and should therefore prevent smaller masses even more efficiently from entering the ion source than in the study by Kürten et al. (2015). In addition, the absence of any trimer signal ($(\text{H}_2\text{SO}_4)_2\text{HSO}_4^-$) in the spectra argues against ambient ion detection. In a previous study by Eisele et al. (2006) ambient ion measurements also showed, besides signals for $(\text{H}_2\text{SO}_4)\text{HSO}_4^-$, signals for $(\text{H}_2\text{SO}_4)_2\text{HSO}_4^-$ which were on average $\sim 50\%$ of the dimer signals. Since the CI-API-TOF design, with its repulsing voltages towards ambient ions in the ion reaction zone, should be more sensitive towards the trimer than towards the dimer, the absence of sulfuric acid trimer signals argues against a significant bias in the data due to charged ambient clusters.

3.8 Highly oxidized organic molecules (HOMs)

Recently, the rapid autoxidation of atmospherically relevant organic molecules, such as isoprene and monoterpenes, was described (Crouse et al., 2013; Ehn et al., 2014). There is evidence that these HOMs are involved in the formation of secondary aerosol and can even promote the formation of new aerosol particles (Jokinen et al., 2015; Kirkby et al., 2016). Nitrate chemical ionization mass spectrometry is capable of detecting a suite of HOMs when the O:C ratio is high (e.g., $> \sim 0.6$ for C_{10} and $> \sim 0.35$ for $\text{C}_{19}/\text{C}_{20}$ compounds) through association of an NO_3^- primary ion (Ehn et al., 2014), while other ionization techniques are more selective towards less oxidized compounds (Aljawhary et al., 2013). Many recent publications report peak lists for different compounds identified from chamber or ambient measurements with nitrate chemical ionization (Ehn et al., 2012, 2014; Kulmala et al., 2013; Mutzel et al., 2015; Praplan et al., 2015; Jokinen et al., 2015; Kirkby et al., 2016). The species from the previous studies are mainly C_{10} (containing 10 carbon atoms) or C_{20} (containing 19 or 20 carbon atoms) compounds originating from reactions between monoterpenes (in most cases from α -pinene) and ozone and/or OH.

The C_{10} compounds can be further segregated into HOM radicals (RO_2 , i.e., $\text{C}_{10}\text{H}_{15}\text{O}_{i \geq 6}$), HOM monomers

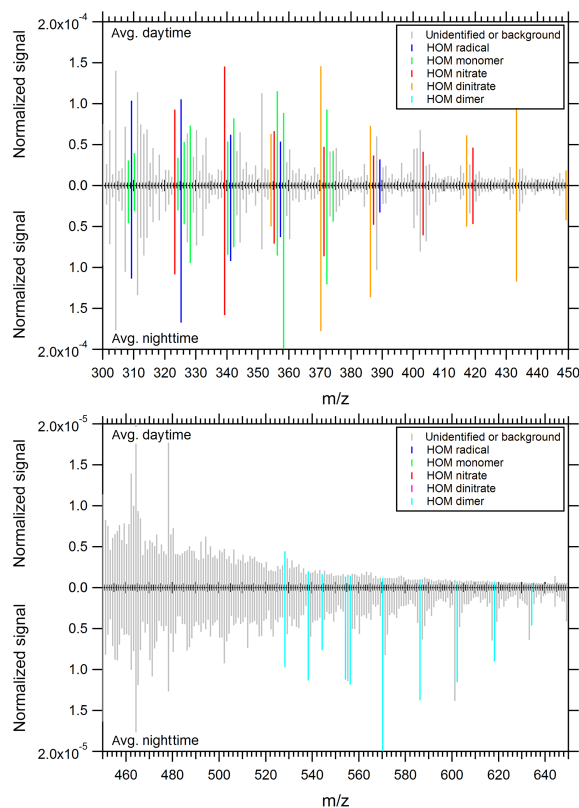


Figure 7. Comparison between average daytime and nighttime mass spectra measured with the nitrate CI-API-TOF. The daytime spectrum was averaged for periods when no nucleation was observed.

($\text{C}_{10}\text{H}_{14}\text{O}_{i \geq 7}$ and $\text{C}_{10}\text{H}_{16}\text{O}_{i \geq 6}$) and HOMs involving reactions with nitrate ($\text{C}_{10}\text{H}_{15}\text{NO}_{i \geq 7}$ and $\text{C}_{10}\text{H}_{16}\text{N}_2\text{O}_{i \geq 8}$; Jokinen et al., 2014). Dimers ($\text{C}_{19}/\text{C}_{20}$ compounds) originate from reactions among HOM RO_2 radicals (Ehn et al., 2014).

The spectra were evaluated according to the peak list shown in Table 2 regarding HOMs. It should be noted that the listed compounds represent some fraction of the observed signal in the monomer and dimer region, although not all of the peaks that are present are identified yet. Figure 7 shows a comparison between the average daytime and the average nighttime spectra for the mass to charge range between m/z 300 and 650. According to Fig. 7 the main difference between day and night is the significantly higher signals in the dimer region during the night.

Figure 8 shows the diurnal variation of the HOMs (separated into HOM radicals, HOM monomers, HOM nitrates and HOM dimers according to Table 2) together with other parameters (NO , NO_2 , O_3 and global radiation). One striking feature is the pronounced maximum concentration of HOM dimers during the night. During the day, when the global ra-

12804

A. Kürten et al.: Observation of new particle formation

Table 2. Peak list of the highly oxidized organic molecules (HOMs) used in this study.

Ion sum formula	Cluster ion	Exact mass	Compound
C ₁₀ H ₁₅ NO ₉ ⁻	(C ₁₀ H ₁₅ O ₆)NO ₃ ⁻	293.0752	HOM RO ₂ radical
C ₁₀ H ₁₅ NO ₁₀ ⁻	(C ₁₀ H ₁₅ O ₇)NO ₃ ⁻	309.0701	HOM RO ₂ radical
C ₁₀ H ₁₅ NO ₁₁ ⁻	(C ₁₀ H ₁₅ O ₈)NO ₃ ⁻	325.0651	HOM RO ₂ radical
C ₁₀ H ₁₅ NO ₁₂ ⁻	(C ₁₀ H ₁₅ O ₉)NO ₃ ⁻	341.0600	HOM RO ₂ radical
C ₁₀ H ₁₅ NO ₁₃ ⁻	(C ₁₀ H ₁₅ O ₁₀)NO ₃ ⁻	357.0549	HOM RO ₂ radical
C ₁₀ H ₁₅ NO ₁₅ ⁻	(C ₁₀ H ₁₅ O ₁₂)NO ₃ ⁻	389.0447	HOM RO ₂ radical
C ₈ H ₁₂ NO ₁₁ ⁻	(C ₈ H ₁₂ O ₈)NO ₃ ⁻	298.0416	HOM monomer
C ₉ H ₁₄ NO ₁₂ ⁻	(C ₉ H ₁₄ O ₉)NO ₃ ⁻	328.0521	HOM monomer
C ₁₀ H ₁₄ NO ₁₀ ⁻	(C ₁₀ H ₁₄ O ₇)NO ₃ ⁻	308.0623	HOM monomer
C ₁₀ H ₁₄ NO ₁₁ ⁻	(C ₁₀ H ₁₄ O ₈)NO ₃ ⁻	324.0572	HOM monomer
C ₁₀ H ₁₄ NO ₁₂ ⁻	(C ₁₀ H ₁₄ O ₉)NO ₃ ⁻	340.0521	HOM monomer
C ₁₀ H ₁₄ NO ₁₃ ⁻	(C ₁₀ H ₁₄ O ₁₀)NO ₃ ⁻	356.0471	HOM monomer
C ₁₀ H ₁₄ NO ₁₄ ⁻	(C ₁₀ H ₁₄ O ₁₁)NO ₃ ⁻	372.0420	HOM monomer
C ₁₀ H ₁₆ NO ₉ ⁻	(C ₁₀ H ₁₆ O ₆)NO ₃ ⁻	294.0831	HOM monomer
C ₁₀ H ₁₆ NO ₁₀ ⁻	(C ₁₀ H ₁₆ O ₇)NO ₃ ⁻	310.0780	HOM monomer
C ₁₀ H ₁₆ NO ₁₁ ⁻	(C ₁₀ H ₁₆ O ₈)NO ₃ ⁻	326.0729	HOM monomer
C ₁₀ H ₁₆ NO ₁₂ ⁻	(C ₁₀ H ₁₆ O ₉)NO ₃ ⁻	342.0678	HOM monomer
C ₁₀ H ₁₆ NO ₁₃ ⁻	(C ₁₀ H ₁₆ O ₁₀)NO ₃ ⁻	358.0627	HOM monomer
C ₁₀ H ₁₆ NO ₁₄ ⁻	(C ₁₀ H ₁₆ O ₁₁)NO ₃ ⁻	374.0576	HOM monomer
C ₁₀ H ₁₅ N ₂ O ₁₀ ⁻	(C ₁₀ H ₁₅ NO ₇)NO ₃ ⁻	323.0732	HOM nitrate
C ₁₀ H ₁₅ N ₂ O ₁₁ ⁻	(C ₁₀ H ₁₅ NO ₈)NO ₃ ⁻	339.0681	HOM nitrate
C ₁₀ H ₁₅ N ₂ O ₁₂ ⁻	(C ₁₀ H ₁₅ NO ₉)NO ₃ ⁻	355.0630	HOM nitrate
C ₁₀ H ₁₅ N ₂ O ₁₃ ⁻	(C ₁₀ H ₁₅ NO ₁₀)NO ₃ ⁻	371.0580	HOM nitrate
C ₁₀ H ₁₅ N ₂ O ₁₄ ⁻	(C ₁₀ H ₁₅ NO ₁₁)NO ₃ ⁻	387.0529	HOM nitrate
C ₁₀ H ₁₅ N ₂ O ₁₅ ⁻	(C ₁₀ H ₁₅ NO ₁₂)NO ₃ ⁻	403.0478	HOM nitrate
C ₁₀ H ₁₅ N ₂ O ₁₆ ⁻	(C ₁₀ H ₁₅ NO ₁₃)NO ₃ ⁻	419.0427	HOM nitrate
C ₁₀ H ₁₆ N ₃ O ₁₁ ⁻	(C ₁₀ H ₁₆ N ₂ O ₈)NO ₃ ⁻	354.0790	HOM dinitrate
C ₁₀ H ₁₇ N ₄ O ₁₄ ⁻	(C ₁₀ H ₁₆ N ₂ O ₈)(HNO ₃)NO ₃ ⁻	417.0747	HOM dinitrate
C ₁₀ H ₁₆ N ₃ O ₁₂ ⁻	(C ₁₀ H ₁₆ N ₂ O ₉)NO ₃ ⁻	370.0739	HOM dinitrate
C ₁₀ H ₁₇ N ₄ O ₁₅ ⁻	(C ₁₀ H ₁₆ N ₂ O ₉)(HNO ₃)NO ₃ ⁻	433.0696	HOM dinitrate
C ₁₀ H ₁₆ N ₃ O ₁₃ ⁻	(C ₁₀ H ₁₆ N ₂ O ₁₀)NO ₃ ⁻	386.0689	HOM dinitrate
C ₁₀ H ₁₇ N ₄ O ₁₆ ⁻	(C ₁₀ H ₁₆ N ₂ O ₁₀)(HNO ₃)NO ₃ ⁻	449.0645	HOM dinitrate
C ₁₉ H ₃₀ NO ₁₆ ⁻	(C ₁₉ H ₃₀ O ₁₃)NO ₃ ⁻	528.1570	HOM dimer
C ₁₉ H ₃₀ NO ₁₇ ⁻	(C ₁₉ H ₃₀ O ₁₄)NO ₃ ⁻	544.1519	HOM dimer
C ₂₀ H ₂₈ NO ₁₆ ⁻	(C ₂₀ H ₂₈ O ₁₃)NO ₃ ⁻	538.1414	HOM dimer
C ₂₀ H ₂₈ NO ₁₇ ⁻	(C ₂₀ H ₂₈ O ₁₄)NO ₃ ⁻	554.1363	HOM dimer
C ₂₀ H ₂₈ NO ₁₈ ⁻	(C ₂₀ H ₂₈ O ₁₅)NO ₃ ⁻	570.1312	HOM dimer
C ₂₀ H ₂₈ NO ₁₉ ⁻	(C ₂₀ H ₂₈ O ₁₆)NO ₃ ⁻	586.1261	HOM dimer
C ₂₀ H ₂₈ NO ₂₀ ⁻	(C ₂₀ H ₂₈ O ₁₇)NO ₃ ⁻	602.1210	HOM dimer
C ₂₀ H ₂₈ NO ₂₁ ⁻	(C ₂₀ H ₂₈ O ₁₈)NO ₃ ⁻	618.1159	HOM dimer
C ₂₀ H ₂₈ NO ₂₂ ⁻	(C ₂₀ H ₂₈ O ₁₉)NO ₃ ⁻	634.1108	HOM dimer
C ₂₀ H ₂₈ NO ₂₃ ⁻	(C ₂₀ H ₂₈ O ₂₀)NO ₃ ⁻	650.1058	HOM dimer
C ₂₀ H ₃₀ NO ₁₇ ⁻	(C ₂₀ H ₃₀ O ₁₄)NO ₃ ⁻	556.1519	HOM dimer

diation shows values above zero, the dimer signals drop by about 1 order of magnitude and reach levels which are close to the detection limit of the instrument. The low daytime dimer concentrations are probably due to enhanced NO, HO₂ and R'O₂ concentrations during the day. These compounds can react with HOM RO₂ radicals and thereby inhibit the for-

mation of dimers, which are a result of the reaction between two RO₂ radicals. As can be seen from Fig. 8, the NO concentration peaks in the morning, HO₂ was not measured but typically peaks around noon or in the later afternoon (Monks, 2005). Direct photolysis of HOM dimers has to our knowl-

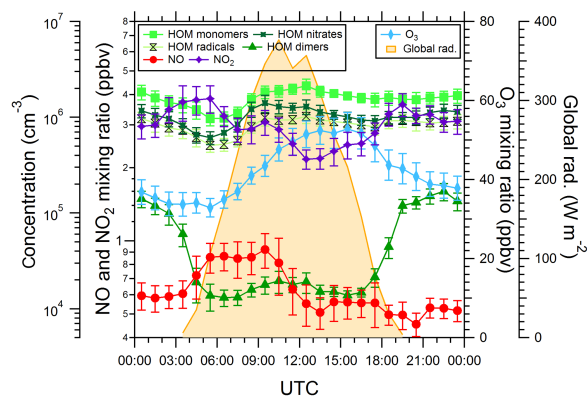


Figure 8. Diurnal profiles of the NO, NO₂ and O₃ mixing ratios. The signals for highly oxidized organic molecules (HOMs) are shown for some C₁₀ (HOM monomers, HOM nitrates and HOM radicals) and C₁₉/C₂₀ compounds (HOM dimers), which show a distinct maximum during the night. The HOM dinitrates show a similar pattern as the other C₁₀ compounds and are not included in the figure. The global radiation is shown in addition. Error bars indicate 1 standard deviation for the 30 min averages.

edge not been reported in the literature but could in principle also explain the dimer pattern seen in Fig. 8.

The HOM monomer signal (Fig. 8) does not show a pronounced diurnal cycle; only in the early morning are the signals reduced by about 50% compared to the daily average. Slightly higher values around noon could be explained by the higher O₃ and OH concentrations during midday, which lead to enhanced formation of HOMs through reactions between these compounds and monoterpenes (Jokinen et al., 2015; Kirkby et al., 2016). The HOM nitrates, dinitrates and radicals show almost the same profile as the HOM monomers. This might be expected for the HOM radicals as these can be regarded as the precursors for the HOM monomers, but the fact that the HOM nitrates follow an almost identical pattern is somewhat surprising as the NO mixing ratio shows a different profile and is thought to be involved in the formation of the HOM nitrates. However, further involvement of, for example, OH, HO₂ and R'O₂ in the HOM formation should also play a role and therefore influence their diurnal pattern. The elucidation of the HOM formation mechanisms is beyond the scope of this article and will therefore not be discussed further. More field and chamber experiments are needed to identify the influence of different trace gases and radicals on the formation and concentration of HOMs.

3.9 Particle formation rates

The presence of small particles (<~20 nm) was observed on almost every day during the campaign. However, often nanometer-sized particles appeared suddenly without clear growth from the smallest size the nDMA covered (slightly

above 3 nm). In total there were seven events where clear growth was detectable, and these events were the only ones for which a NPF rate (J) was derived. It should be noted that clear NPF was observed only on 6 days; however, for one day two NPF rates were derived, which results in a total of seven NPF rates.

In accordance with other previous studies (Metzger et al., 2010; Kirkby et al., 2011), we have first derived a NPF rate at a larger mobility diameter d_{p2} (2.5 nm in the present study), which was corrected to a smaller diameter of $d_{p1} = 1.7$ nm in a second step. The formation rate J_{dp2} is obtained from the time derivative of the small particle concentration, which follows from the difference in particle concentrations ($N_{2.5-10}$) measured by the TSI model 3776 (cut-off diameter of 2.5 nm) and 3010 (cut-off diameter of 10 nm) CPCs:

$$J_{dp2} = \frac{dN_{2.5-10}}{dt} + CS_{dp2} \cdot N_{2.5-10} + \frac{GR}{10 \text{ nm} - 2.5 \text{ nm}} \cdot N_{2.5-10}. \quad (7)$$

The second term on the right-hand side in Eq. (7) accounts for the loss of small particles on particles larger than 2.5 nm, while the third term accounts for the growth of particles out of the size range under consideration (Kulmala et al., 2012). The coagulation sink CS_{dp2} is calculated from the particle size distribution measured by the nDMA and the SMPS. The second step involves an exponential correction to obtain the particle formation rate at the smaller size, J_{dp1} , by taking into account the coagulation sink and the growth rate (GR) of particles (Lehtinen et al., 2007):

$$J_{dp1} = J_{dp2} \cdot \exp\left(\frac{CS_{dp1}}{GR} \cdot dp1 \cdot \gamma\right). \quad (8)$$

The factor γ is defined as follows (Lehtinen et al., 2007):

$$\gamma = \frac{1}{s+1} \cdot \left(\left(\frac{dp2}{dp1} \right)^{s+1} - 1 \right), \quad (9)$$

where s is the slope of the coagulation sink as a function of size for the size range between d_{p1} and d_{p2} ($s = \log(CS_{dp2}/CS_{dp1})/\log(dp2/dp1)$). The value of s can be derived from the measured particle size distribution and was found to be around -1.6 for the present study, which is in good agreement with the values reported by Lehtinen et al. (2007). The growth rate was derived from the nDMA measurements in the size range between 3 and 10 nm by fitting a Gaussian function to the particle size distribution to determine the mode diameter for all measured size distributions. Applying a linear fit to the mode diameter as a function of time yields the GR used in Eq. (8) (Hirsikko et al., 2005). Errors are calculated by taking into account the statistical variation of the particle formation rates J_{dp2} as well as systematic errors on GR (factor of 2), d_{p2} (factor of 1.3) and CS (factor of 1.5).

12806

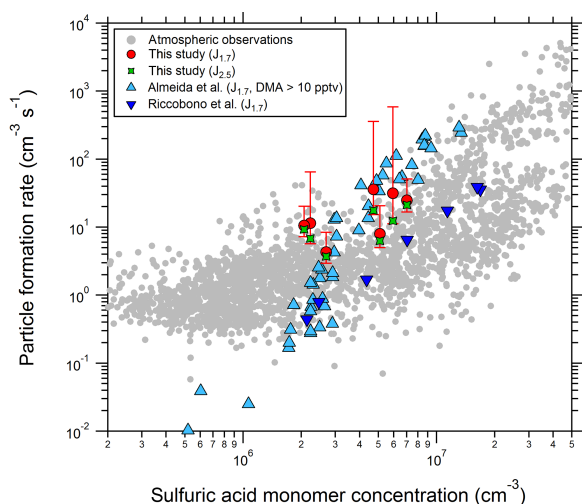


Figure 9. Particle formation rates from this study at a mobility diameter of 1.7 nm ($J_{1.7}$, red circles) and 2.5 nm ($J_{2.5}$, green stars). Data from CLOUD chamber measurements for a diameter of 1.7 nm are shown in addition for the system of sulfuric acid, water and dimethylamine (light blue symbols; see Almeida et al., 2013) and sulfuric acid, water and oxidized organics from pinanediol (dark blue symbols; see Riccobono et al., 2014). The light-gray circles are from other field measurements (Kuang et al., 2008; Paasonen et al., 2010; Kulmala et al., 2013).

Figure 9 shows a comparison between J_{dp1} from this study, data from other field studies and formation rates from CLOUD chamber studies for the system of sulfuric acid, dimethylamine and water at 278 K (Almeida et al., 2013), as well as for oxidized organic compounds with sulfuric acid and water (Riccobono et al., 2014).

4 Discussion

By comparing time periods where significant NPF occurred to time periods where no NPF was observed, some conclusions can be drawn about the relevance of certain parameters regarding NPF. Figure 10 shows a comparison for a variety of parameters by comparing nucleation days to no-nucleation days (red bars) and periods with high sulfuric acid dimer concentrations to no-nucleation days when there are also no high dimer concentrations (blue bars).

It is evident from Fig. 10 that sulfuric acid is on average a factor of 2 to 2.5 higher on days with nucleation; however, the variability is rather high (error bars take into account the standard deviations of a parameter for both the nucleation days and the no-nucleation days). The enhanced sulfuric acid concentrations confirm the importance of this compound regarding NPF, which has also been shown in numerous other studies (e.g., Weber et al., 1997; Kulmala et al., 2004; Fiedler et al., 2005; Kuang et al., 2008). The OH con-

A. Kürten et al.: Observation of new particle formation

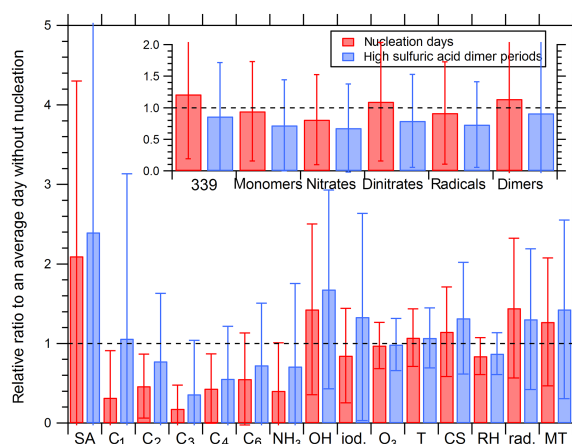


Figure 10. Comparison of various parameters for different time periods (SA: sulfuric acid monomer; C₁, C₂, C₃, C₄ and C₆: amines; iod.: iodic acid; and rad.: global radiation intensity). The subset figure on the upper right shows the signals for the highly oxidized organic compounds with 10 or 20 carbon atoms (339: organic compound C₁₀H₁₅NO₈ clustered with NO₃⁻ having a mass of 339.0681 Th; the definition of other HOMs, i.e., monomers, radicals, nitrates, dinitrates and dimers, can be found in Table 2). The red bars relate nucleation days to days without nucleation and the blue bars show the ratio between periods where high sulfuric acid dimer concentrations were observed (see Fig. 6) to no-nucleation days. Similar times of the day (early morning) were used as reference periods when no nucleation was observed as nucleation and dimer formation was also mainly observed in the morning.

centration and the global radiation are also enhanced during nucleation, which is not surprising given the fact that the parameters H₂SO₄, OH and global radiation are connected. The relative humidity is generally lower during nucleation periods, which has also been reported in previous studies (Hamed et al., 2011; Nieminen et al., 2015).

Regarding amines and ammonia, Fig. 10 reveals an anti-correlation between their concentration and the occurrence of NPF or sulfuric acid dimer formation (factor of 2 to 5 lower during nucleation). However, this does not necessarily mean that these compounds inhibit the formation of particles. On the contrary, it could mean that amines and ammonia are efficiently taken up by small clusters and therefore are also involved in the formation of new particles. Unlike sulfuric acid, amines and ammonia are not produced in the gas phase and therefore their concentration will decrease with increasing distance from their sources depending on the condensation sink. During nucleation the condensation sink is slightly enhanced (Fig. 10), probably because of the newly formed particles. However, the CS is only calculated for particles larger than 3 nm. Also, smaller particles and sulfuric acid clusters can contain amines (Kürten et al., 2014) and even the sulfuric acid monomer can be bound to dimethylamine (Ortega et al., 2012; Kürten et al., 2014). Therefore,

A. Kürten et al.: Observation of new particle formation

12807

continuous production of sulfuric acid and its clusters will lead to a depletion of amines away from their sources, although no mixed clusters of sulfuric acid and amines could be observed; this is probably the case because their concentrations were too low to be measured with the CI-API-TOF. As sulfuric acid concentrations are high during nucleation, this could explain the low amine values. Efficient uptake of amines in the particle phase has also been reported in a previous field study (You et al., 2014). In addition, the limited pool of amines can also be the explanation for the relatively low slope from Fig. 6 (sulfuric acid dimer vs. monomer) for some of the periods with elevated sulfuric acid dimer concentrations. If the sulfuric acid concentration increases, the ratio of the free (unbound) amine to sulfuric acid concentration drops, and there are fewer amines available to stabilize the sulfuric acid dimers. This is a different situation compared to the CLOUD7 experiment, where the amine to sulfuric acid concentration was maintained at a ratio of ~ 100 over the entire duration of the experiments (Kürten et al., 2014). However, from these observations we cannot unambiguously conclude whether the amines are involved in the very first steps of nucleation, or whether they are depleted due to clusters which do not need the help of amines in order to nucleate. One other aspect that could explain the low amine ratios is the somewhat enhanced OH concentration during the nucleation days, as amines react with OH. However, the lifetime of amines regarding their reactions with OH is on the order of hours (Ge et al., 2011), whereas the uptake on particles is significantly faster (if CS is on the order of 10^{-3} to 10^{-2} s $^{-1}$).

Regarding the possibility that sulfuric acid and amines can explain the observed nucleation, it has to be noted that no clusters involving more than two sulfuric acid molecules could be observed. In the following we will calculate the maximum expected sulfuric acid trimer concentration and discuss what parameters can lower this concentration. The maximum measured sulfuric acid dimer concentration is around 1×10^5 molecules cm $^{-3}$ for a sulfuric acid monomer concentration of 1×10^7 molecules cm $^{-3}$. A sulfuric acid trimer will be formed through the collision between a monomer and a dimer (collision rate $K_{1,2}$), whereas the loss rate of the trimer is defined by the sum of the condensation sink (CS) and its evaporation rate ($k_{e,3}$). At steady state this would yield the following equation for the trimer concentration N_3 as function of the monomer and dimer concentrations N_1 and N_2 (for simplicity this neglects a potential contribution from tetramer evaporation):

$$N_3 = \frac{K_{1,2} \cdot N_1 \cdot N_2}{\text{CS} + k_{e,3}}. \quad (10)$$

Using a value of 5×10^{-10} molecule $^{-1}$ cm 3 s $^{-1}$ for $K_{1,2}$ and a condensation sink (CS) of 5×10^{-3} s $^{-1}$ for the above-mentioned monomer and dimer concentrations would yield a trimer concentration of 1×10^5 molecules cm $^{-3}$ if the trimer evaporation rate were zero. This concentration should be detectable with our CI-API-TOF. The fact that we do not see

the trimer could indicate that the trimer evaporation rate is nonzero. For a high amine to sulfuric acid ratio nucleation proceeds at or close to the kinetic limit (Jen et al., 2014; Kürten et al., 2014). However, if the amine concentration is not very high, not every trimer that is formed would be stable (as it is the case for a favored acid–base ratio; see Ortega et al., 2012) and therefore could evaporate rapidly. This would result in lower trimer concentrations, which could be below the detection limit of the CI-API-TOF. From this perspective the absence of larger sulfuric acid amine clusters is not necessarily an indication that this system is not responsible for NPF. In other regions where the sulfuric acid and amine mixing ratios are even higher (i.e., very close to amine sources) such clusters can be observable (Zhao et al., 2011). Recently, Jen et al. (2016b) provided evidence that nitrate chemical ionization could not be sensitive towards sulfuric acid–amine or sulfuric acid–diamine clusters if these contain three or more sulfuric acid molecules because of the lowered acidity of such clusters by the basic amines/diamines. This could also explain the absence of clusters beyond the dimer in the present study. Further measurements using different primary ions are needed to investigate this possibility further.

The C $_{10}$ and C $_{20}$ signals for NPF and no-nucleation days are not significantly different (Fig. 10). This can be interpreted in different ways: (1) the HOMs are not important in terms of NPF, (2) HOMs are generally high enough and it needs just enough sulfuric acid to initiate nucleation involving HOMs, or (3) “HOM” is too broadly defined and only a subgroup of HOMs is involved in the nucleation, but currently we cannot distinguish this group. Neither of the possibilities can be proven right or wrong. However, what can be said is that it is unlikely that the identified HOMs alone are capable of producing new particles to a significant extent at the conditions of the present study. The HOM dimer concentrations (Fig. 8) are significantly higher during the night than during the day. Nevertheless, no nighttime nucleation is observed. This could be interpreted as an indication that if HOMs are involved in NPF, it requires additional compounds such as sulfuric acid to initiate significant nucleation. Alternative explanations for the absence of nighttime nucleation could be the suppression of the formation of HOMs that can nucleate by NO $_3$ during the night, or low [OH], which is required for the formation of nucleating HOMs.

Kulmala et al. (2013) proposed that C $_{10}$ H $_{15}$ NO $_8$ (detected as a cluster with NO $_3^-$ at 339.0681 Th) could be important because NPF correlated even better with this compound compared to sulfuric acid. During nucleation days this compound is only slightly elevated (Fig. 10), and this could be due to the generally higher OH levels, although the exact formation mechanism of C $_{10}$ H $_{15}$ NO $_8$ has to our knowledge not been reported yet. During nucleation, no mixed clusters between sulfuric acid and HOMs could be identified. However, this also does not rule out their existence as the concentrations could be below the CI-API-TOF detection limit, or a low charging

12808

efficiency with the nitrate primary ion could prevent their detection. Furthermore, not all signals are identified yet.

The observed particle formation rates (Fig. 9) are consistent with the rates observed at other sites, although at the upper end of the typical ranges that have been previously measured. The present data seem to agree a bit better with CLOUD chamber data for the system of sulfuric acid, water and dimethylamine (Almeida et al., 2013) compared to data for the system of sulfuric acid, water and oxidized organics from pinanediol (Riccobono et al., 2014). However, a direct comparison is difficult as the conditions between this ambient study and the CLOUD chamber experiments are not identical (with respect to T , RH, CS, amine mixing ratios, HOM concentrations, etc.).

5 Summary

In spring 2014 (18 May to 7 June) a field campaign was conducted at a rural site in central Germany (Vielbrunn/Odenwald). The measurement site was in the vicinity (within 450 to 1100 m distance) of three larger dairy farms. The aim of this campaign was to evaluate whether there is a connection between NPF and the concentration of amines and/or ammonia. Furthermore, the impact of highly oxidized organic molecules (HOMs) from surrounding forests was investigated. A nitrate chemical ionization–atmospheric pressure interface time-of-flight mass spectrometer (CI-API-TOF) was used to identify gas-phase compounds and clusters. Particle counters and differential mobility analyzers were used to characterize the aerosol size distribution and number density. The following conclusions can be drawn from our measurements:

- Nitrate CI-API-TOF can be used to measure sulfuric acid, iodic acid, amines, a nitrosamine, ammonia and HOMs. The measurement of iodic acid, ammonia and the nitrosamine has not been described before; therefore, the method is even more versatile than previously thought and well suited to studying all of the abovementioned compounds during field measurements.
- The sulfuric acid concentration can be well described by proxies (SO_2 , global radiation, RH and CS or just by SO_2 and global radiation) for this site, with a similar accuracy to that reported in a previous study (Mikkonen et al., 2011).
- Significant sulfuric acid dimer concentrations were measured. It is, however, not clear what compound stabilizes the neutral dimers. Larger sulfuric acid clusters (trimer and beyond) were not observed.
- Amines (C_1 , C_2 , C_3 , C_4 and C_6 amines) are present at estimated mixing ratios between approximately 1 and 5 pptv, which is consistent with other studies; the C_4 and

A. Kürten et al.: Observation of new particle formation

C_6 amines as well as ammonia show a diurnal variation, which follows the temperature profile.

- Iodine was observed (probably iodic acid) on every day, which is somewhat surprising for a continental site located more than 400 km away from the ocean. The nitrate CI-API-TOF has a high sensitivity towards iodic acid and its presence indicates long-range transport of iodine-containing substances (although a local source cannot entirely be ruled out). OIO concentrations can also be estimated using OH concentrations; however, both $[\text{HIO}_3]$ ($\sim 3 \times 10^5$ molecules cm^{-3}) and $[\text{OIO}]$ ($\sim 5 \times 10^6$ molecules cm^{-3}) are probably too low to affect NPF significantly at this site.
- The diurnal pattern of HOM dimers shows maximum concentrations during the night but no nighttime nucleation is observed; the daytime concentration could be low due to the presence of NO and/or HO_2 , which suppress the HOM dimer formation.
- Relatively high particle formation rates are found, which are rather at the upper end of the atmospheric observations for other rural sites; the rates are compatible with CLOUD chamber data both for the systems of sulfuric acid, water and dimethylamine (Almeida et al., 2013) and for a system involving sulfuric acid, water and oxidized organics (Riccobono et al., 2014). No definitive answer can be given as to which system is more relevant.
- Nucleation seems to be favored on days with relatively low RH and high sulfuric acid. An anti-correlation with the amine and ammonia signals is observed; this could be due to efficient uptake of these compounds on clusters and particles during NPF as amines and ammonia are not produced in the gas phase.

The above points seem to support recent findings about the relevance of amines in terms of NPF and early growth (Chen et al., 2012; Almeida et al., 2013; Kulmala et al., 2013; Lehtipalo et al., 2016). However, it cannot be unambiguously concluded that amines are more relevant for NPF than HOMs at this site because no nucleating clusters could be directly observed. More studies like the present one are necessary in the future to obtain better statistics about the parameters relevant for NPF (Fig. 10). Ideally, such measurements should include further instrumentation, including a particle size magnifier (Vanhanen et al., 2011) for the measurement of clusters and small particles (< 3 nm), an API-TOF (Junninen et al., 2010) for identification of charged nucleating clusters, an instrument for HO_x/RO_x measurements and an instrument for sensitive amine measurements capable of speciating the amines.

A. Kürten et al.: Observation of new particle formation

12809

6 Data availability

All data presented in this study are available upon request from the corresponding author.

Acknowledgements. We thank the German Weather Service (Deutscher Wetterdienst, DWD) for providing infrastructure and meteorological data. Funding from the German Federal Ministry of Education and Research (grant no. 01LK1222A) and the Marie Curie Initial Training Network “CLOUD-TRAIN” (grant no. 316662) is gratefully acknowledged.

Edited by: T. Karl

Reviewed by: two anonymous referees

References

- Aljawhary, D., Lee, A. K. Y., and Abbatt, J. P. D.: High-resolution chemical ionization mass spectrometry (ToF-CIMS): application to study SOA composition and processing, *Atmos. Meas. Tech.*, 6, 3211–3224, doi:10.5194/amt-6-3211-2013, 2013.
- Almeida, J., Schobesberger, S., Kürten, A., Ortega, I. K., Kupiainen-Määttä, O., Praplan, A. P., Adamov, A., Amorim, A., Bianchi, F., Breitenlechner, M., David, A., Dommen, J., Donahue, N. M., Downard, A., Dunne, E. M., Duplissy, J., Ehrhart, S., Flagan, R. C., Franchin, A., Guida, R., Hakala, J., Hansel, A., Heinritzi, M., Henschel, H., Jokinen, T., Junninen, H., Kajos, M., Kangasluoma, J., Keskinen, H., Kupc, A., Kurtén, T., Kvashin, A. N., Laaksonen, A., Lehtipalo, K., Leiminger, M., Leppä, J., Loukonen, V., Makhmutov, V., Mathot, S., McGrath, M. J., Nieminen, T., Olenius, T., Onnela, A., Petäjä, T., Riccobono, F., Riipinen, I., Rissanen, M., Rondo, L., Ruuskanen, T., Santos, F. D., Sarnela, N., Schallhart, S., Schnitzhofer, R., Seinfeld, J. H., Simon, M., Sipilä, M., Stozhkov, Y., Stratmann, F., Tomé, A., Tröstl, J., Tsagkogeorgas, G., Vaattovaara, P., Visanen, Y., Virtanen, A., Vrtala, A., Wagner, P. E., Weingartner, E., Wex, H., Williamson, C., Wimmer, D., Ye, P., Yli-Juuti, T., Carslaw, K. S., Kulmala, M., Curtius, J., Baltensperger, U., Worsnop, D. R., Vehkamäki, H., and Kirkby, J.: Molecular understanding of sulphuric acid-amine particle nucleation in the atmosphere, *Nature*, 502, 359–363, doi:10.1038/nature12663, 2013.
- Berndt, T., Jokinen, T., Sipilä, M., Mauldin III, R. L., Herrmann, H., Stratmann, F., Junninen, H., and Kulmala, M.: H₂SO₄ formation from the gas-phase reaction of stabilized Criegee Intermediates with SO₂: Influence of water vapour content and temperature, *Atmos. Environ.*, 89, 603–612, doi:10.1016/j.atmosenv.2014.02.062, 2014.
- Berresheim, H., Elste, T., Plass-Dülmer, C., Eisele, F. L., and Tanner, D. J.: Chemical ionization mass spectrometer for long-term measurements of atmospheric OH and H₂SO₄, *Int. J. Mass Spectrom.*, 202, 91–109, doi:10.1016/S1387-3806(00)00233-5, 2000.
- Bianchi, F., Tröstl, J., Junninen, H., Frege, C., Henne, S., Hoyle, C. R., Molteni, U., Herrmann, E., Adamov, A., Bukowiecki, N., Chen, X., Duplissy, J., Gysel, M., Hutterli, M., Kangasluoma, J., Kontkanen, J., Kürten, A., Manninen, H. E., Münch, S., Peräkylä, O., Petäjä, T., Rondo, L., Williamson, C., Weingartner, E., Curtius, J., Worsnop, D. R., Kulmala, M., Dommen, J., and Baltensperger, U.: New particle formation in the free troposphere: A question of chemistry and timing, *Science*, 352, 1109–1112, doi:10.1126/science.aad5456, 2016.
- Blake, R. S., Monks, P. S., and Ellis, A. M.: Proton-Transfer Reaction Mass Spectrometry, *Chem. Rev.*, 109, 861–896, doi:10.1021/cr800364q, 2009.
- Boy, M., Mogensen, D., Smolander, S., Zhou, L., Nieminen, T., Paasonen, P., Plass-Dülmer, C., Sipilä, M., Petäjä, T., Mauldin, L., Berresheim, H., and Kulmala, M.: Oxidation of SO₂ by stabilized Criegee intermediate (sCI) radicals as a crucial source for atmospheric sulfuric acid concentrations, *Atmos. Chem. Phys.*, 13, 3865–3879, doi:10.5194/acp-13-3865-2013, 2013.
- Cappellin, L., Karl, T., Probst, M., Ismailova, O., Winkler, P. M., Soukoulis, C., Aprea, E., Märk, T. D., Gasperi, F., and Biasoli, F.: On quantitative determination of volatile organic compound concentrations using proton transfer reaction time-of-flight mass spectrometry, *Environ. Sci. Technol.*, 46, 2283–2290, doi:10.1021/es203985t, 2012.
- Chang, D., Song, Y., and Liu, B.: Visibility trends in six megacities in China 1973–2007, *Atmos. Res.*, 94, 161–167, doi:10.1016/j.atmosres.2009.05.006, 2009.
- Chen, M., Titcombe, M., Jiang, J., Jen, C., Kuang, C., Fischer, M. L., Eisele, F. L., Siepmann, J. I., Hanson, D. R., Zhao, J., and McMurry, P. H.: Acid–base chemical reaction model for nucleation rates in the polluted atmospheric boundary layer, *P. Natl. Acad. Sci. USA*, 109, 18713–18718, doi:10.1073/pnas.1210285109, 2012.
- Crouse, J. D., Nielsen, L. B., Jørgensen, S., Kjaergaard, H. G., and Wennberg, P. O.: Autooxidation of organic compounds in the atmosphere, *J. Phys. Chem. Lett.*, 4, 3513–3520, doi:10.1021/jz4019207, 2013.
- Ehn, M., Kleist, E., Junninen, H., Petäjä, T., Lönn, G., Schobesberger, S., Dal Maso, M., Trimborn, A., Kulmala, M., Worsnop, D. R., Wahner, A., Wildt, J., and Mentel, Th. F.: Gas phase formation of extremely oxidized pinene reaction products in chamber and ambient air, *Atmos. Chem. Phys.*, 12, 5113–5127, doi:10.5194/acp-12-5113-2012, 2012.
- Ehn, M., Thornton, J. A., Kleist, E., Sipilä, M., Junninen, H., Pullinen, I., Springer, M., Rubach, F., Tillmann, R., Lee, B., Lopez-Hilfiker, F., Andres, S., Acir, I.-H., Rissanen, M., Jokinen, T., Schobesberger, S., Kangasluoma, J., Kontkanen, J., Nieminen, T., Kurtén, T., Nielsen, L. B., Jørgensen, S., Kjaergaard, H. G., Canagaratna, M., Dal Maso, M., Berndt, T., Petäjä, T., Wahner, A., Kerminen, V.-M., Kulmala, M., Worsnop, D. R., Wildt, J., and Mentel, T. F.: A large source of low-volatility secondary organic aerosol, *Nature*, 506, 476–479, doi:10.1038/nature13032, 2014.
- Eisele, F. L. and Tanner, D. J.: Measurement of the gas phase concentration of H₂SO₄ and methane sulfonic acid and estimates of H₂SO₄ production and loss in the atmosphere, *J. Geophys. Res.*, 98, 9001–9010, doi:10.1029/93JD00031, 1993.
- Eisele, F. L., Lovejoy, E. R., Kosciuch, E., Moore, K. F., Mauldin III, R. L., Smith, J. N., McMurry, P. H., and Iida, K.: Negative atmospheric ions and their potential role in ion-induced Nucleation, *J. Geophys. Res.*, 111, D04305, doi:10.1029/2005JD006568, 2006.
- Fiedler, V., Dal Maso, M., Boy, M., Aufmhoff, H., Hoffmann, J., Schuck, T., Birmili, W., Hanke, M., Uecker, J., Arnold, F., and Kulmala, M.: The contribution of sulphuric acid to atmospheric particle formation and growth: a comparison between boundary

12810

- layers in Northern and Central Europe, *Atmos. Chem. Phys.*, 5, 1773–1785, doi:10.5194/acp-5-1773-2005, 2005.
- Forester, C. D. and Wells, J. R.: Hydroxyl radical yields from reactions of terpene mixtures with ozone, *Indoor Air*, 21, 400–409, doi:10.1111/j.1600-0668.2011.00718.x, 2011.
- Freshour, N. A., Carlson, K. K., Melka, Y. A., Hinz, S., Panta, B., and Hanson, D. R.: Amine permeation sources characterized with acid neutralization and sensitivities of an amine mass spectrometer, *Atmos. Meas. Tech.*, 7, 3611–3621, doi:10.5194/amt-7-3611-2014, 2014.
- Ge, X., Wexler, A. S., and Clegg, S. L.: Atmospheric amines – Part I, A review, *Atmos. Environ.*, 45, 524–546, doi:10.1016/j.atmosenv.2010.10.012, 2011.
- Geron, C., Rasmussen, R., Arnsts, R. R., and Guenther, A.: A review and synthesis of monoterpene speciation from forests in the United States, *Atmos. Environ.*, 34, 1761–1781, doi:10.1016/S1352-2310(99)00364-7, 2000.
- Glasoe, W. A., Volz, K., Panta, B., Freshour, N., Bachman, R., Hanson, D. R., McMurry, P. H., and Jen, C.: Sulfuric acid nucleation: An experimental study of the effect of seven bases, *J. Geophys. Res.-Atmos.*, 120, 1933–1950, doi:10.1002/2014JD022730, 2015.
- Hamed, A., Korhonen, H., Sihto, S.-L., Joutsensaari, J., Järvinen, H., Petäjä, T., Arnold, F., Nieminen, T., Kulmala, M., Smith, J. N., Lehtinen, K. E. J., and Laaksonen, A.: The role of relative humidity in continental new particle formation, *J. Geophys. Res.*, 116, D03202, doi:10.1029/2010JD014186, 2011.
- Hanson, D. R. and Eisele, F. L.: Measurement of prenucleation molecular clusters in the NH_3 , H_2SO_4 , H_2O system, *J. Geophys. Res.*, 107, D124158, doi:10.1029/2001JD001100, 2002.
- Hanson, D. R. and Lovejoy, E. R.: Measurement of the thermodynamics of the hydrated dimer and trimer of sulfuric acid, *J. Phys. Chem. A*, 110, 9525–9528, doi:10.1021/jp062844w, 2006.
- Hanson, D. R., McMurry, P. H., Jiang, J., Tanner, D., and Huey, L. G.: Ambient pressure proton transfer mass spectrometry: detection of amines and ammonia, *Environ. Sci. Technol.*, 45, 8881–8888, doi:10.1021/es201819a, 2011.
- Hellén, H., Kieloaho, A.-J., and Hakola, H.: Gas-phase alkyl amines in urban air; comparison with a boreal forest site and importance for local atmospheric chemistry, *Atmos. Environ.*, 94, 192–197, doi:10.1016/j.atmosenv.2014.05.029, 2014.
- Hirsikko, A., Laakso, L., Hörrak, U., Aalto, P. P., Kerminen, V.-M., and Kulmala, M.: Annual and size dependent variation of growth rates and ion concentrations in boreal forest, *Boreal Environ. Res.*, 10, 357–369, 2005.
- Heinritzi, M., Simon, M., Steiner, G., Wagner, A. C., Kürten, A., Hansel, A., and Curtius, J.: Characterization of the mass-dependent transmission efficiency of a CIMS, *Atmos. Meas. Tech.*, 9, 1449–1460, doi:10.5194/amt-9-1449-2016, 2016.
- Janson, R. and de Serves, C.: Acetone and monoterpene emissions from the boreal forest in northern Europe, *Atmos. Environ.*, 35, 4629–4637, doi:10.1016/S1352-2310(01)00160-1, 2001.
- Jen, C., McMurry, P. H., and Hanson, D. R.: Stabilization of sulfuric acid dimers by ammonia, methylamine, dimethylamine, and trimethylamine, *J. Geophys. Res.-Atmos.*, 119, 7502–7514, doi:10.1002/2014JD021592, 2014.
- Jen, C. N., Bachman, R., Zhao, J., McMurry, P. H., and Hanson, D. R.: Diamine-sulfuric acid reactions are a potent source of new particle formation, *Geophys. Res. Lett.*, 43, 867–873, doi:10.1002/2015GL066958, 2016a.
- Jen, C. N., Zhao, J., McMurry, P. H., and Hanson, D. R.: Chemical ionization of clusters formed from sulfuric acid and dimethylamine or diamines, *Atmos. Chem. Phys.*, 16, 12513–12529, doi:10.5194/acp-16-12513-2016, 2016.
- Jiang, J., Zhao, J., Chen, M., Eisele, F. L., Scheckman, J., Williams, B. J., Kuang, C., and McMurry, P. H.: First measurements of neutral atmospheric cluster and 1–2 nm particle number size distributions during nucleation events, *Aerosol Sci. Technol.*, 45, ii–v, doi:10.1080/02786826.2010.546817, 2011.
- Jokinen, T., Sipilä, M., Junninen, H., Ehn, M., Lönn, G., Hakala, J., Petäjä, T., Mauldin III, R. L., Kulmala, M., and Worsnop, D. R.: Atmospheric sulphuric acid and neutral cluster measurements using CI-API-TOF, *Atmos. Chem. Phys.*, 12, 4117–4125, doi:10.5194/acp-12-4117-2012, 2012.
- Jokinen, T., Sipilä, M., Richters, S., Kerminen, V.-M., Paasonen, P., Stratmann, F., Worsnop, D., Kulmala, M., Ehn, M., Herrmann, H., and Berndt, T.: Rapid autooxidation forms highly oxidized RO_2 radicals in the atmosphere, *Angew. Chem. Int. Ed.*, 53, 14596–14600, doi:10.1002/anie.201408566, 2014.
- Jokinen, T., Berndt, T., Makkonen, R., Kerminen, V.-M., Junninen, H., Paasonen, P., Stratmann, F., Herrmann, H., Guenther, A. B., Worsnop, D. R., Kulmala, M., Ehn, M., and Sipilä, M.: Production of extremely low volatile organic compounds from biogenic emissions: Measured yields and atmospheric implications, *P. Natl. Acad. Sci. USA*, 112, 7123–7128, doi:10.1073/pnas.1423977112, 2015.
- Junninen, H., Ehn, M., Petäjä, T., Luosujärvi, L., Kotiaho, T., Kostianen, R., Rohner, U., Gonin, M., Fuhrer, K., Kulmala, M., and Worsnop, D. R.: A high-resolution mass spectrometer to measure atmospheric ion composition, *Atmos. Meas. Tech.*, 3, 1039–1053, doi:10.5194/amt-3-1039-2010, 2010.
- Kirkby, J., Curtius, J., Almeida, J., Dunne, E., Duplissy, J., Ehrhart, S., Franchin, A., Gagné, S., Ickes, L., Kürten, A., Kupc, A., Metzger, A., Riccobono, F., Rondo, L., Schobesberger, S., Tsagko-georgas, G., Wimmer, D., Amorim, A., Bianchi, F., Breitenlechner, M., David, A., Dommen, J., Downard, A., Ehn, M., Flanagan, R. C., Haider, S., Hansel, A., Hauser, D., Jud, W., Junninen, H., Kreissl, F., Kvashin, A., Laaksonen, A., Lehtipalo, K., Lima, J., Lovejoy, E. R., Makhmutov, V., Mathot, S., Mikkilä, J., Minginette, P., Mogo, S., Nieminen, T., Onnela, A., Pereira, P., Petäjä, T., Schnitzhofer, R., Seinfeld, J. H., Sipilä, M., Stozhkov, Y., Stratmann, F., Tomé, A., Vanhanen, J., Viisanen, Y., Vrtala, A., Wagner, P. E., Walther, H., Weingartner, E., Wex, H., Winkler, P. M., Carslaw, K. S., Worsnop, D. R., Baltensperger, U., and Kulmala, M.: Role of sulphuric acid, ammonia and galactic cosmic rays in atmospheric aerosol nucleation, *Nature*, 476, 429–435, doi:10.1038/nature10343, 2011.
- Kirkby, J., Duplissy, J., Sengupta, K., Frege, C., Gordon, H., Williamson, C., Heinritzi, M., Simon, M., Yan, C., Almeida, J., Tröstl, J., Nieminen, T., Ortega, I. K., Wagner, R., Adamov, A., Amorim, A., Bernhammer, A.-K., Bianchi, F., Breitenlechner, M., Brilke, S., Chen, X., Craven, J., Dias, A., Ehrhart, S., Flanagan, R. C., Franchin, A., Fuchs, C., Guida, R., Hakala, J., Hoyle, C. R., Jokinen, T., Junninen, H., Kangasluoma, J., Kim, J., Krapf, M., Kürten, A., Laaksonen, A., Lehtipalo, K., Makhmutov, V., Mathot, S., Molteni, U., Onnela, A., Peräkylä, O., Piel, F., Petäjä, T., Praplan, A. P., Pringle, K., Rap, A., Richards, N. A. D., Riip-

A. Kürten et al.: Observation of new particle formation

12811

- inen, I., Rissanen, M. P., Rondo, L., Sarnela, N., Schobesberger, S., Scott, C. E., Seinfeld, J. H., Sipilä, M., Steiner, G., Stozhkov, Y., Stratmann, F., Tomé, A., Virtanen, A., Vogel, A. L., Wagner, A., Wagner, P. E., Weingartner, E., Wimmer, D., Winkler, P. M., Ye, P., Zhang, X., Hansel, A., Dommen, J., Donahue, N. M., Worsnop, D. R., Baltensperger, U., Kulmala, M., Carslaw, K. S., and Curtius, J.: Ion-induced nucleation of pure biogenic particles, *Nature*, 533, 521–526, doi:10.1038/nature17953, 2016.
- Kuang, C., McMurry, P. H., McCormick, A. V., and Eisele, F. L.: Dependence of nucleation rates on sulfuric acid vapor concentration in diverse atmospheric locations, *J. Geophys. Res.*, 113, D10209, doi:10.1029/2007JD009253, 2008.
- Kulmala, M., Vehkamäki, H., Petäjä, T., Dal Maso, M., Lauri, A., Kerminen, V.-M., Birmili, W., and McMurry, P. H.: Formation and growth rates of ultrafine atmospheric particles: a review of observations, *J. Aerosol Sci.*, 35, 143–176, doi:10.1016/j.jaerosci.2003.10.003, 2004.
- Kulmala, M., Petäjä, T., Nieminen, T., Sipilä, M., Manninen, H. E., Lehtipalo, K., Dal Maso, M., Aalto, P. P., Junninen, H., Paasonen, P., Riipinen, I., Lehtinen, K. E. J., Laaksonen, A., and Kerminen, V.-M.: Measurement of the nucleation of atmospheric aerosol particles, *Nat. Protoc.*, 7, 1651–1667, doi:10.1038/nprot.2012.091, 2012.
- Kulmala, M., Kontkanen, J., Junninen, H., Lehtipalo, K., Manninen, H. E., Nieminen, T., Petäjä, T., Sipilä, M., Schobesberger, S., Rantala, P., Franchin, A., Jokinen, T., Järvinen, E., Äijälä, M., Kangasluoma, J., Hakala, J., Aalto, P. P., Paasonen, P., Mikkilä, J., Vanhanen, J., Aalto, J., Hakola, H., Makkonen, U., Ruuskanen, T., Mauldin III, R. L., Duplissy, J., Vehkamäki, H., Bäck, J., Kortelainen, A., Riipinen, I., Kurtén, T., Johnston, M. V., Smith, J. N., Ehn, M., Mentel, T. F., Lehtinen, K. E. J., Laaksonen, A., Kerminen, V.-M., and Worsnop, D. R.: Direct observations of atmospheric aerosol nucleation, *Science*, 339, 943–946, doi:10.1126/science.1227385, 2013.
- Kürten, A., Rondo, L., Ehrhart, S., and Curtius, J.: Performance of a corona ion source for measurement of sulfuric acid by chemical ionization mass spectrometry, *Atmos. Meas. Tech.*, 4, 437–443, doi:10.5194/amt-4-437-2011, 2011.
- Kürten, A., Rondo, L., Ehrhart, S., and Curtius, J.: Calibration of a chemical ionization mass spectrometer for the measurement of gaseous sulfuric acid, *J. Phys. Chem. A*, 116, 6375–6386, doi:10.1021/jp212123n, 2012.
- Kürten, A., Jokinen, T., Simon, M., Sipilä, M., Sarnela, N., Junninen, H., Adamov, A., Almeida, J., Amorim, A., Bianchi, F., Breitenlechner, M., Dommen, J., Donahue, N. M., Duplissy, J., Ehrhart, S., Flagan, R. C., Franchin, A., Hakala, J., Hansel, A., Heinritzi, M., Hutterli, M., Kangasluoma, J., Kirkby, J., Laaksonen, A., Lehtipalo, K., Leiminger, M., Makhmutov, V., Mathot, S., Onnela, A., Petäjä, T., Praplan, A. P., Riccobono, F., Rissanen, M. P., Rondo, L., Schobesberger, S., Seinfeld, J. H., Steiner, G., Tomé, A., Tröstl, J., Winkler, P. M., Williamson, C., Wimmer, D., Ye, P., Baltensperger, U., Carslaw, K. S., Kulmala, M., Worsnop, D. R., and Curtius, J.: Neutral molecular cluster formation of sulfuric acid-dimethylamine observed in real-time under atmospheric conditions, *P. Natl. Acad. Sci. USA*, 111, 15019–15024, doi:10.1073/pnas.1404853111, 2014.
- Kürten, A., Münch, S., Rondo, L., Bianchi, F., Duplissy, J., Jokinen, T., Junninen, H., Sarnela, N., Schobesberger, S., Simon, M., Sipilä, M., Almeida, J., Amorim, A., Dommen, J., Donahue, N. M., Dunne, E. M., Flagan, R. C., Franchin, A., Kirkby, J., Kupc, A., Makhmutov, V., Petäjä, T., Praplan, A. P., Riccobono, F., Steiner, G., Tomé, A., Tsagkogeorgas, G., Wagner, P. E., Wimmer, D., Baltensperger, U., Kulmala, M., Worsnop, D. R., and Curtius, J.: Thermodynamics of the formation of sulfuric acid dimers in the binary ($\text{H}_2\text{SO}_4\text{--H}_2\text{O}$) and ternary ($\text{H}_2\text{SO}_4\text{--H}_2\text{O--NH}_3$) system, *Atmos. Chem. Phys.*, 15, 10701–10721, doi:10.5194/acp-15-10701-2015, 2015.
- Kürten, A., Bianchi, F., Almeida, J., Kupiainen-Määttä, O., Dunne, E. M., Duplissy, J., Williamson, C., Barnet, P., Breitenlechner, M., Dommen, J., Donahue, N. M., Flagan, R. C., Franchin, A., Gordon, H., Hakala, J., Hansel, A., Heinritzi, M., Ickes, L., Jokinen, T., Kangasluoma, J., Kim, J., Kirkby, J., Kupc, A., Lehtipalo, K., Leiminger, M., Makhmutov, V., Onnela, A., Ortega, I. K., Petäjä, T., Praplan, A. P., Riccobono, F., Rissanen, M. P., Rondo, L., Schnitzhofer, R., Schobesberger, S., Smith, J. N., Steiner, G., Stozhkov, Y., Tomé, A., Tröstl, J., Tsagkogeorgas, G., Wagner, P. E., Wimmer, D., Ye, P., Baltensperger, U., Carslaw, K., Kulmala, M., and Curtius, J.: Experimental particle formation rates spanning tropospheric sulfuric acid and ammonia abundances, ion production rates and temperatures, *J. Geophys. Res.-Atmos.*, accepted, doi:10.1002/2015JD023908, 2016.
- Kurtén, T., Loukonen, V., Vehkamäki, H., and Kulmala, M.: Amines are likely to enhance neutral and ion-induced sulfuric acid-water nucleation in the atmosphere more effectively than ammonia, *Atmos. Chem. Phys.*, 8, 4095–4103, doi:10.5194/acp-8-4095-2008, 2008.
- Lehtinen, K. E. J., Dal Maso, M., Kulmala, M., and Kerminen, V.-M.: Estimating nucleation rates from apparent particle formation rates and vice versa: Revised formulation of the Kerminen–Kulmala equation, *J. Aerosol Sci.*, 38, 988–994, doi:10.1016/j.jaerosci.2007.06.009, 2007.
- Lehtipalo, K., Rondo, L., Kontkanen, J., Schobesberger, S., Jokinen, T., Sarnela, N., Kürten, A., Ehrhart, S., Franchin, A., Nieminen, T., Riccobono, F., Sipilä, M., Yli-Juuti, T., Duplissy, J., Adamov, A., Ahlm, L., Almeida, J., Amorim, A., Bianchi, F., Breitenlechner, M., Dommen, J., Downard, A. J., Dunne, E. M., Flagan, R. C., Guida, R., Hakala, J., Hansel, A., Jud, W., Kangasluoma, J., Kerminen, V.-M., Keskinen, H., Kim, J., Kirkby, J., Kupc, A., Kupiainen-Määttä, O., Laaksonen, A., Lawler, M. J., Leiminger, M., Mathot, S., Olenius, T., Ortega, I. K., Onnela, A., Petäjä, T., Praplan, A., Rissanen, M. P., Ruuskanen, T., Santos, F. D., Schallhart, S., Schnitzhofer, R., Simon, M., Smith, J. N., Tröstl, J., Tsagkogeorgas, G., Tomé, A., Vaattovaara, P., Vehkamäki, H., Virtala, A. E., Wagner, P. E., Williamson, C., Wimmer, D., Winkler, P. M., Virtanen, A., Donahue, N. M., Carslaw, K. S., Baltensperger, U., Riipinen, I., Curtius, J., Worsnop, D. R., and Kulmala, M.: The effect of acid-base clustering and ions on the growth of atmospheric nano-particles, *Nat. Commun.*, 7, 11594, doi:10.1038/ncomms11594, 2016.
- Luts, A., Parts, T.-E., Hörrak, U., Junninen, H., and Kulmala, M.: Composition of negative air ions as a function of ion age and selected trace gases: Mass- and mobility distribution, *J. Aerosol Sci.*, 42, 820–838, doi:10.1016/j.jaerosci.2011.07.007, 2011.
- Mauldin III, R. L., Berndt, T., Sipilä, M., Paasonen, P., Petäjä, T., Kim, S., Kurtén, T., Stratmann, F., Kerminen, V.-M., and Kulmala, M.: A new atmospherically relevant oxidant of sulphur dioxide, *Nature*, 488, 193–196, doi:10.1038/nature11278, 2012.

12812

- Merikanto, J., Spracklen, D. V., Mann, G. W., Pickering, S. J., and Carslaw, K. S.: Impact of nucleation on global CCN, *Atmos. Chem. Phys.*, 9, 8601–8616, doi:10.5194/acp-9-8601-2009, 2009.
- Metzger, A., Verheggen, B., Dommen, J., Duplissy, J., Prevot, A. S. H., Weingartner, E., Riipinen, I., Kulmala, M., Spracklen, D. V., Carslaw, K. S., and Baltensperger, U.: Evidence for the role of organics in aerosol particle formation under atmospheric conditions, *P. Natl. Acad. Sci. USA*, 107, 6646–6651, doi:10.1073/pnas.0911330107, 2010.
- Mikkonen, S., Romakkaniemi, S., Smith, J. N., Korhonen, H., Petäjä, T., Plass-Dümler, C., Boy, M., McMurry, P. H., Lehtinen, K. E. J., Joutsensaari, J., Hamed, A., Mauldin III, R. L., Birmili, W., Spindler, G., Arnold, F., Kulmala, M., and Laaksonen, A.: A statistical proxy for sulphuric acid concentration, *Atmos. Chem. Phys.*, 11, 11319–11334, doi:10.5194/acp-11-11319-2011, 2011.
- Monks, P. S.: Gas-phase radical chemistry in the troposphere, *Chem. Soc. Rev.*, 34, 376–395, doi:10.1039/B307982C, 2005.
- Mutzel, A., Poulain, L., Berndt, T., Iinuma, Y., Rodigast, M., Böge, O., Richters, S., Spindler, G., Sipilä, M., Jokinen, T., Kulmala, M., and Herrmann, H.: Highly oxidized multifunctional organic compounds observed in tropospheric particles: A field and laboratory study, *Environ. Sci. Technol.*, 49, 7754–7761, doi:10.1021/acs.est.5b00885, 2015.
- Nel, A.: Air pollution–related illness: Effects of particles, *Science*, 308, 804–806, doi:10.1126/science.1108752, 2005.
- Nielsen, C. J., Herrmann, H., and Weller, C.: Atmospheric chemistry and environmental impact of the use of amines in carbon capture and storage (CCS), *Chem. Soc. Rev.*, 41, 6684–6704, doi:10.1039/c2cs35059a, 2012.
- Nieminen, T., Yli-Juuti, T., Manninen, H. E., Petäjä, T., Kerminen, V.-M., and Kulmala, M.: Technical note: New particle formation event forecasts during PEGASOS-Zeppelin Northern mission 2013 in Hyttälä, Finland, *Atmos. Chem. Phys.*, 15, 12385–12396, doi:10.5194/acp-15-12385-2015, 2015.
- Ortega, I. K., Kupiainen, O., Kurtén, T., Olenius, T., Wilkman, O., McGrath, M. J., Loukonen, V., and Vehkamäki, H.: From quantum chemical formation free energies to evaporation rates, *Atmos. Chem. Phys.*, 12, 225–235, doi:10.5194/acp-12-225-2012, 2012.
- Ortega, I. K., Olenius, T., Kupiainen-Määttä, O., Loukonen, V., Kurtén, T., and Vehkamäki, H.: Electrical charging changes the composition of sulfuric acid-ammonia/dimethylamine clusters, *Atmos. Chem. Phys.*, 14, 7995–8007, doi:10.5194/acp-14-7995-2014, 2014.
- Paasonen, P., Nieminen, T., Asmi, E., Manninen, H. E., Petäjä, T., Plass-Dümler, C., Flentje, H., Birmili, W., Wiedensohler, A., Hörrak, U., Metzger, A., Hamed, A., Laaksonen, A., Facchini, M. C., Kerminen, V.-M., and Kulmala, M.: On the roles of sulphuric acid and low-volatility organic vapours in the initial steps of atmospheric new particle formation, *Atmos. Chem. Phys.*, 10, 11223–11242, doi:10.5194/acp-10-11223-2010, 2010.
- Petäjä, T., Mauldin, III, R. L., Kosciuch, E., McGrath, J., Nieminen, T., Paasonen, P., Boy, M., Adamov, A., Kotiaho, T., and Kulmala, M.: Sulfuric acid and OH concentrations in a boreal forest site, *Atmos. Chem. Phys.*, 9, 7435–7448, doi:10.5194/acp-9-7435-2009, 2009.
- Plane, J. M. C., Joseph, D. M., Allan, B. J., Ashworth, S. H., and Francisco, J. S.: An experimental and theoretical study of the reactions $\text{OIO} + \text{NO}$ and $\text{OIO} + \text{OH}$, *J. Phys. Chem. A*, 110, 93–100, doi:10.1021/jp055364y, 2006.
- Praplan, A. P., Schobesberger, S., Bianchi, F., Rissanen, M. P., Ehn, M., Jokinen, T., Junninen, H., Adamov, A., Amorim, A., Dommen, J., Duplissy, J., Hakala, J., Hansel, A., Heinritzi, M., Kangasluoma, J., Kirkby, J., Krapf, M., Kürten, A., Lehtipalo, K., Riccobono, F., Rondo, L., Sarnela, N., Simon, M., Tomé, A., Tröstl, J., Winkler, P. M., Williamson, C., Ye, P., Curtius, J., Baltensperger, U., Donahue, N. M., Kulmala, M., and Worsnop, D. R.: Elemental composition and clustering behaviour of α -pinene oxidation products for different oxidation conditions, *Atmos. Chem. Phys.*, 15, 4145–4159, doi:10.5194/acp-15-4145-2015, 2015.
- Rantala, P., Taipale, R., Aalto, J., Kajos, M. K., Patokoski, J., Ruuskanen, T. M., and Rinne, J.: Continuous flux measurements of VOCs using PTR-MS – reliability and feasibility of disjunct-eddy-covariance, surface-layer-gradient, and surface-layer-profile methods, *Boreal Environ. Res.*, 19, 87–107, 2014.
- Riccobono, F., Schobesberger, S., Scott, C. E., Dommen, J., Ortega, I. K., Rondo, L., Almeida, J., Amorim, A., Bianchi, F., Breitenlechner, M., David, A., Downard, A., Dunne, E. M., Duplissy, J., Ehrhart, S., Flagan, R. C., Franchin, A., Hansel, A., Junninen, H., Kajos, M., Keskinen, H., Kupc, A., Kürten, A., Kvashin, A. N., Laaksonen, A., Lehtipalo, K., Makhmutov, V., Mathot, S., Nieminen, T., Onnela, A., Petäjä, T., Praplan, A. P., Santos, F. D., Schallhart, S., Seinfeld, J. H., Sipilä, M., Spracklen, D. V., Stozhkov, Y., Stratmann, F., Tomé, A., Tsagkogeorgas, G., Vaattovaara, P., Viisanen, Y., Vrtala, A., Wagner, P. E., Weingartner, E., Wex, H., Wimmer, D., Carslaw, K. S., Curtius, J., Donahue, N. M., Kirkby, J., Kulmala, M., Worsnop, D. R., and Baltensperger, U.: Oxidation products of biogenic emissions contribute to nucleation of atmospheric particles, *Science*, 344, 717–721, doi:10.1126/science.1243527, 2014.
- Rohrer, F. and Berreheim, H.: Strong correlation between levels of tropospheric hydroxyl radicals and solar ultraviolet radiation, *Nature*, 442, 184–187, doi:10.1038/nature04924, 2006.
- Rondo, L., Kürten, A., Ehrhart, S., Schobesberger, S., Franchin, A., Junninen, H., Petäjä, T., Sipilä, M., Worsnop, D. R., and Curtius, J.: Effect of ions on the measurement of sulfuric acid in the CLOUD experiment at CERN, *Atmos. Meas. Tech.*, 7, 3849–3859, doi:10.5194/amt-7-3849-2014, 2014.
- Saiz-Lopez, A., Plane, J. M. C., Baker, A. R., Carpenter, L. J., von Glasow, R., Martín, J. C. G., McFiggans, G., and Saunders, R. W.: Atmospheric chemistry of iodine, *Chem. Rev.*, 112, 1773–1804, doi:10.1021/cr200029u, 2012.
- Saiz-Lopez, A., Baidar, S., Cuevas, C. A., Koenig, T. K., Fernandez, R. P., Dix, B., Kinnison, D. E., Lamarque, J.-F., Rodriguez-Lloveras, X., Campos, T. L., and Volkamer, R.: Injection of iodine to the stratosphere, *Geophys. Res. Lett.*, 42, 6852–6859, doi:10.1002/2015GL064796, 2015.
- Sarnela, N., Jokinen, T., Nieminen, T., Lehtipalo, K., Junninen, H., Kangasluoma, J., Hakala, J., Taipale, R., Schobesberger, S., Sipilä, M., Larmimaa, K., Westerholm, H., Heijari, J., Kerminen, V.-M., Petäjä, T., and Kulmala, M.: Sulphuric acid and aerosol particle production in the vicinity of an oil refinery, *Atmos. Environ.*, 119, 156–166, doi:10.1016/j.atmosenv.2015.08.033, 2015.
- Sarwar, G., Fahey, K., Kwok, R., Gilliam, R. C., Roselle, S. J., Mathur, R., Xue, J., Yu, J., and Carter, W. P. L.: Potential impacts of two SO_2 oxidation pathways on regional sulphate con-

A. Kürten et al.: Observation of new particle formation

12813

- centrations: Aqueous-phase oxidation by NO₂ and gas-phase oxidation by stabilized Criegee intermediate, *Atmos. Environ.*, 68, 186–197, doi:10.1016/j.atmosenv.2012.11.036, 2013.
- Schade, G. W. and Crutzen, P. J.: Emission of aliphatic amines from animal husbandry and their reactions: Potential source of N₂O and HCN, *J. Atmos. Chem.*, 22, 319–346, doi:10.1007/BF00696641, 1995.
- Schobesberger, S., Junninen, H., Bianchi, F., Lönn, G., Ehn, M., Lehtipalo, K., Dommen, J., Ehrhart, S., Ortega, I. K., Franchin, A., Nieminen, T., Riccobono, F., Hutterli, M., Duplissy, J., Almeida, J., Amorim, A., Breitenlechner, M., Downard, A. J., Dunne, E. M., Flagan, R. C., Kajos, M., Keskinen, H., Kirkby, J., Kupc, A., Kürten, A., Kurtén, T., Laaksonen, A., Mathot, S., Onnela, A., Praplan, A. P., Rondo, L., Santos, F. D., Schallhart, S., Schnitzhofer, R., Sipilä, M., Tomé, A., Tsagkogeorgas, G., Vehkamäki, H., Wimmer, D., Baltensperger, U., Carslaw, K. S., Curtius, J., Hansel, A., Petäjä, T., Kulmala, M., Donahue, N. M., and Worsnop, D. R.: Molecular understanding of atmospheric particle formation from sulfuric acid and large oxidized organic molecules, *Proc. Natl. Acad. Sci. USA*, 110, 17223–17228, doi:10.1073/pnas.1306973110, 2013.
- Sihto, S.-L., Kulmala, M., Kerminen, V.-M., Dal Maso, M., Petäjä, T., Riipinen, I., Korhonen, H., Arnold, F., Janson, R., Boy, M., Laaksonen, A., and Lehtinen, K. E. J.: Atmospheric sulphuric acid and aerosol formation: implications from atmospheric measurements for nucleation and early growth mechanisms, *Atmos. Chem. Phys.*, 6, 4079–4091, doi:10.5194/acp-6-4079-2006, 2006.
- Simon, M., Heinritzi, M., Herzog, S., Leiminger, M., Bianchi, F., Praplan, A., Dommen, J., Curtius, J., and Kürten, A.: Detection of dimethylamine in the low pptv range using nitrate chemical ionization atmospheric pressure interface time-of-flight (CI-API-TOF) mass spectrometry, *Atmos. Meas. Tech.*, 9, 2135–2145, doi:10.5194/amt-9-2135-2016, 2016.
- Sintermann, J., Schallhart, S., Kajos, M., Jocher, M., Bracher, A., Mürner, A., Johnson, D., Neftel, A., and Ruuskanen, T.: Trimethylamine emissions in animal husbandry, *Biogeosciences*, 11, 5073–5085, doi:10.5194/bg-11-5073-2014, 2014.
- Sipilä, M., Jokinen, T., Berndt, T., Richters, S., Makkonen, R., Donahue, N. M., Mauldin III, R. L., Kurtén, T., Paasonen, P., Sarnela, N., Ehn, M., Junninen, H., Rissanen, M. P., Thornton, J., Stratmann, F., Herrmann, H., Worsnop, D. R., Kulmala, M., Kerminen, V.-M., and Petäjä, T.: Reactivity of stabilized Criegee intermediates (sCIs) from isoprene and monoterpene ozonolysis toward SO₂ and organic acids, *Atmos. Chem. Phys.*, 14, 12143–12153, doi:10.5194/acp-14-12143-2014, 2014.
- Sipilä, M., Sarnela, N., Jokinen, T., Junninen, H., Hakala, J., Rissanen, M. P., Praplan, A., Simon, M., Kürten, A., Bianchi, F., Dommen, J., Curtius, J., Petäjä, T., and Worsnop, D. R.: Bisulfate – cluster based atmospheric pressure chemical ionization mass spectrometer for high-sensitivity (<100 ppqV) detection of atmospheric dimethyl amine: proof-of-concept and first ambient data from boreal forest, *Atmos. Meas. Tech.*, 8, 4001–4011, doi:10.5194/amt-8-4001-2015, 2015.
- Stein, A. F., Draxler, R. R., Rolph, G. D., Stunder, B. J. B., Cohen, M. D., and Ngan, F.: NOAA's HYSPLIT atmospheric transport and dispersion modeling system, *B. Am. Meteorol. Soc.*, 96, 2059–2077, doi:10.1175/BAMS-D-14-00110.1, 2015.
- Tani, A., Hayward, S., and Hewitt, C. N.: Measurement of monoterpenes and related compounds by proton transfer reaction-mass spectrometry (PTR-MS), *Int. J. Mass Spectrom.*, 223, 561–578, doi:10.1016/S1387-3806(02)00880-1, 2003.
- Vanhanen, J., Mikkilä, J., Lehtipalo, K., Sipilä, M., Manninen, H. E., Siivola, E., Petäjä, T., and Kulmala, M.: Particle size magnifier for nano-CN detection, *Aerosol Sci. Technol.*, 45, 533–542, doi:10.1080/02786826.2010.547889, 2011.
- von Bobruzki, K., Braban, C. F., Famulari, D., Jones, S. K., Blackall, T., Smith, T. E. L., Blom, M., Coe, H., Gallagher, M., Ghahaieny, M., McGillen, M. R., Percival, C. J., Whitehead, J. D., Ellis, R., Murphy, J., Mohacsi, A., Pogany, A., Junninen, H., Rantanen, S., Sutton, M. A., and Nemitz, E.: Field inter-comparison of eleven atmospheric ammonia measurement techniques, *Atmos. Meas. Tech.*, 3, 91–112, doi:10.5194/amt-3-91-2010, 2010.
- Weber, R. J., Marti, J. J., McMurry, P. H., Eisele, F. L., Tanner, D. J., and Jefferson, A.: Measurements of new particle formation and ultrafine particle growth rates at a clean continental site, *J. Geophys. Res.*, 102, 4375–4385, doi:10.1029/96JD03656, 1997.
- You, Y., Kanawade, V. P., de Gouw, J. A., Guenther, A. B., Madronich, S., Sierra-Hernández, M. R., Lawler, M., Smith, J. N., Takahama, S., Ruggeri, G., Koss, A., Olson, K., Baumann, K., Weber, R. J., Nenes, A., Guo, H., Edgerton, E. S., Porcelli, L., Brune, W. H., Goldstein, A. H., and Lee, S.-H.: Atmospheric amines and ammonia measured with a chemical ionization mass spectrometer (CIMS), *Atmos. Chem. Phys.*, 14, 12181–12194, doi:10.5194/acp-14-12181-2014, 2014.
- Yu, H. and Lee, S.-H.: Chemical ionisation mass spectrometry for the measurement of atmospheric amines, *Environ. Chem.*, 9, 190–201, doi:10.1071/EN12020, 2012.
- Zhang, R., Khalizov, A., Wang, L., Hu, M., and Xu, W.: Nucleation and growth of nanoparticles in the atmosphere, *Chem. Rev.*, 1957–2011, doi:10.1021/cr2001756, 2012.
- Zhao, J., Eisele, F. L., Titcombe, M., Kuang, C., and McMurry, P. H.: Chemical ionization mass spectrometric measurements of atmospheric neutral clusters using the cluster-CIMS, *J. Geophys. Res.*, 115, D08205, doi:10.1029/2009JD012606, 2010.
- Zhao, J., Smith, J. N., Eisele, F. L., Chen, M., Kuang, C., and McMurry, P. H.: Observation of neutral sulfuric acid-amine containing clusters in laboratory and ambient measurements, *Atmos. Chem. Phys.*, 11, 10823–10836, doi:10.5194/acp-11-10823-2011, 2011.
- Zhao, J., Ortega, J., Chen, M., McMurry, P. H., and Smith, J. N.: Dependence of particle nucleation and growth on high-molecular-weight gas-phase products during ozonolysis of α -pinene, *Atmos. Chem. Phys.*, 13, 7631–7644, doi:10.5194/acp-13-7631-2013, 2013.

4.4 Characterization of the mass-dependent transmission efficiency of a CIMS (Heinritzi et al. (2016))

Atmos. Meas. Tech., 9, 1449–1460, 2016
www.atmos-meas-tech.net/9/1449/2016/
doi:10.5194/amt-9-1449-2016
© Author(s) 2016. CC Attribution 3.0 License.



Atmospheric
Measurement
Techniques
Open Access
EGU

Characterization of the mass-dependent transmission efficiency of a CIMS

Martin Heinritzi¹, Mario Simon¹, Gerhard Steiner^{2,3}, Andrea C. Wagner¹, Andreas Kürten¹, Armin Hansel^{3,4}, and Joachim Curtius¹

¹Goethe University Frankfurt, Institute for Atmospheric and Environmental Sciences, 60438 Frankfurt am Main, Germany

²University of Vienna, Faculty of Physics, 1090 Wien, Austria

³University of Innsbruck, Institute for Ion and Applied Physics, 6020 Innsbruck, Austria

⁴Ionicon Analytik GmbH, 6020 Innsbruck, Austria

Correspondence to: Martin Heinritzi (heinritzi@iau.uni-frankfurt.de)

Received: 21 August 2015 – Published in Atmos. Meas. Tech. Discuss.: 2 November 2015

Revised: 5 March 2016 – Accepted: 12 March 2016 – Published: 4 April 2016

Abstract. Knowledge about mass discrimination effects in a chemical ionization mass spectrometer (CIMS) is crucial for quantifying, e.g., the recently discovered extremely low volatile organic compounds (ELVOCs) and other compounds for which no calibration standard exists so far. Here, we present a simple way of estimating mass discrimination effects of a nitrate-based chemical ionization atmospheric pressure interface time-of-flight (CI-API-TOF) mass spectrometer. Characterization of the mass discrimination is achieved by adding different perfluorinated acids to the mass spectrometer in amounts sufficient to deplete the primary ions significantly. The relative transmission efficiency can then be determined by comparing the decrease of signals from the primary ions and the increase of signals from the perfluorinated acids at higher masses. This method is in use already for PTR-MS; however, its application to a CI-API-TOF brings additional difficulties, namely clustering and fragmentation of the measured compounds, which can be treated with statistical analysis of the measured data, leading to self-consistent results. We also compare this method to a transmission estimation obtained with a setup using an electrospray ion source, a high-resolution differential mobility analyzer and an electrometer, which estimates the transmission of the instrument without the CI source. Both methods give different transmission curves, indicating non-negligible mass discrimination effects of the CI source. The absolute transmission of the instrument without the CI source was estimated with the HR-DMA method to plateau between the m/z

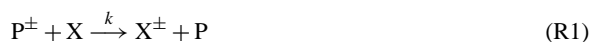
range of 127 and 568 Th at around 1.5 %; however, for the CI source included, the depletion method showed a steady increase in relative transmission efficiency from the m/z range of the primary ion (mainly at 62 Th) to around 550 Th by a factor of around 5. The main advantages of the depletion method are that the instrument is used in the same operation mode as during standard measurements and no knowledge of the absolute amount of the measured substance is necessary, which results in a simple setup.

1 Introduction

The nitrate-based chemical ionization atmospheric pressure interface time-of-flight (CI-API-TOF) mass spectrometer has been established as an important tool for atmospheric sciences over the last years. It is capable of measuring sulfuric acid down to levels of $5 \times 10^4 \text{ cm}^{-3}$ (Kürten et al., 2011; Jokinen et al., 2012) and clusters of sulfuric acid with dimethylamine (Kürten et al., 2014), as well as the newly described class of extremely low volatile organic compounds (ELVOCs, Ehn et al., 2014), which play a role in the formation of secondary organic aerosol (SOA). However, proper quantification of the measured signals remains challenging, as direct calibration gas standards for sulfuric acid, as well as for ELVOCs do not exist so far. For comparison, for proton-transfer-reaction mass spectrometry (PTR-MS), which is capable of measuring precursors for ELVOCs like α -pinene at

the ppt level (Graus et al., 2010), calibration gas standards for many volatile organic compounds (VOCs) are commercially available with a typical uncertainty of $\pm 5\%$. The lack of calibration gas standards for the CI-API-TOF led to the development of a dedicated calibration system for sulfuric acid (Kürten et al., 2012). Here, a known amount of gaseous sulfuric acid is produced via UV-light induced generation of OH• radicals (Tanner and Eisele, 1995) and subsequent oxidation of SO₂ to H₂SO₄ (Eisele and Tanner, 1991). The UV system is characterized with a separate experiment, using photolytical conversion of N₂O to NO_x (Edwards et al., 2003), where both reactant and product can be measured. With this system calibration factors for the CI-API-TOF can be obtained for sulfuric acid with an overall uncertainty of around 33%. However, this leaves still open the question of quantifying ELVOCs properly. Ehn et al. (2014) have performed a gravimetric calibration of the CI-API-TOF using perfluorinated heptanoic acid, which appears mainly in the m/z range of 319 to 426 Th (monomers) and at 727 Th (dimers). They obtained a similar calibration factor for this compound as for sulfuric acid; however, the detailed transmission efficiency of the instrument over the entire mass range cannot be resolved with this method.

The theoretical framework for deriving concentrations of a certain compound from ion count rates for the CI-API-TOF is essentially the same as given by Eisele and Tanner (1993) for sulfuric acid measurements or by Hansel et al. (1995) for a PTR-MS. Ionization of a compound X via primary ions P[±] can be described by the following reaction:



The relation between primary ion concentration [P[±]] and the concentration of the desired compound [X] in the reaction tube of the instrument is given by the following expression, where k is the reaction rate constant for the ionization reaction:

$$\frac{d[\text{P}^{\pm}]}{dt} = -k[\text{P}^{\pm}][\text{X}]. \quad (1)$$

Assuming [X] as constant over the reaction time t (pseudo first order reaction approximation) enables a simple integration. The additional assumption that the total amount of charge is constant in the reaction tube leads to the following expression for the concentration of [X]:

$$[\text{X}] = \frac{1}{kt} \ln \left(1 + \frac{[\text{X}^{\pm}]}{[\text{P}^{\pm}]} \right) \approx \frac{1}{kt} \cdot \frac{[\text{X}^{\pm}]}{[\text{P}^{\pm}]} \quad (2)$$

Assuming $[\text{X}^{\pm}] \ll [\text{P}^{\pm}]$, which is usually fulfilled, allows for the first order approximation in Eq. (2). The concentration of compound X is proportional to the ratio of concentrations of product ions [X[±]] and primary ions [P[±]]. However, the mass spectrometer does not measure the ion concentrations in the reaction chamber directly, but only ion count rates at the location of the detector of the instrument. Therefore replacing

the concentrations [X[±]] and [P[±]] in Eq. (2) by ion count rates $i(\text{X}^{\pm})$ and $i(\text{P}^{\pm})$ is only justified if we account for the relative mass discrimination of the two ion species inside the mass spectrometer:

$$[\text{X}] \approx \frac{1}{kt} \cdot \frac{i(\text{X}^{\pm})}{i(\text{P}^{\pm})} \cdot \frac{1}{T_{\text{X}}}. \quad (3)$$

Here, T_{X} is the factor that describes the mass discrimination of ions X[±] relative to that of the primary ions P[±]. This factor can be strongly dependent on the m/z ratio of the involved ions. Calibration with an external gas standard or the above described H₂SO₄ calibration intrinsically accounts for this factor. However, if a direct calibration is not available, the factor T_{X} has to be known for the m/z range of the desired compound. Therefore the calculated concentration of X depends on the ratio of product ions to primary ions, as well as the reaction time t , the reaction rate constant k and the relative transmission factor T_{X} . Ehn et al. (2014) showed with quantum chemical calculations that the collision rates of characteristic ELVOC molecules with the nitrate primary ions (NO₃⁻(HNO₃)₀₋₂) are equal to the collision rate of sulfuric acid with the nitrate primary ions, respectively. Furthermore, due to the assumed high binding energy between the highly oxidized ELVOC molecules and the nitrate primary ions, a charging at the kinetic limit is assumed, resulting in approximately the same reaction rate constant for ELVOCs as for sulfuric acid. This is, however, a rough approximation as the chemical composition of ELVOC molecules differs strongly and may thus result in varying reaction rate constants. As the reaction time is assumed to be equal for all compounds, only depending on the geometry of the ion source and the applied flows, the factor $1/kt$ in Eq. (3) for ELVOC molecules would be approximately the same as for sulfuric acid, leaving the mass discrimination factor T_{X} as the only remaining unknown. This factor is of great importance for quantification of any uncalibrated compound and especially for ELVOC molecules, as their m/z range (peaks between 235 and 625 Th) differs strongly from that of sulfuric acid (main peak at 97 Th).

In this study we show the application of the method of depleting primary ions to the nitrate-based CI-API-TOF for obtaining transmission curves. We describe the measurement setup and the used compounds as well as the statistical analysis that became necessary due to the high level of clustering of compounds inside the CI-API-TOF. Additionally we compare this method with a second approach for transmission estimations that uses a high-resolution differential mobility analyzer and an electrometer.

2 Mass discrimination effects

Various parts of the time-of-flight mass spectrometer (Tofwerk AG, Thun, Switzerland) can cause mass discrimination

effects, especially the two quadrupole units in the APi interface, the orthogonal extraction unit in the TOF and the multi-channel plate (MCP) detector. The CI source itself (Kürten et al., 2011) may also cause mass discrimination effects, as several negative voltages are applied to the source to guide the ions to the pinhole, which marks the entrance of the vacuum region of the instrument. After the pinhole, three differentially pumped chambers are installed, two of which contain a segmented quadrupole operating in RF-only mode, and the last one contains an Einzel lens system. The main task of these transfer units is to guide and focus the ion beam to the high vacuum TOF region. Quadrupoles in RF-only mode act as a high pass filter for ions as the trajectories of ions below a certain m/z ratio are not stable any more (Chernushevich et al., 2001). On the other hand, as the potential well provided by a quadrupole is inversely proportional to m/z , heavier ions suffer poorer focusing and thus reduced transmission (Gerlich, 1992). The m/z range with maximum transmission can however be modulated with the applied RF-voltage. According to Chernushevich et al. (2001), higher RF voltages lead to a stronger suppression of lighter ions and vice versa. Additionally, the shape of the transmission curve depends on the ion beam shape at the entrance of the quadrupole. Muntean (1995) showed ion trajectory calculations taking into account ion beam divergence as well as off-axis beam profiles. While beam divergence shifts the maximum transmission to small values, meaning an additional suppression of heavy ions, off-axis intensities have the opposite effect. In practice, there will be a suppression of ion transmission at both ends of the m/z range, with the shape and position of the transmission window depending on the detailed settings and the quality of the beam focusing.

The orthogonal extraction unit of a TOF shows a systematic discrimination of lower m/z ratios under the assumption of a mono-energetic ion beam entering the extraction unit in axial direction (Chernushevich et al., 2001). This discrimination is a result of the higher axial velocity and thus larger spatial spread of lighter ions along the axis. Therefore as a larger fraction of lighter ions has already left the extraction region compared to heavier ions, fewer of the lighter ions are accelerated orthogonally to the detector. As the velocity of the ions is proportional to $\sqrt{m/z}^{-1}$ the geometric duty cycle is proportional to $\sqrt{m/z}$.

Also the multi-channel plate detector in the TOF can show mass discrimination effects. Müller et al. (2014) showed for a PTR-TOF, which utilizes the same MCP as the TOF in this study (PHOTONIS Inc., Sturbridge, MA, USA), that the mass discrimination can change due to aging of the detector and is strongly dependent on the operating voltage of the MCP. Especially at low gain voltages, higher masses are discriminated against more strongly. Gilmore and Seah (2000) showed that the mass discrimination effects of an MCP also vary with the total impact energy of the ions, which is defined by the post accelerating voltage in a TOF. This study found a

reduced detection efficiency for heavier ions at lower impact energies.

Finally, even the smallest changes of the inner geometry of the instrument, e.g., caused by shipping, can affect ion beam alignment and thus cause different transmission characteristics. This variety of effects makes it almost impossible to calculate the transmission efficiency, so methods for a measurement of this property are crucial.

3 Methods

3.1 HR-DMA

The development of high-resolution differential mobility analyzers (HR-DMA) led to the ability of classifying particles and clusters down to a size of around 1 nm (Steiner et al., 2010; Fernández de la Mora et al., 2013). As this corresponds to a mass range the CI-APi-TOF is able to measure, these two instruments can be combined for a characterization of the latter. Here, a version of the so called “Vienna-type” DMA was used (Steiner et al., 2010). It is a closed loop, medium flow (up to around 700 slpm) size classifier, with a maximum resolution power of around 20. The resolution power is derived from the ratio of the electrical mobility Z of a certain cluster and the full-width half maximum (FWHM) of the corresponding peak in a mobility scan. However, for the operating conditions in this study a resolution power between 10 and 15 was achieved, which was sufficient to clearly separate monomers and dimers of almost all compounds tested. The high resolution, in principle, is necessary to distinguish between small clusters with only one molecule difference in mass. To generate these clusters, an electrospray ion source was used, which can be operated in either negative or positive mode. As the nitrate-based CI-APi-TOF is operating in negative ion mode, we produced negatively charged clusters of several bromide and iodide salts as well as an ionic liquid (see Table 1). After production by electrospray ionization (ESI) and size selection in the HR-DMA the cluster ion flow is split up between a Faraday cup electrometer (EM) to measure the ion count rate in front of the mass spectrometer and the CI-APi-TOF. The transmission efficiency of the mass spectrometer at a certain m/z ratio is obtained by dividing the ion count rates from the TOF by the corrected EM ion count rate. The configurations that were tested are shown in Fig. 1a and b. This method is in use already for characterizing the transmission efficiency of APi-TOF instruments (Junninen et al., 2010) and does not account for mass discrimination effects of the CI source. The pinhole plate of an APi-TOF is usually set to a certain voltage to attract ions. In the CI-APi-TOF this is achieved by applying negative voltages to the CI source, whereas the pinhole plate itself is at ground potential. In the configurations used here, the pinhole plate was at ground as well in order not to disturb the potential steps on the vacuum side of the instrument. In the

Table 1. Compounds used for HR-DMA method with according monomer, dimer, and trimer. Trimers were not always quantifiable as the HR-DMA also selected multiply charged higher clusters when adjusted for trimers (indicated by italics). This was also the case for the tetradodecylammonium bromide dimer.

Name	Monomer, m/z [Th]	Dimer, m/z [Th]	Trimer, m/z [Th]
Methyloctylammonium bis(trifluoromethylsulfonyl)imide, MTOA	$C_2NO_4F_6S_2^-$, 279.92	$C_{29}H_{54}N_3O_8F_{12}S_4^-$, 928.26	$C_{56}H_{108}N_5O_{12}F_{18}S_6^-$, 1576.60
Tetrabutylammonium iodide, TBAI	I^- , 126.90	$C_{16}H_{36}NI_2^-$, 496.09	
Tetrapropylammonium iodide, TPPAI	I^- , 126.90	$C_{12}H_{28}NI_2^-$, 440.03	
Tetraheptylammonium bormide, THABr	Br^- , 78.92	$C_{28}H_{60}NBr_2^-$, 568.31	
Tetradodecylammonium bromide, TDABr	Br^- , 78.92	$C_{48}H_{100}NBr_2^-$, 848.62	

first setup the cluster ions are directly guided to the pinhole of the TOF, which marks the entrance to the vacuum region. The goal of this setup was to determine the mass discrimination of the TOF itself, including the APi section from the point of the pinhole to the detector (sampling line effects are discussed below). However, we also chose a second setup, where the CI source of the instrument was installed, with the goal of studying possible effects from this section on the transmission curve. All the voltages of the CI source were set to standard operation values, as well as all flows. The corona discharge was shut off and nitric acid was not fed into the instrument. Choosing this setup, one faces the problem that the CI source is operated at negative voltages up to -500 V, so feeding negative ions from outside into the source means climbing a very large potential step. This step can of course affect ions with different masses in different ways; we expect high losses of light ions due to their high electrical mobility. Instead of placing this potential step at the end of the $1/2''$ sampling line inside the CI source, we chose to set it outside the ion source, where we installed a 6 mm nylon insulator (Fig. 1b). Due to the smaller inner diameter, the velocity of the flow is higher which should give smaller losses of ions at the voltage step. However, this way the usually grounded sampling line as well as the first part of the ion source had to be set to -500 V.

Measuring only in the configurations given in Fig. 1a and b yields the total transmission curve of the whole setup including tubing effects. For technical reasons the sampling line to the TOF did not have the same length as the line to the EM, therefore the losses of ions in the lines cannot be assumed to be identical. Additionally, the sampling line of the TOF increases in diameter from 6 mm to $1/2''$ in front of the CI source in the second setup. It is crucial to correct for these losses, as diffusion to the walls is mass-dependent and thus affects the shape of the transmission curve. We have made additional measurements to obtain mass-dependent EM correction factors that account for the different tubing lengths and flows (see Fig. 2). By doing so, we can estimate the ion concentration not only at the position of the EM, but directly in front of the mass spectrometer which is the important measure for the transmission estimation. For that we

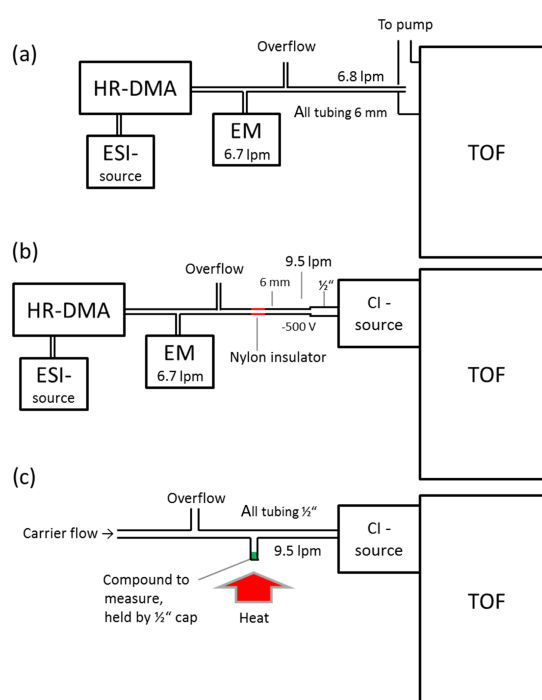


Figure 1. Schematic setup for the three types of experiments conducted. (a) HR-DMA measurement without CI source, API-TOF only. (b) HR-DMA setup with CI ion source. The $1/2''$ sampling line of the CI source was at a potential of -500 V. To minimize losses the potential step from ground to -500 V was installed at the 6 mm line with a nylon insulator. (c) Setup for the depletion method. A small sample was stored in a $1/2''$ cap and slowly heated with a standard heat gun. Potential overly high or overly small diffusion of the sample into the carrier flow can be controlled by varying length and inner diameter of the vertical connection between the sample and the carrier flow line.

placed the EM at the position of the TOF and applied equal flows as during the standard measurements. However, as the inlet of the EM has 6 mm diameter, the transition from 6 mm to the $1/2''$ TOF sampling line could not be accounted for.

This is a remaining source of uncertainty as losses at this point may be mass-dependent as well. For the CI setup we also tried to simulate the potential step of -500 V by using a nylon insulator; however, we used a second nylon insulator to set the sampling line to ground again in front of the EM. As only one EM was available the losses could not be measured simultaneously, but only after reassembling the setup, assuming the ESI source performance stayed constant over the duration of the measurement and reassembling. This was checked by measuring in the initial position of the EM before and after assembling, which showed reasonable agreement. The measurements were performed with the monomer, dimer, and trimer of MTOA (methyltrioctylammonium bis(trifluoromethylsulfonyl)imide), which correspond to m/z ratios of 279.9, 928.3, and 1576.6 Th, respectively. The mobility spectra for these measurements are shown in Fig. 2a and b. Each mobility spectrum is the average of 5 individual scans. The ratios of the individual peak areas for EM at original position and at TOF position give the mass-dependent correction factors. Peak areas were obtained by fitting triple Gaussian peaks to the spectra. The MTOA trimer signal is strongly affected by multiply charged heavier clusters selected by the HR-DMA due to their identical electrical mobility. The shoulder in the data caused by these higher clusters was fitted with a double Gaussian peak and subtracted from the trimer signal before obtaining trimer peak areas. As these measurements were only performed for MTOA monomer, dimer, and trimer, covering a m/z range from 280 to 1576 Th, we had to extrapolate the EM correction to smaller clusters (see Fig. 2c). For that an exponential fit with offset 1 was applied to the correction factors, whereas the MTOA trimer was only weighted with 50 % due to the effects of multiply charged higher clusters. With this extrapolation, additional uncertainty is introduced to the EM correction of especially negative monomers of bromide and iodide salts (Br^- at 79 Th and I^- at 127 Th). In general, both setups are not perfect; as in the APi setup, the ions are not drawn to the pinhole, whereas in the CI setup a large potential step and thus large correction factors are involved. The total uncertainty consists of contributions from the EM correction for MTOA (8 %), the extrapolation of the fit to other masses (estimated by using 68 % confidence bonds of the EM correction fit to be around 7 %), and for dimers possible fragmentation to monomers. Especially iodide dimers fragmented strongly to I^- , the EM values were corrected for that with the independently obtained monomer transmission efficiency. The percentage of EM signal attributed to lower clusters was used to estimate the additional uncertainty introduced by fragmentation. As the MTOA trimer signal overlaps with signals from multiply charged heavier clusters and the maximum correction of the MTOA peak in the mobility spectrum due to the shoulder was 31 %, this number was used as additional uncertainty for the MTOA trimer. During the EM correction measurements for the CI mode a second nylon insulator was installed to operate the EM at ground potential.

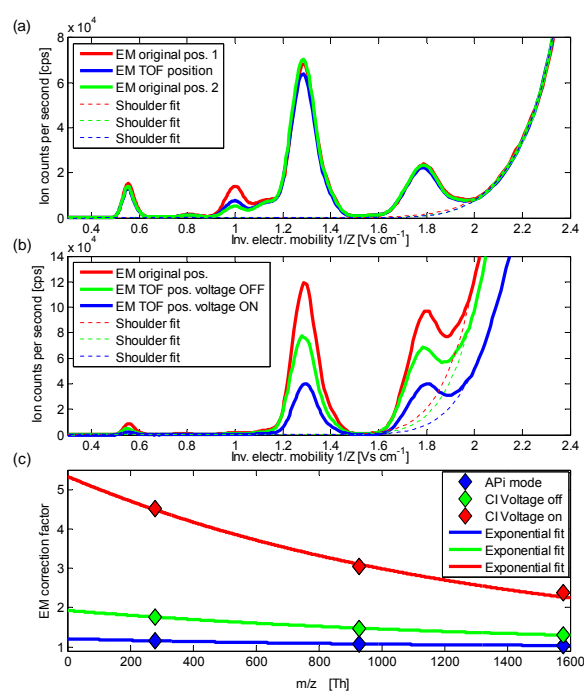


Figure 2. (a) Mobility spectrum for MTOA generated by the HR-DMA with the EM at original position and when its position was interchanged with that of the APi-TOF. The shoulder on the right originates from multiply charged higher clusters. The fit of the shoulder to correct the trimer concentration is shown as well. (b) Same as (a) but with two nylon insulators and potential step of -500 V added to the setup. Applying the voltage results in additional drastic losses. (c) Calculated correction factors for MTOA monomer, dimer, and trimer and exponential fit for extension to smaller m/z ratios.

Ion losses in this second insulator were not quantifiable and are thus not represented by error bars, but we note that there may be additional uncertainty for the data points of the CI mode. This may lead to an underprediction of ion concentration in front of the pinhole and thus an overprediction of the CI mode transmission values.

3.2 Depletion of primary ions

The basic idea of the depletion method is to add different substances to the instrument one after the other in amounts that lead to a significant decrease in primary ions (Steinbacher et al., 2004; Huey et al., 1995). Charge provided by the primary ions is therefore shifted to the m/z region of the product ions. Comparing the loss of charge at the primary ion mass with the appearance of charge at the product ion mass yields the relative transmission factor between these two masses. The underlying assumption is that the total amount of charge in the system is constant over the duration of the experiment,

which is usually the case for both PTR-MS, as well as CI-API-TOF. The substances should ideally not fragment significantly nor cluster with themselves as this leads to a charge transfer to a third mass region; however, we will face this problem for the CI-API-TOF. The relation between reacted primary ions and product ions should be linear and the slope of the linear fit gives the relative transmission of the m/z range of the product ions compared to the m/z range of the primary ions. Adding different compounds one after the other leads to a transmission curve over a certain m/z range. The first main advantage of this method is that it is not necessary to know how much of the compound of interest is added to the instrument. This leads to a very simple measurement setup without the need for further instrumentation. The second main advantage is that the instrument is used in standard operating mode including the CI source, which is not the case for the HR-DMA method. Therefore the depletion method intrinsically accounts for mass discrimination effects of the CI source. Note that this method only reveals the relative mass discrimination of the product ions compared to the m/z range of the primary ions, which is however sufficient for quantification (Eq. 3). If the absolute transmission is needed, the HR-DMA method should be chosen.

The saturation method works fine for a PTR-MS as this technique is a rather soft ionization method and there is almost no clustering of a substance with itself. Therefore the shift of charge from the m/z range of the primary ions to the desired m/z range is usually rather complete, and almost no charge appears at a third m/z range; however, this may change for certain substances. Good compounds for applying this method to a PTR-MS are for example acetone or xylene, whereas monoterpenes usually show a considerable degree of fragmentation. The picture changes, however, when we want to apply this technique to the CI-API-TOF. First of all, we need different substances that can be easily measured with the CI-API-TOF and should cover substantial parts of the m/z range (ideally from around 100 to around 1500 Th). We have chosen several perfluorinated acids ($\text{CF}_3(\text{CF}_2)_{3,5,6,7,8}\text{COOH}$, Sigma Aldrich, purity $\geq 95\%$) as fluorine is very electronegative and is thus supposed to easily take over the negative charge from NO_3^- , while the hydrogen atom of the acid group can perform a proton transfer reaction with the primary ion. On the other hand, perfluorinated acids are available at different molecular weights, with a variable number of CF_2 building blocks included. CF_2 has a molecular mass of 50 amu, so the m/z range can be stepped through easily by adding differently sized compounds. We have tried also perfluorododecyltrichlorosilane ($\text{C}_{12}\text{H}_4\text{Cl}_3\text{F}_{21}\text{Si}$, Sigma Aldrich, purity 97%). Table 2 shows an overview of the substances that were applied.

The measurement setup has to ensure that sufficient amounts of the desired compound enter the CI source of the instrument to deplete the primary ions, but on the other hand one has to be careful not to put too much into the system to avoid long term contamination. One way to achieve this

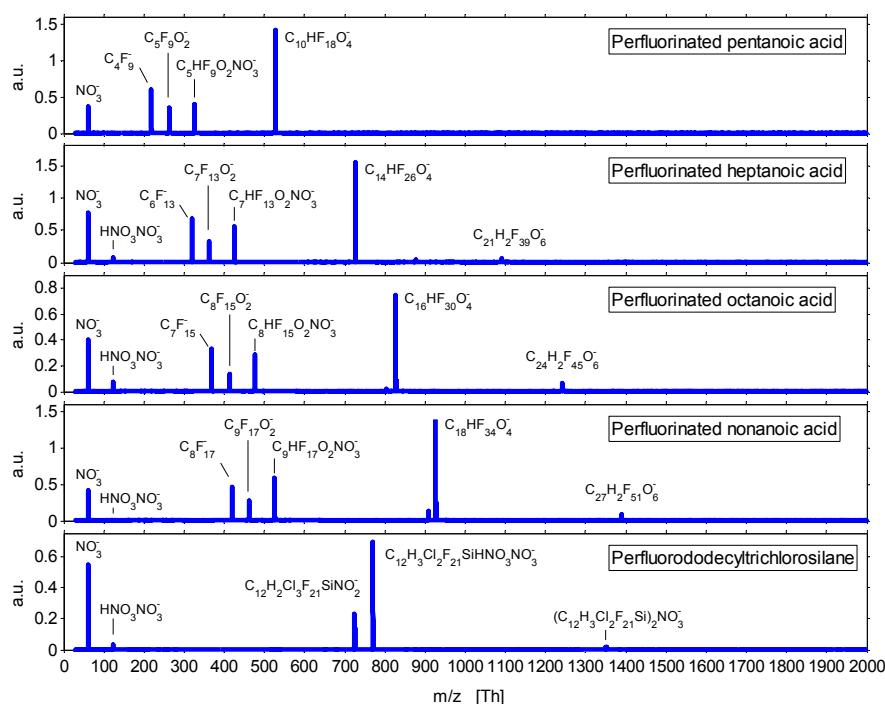
is to inject a gas sample from the headspace of the desired compound with a needle into the sample flow of the instrument through a rubber sealing. This works in principle, but gives only very short signal spikes as the volume in the needle is quickly diluted. A better approach is shown in Fig. 1c), where a $1/2''$ T-piece was added to the sampling line with a short $1/2''$ tube and a $1/2''$ cap at the end of the tube. The chosen compound is placed inside the cap. It is important to only use very small amounts in order not to contaminate the whole system for long periods of time. All the substances used evaporated either from liquid (perfluorinated pentanoic acid) or solid phase (all others) and diffused along the short vertical $1/2''$ line into the sample flow. Different concentration levels of the compounds were achieved by heating the cap slowly with a heat gun. If the amount of a compound in the cap is too large, a permanent complete depletion of all primary ions can occur. As will be described below, we need, however, varying degrees of depletion to deliver meaningful transmission curves; a complete and permanent depletion of the primary ions is not useful. To avoid this, it is important to only use a small grain/drop of the respective compound and/or to install a longer and/or thinner vertical diffusion tube in the inlet setup (see Fig. 1c).

The spectra for the different compounds are shown in Fig. 3. It is evident that the charge provided by the primary ions is not only shifted to one distinct m/z region like it is the case for this method in PTR-MS, but distributed over a wider range of masses. The monomer of all perfluorinated acids appears at three main channels, namely proton transfer to NO_3^- (middle peak), clustering with NO_3^- (right peak) and fragmentation (loss of the acid group; left peak). These three monomer peaks alone span already over a m/z range of 106 Th, which is a disadvantage of this method. Furthermore, the perfluorinated acids, as well as the silane compound tend to cluster strongly with themselves. However, for dimers and trimers of these acids, only one main peak was measured originating from a proton transfer reaction. Higher clusters like tetramers or pentamers were not observed. Especially for smaller perfluorinated acids, the tetramers would lie well below 2000 Th, which is the highest m/z ratio the CI-API-TOF is able to measure; so it is reasonable to assume that we are not missing any charge at m/z ratios higher than 2000 Th. We also know from different experiments that the transmission efficiency for high m/z ratios of up to 2000 Th is not zero.

To obtain time series of the data we used the MATLAB based *tofTools* software. For the monomer intensities of the perfluorinated acids and the silane compound, all monomer peaks were added up without any further correction for transmission. The measurement data from the heating experiments with perfluorinated heptanoic and nonanoic acid (Fig. 4) show a decrease of the primary ion signal (sum of NO_3^- and $\text{HNO}_3\text{NO}_3^-$) when the heating started at the beginning of the experiment and a strong increase in the perfluorinated acid signal. The sum of all signals also increases by

Table 2. Compounds used for depletion method. The perfluorinated acids only differ in the number of CF₂ building blocks.

Name	Formula	Mol. weight [amu]	Purity [%]
Perfluorinated pentanoic acid	CF ₃ (CF ₂) ₃ COOH	264.05	97
Perfluorinated heptanoic acid	CF ₃ (CF ₂) ₅ CO ₂ H	364.06	99
Perfluorinated octanoic acid	CF ₃ (CF ₂) ₆ COOH	414.07	96
Perfluorinated nonanoic acid	CF ₃ (CF ₂) ₇ COOH	464.08	97
Perfluorinated decanoic acid	CF ₃ (CF ₂) ₈ CO ₂ H	564.09	95
Perfluorododecyltrichlorosilane	C ₁₂ H ₄ Cl ₃ F ₂₁ Si	681.57	97

**Figure 3.** Spectra for all compounds used for depletion mode experiments. Primary ions are NO₃⁻ at 62 Th and HNO₃NO₃⁻ at 125 Th. The three monomer peaks for the perfluorinated acids originate from proton transfer to NO₃⁻ (middle peak), clustering with NO₃⁻ (right peak) and fragmentation (loss of the acid group, left peak). Dimers and trimers of the perfluorinated acids are present only as one main peak. Notice the stepwise addition of CF₂ building blocks for the perfluorinated acids.

more than a factor of 2. The total amount of charge in the CI source is given by the primary ion production in the corona discharge and is assumed to be constant over the experiment. As we count more charge during the heating at higher m/z regimes, the transmission efficiency of charge through the instrument must be higher for the m/z range of heptanoic and nonanoic acid monomer and dimer compared to the m/z range of the primary ions.

However, as the charge from the primary ions is not only transferred to one distinct mass, but distributed over a wider range, we cannot apply a linear fit to the data. We therefore introduce a relation that combines the measured signal with the theoretical total amount of charge in the system via

weighting factors, which will lead to relative transmission factors:

$$s_{\text{prim}} \cdot f_{\text{prim}} + s_{\text{mon}} \cdot f_{\text{mon}} + s_{\text{dim}} \cdot f_{\text{dim}} + s_{\text{trim}} \cdot f_{\text{trim}} = 1 \quad (4)$$

or $\sum_i s_i f_i = 1$, where i indicates primary ions and monomers, dimer, and trimer of the perfluorinated acids. s_i is the signal of the corresponding compound in counts per second at a given time and f_i are the weighting factors that need to be introduced to yield the right hand side of the equation, which is a normalized expression of the total amount of charge present in the CI source. This is a quantity not directly measurable

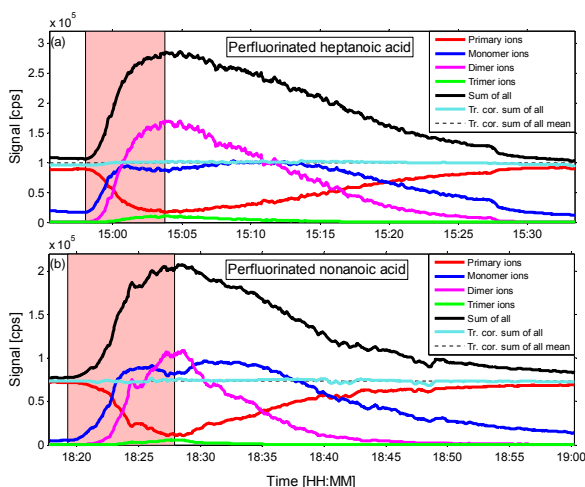


Figure 4. Measurement examples for (a) perfluorinated heptanoic acid and (b) perfluorinated nonanoic acid. Data are slightly smoothed (moving average). Heating (indicated by red shaded areas) leads to increased evaporation of the perfluorinated acids and a depletion of primary ions. After the heating period the system cooled down to room temperature, with the corresponding decrease in signal for perfluorinated acids and recovery of the primary ions. The sum of all signals shows a clear increase due to the heating periods, as charge is shifted to higher m/z regions. As the amount of charge is limited by the primary ions, this indicates that a higher fraction of ions reaches the detector when the ions are at the m/z range of the monomer or dimer of pentanoic or nonanoic acid. This is direct evidence for higher transmission efficiencies at these m/z ranges.

with the TOF unless the absolute transmission efficiency is known. We are not interested in its absolute value, but just need to assume that it is constant over the duration of the experiment. Equation (4) has four knowns and four unknowns, but it must be true for every time step of the experiment, so this one equation expands into an overdetermined system of linear equations, which can readily be solved via regression analysis. After obtaining the four weighting factors f_i , we normalize them to the weighting factor of the primary ions and invert them to get the relative transmission factors for the mass range of monomer, dimer, and trimer of the used perfluorinated acid with respect to the mass range of the primary ions.

The relative uncertainty was estimated via the 95 % confidence bonds of the regression analysis. Additional uncertainty for the relative transmission factors comes from possible fragmentation of larger clusters to primary or monomer ions. However, as fragmentation to primary ions implicates that their signal cannot be fully depleted, and during the strongest heating the primary ion level goes, e.g., below 4 and 5 % of the original level for heptanoic and nonanoic acid, respectively, we use 5 % as upper limit for fragmen-

tation to primary ions. For fragmentation to monomer ions, we compare the highest dimer signal to the monomer signal at the same point of time (the right peak of the monomers can be excluded for this, as no dimer contains NO_3^- and thus cannot fragment to this peak). We find minimum monomer to dimer ratios of 12 and 20 % for heptanoic and nonanoic acid, respectively. These ratios might go down even further for stronger heating, so we have added an additional uncertainty for primary ion signals of 5 % and for all the others of 15 %. As the relative transmission of the primary ions was set to 1, their uncertainty was added in quadrature to the one of all other compounds involved. Time resolution of the data affects the uncertainty originating from the regression analysis; we chose a 3 s resolution for all compounds, which leads to relatively small error bars. As the monomer peaks of all involved compounds spread over a certain m/z range and the transmission efficiency may change over this span, summing up the three monomer peaks introduces additional uncertainty. Note that the ratios of primary ions, monomers, dimers and trimers to each other should vary ideally significantly over the duration of the experiment to obtain reliable results with this method, otherwise close to linearly dependent equations cause a large scatter of the results. At this point also the advantage of the heating method over the injection method becomes obvious as the first one produces smooth increases and decreases of perfluorinated acids and so much more data points for the statistical analysis.

4 Results

We have obtained two transmission curves for the HR-DMA method and one for the depletion method, which are shown in Fig. 5. The curves were obtained by applying least-squares fits to a 2-fold Gaussian distribution for the APi-, CI-mode and depletion data. To ensure reasonably good representation of the measured data, we had to set lower limits for the two parameters in the denominator of the exponent (200 for the CI-mode and depletion method and 350 and 500 for the APi-mode fit). The overall transmission for the APi mode is in the range of 1 % with a steep increase from m/z 80 Th (Br^-) to m/z 127 Th (I^-) and a shallow decrease at higher m/z ranges above around 700 Th. The shape of the transmission curve is in agreement with earlier estimates for an APi-TOF using a similar method by Ehn et al. (2011); however, in our study we found around transmission levels a factor of 2 higher than Ehn et al. (2011). The data points of the APi setup are systematically higher than for the CI setup, with a larger difference for smaller masses. This difference is due to a combined effect of the CI ion source as well as the discussed voltage step of -500 V in front of the ion source. The result is a stronger suppression of lighter ions in the CI setup and a shift of the maximum of the curve towards higher masses. Furthermore, the difference in transmission between Br^- and I^- is much smaller for the CI setup. Note that io-

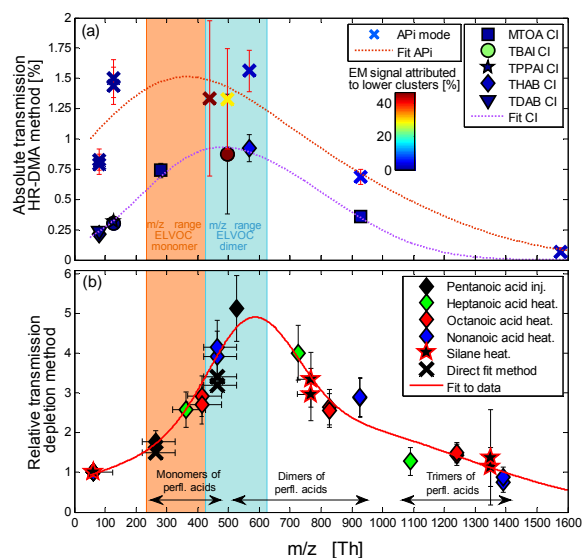


Figure 5. (a) Absolute transmission data obtained with the HR-DMA method for API only (crosses) and CI mode. Each data point is the ratio of TOF signal to corrected EM signal of a certain cluster. Iodide containing dimers fragment significantly to I^- , which enhances uncertainty. (b) Transmission curve obtained by depletion method with included mass discrimination effects of the CI source. The data points obtained with the direct fit method represent lower limits of relative transmission. A least-squares fit to a 2-fold Gaussian distribution was applied to the data (direct fit data was not used for this fit). The transmission curve obtained by the depletion method changes significantly over the m/z range of ELVOC molecules, indicated by orange and blue shaded areas for ELVOC monomer and dimer, respectively.

dide dimers show a high degree of fragmentation indicated by color code in Fig. 5a, whereas bromide dimers fragment very little. Therefore, bromide salts together with the ionic liquid MTOA work best for this method. Error bars in Fig. 5a represent results of Gaussian error propagation of the above mentioned uncertainties.

The results for the relative transmission efficiency estimated with the depletion method are shown in Fig. 5b. The agreement between the individual perfluorinated acids and the silane compound is remarkably good. There is a clear maximum of transmission efficiency in the range around 600 Th. Especially the m/z range from 235 to 625 Th shows a steep increase in transmission efficiency. This m/z range corresponds to the ELVOC monomer and dimer range as indicated by light orange and blue color in Fig. 5 and is thus of great importance for ELVOC quantification. The direct fit method was applied to some of the data obtained during depletion experiments. It is a linear fit of product ions vs. reacted primary ions (as used in PTR-MS) during periods of time, where mostly monomers were present. These data points (black crosses in Fig. 5b) can be seen as a lower limit

for the relative transmission. The above mentioned fit to the 2-fold Gaussian distribution of the results of the regression analysis was used as transmission curve of the instrument and to correct data sets from other experiments obtained under similar conditions. Horizontal error bars in Fig. 5b indicate the spread of the primary ions, as well as the monomers of the perfluorinated acids and the silane compound along the m/z axis. All monomers of perfluorinated acids were set to the m/z value of the deprotonated monomer peak (middle monomer peak, see Fig. 3). Vertical error bars originate from the regression analysis as described above. As the monomer peaks of all involved compounds spread over a certain m/z range and the transmission efficiency changes over this span, summing up the three monomer peaks introduces additional uncertainty. However, as the left monomer peak of the perfluorinated acids has a lower transmission efficiency than the middle peak and the right monomer peak a higher one, this effect tends to cancel out. We tested this for all used compounds by correcting monomer peaks individually for transmission and found an effect ranging from 2 % for perfluorinated pentanoic acid to 10 % for the silane compound. These uncertainties were added in quadrature to the ones of the regression analysis and affect only monomers but not dimers and trimers.

If we use the results of the regression analysis for the individual acids and correct the corresponding time traces in Fig. 4 for transmission, their sum should yield a constant level over the duration of the experiment. This is the case for both acids shown in Fig. 4 (light blue line). The constant signal confirms our method and represents now the constant ion production in the CI source.

The shape and the position of maximum transmission differ from the two curves obtained by the HR-DMA method. These differences may be attributed to mass discrimination effects of the CI source because the HR-DMA method does, in principle, not account for this. The CI setup shown in Fig. 1b tried to simulate these effects, but for the price of introducing an additional potential step of -500 V, which also may change the shape of the transmission curve. The HR-DMA method is a valid and established method for estimating the transmission efficiency of an API-TOF. However, for a CI-API-TOF the depletion method produces more reliable results as the CI source is included in the characterization as well. This method shows two main advantages: The first is that the instrument is used in its standard operation mode with the exact same settings as during sulfuric acid or ELVOC measurements, so no additional corrections have to be applied in order to obtain the transmission efficiency. The second main advantage is that no knowledge of the amounts of perfluorinated acids that enter the instrument is required for estimating the relative transmission efficiency. We just have to add sufficient amounts to deplete the primary ions significantly. This results in a simple and inexpensive measurement setup.

5 Conclusion

We have presented an easy-to-use and straight-forward way of estimating the mass-dependent transmission efficiency of a nitrate-based CI-APi-TOF via the depletion of primary ions. This method is in use already for PTR-MS, but to our knowledge has not been applied to a nitrate-based CI-APi-TOF before. The additional difficulty compared to PTR-MS is a strong clustering of the tested substances, which is treated with statistical analysis of the measurement data. We used different perfluorinated acids and one silane compound to estimate relative transmission factors over the m/z range from around 250 to 1400 Th. The results for all compounds are very consistent and show a steady increase in transmission efficiency from the m/z region of the nitrate primary ions up to about 500 Th by a factor of ~ 5 . A second method, which estimates the transmission efficiency of the APi-TOF alone without the CI source by use of an HR-DMA and an electrometer, shows a differently shaped transmission curve with a transmission efficiency of $\sim 1.5\%$ in the m/z region from 127 to 568 Th. We thus conclude that there most probably exist non-negligible mass discrimination effects of the CI source. These effects have to be taken into account for the quantification of ELVOCs and other compounds. As the transmission efficiency strongly depends on the chosen settings of the instrument, our transmission estimation cannot be generalized to other instruments. Ehn et al. (2014) found similar calibration coefficients for sulfuric acid and perfluorinated heptanoic acid, indicating similar transmission efficiencies for both m/z ranges. However, a detailed transmission curve cannot be obtained by a standard gravimetric calibration with one compound, so the method presented in this study can further enhance the accuracy of quantification for ELVOCs and other molecules. The depletion method has the advantage of a simple setup, as no need for quantification of the measured compounds exists and the instrument is used in its normal operation mode. We also want to point out that this method should, in principle, work as well for other chemical ionization schemes like acetate or iodide; however, different substances than the ones used in our study will have to be applied.

Appendix A

Here we present the detailed settings of the CI-APi-TOF used in this study. The settings were applied for the depletion method as well as for HR-DMA experiments.

Table A1. Voltage and flow settings of the CI source. The basic design of the CI source is given in Kürten et al. (2011); however, the HNO₃ and corona mixing flow were not fed into the source together with the N₂ sheath flow, but directly over the corona needle. The electrostatic lens in front of the pinhole and the N₂ buffer flow were omitted in our CI source. The corona needle voltage given below is reduced by a 500 MΩ resistor before being applied to the needle itself.

Gas flows in CI source	[L min ⁻¹]	Voltages CI source	[V]
N ₂ sheath flow	20	Corona cylinder	-500
Exhaust flow	31.85	Drift tube	-210
HNO ₃ flow	0.050	Pinhole plate	0
Corona mixing flow	1.5	Corona needle	-6000
Sample flow CI source	9.5		
Sample flow TOF	0.80		

Table A2. Voltages and frequencies in the APi section.

SSQ low voltages [V]	BSQ low voltages [V]	Quadrupoles RF
IMR	0	Q2 Front 10
Nozzle	10	Q2 Back 13.5
Q1 EP	5	Skimmer 2 16
Q1 Front	8	Reference (bias) 17
Q1 Back	8	Ion-lens 2 135
Lens skimmer	8	Detector flange 39
Skimmer	8	Deflector 38.1
		SSQ Frequency 620 kHz
		SSQ Amplitude 180 V
		BSQ Frequency 1.15 MHz
		BSQ Amplitude 100 V

Table A3. Voltages and pressures in the TOF section (operated in negative high sensitivity mode).

Extraction pulser [V]	TOF high voltages [V]	TOF pressures [mbar]
TOF Pulse	700	Lens 500
TOF Ref.	42	Drift 3000
TOF Extr. 1	35	RG 649
TOF Extr. 2	700	RB 700
		HM 0
		A 2700
		MCP 2155
		Fore pressure 3.52
		SSQ 2.29
		BSQ 3.48×10^{-2}
		PB 9.55×10^{-5}
		TOF 9.61×10^{-7}

1460

M. Heinritzi et al.: Characterization of the mass-dependent transmission efficiency of a CIMS

Acknowledgements. We thank Jay Slowik for the fruitful discussion. We also thank the tofTools team for providing tools for mass spectrometry analysis. This work was funded by: EC Seventh Framework Programme (Marie Curie Initial Training Network, MC-ITN “CLOUD-TRAIN” no. 316662), German Federal Ministry of Education and Research (project no. 01LK1222A), the University of Innsbruck Research Grant for Young Scientists and the Austrian Science Fund, FWF (grant no. P27295-N20).

Edited by: F. Stroh

References

- Chernushevich, I. V., Loboda, A. V., and Thomson, B. A.: An introduction to quadrupole–time-of-flight mass spectrometry, *J. Mass Spectrom.*, 36, 849–865, 2001.
- Edwards, G. D., Cantrell, C. A., Stephens, S., Brian, H., Goyea, O., Shetter, R. E., Mauldin III, R. L., Kosciuch, E., Tanner, D. J. and Eisele, F. L.: Chemical Ionization Mass Spectrometer Instrument for the Measurement of Tropospheric HO₂ and RO₂, *Anal. Chem.*, 75, 5317–5327, 2003.
- Ehn, M., Junninen, H., Schobesberger, S., Manninen, H. E., Franchin, A., Sipilä, M., Petäjä, T., Kerminen, V.-M., Tammet, H., Mirme, A., Mirme, S., Hörrak, U., Kulmala, M., and Worsnop, D. R.: An Instrumental Comparison of Mobility and Mass Measurements of Atmospheric Small Ions, *Aerosol Sci. Tech.*, 45, 522–532, 2011.
- Ehn, M., Thornton, J., Kleist, E., Sipilä, M., Junninen, H., Pullinen, I., Springer, M., Rubach, F., Tillmann, R., Lee, B., Lopez-Hilfiker, F., Andres, S., Acir, I.-H., Rissanen, M., Jokinen, T., Schobesberger, S., Kangasluoma, J., Kontkanen, J., Nieminen, T., Kurten, T., Nielsen, L. B., Jorgensen, S., Kjaergaard, H., Canagaratna, M., Dal Maso, M., Berndt, T., Petaja, T., Wahner, A., Kerminen, V.-M., Kulmala, M., Worsnop, D. R., Wildt, J., and Mentel, T. F.: A large source of low-volatility secondary organic aerosol, *Nature*, 506, 476–479, 2014.
- Eisele, F. L. and Tanner, D. J.: Ion-assisted tropospheric OH measurements, *J. Geophys. Res.*, 96, 9295–9308, 1991.
- Eisele, F. L. and Tanner, D. J.: Measurement of the gas phase concentration of H₂SO₄ and methane sulfonic acid and estimates of H₂SO₄ production and loss in the atmosphere, *J. Geophys. Res.*, 98, 9001–9010, 1993.
- Fernández de la Mora, J. F. and Kozlowski, J.: Hand-held differential mobility analyzers of high resolution for 1–30 nm particles: Design and fabrication considerations, *J. Aerosol. Sci.*, 57, 45–53, 2013.
- Gerlich, D.: Inhomogeneous RF fields: a versatile tool for the study of processes with slow ions, in: *Advances in Chemical Physics: State-Selected and State-To-State Ion-Molecule Reaction Dynamics, Part 1, Experiment*, edited by: Ng, C.-Y. and Baer, M., John Wiley & Sons, New York, USA, 82, 1–176, 1992.
- Gilmore, I. S. and Seah, M. P.: Ion detection efficiency in SIMS: Dependencies on energy, mass and composition for microchannel plates used in mass spectrometry, *Int. J. Mass. Spectrom.*, 202, 217–229, 2000.
- Graus, M., Müller, M., and Hansel, A.: High resolution PTR-TOF: quantification and formula confirmation of VOC in real time, *J. Am. Soc. Mass Spec.*, 21, 1037–1044, 2010.
- Hansel, A., Jordan, A., Holzinger, R., Prazeller, P., Vogel, W., and Lindinger, W.: Proton transfer reaction mass spectrometry: on-line trace gas analysis at the ppb level, *Int. J. Mass Spectrom.*, 149–150, 609–619, 1995.
- Huey, L. G., David R. H., and Carleton J. H.: Reactions of SF₆⁻ and I⁻ with atmospheric trace gases, *J. Phys. Chem. US*, 99, 5001–5008, 1995.
- Jokinen, T., Sipilä, M., Junninen, H., Ehn, M., Lönn, G., Hakala, J., Petäjä, T., Mauldin III, R. L., Kulmala, M., and Worsnop, D. R.: Atmospheric sulphuric acid and neutral cluster measurements using CI-API-TOF, *Atmos. Chem. Phys.*, 12, 4117–4125, doi:10.5194/acp-12-4117-2012, 2012.
- Junninen, H., Ehn, M., Petäjä, T., Luosujärvi, L., Kotiaho, T., Kostianen, R., Rohner, U., Gonin, M., Fuhrer, K., Kulmala, M., and Worsnop, D. R.: A high-resolution mass spectrometer to measure atmospheric ion composition, *Atmos. Meas. Tech.*, 3, 1039–1053, doi:10.5194/amt-3-1039-2010, 2010.
- Kürten, A., Rondo, L., Ehrhart, S., and Curtius, J.: Performance of a corona ion source for measurement of sulfuric acid by chemical ionization mass spectrometry, *Atmos. Meas. Tech.*, 4, 437–443, doi:10.5194/amt-4-437-2011, 2011.
- Kürten, A., Rondo, L., Ehrhart, S., and Curtius, J.: Calibration of a chemical ionization mass spectrometer for the measurement of gaseous sulfuric acid, *J. Phys. Chem. A*, 116, 6375–6386, 2012.
- Kürten, A., Jokinen, T., Simon, M., Sipilä, M., Sarnela, N., Junninen, H., Adamov, A., Almeida, J., Amorim, A., Bianchi, F., Breitenlechner, M., Dommen, J., Donahue, N. M., Duplissy, J., Ehrhart, S., Flagan, R.C., Franchin, A., Hakala, J., Hansel, A., Heinritzi, M., Hutterli, M., Kangasluoma, J., Kirkby, J., Laaksonen, A., Lehtipalo, K., Leiminger, M., Makhmutov, V., Mathot, S., Onnela, A., Petäjä, T., Praplan, A. P., Riccobono, F., Rissanen, M. P., Rondo, L., Schobesberger, S., Seinfeld, J. H., Steiner, G., Tomé, A., Tröstl, J., Winkler, P. M., Williamson, C., Wimmer, D., Ye, P., Baltensperger, U., Carslaw, K. S., Kulmala, M., Worsnop, D. R., and Curtius, J.: Neutral molecular cluster formation of sulfuric acid–dimethylamine observed in real time under atmospheric conditions, *P. Natl. Acad. Sci. USA*, 111, 15019–15024, 2014.
- Muntean, F.: Transmission study for rf-only quadrupoles by computer simulation, *Int. J. Mass Spectrom.*, 151, 197–206, 1995.
- Müller, M., Mikoviny, T., and Wisthaler, A.: Detector aging induced mass discrimination and non-linearity effects in PTR-ToF-MS, *Int. J. Mass. Spectrom.*, 365, 93–97, 2014.
- Steinbacher, M., Dommen, J., Ammann, C., Spirig, C., Nefel, A., and Prevot, A. S. H.: Performance characteristics of a proton-transfer-reaction mass spectrometer (PTR-MS) derived from laboratory and field measurements, *Int. J. Mass. Spectrom.*, 239, 117–128, 2004.
- Steiner, G., Attoui, M., Wimmer, D., and Reischl, G. P.: A medium flow, high-resolution Vienna DMA running in recirculating mode, *Aerosol Sci. Tech.*, 44, 308–315, 2010.
- Tanner, D. J. and Eisele, F. L.: Present OH measurement limits and associated uncertainties, *J. Geophys. Res.*, 100, 2883–2892, 1995.

4.5 Ion-induced nucleation of pure biogenic particles

(Kirkby et al. (2016))

LETTER

OPEN

doi:10.1038/nature17953

Ion-induced nucleation of pure biogenic particles

Jasper Kirkby^{1,2}, Jonathan Duplissy^{3,4}, Kamalika Sengupta⁵, Carla Frege⁶, Hamish Gordon², Christina Williamson^{1,†}, Martin Heinritzi^{1,7}, Mario Simon¹, Chao Yan³, João Almeida^{1,2}, Jasmin Tröstl⁶, Tuomo Nieminen^{3,4}, Ismael K. Ortega⁸, Robert Wagner³, Alexey Adamov³, Antonio Amorim⁹, Anne-Kathrin Bernhammer^{7,10}, Federico Bianchi^{6,11}, Martin Breitenlechner^{7,10}, Sophia Brilke¹, Xuemeng Chen³, Jill Craven¹², Antonio Dias², Sebastian Ehrhart^{1,2}, Richard C. Flagan¹², Alessandro Franchin³, Claudia Fuchs⁶, Roberto Guida², Jani Hakala³, Christopher R. Hoyle^{6,13}, Tuija Jokinen³, Heikki Junninen³, Juha Kangasluoma³, Jaeseok Kim^{14,†}, Manuel Krapf⁶, Andreas Kürten¹, Ari Laaksonen^{14,15}, Katrianne Lehtipalo^{3,6}, Vladimir Makhmutov¹⁶, Serge Mathot², Ugo Molteni⁶, Antti Onnela², Otso Peräkylä³, Felix Piel¹, Tuukka Petäjä³, Arnaud P. Praplan³, Kirsty Pringle⁵, Alexandru Rap⁵, Nigel A. D. Richards^{5,17}, Ilona Riipinen¹⁸, Matti P. Rissanen³, Linda Rondo¹, Nina Sarnela³, Siegfried Schobesberger^{3,†}, Catherine E. Scott⁵, John H. Seinfeld¹², Mikko Sipilä^{3,4}, Gerhard Steiner^{3,7,19}, Yuri Stozhkov¹⁶, Frank Stratmann²⁰, Antonio Tomé²¹, Annele Virtanen¹⁴, Alexander L. Vogel², Andrea C. Wagner¹, Paul E. Wagner¹⁹, Ernest Weingartner⁶, Daniela Wimmer^{1,3}, Paul M. Winkler¹⁹, Penglin Ye²², Xuan Zhang¹², Armin Hansel^{7,10}, Josef Dommen⁶, Neil M. Donahue²², Douglas R. Worsnop^{3,14,23}, Urs Baltensperger⁶, Markku Kulmala^{3,4}, Kenneth S. Carslaw⁵ & Joachim Curtius¹

Atmospheric aerosols and their effect on clouds are thought to be important for anthropogenic radiative forcing of the climate, yet remain poorly understood¹. Globally, around half of cloud condensation nuclei originate from nucleation of atmospheric vapours². It is thought that sulfuric acid is essential to initiate most particle formation in the atmosphere^{3,4}, and that ions have a relatively minor role⁵. Some laboratory studies, however, have reported organic particle formation without the intentional addition of sulfuric acid, although contamination could not be excluded^{6,7}. Here we present evidence for the formation of aerosol particles from highly oxidized biogenic vapours in the absence of sulfuric acid in a large chamber under atmospheric conditions. The highly oxygenated molecules (HOMs) are produced by ozonolysis of α -pinene. We find that ions from Galactic cosmic rays increase the nucleation rate by one to two orders of magnitude compared with neutral nucleation. Our experimental findings are supported by quantum chemical calculations of the cluster binding energies of representative HOMs. Ion-induced nucleation of pure organic particles constitutes a potentially widespread source of aerosol particles in terrestrial environments with low sulfuric acid pollution.

It is thought that aerosol particles rarely form in the atmosphere without sulfuric acid^{3,4}, except in certain coastal regions where iodine oxides are involved⁸. Furthermore, ions are thought to be relatively unimportant in the continental boundary layer, accounting for only around 10% of particle formation⁵. Sulfuric acid derives from anthropogenic and volcanic sulfur dioxide emissions as well as dimethyl sulfide from marine biota. However, typical daytime sulfuric acid concentrations (10^5 – 10^7 cm⁻³, or 0.004–0.4 parts per trillion by volume (p.p.t.v.) at standard conditions) are too low for sulfuric acid and water alone to account for the particle formation rates observed in the lower atmosphere⁹, so additional vapours are required to stabilize any embryonic sulfuric acid clusters against evaporation. Base species such as amines can do this and can explain part of atmospheric particle

nucleation¹⁰. It is well established that oxidation products of volatile organic compounds (VOCs) are important for particle growth¹¹, but whether their role in the smallest particles is in nucleation or growth alone has remained ambiguous^{4,12,13}. Recently, however, it has been shown that oxidized organic compounds do indeed help to stabilize sulfuric acid clusters and probably play a major role in atmospheric particle nucleation^{6,14,15}. We refer to these compounds as HOMs (highly oxygenated molecules) rather than ELVOCs (extremely low-volatility organic compounds)¹⁶ because the measured compounds span a wide range of low volatilities.

Here we report atmospheric particle formation solely from biogenic vapours. The data were obtained at the CERN CLOUD chamber (Cosmics Leaving Outdoor Droplets; see Methods for experimental details) between October 2012 and November 2013. In contrast with other works that have reported organic particle formation without intentional addition of sulfuric acid^{6,7}, here we measure the cluster chemistry and the role of ions, and rule out contamination.

Precursor VOCs in the atmosphere arise predominantly from natural sources such as vegetation and largely comprise isoprene (C₅H₈), monoterpenes (C₁₀H₁₆), sesquiterpenes (C₁₅H₂₄) and diterpenes (C₂₀H₃₂). Here we have studied α -pinene (C₁₀H₁₆) because it is the most abundant monoterpene, often exceeding 50 p.p.t.v. in the continental boundary layer¹⁷. We oxidized α -pinene by exposure to ozone and also to hydroxyl radicals (OH \cdot) produced from ozone photolysis and secondary reactions. To measure the relative importance of these oxidants we also performed a few pure ozonolysis experiments (in which we removed OH \cdot with a 0.1% H₂ scavenger) and a few pure hydroxyl experiments (in which we generated OH \cdot by photolysis of gas-phase nitrous acid, HONO). Two nitrate chemical ionization atmospheric pressure interface time-of-flight (CI-API-TOF) mass spectrometers measured neutral gas-phase compounds in the chamber (H₂SO₄ and HOMs). Therefore, for this study, HOMs are implicitly defined as oxidized organic compounds that can be detected by a nitrate CI-API-TOF; related molecules with a lower oxidation state

¹Goethe University Frankfurt, Institute for Atmospheric and Environmental Sciences, 60438 Frankfurt am Main, Germany. ²CERN, CH-1211 Geneva, Switzerland. ³Department of Physics, University of Helsinki, FI-00014 Helsinki, Finland. ⁴Helsinki Institute of Physics, University of Helsinki, FI-00014 Helsinki, Finland. ⁵School of Earth and Environment, University of Leeds, Leeds LS2 9JT, UK. ⁶Paul Scherrer Institute, Laboratory of Atmospheric Chemistry, CH-5232 Villigen, Switzerland. ⁷Institute for Ion and Applied Physics, University of Innsbruck, 6020 Innsbruck, Austria. ⁸Onera—The French Aerospace Lab, F-91123 Palaiseau, France. ⁹SIM, University of Lisbon, 1849-016 Lisbon, Portugal. ¹⁰Ionicon Analytik GmbH, 6020 Innsbruck, Austria. ¹¹Institute for Atmospheric and Climate Science, ETH Zurich, CH-8092 Zurich, Switzerland. ¹²Division of Chemistry and Chemical Engineering, California Institute of Technology, Pasadena, California 91125, USA. ¹³WSL Institute for Snow and Avalanche Research SLF, CH-7260 Davos, Switzerland. ¹⁴University of Eastern Finland, FI-70211 Kuopio, Finland. ¹⁵Finnish Meteorological Institute, FI-00101 Helsinki, Finland. ¹⁶Solar and Cosmic Ray Research Laboratory, Lebedev Physical Institute, 119991 Moscow, Russia. ¹⁷University of Leeds, National Centre for Earth Observation, Leeds LS2 9JT, UK. ¹⁸Department of Applied Environmental Science, University of Stockholm, SE-10961 Stockholm, Sweden. ¹⁹Faculty of Physics, University of Vienna, 1090 Vienna, Austria. ²⁰Leibniz Institute for Tropospheric Research, 04318 Leipzig, Germany. ²¹University of Beira Interior, 6201-001 Covilhã, Portugal. ²²Center for Atmospheric Particle Studies, Carnegie Mellon University, Pittsburgh, Pennsylvania 15213, USA. ²³Aerodyne Research Inc., Billerica, Massachusetts 01821, USA. †Present addresses: CIREN, University of Colorado Boulder, Boulder, Colorado 80309, USA (C.W.); Arctic Research Center, Korea Polar Research Institute, Incheon 406-840, South Korea (J. Kim); Department of Atmospheric Sciences, University of Washington, Seattle, Washington 98195, USA (S.S.).

RESEARCH LETTER

or different functional groups could be present in the chamber, but undetected by our nitrate chemical ionization set-up.

Before starting measurements, we carefully cleaned the CLOUD chamber (see Methods) and established extremely low contaminant concentrations: at 38% relative humidity and 278 K, the contaminants were below the detection limit for SO₂ (<15 p.p.t.v.) and H₂SO₄ (<5 × 10⁴ cm⁻³), and total organics (largely comprising high volatility C₁–C₃ compounds) were below 150 p.p.t.v. Contaminants with a high proton affinity or a high gas-phase acidity can be detected as ions by the API-TOF operating in positive or negative mode, respectively, even at neutral molecule concentrations as low as 10⁴ cm⁻³. The API-TOF measured contaminant C₅H₅NH⁺ (protonated pyridine) and contaminant NO₃⁻ to be the dominant positive and negative ions, respectively, before we added any trace gases to the chamber other than water vapour and ozone (Extended Data Fig. 1a, b). Despite its higher gas-phase acidity, we detected contaminant HSO₄⁻ at only 1% of the NO₃⁻ signal (Extended Data Fig. 1b), ruling out any contribution of sulfuric acid to the nucleation measurements. From previous studies and molecular analysis of the charged clusters (see below), the most abundant positive ion is likely to be contaminant ammonium (NH₄⁺), but its mass is below the acceptance cut-off of the API-TOF as operated in this study.

Within a few minutes of the initial exposure of α-pinene to O₃ in the chamber, we detected gas-phase HOM monomers and dimers (Fig. 1a). Particles appeared shortly afterwards (Fig. 1b). HOM monomers (denoted E₁) broadly comprise highly oxidized C_{8–10}H_{14,16}O_{6–12} species with an oxygen-to-carbon ratio (O/C) above about 0.6. HOM dimers (E₂) are two covalently bound monomers (see below), which generally have lower oxygen-to-carbon ratios, but, almost certainly, a lower volatility. For the present study we define E₁ (E₂) to be the summed HOM peaks in the mass/charge range $m/z = 235–424$ Th (425–625 Th), where 1 Th = 1 Da/e and *e* is the elementary charge. This definition excludes peaks in the E₁ mass band distinguished by an odd H number (C₁₀H₁₅O_{6,8,10,12}), which we assign to the RO₂· peroxy radical. These *m/z* values include a contribution of 62 Th due to the NO₃⁻ ion from the CI-API-TOF ionizer. We define the total HOMs as the sum RO₂· + E₁ + E₂.

We measure high HOM molar yields (Extended Data Fig. 2): approximately 1.2% per hydroxyl radical (OH·) reaction with α-pinene, 3.2% per ozone reaction with α-pinene, and 2.9% from pure ozonolysis. We find a high E₂ yield from ozonolysis (10%–20% of total HOMs), but negligible E₂ yield from hydroxyl-initiated oxidation. Neutral trimers are close to the detection limit of the CI-API-TOF (below 0.1% of total HOMs). High yields of these same HOMs have previously been reported^{6,16}, although our ozonolysis yields are less than half those of ref. 16. For our experiments, α-pinene was in the range 0.1–2 parts per billion by volume (p.p.b.v.), with 20–40 p.p.b.v. of O₃. The OH· concentrations were (0.5–0.8) × 10⁶ cm⁻³ during ozonolysis experiments, and (0.4–2) × 10⁵ cm⁻³ during pure hydroxyl experiments with 0.5–3 p.p.b.v. of HONO.

This remarkably fast production of HOMs is likely to proceed via an autoxidation mechanism involving peroxy radicals^{16,18–20} (Extended Data Fig. 3). There is simply insufficient time for oxidation to proceed in multiple steps through stable intermediate molecules. Here, initial ozonolysis of an α-pinene molecule proceeds via a Criegee intermediate and further steps to form an RO₂· radical, followed by several repeated cycles of intramolecular H abstraction and O₂ addition to re-form a new RO₂· radical. We measure an RO₂· fraction of total HOMs between 15% and 1% for HOMs from 0.1 p.p.t.v. to 10 p.p.t.v., respectively. A combination reaction of differently oxidized peroxy radicals explains the rapid high yield of covalently bound E₂. The negligible E₂ yield from hydroxyl-initiated oxidation could result from additional NO_x chemistry that terminates the peroxy radicals before they can combine. Our theoretical calculations further indicate that E₂ must be covalently bound because the neutral molecular cluster formed from two monomers (denoted E₁E₁) is expected to be unstable (see below).

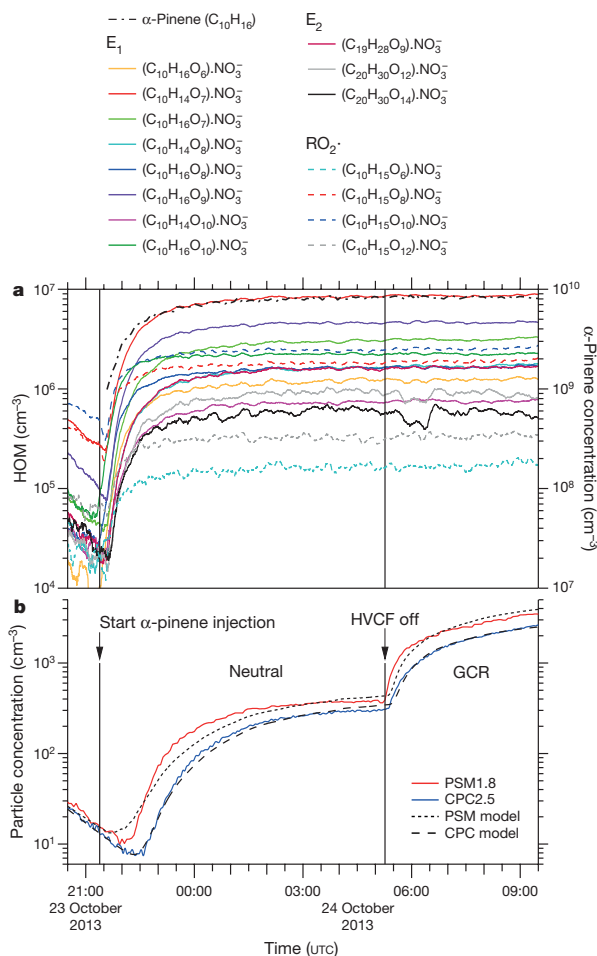


Figure 1 | Evolution of HOMs and particles during a typical run.

a, Evolution of selected HOM monomers (E₁), dimers (E₂) and peroxy radicals (RO₂·) at 300 p.p.t.v. α-pinene, 33 p.p.b.v. O₃, zero H₂ or HONO, 38% relative humidity, 278 K and [H₂SO₄] < 5 × 10⁴ cm⁻³ (the same run as shown in Extended Data Fig. 4). The HOMs start to appear soon after the first injection of α-pinene into the chamber at 21:22, 23 October 2013. A HOM monomer is a highly oxygenated molecule derived from α-pinene (C₁₀H₁₆), and a HOM dimer is a covalently bound pair of monomers. Peroxy radicals are identified by an odd H number. The HOMs are charged with an NO₃⁻ ion in the CI-API-TOF mass spectrometer. The systematic scale uncertainty on the HOM concentrations is +80%/–45%. **b**, Evolution of the particle number concentrations measured in the PSM1.8 (red curve) and CPC2.5 (blue curve) particle counters. The high-voltage clearing field (HVCF) was switched off at 05:16, 24 October 2013, marking the transition from neutral (ion-free) to GCR conditions in the chamber. A sharp increase in the rate of particle formation is seen, due to ion-induced nucleation of pure biogenic particles. However, no change occurs in the HOM concentrations (**a**), because these are predominantly neutral gas-phase molecules. The dotted and dashed curves in **b** show the PSM1.8 and CPC2.5 distributions, respectively, simulated for this run with the AEROCLOUD kinetic model, which is used to derive the experimental nucleation rates (see Methods).

We measured nucleation rates under neutral (J_n), Galactic cosmic ray (GCR; J_{gcr}) and π^+ beam (J_π) conditions, corresponding to ion-pair concentrations of around 0 cm⁻³, 700 cm⁻³ and 3,000 cm⁻³, respectively. This range spans atmospheric ion concentrations between ground level and 15-km altitude. The nucleation rate J_n describes the neutral rate alone, whereas J_{gcr} and J_π describe the sum of the neutral and ion-induced rates, $J_n + J_{ion}$. We determine the nucleation rates at

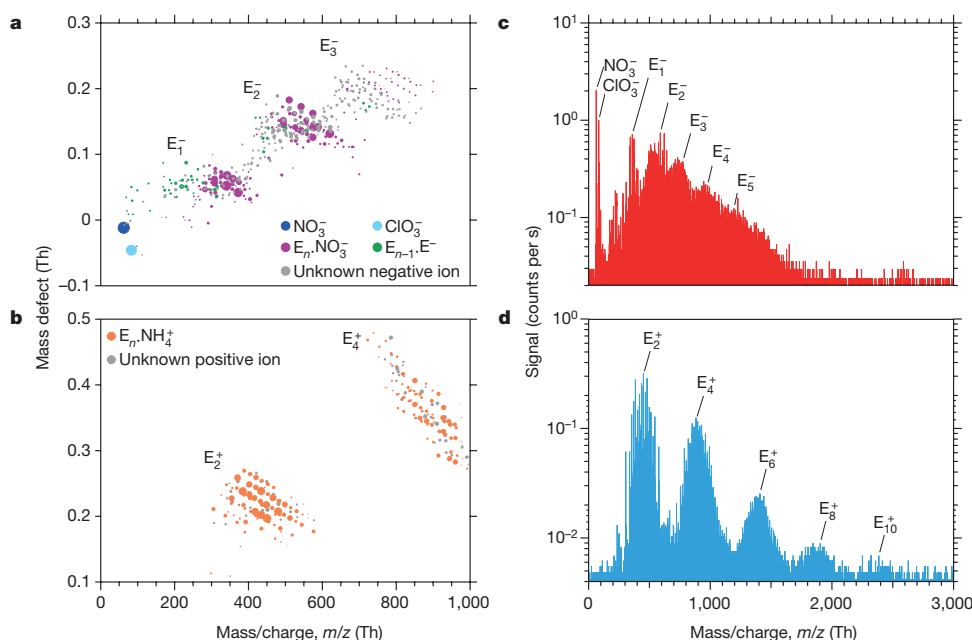


Figure 2 | Molecular composition and mass spectra of charged clusters during GCR nucleation events without sulfuric acid. a, b, Cluster mass defect (difference from integer mass) versus m/z of negatively (a) and positively (b) charged clusters measured with the API-TOF at 240 p.p.t.v. α -pinene, 34 p.p.b.v. O_3 , zero H_2 or HONO, 38% relative humidity, 278 K and $[H_2SO_4]$ below the detection limit ($5 \times 10^4 \text{ cm}^{-3}$). The values of J_{GCR} and total HOMs concentration are, respectively, $3.4 \text{ cm}^{-3} \text{ s}^{-1}$ and $1.7 \times 10^7 \text{ cm}^{-3}$ (a), and $3.3 \text{ cm}^{-3} \text{ s}^{-1}$ and $2.4 \times 10^7 \text{ cm}^{-3}$ (b). The mass bands are labelled according to the number of HOM monomer units in the cluster, E_n . Each circle represents a distinct molecular composition and its area represents the counts per second. The most highly oxidized compounds are located at the lower right-hand edge of each band.

The dark blue circle represents NO_3^- ions; the light blue circle represents ClO_3^- ions. Clusters with fully identified molecular composition are coloured according to their core ion: purple (NO_3^-), green (E^-) or orange (NH_4^+). Grey circles are unidentified clusters. c, d, Mass spectra from the same events for negative (c) and positive (d) clusters up to $m/z = 3,000$ Th. A particle of 1.7-nm mobility diameter has a mass of about 1,200 Th. The 'Nessie' plot (d) shows that positive-ion-induced nucleation involves HOM dimers alone ($E_1\text{NH}_4^+$ clusters are not seen owing to instrument tuning). The decreasing signal amplitude at larger masses is due to the lower concentration and decreasing detection efficiency of the API-TOF mass spectrometer (the efficiency versus m/z depends on the instrument tune and polarity).

1.7-nm mobility diameter, at which size a particle is generally considered to be stable against evaporation. To determine the nucleation rates, we fit the time-dependent particle concentrations with a numerical model that treats particle nucleation and growth kinetically at the molecular level (an example is shown in Fig. 1b; see Methods for further details).

A typical run sequence (Extended Data Fig. 4) begins by establishing ion-free conditions with a high-voltage clearing field and introducing α -pinene to the chamber, where it mixes with ozone. Particles then start to form and, after measuring J_n at steady-state α -pinene concentration, we turn off the high voltage and measure J_{GCR} under otherwise identical chamber conditions. A sharp enhancement of particle formation is seen when the high voltage was turned off (Extended Data Fig. 4b, e), due to ion-induced nucleation of both charge signs (Extended Data Figs 4c, d and 5).

Figure 2 shows the molecular composition and mass spectra of negatively and positively charged ions, monomers, dimers and clusters during ion-induced nucleation events. The dominant core ions in the clusters are identified as NH_4^+ , NO_3^- and E^- . Here E^- is inferred for negatively charged ions or clusters that contain only C, H and O; the E^- ion corresponds to a HOM of high gas-phase acidity. In contrast to negative clusters, the positive clusters nucleate only with dimers, producing distinct mass bands that are detected up to E_{10} in the API-TOF (Fig. 2c, d). This indicates the importance of dimers for pure biogenic nucleation. Dimers are expected to be less volatile than monomers, owing primarily to higher molecular weight, but also to additional functional groups. Our previously described definition for neutral gas-phase HOMs encompasses compounds with a wide range

of low volatilities^{19,21}, of which only a subset drive nucleation (ELVOCs, which comprise about 36% of measured total HOMs²¹). From the strong ion enhancement of nucleation we conclude that the API-TOF mass peaks above the dimer in Fig. 2 are clusters of ELVOC monomers and dimers. Although we can precisely determine their molecular composition ($\text{C}_x\text{H}_y\text{O}_z$), we can only infer their specific structure and functional groups.

We show the experimental neutral and GCR nucleation rates in Fig. 3 over the total HOMs range 0.1–10 p.p.t.v., which spans the range of atmospheric interest. Below 1 p.p.t.v. HOM, ionization at ground-level GCR intensities enhances the nucleation rate by between one and two orders of magnitude compared with neutral nucleation. At higher concentrations, the neutral and GCR nucleation rates converge because the ion-induced rate, J_{ion} , reaches the limit set by the GCR total ion production rate ($3.4 \text{ cm}^{-3} \text{ s}^{-1}$). Positive and negative clusters nucleate at comparable rates (an example is shown in Extended Data Fig. 5). Relative humidity has little effect on J_{GCR} over the range 6%–80% relative humidity, whereas J_n increases substantially at higher relative humidity (Extended Data Fig. 6).

The large GCR enhancement indicates that biogenic molecular clusters are relatively unstable unless an ion is present. A charged cluster is also likely to experience higher collision rates with HOMs because they are expected to have high electric polarizability and, depending on their structure, large dipole moments. We further investigated the dependence on ion species by adding small amounts of SO_2 to the chamber, up to around 1,000 p.p.t.v. When $[H_2SO_4]$ exceeds about $1 \times 10^5 \text{ cm}^{-3}$, the major negative ion species shift to HSO_4^- , SO_5^- and SO_4^- (Extended Data Fig. 1c), owing to their lower proton affinity (higher gas-phase

RESEARCH LETTER

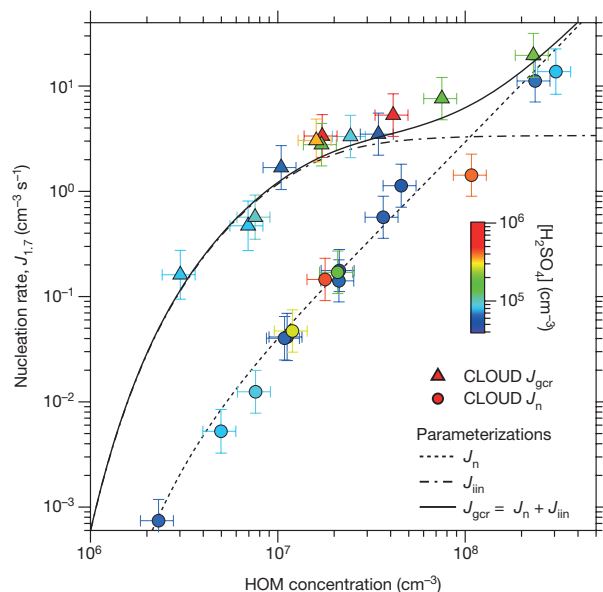


Figure 3 | Pure biogenic nucleation rates versus HOM concentration. Neutral (J_n ; circles) and GCR (J_{gr} ; triangles) nucleation rates versus total HOMs concentration ($\text{RO}_2 + \text{E}_1 + \text{E}_2$). The fraction of total HOMs that participate in nucleation (ELVOCs) is about 36% (ref. 21). The experimental conditions are 10–1,300 p.p.t.v. α -pinene (for measurements below $J_{1.7} = 10 \text{ cm}^{-3} \text{ s}^{-1}$), 30–35 p.p.b.v. O_3 , zero H_2 or HONO, 38% relative humidity, 278 K and $< 8 \times 10^5 \text{ cm}^{-3} \text{ H}_2\text{SO}_4$. The colour scale shows $[\text{H}_2\text{SO}_4]$; purple and blue points correspond to contaminant level (below the detection threshold); other colours correspond to measurements after SO_2 was added to the chamber. The fitted curves show parameterizations (described in Methods) for J_n (dashed), J_{gr} (solid) and ion-induced nucleation ($J_{in} = J_{gr} - J_n$; dot-dashed). The J_{in} parameterization assumes that the nucleation rate falls steeply at HOM concentrations below the experimental measurements, following a similar slope to that for J_n . The bars indicate 1σ total errors, although the overall systematic scale uncertainty of $+80\%/-45\%$ on the HOM concentration is not shown.

acidity) than contaminant compounds. However, the nucleation rates with sulfur ion species remain unchanged (Fig. 3). Taken together, our observations therefore show that ubiquitous ion species can stabilize embryonic biogenic clusters. However, we do not observe chlorine in nucleating clusters, even though contaminant chlorine ion species are present (Fig. 2 and Extended Data Fig. 1), which indicates that not all ions have a suitable chemical structure to bond strongly with the oxidized organic compounds²².

Figure 4 shows the CLOUD biogenic nucleation rates extended to $[\text{H}_2\text{SO}_4] = 6 \times 10^6 \text{ cm}^{-3}$ and compared with atmospheric boundary-layer observations^{3,4,23,24}. Biogenic nucleation rates show no significant dependence on sulfuric acid concentration over this range (that is, within the experimental measurement errors, the nucleation rate is consistent with zero dependency on sulfuric acid concentration). This finding sharply contrasts with base-stabilized nucleation of sulfuric acid in the presence of ammonia⁹ or amines¹⁰, where nucleation rates at 1.7 nm show a steep dependency on $[\text{H}_2\text{SO}_4]$ above 10^6 cm^{-3} . Comparison of the atmospheric observations (Fig. 4) with our measurements therefore suggests that nucleation in the lower atmosphere may involve a mixture of two distinct mechanisms. The first, which is more important in polluted environments, involves nucleation of sulfuric acid and water together with a combination of amines or ammonia with oxidized organics, and has a strong dependence on sulfuric acid. The second, which is more important in pristine environments, involves nucleation of pure organic particles and depends on only oxidized organics and ions.

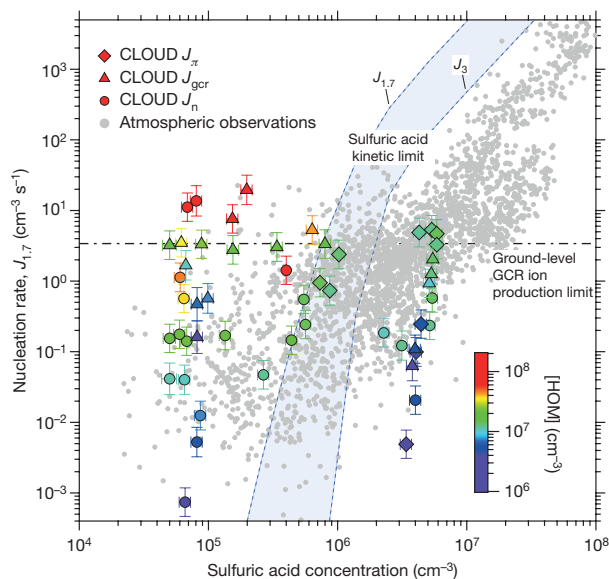


Figure 4 | Experimental and atmospheric nucleation rates versus H_2SO_4 concentration. CLOUD measurements of the neutral (J_n ; circles), GCR (J_{gr} ; triangles) and π beam (J_{pi} ; diamonds) biogenic nucleation rates at 1.7 nm ($J_{1.7}$) versus $[\text{H}_2\text{SO}_4]$. The CLOUD experimental conditions are 10–1,300 p.p.t.v. α -pinene (for measurements below $J_{1.7} = 10 \text{ cm}^{-3} \text{ s}^{-1}$), 25–35 p.p.b.v. O_3 , zero H_2 or HONO, 20%–40% relative humidity and 278 K. Measurements below $1 \times 10^5 \text{ cm}^{-3}$ for $[\text{H}_2\text{SO}_4]$ are near to the detection limit of the CI-API-TOF and should be considered as upper estimates (to avoid overlap, some data points at the H_2SO_4 detection limit are displaced by up to $1 \times 10^4 \text{ cm}^{-3}$). The total HOMs concentration from α -pinene oxidation is indicated by the colour scale. Observations of particle formation in the atmospheric boundary layer (mainly at 3-nm threshold size) are indicated by small grey circles^{3,4,23,24}. Following convention, the H_2SO_4 concentration refers to monomers alone; that is, H_2SO_4 bound in molecular clusters is not included. The kinetic upper limit on sulfuric acid nucleation is indicated by the blue band, which is bounded by dashed lines indicating $J_{1.7}$ and J_3 . This band assumes the CLOUD condensation sink, which is comparable to that of a pristine atmosphere. The upper limit on J_{in} from the GCR ion-pair production rate at ground level is indicated by the dot-dashed line. The bars indicate 1σ total errors, although the overall $+50\%/-33\%$ systematic scale uncertainty on $[\text{H}_2\text{SO}_4]$ is not shown.

To gain further insight into the stability of initial neutral and charged clusters of highly oxidized biogenic molecules, we calculated their Gibbs free energies of formation, ΔG , using quantum chemical methods (see Methods). For this study we chose $\text{C}_{10}\text{H}_{14}\text{O}_7$ and $\text{C}_{20}\text{H}_{30}\text{O}_{14}$ as E_1 and E_2 surrogates, respectively (Extended Data Fig. 7). We observe these compounds both in the gas (Fig. 1) and particle phases in the CLOUD chamber. We show proposed formation mechanisms and structures^{19,20} in Extended Data Fig. 3. Our calculations, summarized in Extended Data Table 1 and Extended Data Fig. 8, confirm that ELVOC clusters formed with an E_1^- , HSO_4^- , NO_3^- or NH_4^+ ion are expected to be stable (that is, their growth rate exceeds the evaporation rate) at around 0.1 p.p.t.v. ELVOC, or below. In contrast, the initial neutral clusters are weakly bound and so neutral nucleation is expected to be weaker. Although limited to a single surrogate pair, our theoretical calculations thus provide independent support for the experimental measurements.

Comparisons with atmospheric observations should be considered as preliminary because our measurements were made at only one temperature, with a single monoterpene, in the absence of isoprene and mostly in the absence of NO_x , which can influence HOM yields. Nevertheless, our results may provide fresh insights into several seemingly disparate

phenomena associated with low atmospheric concentrations of sulfuric acid. First, pure HOM nucleation could provide a mechanism to account for nucleation-mode particles observed at night-time, under low- $[\text{H}_2\text{SO}_4]$ conditions^{25,26}. Second, although observations are rare, nucleation-mode particles are seen in the Amazon²⁷, where SO_2 levels are extremely low (20–30 p.p.t.v.). Peak particle concentrations often occur at sunrise and sunset²⁷, and appear to be associated with rain, which reduces the aerosol condensation sink and may generate high ion concentrations by evaporation of charged droplets at the Rayleigh limit. Third, pure biogenic nucleation could explain new particle formation observed in the upper troposphere in cloud outflows depleted of SO_2 , such as over the Amazon^{27–29}. Low-solubility biogenic precursor vapours can be efficiently convected inside clouds to high altitudes where HOMs will form in the cloud outflows on exposure to oxidants, and nucleation is likely to be enhanced by the low temperatures. Fourth, since high HOM yields are also found from other organic compounds with an endocyclic double bond such as cyclohexene¹⁶, pure HOM nucleation involving anthropogenic organic precursors could be expected when $[\text{H}_2\text{SO}_4]$ is low³⁰. Finally, ion-induced pure biogenic nucleation might shed new light on the long-standing question of a physical mechanism for solar-climate variability in the pristine pre-industrial climate^{31,32}.

Direct observational evidence of pure biogenic nucleation has not been reported so far, owing to atmospheric pollution or lack of suitable instrumentation. The pure biogenic mechanism is likely to dominate nucleation in pristine terrestrial regions such as tropical rainforests or at higher altitudes above forests in convective cloud outflows. Pure biogenic nucleation might also take place over forested areas at high northern latitudes during periods of especially low pollution. Identification of pure biogenic nucleation in the atmosphere will require simultaneous measurements with several newly developed mass spectrometers, API-TOF (for molecular composition of ions and nucleating charged clusters) and CI-API-TOF (gas-phase HOMs and H_2SO_4), together with standard instruments such as low-threshold particle counters, PTR-TOF (precursor organic vapours) and NAIS (size spectra of ions and charged particles).

In summary, we find that highly oxidized organic compounds play a role in atmospheric particle nucleation comparable to that of sulfuric acid; together with a suitable stabilizing agent, each has sufficiently low volatility to form new particles in the lower atmosphere at vapour concentrations near 10^7 cm^{-3} . The stabilizing agent for pure biogenic particles is a suitable ion, whereas for sulfuric acid particles the stabilizing agents are amines, or ammonia with oxidized organics. Ion-induced nucleation of pure biogenic particles may have important consequences for pristine climates because it provides a mechanism by which nature produces particles without pollution. This could raise the baseline aerosol state of the pristine pre-industrial atmosphere and so could reduce the estimated anthropogenic radiative forcing from increased aerosol-cloud albedo over the industrial period.

Online Content Methods, along with any additional Extended Data display items and Source Data, are available in the online version of the paper; references unique to these sections appear only in the online paper.

Received 6 July 2015; accepted 16 March 2016.

- Boucher, O. *et al.* in *Climate Change 2013: The Physical Science Basis. Working Group I Contribution to the Fifth Assessment Report of the Intergovernmental Panel on Climate Change* (eds Stocker, T. F. *et al.*) 571–658 (Cambridge Univ. Press, 2013).
- Merikanto, J., Spracklen, D. V., Mann, G. W., Pickering, S. J. & Carslaw, K. S. Impact of nucleation on global CCN. *Atmos. Chem. Phys.* **9**, 8601–8616 (2009).
- Kuang, C., McMurry, P. H., McCormick, A. V. & Eisele, F. L. Dependence of nucleation rates on sulfuric acid vapor concentration in diverse atmospheric locations. *J. Geophys. Res. Atmos.* **113**, D10209 (2008).
- Kulmala, M. *et al.* Direct observations of atmospheric aerosol nucleation. *Science* **339**, 943–946 (2013).
- Hirsikko, A. *et al.* Atmospheric ions and nucleation: a review of observations. *Atmos. Chem. Phys.* **11**, 767–798 (2011).
- Zhao, J., Ortega, J., Chen, M., McMurry, P. H. & Smith, J. N. Dependence of particle nucleation and growth on high-molecular-weight gas-phase products during ozonolysis of α -pinene. *Atmos. Chem. Phys.* **13**, 7631–7644 (2013).
- Gao, S. *et al.* Low-molecular-weight and oligomeric components in secondary organic aerosol from the ozonolysis of cycloalkenes and α -pinene. *J. Phys. Chem. A* **108**, 10147–10164 (2004).
- O'Dowd, C. D. *et al.* Marine aerosol formation from biogenic iodine emissions. *Nature* **417**, 632–636 (2002).
- Kirkby, J. *et al.* Role of sulphuric acid, ammonia and galactic cosmic rays in atmospheric aerosol nucleation. *Nature* **476**, 429–433 (2011).
- Almeida, J. *et al.* Molecular understanding of sulphuric acid–amine particle nucleation in the atmosphere. *Nature* **502**, 359–363 (2013).
- Riipinen, I. *et al.* Organic condensation: a vital link connecting aerosol formation to cloud condensation nuclei (CCN) concentrations. *Atmos. Chem. Phys.* **11**, 3865–3878 (2011).
- Zhang, R. *et al.* Atmospheric new particle formation enhanced by organic acids. *Science* **304**, 1487–1490 (2004).
- Metzger, A. *et al.* Evidence for the role of organics in aerosol particle formation under atmospheric conditions. *Proc. Natl Acad. Sci. USA* **107**, 6646–6651 (2010).
- Schobesberger, S. *et al.* Molecular understanding of atmospheric particle formation from sulfuric acid and large oxidized organic molecules. *Proc. Natl Acad. Sci. USA* **110**, 17223–17228 (2013).
- Riccobono, F. *et al.* Oxidation products of biogenic emissions contribute to nucleation of atmospheric particles. *Science* **344**, 717–721 (2014).
- Ehn, M. *et al.* A large source of low-volatility secondary organic aerosol. *Nature* **506**, 476–479 (2014).
- Guenther, A. B. *et al.* The Model of Emissions of Gases and Aerosols from Nature version 2.1 (MEGAN2.1): an extended and updated framework for modeling biogenic emissions. *Geosci. Model Dev.* **5**, 1471–1492 (2012).
- Crounse, J. D., Nielsen, L. B., Jørgensen, S., Kjaergaard, H. G. & Wennberg, P. O. Autoxidation of organic compounds in the atmosphere. *J. Phys. Chem. Lett.* **4**, 3513–3520 (2013).
- Zhang, X. *et al.* Formation and evolution of molecular products in α -pinene secondary organic aerosol. *Proc. Natl Acad. Sci. USA* **112**, 14168–14173 (2015).
- Kurtén, T. *et al.* Computational study of hydrogen shifts and ring-opening mechanisms in α -pinene ozonolysis products. *J. Phys. Chem. A* **119**, 11366–11375 (2015).
- Tröstl, J. *et al.* The role of low-volatility organic compounds in initial particle growth in the atmosphere. *Nature* **533**, <http://dx.doi.org/10.1038/nature18271> (2016).
- Kathmann, S. M., Schenter, G. K. & Garrett, B. C. Ion-induced nucleation: the importance of chemistry. *Phys. Rev. Lett.* **94**, 116104 (2005).
- Paasonen, P. *et al.* On the roles of sulphuric acid and low-volatility organic vapours in the initial steps of atmospheric new particle formation. *Atmos. Chem. Phys.* **10**, 11223–11242 (2010).
- Sihto, S.-L. *et al.* Atmospheric sulphuric acid and aerosol formation: implications from atmospheric measurements for nucleation and early growth mechanisms. *Atmos. Chem. Phys.* **6**, 4079–4091 (2006).
- Suni, T. *et al.* Formation and characteristics of ions and charged aerosol particles in a native Australian eucalyptus forest. *Atmos. Chem. Phys.* **8**, 129–139 (2008).
- Lee, S.-H. *et al.* Observations of nighttime new particle formation in the troposphere. *J. Geophys. Res. Atmos.* **113**, D10210 (2008).
- Martin, S. T. *et al.* Sources and properties of Amazonian aerosol particles. *Rev. Geophys.* **48**, RG2002 (2010).
- Kulmala, M. *et al.* Deep convective clouds as aerosol production engines: role of insoluble organics. *J. Geophys. Res. Atmos.* **111**, D17202 (2006).
- Ekman, A. M. L. *et al.* Do organics contribute to small particle formation in the Amazonian upper troposphere? *Geophys. Res. Lett.* **35**, L17810 (2008).
- Bianchi, F. *et al.* New particle formation in the free troposphere: a question of chemistry and timing. *Science* **352**, <http://dx.doi.org/10.1126/science.aad5456> (2016).
- Herschel, W. Observations tending to investigate the nature of the Sun, in order to find the causes or symptoms of its variable emission of light and heat; with remarks on the use that may possibly be drawn from solar observations. *Philos. Trans. R. Soc. Lond.* **91**, 265–318 (1801).
- Kirkby, J. Cosmic rays and climate. *Surv. Geophys.* **28**, 333–375 (2007).

Acknowledgements We thank CERN for supporting CLOUD with important technical and financial resources, and for providing a particle beam from the CERN Proton Synchrotron. We also thank P. Carrie, L.-P. De Menezes, J. Dumollard, F. Josa, I. Krasin, R. Kristic, A. Laassiri, O. S. Maksimov, B. Marichy, H. Martinati, S. V. Mizin, R. Sitals, A. Wasem and M. Wilhelmsson for their contributions to the experiment. We thank the CSC Centre for Scientific Computing in Espoo, Finland for computer time. This research has received funding from the EC Seventh Framework Programme (Marie Curie Initial Training Network MC-ITN CLOUD-TRAIN no. 316662, EU Horizon 2020 Marie Curie grant no. 656994, ERC-Consolidator grant NANODYNAMITE no. 616075 and ERC-Advanced grant ATMNUCLE no. 227463), the German Federal Ministry of Education and Research (project no. 01LK1222A), the Swiss National Science Foundation (project nos 200020_135307, 200021_140663, 206021_144947/1 and 20FI20_149002/1), the Academy of Finland (Center of Excellence project no. 1118615), the Academy of Finland (135054, 133872,


RESEARCH LETTER

251427, 139656, 139995, 137749, 141217, 141451), the Finnish Funding Agency for Technology and Innovation, the Väisälä Foundation, the Nessling Foundation, the Austrian Science Fund (FWF; project no. L593), the Portuguese Foundation for Science and Technology (project no. CERN/FP/116387/2010), the Swedish Research Council, Vetenskapsrådet (grant 2011-5120), the Presidium of the Russian Academy of Sciences and Russian Foundation for Basic Research (grant 12-02-91522-CERN), the UK Natural Environment Research Council (grant NE/K015966/1), the Royal Society (Wolfson Merit Award), the US National Science Foundation (grants AGS1136479, AGS1447056 and CHE1012293), Caltech ESE Grant (Davidow Foundation), Dreyfus Award EP-11-117, the French National Research Agency (ANR), the Nord-Pas de Calais, and the European Funds for Regional Economic Development (FEDER, Labex-Cappa, ANR-11-LABX-0005-01).

Author Contributions J.A., H.G., A.K., T.N., J.T. and C.W. analysed the nucleation rates; C.Fr. analysed the API-TOF charged clusters; M.H., M.Sim. and C.Y. performed the Cl-API-TOF HOM and H₂SO₄ analyses; A.-K.B. analysed the PTR-TOF α -pinene; J.H.S. and X.Z. analysed the ELVOC structures and formation mechanisms; I.K.O. performed the quantum chemical calculations; A.Ad., J.A., A.Am., A.-K.B., F.B., M.B., S.B., J.Cu., J.Cr., A.D., J.Do., J.Du., S.E., C.Fr., C.Fu., H.G., M.H., C.R.H., T.J., H.J., J.Ka., J. Kim, J.Kir., M.Kr., A.K., K.L., V.M., U.M., T.N., F.P., T.P., A.P.P., M.P.R., N.S., K.S., M.Sim., M.Sip., G.S., A.T., J.T., A.W., D.W., R.W., C.W.,

C.Y. and P.Y. collected the data and contributed to the analysis; K.S.C., H.G., K.P., A.R., N.A.D.R., K.S. and C.E.S. evaluated the atmospheric relevance; J.Kir. wrote the manuscript; J.A., J.Do., N.M.D., C.Fr., H.G., M.H., J.H.S., M.Sim., C.W., R.W., C.Y. and X.Z. contributed to Methods and Extended Data; and U.B., K.S.C., J.Cu., J.Do., N.M.D., R.C.F., A.H., J.Kir., M.Ku., J.H.S. and D.R.W. contributed to data interpretation and editing of manuscript. All authors contributed to the development of the CLOUD facility and analysis instruments, and commented on the manuscript.

Author Information Reprints and permissions information is available at www.nature.com/reprints. The authors declare no competing financial interests. Readers are welcome to comment on the online version of the paper. Correspondence and requests for materials should be addressed to J.Kir. (jasper.kirkby@cern.ch).

 This work is licensed under a Creative Commons Attribution 4.0 International (CC BY 4.0) licence. The images or other third party material in this article are included in the article's Creative Commons licence, unless indicated otherwise in the credit line; if the material is not included under the Creative Commons licence, users will need to obtain permission from the licence holder to reproduce the material. To view a copy of this licence, visit <http://creativecommons.org/licenses/by/4.0/>.

METHODS

Overview of the CLOUD facility. The CLOUD experiment at CERN is designed to study the effects of cosmic rays on aerosols, cloud droplets and ice particles, under precisely controlled laboratory conditions. The 3-m-diameter stainless-steel CLOUD chamber and its gas system have been built to the highest technical standards of cleanliness and performance. The CLOUD chamber is periodically cleaned by rinsing the walls with ultra-pure water, followed by heating to 373 K and flushing at a high rate with humidified synthetic air and elevated ozone (several parts per million by volume). Contaminant levels of condensable vapours are in the sub-p.p.t.v. range. The high cleanliness of the chamber, together with its large volume (26.1 m³) and highly stable operating conditions, allows particle formation to be studied under atmospheric conditions at nucleation rates between about 0.001 cm⁻³ s⁻¹ and 100 cm⁻³ s⁻¹. The loss rate of condensable vapours and particles onto the chamber walls is comparable to the ambient condensation sink of the pristine boundary layer.

Ion production in the chamber can be controlled using an internal electric clearing field (which creates an ion-free environment), GCRs or an adjustable π^+ beam^{9,33} from the CERN Proton Synchrotron. The π^+ beam is de-focused to a transverse size of about 1.5 m × 1.5 m when it passes through the CLOUD chamber. With the electric field set to zero, the equilibrium ion-pair concentration in the chamber due to GCRs is around 700 cm⁻³. With the π^+ beam, this can be increased to any value up to about 3,000 cm⁻³. Hence, ion concentrations corresponding to any altitude in the troposphere can be generated in the CLOUD chamber.

The experiment has precise control of the trace vapours inside the chamber and also of the environmental temperature between 300 K and 203 K. Uniform mixing is achieved with magnetically coupled stainless-steel fans mounted at the top and bottom of the chamber. The characteristic gas mixing time in the chamber is a few minutes, depending on the fan speeds. Photochemical processes are initiated by illumination with an ultraviolet fibre-optic system, providing highly stable gas-phase reactions with a precise start time. The contents of the chamber are continuously analysed by instruments connected to sampling probes that project into the chamber. The sampling analysers are tailored for each experimental campaign, but typically comprise around 30–35 instruments, of which up to 10 are mass spectrometers.

Summary of analysing instruments. For the results reported here, the analysing instruments attached to the chamber included a chemical ionization mass spectrometer (CIMS) for H₂SO₄ concentration³⁴; an atmospheric pressure interface time-of-flight (APi-TOF; Aerodyne Research Inc. and ToFwerk AG)³⁵ mass spectrometer for molecular composition of positively or negatively charged ions and clusters; two chemical ionization atmospheric pressure interface time-of-flight (CI-APi-TOF; Aerodyne Research Inc. and ToFwerk AG)^{36,37} mass spectrometers for molecular composition and concentration of neutral gas-phase H₂SO₄ and HOMs; a proton transfer reaction time-of-flight (PTR-TOF; Ionicon Analytik GmbH)³⁸ mass spectrometer for organic vapours; a neutral cluster and air ion spectrometer (NAIS; Airel Ltd)³⁹ for concentrations of positive ions, negative ions and charged clusters in the range 1–40 nm; a nano-radial differential mobility analyser (nRDMA)⁴⁰ and a nano scanning mobility particle sizer (nano-SMPS) for particle size spectra; and several condensation particle counters (CPCs) with 50% detection efficiency thresholds between 1 nm and 4 nm: two Airmodus A09 particle size magnifiers, PSM⁴¹, (one fixed-threshold and the other scanning), two diethylene glycol CPCs, DEG-CPC^{42,43}, a butanol TSI 3776 CPC and a water TSI 3786 CPC (TSI Inc.).

Additional gas analysers included dew-point sensors (EdgeTech), sulfur dioxide (Thermo Fisher Scientific, Inc. 42i-TLE) and ozone (Thermo Environmental Instruments TEI 49C). For certain tests, HONO vapour was supplied to the chamber and photolysed with ultraviolet light to produce OH· in the absence of O₃. The gaseous HONO was generated by continual mixing of H₂SO₄ with NaNO₂ (ref. 44) in a specially designed stainless-steel reactor, and then steadily flowed into the chamber. The HONO analyser involved a specially designed probe that passed samples of air from the chamber through a solution of H₂SO₄ and sulfanilamide, which was then analysed online with a long path absorption photometer (LOPAP)⁴⁵.

Determination of the nucleation and growth rates. The nucleation rates (in cm⁻³ s⁻¹) were measured under neutral (J_n), ground-level GCR (J_{gcr}) and π^+ beam (J_π) conditions. Neutral nucleation rates are measured with the clearing field electrodes set to ± 30 kV, which establishes an electric field of about 20 kV m⁻¹ in the chamber. This completely suppresses ion-induced nucleation because, under these conditions, small ions or molecular clusters are swept from the chamber in about 1 s. Because all of the nucleation and growth processes under consideration take place on substantially longer timescales, neutral nucleation rates can be measured with zero background from ion-induced nucleation. For GCR and π^+ beam conditions, the electric field was set to zero, leading to equilibrium ion-pair concentrations around 700 cm⁻³ and 3,000 cm⁻³, respectively. The nucleation rate

J_n measures the neutral rate alone, whereas J_{gcr} and J_π measure the sum of the neutral and ion-induced nucleation rates, $J_n + J_{in}$.

The nucleation rates reported here were obtained primarily with the Airmodus scanning PSM at 1.8-nm threshold (PSM1.8) and the TSI 3776 CPC (CPC2.5), nominally 2.5-nm threshold, but measured at 3.2-nm threshold with WO_x particles⁴⁶. The nucleation rates $J_{1.7}$ are determined at 1.7-nm mobility diameter (1.4-nm mass diameter), at which size a particle is normally considered to be above its critical size and, therefore, thermodynamically stable. The critical size corresponds to the cluster size at which the evaporation and growth rates are equal. It varies with temperature, chemical species, charge and vapour concentrations, and may even be absent when evaporation rates are highly suppressed, such as for sulfuric acid–dimethylamine clusters^{10,37}. Our measurements indicate that the smallest neutral HOM clusters are relatively unstable; therefore, 1.7 nm, which is equivalent to around 5 HOM monomer units, is a reasonable size at which to derive the experimental nucleation rates.

AEROCLOUD model. To determine nucleation rates at 1.7 nm, the time-dependent particle concentrations measured with the PSM1.8 and CPC2.5 are fitted with a simplified numerical model (AEROCLOUD) that treats particle nucleation and growth kinetically at the molecular level. The model uses HOM monomer, HOM dimer and H₂SO₄ production rates derived from the CI-APi-TOF experimental data. The measured HOM production rates are scaled by a factor of 1.8 to match the observed particle appearance times and growth rates. This scaling results in good agreement of the model with the experimental data over the full experimental range of HOM concentrations. The scaling factor is within the systematic measurement uncertainty of the CI-APi-TOF, and could arise if a nitrate CI-APi-TOF does not detect all the HOMs that contribute to particle growth.

Primary ions from GCRs are generated in the model at the known rate of $q = 1.7$ ion pairs per cubic centimetre per second. A fixed parameter of the model, f_c , accounts for the charge sign asymmetry due to differences in the diffusional loss rates of positive and negative primary ions to the chamber walls:

$$q_+ = f_c (2q)$$

$$q_- = (1 - f_c) (2q)$$

The parameter f_c is determined by the experimentally measured positive and negative ion concentrations in the NAIS to have the value 0.52.

Molecules and particles collide kinetically, and cluster with each other. The model uses a reduced clustering probability (termed a 'sticking probability' below) to account for unstable small clusters, rather than allowing clusters to evaporate once they have formed. This greatly increases the speed of the computation. If the particle formed by a collision exceeds a certain size (corresponding to around 1.7-nm mobility diameter for pure biogenic clusters; see below), then it is assumed to be effectively stable and subsequently grows at near the kinetic limit. The particle growth rate between the PSM1.8 and CPC2.5 is therefore implicitly treated in the model essentially as kinetically limited growth by particle coagulation plus HOM and H₂SO₄ vapour condensation. Particles grow through size bins that are linearly spaced for small sizes and logarithmically spaced from about 2 nm to a maximum size of 400 nm. The time-steps for clustering processes range from 0.9 s to 10 s, depending on the conditions of the experimental run under analysis. The time-step is 10 s for all other processes (for example, updates of gas concentrations, high-voltage clearing-field changes, fan changes, and particle losses due to dilution of the chamber contents or diffusion to the walls). The density of the pure HOM clusters is fixed at 1.3 g cm⁻³, and at 1.85 g cm⁻³ for a pure H₂SO₄ cluster.

For neutral–neutral collisions, the number of particles in size bins 1 and 2 that coagulate in a time interval Δt to produce a particle of mass m_{12} is:

$$n_{12} = K_{00} S'_{00} n_1 n_2 V_{12} \Delta t \quad (1)$$

where K_{00} is the neutral–neutral collision kernel, n_1 , n_2 and n_{12} are the particle number concentrations, and V_{12} is the van der Waals enhancement factor (see below). The neutral–neutral sticking probability for pure biogenic particles, $S'_{00,B}$, is:

$$S'_{00,B} = \exp[-0.693(C_B/m_{12})^{S_B}]$$

where C_B and S_B are free parameters. The parameter C_B effectively defines the threshold mass of stable clusters because the sticking probability $S'_{00,B} = 0.5$ when $C_B = m_{12}$, whereas the parameter S_B controls the sharpness of the threshold. The sticking probability for collisions where at least one particle is mainly sulfuric acid is similarly defined as:

$$S'_{00,A} = \exp[-0.693(C_A/m_{12})^{S_A}]$$

where C_A and S_A are free parameters.

RESEARCH LETTER

The neutral–neutral collision kernel, K_{00} , in equation (1) is the Fuchs form of the Brownian coagulation coefficient^{47,48}. The van der Waals enhancement factor is the modification to Fuchs theory due to Sceats⁴⁹, as described in ref. 50, for a Knudsen number in the kinetic (free molecular) regime. The enhancement factor is:

$$V_{12} = 1 + \frac{\sqrt{A'/3}}{1 + b_0\sqrt{A'}} + b_1\ln(1 + A') + b_2\ln(1 + A')^3$$

where the reduced Hamaker constant, A' , is:

$$A' = \frac{A}{kT} \frac{r_1 r_2}{(r_1 + r_2)^2}$$

where $r_{1,2}$ are the particle radii, $A = 6.4 \times 10^{-20}$ J (the Hamaker constant for sulfuric acid⁵⁰), $b_0 = 0.0151$, $b_1 = -0.186$, $b_2 = -0.0163$, k is the Boltzmann constant and T is temperature. The same Hamaker constant is used for both sulfuric acid and HOMs because it does not noticeably change the model predictions.

Ions and charged clusters collide according to a similar expression as equation (1):

$$n_{12} = (E \times K_{00}) S' n_1 n_2 \Delta t \quad (2)$$

where E is an enhancement factor to obtain the charged collision kernels (described below). The sticking probability for collisions between a neutral particle and a charged particle, S'_{0+0-} , is:

$$S'_{0+0-} = \exp[-0.693(C/m_{12})^{S_{0+0-}}]$$

where S_{0+0-} is a free parameter and $C = C_B$ or C_A for biogenic or acid particles, respectively. Ion–ion recombination results in a neutral particle, which may evaporate at small sizes. The model allows partial evaporation of such recombination particles; in this case the cluster divides into monomers and the mass is conserved. The probability of cluster survival after ion–ion recombination, S'_{+-} , is:

$$S'_{+-} = \exp[-0.693(C_{+-}/m_{12})^{S_{+-}}]$$

where C_{+-} is a free parameter. A power of unity ($S_{+-} = 1$) is used because the data do not constrain this parameter well.

To obtain the charged collision kernels, the neutral–neutral collision kernel is multiplied by size-dependent enhancement factors, E :

$$\begin{aligned} E'_{0+0-} &= K_{0+0-}/K_{00} \\ E_{++--} &= K_{++--}/K_{00} \\ E_{+-} &= K_{+-}/K_{00} \end{aligned}$$

where K are the collision kernels and the subscripts refer to the charge of the colliding particles. The charged collision kernels in equation (2) are obtained from ref. 51, which refers to sulfuric acid particles. Because biogenic particles may have different neutral–charged collision kernels, their enhancement factor is left free in the fit:

$$E_{0+0-} = \frac{E'_{0+0-} - 1}{f_{0+0-}} + 1 \quad (3)$$

where f_{0+0-} is a free parameter.

Ions, monomers, clusters and larger particles are continually lost by diffusion to the walls and by dilution of the chamber contents with fresh gas mixture. The dilution lifetime is near 3 h (10^{-4} s⁻¹), depending on the total sampling rate of all instruments attached to the chamber. The wall loss rate is 1.8×10^{-3} s⁻¹ for H₂SO₄ monomers, and decreases with increasing cluster or molecule diameter as $1/d$. The same scaling law is used to obtain the wall loss rate for HOMs; that is, it is assumed that HOMs and particles that collide with the walls are irreversibly lost. For experimental runs for which there is a pre-existing population of particles in the chamber at the start of a run due to incomplete cleaning of the chamber, losses to this coagulation sink are accounted for by inserting the initial size distribution into the size bins of the model.

To determine the nucleation rates, the five free parameters of the model (S_B , S_A , S_{0+0-} , f_{0+0-} and C_{+-}) are fitted to the experimental particle concentrations in the PSM1.8 and CPC2.5 versus time. For example, for neutral pure biogenic runs, only one free parameter (S_B) is involved in the fit. The value of S_B ranges from 12 to 14, S_A from 4 to 6, S_{0+0-} from 0.1 to 1.0, f_{0+0-} is near 4 and C_{+-} is near 10,000 Th. The parameters C_B , C_A , S_{+-} and f_c were determined by a global fit to all runs in the dataset and then subsequently fixed at these values. The fitted threshold masses for C_B and C_A are around 1,300 Th and 700 Th, respectively. The parameter S_{+-} is set to 1.0 and f_c is set to 0.52. The time development of the particle number

concentrations in both counters throughout all of the nucleation events in our dataset is well reproduced by the model (an example is shown in Extended Data Fig. 4b).

After fitting the data with the model, the nucleation rate $J_{1.7}$ is determined as the number of particles that grow to a mobility diameter of 1.7 nm or larger in any time-step, divided by the time increment. In each nucleation run at fixed conditions, the time t_{\max} is determined at which $J_{1.7}$ is maximum; the value of $J_{1.7}$ for that run is then calculated as the mean measurement over the interval ($t_{\max} \pm 300$ s).

There are three major advantages of using a data-driven kinetic model to determine nucleation rates rather than making direct measurements with the PSM1.8 or CPC2.5 data. First, it avoids the need for time derivatives of the data, which are subject to large errors at low counting rates. Second, particle growth rates are determined by kinetics and properly account for growth due to collisions both with monomers and with other particles. The model treatment of the data therefore avoids the exponential sensitivity on experimental growth rates that occurs with other methods^{52–55}. Experimental growth rates are determined from particle counter rise times and have relatively large uncertainties in the 1–3-nm size range. Finally, the model requires consistency between the PSM1.8 and CPC2.5 so the formation rates are experimentally constrained both near the 1.7-nm threshold size and near 3 nm.

Verification of the model nucleation rates. We performed extensive cross-checks of the nucleation rates obtained with the model by calculating the nucleation rates independently in two additional ways: (1) direct measurements at 1.8 nm using the scanning PSM and (2) CPC2.5 measurements that are stepwise-corrected to 1.7-nm threshold size. Within their experimental uncertainties, the nucleation rates obtained by both these methods agree well with the values obtained with the AEROCLOUD kinetic model.

The stepwise-corrected method is described in detail in ref. 55, but a brief summary is provided here. The nucleation rates are derived from the rate of change of the formation rates, dN_{CPC}/dt , where N_{CPC} is the particle number concentration measured with the CPC2.5 above its detection threshold, d_{th} . The formation rate is corrected in two sequential steps for particle losses to chamber walls, dilution and coagulation: (1) particle losses above d_{th} and (2) particle losses during growth from 1.7 nm to d_{th} . The dilution and wall loss rates are the same as in the kinetic model. To calculate the coagulation rate, the particles are divided into size bins and then the loss rate in each bin i is computed by summing the size-dependent collision (coagulation-loss) rate of the particles in bin i with those in all other bins. The total coagulation loss rate is then the sum of the particle loss rates in each bin i .

Correcting for particle losses during growth from 1.7 nm to d_{th} (item (2) above) requires knowledge of the particle growth rate. This is experimentally determined with several instruments, for example, from the appearance times measured in the scanning PSM⁵⁶, which detects particles over a range of threshold diameters between 1 nm and 2.5 nm. The growth rates were also measured over different size ranges with several other instruments, including a fixed-threshold PSM, two DEGCPCs, a TSI 3776 CPC, an API-TOF, an NAIS, an nRDMA and a nano-SMPS. The experimental growth rates are parameterized because they cannot be measured sufficiently precisely at each point in time during all events. To determine the nucleation rate at 1.7 nm from the corrected formation rate at d_{th} , the size interval is divided into m log-normally spaced bins, $d\log(D_p)$, chosen to match the spacing of the SMPS bins at larger sizes. The residence time of a particle in each bin is $\delta t = \delta d_i / (\text{growth rate})$, where δd_i is the size of bin i . Starting with the measured particle distribution above d_{th} , the size distribution and formation rate is then extended towards 1.7 nm in a stepwise process. In the first step, using the known loss rates due to the chamber walls, dilution and coagulation, as well as the time δt , the concentration in the largest new bin is calculated, as well as the formation rate into this bin. Using this concentration, the size distribution is updated and the process is repeated until, after m steps, the smallest size bin at 1.7 nm is reached, where the nucleation rate is determined.

The NAIS. The neutral cluster and air ion spectrometer (NAIS)⁵⁷ measures the size distributions of positively and negatively charged particles, and also of total (charged plus neutral) particles, between mobility-equivalent diameters of 0.75 nm and 45 nm. Because the instrument includes two mobility analysers operating in parallel, positive and negative spectra are obtained simultaneously, each with 21 electrometers. Taking into account the internal diffusion losses, the mobility distribution is then calculated in 28 size bins from the measured electrometer currents.

The instrument operates sequentially in three modes: ion, particle and offset mode (one cycle takes 150 s). The aerosol sample first passes through a pre-conditioning section containing a discharger, an electric filter, a charger and a second electric filter (post-filter). The charger and discharger are corona needles of opposite polarities. In ion mode, the pre-conditioning unit is switched off and the sample passes through unaffected. In this way, the mobility analysers

measure only ions and charged particles from the CLOUD chamber. In particle mode—which was not used for the results reported here—both chargers are switched on and so neutral particles from the CLOUD chamber can be classified. The post-filters improve the measurements by removing residual ions from the charger. In offset mode, the dischargers and corresponding filters are switched on. The sample is charged to the opposite polarity as the subsequent analyser and so no detectable particles can enter. In this way, the noise levels and possible parasitic currents are measured to provide corrections for the preceding ion and particle measurement.

After preconditioning, the aerosol sample is classified in two cylindrical mobility analysers. The central electrode consists of several sections, each at a different fixed electric potential. The particles enter the analysers through a circular slit near the central electrode and are collected at the 21 outer electrodes where they transfer their charge to the connected electrometer and the resulting current is measured. The analysers operate at a sheath flow rate of 60 l min⁻¹. Filtered excess air serves as sheath gas to ensure conditions similar to the sample flow. The data inversion that converts the measured electrometer currents to particle concentrations is based on model calculations simulating trajectories of particles with different mobilities, and on calibration measurements of the internal losses. The performance of the NAIS for ion-mobility (size) and concentration measurements is described in refs 58, 59.

The APi-TOF mass spectrometer. The atmospheric pressure interface time-of-flight (APi-TOF) mass spectrometer¹⁴ measures the mass-to-charge ratio of positive or negative ions with an inlet at atmospheric pressure. The first stage of the instrument consists of an atmospheric pressure interface (APi) section where ions are focused and guided by two quadrupoles and an ion lens through three chambers at progressively lower pressures down to 10⁻⁴ mbar. The second stage of the instrument is a time-of-flight (TOF) mass spectrometer at 10⁻⁶ mbar.

The APi-TOF was connected to the CLOUD chamber via a 1" (21.7-mm inner diameter) sampling probe shared with the NAIS. A Y-splitter divided the total flow of 20 l min⁻¹ equally between the two instruments. The sample flow for the APi-TOF was 0.8 l min⁻¹, with the remainder being discarded.

The APi-TOF measurements were made during GCR and π^+ beam runs; that is, the ions were charged by GCRs or charged pions traversing the CLOUD chamber. Because the APi-TOF can measure only one polarity at a time, positive and negative ions were measured in different runs. Different instrument settings were used during the campaigns to optimize detection in the low- or high-mass regions of the spectrum. The data were analysed with *tofTools*³⁵, developed by the University of Helsinki. The tool is implemented in MATLAB and allows complete processing of TOF data: averaging, mass calibration, baseline detection, peak fitting and high-resolution analysis.

The CI-APi-TOF mass spectrometer. Two nitrate chemical ionization atmospheric pressure interface time-of-flight (CI-APi-TOF) mass spectrometers were used to measure neutral sulfuric acid and HOMs. The instruments were operated by the University of Frankfurt (UFRA-CI) and the University of Helsinki (UHEL-CI); differences between the two instruments are indicated in this section by adding the UHEL-CI characteristics in parentheses after those of the UFRA-CI. The CI-APi-TOF has been described previously^{36,37}. The sample air from the CLOUD chamber was drawn in through a 1/2" stainless steel tube at flow rate of 9 l min⁻¹ (10 l min⁻¹). An electrostatic filter was installed in front of each instrument to remove ions and charged clusters formed in the chamber. The geometry of both ion sources follows the design of ref. 60, but a corona charger³⁴ (X-ray generator) is used for ion generation. Dry air with nitric acid vapour is flushed over the ionizer to generate NO₃⁻ (HNO₃)_{j=0,2} ions. The ions are guided into the sample flow with an electric field, where they react with sulfuric acid and HOMs. The reaction time is approximately 50 ms (200 ms) before the ions enter the APi section through a pinhole with a diameter of 350 μ m (300 μ m). The APi section consists of three consecutive differentially pumped chambers where the pressure is progressively reduced and the ions are focused by two sets of quadrupoles and an ion lens system. The mass-to-charge ratios, m/z , of the ions that pass through these chambers are measured by a time-of-flight (TOF) mass spectrometer (Tofwerk AG).

The voltage settings in the APi-TOF section influence the mass-dependent transmission efficiency. The transmission curves were determined in a series of calibration measurements in which various perfluorinated acid vapours of different m/z were passed into the instrument in sufficient amounts to saturate all the primary ions. In this way, a constant ion signal could be generated at each m/z and so the transmission efficiency could be determined relative to that of the primary ions mass range. The UFRA-CI operated at the same voltage settings for the entire data collection period; the UHEL-CI was operated in a switching mode between two voltage settings optimized for low and high m/z , respectively.

The raw data were analysed with the MATLAB *tofTools* package³⁵. The mass scale is calibrated to an accuracy of better than 10 p.p.m. using a two-parameter fit.

The concentration of sulfuric acid is calculated from the ratio of bisulfate ion counting rates (in s⁻¹) relative to primary ions as follows:

$$[\text{H}_2\text{SO}_4] = C \times \text{SL}_{\text{H}_2\text{SO}_4} \ln \left[1 + \frac{\text{HSO}_4^- + \text{HSO}_4^- \cdot \text{HNO}_3}{\sum_{j=0}^2 \text{NO}_3^- \cdot (\text{HNO}_3)_j} \right]$$

The factor $\text{SL}_{\text{H}_2\text{SO}_4}$ corrects for losses in the sampling line from the CLOUD chamber. The calibration coefficient, C , is determined by connecting the CI-APi-TOF to a well-characterized H₂SO₄ generator⁶¹. The value of C depends on the voltage settings in the APi-TOF section and was determined to be 6.5 \times 10⁹ cm⁻³ (1.2 \times 10¹⁰ cm⁻³ and 2.8 \times 10⁹ cm⁻³ for the high and low m/z settings, respectively), with an uncertainty of +50%/-33%. The H₂SO₄ detection limit is 5 \times 10⁴ cm⁻³ or slightly lower.

The concentration of a HOM at $m/z = i$ is calculated as follows:

$$[\text{HOM}] = CT_i \times \text{SL}_{E_1/E_2} \ln \left[1 + \frac{\text{HOM}_i \cdot \text{NO}_3^-}{\sum_{j=0}^2 \text{NO}_3^- \cdot (\text{HNO}_3)_j} \right]$$

Here, $\text{HOM}_i \cdot \text{NO}_3^-$ is the background-subtracted counting rate of the HOM. Background levels were measured by sampling air from the clean CLOUD chamber without any α -pinene present. The factor T_i is the mass-dependent transmission efficiency. The calibration coefficient, C , is the same as that obtained for sulfuric acid because HOMs and sulfuric acid were shown to have similar molecular collision rates with the nitrate ions¹⁶. Furthermore, the binding of NO₃⁻ with highly oxidized HOMs is found in the present study to be strong, so clustering should proceed at near the kinetic limit, as it does for NO₃⁻ with sulfuric acid. The factor SL_{E_1/E_2} corrects for losses in the sampling line from the CLOUD chamber. The values were determined for E_1 and E_2 separately, using experimentally determined diffusion coefficients, as $\text{SL}_{E_1} = 1.443$ and $\text{SL}_{E_2} = 1.372$.

The HOM monomers, E_1 , are the background-subtracted sum of the peaks in the m/z band 235–424 Th; the HOM dimers, E_2 , are the corresponding sum for 425–625 Th. Instrumental contamination peaks are excluded from the band summation, as are peaks assigned to the RO₂⁻ radical (C₁₀H₁₅O_{6,8,10,12}, which correspond to $m/z = 293$ Th, 325 Th, 357 Th and 389 Th). Total HOMs is defined as the sum RO₂⁻ + E_1 + E_2 .

HOM yields. The HOM yields from either ozonolysis or OH \cdot chemistry were calculated by assuming equal production and loss rates during steady-state¹⁶:

$$\frac{d[\text{HOM}]}{dt} = \gamma_{\text{Ox}} k_{\text{AP}+\text{Ox}} [\text{AP}] [\text{Ox}] - k_{\text{loss}} [\text{HOM}] = 0$$

where the yield, γ_{Ox} , is the fraction of α -pinene (AP) oxidation reactions leading to HOM formation, and 'Ox' signifies O₃ or OH \cdot . The values of the rate constants (in cm³ per molecule per second) at 278 K for oxidation of α -pinene are $k_{\text{AP}+\text{O}_3} = 8.05 \times 10^{-17}$ and $k_{\text{AP}+\text{OH}\cdot} = 5.84 \times 10^{-11}$, from the International Union of Pure and Applied Chemistry (IUPAC)⁶² (the α -pinene + O₃ rate constant is updated on the IUPAC website at http://iupac.pole-ether.fr/htdocs/datasheets/pdf/Ox_VOC8_O3_apinene.pdf). The HOM wall loss rate was determined to be 1.1 \times 10⁻³ s⁻¹, assuming they are irreversibly lost. An additional loss is due to dilution of the chamber contents by makeup gases (0.1 \times 10⁻³ s⁻¹). The total loss rates for HOMs is then $k_{\text{loss}} = 1.2 \times 10^{-3}$ s⁻¹.

During the experiments involving pure OH \cdot chemistry, nitrous acid (HONO) concentrations ranging from 0.5 p.p.b.v. to 3 p.p.b.v. were photolysed by ultraviolet radiation from the fibre optic system to produce OH \cdot . This led to a small contamination of NO in the chamber, which may potentially influence the HOM yield. The OH \cdot concentrations in the CLOUD chamber were estimated using the PTR-TOF measurements of the difference of the α -pinene concentrations with no OH \cdot present (ultraviolet off) and OH \cdot present (ultraviolet on at different intensities). The decrease in α -pinene was due to only OH \cdot reactions, because no O₃ was present in the chamber during these experiments. The accuracy for [OH \cdot] is estimated to be $\pm 30\%$ (1 σ) including uncertainties in α -pinene measurements and reaction rate constant, which leads to a systematic scale uncertainty on the HOM production rate, $k_{\text{AP}+\text{OH}\cdot} [\text{AP}] [\text{OH}\cdot]$, of $\pm 40\%$ (1 σ). However, run-to-run uncertainties contribute substantially to the overall uncertainty as indicated by the error bars in Extended Data Fig. 2.

The SO₂-CIMS. The SO₂ chemical ionization mass spectrometer (SO₂-CIMS) uses CO₃⁻ primary ions to convert SO₂ to SO₅⁻, which is then measured in a quadrupole mass spectrometer with an APi interface (Georgia Tech). The general design of the ion source is shown in ref. 60, but the primary ions are generated with a corona discharge³⁴. The corona needle holder was modified so that CO₂, O₂ and Ar are fed directly over the corona discharge. In this way, direct contact between the N₂ sheath flow and the discharge needle is avoided, which leads to a reduced

RESEARCH LETTER

contamination by NO_3^- and maximizes the ratio of CO_3^- to NO_3^- . The reaction scheme for the ionization of SO_2 to SO_5^- can be found in ref. 63. The use of a dry N_2 buffer flow in front of the pinhole of the mass spectrometer evaporates associated water molecules from SO_5^- ions, and so sulfur dioxide is detected in the mass spectrum at $m/z = 112$ Th (SO_5^-).

The SO_2 concentration (in p.p.t.v.) is calculated from the ion count rates, $R_{m/z}$, as follows:

$$\text{SO}_2 = C_S \ln(1 + R_{112}/R_{60})$$

where R_{112} corresponds to the background-corrected ion count rate of SO_5^- and R_{60} is the ion count rate of the primary ion CO_3^- . The calibration factor C_S was obtained by periodically calibrating the instrument with a SO_2 gas standard (Carbagas AG) during the campaign. During a calibration, the gas standard was diluted with ultraclean humidified air at 38% relative humidity (the same as that supplied to the CLOUD chamber) to achieve a range of different SO_2 mixing ratios between 12 p.p.t.v. and 11 p.p.b.v. The calibration factor was found to be 1.3×10^5 p.p.t.v., with an estimated uncertainty of $\pm 11\%$. The error includes uncertainties in the flow rates during a calibration and in the gas standard concentration, as well as statistical uncertainties. However, we also observed that temperature changes in the experimental hall where the experiments were conducted led to a drift in the SO_5^- background signal when no SO_2 was applied to the CIMS. This effect contributes to the overall uncertainty and mainly affects the measurement at low SO_2 levels (< 100 p.p.t.v.), with lower precision in this concentration range. For example, at 30 p.p.t.v. SO_2 , the estimated uncertainty is $\pm 23\%$, but it becomes progressively smaller with higher SO_2 levels, reaching $\pm 13\%$ above 100 p.p.t.v. SO_2 . The detection limit of the instrument is 15 p.p.t.v. SO_2 .

Experimental errors. To determine $J_{1,7}$, the measured particle concentrations in the PSM1.8 and CPC2.5 versus time are fitted with the AEROCLOUD model (see above). The nucleation rate error, σ_J , has three main components. The dominant error at slow growth rates is due to uncertainties in the PSM1.8 and CPC2.5 detection thresholds for HOM particles⁶⁴. The threshold error components are first determined numerically for each nucleation measurement by performing additional AEROCLOUD fits after shifting the PSM1.8 particle detection threshold by $+0.2/-0.1$ nm and the CPC2.5 threshold by ± 0.4 nm. This provides four fractional $J_{1,7}$ errors which are then averaged for each counter to provide a mean fractional uncertainty, σ_{psm} and σ_{cpc} , respectively. The total error due to detection threshold uncertainties, σ_{thr} , for the combined fit to the PSM1.8 and CPC2.5 data is then:

$$\frac{1}{\sigma_{\text{thr}}^2} = \frac{1}{\sigma_{\text{psm}}^2} + \frac{1}{\sigma_{\text{cpc}}^2}$$

$$\sigma_{\text{thr}} = \frac{\sigma_{\text{psm}}\sigma_{\text{cpc}}}{(\sigma_{\text{psm}}^2 + \sigma_{\text{cpc}}^2)^{1/2}}$$

The total fractional $J_{1,7}$ error, σ_J , is then obtained by adding σ_{thr} in quadrature with an experimental error due to run-to-run reproducibility under nominally identical chamber conditions, σ_{exp} , and an error to account for model approximations, σ_{model} :

$$\sigma_J^2 = \sigma_{\text{thr}}^2 + \sigma_{\text{exp}}^2 + \sigma_{\text{model}}^2$$

where $\sigma_{\text{exp}} = 30\%$ and $\sigma_{\text{model}} = 50\%$.

The concentration of O_3 is measured with a calibrated instrument and is known to $\pm 10\%$. The α -pinene concentration in the PTR-TOF is known to $\pm 10\%$. As discussed above, the uncertainty on SO_2 is $\pm 13\%$ above 150 p.p.t.v., increasing at lower values to $\pm 23\%$ at 30 p.p.t.v.

For CI-API-TOF measurements, the run-to-run experimental uncertainties are $\pm 10\%$ for $[\text{H}_2\text{SO}_4]$ and $\pm 20\%$ for $[\text{HOM}]$. However, there is a larger overall systematic error that scales all measurements by the same amount. The systematic scale uncertainty for $[\text{H}_2\text{SO}_4]$ is estimated to be $+50\%/-33\%$. This estimate is based on a comparison of $[\text{H}_2\text{SO}_4]$ measurements with a CIMS and a calibrated H_2SO_4 generator⁶¹. The systematic uncertainties for $[\text{HOM}]$ have the following sources and fractional errors (1σ): sulfuric acid calibration (50%), charging efficiency of HOMs in the ion source (25%), mass dependent transmission efficiency (50%) and sampling line losses (20%). This results in an overall systematic scale uncertainty for $[\text{HOM}]$ of $+80\%/-45\%$. The uncertainty in the HOM yield from ozonolysis or hydroxyl chemistry is estimated by adding the $[\text{HOM}]$ uncertainty in quadrature with the errors for α -pinene (10%), O_3 (10%), OH \cdot (30%), HOM wall loss rate (6%) and rate constants (35% for the α -pinene O_3 reaction and 20% for the α -pinene OH \cdot reaction). This results in a mean estimated uncertainty in HOM yield for either ozonolysis or hydroxyl chemistry of $+100\%/-60\%$.

Quantum chemical calculations. To estimate the characteristic binding energies and evaporation rates expected for ELVOC clusters, we chose $\text{C}_{10}\text{H}_{14}\text{O}_7$ (molecular

weight of 246) to represent the ELVOC monomer, E_1 , and $\text{C}_{20}\text{H}_{30}\text{O}_{14}$ (molecular weight of 494) to represent the covalently bound ELVOC dimer, E_2 . Their formation mechanism and structures are shown in Extended Data Figs 3 and 7. To evaluate the effect of charge on the formation of ELVOC clusters, we studied initial molecular clusters of E_1 and E_2 that are either neutral or else include an ion of the type E_1^- , HSO_4^- , NO_3^- or NH_4^+ (Extended Data Table 1).

We calculated formation Gibbs free energies at 278 K, $\Delta G_{278\text{K}}$, of different clusters with the MO62X functional⁶⁵ and the 6-31+G(d) basis set⁶⁶ using the Gaussian09 program⁶⁷. The formation Gibbs free energy can be related to evaporation rate as described in refs 68, 69. In previous works^{10,15}, we used the method proposed in ref. 68 for calculating the formation free energy of different clusters. However, this method is too computationally demanding for the large clusters of the present study. The MO62X functional has been shown to be well suited to the study of atmospheric clusters⁷⁰. Ref. 70 has shown how reducing the basis set from the largest Pople basis set available (6-311++G(3df,3pd)) to the basis set used in this work (6-31+G(d)) leads to differences in the calculated formation free energies below 1 kcal mol⁻¹. Therefore, MO62X/6-31+(d) is a good alternative to the B3RICC2 method⁶⁸ when studying large clusters. We confirmed this by comparing the formation free energies previously calculated¹⁵ using the B3RICC2 method with those calculated here using the MO62X/6-31+G(d) method. The differences were found to be below 2 kcal mol⁻¹.

Parameterization of the pure biogenic nucleation rate. We parameterized the experimentally measured pure biogenic nucleation rates in a form suitable for global aerosol models. The neutral and ion-induced pure biogenic nucleation rates (in cm⁻³s⁻¹) are parameterized as:

$$J_n = a_1[\text{HOM}]^{a_2+a_5/[\text{HOM}]}$$

$$J_{\text{ion}} = 2[n_{\pm}]a_3[\text{HOM}]^{a_4+a_5/[\text{HOM}]}$$
(4)

where $[n_{\pm}] = [n_+] = [n_-]$ is the small-ion concentration of either sign. Expressions for $[\text{HOM}]$ and $[n_{\pm}]$ are given in equations (7) and (10) below, respectively. The parameters a_n are determined from fits to the data in Fig. 3 and have the values $a_1 = 0.04001$, $a_2 = 1.848$, $a_3 = 0.001366$, $a_4 = 1.566$ and $a_5 = 0.1863$, with $[\text{HOM}]$ expressed in units of 10⁷ cm⁻³. The parameterized rates are shown by the curves in Fig. 3. The R^2 value of the fit is 0.97. The terms a_{1-4} describe simple power laws, whereas the term a_5 accounts for the steepening of the nucleation rate at low HOM concentrations. The nucleation rates are assumed to be independent of temperature, except for the effect of rate constants (equation (6) below), because the experimental measurements exist at only a single temperature.

The HOM concentration in equation (4) is determined from its production and loss rates:

$$\frac{d[\text{HOM}]}{dt} = Y_{\text{HOM}+\text{O}_3}k_{\text{MT}+\text{O}_3}[\text{MT}][\text{O}_3] + Y_{\text{HOM}+\text{OH}\cdot}k_{\text{MT}+\text{OH}\cdot}[\text{MT}][\text{OH}\cdot] - k_{\text{HOM}}[\text{HOM}]$$
(5)

where MT represents total monoterpenes. The IUPAC⁶² reaction rate constants (in cm³ per molecule per second) for oxidation of α -pinene by ozone and hydroxyl radicals are, respectively:

$$k_{\text{MT}+\text{O}_3} = 8.05 \times 10^{-16} \exp(-640/T)$$

$$k_{\text{MT}+\text{OH}\cdot} = 1.2 \times 10^{-11} \exp(440/T)$$
(6)

where T (in K) is the temperature (the α -pinene+ O_3 rate constant is updated on the IUPAC website at http://iupac.pole-ether.fr/htdocs/datasheets/pdf/Ox_VOC8_O3_apinene.pdf). The HOM yields in each ozone-monoterpene and hydroxyl-monoterpene reaction are $Y_{\text{HOM}+\text{O}_3}$ and $Y_{\text{HOM}+\text{OH}\cdot}$, respectively. The parameter k_{HOM} is the HOM loss rate or, equivalently, the atmospheric condensation sink, CS (in s⁻¹). The condensation sink is determined assuming the diffusion characteristics of a typical α -pinene oxidation product (see appendix A1 of ref. 71). Assuming steady-state in equation (5), the HOM concentration becomes:

$$[\text{HOM}] = \frac{Y_{\text{HOM}+\text{O}_3}k_{\text{MT}+\text{O}_3}[\text{MT}][\text{O}_3] + Y_{\text{HOM}+\text{OH}\cdot}k_{\text{MT}+\text{OH}\cdot}[\text{MT}][\text{OH}\cdot]}{\text{CS}}$$
(7)

where the HOM yield from ozonolysis is $Y_{\text{HOM}+\text{O}_3} = 2.9\%$, and from reaction with the hydroxyl radical is $Y_{\text{HOM}+\text{OH}\cdot} = 1.2\%$ (Extended Data Fig. 2). The HOM yield from ozonolysis is determined from CLOUD measurements in the presence of a hydroxyl scavenger (0.1% H_2). The HOM yield from reaction with hydroxyl radicals is determined from CLOUD measurements in the absence of ozone, and where photolysed HONO provides the OH \cdot source. Therefore, the experimental measurement of hydroxyl-initiated oxidation is made in the presence of NO_x , as occurs in the atmosphere.

The small-ion concentration in equation (4) is calculated from the steady-state solution of the ion balance equation:

$$\frac{d[n_{\pm}]}{dt} = q - \alpha[n_{\pm}]^2 - k_i[n_{\pm}] \quad (8)$$

where q (in $\text{cm}^{-3}\text{s}^{-1}$) is the ion-pair production rate and α is the ion-ion recombination coefficient (in cm^3s^{-1}). The factor of 2 in equation (4) accounts for nucleation from positive and negative ions. For the CLOUD GCR data, $q = 1.7\text{cm}^{-3}\text{s}^{-1}$. Terrestrial radioactivity such as radon contributes additional ionization in the boundary layer over land masses⁷². The ion loss rate, k_i , is due to the condensation sink, CS, and ion-induced nucleation:

$$k_i = \text{CS} + \frac{J_{\text{in}}}{2[n_{\pm}]} \quad (9)$$

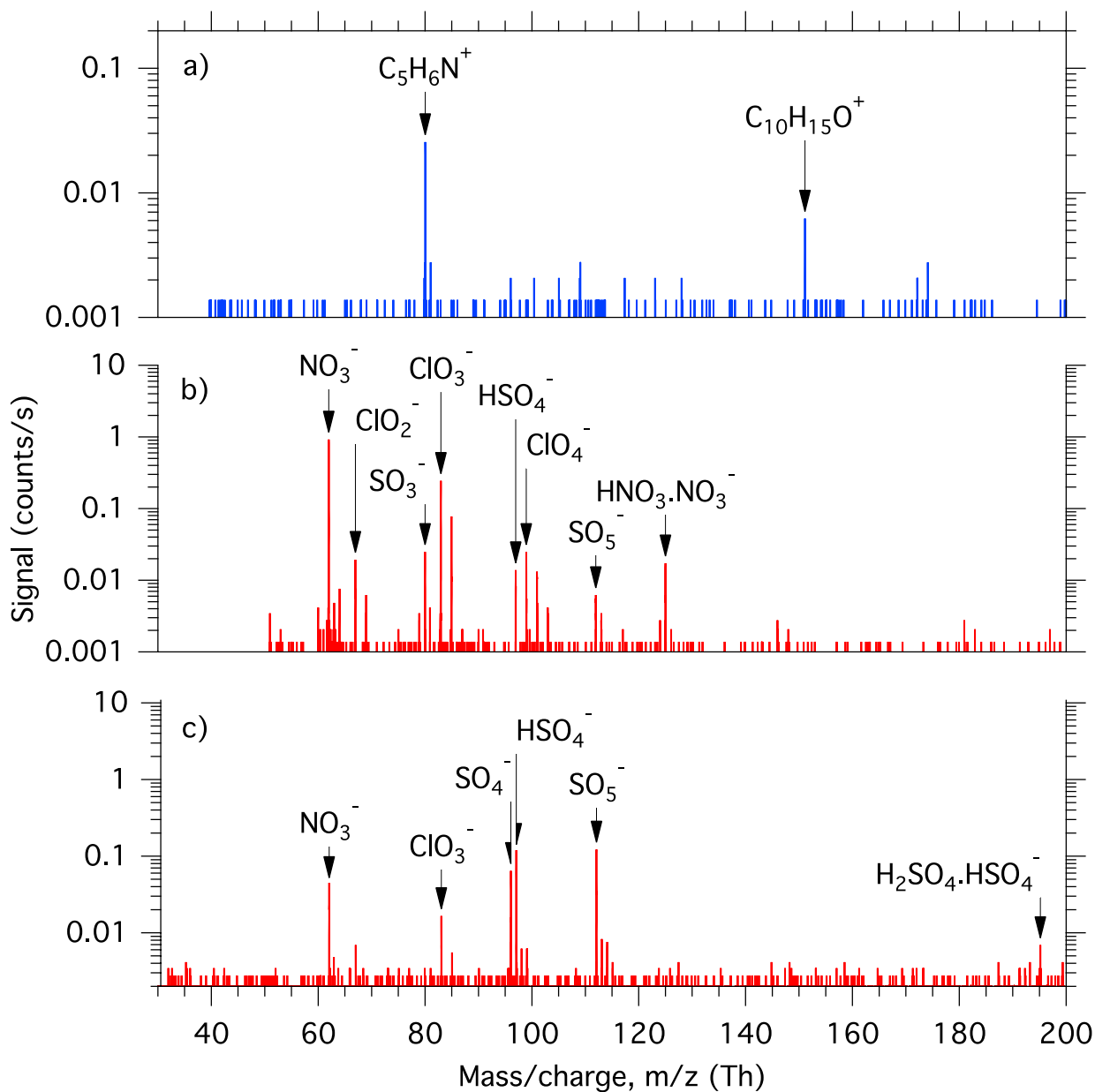
where $J_{\text{in}}/(2[n_{\pm}])$ is given by equation (4) and the steady-state concentration of small ions is, from equation (8):

$$[n_{\pm}] = \frac{(k_i^2 + 4\alpha q)^{1/2} - k_i}{2\alpha} \quad (10)$$

From equations (8) and (9), J_{in} saturates at $2q$ at high nucleation rates (see Fig. 3).

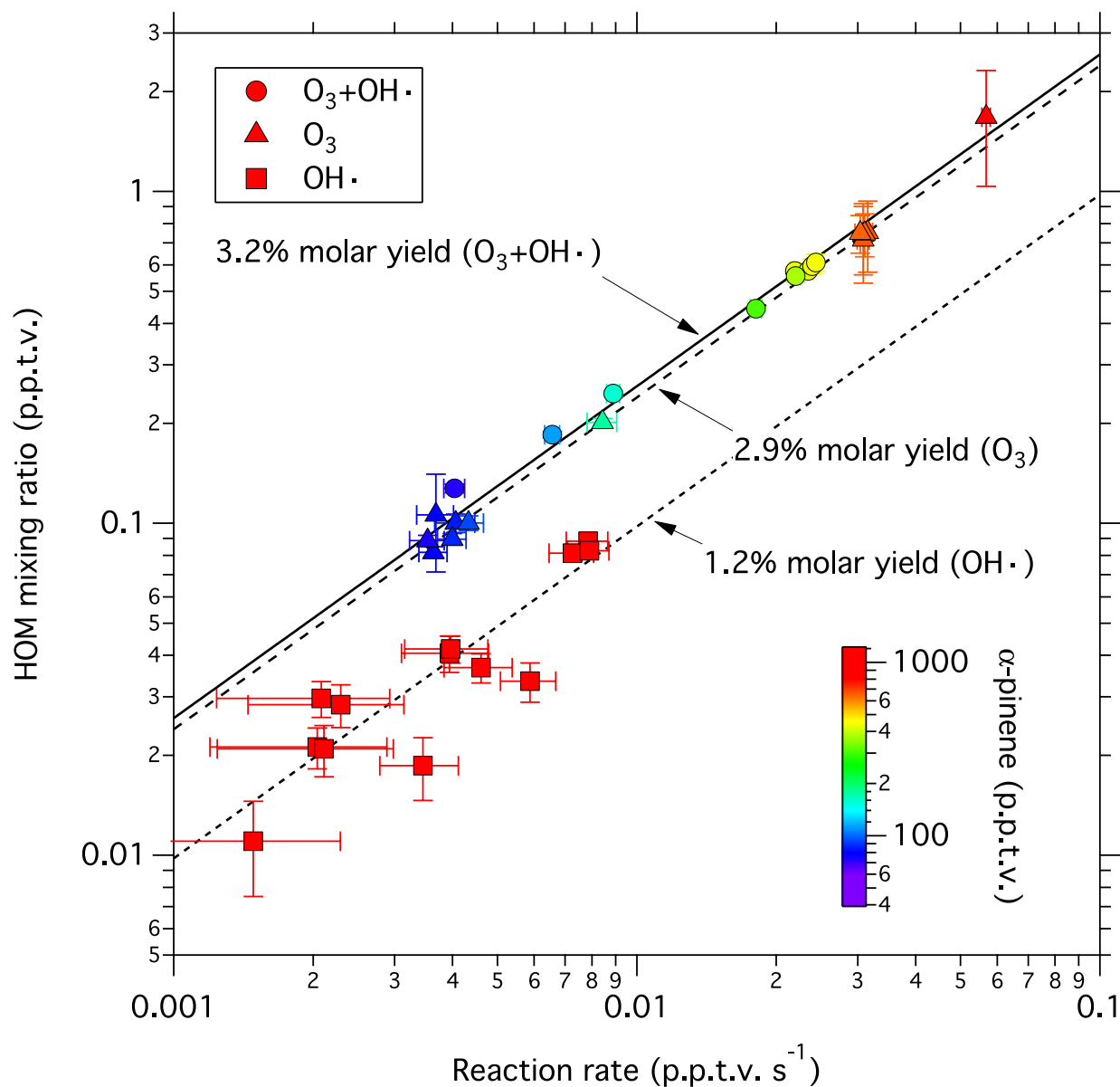
33. Enghoff, M. B., Pedersen, J. O. P., Uggerhøj, U. I., Paling, S. M. & Svensmark, H. Aerosol nucleation induced by a high energy particle beam. *Geophys. Res. Lett.* **38**, L09805 (2011).
34. Kürten, A., Rondo, L., Ehrhart, S. & Curtius, J. Performance of a corona ion source for measurement of sulphuric acid by chemical ionisation mass spectrometry. *Atmos. Meas. Tech.* **4**, 437–443 (2011).
35. Junninen, H. *et al.* A high-resolution mass spectrometer to measure atmospheric ion composition. *Atmos. Meas. Tech.* **3**, 1039–1053 (2010).
36. Jokinen, T. *et al.* Atmospheric sulphuric acid and neutral cluster measurements using CI-API-TOF. *Atmos. Chem. Phys.* **12**, 4117–4125 (2012).
37. Kürten, A. *et al.* Neutral molecular cluster formation of sulfuric acid-dimethylamine observed in real time under atmospheric conditions. *Proc. Natl Acad. Sci. USA* **111**, 15019–15024 (2014).
38. Graus, M., Müller, M. & Hansel, A. High resolution PTR-TOF: quantification and formula confirmation of VOC in real time. *J. Am. Soc. Mass Spectrom.* **21**, 1037–1044 (2010).
39. Mirme, S. *et al.* Atmospheric sub-3 nm particles at high altitude. *Atmos. Chem. Phys.* **10**, 437–451 (2010).
40. Zhang, S. H., Akutsu, Y., Russell, L. M., Flagan, R. C. & Seinfeld, J. H. Radial differential mobility analyzer. *Aerosol Sci. Technol.* **23**, 357–372 (1995).
41. Vanhanen, J. *et al.* Particle size magnifier for nano-CN detection. *Aerosol Sci. Technol.* **45**, 533–542 (2011).
42. Iida, K., Stolzenburg, M. R. & McMurry, P. H. Effect of working fluid on sub-2 nm particle detection with a laminar flow ultrafine condensation particle counter. *Aerosol Sci. Technol.* **43**, 81–96 (2009).
43. Wimmer, D. *et al.* Performance of diethylene glycol-based particle counters in the sub-3 nm size range. *Atmos. Meas. Tech.* **6**, 1793–1804 (2013).
44. Taira, M. & Kanda, Y. Continuous generation system for low-concentration gaseous nitrous acid. *Anal. Chem.* **62**, 630–633 (1990).
45. Heland, J., Kleffmann, J., Kurtenbach, R. & Wiesen, P. A new instrument to measure gaseous nitrous acid (HONO) in the atmosphere. *Environ. Sci. Technol.* **35**, 3207–3212 (2001).
46. Riccobono, F. *et al.* Contribution of sulfuric acid and oxidized organic compounds to particle formation and growth. *Atmos. Chem. Phys.* **12**, 9427–9439 (2012).
47. Fuchs, N. A. *The Mechanics of Aerosols* (Pergamon, 1964).
48. Seinfeld, J. H. & Pandis, S. N. *Atmospheric Chemistry and Physics: From Air Pollution to Climate Change* 2nd edn, 600 (Wiley, 2006).
49. Scaets, M. G. Brownian coagulation in aerosols—the role of long range forces. *J. Coll. Interf. Sci.* **129**, 105–112 (1989).
50. Chan, T. W. & Mozurkewich, M. Measurement of the coagulation rate constant for sulfuric acid particles as a function of particle size using tandem differential mobility analysis. *J. Aerosol Sci.* **32**, 321–339 (2001).
51. Laakso, L. *et al.* Kinetic nucleation and ions in boreal forest particle formation events. *Atmos. Chem. Phys.* **4**, 2353–2366 (2004).
52. Kerminen, V.-M. & Kulmala, M. Analytical formulae connecting the “real” and the “apparent” nucleation rate and the nuclei number concentration for atmospheric nucleation events. *J. Aerosol Sci.* **33**, 609–622 (2002).
53. Kulmala, M. & Kerminen, V.-M. On the formation and growth of atmospheric nanoparticles. *Atmos. Res.* **90**, 132–150 (2008).
54. Ehrhart, S. & Curtius, J. Influence of aerosol lifetime on the interpretation of nucleation experiments with respect to the first nucleation theorem. *Atmos. Chem. Phys.* **13**, 11465–11471 (2013).
55. Kürten, A., Williamson, C., Almeida, J., Kirkby, J. & Curtius, J. On the derivation of particle nucleation rates from experimental formation rates. *Atmos. Chem. Phys.* **15**, 4063–4075 (2015).
56. Lehtipalo, K. *et al.* Methods for determining particle size distribution and growth rates between 1 and 3 nm using the Particle Size Magnifier. *Bor. Environ. Res.* **19** (Suppl. B), 215–236 (2014).
57. Mirme, S. & Mirme, A. The mathematical principles and design of the NAIS – a spectrometer for the measurement of cluster ion and nanometer aerosol size distributions. *Atmos. Meas. Tech.* **6**, 1061–1071 (2013).
58. Asmi, E. *et al.* Results of the first air ion spectrometer calibration and intercomparison workshop. *Atmos. Chem. Phys.* **9**, 141–154 (2009).
59. Gagné, S. *et al.* Intercomparison of air ion spectrometers: an evaluation of results in varying conditions. *Atmos. Meas. Tech.* **4**, 805–822 (2011).
60. Eisele, F. L. & Tanner, D. J. Measurement of the gas-phase concentration of H₂SO₄ and methane sulfonic acid and estimates of H₂SO₄ production and loss in the atmosphere. *J. Geophys. Res. Atmos.* **98**, 9001–9010 (1993).
61. Kürten, A., Rondo, L., Ehrhart, S. & Curtius, J. Calibration of a chemical ionization mass spectrometer for the measurement of gaseous sulphuric acid. *J. Phys. Chem. A* **116**, 6375–6386 (2012).
62. Atkinson, R. *et al.* Evaluated kinetic and photochemical data for atmospheric chemistry: volume II – gas phase reactions of organic species. *Atmos. Chem. Phys.* **6**, 3625–4055 (2006).
63. Möhler, O., Reiner, T. H. & Arnold, F. The formation of SO₂ by gas-phase ion-molecule reactions. *J. Chem. Phys.* **97**, 8233–8239 (1992).
64. Kangasluoma, J. *et al.* Sub-3 nm particle size and composition dependent response of a nano-CPC battery. *Atmos. Meas. Tech.* **7**, 689–700 (2014).
65. Zhao, Y. & Truhlar, D. G. The M06 suite of density functionals for main group thermochemistry, thermochemical kinetics, noncovalent interactions, excited states, and transition elements: two new functionals and systematic testing of four M06-class functionals and 12 other functionals. *Theor. Chem. Acc.* **120**, 215–241 (2008).
66. Ditchfield, R., Hehre, W. J. & Pople, J. A. Self-consistent molecular-orbital methods. IX. An extended Gaussian-type basis for molecular-orbital studies of organic molecules. *J. Chem. Phys.* **54**, 724–728 (1971).
67. Frisch, M. J. *et al.* Gaussian 09 Revision A.01, http://www.gaussian.com/g_prod/g09.htm (Gaussian, Inc., 2009).
68. Ortega, I. K. *et al.* From quantum chemical formation free energies to evaporation rates. *Atmos. Chem. Phys.* **12**, 225–235 (2012).
69. Ortega, I. K. *et al.* Can highly oxidized organics contribute to atmospheric new particle formation? *J. Phys. Chem. A* **120**, 1452–1458 (2016).
70. Elm, J. & Mikkelsen, K. V. Computational approaches for efficient modelling of small atmospheric clusters. *Chem. Phys. Lett.* **615**, 26–29 (2014).
71. Mann, G. W. *et al.* Intercomparison of modal and sectional aerosol microphysics representations within the same 3-D global chemical transport model. *Atmos. Chem. Phys.* **12**, 4449–4476 (2012).
72. Zhang, K. *et al.* Radon activity in the lower troposphere and its impact on ionization rate: a global estimate using different radon emissions. *Atmos. Chem. Phys.* **11**, 7817–7838 (2011).
73. Rissanen, M. P. *et al.* The formation of highly oxidized multifunctional products in the ozonolysis of cyclohexene. *J. Am. Chem. Soc.* **136**, 15596–15606 (2014).
74. Rissanen, M. P. *et al.* Effects of chemical complexity on the autoxidation mechanisms of endocyclic alkene ozonolysis products: from methylcyclohexenes toward understanding α -pinene. *J. Phys. Chem. A* **119**, 4633–4650 (2015).

RESEARCH LETTER



Extended Data Figure 1 | Small-ion mass spectra. a, b, Composition of positive (a) and negative (b) small ions measured by the APi-TOF under GCR conditions and before adding any SO_2 to the chamber. The experimental conditions are zero α -pinene, 35 p.p.b.v. O_3 , zero H_2 or HONO, 38% relative humidity, 278 K and $[H_2SO_4] < 5 \times 10^4 \text{ cm}^{-3}$. Collisions will transfer positive charge to contaminant molecules having the highest proton affinity (a), and negative charge to contaminant molecules with the lowest proton affinity, that is, highest gas-phase acidity (b). From molecular cluster measurements, the positive ions

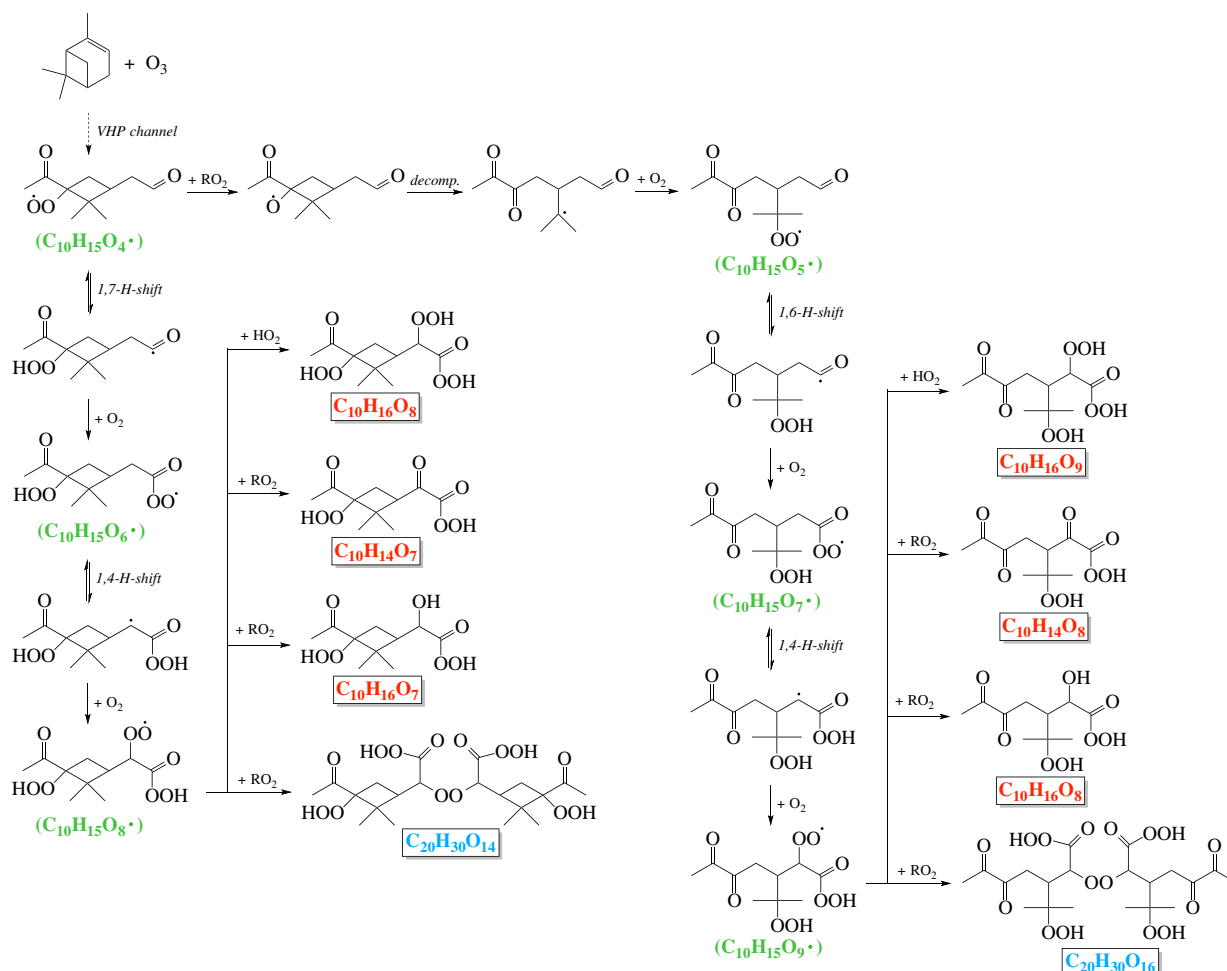
also include ammonium (NH_4^+), but its mass is below the set acceptance cut-off of the APi-TOF. c, The negative small-ion spectrum at $[H_2SO_4] = 1.2 \times 10^5 \text{ cm}^{-3}$, after adding 32 p.p.t.v. SO_2 to the chamber, showing that the dominant ions species shift from nitrate to sulfur-containing. The experimental conditions are 340 p.p.t.v. α -pinene, 35 p.p.b.v. O_3 , zero H_2 or HONO, 38% relative humidity and 278 K. Water molecules evaporate rapidly from most hydrated ions in the APi-TOF and so are not detected.



Extended Data Figure 2 | HOM yields versus α -pinene oxidation rates with O_3 and $OH\cdot$. Total HOM mixing ratios versus α -pinene reaction rate with (i) O_3 plus $OH\cdot$ (ozone without H_2 scavenger; circles and solid line), (ii) O_3 alone (ozone with 0.1% H_2 scavenger; triangles and dashed line) and (iii) $OH\cdot$ alone (produced by ultraviolet photolysis of nitrous acid, HONO, in the absence of O_3 ; squares and dotted line). The yields are shown for total HOMs = $RO_2\cdot + E_1 + E_2$. The experimental conditions are 38% relative humidity, 278 K and (i) 70–440 p.p.t.v. α -pinene,

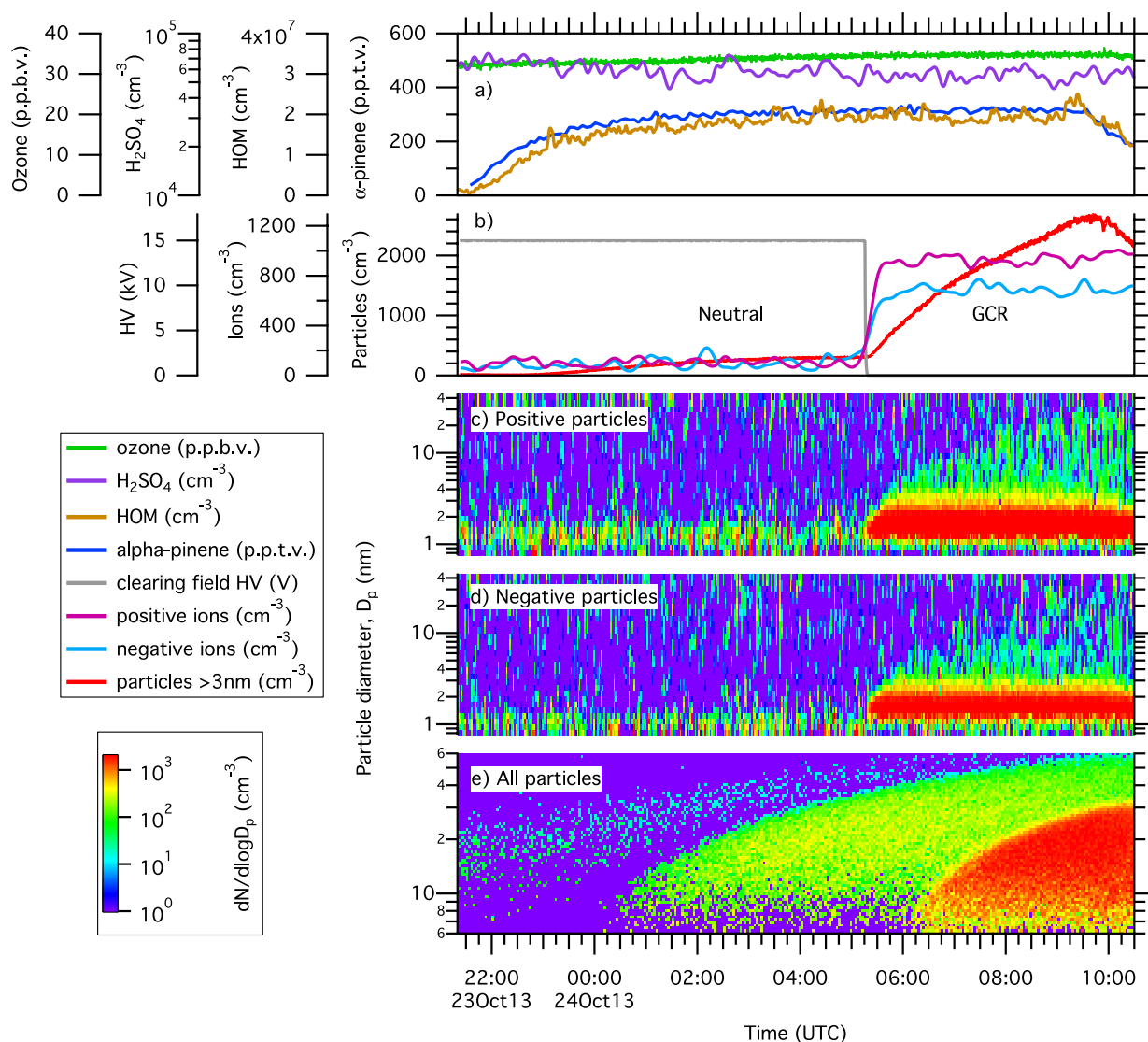
21–35 p.p.b.v. O_3 , zero H_2 or HONO, 0%–100% ultraviolet, (ii) 80–1,230 p.p.t.v. α -pinene, 21–35 p.p.b.v. O_3 , 0.1% H_2 , zero HONO, 0%–100% ultraviolet, and (iii) 840–910 p.p.t.v. α -pinene, zero O_3 or H_2 , 0.5–3 p.p.b.v. HONO, 0%–100% ultraviolet. The bars indicate 1σ point-to-point errors. Overall systematic scale uncertainties of $\pm 40\%$ for the reaction rates and $+80\%/ -45\%$ for the HOM mixing ratios are not shown. The combined errors on the HOM molar yields for either ozonolysis or hydroxyl chemistry are $+100\%/ -60\%$ ($\pm 1\sigma$).

RESEARCH LETTER



Extended Data Figure 3 | Proposed mechanism for the formation of the E₁ and E₂ surrogates via peroxy radical formation. The proposed scheme for the formation of the ELVOC monomer (C₁₀H₁₄O₇) and dimer (C₂₀H₃₀O₁₄) surrogates selected for quantum chemical calculations (Extended Data Fig. 7) is based on recently established autooxidation mechanisms for a series of cycloalkane + O₃ systems.^{16,18–20,73,74} Peroxy radicals in the figure are indicated by a green label, E₁ by a red label and E₂ by a blue label. Addition of ozone to the double bond of α -pinene produces two carbonyl-substituted Criegee biradicals. The energy-rich Criegee biradical is either collisionally stabilized, or isomerizes via 1,4-H-shift to a vinylhydroperoxide (VHP), which then decomposes to yield an OH· and an alkenoxy radical. The alkenoxy radical reacts with O₂, leading to a peroxy radical, which is the potential precursor to a sequence of autooxidation reactions leading to the formation of HOMs¹⁶. Here the peroxy radical C₁₀H₁₅O₄· is chosen as the starting point for HOM formation. The first intramolecular hydrogen abstraction is likely to take place at the aldehydic carbon from the opposite side of the peroxy group, although the rigid four-carbon-atom ring could hinder bending of the structure. For the *cis* configuration where the peroxy group and the aldehydic hydrogen are on the same side of the cyclobutyl ring, the 1,7-H shift rate is calculated²⁰ to be 0.14 s⁻¹, which initiates the autooxidation chemistry on a fast timescale compared to the HOM lifetime resulting from loss to the CLOUD chamber walls (about 900 s). The resultant acyclic radical undergoes rapid O₂ addition, leading to an -OOH functionalized peroxyacyl radical (C₁₀H₁₅O₆·). The second intramolecular hydrogen abstraction is expected to proceed at the carbon atom in the α position of the peroxyacyl group via 1,4-H isomerization. The resultant C₁₀H₁₅O₈·

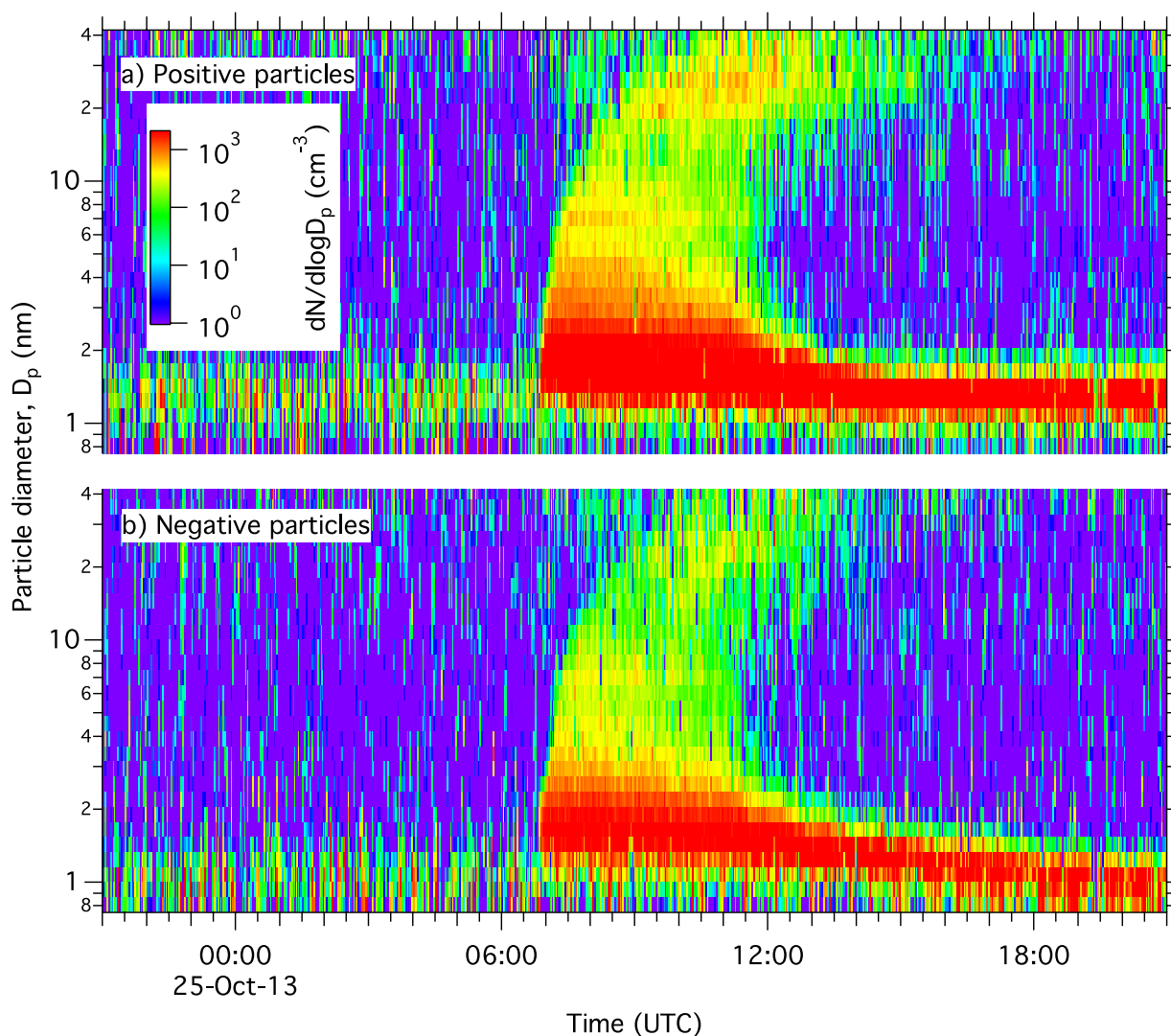
terminates by known reactions of peroxy radicals (HO₂· or RO₂· under the present experimental conditions), producing a spectrum of HOM monomers that includes the E₁ surrogate, C₁₀H₁₄O₇. The homogeneous recombination of two peroxy radicals via elimination of O₂ produces the covalently bound dimer C₂₀H₃₀O₁₄ chosen as the E₂ surrogate. Alternatively, C₁₀H₁₅O₈· can undergo further autooxidation, if sufficiently labile hydrogen atoms are available, leading to the observed closed-shell monomers with ≥ 9 O (Fig. 1). The self/cross-reaction of the C₁₀H₁₅O₄· peroxy radical produces an alkoxy radical, which decomposes rapidly, leading to a carbonyl-functionalized peroxy radical (C₁₀H₁₅O₅·). This peroxy radical is another potential starting structure for HOM formation. The carbon-ring-opening reaction pathway, while increasing the steric availability of the H atom, might be a slow step. The effective formation rate of the C=O-functionalized peroxy radical is calculated to be less than about 10⁻³ s⁻¹, which is comparable to its wall deposition rate. The timescale with respect to the subsequent autooxidation reaction, on the other hand, is expected to be of the order of seconds, by analogy with that for branched-chain peroxy radicals⁷³. The unbalanced sources and sinks potentially account for the low signals of peroxy radicals with odd oxygen numbers (for example, C₁₀H₁₅O₅·, C₁₀H₁₅O₇· and C₁₀H₁₅O₉·). The autooxidation process of C₁₀H₁₅O₅· is presumed to proceed by an autooxidative reaction pathway similar to that for C₁₀H₁₅O₄·, eventually leading to the spectrum of HOM monomers and dimers observed in the CLOUD chamber. Except for the autooxidation channel, all the peroxy radicals are still subject to well-established reactions such as R(·)O₂ + RO₂/HO₂, which are potentially important if the reaction rate is comparable to that for the autooxidation channel.



Extended Data Figure 4 | Typical nucleation run sequence. Example of a typical measurement sequence of the neutral and GCR nucleation rates as a function of coordinated universal time (UTC), at zero H_2 or HONO, 38% relative humidity and 278 K. **a**, The run began at 21:22, 23 October 2013, by starting the α -pinene flow into the chamber to reach a chosen equilibrium value near 300 p.p.t.v., which produced an equilibrium total HOMs concentration near $2 \times 10^7 \text{ cm}^{-3}$ (0.8 p.p.t.v.). **b**, Particles (red curve) formed at a slow rate in the chamber without ions present ('neutral' conditions). The clearing field high voltage (HV) was turned off at 05:16, 24 October 2013, and the subsequent presence of ions in the chamber from GCRs caused a sharp increase in the particle formation rate by about one order of magnitude (as seen by the increase in the gradient of the red curve). The nucleation rates are measured under constant gas conditions in the period before ($J_n = 0.14 \text{ cm}^{-3} \text{ s}^{-1}$) and after ($J_{\text{GCR}} = 3.3 \text{ cm}^{-3} \text{ s}^{-1}$) turning off the clearing field high voltage. **c**, **d**, Ion-induced nucleation is

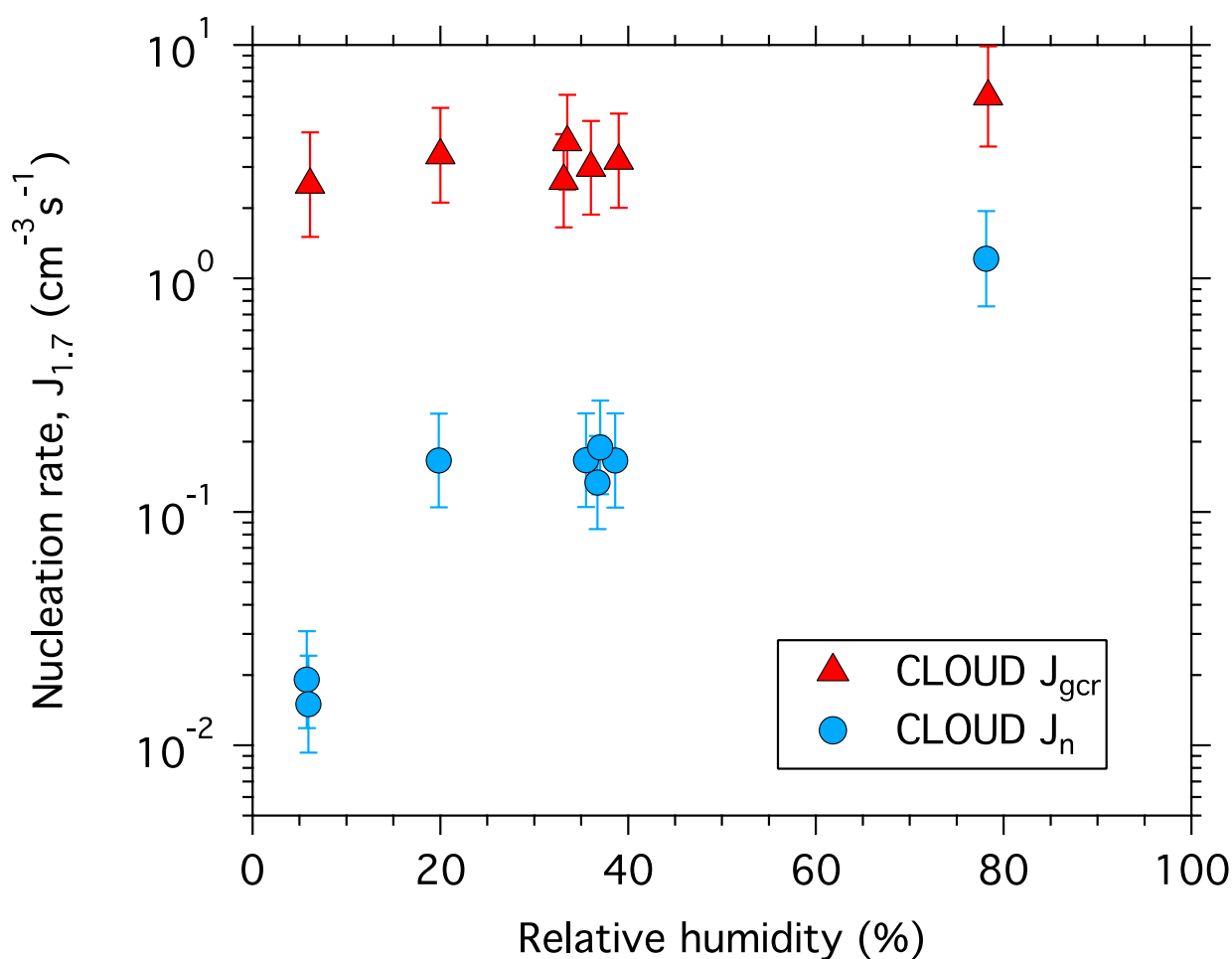
observed both for positive (**c**) and negative (**d**) charged particles, followed by rapid particle growth to sizes above 10 nm. **e**, The nucleated particles grew over a period of several hours to diameters approaching 50 nm, where they begin to constitute cloud condensation nuclei. A sharp increase in the formation rate of particles above the SMPS detection threshold of 5 nm can be seen when GCR ions are present. The colour scale in **c–e** indicates $dN/d\log(D_p)$, where N (in cm^{-3}) is the particle number concentration and D_p (in nm) is the particle diameter. The concentrations of ozone and contaminant H_2SO_4 were essentially constant during the run, which ended at 09:30 when the α -pinene flow to the chamber was turned off. The H_2SO_4 measurement near $5 \times 10^4 \text{ cm}^{-3}$ corresponds to the instrumental background level of the CI-API-TOF mass spectrometer and so represents an upper limit on the actual concentration. Further characteristics of this run can be seen in Fig. 1.

RESEARCH LETTER



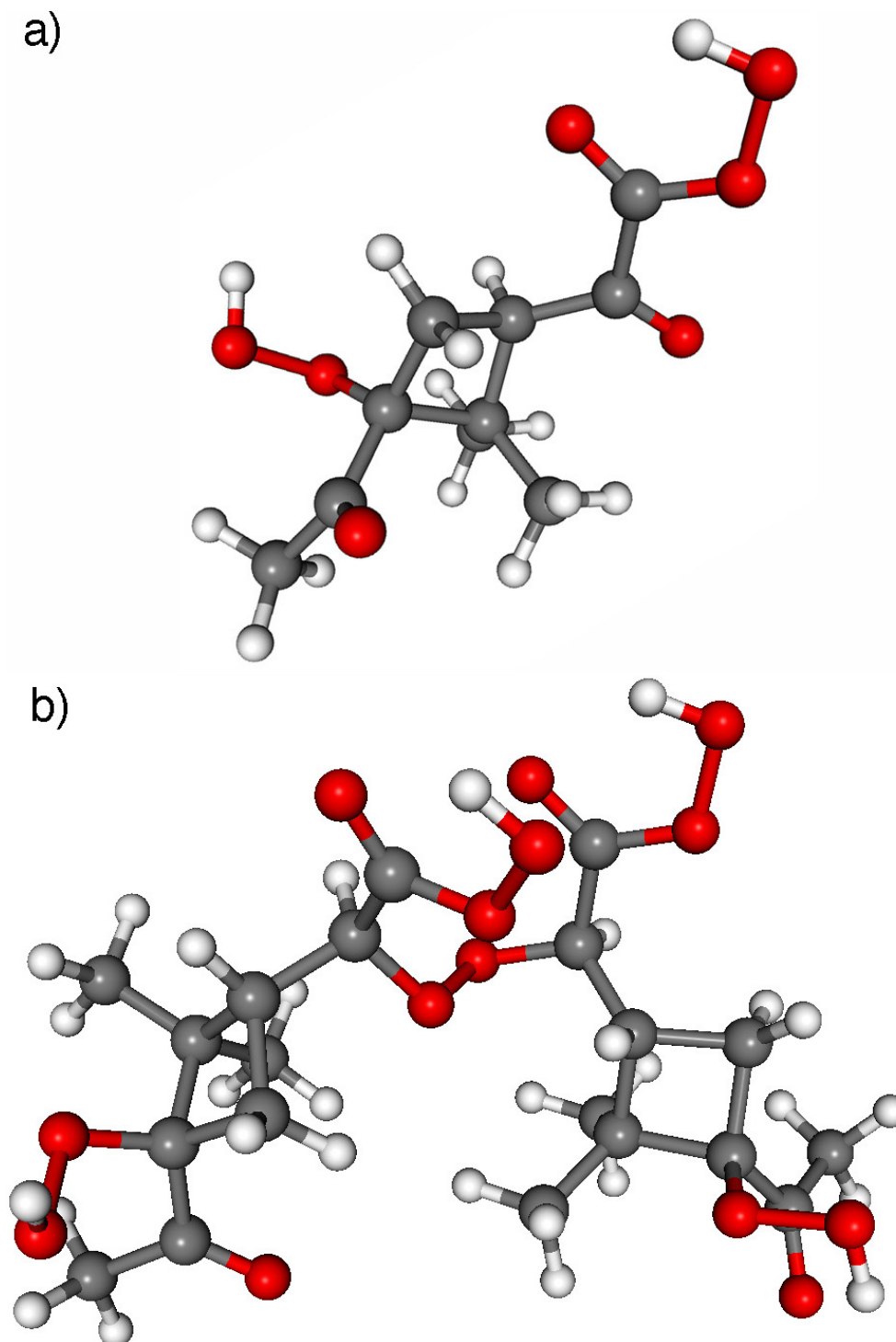
Extended Data Figure 5 | Ion-induced nucleation event without H_2SO_4 , measured in the NAIS. a, b, Example of a nucleation event showing the growth versus time of positive (a) and negative (b) charged particles at 530 p.p.t.v. α -pinene, 35 p.p.b.v. O_3 , zero H_2 or HONO, 3.4×10^7 cm⁻³ HOM, 38% relative humidity, 278 K and $[H_2SO_4] < 5 \times 10^4$ cm⁻³. The clearing field high voltage was turned off at 06:48, marking the start of

GCR ionization conditions in the chamber, and the α -pinene flow into the chamber was stopped at 10:52. Ion-induced nucleation can be seen for positive and negative charged particles, followed by rapid growth to sizes above 10 nm. Ion-ion recombination progressively neutralizes the charged particles as they grow, but some reappear at larger sizes, owing to diffusion charging.



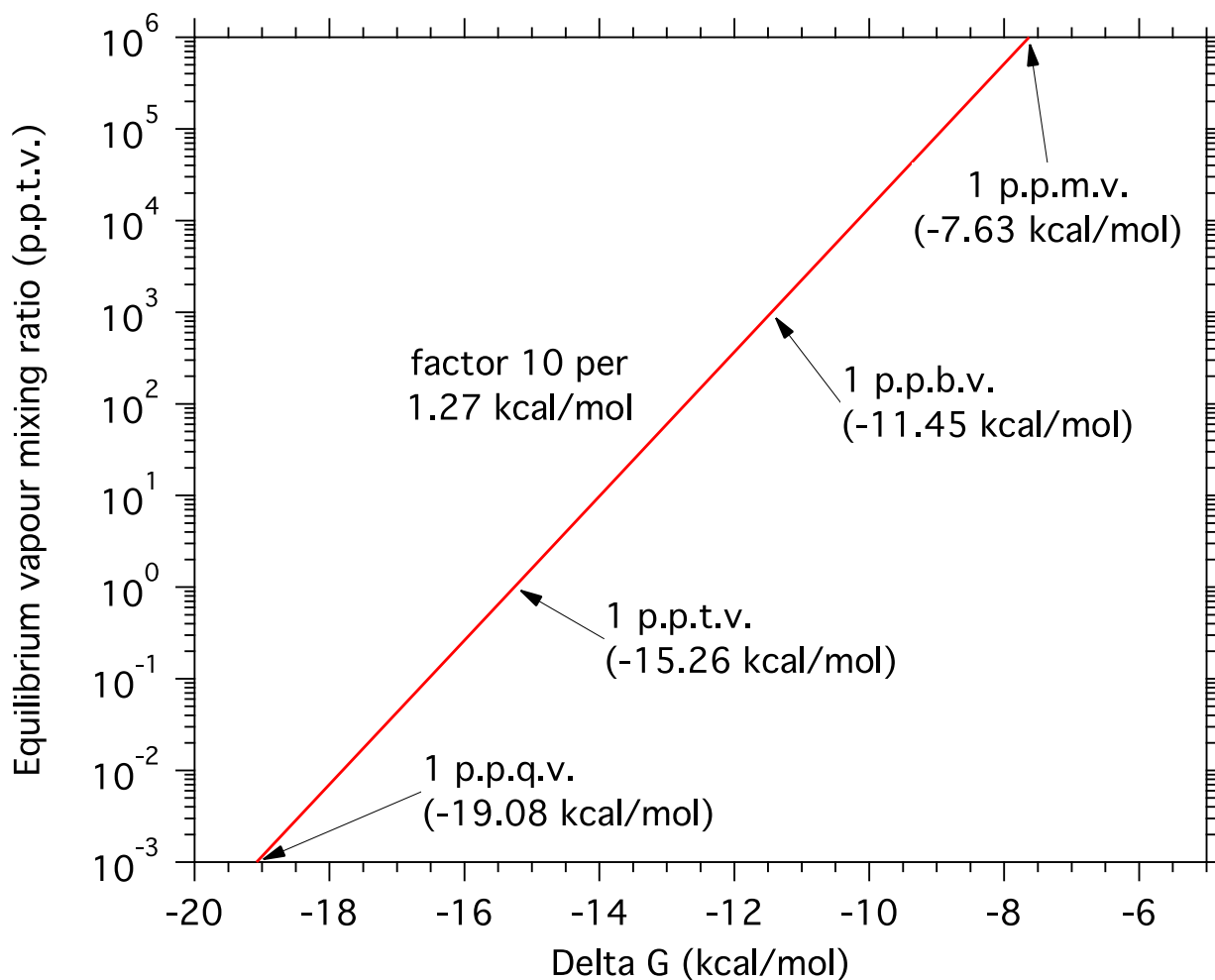
Extended Data Figure 6 | Nucleation rates versus relative humidity. Neutral (J_{n} ; circles) and GCR (J_{gcr} ; triangles) nucleation rates versus relative humidity. The experimental conditions are 250–800 p.p.t.v. α -pinene, 30–35 p.p.b.v. O_3 , zero H_2 or HONO, $(1.1\text{--}2.9) \times 10^7 \text{ cm}^{-3}$ HOM, 278 K and $(0.5\text{--}1.5) \times 10^5 \text{ cm}^{-3}$ H_2SO_4 . All measurements have

been corrected to the same total HOMs concentration ($2.05 \times 10^7 \text{ cm}^{-3}$) using the curves shown in Fig. 3. The bars indicate 1σ total errors, although these are not shown in the x direction because they are smaller than the symbols.



Extended Data Figure 7 | Surrogate molecules chosen for quantum chemical calculations. a, b, Structures of the surrogate molecules chosen for quantum chemical calculations to represent the ELVOC monomer, E_1 , $C_{10}H_{14}O_7$ (a) and the covalently bound dimer, E_2 , $C_{20}H_{30}O_{14}$ (b).

Grey spheres represent carbon atoms, red are oxygen atoms and white are hydrogen atoms. We show their proposed formation mechanisms in Extended Data Fig. 3.



Extended Data Figure 8 | Relationship between cluster formation energies and equilibrium evaporation/condensation rates.

Estimated ELVOC vapour mixing ratios versus the $\Delta G_{278\text{K}}$ at which the condensation and evaporation rates of the cluster at 278 K are in equilibrium^{68,69}. For example, a formation free energy of $-15.3 \text{ kcal mol}^{-1}$

corresponds to equal rates for particle evaporation and vapour condensation at 278 K and 1 p.p.t.v. ELVOC vapour mixing ratio ($2.6 \times 10^7 \text{ cm}^{-3}$). The evaporation rate increases by a factor of 10 for each $1.27 \text{ kcal mol}^{-1}$ reduction of the cluster formation energy.

RESEARCH LETTER

Extended Data Table 1 | Quantum chemical calculations of ELVOC cluster formation energies

Neutral clusters		Negative clusters		Positive clusters	
Cluster process	ΔG_{278K} (kcal/mol)	Cluster process	ΔG_{278K} (kcal/mol)	Cluster process	ΔG_{278K} (kcal/mol)
$E_1 + E_1$	-5.76	$E_1 + E_1^-$	-20.95	$E_1 + \text{NH}_4^+$	-22.46
$E_2 + E_1$	-2.15	$E_2 + E_1^-$	-19.90	$E_2 + \text{NH}_4^+$	-30.87
				$E_1 + E_1.\text{NH}_4^+$	-11.71
				$E_2 + E_1.\text{NH}_4^+$	-24.35
				$E_1 + E_2.\text{NH}_4^+$	-15.94
$E_1 + \text{H}_2\text{SO}_4$	-9.90	$E_1 + \text{HSO}_4^-$	-26.97		
$E_2 + \text{H}_2\text{SO}_4$	-12.04	$E_2 + \text{HSO}_4^-$	-30.30		
$E_1 + E_1.\text{H}_2\text{SO}_4$	+2.49	$E_1 + E_1.\text{HSO}_4^-$	-15.28		
$E_2 + E_1.\text{H}_2\text{SO}_4$	+3.13				
$E_1 + E_2.\text{H}_2\text{SO}_4$	-5.69				
		$E_1 + \text{NO}_3^-$	-25.99		
		$E_2 + \text{NO}_3^-$	-25.65		
		$E_1 + E_1.\text{NO}_3^-$	-10.09		

Formation Gibbs free energies at 278K, ΔG_{278K} , for neutral, negatively charged and positively charged ELVOC clusters. The cluster processes indicate the incident E_1/E_2 vapour molecule + the target cluster. Quantum chemical calculations made at other temperatures (not shown) indicate that the binding energies strengthen by $-1.0 \text{ kcal mol}^{-1}$ per 20K reduction in temperature. The uncertainty in the calculated energies is less than 2 kcal mol^{-1} . Our calculations indicate the following approximate order for different functional groups to contribute to the cluster binding energies involving HSO_4^- or H_2SO_4 (starting with the strongest): (i) carboxylic acids, R-C(=O)-OH ; (ii) hydroxyls, R-OH ; (iii) hydroperoxy acids, R-C(=O)-O-OH ; (iv) hydroperoxides, R-O-OH ; and (v) carbonyls, R-(R')C=O . In the case of NH_4^+ , the main interacting group is carbonyl, independently of which other groups are attached to it; therefore ammonium will form stronger clusters with carboxylic acids, hydroperoxy acids or carbonyls than it will with hydroxyls or hydroperoxides.

**4.6 The role of low-volatility organic compounds
in initial particle growth in the atmosphere
(Tröstl et al. (2016))**

LETTER

OPEN

doi:10.1038/nature18271

The role of low-volatility organic compounds in initial particle growth in the atmosphere

Jasmin Tröstl¹, Wayne K. Chuang², Hamish Gordon³, Martin Heinritzi⁴, Chao Yan⁵, Ugo Molteni¹, Lars Ahlm⁶, Carla Frege¹, Federico Bianchi^{1,5,7}, Robert Wagner⁵, Mario Simon⁴, Katrianne Lehtipalo^{1,5}, Christina Williamson^{4,8,†}, Jill S. Craven⁹, Jonathan Duplissy^{5,10}, Alexey Adamov⁵, Joao Almeida³, Anne-Kathrin Bernhammer^{11,12}, Martin Breitenlechner^{11,12}, Sophia Brilke⁴, António Dias³, Sebastian Ehrhart³, Richard C. Flagan⁹, Alessandro Franchin⁵, Claudia Fuchs¹, Roberto Guida³, Martin Gysel¹, Armin Hansel^{11,12}, Christopher R. Hoyle^{1,13}, Tuija Jokinen⁵, Heikki Junninen⁵, Juha Kangasluoma⁵, Helmi Keskinen^{5,14,†}, Jaeseok Kim^{14,†}, Manuel Krapf¹, Andreas Kürten⁴, Ari Laaksonen^{14,15}, Michael Lawler^{14,16}, Markus Leiminger⁴, Serge Mathot³, Ottmar Möhler¹⁷, Tuomo Nieminen^{5,10}, Antti Onnela³, Tuukka Petäjä⁵, Felix M. Piel⁴, Pasi Miettinen¹⁴, Matti P. Rissanen⁵, Linda Rondo⁴, Nina Sarnela⁵, Siegfried Schobesberger^{5,†}, Kamalika Sengupta¹⁸, Mikko Sipilä⁵, James N. Smith^{14,19}, Gerhard Steiner^{5,11,20}, António Tomé²¹, Annele Virtanen¹⁴, Andrea C. Wagner⁴, Ernest Weingartner^{1,†}, Daniela Wimmer^{4,5}, Paul M. Winkler²⁰, Penglin Ye², Kenneth S. Carslaw¹⁸, Joachim Curtius⁴, Josef Dommen¹, Jasper Kirkby^{3,4}, Markku Kulmala⁵, Ilona Riipinen⁶, Douglas R. Worsnop^{5,10,22}, Neil M. Donahue^{2,5} & Urs Baltensperger¹

About half of present-day cloud condensation nuclei originate from atmospheric nucleation, frequently appearing as a burst of new particles near midday¹. Atmospheric observations show that the growth rate of new particles often accelerates when the diameter of the particles is between one and ten nanometres^{2,3}. In this critical size range, new particles are most likely to be lost by coagulation with pre-existing particles⁴, thereby failing to form new cloud condensation nuclei that are typically 50 to 100 nanometres across. Sulfuric acid vapour is often involved in nucleation but is too scarce to explain most subsequent growth^{5,6}, leaving organic vapours as the most plausible alternative, at least in the planetary boundary layer^{7–10}. Although recent studies^{11–13} predict that low-volatility organic vapours contribute during initial growth, direct evidence has been lacking. The accelerating growth may result from increased photolytic production of condensable organic species in the afternoon², and the presence of a possible Kelvin (curvature) effect, which inhibits organic vapour condensation on the smallest particles (the nano-Köhler theory)^{2,14}, has so far remained ambiguous. Here we present experiments performed in a large chamber under atmospheric conditions that investigate the role of organic vapours in the initial growth of nucleated organic particles in the absence of inorganic acids and bases such as sulfuric acid or ammonia and amines, respectively. Using data from the same set of experiments, it has been shown¹⁵ that organic vapours alone can drive nucleation. We focus on the growth of nucleated particles and find that the organic vapours that drive initial growth have extremely low volatilities (saturation concentration less than 10^{−4.5} micrograms per cubic metre). As the particles increase in size and the Kelvin barrier falls, subsequent growth is primarily

due to more abundant organic vapours of slightly higher volatility (saturation concentrations of 10^{−4.5} to 10^{−0.5} micrograms per cubic metre). We present a particle growth model that quantitatively reproduces our measurements. Furthermore, we implement a parameterization of the first steps of growth in a global aerosol model and find that concentrations of atmospheric cloud condensation nuclei can change substantially in response, that is, by up to 50 per cent in comparison with previously assumed growth rate parameterizations.

Two measurement campaigns at the CERN CLOUD (Cosmic Leaving Outdoor Droplets) chamber (Methods) focused on aerosol growth with different levels of sulfuric acid and α -pinene oxidation products. With the chamber at 278 K and 38% relative humidity, tropospheric concentrations of α -pinene, ozone (O₃) and SO₂ were introduced (see Extended Data Table 1). Using various instruments (Methods and Extended Data Fig. 1) we measured the behaviour of freshly nucleated particles of 1–2 nm diameter and their subsequent growth up to 80 nm. Two chemical ionization mass spectrometers (Methods) using nitrate as the reagent ion (nitrate-CI-API-TOF) measured the concentrations of sulfuric acid and highly oxygenated organic compounds^{16,17}. Nitrate anions tend to cluster with highly oxygenated molecules (HOMs), and the measured HOMs fall broadly into two product ranges based on carbon number (Extended Data Fig. 2): monomers (C_xH_yO_z with $x = 8–10$, $y = 12–16$ and $z = 6–12$), and dimers (C_xH_yO_z with $x = 17–20$, $y = 26–32$ and $z = 8–18$). Here we refer to these measured compounds as HOMs rather than extremely low-volatility organic compounds (ELVOCs), as previously reported¹⁷. As we shall show, the HOM volatility spans a wide range (although it is always very low), and we shall separate HOMs into volatility bins using the volatility basis set (VBS)¹⁸.

¹Paul Scherrer Institute, Laboratory of Atmospheric Chemistry, CH-5232 Villigen, Switzerland. ²Carnegie Mellon University, Center for Atmospheric Particle Studies, Pittsburgh, Pennsylvania 15213, USA. ³CERN, CH-1211 Geneva, Switzerland. ⁴Goethe University Frankfurt, Institute for Atmospheric and Environmental Sciences, 60438 Frankfurt am Main, Germany. ⁵Department of Physics, University of Helsinki, PO Box 64, FI-00014 Helsinki, Finland. ⁶Department of Applied Environmental Science, University of Stockholm, SE-10961 Stockholm, Sweden. ⁷Institute for Atmospheric and Climate Science, ETH Zürich, 8092 Zürich, Switzerland. ⁸Chemical Sciences Division, Earth System Research Laboratory, NOAA, Boulder, Colorado, USA. ⁹Division of Chemistry and Chemical Engineering, California Institute of Technology, Pasadena, California 91125, USA. ¹⁰Helsinki Institute of Physics, University of Helsinki, PO Box 64, FI-00014 Helsinki, Finland. ¹¹Institute for Ion and Applied Physics, University of Innsbruck, 6020 Innsbruck, Austria. ¹²Ionicon Analytik GmbH, 6020 Innsbruck, Austria. ¹³WSL Institute for Snow and Avalanche Research SLF, 7260 Davos, Switzerland. ¹⁴University of Eastern Finland, 70211 Kuopio, Finland. ¹⁵Finnish Meteorological Institute, 00101 Helsinki, Finland. ¹⁶National Center for Atmospheric Research, Atmospheric Chemistry Observations and Modeling Laboratory, Boulder, Colorado 80301, USA. ¹⁷Institute of Meteorology and Climate Research, Karlsruhe Institute of Technology, Karlsruhe, Germany. ¹⁸School of Earth and Environment, University of Leeds, LS2 9JT Leeds, UK. ¹⁹Department of Chemistry, University of California, Irvine, California 92697, USA. ²⁰Faculty of Physics, University of Vienna, 1090 Vienna, Austria. ²¹SIM, University of Lisbon and University of Beira Interior, 1849-016 Lisbon, Portugal. ²²Aerodyne Research, Inc., Billerica, Massachusetts 01821, USA. †Present addresses: Cooperative Institute for Research in Environmental Sciences, University of Colorado Boulder, Boulder, Colorado, USA and Chemical Sciences Division NOAA Earth System Research Laboratory, Boulder, Colorado, USA (C.W.); SMEAR II, Hyytiälä Forestry Field Station, University of Helsinki, Hyytiäläntie 124, FI-35500 Korkeakoski, Finland (H.K.); Arctic Research Center, Korea Polar Research Institute, 21990 Incheon, South Korea (J. Kim); Department of Atmospheric Sciences, University of Washington, Seattle, Washington 98195, USA (S.S.); Institute for Aerosol and Sensor Technology, University of Applied Science Northwestern Switzerland, 5210 Windisch, Switzerland (E.W.).

RESEARCH LETTER

In Fig. 1 we plot the growth rates measured in CLOUD as a function of sulfuric acid and HOM concentration, focusing on size ranges from 1.1 nm to 3.2 nm and >5 nm (mobility) diameter. It is evident from Fig. 1a and b that the observed growth cannot be explained in either size range by the condensation of sulfuric acid even at the kinetic limit, where sulfuric acid is assumed to be completely non-volatile. Furthermore, for sulfuric acid molecular concentrations below 10^7 cm^{-3} , the growth rate is uncorrelated with sulfuric acid. In contrast, the growth is clearly correlated with organics for all size ranges up to the size of cloud condensation nuclei (CCN) for HOM concentrations $>10^6 \text{ cm}^{-3}$ (Fig. 1c and d). For experiments with sulfuric acid concentrations $<5.5 \times 10^5 \text{ cm}^{-3}$ we have separately reported a large charge enhancement for the nucleation rate¹⁵. However, there is no corresponding charge influence on the growth rates of either 1.1–3.2 nm or >5 nm particles (grey versus blue symbols in Fig. 1c and d). Most of the HOMs in the chamber are neutral ($\sim 10^7 \text{ cm}^{-3}$ neutral HOMs versus $\sim 10^3 \text{ cm}^{-3}$ charged molecules), so a charge enhancement is not expected, especially with increasing size¹⁹. However, owing to the experimental uncertainties we cannot exclude the possibility of an ion enhancement at sizes below 3 nm.

A non-volatile (collision-limited) model of HOM condensation (Methods) cannot explain the observed growth rates across the full range of particle diameters we studied. We modelled growth at 1.1 nm, 3.2 nm, 5 nm, 15 nm and 50 nm (labelled curves, Fig. 1c and d) assuming that observed HOM monomers and dimers are non-volatile, with a density of $1,400 \text{ kg m}^{-3}$ and a mass of 300 Da. Contrary to the common

misconception that non-volatile diameter growth rate should be constant with size (in the free molecular regime), the predicted growth rate with this assumption is highest at any given HOM concentration for the smallest particles and decreases rapidly with increasing size up to $\sim 5 \text{ nm}$ (Fig. 1c, d). This predicted decreasing growth rate with increasing particle size is because the cross-section and collision velocity are highest relative to particle size for the smallest particles (Methods). However, the observations show the reverse, with growth rates for sizes above 5 nm exceeding those near 2 nm by a factor of 1.5 ± 0.2 , obtained from normalizing (to 10^7 cm^{-3} HOMs) and averaging the growth rates in the considered size ranges. The ratio of observed growth rates to modelled non-volatile growth rates increases from 0.7 ± 0.1 at 1.1 nm to 2.8 ± 0.2 at 5 nm, where in each case the quoted error is the standard error of the mean. This large discrepancy is strong evidence that the measured HOMs cannot fully describe the observed growth, and that additional organic material must be contributing to particle growth above roughly 5 nm particle diameter.

To explore the potential role of HOM volatility, we use the SIMPOL model²⁰ to estimate the saturation mass concentration (C^* , $\mu\text{g m}^{-3}$) and saturation molecular concentration (N^* , cm^{-3}) of each HOM using its measured atomic composition together with an estimation of its likely chemical structure (see Extended Data Fig. 3). We grouped the HOMs in volatility bins (separated by factors of ten) and assigned them to several volatility classes (see Extended Data Fig. 4). The HOMs span a wide range from extremely low-volatility (ELVOC, $C^* < 10^{-4.5} \mu\text{g m}^{-3}$; $N^* < 5 \times 10^4 \text{ cm}^{-3}$ assuming a molecular mass

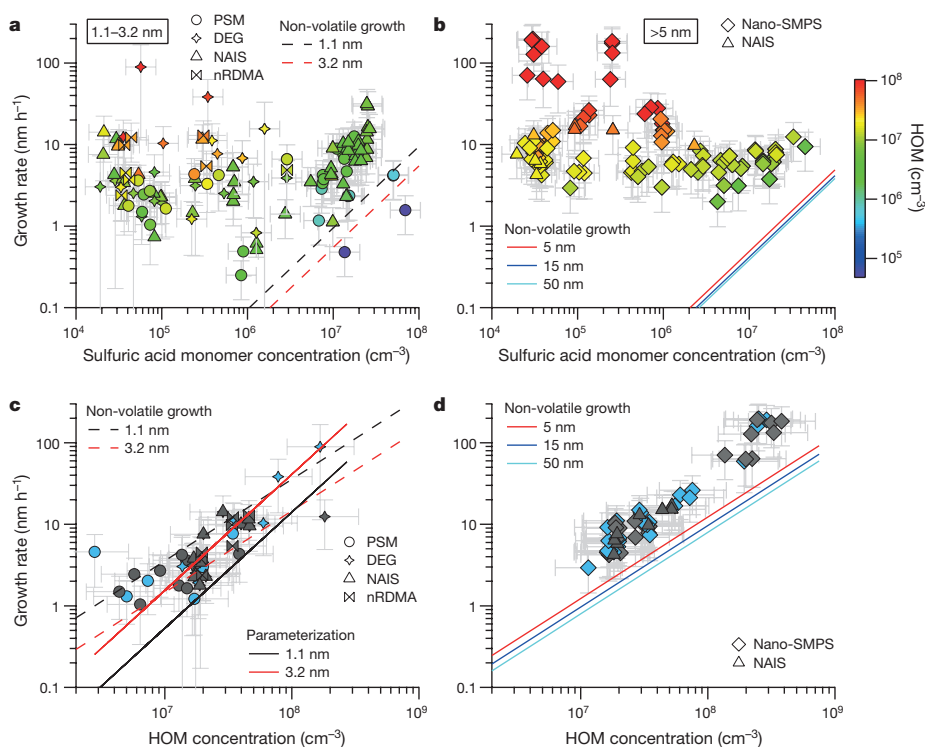


Figure 1 | Growth rates as a function of sulfuric acid and highly oxygenated molecule (HOM) concentrations. Symbol shapes represent the different instruments to derive the growth rates (see key and Methods), symbol colours indicate the HOM concentration (colour scale at right). **a, b**, Growth rate versus sulfuric acid concentration for particles from 1.1 nm to 3.2 nm (**a**), and for particles 5–15 nm, 15–30 nm, 30–60 nm and >60 nm (**b**). Non-volatile growth rates by condensation of sulfuric acid⁵ are displayed for different diameters. **c**, Measured growth rates from 1.1 nm to 3.2 nm versus the HOM concentration for sulfuric acid concentrations $<5 \times 10^5 \text{ cm}^{-3}$; **d**, as **c** but for size ranges 5–15 nm,

15–30 nm, 30–60 nm and >60 nm. Linear growth was observed for particles >5 nm, thus no differentiation was made in **b** and **d**. Panel **c** additionally shows the parameterization for 1.1 nm and 3.2 nm based on our volatility-distribution modelling results. Symbol colours in **c** and **d** indicate the ion conditions in the chamber (blue, neutral; grey, ions from Galactic cosmic rays (GCR); see Methods). The HOM and sulfuric acid concentration uncertainty (error bars) is estimated to be $+80\%/-45\%$ and $+50\%/-33\%$, respectively. Growth rate error bars indicate 1σ total errors.

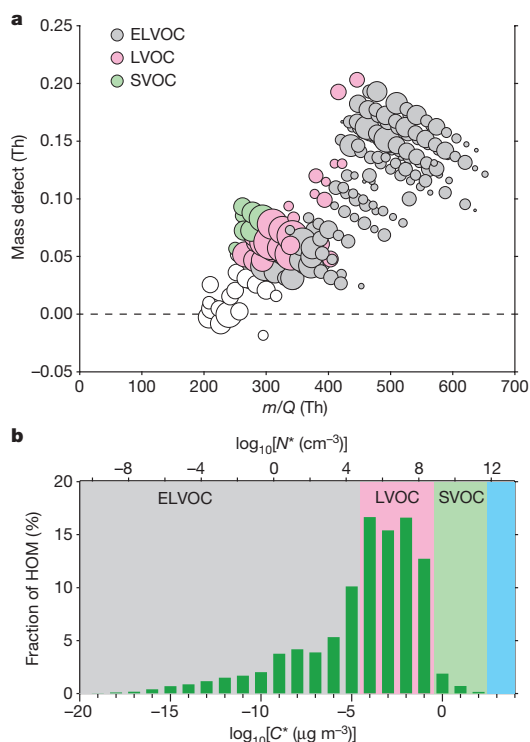


Figure 2 | Observed gas-phase HOMs and their volatility distribution. a, Mass defect (in Th; $1 \text{ Th} = 1 \text{ Da}/e$, where e is the elementary charge) of all HOMs versus their nominal mass to charge ratio (m/Q) including the estimated volatility distribution based on the proposed structures (Extended Data Fig. 3). The size of the plotting symbols is proportional to the logarithm of the counting rate. White circles are C_5 – C_7 compounds, which were not included in the volatility analysis. b, HOMs binned to a volatility distribution showing the measured relative counting rates in per cent, with ELVOCs comprising $\sim 36\%$.

of 300 Da) to low-volatility (LVOC, $10^{-4.5} \mu\text{g m}^{-3} \leq C^* \leq 10^{-0.5} \mu\text{g m}^{-3}$; $5 \times 10^4 \text{ cm}^{-3} \leq N^* \leq 5 \times 10^8 \text{ cm}^{-3}$) to some semi-volatile (SVOC, $10^{-0.5} \mu\text{g m}^{-3} \leq C^* \leq 10^{2.5} \mu\text{g m}^{-3}$; $5 \times 10^8 \text{ cm}^{-3} \leq N^* \leq 5 \times 10^{11} \text{ cm}^{-3}$) organic compounds. In Fig. 2a we show a mass defect plot (Methods) of the observed compounds during a representative run, and in Fig. 2b we show the corresponding volatility distribution (colours based on ref. 18). The binned volatility distribution of measured gas-phase organic species (Fig. 2b) shows a substantial fraction of ELVOCs, maximal contribution in the LVOC range and even low levels of SVOCs. Because the LVOCs and SVOCs do not build up a sufficient saturation ratio to overcome the Kelvin barrier, they should not be able to condense onto the smallest particles, so that only the ELVOCs should contribute to the initial growth. While nitrate ions cluster efficiently with ELVOCs and calibration based on sulfuric acid should be fairly accurate, the concentration of LVOCs and SVOCs is likely to be underestimated because of inefficient clustering²¹. Indeed, SVOCs are formed with high yield in α -pinene oxidation²² but most of them evidently are not detected by the nitrate-CI-API-TOF instrument (Fig. 2). The fact that even the non-volatile model based on measured HOMs underestimates the observed growth rates for particles $> 5 \text{ nm}$ by a factor of three strongly indicates that the concentration of condensing organic vapours is substantially higher than measured, at least after the Kelvin barrier has diminished.

We further consider two very different experiments. During the first experiment, the HOM concentration increased nonlinearly with time, which replicates the diurnal variation of biogenic emissions and oxidants in the ambient for the morning and early afternoon (Fig. 3a). This situation leads to a nonlinear increase in the growth rate. During the second experiment, the HOM concentration remained at a constant steady state (production balanced by wall loss). This allowed us to test whether the accelerating growth seen in the first experiment was due to the diminishing Kelvin effect or the increasing HOM concentration. The constant HOM concentration led to a nearly constant growth rate, except for the smallest particles below $\sim 5 \text{ nm}$ (Fig. 3d).

In order to quantify the importance of the Kelvin effect and HOM measurement biases, we analysed the contribution of HOMs to early growth and assessed the dependence on HOM volatility by using a dynamic volatility-distribution model²³ for these two cases. The HOM volatility-distribution model comprises nine C^* bins ranging from

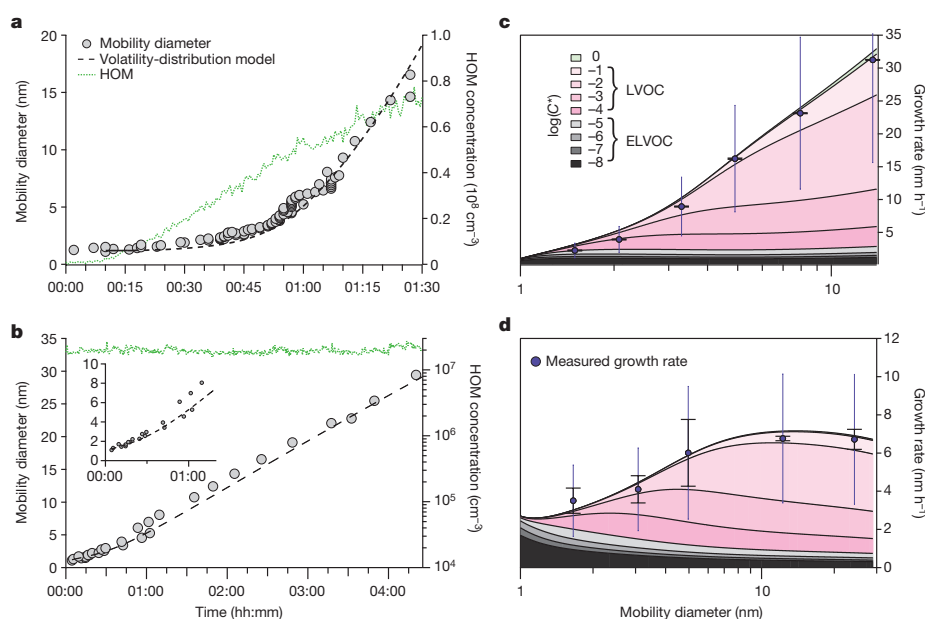


Figure 3 | Comparison of the growth rates in two experiments with a dynamic volatility basis set (VBS) model. a, b, Temporal evolution of the particle size (filled circles) and the modelled particle size (dashed lines) for an experiment with increasing HOM concentration (a), and for constant HOM concentration (b), with the inset magnifying the time evolution of the first 5 nm. c, d, Size-dependent modelled (lines) and measured (filled circles) growth rate for the increasing HOM concentration (c), and for the constant HOM concentration (d). Colours (key in c) indicate the contribution of different volatility bins to the condensational growth. Error bars indicate the error of the fit alone, whiskers the 1σ systematic scale uncertainty of the determined growth rates.

RESEARCH LETTER

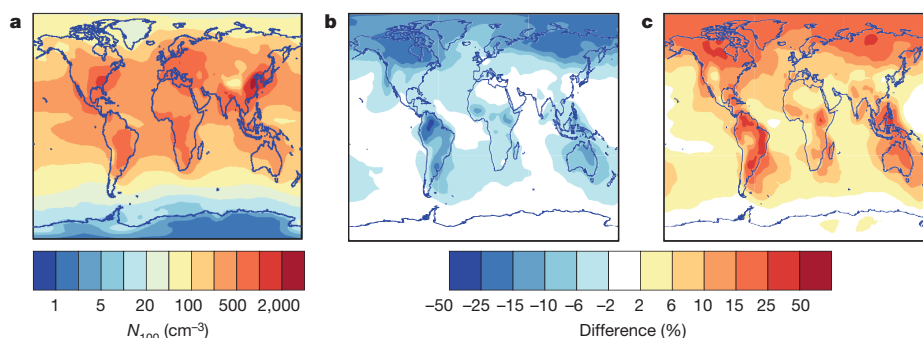


Figure 4 | Modelled influence on global CCN of different organic growth rates from 1.7 nm to 3 nm simulated by the GLOMAP aerosol model. a, The annual mean number concentration of soluble particles of at least 100 nm diameter (N_{100} on colour scale, taken as a proxy for CCN) at cloud base level. We treat irreversible (collision-limited) condensation of sulfuric acid for particle growth from 1.7 nm to 3 nm, together with a size-dependent growth rate due to HOMs from the present work.

$10^{-8} \mu\text{g m}^{-3}$ to $1 \mu\text{g m}^{-3}$ (10^1 cm^{-3} to 10^9 cm^{-3}), split into three ranges (see Fig. 2 and Extended Data Fig. 5): ELVOC (grey), LVOC (pink) and SVOC (light green). When we run the HOM volatility-distribution model using the directly measured volatility-binned HOM concentrations as input, the simulated growth rates for particles >2 nm are underestimated by a large factor (see Extended Data Fig. 6, blue dashed line). This is consistent with the expectation that the detection efficiency of LVOCs in the nitrate-CI-API-TOF is lower as discussed above. An attempt to adjust the HOM volatility distribution by increasing the LVOCs to reproduce the observed growth rates was not successful (see Extended Data Fig. 6, blue solid line). The model can be brought into agreement with observations by increasing the LVOC concentrations and introducing a Kelvin effect (Fig. 3 and Extended Data Fig. 6 grey line). This tuned model, adjusting for inefficient LVOC measurement in the nitrate-CI-API-TOF and considering the Kelvin effect (see Methods, Extended Data Fig. 5b and Extended Data Fig. 7 for details), captures the observed particle growth in both example cases with high fidelity (Fig. 3). While the agreement at 10 nm diameter is ensured by our LVOC correction, the Kelvin term is essential to reproduce the observed growth rate over the full size range for these two quite different cases, although the strong size dependence in Fig. 3a is primarily due to the increasing HOM concentration. This is evidence that the Kelvin term (along with abundant LVOCs) is responsible for the acceleration in growth observed in field experiments in the afternoon, and that only ELVOCs have a sufficiently high saturation ratio to overcome the Kelvin barrier at the smallest sizes.

The pool of ELVOCs, many having $C^* \ll 10^{-8} \mu\text{g m}^{-3}$ (Fig. 2b), implies continuous production of relatively stable clusters smaller than 2 nm (continuous nucleation is observed, as shown in Extended Data Fig. 8). ELVOCs govern the contribution to growth up to ~ 2 nm; beyond this, LVOCs take over in sequence as the Kelvin effect becomes progressively weaker with increasing size. Thus, while growth rates in the non-volatile HOM model decrease by a factor of ~ 3 between 1 nm and 5 nm, in the volatility-distribution HOM model they increase by a factor of ~ 3 over this range, consistent with observations. This volatility-distribution growth model is a version of ‘nano-Köhler theory’, in which the effects of condensed-phase mixing (Raoult’s law) and particle curvature (the Kelvin term) combine for miscible organics. The Kelvin effect dominates because curvature enhances condensed-phase activities by orders of magnitude for the smallest particles, regardless of their composition, and the critical issue is whether the saturation ratio of an LVOC volatility bin exceeds this threshold (see Extended Data Fig. 7 for detailed model results). Finally, the volatility-distribution model shows that, in the experiments, SVOCs cannot contribute to the observed growth via non-reactive uptake as their gas-phase saturation ratio never

rises high enough for them to contribute (see Extended Data Fig. 7 and Methods).
b, The percentage change in CCN concentration (colour scale) when growth from 1.7 nm to 3 nm is due to sulfuric acid alone. **c**, The percentage change in CCN concentration when we parameterize growth from 1.7 nm to 3 nm as irreversible condensation of sulfuric acid together with an organic contribution following ref. 30, which assumes a Kelvin barrier to organic condensation below 2.5 nm. All simulations assume the same nucleation rates at 1.7 nm and the same particle growth rates above 3 nm.

risers high enough for them to contribute (see Extended Data Fig. 7 and Methods).

The α -pinene + ozone system explored here is among the most efficient sources of ELVOCs yet observed^{16,17}, but it is likely that many sources of LVOCs may be important in the atmosphere. The latter include the first-generation compounds described here but also later-generation ‘ageing’ products formed by reaction with OH radicals^{10,24,25}. Different sources are almost certain to produce LVOCs with differing volatility distributions and chemical properties, which also might influence their reactivity in the condensed phase, including oligomerization²³ and reactive uptake²⁶, resulting in different growth patterns compared to those in Fig. 3. These growth patterns thus constitute a critical and variable link between new particle formation and CCN formation.

Strongly size-dependent nanoparticle growth has been observed and parameterized based on atmospheric observations^{3,27–29}, although during nucleation events in the field it has not been possible to determine whether changes in the growth rate are due to the Kelvin effect or due to changes in the HOM concentrations during the event. To assess the global implications of our findings, we parameterized the growth between 1.7 nm and 3 nm using the size-resolved growth rates from the HOM volatility-distribution modelling results (Fig. 1 and Methods). Using a global aerosol model (Methods), we find that CCN concentrations are sensitive to whether, and how, organic compounds participate in the first stages of the growth of freshly nucleated particles. Figure 4a shows the concentrations of soluble 100 nm particles (N_{100}), a proxy for CCN, using our parameterized growth rates, which are up to a factor of two higher than those in a simulation without organics participating in the initial growth (Fig. 4b). Conversely, a previous parameterization³⁰ which empirically accounts for the Kelvin effect below 2.5 nm but assumes that all condensable organic products (not just HOMs) contribute to the growth of these particles, produces CCN concentrations up to 50% higher than our parameterization (Fig. 4c). Our model results show that CCN concentrations can be sensitive to the processes and concentrations of species driving the growth of the smallest atmospheric particles as reflected in the pronounced differences of the corresponding growth rates (Extended Data Fig. 9). On the basis of the combined modelling results and experimental data that we report here, we suggest that low-volatility organic vapours are the key to particle growth at the initial sizes.

Online Content Methods, along with any additional Extended Data display items and Source Data, are available in the online version of the paper; references unique to these sections appear only in the online paper.


Received 1 September 2015; accepted 22 April 2016.

- Merikanto, J., Spracklen, D. V., Mann, G. W., Pickering, S. J. & Carslaw, K. S. Impact of nucleation on global CCN. *Atmos. Chem. Phys.* **9**, 8601–8616 (2009).
- Kulmala, M. *et al.* Direct observations of atmospheric aerosol nucleation. *Science* **339**, 943–946 (2013).
- Kuang, C. *et al.* Size and time-resolved growth rate measurements of 1 to 5 nm freshly formed atmospheric nuclei. *Atmos. Chem. Phys.* **12**, 3573–3589 (2012).
- Lehtinen, K. E., Dal Maso, M., Kulmala, M. & Kerminen, V.-M. Estimating nucleation rates from apparent particle formation rates and vice versa: revised formulation of the Kerminen-Kulmala equation. *J. Aerosol Sci.* **38**, 988–994 (2007).
- Nieminen, T., Lehtinen, K. E. J. & Kulmala, M. Sub-10 nm particle growth by vapor condensation-effects of vapor molecule size and particle thermal speed. *Atmos. Chem. Phys.* **10**, 9773–9779 (2010).
- Riccobono, F. *et al.* Contribution of sulfuric acid and oxidized organic compounds to particle formation and growth. *Atmos. Chem. Phys.* **12**, 9427–9439 (2012).
- Riipinen, I. *et al.* The contribution of organics to atmospheric nanoparticle growth. *Nat. Geosci.* **5**, 453–458 (2012).
- Smith, J. N. *et al.* Chemical composition of atmospheric nanoparticles formed from nucleation in Tecamac, Mexico: evidence for an important role for organic species in nanoparticle growth. *Geophys. Res. Lett.* **35**, L04808 (2008).
- Laaksonen, A. *et al.* The role of VOC oxidation products in continental new particle formation. *Atmos. Chem. Phys.* **8**, 2657–2665 (2008).
- Donahue, N. M. *et al.* How do organic vapors contribute to new-particle formation? *Faraday Discuss.* **165**, 91–104 (2013).
- Zhao, J., Ortega, J., Chen, M., McMurry, P. & Smith, J. Dependence of particle nucleation and growth on high-molecular-weight gas-phase products during ozonolysis of α -pinene. *Atmos. Chem. Phys.* **13**, 7631–7644 (2013).
- Donahue, N. M., Trump, E. R., Pierce, J. R. & Riipinen, I. Theoretical constraints on pure vapor-pressure driven condensation of organics to ultrafine particles. *Geophys. Res. Lett.* **38**, L16801 (2011).
- Pierce, J. R. *et al.* Quantification of the volatility of secondary organic compounds in ultrafine particles during nucleation events. *Atmos. Chem. Phys.* **11**, 9019–9036 (2011).
- Kulmala, M., Kerminen, V.-M., Anttila, T., Laaksonen, A. & O'Dowd, C. D. Organic aerosol formation via sulphate cluster activation. *J. Geophys. Res.* **D 109**, D04205 (2004).
- Kirkby, J. *et al.* Ion-induced nucleation of pure biogenic particles. *Nature* **533**, <http://dx.doi.org/10.1038/nature17953> (2016).
- Jokinen, T. *et al.* Production of extremely low volatile organic compounds from biogenic emissions: measured yields and atmospheric implications. *Proc. Natl Acad. Sci. USA* **112**, 7123–7128 (2015).
- Ehn, M. *et al.* A large source of low-volatility secondary organic aerosol. *Nature* **506**, 476–479 (2014).
- Donahue, N. M., Kroll, J. H., Pandis, S. N. & Robinson, A. L. A two-dimensional volatility basis set — part 2: diagnostics of organic-aerosol evolution. *Atmos. Chem. Phys.* **12**, 615–634 (2012).
- Lovejoy, E. R., Curtius, J. & Froyd, K. D. Atmospheric ion-induced nucleation of sulfuric acid and water. *J. Geophys. Res.* **D 109**, D08204 (2004).
- Pankow, J. F. & Asher, W. E. SIMPOL. 1: A simple group contribution method for predicting vapor pressures and enthalpies of vaporization of multifunctional organic compounds. *Atmos. Chem. Phys.* **8**, 2773–2796 (2008).
- Hytinen, N. *et al.* Modeling the charging of highly oxidized cyclohexene ozonolysis products using nitrate-based chemical ionization. *J. Phys. Chem. A* **119**, 6339–6345 (2015).
- Presto, A. A. & Donahue, N. M. Investigation of α -pinene + ozone secondary organic aerosol formation at low total aerosol mass. *Environ. Sci. Technol.* **40**, 3536–3543 (2006).
- Trump, E. R. & Donahue, N. M. Oligomer formation within secondary organic aerosols: equilibrium and dynamic considerations. *Atmos. Chem. Phys.* **14**, 3691–3701 (2014).
- Schobesberger, S. *et al.* Molecular understanding of atmospheric particle formation from sulfuric acid and large oxidized organic molecules. *Proc. Natl Acad. Sci. USA* **110**, 17223–17228 (2013).
- Riccobono, F. *et al.* Oxidation products of biogenic emissions contribute to nucleation of atmospheric particles. *Science* **344**, 717–721 (2014).
- Wang, L. *et al.* Atmospheric nanoparticles formed from heterogeneous reactions of organics. *Nat. Geosci.* **3**, 238–242 (2010).
- Yli-Juuti, T. *et al.* Growth rates of nucleation mode particles in Hyytiälä during 2003–2009: variation with particle size, season, data analysis method and ambient conditions. *Atmos. Chem. Phys.* **11**, 12865–12886 (2011).
- Häkkinen, S. A. K. *et al.* Semi-empirical parameterization of size-dependent atmospheric nanoparticle growth in continental environments. *Atmos. Chem. Phys.* **13**, 7665–7682 (2013).
- Bianchi, F. *et al.* New particle formation in the free troposphere: a question of chemistry and timing. *Science* **352**, <http://dx.doi.org/10.1126/science.aad5456> (2016).
- D'Andrea, S. D. *et al.* Understanding global secondary organic aerosol amount and size-resolved condensational behavior. *Atmos. Chem. Phys.* **13**, 11519–11534 (2013).

Acknowledgements We thank CERN for supporting CLOUD with technical and financial resources, and for providing a particle beam from the CERN Proton Synchrotron. This research has received funding from the EC Seventh Framework Programme (Marie Curie Initial Training Network 'CLOUD-ITN' no. 215072, MC-ITN 'CLOUD-TRAIN', no. 316662, and ERC-StG-ATMOGAIN (278277) and ERC-Advanced 'ATMNUCLE' grant no. 227463), the German Federal Ministry of Education and Research (project nos 01LK0902A and 01LK1222A), the Swiss National Science Foundation (project nos 200020_135307, 200020_152907, 20FI20_149002 and 200021_140663), the Academy of Finland Center of Excellence programme (project no. 1118615), the Academy of Finland (CoE project no. 1118615, LASTU project no. 135054), the Nessling Foundation, the Austrian Science Fund (FWF; project no. J3198-N21), the EU's Horizon 2020 research and innovation programme under the Marie Skłodowska-Curie (no. 656994), the Swedish Research Council, Vetenskapsrådet (grant no. 2011-5120), the Portuguese Foundation for Science and Technology (project no. CERN/FP/116387/2010), the Presidium of the Russian Academy of Sciences and Russian Foundation for Basic Research (grants 08-02-91006-CERN and 12-02-91522-CERN), Dreyfus Award EP-11-117, the Davidow Foundation, the US National Science Foundation (grants AGS1136479, AGS1447056, AGS1439551 and CHE1012293), US Department of Energy (grant DE-SC00014469) and the FP7 project BACCHUS (grant agreement 603445).

Author Contributions A.A., J.A., U.B., A.-K.B., M.B., F.B., K.S.C., J.S.C., J.C., A.D., J.Do., N.M.D., J.Du., S.E., R.C.F., A.F., C.Fr., C.Fu., R.G., M.G., M.H., T.J., H.K., J.Kir., M.Kr., M.Ku., A.K., A.L., K.L., P.M., U.M., T.N., T.P., F.M.P., M.P.R., S.S., M.Sim., M.Sip., J.N.S., G.S., A.T., J.T., A.V., A.C.W., R.W., E.W., D.W., P.M.W., D.W. and C.Y. designed the experiment or prepared the CLOUD facility or instruments. A.A., J.A., A.-K.B., M.B., F.B., S.B., J.S.C., J.C., A.D., J.Du., S.E., A.F., C.Fr., C.Fu., H.G., M.H., C.R.H., T.J., J.Ka., H.K., J. Kim, J.Kir., M.Kr., A.K., M.L., K.L., P.M., U.M., T.N., F.M.P., I.R., M.P.R., N.S., S.S., K.S., M.Sim., M.Sip., J.N.S., G.S., A.T., J.T., A.V., A.C.W., R.W., C.W., D.W., C.Y. and P.Y. collected data. L.A., A.K.B., F.B., S.B., J.S.C., N.M.D., R.C.F., A.F., C.F., M.H., C.R.H., T.J., K.L., U.M., T.N., N.S., S.S., M.Sim., M.Sip., G.S., J.T., R.W., C.W., D.W. and C.Y. performed data analysis. J.Do. and U.M. contributed HOM structures. W.K.C., N.M.D., L.A., I.R. and J.T. performed aerosol growth modelling. H.G. performed GLOMAP modelling. J.T., L.A., U.B., F.B., K.S.C., J.C., J.Do., N.M.D., J.Du., R.C.F., C.Fr., H.G., M.G., M.H., C.R.H., T.J., J.Kir., M.Ku., K.L., U.M., T.P., I.R., M.P.R., N.S., S.S., M.Sim., C.W., D.W. and C.Y. were involved in the scientific interpretation and discussion. J.T., U.B., J.Do., N.M.D. and H.G. wrote the manuscript. All commented on the paper.

Author Information Reprints and permissions information is available at www.nature.com/reprints. The authors declare no competing financial interests. Readers are welcome to comment on the online version of the paper. Correspondence and requests for materials should be addressed to U.B. (urs.baltensperger@psi.ch).

 This work is licensed under a Creative Commons Attribution 4.0 International (CC BY 4.0) licence. The images or other third party material in this article are included in the article's Creative Commons licence, unless indicated otherwise in the credit line; if the material is not included under the Creative Commons licence, users will need to obtain permission from the licence holder to reproduce the material. To view a copy of this licence, visit <http://creativecommons.org/licenses/by/4.0/>.

RESEARCH LETTER

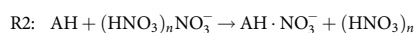
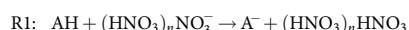
METHODS

The CLOUD chamber. We conducted two measurement campaigns at the CERN CLOUD chamber, a 26 m³ stainless steel vessel which enables aerosol experiments under the full range of tropospheric conditions^{31,32}. CLOUD7, in the autumn of 2012, included mostly high sulfuric acid concentrations, while CLOUD8, in 2013, addressed low sulfuric acid concentrations. To avoid contamination, pure air is generated by the evaporation of cryogenic liquid nitrogen (N₂) and liquid oxygen (O₂), combined at a ratio of 79:21. A UV light (250–400 nm) system enables the formation of hydroxyl (OH) radicals via the photolysis of ozone³³. By applying a high voltage field (30 kV m⁻¹) all charged particles in the chamber can be removed rapidly (neutral conditions); when the high voltage field is turned off, natural ions are produced in the chamber by Galactic cosmic rays (GCR condition) reaching ground level. With the 3.5 GeV/c secondary pion beam (π condition) from the CERN Proton Synchrotron passing through the chamber, ion concentrations representative for those of the upper troposphere can be achieved^{31,34}. A dedicated inlet system is available for every gas. In order to clean the chamber, the chamber can be heated by raising the temperature to 373 K, and, in addition, flushed with ultra pure water. All gas pipes are made from stainless steel to avoid contamination, and chamber and gas seals are chemically inert gold coated metal. Two fans running in counter flow ensure a good mixture of the gases in the chamber³⁵. Traces of contaminants, for example, low molecular weight volatile organic compounds (VOCs)³⁶ or ammonia³⁷, were sometimes observed in the chamber. However, as shown elsewhere³⁸, extremely clean conditions can be achieved.

Experimental settings. A typical experiment started with the injection of α -pinene under neutral (ion free) conditions. The ozone already present in the chamber immediately reacts with the α -pinene leading to aerosol nucleation (see also ref. 15). Using the UV fibre system in the chamber, additional OH could be photochemically produced. The major fraction of HOM (~60%) were chemically produced via the ozonolysis of α -pinene. This experiment was continued until a steady-state—that is, a stable HOM concentration, was achieved. Afterwards the high-voltage field, used in neutral experiments for sweeping out ions, was turned off. This allowed ions (~700 cm⁻³) produced by Galactic cosmic rays to accumulate in the chamber, and resulted in a second nucleation event (see also ref. 15). In addition experiments were also started under GCR conditions to prove consistency. In total, approximately 40% of the runs started (with increasing HOM concentration) in neutral conditions, 18% in GCR condition and 20% in π condition. Plateau conditions (with steady-state HOM concentration) in GCR constitute approximately 18% of the runs and in π condition approximately 4%. π conditions relate to experiments where the Proton Synchrotron was also used to produce higher ion concentrations (~3,000 cm⁻³), as encountered in the upper troposphere. This was only possible during CLOUD 7, as during CLOUD 8 the Proton Synchrotron was not in operation due to maintenance work. A typical experiment is shown in Extended Data Fig. 8. For pure biogenic experiments, we added no SO₂ for sulfuric acid experiments, we injected SO₂ into the chamber as an additional precursor. All experimental steady-state conditions can be found in Extended Data Table 1. For each run several growth rates at different diameters could be quantified (see Extended Data Figs 1 and 8). Extended Data Fig. 8 shows two nucleation events that were observed during one run, one under neutral and the second one under GCR conditions. Thus, one run can yield several points in Fig. 1.

Cluster composition. *Atmospheric pressure interface time of flight mass spectrometer (API-TOF).* One API-TOF (Tofwerk AG) measured the mass-to-charge ratio of positive or negative clusters present in the CLOUD chamber²⁴. Since this instrument only measures charged clusters, the measurements were made during GCR or π conditions. It is only possible to measure one polarity at a time thus positive and negative spectra were measured alternately. *Chemical ionization atmospheric pressure interface time of flight mass spectrometer (nitrate-CI-API-TOF).* Two nitrate-CI-API-TOFs³⁸ measured the concentration of sulfuric acid, oxidized organics and other clusters and molecules in the cloud chamber.

The instruments use an ion source (one an X-ray generator, one a corona needle) to ionize the reagent gas nitric acid in a nitrogen flow. In a drift tube an electric field is then applied to guide the primary ions to the sample flow where they react with the neutral molecules and clusters with an overall reaction time of about 200 ms in one instrument and 50 ms in the other. Inside the drift tube, two possible reactions can then take place to ionize the neutral molecules or clusters A in the sample flow:



The first reaction (R1) corresponds to a proton transfer reaction (acid/base reaction) which is, for example, the case for sulfuric acid. The second reaction (R2) is a ligand switching reaction, forming a more stable adduct, which is the case for

highly oxygenated molecules (HOMs). Using an electrostatic field, the charged molecules and clusters are then guided through a small pinhole with a diameter of 350 (300) μm to the API-TOF section.

The voltage settings in the API and TOF sections determine the mass dependent transmission efficiency of the instrument. The transmission curves were determined with separate measurements, by adding certain compounds (perfluorinated acids) to the instrument in sufficient amounts to deplete the primary ions. With this method the transmission relative to the mass to charge ratio (m/Q) of the primary ions was determined³⁹. One instrument operated at the same voltage settings for the whole campaign while the other one was operated in a switching mode between voltage settings optimized for a low or high m/Q range.

We analysed the raw data with the MATLAB *tofTools* package^{32,40}. The mass scale is calibrated to better than 10 p.p.m. accuracy, using a two-parameter fit. The concentration of sulfuric acid is calculated from the count rates of each ion species as follows:

$$[\text{H}_2\text{SO}_4] = C \times \text{SL}_{\text{H}_2\text{SO}_4} \times \ln \left(1 + \frac{[\text{HSO}_4^-] + [\text{HSO}_4^- \cdot \text{HNO}_3]}{\sum_{j=0}^2 [\text{NO}_3^- \cdot (\text{HNO}_3)_j]} \right) \quad (1)$$

where $[\text{H}_2\text{SO}_4]$ is the concentration of sulfuric acid. The corresponding ion count rates, including the primary ions, appear on the right hand side of the equation. C is a calibration coefficient, which was determined by connecting the nitrate-CI-API-TOF to a well characterized H₂SO₄ generator⁴¹. Line losses for H₂SO₄ were corrected with the term $\text{SL}_{\text{H}_2\text{SO}_4}$. SL can be calculated from empirical equations for straight circular tubes with a laminar flow⁴².

Measurement of oxidized organics. During nucleation and growth, we observed two distinct signal patterns—monomers and dimers—in the nitrate-CI-API-TOF (Extended Data Fig. 2, Run 1209) corresponding to the monomers and dimers of the α -pinene oxidation products. These bands contain highly oxygenated molecules (HOMs), which have been found to play a potentially major role in aerosol growth¹⁷. Owing to their structure and their high O:C, these clusters have a low saturation vapour concentration. In ref. 17, it was assumed that all observed oxygenated organics are extremely low-volatility organic compounds (ELVOCs) and condense on the added seed aerosol.

We define monomers (mainly C_xH_yO_z with $x = 8-10$, $y = 12-16$ and $z = 6-12$) as the sum of the peaks in the m/Q range from 235–424 Th (1 Th = 1 Da/e, where e is the elementary charge) and dimers (mainly C_xH_yO_z with $x = 17-20$, $y = 26-32$ and $z = 8-18$) as the sum from 425–625 Th. We excluded contamination peaks from the summation within a band, as well as peaks assigned to RO₂ radicals (C₁₀H₁₅O_{6,8,10,12}, corresponding to m/Q of 293, 325, 357 and 389 Th).

The API-TOF also detected naturally charged clusters between 670 and 850 Th (trimers) and between 900 and 1,200 Th (tetramers). For the nitrate-CI-API-TOF the trimer band was only observed for a very long integration time, indicating either a low concentration of neutral trimers or a low transmission efficiency. We also observed intermediate species with a carbon number of 11 to 17, which may be dimers formed from reactions of RO₂ radicals with RO₂ radicals formed from fragments. However, their concentration is small (see cyan peaks in Extended Data Fig. 2).

To estimate the concentration of each highly oxygenated molecule (HOM_{*i*}), we applied the following equation:

$$[\text{HOM}_i] = C \times T_i \times \text{SL}_{\text{HOM}_i} \times \ln \left(1 + \frac{[\text{HOM}_i \cdot \text{NO}_3^-]}{\sum_{j=0}^2 [\text{NO}_3^- \cdot (\text{HNO}_3)_j]} \right) \quad (2)$$

In this equation, $[\text{HOM}_i \cdot \text{NO}_3^-]$ is the integrated area of a background corrected HOM peak in counts per second (c.p.s.). We corrected for the losses through the sampling line with the term SL_{HOM} . Here, we used the diffusion coefficients for the monomers (0.0297 cm² s⁻¹) and for the dimers (0.0240 cm² s⁻¹), which we determined in the CLOUD chamber experimentally. This results in correction factors for the monomers of a factor of 1.44 and for dimers of a factor of 1.37. The total HOM concentration is defined as the sum of all $[\text{HOM}_i]$, which includes all identified monomers, dimers and intermediate clusters (see Extended Data Fig. 2).

We assume that the binding between the nitrate ion and the HOM is strong and proceeds at the kinetic limit and therefore use the same calibration constant C as for sulfuric acid. This assumption does hold for highly oxygenated species with extremely low volatilities, but not for less oxygenated species as the ionization efficiency decreases²¹. Quantum chemical calculations have shown that the nitrate

preferably clusters with ELVOC²¹. Less oxidized species are, therefore, observed to a lesser extent under our experimental conditions (HNO₃ concentration).

The transmission efficiency T_i of each individual HOM_{*i*} depends strongly on the mass of each molecule and the different voltage settings in the nitrate-CI-APi-TOF. To correct this transmission factor, we derived a transmission curve over the whole mass range of the HOMs. For more details see ref. 43.

The uncertainty in HOM measurement was caused by the following sources: uncertainty in sulfuric acid calibration, charging efficiency of HOMs by the nitrate ion, mass dependent transmission efficiency and sampling line losses. This results in an overall scaling uncertainty for the measured [ELVOC] of +80%–45% assuming a charging efficiency of one. We cannot give an uncertainty of the LVOC concentration. Instead we used a scaling factor to match the observation. On the basis of that and because LVOC ≫ ELVOC, the HOM concentration is presumably underestimated by a factor of four. Nobody, at least to our knowledge, has been able to calibrate the nitrate chemical ionization source for charging efficiency so far.

For the analysis, the data from only one nitrate-CI-APi-TOF (University of Frankfurt–UFRA) was used. The main reason for this was that a transmission calibration of the APi-TOF section was performed with this instrument (see also ref. 43) and thus the data are expected to be quantitatively correct. The other nitrate-CI-APi-TOF (University of Helsinki–UHEL) agrees very well for the monomer concentration, but less well for the oligomers. In addition, the UHEL nitrate-CI-APi-TOF was operated under different settings. It was switched between several modes—(1) high fragmentation, (2) high mass and (3) low mass—to get further information on the fragmentation of the molecules and clusters.

Mass defect. In a mass defect plot, the difference between the exact mass of a compound and its nominal mass (*Th*) is depicted as function of its mass to charge ratio (*Th*). Depending on the element the mass defect can be negative or positive. In case of oxygen the mass defect is negative, so that a slope downwards represents an increase in oxygen molecules. Thus, the analysis of a complex high resolution spectrum is simplified by a convenient visualization where the pattern of compounds belonging to the same family is clearly shown.

Proton transfer reaction time of flight mass spectrometer (PTR-TOF-MS). We used a PTR-TOF-MS (Ionicon Analytik) to determine α-pinene concentrations in the chamber; it also provides information about the overall cleanliness regarding VOCs in the chamber. VOCs are ionized in a reaction chamber by means of a proton transfer reaction under precisely defined conditions (reaction time, pressure, temperature) and then analysed by a time-of-flight (TOF) mass spectrometer (ToFwerk AG). A mass resolving power of 4,000 ($m/\Delta m$, FWHM) and a mass accuracy within 10 p.p.m. enables unambiguous identification of pure hydrocarbons and volatile organic compounds up to $m/Q = 250$ Th (ref. 39). Direct calibration allows determination of α-pinene volume mixing ratios with an accuracy of 5% and a lower detection limit of 25 parts per trillion by volume (p.p.t.v.).

SO₂ chemical ionization mass spectrometer (SO₂-CIMS). The very low SO₂ volume mixing ratios were determined with an SO₂ chemical ionization mass spectrometer (SO₂-CIMS). It uses the primary ion (CO₃⁻) to convert SO₂ to SO₃⁻ (reaction scheme can be found elsewhere⁴⁴). The SO₃⁻ is then measured in a quadrupole mass spectrometer with an atmospheric pressure interface (Georgia Tech). The primary ions are generated with a corona discharge⁴⁵. The ratio of CO₃⁻ to NO₃⁻ was maximized by feeding CO₂, O₂ and Ar directly over the corona discharge, leading to a reduced contamination by NO₃⁻. The SO₂ concentration is then calculated as follows:

$$[\text{SO}_2] = C_s \ln(1 + R_{112}/R_{60}) \quad (3)$$

where R_{112} is the background-corrected ion count rate of SO₃⁻, R_{60} the ion count rate of CO₃⁻ and C_s the calibration factor. C_s was obtained by using an SO₂ gas standard (Carbagas AG). The calibration was repeated periodically during the campaign. The resulting calibration factor was found to be 1.3×10^5 p.p.t.v. Its detection threshold of SO₂ is about 15 p.p.t.v.; the uncertainty is within 23% for low SO₂ volume mixing ratios (around 30 p.p.t.v.), and 13% for volume mixing ratios >150 p.p.t.v. This uncertainty is mostly related to temperature changes in the experimental hall where the SO₂-CIMS was located. This change led to a drift in the SO₃⁻ background signal.

Aerosol properties. *Nano radial differential mobility analyser (nRDMA).* A custom-built aerosol size classifier and counter assembly was used to measure positively charged particles in the 1.1 to 10 nm diameter size range with a time resolution of 60 s. The classifier was a Caltech Nano-Radial Differential Mobility Analyser (herein referred to as nRDMA⁴⁶). The counter that was employed downstream of the nRDMA was an Airmodus Particle Size Magnifier with a 78 °C saturator coupled to a Brechtel Manufacturing Inc. Mixing Condensation Particle Counter, model 1710⁴⁷. The raw data from the Caltech assembly was inverted using transfer function parameters, effective length, and penetration efficiency functions⁴⁸.

Nano scanning mobility particle sizer (nano-SMPS). The nano-SMPS⁴⁹ measured the dry aerosol size distribution from 5 nm to 80 nm with a time resolution of 130 s. It was located within a temperature controlled rack and was kept at chamber temperature. The nano-SMPS consisted of the TSI condensation particle counter (CPC) 3772 with a modified cut-off ($D_{50} = 5.6$ nm, $D_{10} = 3.5$ nm)⁶, a TSI-type PSI-built short differential mobility analyser (DMA) and a neutralizer (Kr-85 source). The data were corrected for single charging efficiency, multiple charges, diffusion losses, and CPC detection efficiency. The diffusion loss correction assumes a laminar flow⁵⁰ and includes all parts of the nano-SMPS system (tubes, Kr-source, DMA inlet, DMA column).

Neutral cluster and air ion spectrometer (NAIS). The NAIS (Airel) is an ion mobility spectrometer designed to determine the number size distribution of ions in the size range 0.75–45 nm, as well as total (charged and neutral) particles in the size range ~2–45 nm (ref. 51). Previous studies have verified the performance of the NAIS^{52,53}. It consists of two differential mobility analysers (DMAs) in parallel. Each is equipped with 21 electrometers, to separate the mobilities and determine the concentrations of positive and negative ions simultaneously. A corona charger is used when measuring the total particle size distribution.

Particle counters. Several particle counters with different 50% cut-offs were deployed at the CLOUD chamber including two DEG-CPCs^{54,55} (1.5 and 2.7 nm cut-off), one butanol CPC (TSI 3776, 3.2 nm cut-off) and one Particle Size Magnifier (PSM, Airmodus, model A10)⁵⁶. The PSM was run in scanning mode and was used to determine the number size distributions between 1.4 nm and 3.4 nm mobility diameter.

Volatility of oxygenated organics. Recent studies have focused on the formation mechanism of highly oxygenated organics^{17,57,58}. Here we considered the propagation and termination reactions as proposed in refs 57 and 59. We used the radicals from α-pinene ozonolysis proposed in ref. 60 as a starting point and evaluated the possible chemical structures for monomers and dimers (Extended Data Fig. 3). We assume that dimers are covalently bound^{15,17}. This is supported by the chemical formulae of the observed compounds which cannot be explained by a cluster consisting of two monomers.

Instead of assuming an average reduction of the saturation vapour concentration with oxidation, we used this set of chemical structures to calculate the saturation vapour concentration with SIMPOL²⁰.

We then plotted the oxygen to carbon ratio (O:C) as a function of C^* (see Extended Data Fig. 4). We applied a linear least squares fit and used the fit parameters to estimate the volatility for molecules for which we did not derive the structure. The intermediate cluster volatilities were roughly estimated assuming different numbers and types of functional groups (aldehydes, ketones, hydroperoxyacids). The concentration of these clusters is low and will therefore not influence the results significantly. SIMPOL was originally derived at 293 K, but a temperature dependence is given. Thus, we extrapolated C^* to 278 K (resulting in approximately one order of magnitude lower C^* values). Then we separated all observed HOM peaks into volatility regimes¹⁸, as shown in Fig. 2a and b. For this, the HOM concentrations observed in CLOUD for a steady-state run (1209) with ~600 p.p.t.v. of injected α-pinene was used. It needs to be noted that the SIMPOL data set does not contain the smallest saturation vapour pressures (as they are difficult to measure quantitatively). Thus, the predicted saturation vapour concentrations for low-volatility compounds could deviate from the actual values. However, the binned volatility distribution is rather flat especially in the ELVOC range. So even if the saturation concentration were to deviate by an order of magnitude, this would not change the conclusions of this work.

Aerosol growth model. The net condensation flux is defined as⁶¹:

$$\dot{\phi}_{i,p}^c = N_p \underbrace{(\pi/4(D_p + D_i)^2)}_{\text{particle-vapour collision cross-section } \sigma_{i,p}} \underbrace{\nu_{i,p}^c}_{\text{deposition rate of vapours at the surface}} \underbrace{[C_i^y - a'_{i,p} C_i^0]}_{\text{driving force of condensation } F_{i,p}} = \alpha'_{i,p} \nu_{i,p}^c C_i^0 [S_i - a'_{i,p}] \quad (4)$$

with N_p the particle number concentration, D_p the particle diameter, D_i the vapour diameter, $\alpha'_{i,p}$ the accommodation coefficient, the vapour concentration C_i^y and the saturation vapour concentration of C_i^0 . In the following the indicated terms of equation (4) will be further explained.

Deposition rate coefficient. In the molecular regime the collision cross-section is the appropriate metric of a collision probability. Here we assume hard-sphere limit, neglecting charge interactions. The deposition rate coefficient is corrected for the transition regime using the $\beta_{i,p}$ correction factor, to account for non-continuum effects, that is⁶²:

$$\beta_{i,p} = \frac{\text{Kn}(1 + \text{Kn})}{\text{Kn}^2 + \text{Kn} + 0.283\text{Kn}\alpha'_{i,p} + 0.75\alpha'_{i,p}}; \quad \text{Kn} = \frac{2\lambda}{D_p} \quad (5)$$

RESEARCH LETTER

The $\beta_{i,p}$ correction term and the mass accommodation coefficient $\alpha_{i,p}$ are connected, as the correction term considers the onset of the gas-phase concentration gradients near the particle. For very small particles (Knudsen number, $\text{Kn} \gg 1$), no gradients exist. However, for very large particles ($\text{Kn} \ll 1$), the gas concentration at the particle surface can be near zero even with $\alpha_{i,p} < 1$. The effective mass accommodation coefficient, $a'_{i,p}$, is therefore introduced as well.

For the collision between vapours and ultrafine particles, the reduced mass $\mu_{i,p}$ needs to be considered; $v_{i,p}$ is then the centre of mass velocity:

$$v_{i,p} = \sqrt{8RT/(\pi\mu_{i,p})}; \quad \mu_{i,p} = M_i M_p / (M_i + M_p) \quad (6)$$

The two first terms—collision cross-section and the deposition rate—can be combined. Instead of using the cross-section, the suspended surface area ($N_p \pi D_p^2$) can be used. The modified deposition rate coefficient is then given by:

$$s_{i,p} = \frac{(D_p + D_i)^2}{D_p^2} \frac{v_i}{4} \alpha_{i,p} \beta_{i,p} \quad (7)$$

Condensation sink. Combining the surface area and the deposition rate coefficient we can calculate the collision frequency, which is the frequency with which species i collides with the particle surface:

$$\nu_{i,p}^c = v_i \beta_{i,p} (D_p \alpha_i = 1) (\pi D_p^2 N_p) \quad (8)$$

The condensation sink, $k_c = \sum_p \alpha'_{i,p} \nu_{i,p}^c$, gives the actual time constant for interaction of vapours with particles. The condensation sink is also the fundamental equilibration timescale between the gas and particle phases when condensation is the main loss of vapours.

Driving force of condensation. The driving force of condensation $F_{i,p}$ and excess saturation ratio S_i^{XS} are:

$$F_{i,p} = [C_i^y - a'_{i,p} C_i^0] = C_i^0 \frac{[S_i - a'_{i,p}]}{S_i^{XS}} \quad (9)$$

The saturation ratio (gas-phase activity) is $S_i = C_i^y / C_i^0$. The term $a_{i,p}$ is the activity of the species i at the condensed-phase surface of the particle ($a_{i,p} = X_{i,p} \gamma_{i,p}$, Raoult term), where $X_{i,p} = C_{i,p}^s / C_p^s$ is the mass fraction, and $\gamma_{i,p}$ the mass based activity coefficient in the organic condensed phase. Owing to their curved surfaces, the activity of a small particle— $a'_{i,p} = a_{i,p} K_{i,p}$ —includes the Kelvin term $K_{i,p}$. The Kelvin term is defined as⁶¹:

$$K_{i,p} = 10^{D_{K10}/D_p} = \exp\left(\frac{4\sigma_i M_i}{RT\rho_i D_p}\right) \quad (10)$$

$$D_{K10} = \log_{10}(e) \times \frac{4\sigma_i M_i}{RT\rho_i} \quad (11)$$

with the surface tension σ , the molar weight M and the density ρ . For very small particles a large supersaturation is needed to allow for condensation. For $\sigma = 0.023 \text{ N m}^{-1}$, a molar weight of 300 g mol^{-1} at 300 K , $D_K = 3.75 \text{ nm}$. Any charge effect on the growth rate would appear in either an enhancement to the collision cross-section, $\sigma_{i,p}$, due to charge-dipole interactions, or a change in the effective Kelvin diameter reflecting enhanced stability of small clusters. Further investigation of a possible enhancement in the growth rate caused by ions requires dedicated experiments.

Equilibrium solution. At equilibrium, $F_{i,p}$ is zero. In this case, equilibrium partitioning is the basis for organic aerosol calculations. Aerosol partitioning theory describes the condensation and evaporation of gas phase species on or from an aerosol surface⁶³. The fraction of the condensed phase (s) of a species i in the suspended aerosol particle within the partitioning framework is defined as:

$$f_i^s = \frac{1}{1 + C_i^s / C_{OA}^s} \quad (12)$$

C_i^s is the effective saturation concentration of the vapour and C_{OA}^s the concentration of species k in the particle phase.

Steady-state solution. Organic aerosol production, P_i (or loss) is inherently not an equilibrium process, but many terms will reach a steady state in different situations. There are two relevant limits: one where condensation to suspended particles controls the vapour concentrations on a timescale given by the condensation sink ($\alpha' \nu_{i,p}^c$), and one where losses, k_i (that is, wall losses), control those vapour concentrations. We are interested in the steady-state saturation ratios S_i^{SS} and excess saturation ratio $S_i^{XS,SS}$.

When losses control the steady-state, $S_i^{SS} = (P_i / C_i^0) / k_i$. If the suspended particles control the steady-state, the excess saturation ratio will be in steady state. A fraction of P_i will go to vapours and a fraction to the particles. The latter fraction will be approximately f_i^s .

$$\phi_i^{XS} = f_i^s P_i = \alpha' k^c C_i^0 [S_i - a_i] = \alpha' k^c C_i^0 S_i^{XS,SS}; \quad S_i^{XS,SS} = f_i^s \frac{P_i / C_i^0}{\alpha' k^c} \quad (13)$$

$S_i^{XS,SS}$ is a key diagnostic for organic condensation. If $S_i^{XS,SS} \gg 1$, the condensation will be essentially 'non-volatile' ($a'_{i,p}$ will have no influence on the condensation), while if $S_i^{XS,SS} \leq 1$ then the condensation will be 'semi-volatile'. Finally, if $S_i^{XS,SS} \ll 1$, species i cannot be an important driver of the condensation, as $a'_{i,p}$ cannot grow larger than S_i during net gas-phase production.

Dynamic volatility-distribution modelling of aerosol growth. From ref. 15, where the yields were derived from the same experiments, we know the molar yield of HOMs to be roughly $\sim 2.9\%$ from α -pinene ozonolysis. The molar weight of the HOMs is on average twice the molar weight of α -pinene, and we approximate a mass yield of the HOMs of about 6%. The HOMs used include monomers, dimers and intermediate compounds as seen by the nitrate-CI-API-TOF. The concentration of other neutral multimers was either too low or below detection limit (and thus also too low) to contribute significantly to the growth and were neglected in the model. The dynamic volatility-distribution model then condenses the observations into nine volatility bins ranging from $C^* = 10^{-8} \mu\text{g m}^{-3}$ to $C^* = 1 \mu\text{g m}^{-3}$. ELVOC and LVOC were defined as $C^* < 10^{-4.5} \mu\text{g m}^{-3}$ and $10^{-4.5} \mu\text{g m}^{-3} < C^* < 10^{-0.5} \mu\text{g m}^{-3}$ respectively, which is slightly modified compared to ref. 18. This is justified as species with $C^* = 10^{-4} \mu\text{g m}^{-3}$ (typically ELVOC) behaved rather like LVOC, that is, the condensation flux increases with diameter. In Fig. 1 we have seen that the measured HOMs alone cannot explain the observed growth in all size ranges. Therefore, a larger yield of $C^* = 1 \mu\text{g m}^{-3}$ was assumed (light shaded area in Extended Data Fig. 5a), which represents the compounds participating in the formation of the traditional secondary organic aerosol (SOA). Species with $C^* \leq 10^{-8} \mu\text{g m}^{-3}$ were brought into one single bin with $C^* = 10^{-8} \mu\text{g m}^{-3}$. The CI-API-TOF transmission calibration was multiplied by a factor of 1.3, which is within the transmission efficiency uncertainties. The resulting HOM distribution (in percentage) is displayed in Extended Data Fig. 5a.

Using this adjusted HOM distribution, we modelled the growth rate due to condensation assuming no Kelvin effect. Extended Data Fig. 6 shows that the model overestimates the early growth rate and substantially underestimates the observed particle growth rates at larger sizes (blue dashed line). In a next step we modified the charging efficiencies, to match the observation better. Our best result was achieved with values of [0.5, 0.4, 0.3, 0.1] for the VBS bins from 10^{-4} to $10^{-1} \mu\text{g m}^{-3}$, meaning that we increased the raw measured values by [2, 2.5, 3.3, and 10]. Still, it is not possible to describe the observations as depicted by the solid blue line in Extended Data Fig. 6.

Therefore it is essential to introduce the Kelvin effect to reproduce the observed growth rate. In the model we use a Kelvin diameter $D_K = 3.75 \text{ nm}$. This corresponds to a surface tension of 23 mN m^{-1} , which is a reasonable value for organics⁶⁴. If we attempt to model the observed growth using the HOM volatility distribution in Extended Data Fig. 5a, Extended Data Fig. 6 shows that the model substantially underestimates the observed particle growth (pink dashed line), as expected.

The efficiency of HOM charging by the nitrate anion (NO_3^-) depends upon the number and location of OOH groups²¹. As the probability of two OOH groups at optimal configuration is highest for the least volatile species (ELVOC), their charging efficiency is near unity. For products with higher volatility (LVOC) the efficiency decreases. Many of the oxidized monomers might still have a stiff carbon 4-ring backbone hindering an optimal cluster formation between two OOH groups and the nitrate ion. This decreased charging efficiency has yet to be experimentally quantified. Cycloalkene experiments indicate that the nitrate-CI-API-TOF indeed underestimates the low-oxygenated compounds, if compared with the acetate-CIMS⁶⁵, while the concentration for highly oxygenated compounds is similar. The ELVOC bins cannot be changed to a great extent as this would yield an overestimation in the growth rate at sizes below 3 nm.

Adjusting both the LVOC concentrations and the Kelvin term, it is possible to explain the observed size dependent behaviour in Fig. 3. Our best fit was achieved with charging efficiencies of [0.5, 0.25, 0.1, 0.1] for the VBS bins from 10^{-4} to $10^{-1} \mu\text{g m}^{-3}$ and a Kelvin diameter $D_K = 3.75 \text{ nm}$. The final adjusted yields can be seen in Extended Data Fig. 5b, which displays the HOM fraction in the corresponding volatility bins (in percentage). Other tested Kelvin diameters (for example, $D_K = 4.5 \text{ nm}$) yielded a slightly worse agreement with the measurements, the qualitative picture, however, remained the same. Increasing D_K requires an additional adjustment of the ELVOCs to match the observations, so that several parameter combinations will yield similar results. However, very large D_K are very unlikely, as there is not much space to increase the ELVOC concentration due to the nitrate-CI-API-TOF measurement principle.

Here we do not attempt to constrain the volatility distribution exactly. We show that the distribution matters in the formation of particles. ELVOC condensation dominates the growth up to ~ 1.5 nm. Beyond this size, LVOC can contribute and drive the growth. It should be noted that the HOM distribution will change with chamber operating conditions (temperature, α -pinene concentration, particle concentration).

Here we only show two representative runs, but very different cases. We did not perform experiments with pre-existing particles in the chamber, at least not in such an amount to overcome the sink due to the wall ($k_{\text{wall}} \approx 10^{-3} \text{ s}^{-1}$ versus $k_{\text{cond}} \approx 10^{-4} \text{ s}^{-1}$ or lower). The wall loss does in some way simulate the sink due to pre-existing particles. The measured gas-phase concentration is a result of the existing sink and source terms. These terms will be somewhat different in the chamber compared to ambient conditions. Thus, we cannot say that under the same α -pinene and ozone concentrations the growth is the same. But, measuring the same volatility distribution of HOMs in the ambient (and at the same temperature) should yield similar results. The exact evolution of the particle size and the contribution of the volatility bins will always depend on the observed volatility distribution of the HOM species. The volatility distribution itself will depend on the temperature and the oxidants (for example, NO_x will hinder the formation of ELVOC, lowering the yield¹⁷). But the approach proposed here and the corresponding conclusion will still be applicable.

Model details. For the simulations we assumed a mono-disperse population of nucleated particles at an initial size of 1.2 nm mobility diameter or 0.9 nm physical diameter (which is approximately the monomer size). The key parameter is the concentration gradient (see equation (9)), which in turn reflects the differences in activity between the gas phase (the saturation ratio) and the particle phase (here the mass fraction). This can be seen in Extended Data Fig. 7a. The gas phase is characterized by the balance between the production rate of the α -pinene oxidation products and wall losses yielding a stable gas-phase saturation ratio. In contrast, the condensed phase activities drop as soon as the particles grow and the Kelvin effect decreases.

Looking at the excess saturation (Extended Data Fig. 7b), the least volatile species (mostly ELVOC) have a significant excess saturation at all times; the condensed phase activity is always much lower than the gas-phase saturation ratio. The more volatile species are near equilibrium at the beginning, only gradually (if ever) developing a significant driving force of condensation. The most volatile species are in equilibrium all of the time with a diminishing mass fraction in the condensed phase. For < 2.5 nm, the particles are unstable, with the majority of their constituents showing activities $\gg 1$. They can only grow as a consequence of the excess saturation ratio of the ELVOCs. If the production were rapidly stopped, the particles would evaporate. Extended Data Fig. 7b also shows the condensed phase mass fraction and thus the chemical composition of the particle. Particles < 2.5 nm are mainly composed of ELVOC dominated by species with $C^* = 10^{-8} \mu\text{g m}^{-3}$. For larger particles the LVOC mass fraction increases until each contributes equally to the particle composition. The two most volatile bins never contribute substantially to the particle composition as their gas-phase saturation ratio is too low.

Extended Data Fig. 7c shows the absolute driving force of condensation and the equilibrium concentration of the different volatile species over the growing particles. Here, this transition from ELVOC to LVOC dominated growth is evident in the driving force of condensation. Owing to the stiff coupled differential equations tight tolerances on the solver are required for the solution to converge accurately.

Appearance times and growth rate estimation of clusters and aerosols. The appearance times of clusters and aerosols allow us to investigate the growth process. Cluster and particle appearance times, defined as the 50% rise time of the concentration of a cluster or size channel⁶⁶, were derived for APi-TOF, PSM, NAIS, DEG-CPCs, nRDMA and nano-SMPS. The corresponding diameters (leading edge diameter) were then plotted against the time. The temporal evolution is then representing the growth rate. For linear evolution, a linear fit was applied; the slope yields the growth rate. Extended Data Fig. 1 combines all the calculated appearance times for one example run. It shows an excellent agreement between the different methods and instruments.

To determine the appearance time for APi-TOF, NAIS, and PSM, concentrations in each size bin were analysed and the time when the concentration reaches 50% of its maximum value after the start of a nucleation experiment was determined and linked with the diameter midpoint of the size bin. The growth rate was obtained from a linear fit of the appearance times and the corresponding diameters. For the PSM the growth rate could be determined for the size range 1.5–3.2 nm. For the NAIS: (1) 1.4–3 nm, (2) 5–15 nm and (3) 15–30 nm. In the APi-TOF, appearance times of the monomers, dimers, trimers and tetramers were determined.

A normal (Gauss) function was applied to the size distribution data^{2,67}. The position of the full-width at half-maximum (FWHM) was then defined as the 50% rise time. Nano-SMPS growth rates were determined for the following size

ranges: (1) 5–15 nm, (2) 15–30 nm, (3) 30–60 nm and (4) > 60 nm. In these size ranges, a constant growth rate for constant HOM concentration was observed, so we did not further differentiate these ranges in Fig. 1. For the nRDMA: (1) 1.1–3 nm, (2) 2–7 nm.

The DEG-CPC method was slightly different. In previous studies⁶, the 1% threshold of the CPC and the initial rise of the concentration was used to further extend the growth rate analysis to lower diameters. We decided to also use this approach for the DEG-CPCs. However, owing to the high noise, it was often difficult to determine the 1% rise time, thus the 5% rise time of the DEG-CPCs was used instead, yielding similar results.

Growth rate uncertainties. The method uncertainty is estimated⁶⁶ to be approximately 50%. To consider the run-to-run uncertainty, we used σ_{fit} , as retrieved from the linear fit uncertainty to determine the growth rate (GR). The overall uncertainty then scales as follows:

$$\sigma_{\text{tot}} = \sqrt{0.25[\text{GR}]^2 + \sigma_{\text{fit}}^2} \quad (14)$$

The growth rates in Fig. 1c, d correlate reasonably well with the HOM concentration. Growth rates of larger sizes correlate with a Pearson's correlation coefficient of 0.94, growth rates at smaller size with a Pearson's correlation coefficient of 0.7. The lower correlation at the smaller sizes can be explained by the higher measurement uncertainty at these size ranges, compared to larger sizes.

Parameterization of first steps of growth and global aerosol modelling. We are especially interested in the first steps of growth, that is, from the nucleated cluster size to 3 nm, as there the coagulation losses are highest. In the global model we use here⁶⁸, nucleated clusters have a diameter of 1.7 nm, and particles must grow to 3 nm before being advected through the atmosphere in the nucleation mode. Therefore we parameterize the growth rate in the size range 1.7–3 nm. We use the size-resolved growth rates from the HOM volatility-distribution modelling results to derive a size-dependent parameterization. The Kelvin effect increases the growth rate with increasing size. The considered size range (1.7–3 nm) is small enough that we can approximate the dependence on the particle diameter D_p as linear. We thus parameterize the growth rate (in nm h^{-1}) by fitting the two-dimensional function ([HOM] in cm^{-3} , D_p in nm):

$$\text{GR} = kD_p[\text{HOM}]^p \quad (15)$$

to the HOM volatility-distribution modelling results, with the free parameters $k = (5.2 \pm 0.4) \times 10^{-11}$ and $p = 1.424 \pm 0.004$. Here the uncertainties are those from the fit only; they reflect how well the function describes the data but do not represent the full uncertainty in the parameterization. The parameterization is intended to describe the size-dependent growth that we observe, and does not necessarily reflect the underlying mechanism. Therefore, extrapolations to very high values ($> 5 \times 10^8 \text{ cm}^{-3}$) and low values ($< 2 \times 10^6 \text{ cm}^{-3}$) may not be reliable, as it is likely that the parameterized growth rates deviate from the true growth rates. Such high biogenic HOM values, however, are not expected in the field and should not impact the global modelling results. Conversely, low HOM concentrations far below $2 \times 10^8 \text{ cm}^{-3}$ are expected far from sources of terpenes, especially over oceans and the upper free troposphere. From Fig. 1 it is evident that the growth rate at [HOM] $< 2 \times 10^6 \text{ cm}^{-3}$ is $< 1 \text{ nm h}^{-1}$. Under these conditions, growth is driven by condensation of sulfuric acid, and uncertainties in the parameterization of the very small organic contribution are not expected to affect the results significantly.

This parameterization provides a refined estimate of the growth rate between 1.7 and 3 nm, which is appropriate for models of atmospheric aerosol that treat SOA condensation kinetically. To implement the parameterization, a mechanism and yield for the production of HOMs is required. In our model, HOMs are simulated as being produced directly from the oxidation of monoterpenes (MT) and lost to the condensation sink (CS) in a steady-state approximation:

$$[\text{HOM}] = (Y_1k_1[\text{MT}][\text{O}_3] + Y_2k_2[\text{MT}][\text{OH}])/\text{CS} \quad (16)$$

where Y_1 , the yield of HOMs from the ozonolysis of monoterpenes, is 2.9%, and Y_2 , the yield from the OH-oxidation, is 1.2%. The yields were determined from the nitrate-CI-APi-TOF and PTR-TOF measurements in the CLOUD chamber¹⁵. The constants k_1 and k_2 are the temperature dependent reaction rate constants of α -pinene with ozone and hydroxyl radicals, respectively⁶⁹. Thus the numerator of equation (16) represents the production of HOMs and the denominator the losses.

We do not quote a similar parameterization for growth rates at larger sizes, because it is clear that the nitrate-CI-APi-TOF does not see all of the more volatile molecules that condense onto larger particles, many more compounds are likely to participate than those present in the CLOUD chamber, and at these larger sizes the kinetic condensation approach should be complemented by an equilibrium partitioning treatment (for example, ref. 70).

RESEARCH LETTER

This parameterization represents pure organic growth resulting from biogenic emissions. In the ambient atmosphere, additional organic and inorganic precursors such as sulfuric acid, ammonia, amines and anthropogenic VOCs are also present and influence the growth rate, in addition to the different oxidants. Also temperature and relative humidity could influence the observed growth rates. So, while this parameterization represents a significant advance on the current state of the art, it should not be considered complete. Furthermore, we only consider the size range 1.7 to 3 nm, as the growth in this size range is most decisive for the fate of the freshly nucleated particle⁴.

The parameterization of initial particle growth is incorporated in the global aerosol model GLOMAP-mode⁶⁸, an extension to the TOMCAT chemical transport model⁷¹. GLOMAP includes representations of particle formation, growth via coagulation, condensation and cloud processing, wet and dry deposition and in/below cloud scavenging. The horizontal resolution is 2.8×2.8 degrees and there are 31 vertical sigma-pressure levels extending from ground level to 10 hPa. Aerosol in the model is formed of four components: black carbon, organic carbon, sea salt and sulfate, and is advected through the atmosphere in seven log-normal size modes. These are hygroscopic nucleation, Aitken, accumulation and coarse modes, and non-hygroscopic Aitken, accumulation and coarse modes. Formation of secondary particles in the model is based on CLOUD measurements of ternary H₂SO₄-organic-H₂O nucleation detailed in ref. 25 and on a parameterization of binary H₂SO₄-H₂O nucleation⁷². Simulations are run for the year 2008.

In the aerosol model, particles grow by irreversible condensation of monoterpene oxidation products and sulfuric acid. Monoterpene emissions in the model are taken from the database of ref. 73. Our measurements¹⁵ provide HOM yields of 2.9% from the oxidation of α -pinene by ozone and 1.2% from the hydroxyl radical. In ref. 58 a substantially higher HOM yield was observed from endocyclic monoterpenes such as α -pinene than from exocyclic monoterpenes. These two types are roughly equally abundant in the atmosphere. Thus, we account for this by dividing our measured yields by two. In the light of these results, we also divide the organic nucleation rate of ref. 25 by two, since it also assumed all terpenes were represented by α -pinene in the atmosphere. Above 3 nm in diameter, a fixed 13% of the oxidation products of monoterpenes with OH, O₃ and NO₃ (assuming the reaction rates of α -pinene) condense irreversibly onto aerosol particles at the kinetic limit. These oxidized organic molecules are referred to as SORG and are advected through the troposphere as a tracer in the model, while the HOM concentration is calculated assuming a steady state as described earlier. Below 3 nm, organic molecules condense onto particles according to the parameterization, while sulfuric acid molecules condense at the kinetic limit (collision-limited), which is approximately:

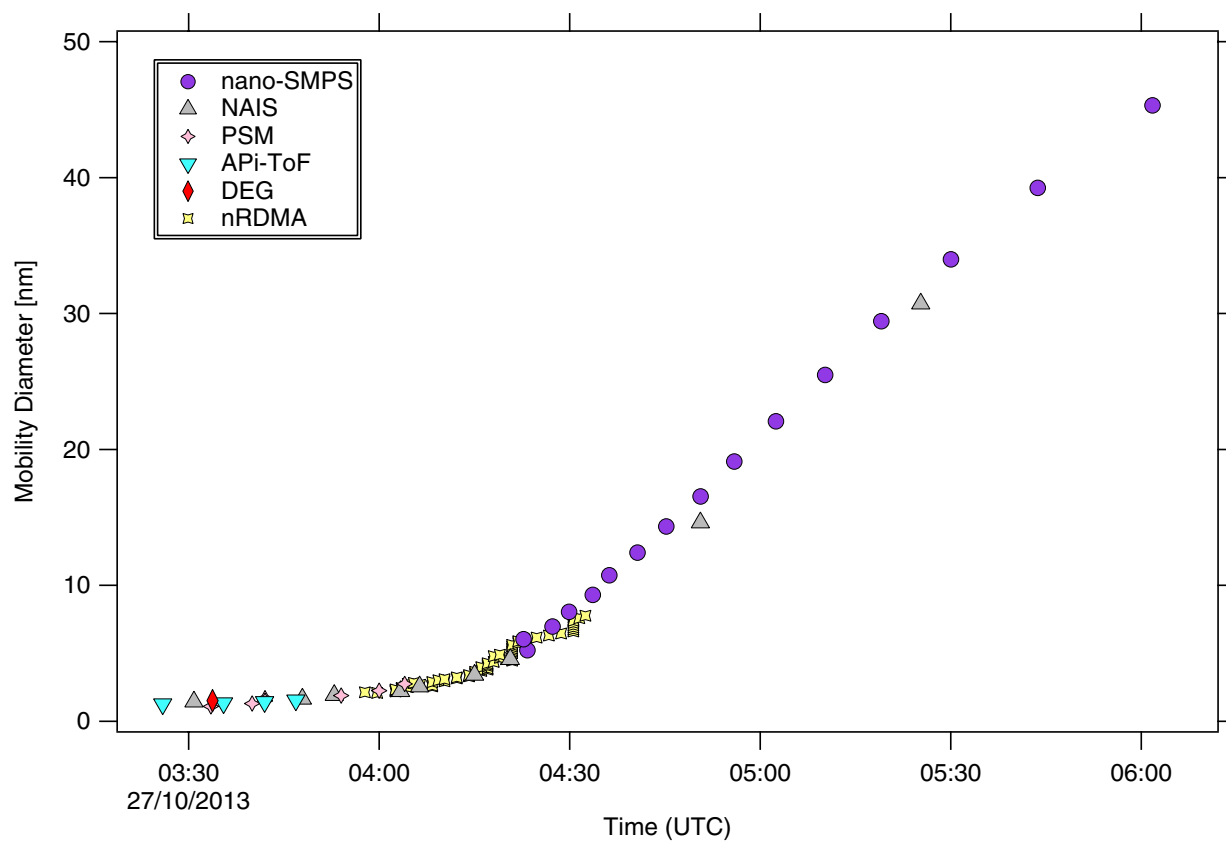
$$GR_S = 7.3 \times 10^{-8} [H_2SO_4] \quad (17)$$

Additional model runs were performed with no organics participating in the initial growth, and with non-volatile size-dependent growth of particles between 1.7 and 3 nm due to condensation of SORG multiplied by the factor determined in ref. 30 for the parameterization of ref. 3,

$$k = 0.47D_p - 0.18 \quad (18)$$

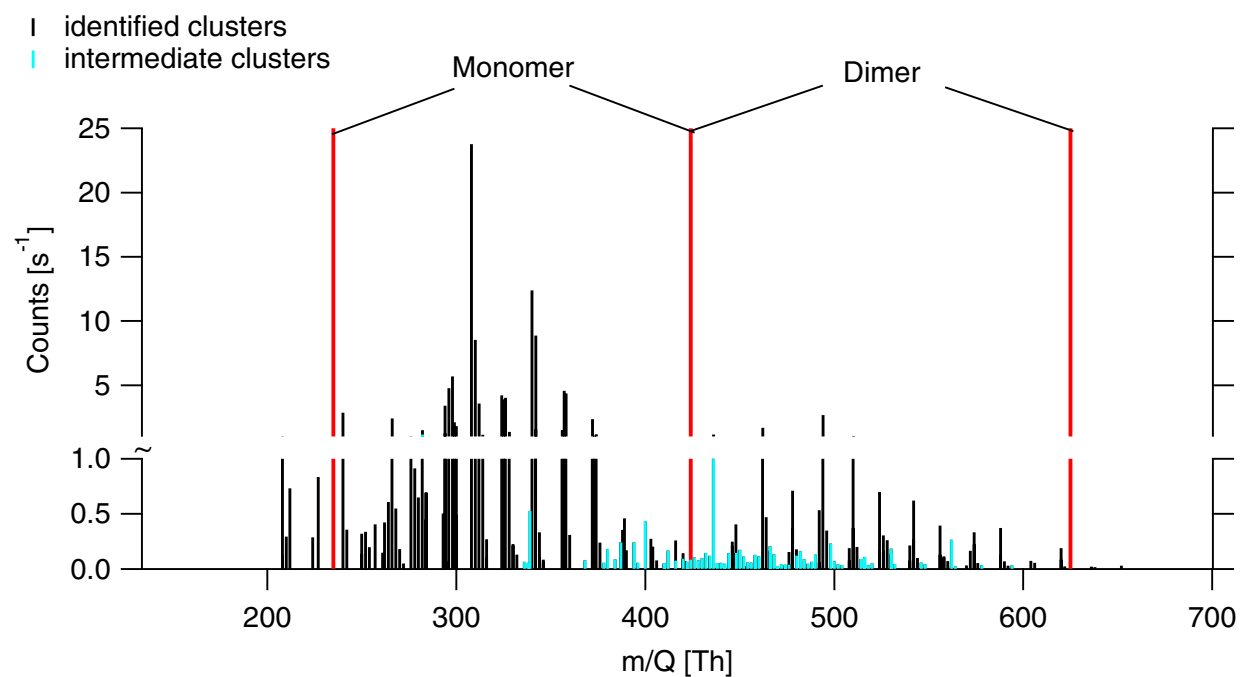
where D_p is the particle diameter in nm and the correction is only applied to particles below 2.5 nm. We note that the SORG in GLOMAP is produced with a 13% yield while that in GEOS-chem is produced with a 10% yield. The growth rates in these three cases are shown in Extended Data Fig. 9, together with the HOM concentration in the model.

31. Kirkby, J. *et al.* Role of sulphuric acid, ammonia and galactic cosmic rays in atmospheric aerosol nucleation. *Nature* **476**, 429–433 (2011).
32. Duplissy, J. *et al.* Effect of ions on sulfuric acid-water binary particle formation: 2. Experimental data and comparison with qc-normalized classical nucleation theory. *J. Geophys. Res. Atmos.* **121**, 1752–1775 (2016).
33. Kupc, A. *et al.* A fibre-optic UV system for H₂SO₄ production in aerosol chambers causing minimal thermal effects. *J. Aerosol Sci.* **42**, 532–543 (2011).
34. Duplissy, J. *et al.* Results from the CERN pilot CLOUD experiment. *Atmos. Chem. Phys.* **10**, 1635–1647 (2010).
35. Voigtländer, J., Duplissy, J., Rondo, L., Kürten, A. & Stratmann, F. Numerical simulations of mixing conditions and aerosol dynamics in the CERN CLOUD chamber. *Atmos. Chem. Phys.* **12**, 2205–2214 (2012).
36. Schnitzhofer, R. *et al.* Characterisation of organic contaminants in the CLOUD chamber at CERN. *Atmos. Meas. Tech.* **7**, 2159–2168 (2014).
37. Bianchi, F., Dommen, J., Mathot, S. & Baltensperger, U. On-line determination of ammonia at low pptv mixing ratios in the CLOUD chamber. *Atmos. Meas. Tech.* **5**, 1719–1725 (2012).
38. Jokinen, T. *et al.* Atmospheric sulphuric acid and neutral cluster measurements using Cl-API-TOF. *Atmos. Chem. Phys.* **12**, 4117–4125 (2012).
39. Graus, M., Müller, M. & Hansel, A. High resolution PTR-TOF: quantification and formula confirmation of VOC in real time. *J. Am. Soc. Mass Spectrom.* **21**, 1037–1044 (2010).
40. Junninen, H. *et al.* A high-resolution mass spectrometer to measure atmospheric ion composition. *Atmos. Meas. Tech.* **3**, 1039–1053 (2010).
41. Kürten, A., Rondo, L., Ehrhart, S. & Curtius, J. Calibration of a chemical ionization mass spectrometer for the measurement of gaseous sulfuric acid. *J. Phys. Chem. A* **116**, 6375–6386 (2012).
42. Cheng, Y.-S. in *Aerosol Measurement: Principles, Techniques, and Applications* (eds Kulkarni, P. *et al.*) 569–601 (John Wiley & Sons, 2001).
43. Heinritzi, M. *et al.* Characterization of the mass-dependent transmission efficiency of a CIMS. *Atmos. Meas. Tech.* **9**, 1449–1460 (2016).
44. Möhler, O., Reiner, T. H. & Arnold, F. The formation of SO₃ by gas phase ion-molecule reactions. *J. Chem. Phys.* **97**, 8233–8239 (1992).
45. Kürten, A., Rondo, L., Ehrhart, S. & Curtius, J. Performance of a corona ion source for measurement of sulfuric acid by chemical ionization mass spectrometry. *Atmos. Meas. Tech.* **4**, 437–443 (2011).
46. Brunelli, N. A., Flagan, R. C. & Giapi, K. P. Radial differential mobility analyzer for one nanometer particle classification. *Aerosol Sci. Technol.* **43**, 53–59 (2009).
47. Wang, J., McNeill, V. F., Collins, D. R. & Flagan, R. C. Fast mixing condensation nucleus counter: application to rapid scanning differential mobility analyzer measurements. *Aerosol Sci. Technol.* **36**, 678–689 (2002).
48. Jiang, J. *et al.* Transfer functions and penetrations of five differential mobility analyzers for sub-2 nm particle classification. *Aerosol Sci. Technol.* **45**, 480–492 (2011).
49. Wang, S. C. & Flagan, R. C. Scanning electrical mobility spectrometer. *Aerosol Sci. Technol.* **13**, 230–240 (1990).
50. Kulkarni, P., Baron, P. A. & Willeke, K. *Aerosol Measurement: Principles, Techniques, and Applications* (John Wiley & Sons, 2011).
51. Mirme, S. & Mirme, A. The mathematical principles and design of the NAIS—a spectrometer for the measurement of cluster ion and nanometer aerosol size distributions. *Atmos. Meas. Tech.* **6**, 1061–1071 (2013).
52. Asmi, E. *et al.* Results of the first air ion spectrometer calibration and intercomparison workshop. *Atmos. Chem. Phys.* **9**, 141–154 (2009).
53. Gagné, S. *et al.* Intercomparison of air ion spectrometers: an evaluation of results in varying conditions. *Atmos. Meas. Tech.* **4**, 805–822 (2011).
54. Wimmer, D. *et al.* Performance of diethylene glycol-based particle counters in the sub-3 nm size range. *Atmos. Meas. Tech.* **6**, 1793–1804 (2013).
55. Iida, K., Stolzenburg, M. R. & McMurry, P. H. Effect of working fluid on sub-2 nm particle detection with a laminar flow ultrafine condensation particle counter. *Aerosol Sci. Technol.* **43**, 81–96 (2009).
56. Vanhanen, J. *et al.* Particle size magnifier for nano-CN detection. *Aerosol Sci. Technol.* **45**, 533–542 (2011).
57. Rissanen, M. P. *et al.* The formation of highly oxygenated multifunctional products in the ozonolysis of cyclohexene. *J. Am. Chem. Soc.* **136**, 15596–15606 (2014).
58. Jokinen, T. *et al.* Rapid autoxidation forms highly oxidized RO₂ radicals in the atmosphere. *Angew. Chem. Int. Ed.* **53**, 14596–14600 (2014).
59. Mentel, T. *et al.* Formation of highly oxidized multifunctional compounds: autoxidation of peroxy radicals formed in the ozonolysis of alkenes deduced from structure product relationships. *Atmos. Chem. Phys.* **15**, 6745–6765 (2015).
60. Zhang, D. & Zhang, R. Ozonolysis of α -pinene and β -pinene: kinetics and mechanism. *J. Chem. Phys.* **122**, 114308 (2005).
61. Seinfeld, J. H. & Pandis, S. N. *Atmospheric Chemistry and Physics: from Air Pollution to Climate Change* (John Wiley & Sons, 2006).
62. Fuchs, N. A. & Sutugin, A. G. *Coagulation rate of Highly Dispersed Aerosols* (Ann Arbor Science, 1970).
63. Pankow, J. F. An absorption model of gas/particle partitioning of organic compounds in the atmosphere. *Atmos. Environ.* **28**, 185–188 (1994).
64. Korosi, G. & Kovats, E. S. Density and surface tension of 83 organic liquids. *J. Chem. Eng. Data* **26**, 323–332 (1981).
65. Berndt, T. *et al.* Gas-phase ozonolysis of cycloalkenes: formation of highly oxidized RO₂ radicals and their reactions with NO, NO₂, SO₂, and other RO₂ radicals. *J. Phys. Chem. A* **119**, 10336–10348 (2015).
66. Lehtipalo, K. *et al.* Methods for determining particle size distribution and growth rates between 1 and 3 nm using the particle size magnifier. *Boreal Environ. Res.* **19**, 215–236 (2014).
67. Kulmala, M. *et al.* Initial steps of aerosol growth. *Atmos. Chem. Phys.* **4**, 2553–2560 (2004).
68. Mann, G. W. *et al.* Description and evaluation of GLOMAP-mode: a modal global aerosol microphysics model for the UKCA composition-climate model. *Geoscientific Model Dev.* **3**, 519–551 (2010).
69. McNaught, A. D. & Wilkinson, A. *Compendium Of Chemical Terminology* Vol. 1669 (Blackwell Science, 1997).
70. Riipinen, I. *et al.* Organic condensation: a vital link connecting aerosol formation to cloud condensation nuclei (CCN) concentrations. *Atmos. Chem. Phys.* **11**, 3865–3878 (2011).
71. Chipperfield, M. P. New version of the TOMCAT/SLIMCAT off-line chemical transport model: Intercomparison of stratospheric tracer experiments. *Q. J. R. Meteorol. Soc.* **132**, 1179–1203 (2006).
72. Kulmala, M., Laaksonen, A. & Pirjola, L. Parameterizations for sulfuric acid/water nucleation rates. *J. Geophys. Res. D* **103**, 8301–8307 (1998).
73. Guenther, A. *et al.* A global model of natural volatile organic compound emissions. *J. Geophys. Res. D* **100**, 8873–8892 (1995).
74. Kurtén, T. *et al.* Computational study of hydrogen shifts and ring-opening mechanisms in α -pinene ozonolysis products. *J. Phys. Chem. A* **119**, 11366–11375 (2015).



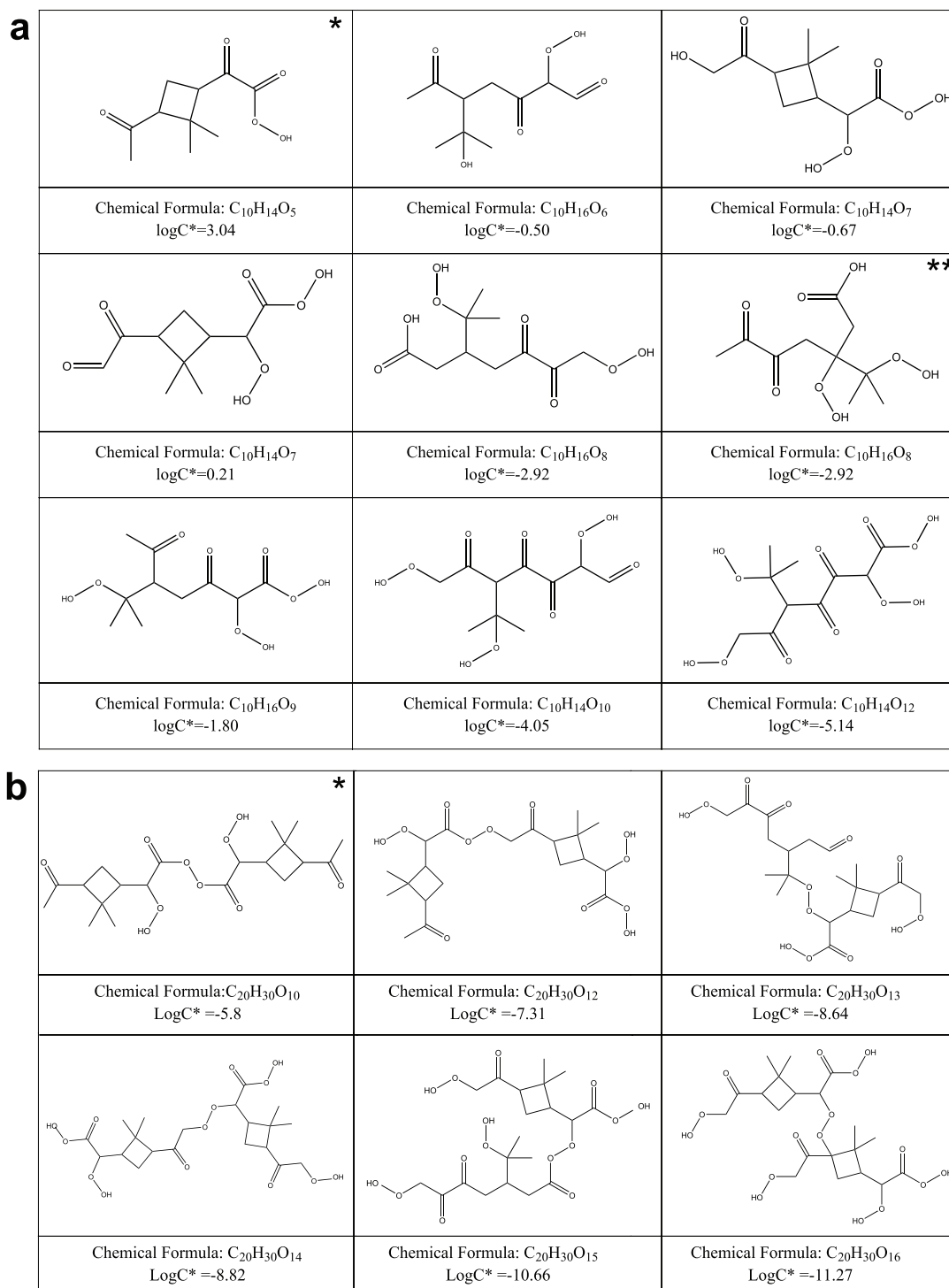
Extended Data Figure 1 | Appearance times of clusters and aerosols as seen by nano-SMPS, NAIS, PSM, APi-TOF, DEG and nRDMA. The different instruments are indicated with different plotting symbols. Instrument descriptions and acronyms can be found in Methods.

RESEARCH LETTER



Extended Data Figure 2 | Observed mass spectrum as seen by the nitrate-CI-APi-TOF at 278 K and 38% relative humidity. A steady-state mixing ratio of approximately 250 p.p.t.v. of α -pinene was established in the chamber in the presence of 35 p.p.b.v. ozone and no injection of SO_2 . Black bars indicate all identified monomers and dimers, with the red

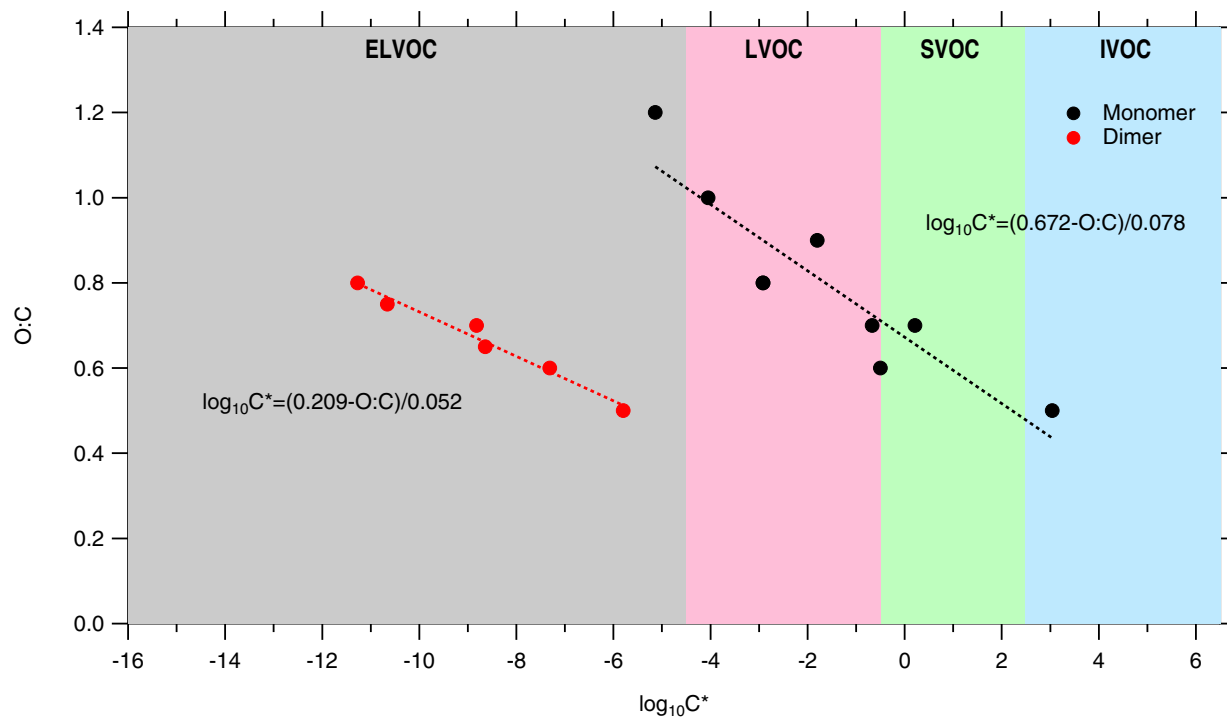
bars indicating the corresponding m/Q range. Intermediate molecules or clusters (with carbon atoms between 11 and 17) that cannot be explained by the formation mechanism shown in Kirkby *et al.*¹⁵ are indicated by the cyan bars.



Extended Data Figure 3 | Possible structures of α -pinene oxidation products. **a**, Possible structures of HOM monomer molecules. C^* was estimated using the SIMPOL method (at 293 K). Note that the volatility is less once the ring structure is open. The volatility generally decreases with

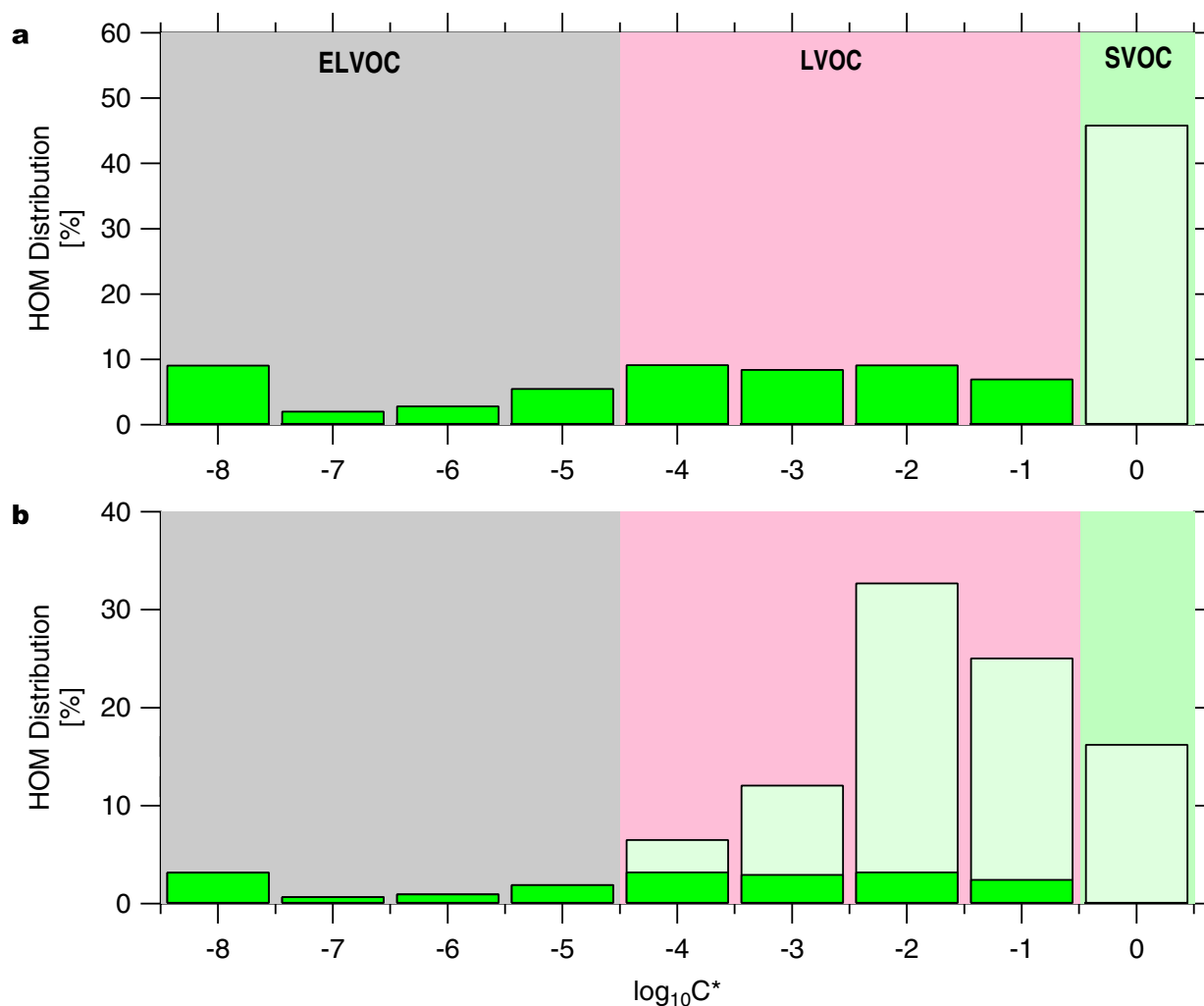
increasing oxidation and decreasing temperature. **b**, Possible structures of HOM dimer molecules. C^* was estimated using the SIMPOL method (at 293 K). Structures in boxes with asterisk(s) at the top right corner were confirmed by (*) or taken from (**) Kurtén *et al.*⁷⁴.

RESEARCH LETTER



Extended Data Figure 4 | Estimation of C* for monomer and dimer molecules at 293 K. Colours indicate the volatility class based on ref. 18. A linear fit was applied to the C* estimates (dashed lines). This fit was then applied to all compounds using their O:C ratio to

estimate their value of C*. Volatility bins comprise ELVOC, LVOC, SVOC and IVOC (intermediate volatile organic compounds with C* from 10^{2.5} to 10^{6.5} μg m⁻³).

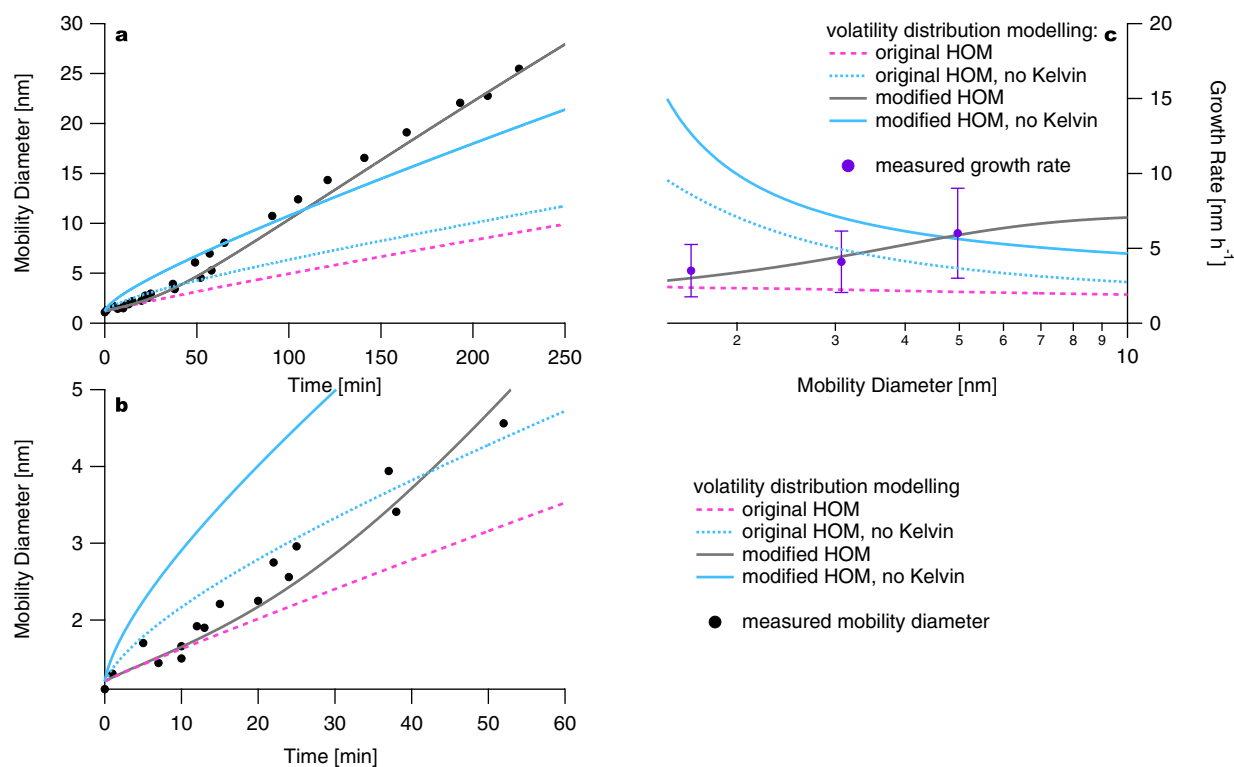


Extended Data Figure 5 | HOM distribution binned to a VBS.

a, Measured HOM distribution (dark green) binned to a VBS. As the nitrate-CI-API-TOF is expected to underestimate SVOC, which are often observed during secondary aerosol formation in smog chamber studies,

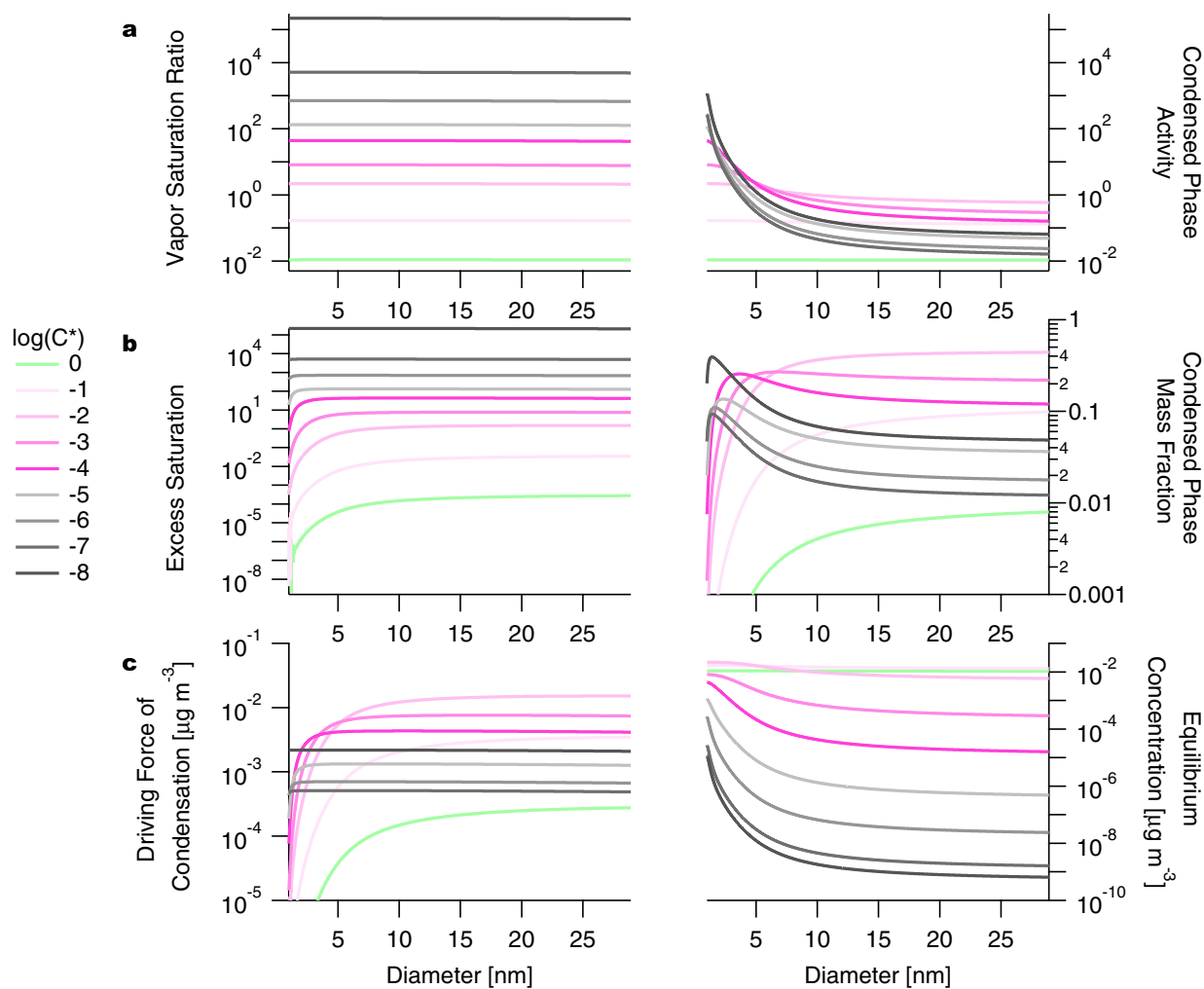
we added a representative SOA bin at $\log C^* = 0$ (light green). **b**, Modified HOM distribution after scaling for the weaker charging efficiency for LVOC (light green). The ELVOC:LVOC:SVOC ratios are **a**, 20:34:46 and **b**, 7:77:16.

RESEARCH LETTER



Extended Data Figure 6 | Dynamic volatility-distribution modelling results with and without a Kelvin term and with original and modified HOM volatility distribution for the case of constant HOMs. a. Different model approaches (key at bottom right) compared to the measured diameter evolution and the first 5 nm of the diameter evolution (key in panel). **c.** Size dependent growth rate for different model approaches (key at bottom right). The Kelvin effect is essential to describe the measured diameter behaviour. Using the original volatility distribution (blue dashed line), the model slightly overestimates the initial growth but strongly underestimates

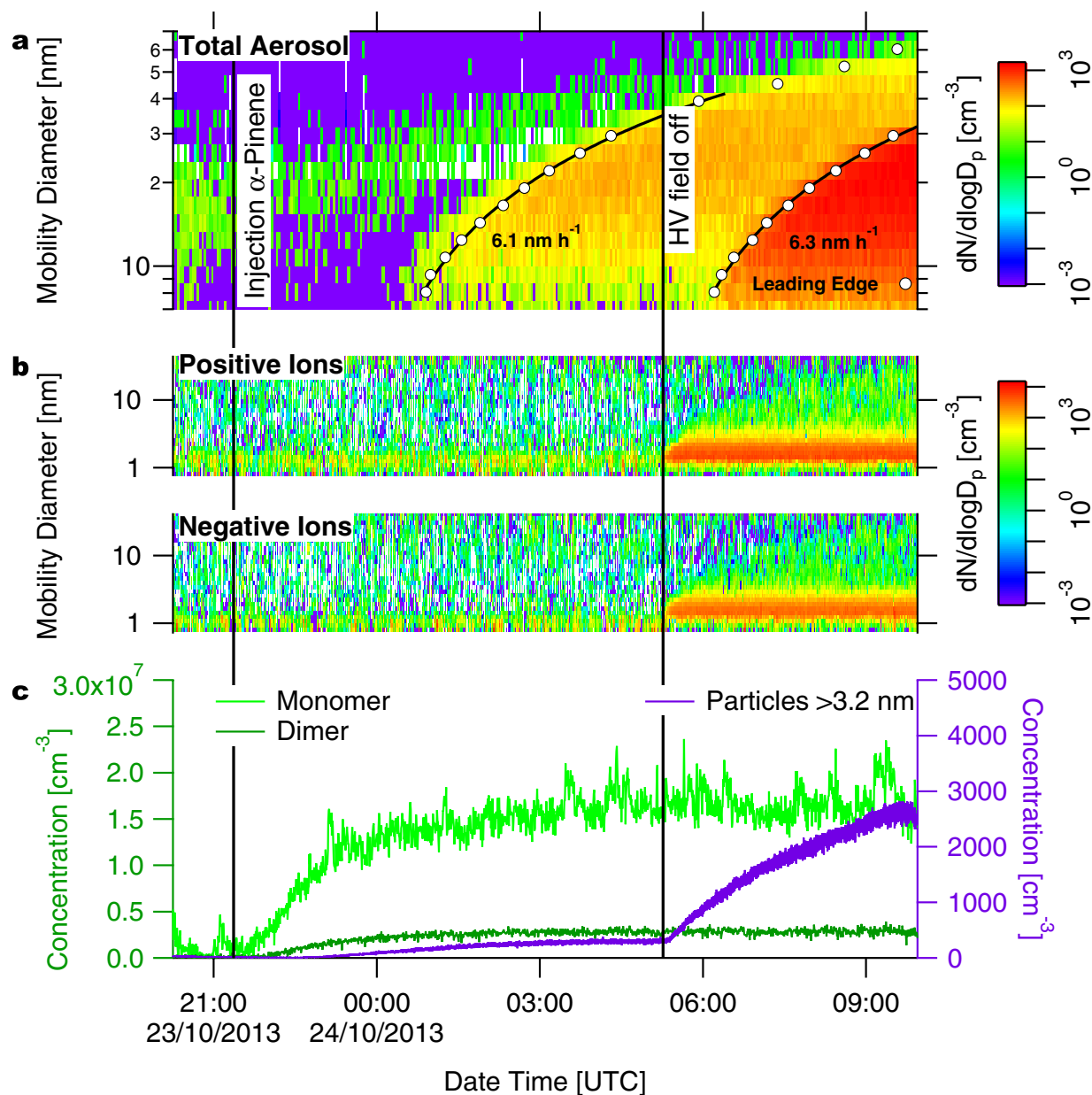
it at larger sizes. Although considering a Kelvin effect fits the initial growth well, growth at larger sizes is underestimated even more (pink dashed line). By adjusting the HOM volatility distribution in the model with no Kelvin effect, the best fit (blue solid curve) still fails to reproduce the observations, substantially overpredicting growth at small sizes and then underpredicting growth at larger sizes. However, adjusting the volatility distribution and treating the Kelvin effect captures the growth well over the full size range (grey solid line). Error bars indicate the 1σ systematic scale uncertainty of the determined growth rates.



Extended Data Figure 7 | Dynamic volatility-distribution model details. **a**, Vapour (left) and condensed-phase (right) activities during a simulated particle growth event in CLOUD (Fig. 3b, d). Vapours are in steady-state with respect to production and wall loss, with the saturation ratio increasing monotonically with decreasing volatility. **b**, Excess saturation ratios (left) and particle composition (mass fractions; right)

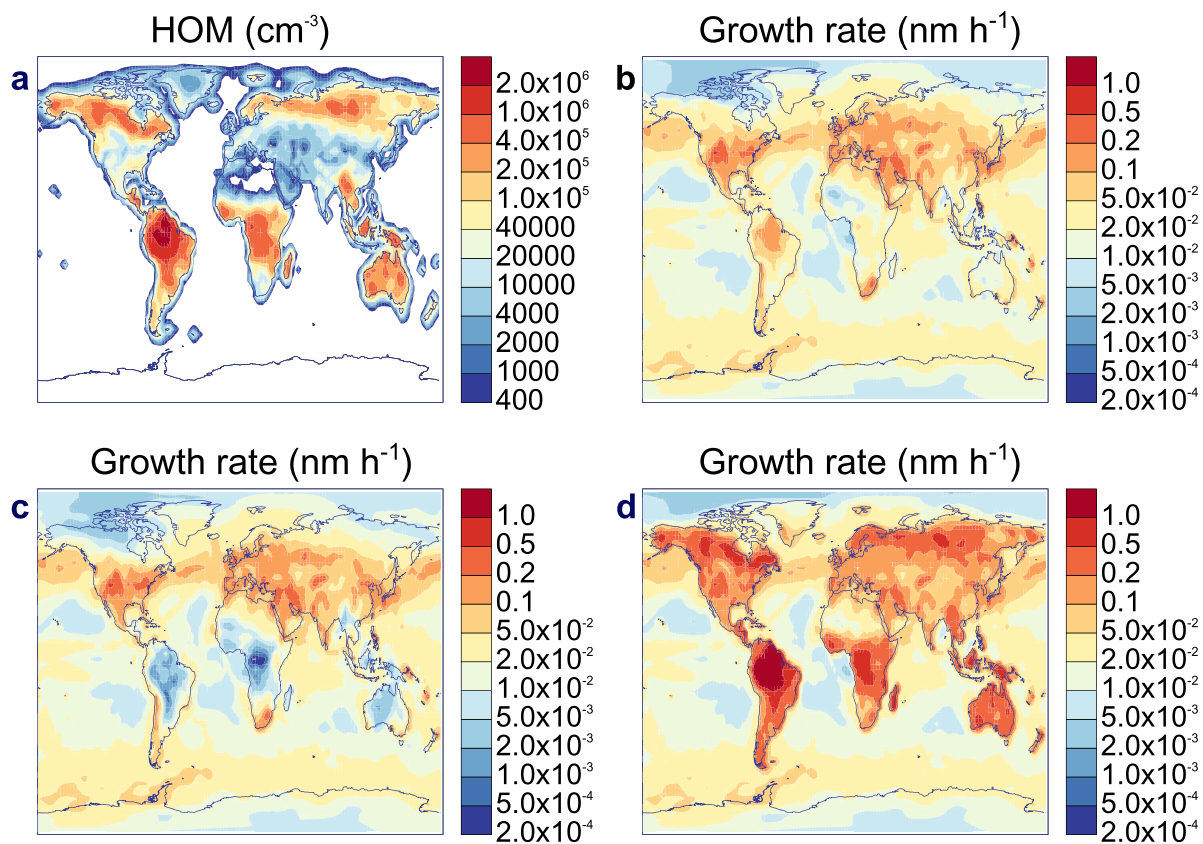
during simulated particle growth event in CLOUD. **c**, Driving force of condensation (left) and equilibrium concentrations of vapours over particles (right) during simulated particle growth events in CLOUD. Volatility is indicated by brightness, with darkest grey corresponding to $C^* = 10^{-8} \mu\text{g m}^{-3}$ (see key).

RESEARCH LETTER



Extended Data Figure 8 | Typical experiment during CLOUD8.
 α -Pinene was injected under neutral conditions. Once stable conditions were achieved, the clearing (HV) field was turned off allowing ions from Galactic cosmic rays to remain in the chamber. This immediately yields a second nucleation. **a**, The nano-SMPS size distribution; **b**, the ion size

distribution as seen by the NAIS ion mode; and **c**, the monomer (light green) and dimer (dark green) and the number particle concentration for particles bigger than 3.2 nm (purple; CPC 3776). The colour keys on the right side relate to the number size distribution ($dN/d\log D_p$).



Extended Data Figure 9 | Annually averaged HOM concentration, and the annually averaged growth rate, simulated by GLOMAP at cloud base level. a, Spatial distribution of HOM concentration (in cm^{-3}). **b–d**, Spatial distribution of growth rates (in nm h^{-1}) using different parameterizations: **b**, using the size-dependent parameterization of initial

particle growth and irreversible condensation of H_2SO_4 , **c**, with growth from 1.7 nm to 3 nm only due to H_2SO_4 , and **d**, with growth from 1.7 nm to 3 nm assuming irreversible condensation of H_2SO_4 together with an organic contribution following ref. 30, which assumes a Kelvin barrier to organic condensation below 2.5 nm.

RESEARCH LETTER

Extended Data Table 1 | Summary of CLOUD runs during CLOUD7 and CLOUD8

CLOUD 7						
RUN	Ozone [p.p.b.v.]	α -pinene [p.p.t.v.]	SO ₂ [p.p.b.v.] [‡]	HOM [cm ⁻³]	Sulfuric Acid [cm ⁻³] [‡]	
1060	20	660	70	1.1·10 ⁷	1.9·10 ⁷	
1061	20	640	70	1.0·10 ⁷	1.8·10 ⁷	
1062	20	180	70	4.2·10 ⁶	7.8·10 ⁶	
1063	20	650	70	1.0·10 ⁷	1.6·10 ⁷	
1065	20	190	70	3.8·10 ⁶	6.5·10 ⁶	
1066	20	650	70	1.3·10 ⁷	8.7·10 ⁶	
1067	20	640	70	1.3·10 ⁷	6.6·10 ⁶	
1068	20	890	70	1.5·10 ⁷	1.2·10 ⁷	
1070	20	1230	70	1.7·10 ⁷	2.4·10 ⁷	
1107	30	420	0.6	1.4·10 ⁷	7.6·10 ⁵	
1108	30	420	0.6	1.4·10 ⁷	6.0·10 ⁵	
1109	30	430	0.6	1.4·10 ⁷	6.3·10 ⁶	
1110	30	430	0.6	1.3·10 ⁷	5.1·10 ⁶	
1111	30	430	1.6	1.4·10 ⁷	5.6·10 ⁶	
1113	30	370	1.6	1.3·10 ⁷	5.5·10 ⁶	
1114	30	390	1.6	5.8·10 ⁶	4.3·10 ⁶	

[‡] measured with SO₂ monitor (Thermo scientific, 43i-TLE)

[‡] measured with CIMS

CLOUD 8						
RUN	Ozone [p.p.b.v.]	α -pinene [p.p.t.v.]	SO ₂ [p.p.b.v.]	HOM [cm ⁻³]	Sulfuric Acid [cm ⁻³]	
1208	32	20	- ^o	2.9·10 ⁶	6.8·10 ⁴	
	34	40	- ^o	5.8·10 ⁶	6·10 ⁴	
	34	110	- ^o	1.4·10 ⁷	7.4·10 ⁴	
1209	35	250	- ^o	2.0·10 ⁷	3.8·10 ⁴	
1210	35	510	- ^o	3.4·10 ⁷	3.4·10 ⁴	
1211	34	240	5	1.7·10 ⁷	-*	
1212	32	1340	20	1.0·10 ⁸	7.5·10 ⁵	
1213	33	1280	10	7.4·10 ⁷	1.3·10 ⁵	
1214	33	170	8	1.4·10 ⁷	8.2·10 ⁴	
1215	33	90	6	7.4·10 ⁶	6.3·10 ⁴	
1217	32	270	40	1.9·10 ⁷	1.1·10 ⁵	
1218	33	250	150	1.7·10 ⁷	4.4·10 ⁵	
1219	34	250	1300	1.4·10 ⁷	2.9·10 ⁶	
1220	33	240	1500	1.2·10 ⁷	3.3·10 ⁶	
1221	31	11000	20	2.1·10 ⁸	3.1·10 ⁴	
1222	31	7750	20	1.8·10 ⁸	2.9·10 ⁴	
1224	33	900	-*	4.2·10 ⁷	9.4·10 ⁵	
1225	31	15700	-*	2.5·10 ⁸	2.6·10 ⁵	
1226	31	60	-*	3.8·10 ⁶	8.2·10 ⁴	
1226	30	700	-*	2.8·10 ⁷	5.1·10 ⁴	
1227	33	460	-*	1.9·10 ⁷	3.1·10 ⁴	
1229	33	290	4000	9.2·10 ⁶	3.1·10 ⁷	

* no measurement available

^o no SO₂ injected

Each run consisted of several stages (increasing gases, steady-state, changing charging state of chamber, see also Extended Data Fig. 8), here only the steady-state plateau values are indicated.

- 4.7 Rapid growth of organic aerosol nanoparticles over a wide tropospheric temperature range**
(Stolzenburg et al. (2018))



Rapid growth of organic aerosol nanoparticles over a wide tropospheric temperature range

Dominik Stolzenburg^a, Lukas Fischer^b, Alexander L. Vogel^{c,d,e}, Martin Heinritzi^c, Meredith Schervish^f, Mario Simon^c, Andrea C. Wagner^c, Lubna Dada^g, Lauri R. Ahonen^g, Antonio Amorim^{h,i}, Andrea Baccarini^e, Paulus S. Bauer^a, Bernhard Baumgartner^a, Anton Bergen^c, Federico Bianchi^g, Martin Breitenlechner^{b,j,k}, Sophia Brilke^a, Stephany Buenrostro Mazon^g, Dexian Chen^f, António Dias^{d,h,i}, Danielle C. Draper^l, Jonathan Duplissy^g, Imad El Haddad^e, Henning Finkenzeller^m, Carla Frege^e, Claudia Fuchs^e, Olga Garmash^g, Hamish Gordon^{d,n}, Xucheng He^g, Johanna Helm^c, Victoria Hofbauer^f, Christopher R. Hoyle^o, Changhyuk Kim^{p,q}, Jasper Kirkby^{c,d}, Jenni Kontkanen^g, Andreas Kürten^c, Janne Lampilahti^g, Michael Lawler^l, Katrianne Lehtipalo^g, Markus Leiminger^b, Huajun Mai^p, Serge Mathot^d, Bernhard Mentler^b, Ugo Molteni^e, Wei Nie^r, Tuomo Nieminen^s, John B. Nowak^t, Andrea Ojdanic^a, Antti Onnela^d, Monica Passananti^g, Tuukka Petäjä^g, Lauriane L. J. Quéléver^g, Matti P. Rissanen^g, Nina Sarnela^g, Simon Schallhart^{g,u}, Christian Tauber^a, António Tomé^v, Robert Wagner^g, Mingyi Wang^l, Lena Weitz^c, Daniela Wimmer^g, Mao Xiao^e, Chao Yan^f, Penglin Ye^{f,t}, Qiaozhi Zha^g, Urs Baltensperger^e, Joachim Curtius^c, Josef Dommen^e, Richard C. Flagan^p, Markku Kulmala^{g,w}, James N. Smith^l, Douglas R. Worsnop^{g,t}, Armin Hansel^{b,x}, Neil M. Donahue^f, and Paul M. Winkler^{a,1}

^aFaculty of Physics, University of Vienna, 1090 Vienna, Austria; ^bInstitute for Ion Physics and Applied Physics, University of Innsbruck, 6020 Innsbruck, Austria; ^cInstitute for Atmospheric and Environmental Sciences, Goethe University Frankfurt, 60438 Frankfurt am Main, Germany; ^dCERN, the European Organization for Nuclear Research, 1211 Geneva, Switzerland; ^eLaboratory of Atmospheric Chemistry, Paul Scherrer Institute, 5232 Villigen, Switzerland; ^fCenter for Atmospheric Particle Studies, Carnegie Mellon University, Pittsburgh, PA 15213; ^gInstitute for Atmospheric and Earth System Research/Physics, Faculty of Science, University of Helsinki, 00014 Helsinki, Finland; ^hCentro Multidisciplinar de Astrofísica, University of Lisbon, 1749-016 Lisbon, Portugal; ⁱFaculdade de Ciências da Universidade de Lisboa, University of Lisbon, 1749-016 Lisbon, Portugal; ^jJohn A. Paulson School of Engineering and Applied Sciences, Harvard University, Cambridge, MA 02138; ^kDepartment of Chemistry and Chemical Biology, Harvard University, Cambridge, MA 02138; ^lDepartment of Chemistry, University of California, Irvine, CA 92697; ^mDepartment of Chemistry and Biochemistry, University of Colorado Boulder, Boulder, CO 80309; ⁿSchool of Earth and Environment, University of Leeds, LS2 9JT Leeds, United Kingdom; ^oInstitute for Atmospheric and Climate Science, ETH Zurich, 8092 Zurich, Switzerland; ^pDivision of Chemistry and Chemical Engineering, California Institute of Technology, Pasadena, CA 91125; ^qDepartment of Environmental Engineering, Pusan National University, 46241 Busan, Republic of Korea; ^rJoint International Research Laboratory of Atmospheric and Earth System Sciences, Nanjing University, 210023 Nanjing, China; ^sDepartment of Applied Physics, University of Eastern Finland, 70211 Kuopio, Finland; ^tAerodyne Research Inc., Billerica, MA 01821; ^uFinnish Meteorological Institute, 00101 Helsinki, Finland; ^vInstituto Infante Dom Luiz, University of Beira Interior, 6200 Covilhã, Portugal; ^wAerosol and Haze Laboratory, Beijing Advanced Innovation Center for Soft Matter Science and Engineering, Beijing University of Chemical Technology, Beijing, China; and ^xIonicon Analytik GmbH, 6020 Innsbruck, Austria

Edited by John H. Seinfeld, California Institute of Technology, Pasadena, CA, and approved July 30, 2018 (received for review May 3, 2018)

Nucleation and growth of aerosol particles from atmospheric vapors constitutes a major source of global cloud condensation nuclei (CCN). The fraction of newly formed particles that reaches CCN sizes is highly sensitive to particle growth rates, especially for particle sizes <10 nm, where coagulation losses to larger aerosol particles are greatest. Recent results show that some oxidation products from biogenic volatile organic compounds are major contributors to particle formation and initial growth. However, whether oxidized organics contribute to particle growth over the broad span of tropospheric temperatures remains an open question, and quantitative mass balance for organic growth has yet to be demonstrated at any temperature. Here, in experiments performed under atmospheric conditions in the Cosmics Leaving Outdoor Droplets (CLOUD) chamber at the European Organization for Nuclear Research (CERN), we show that rapid growth of organic particles occurs over the range from -25°C to 25°C . The lower extent of autoxidation at reduced temperatures is compensated by the decreased volatility of all oxidized molecules. This is confirmed by particle-phase composition measurements, showing enhanced uptake of relatively less oxygenated products at cold temperatures. We can reproduce the measured growth rates using an aerosol growth model based entirely on the experimentally measured gas-phase spectra of oxidized organic molecules obtained from two complementary mass spectrometers. We show that the growth rates are sensitive to particle curvature, explaining widespread atmospheric observations that particle growth rates increase in the single-digit-nanometer size range. Our results demonstrate that organic vapors can contribute to particle growth over a wide range of tropospheric temperatures from molecular cluster sizes onward.

The global budget of cloud condensation nuclei (CCN) significantly influences the Earth's radiative balance, as it affects the albedo and the lifetime of clouds. New particle formation by gas-to-particle conversion is the largest source of CCN (1). Especially the early steps of particle growth between 1 and 10 nm determine the survival chance of freshly formed particles and therefore their climatic relevance (2, 3). The major vapors driving particle growth are sulfuric acid and, maybe more importantly, low-volatility organics resulting from the oxidation of volatile organic compounds (VOCs) (4). Monoterpenes are an important class of atmospheric VOCs with copious emissions from vegetation (5). They are quickly oxidized in the atmosphere and, through a subsequent autoxidation process, rapidly

Author contributions: D.S., L.F., A.L.V., H.G., J. Kirkby, A. Onnela, U.B., J.C., J. Dommen, R.C.F., M.K., D.R.W., A.H., N.M.D., and P.M.W. designed research; D.S., L.F., A.L.V., M.H., M. Simon, A.C.W., L.D., L.R.A., A.A., A. Baccarini, P.S.B., B.B., A. Bergen, F.B., M.B., S.B., S.B.M., D.C., A.D., D.C.D., J. Duplissy, I.E.H., H.F., C. Frege, C. Fuchs, O.G., H.G., X.H., J.H., V.H., C.R.H., C.K., J. Kirkby, J. Kontkanen, A.K., J.L., M. Lawler, K.L., M. Leiminger, H.M., S.M., B.M., U.M., W.N., T.N., J.B.N., A. Ojdanic, A. Onnela, M.P., T.P., L.L.J.Q., M.P.R., N.S., S.S., C.T., A.T., R.W., M.W., L.W., D.W., M.X., C.Y., P.Y., and Q.Z. performed research; D.S., L.F., M.B., A.H., and P.M.W. contributed new reagents/analytic tools; D.S., L.F., A.L.V., M.H., M. Schervish, M. Simon, A.C.W., L.D., D.C.D., M. Lawler, R.W., L.W., and J.N.S. analyzed data; and D.S., L.F., A.L.V., M.H., J. Kirkby, N.M.D., and P.M.W. wrote the paper.

The authors declare no conflict of interest.

This article is a PNAS Direct Submission.

This open access article is distributed under Creative Commons Attribution-NonCommercial-NoDerivatives License 4.0 (CC BY-NC-ND).

¹To whom correspondence should be addressed. Email: paul.winkler@univie.ac.at.

This article contains supporting information online at www.pnas.org/lookup/suppl/doi:10.1073/pnas.1807604115/-DCSupplemental.

Published online August 28, 2018.

aerosols | nanoparticle growth | aerosol formation | CLOUD experiment | volatile organic compounds

Significance

Aerosol particles can form and grow by gas-to-particle conversion and eventually act as seeds for cloud droplets, influencing global climate. Volatile organic compounds emitted from plants are oxidized in the atmosphere, and the resulting products drive particle growth. We measure particle growth by oxidized biogenic vapors with a well-controlled laboratory setup over a wide range of tropospheric temperatures. While higher temperatures lead to increased reaction rates and concentrations of highly oxidized molecules, lower temperatures allow additional, but less oxidized, species to condense. We measure rapid growth over the full temperature range of our study, indicating that organics play an important role in aerosol growth throughout the troposphere. Our finding will help to sharpen the predictions of global aerosol models.

form highly oxygenated molecules (HOMs), which constitute a large source of low-volatility species in the atmosphere (6). Recent studies have shown that HOMs from the ozonolysis of the predominant monoterpene α -pinene are able to form (7) and efficiently grow particles from cluster sizes onward (8). Model simulations suggest that they are major contributors to particle formation on a global scale (9). Moreover, the impact of HOMs on initial particle growth might explain the observations of increasing growth rates with particle size between 1 and 10 nm during particle-formation events (10) by a multicomponent Kelvin effect (8, 11), also known as nano-Köhler theory (12). This is because HOMs span a wide range of volatilities (13), and, with increasing particle size, more and more low-volatility species can contribute to the growth process.

In contrast to sulfuric acid plus ammonia or amines, where growth proceeds close to the kinetic limit (14), growth driven by organics is governed by the resulting volatilities of the wide variety of oxidation products. Therefore, temperature likely plays a decisive role, as the saturation concentration has a steep exponential temperature dependence as described by the Clausius–Clapeyron relation. Additionally, a recent study has shown that temperature crucially influences the chemical composition of the initially formed molecular clusters in α -pinene ozonolysis (15). Therefore, the contribution of biogenic organics to new particle formation might be strongly sensitive to temperature. This, in turn, may significantly influence the importance of new particle formation at high altitudes (16) and in outflow regions of deep-convective clouds—for example, over the Amazon Basin (17–19).

Here, we investigate in the Cosmics Leaving Outdoor Droplets (CLOUD) chamber (20) the effect of temperature on the production of oxygenated molecules and subsequent particle growth from dark α -pinene ozonolysis at three different temperatures (-25°C , 5°C , and 25°C) for various precursor concentrations. The resulting volatility distributions are inferred by combining two types of chemical ionization (CI) high-resolution time of flight mass spectrometers (TOF-MS) (21, 22) using complementary ionization techniques to obtain a detailed representation of the gaseous oxidation products. Together with the precision measurement of particle growth rates (23) and analysis of the particle-phase composition (24), this allows identification of the underlying processes and their temperature dependence responsible for initial growth in biogenic ozonolysis systems (see *Materials and Methods* for details about the experimental setup and measurement procedures).

Results

Observed Gas-Phase Composition and Volatility Distribution. We measured gas-phase composition with a nitrate-CI atmospheric pressure interface (APi)-TOF-MS (nitrate-CI) (21) and a proton

transfer reaction (PTR)-TOF-MS (PTR3) (22) to obtain a more detailed overview of the neutral gas-phase species present during the α -pinene ozonolysis experiments. We obtained overlap for peaks observed in both instruments (*SI Appendix*, Fig. S3) and show a combined mass-defect plot of both instruments for three representative experiments at three different temperatures in *SI Appendix*, Fig. S4. The PTR3 introduces >200 previously undetected molecular ion signals, not only HOMs, which are usually specified by their high oxygen to carbon ratio ($\text{O}:\text{C} > 0.7$ for monomers), but mostly compounds toward lower oxidation states. For molecules with identified chemical composition, a volatility can be assigned according to the number of oxygen atoms n_{O} and the number of carbon atoms n_{C} within the molecule (*SI Appendix*).

As volatilities of organic compounds observed in the atmosphere vary by >10 orders of magnitude and the combined mass spectra contain ~ 500 different molecules, it is convenient to simplify considerations of gas-to-particle partitioning by grouping compounds together within a volatility basis set (VBS) (13, 25). Within this framework, the volatility bins are separated by one decade in C^* at 300 K, and for other temperatures, the binned distribution is shifted toward lower saturation mass concentrations. The saturation mass concentration of oxidized organics should follow the Clausius–Clapeyron relation at a constant evaporation enthalpy ΔH_{vap} , which in turn is linked to C^* at 300 K (13) (*SI Appendix*).

Fig. 1 shows the resulting binned volatility distribution of all observed organic gas-phase compounds for three representative experiments. We averaged observed gas-phase concentrations

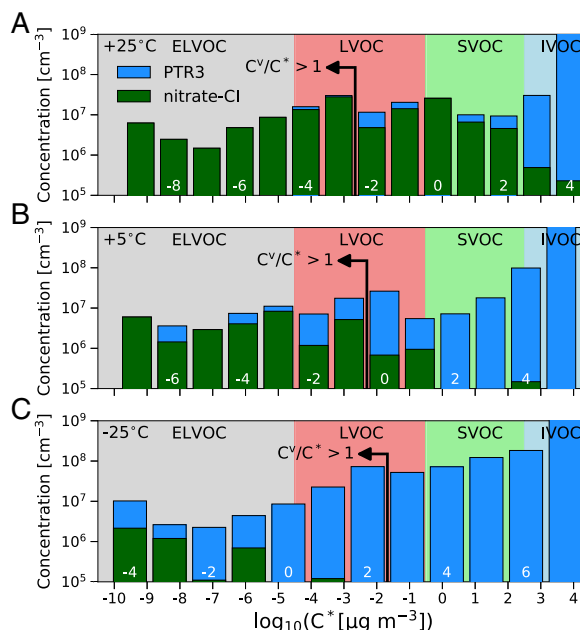


Fig. 1. Volatility distributions for representative experiments with similar α -pinene ozonolysis rate: 25°C (A), 5°C (B), and -25°C (C). The green and blue bars show summed molecular ions observed in the nitrate-CI and PTR3, respectively. The highest and lowest bin are overflow bins. Volatility bins are defined at 300 K, shifted, and widened according to their corresponding temperature. The resulting saturation mass concentration is defined on the x axis, while $\log_{10} C_{300\text{K}}^*$ is specified by white numbers. Additionally, the bins in supersaturation with $C^*/C_{300\text{K}}^* > 1$ are found left of the indicating arrow. ELVOC, extremely low-volatility organic compound; IVOC, intermediate-volatility organic compound; LVOC, low-volatility organic compound; SVOC, semi-volatile organic compound.

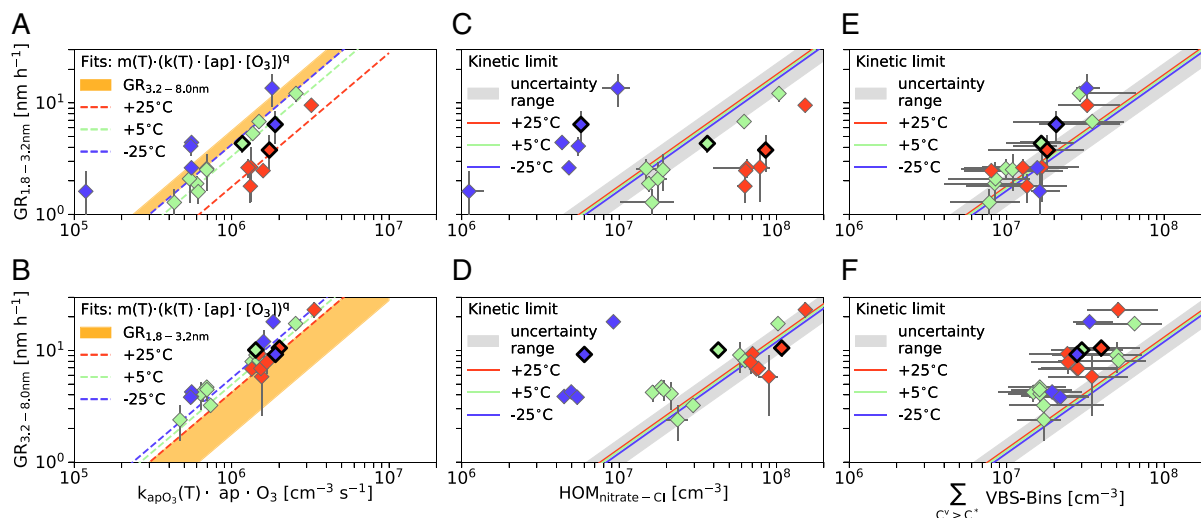


Fig. 2. Growth rates (GR) measured by the DMA train in two size intervals [1.8–3.2 nm (A, C, and E) and 3.2–8 nm (B, D, and F)] vs. several gas-phase variables. Representative experiments are highlighted. On the x axis, A and B show the reacted α -pinene rate, C and D show the HOMs observed in the nitrate-Cl, and E and F show the amount of condensable material determined by the temperature-dependent volatility basis set. Colors in all plots indicate the run temperatures: purple corresponds to -25°C , green to 5°C , and red to 25°C . In A and B, the light yellow areas shows the range of growth rates of the other size interval to demonstrate the observed lower growth rates at small diameters. In C–F, the gray areas illustrate the range of uncertainty on the kinetic condensation limits drawn as solid colored lines. In E and F, the error on the sum over the VBS distribution is determined from the 1-decade uncertainty in the volatility definition.

C^v over a period where comparable particle growth rates are measured with a differential mobility analyzer (DMA) train (23), and the α -pinene ozonolysis rate is similar with $k(T) \cdot [\text{ap}] \cdot [\text{O}_3] \sim 1.4 - 2.0 \cdot 10^6 \text{ cm}^{-3} \text{ s}^{-1}$.

Due to the comparable growth rates of the three examples, the gas-particle partitioning is expected to be comparable, which is confirmed by the similarity of the observed total volatility distribution over the extremely low-volatility organic compound (ELVOC) and low-volatility organic compound (LVOC) ranges. Earlier work on growth of nucleated particles from α -pinene oxidation at 5°C using only a nitrate-Cl found that the measured HOMs could only explain a fraction of the growth and speculated that the nitrate detection efficiency was progressively lower for less polar (and, hence, more volatile) species (8). We confirmed the missing fraction and found that the PTR3 detected many new compounds, mainly less-oxygenated molecules with $n_{\text{O}} \leq 7$, not measured by the nitrate-Cl, independent of temperature. At low temperature, fewer polar functional groups are required for a compound to have a low volatility, and thus at 5°C , and even more significantly at -25°C (Fig. 1 B and C, respectively), these species observed by the PTR3 contribute substantially in the LVOC and even ELVOC range.

Particle-Growth Measurements. We measured growth rates during the experiments with a DMA train over two different size intervals, 1.8–3.2 and 3.2–8 nm, by the appearance time method as it was done in comparable studies (8, 14). It gives robust apparent particle-growth rates for chamber experiments and is not affected by measurement uncertainties in absolute particle concentrations due to possible evaporation effects during the measurement procedure (SI Appendix). Fig. 2 shows the measured growth rates vs. several gas-phase variables. Fig. 2A and B shows the correlation with the estimated reaction rate of the α -pinene ozonolysis during the growth rate measurement. Higher reaction rates, and hence higher product concentrations, lead to higher growth rates, following an exponential relation $m(T, d_p) \cdot$

$(k(T) \cdot [\text{ap}] \cdot [\text{O}_3])^q$ (SI Appendix). For a given α -pinene ozonolysis reaction rate, we find lower growth rates at smaller sizes. The smaller size range also shows a more significant temperature dependency: The growth rates are higher at low temperatures at a given reaction rate. This indicates that the ozonolysis products at the three different temperatures have different properties influencing their ability to condense from molecular cluster sizes onward.

Fig. 2 C and D shows the measured growth rates vs. the total HOM signal observed in the nitrate-Cl only, along with a kinetic curve showing the growth rate if all measured HOMs condensed irreversibly (26). The growth rates of the three different temperatures are clearly separated, but condensation at the kinetic limit for HOMs would give almost identical values. Thus, the total HOM concentration observed in the nitrate-Cl cannot fully describe the observed growth at any temperature. At 25°C , several HOMs measured by the nitrate-Cl are classified as semi-volatile organic compounds and might not be able to condense, and at -25°C , the nitrate-Cl measures only a small fraction of the less-oxygenated α -pinene oxidation products responsible for particle growth (Fig. 1).

Therefore, Fig. 2 E and F shows the growth rates vs. a sum, combining both mass spectrometers, over all VBS bins in supersaturation for a given particle size—that is, with $S = K(D_p) \cdot C_{\text{VBS bin}}^v / C_{\text{VBS bin}}^* > 1$. A Kelvin term $K(D_p) = 10^{D_{K10}/D_p}$ accounts for the curvature of the particles, slowing growth of smaller particles. With this simple approach, it is possible to bring the growth measurements at these three different temperatures into reasonable agreement, aligning the data points roughly parallel to the kinetic line. This approach only accounts for bins in supersaturation, which should condense almost kinetically. Especially for the larger size interval, the measured growth rates were slightly higher than the supersaturated kinetic limits for all temperatures. However, some VBS bins below supersaturation will contribute as well by gas-particle partitioning, which was not considered in this simple approach.

Comparison with an Aerosol Growth Model. We modeled growth with the same framework as used in ref. 8. However, we modified the model to take real-time measured VBS distributions from both mass spectrometers as input, without any adjustments of unknown charging efficiencies (*SI Appendix*).

The most important remaining unknown in the condensation equations is the Kelvin term, $K(D_p) = 10^{D_{K10}/D_p}$, parametrized for simplicity by a decadal Kelvin diameter related to bulk liquid properties $D_{K10} = \log_{10}(e) \cdot (4\sigma M) \cdot (RT\rho)^{-1}$. However, the observed size dependence and especially the growth measurements at diameters $< D_{K10}$ should provide a direct constraint on the curvature effect. For the three representative experiments, we found the best agreement with $D_{K10}(T) = (4.8 \pm 0.8) \cdot (300 \text{ K} \cdot T^{-1}) \text{ nm}$. This corresponds to reasonable average properties (surface tension $\sigma = 0.03 \text{ N}\cdot\text{m}^{-1}$, molecular mass $M = 320 \text{ g}\cdot\text{mol}^{-1}$, and density $\rho = 1,400 \text{ kg}\cdot\text{m}^{-3}$) for the many condensing species, ignoring other possible temperature dependencies in ρ , σ , and M . Fig. 3 shows the resulting predicted growth rates and their size dependence in comparison with the measurements. The agreement between modeled and measured growth rate at the smallest sizes is within the uncertainties of the measurements. Other values for D_{K10} —for example, $D_{K10}(300 \text{ K}) = 3.75 \text{ nm}$, used previously—lead to

a significant overestimation of the observed growth rates at the smallest diameters for all temperatures. Another reason for the higher D_{K10} could be an underestimation of the volatility of the most oxygenated compounds (27). Above 5 nm, the model agreed well with the observations at all temperatures. Considering the 1-decade uncertainty in saturation mass concentration (*SI Appendix*), we achieved reasonable mass balance for growth of freshly nucleated particles between 2 and 30 nm over a wide range of conditions.

Although there was no disagreement of the model with the measurements, within the uncertainties, there are several contributions that we have not considered. First, some condensable compounds might still be undetected by the two used ionization chemistries. Additionally, fragmentation of molecules within the instruments might disturb the volatility estimate. Second, the temperature dependence of organic volatilities is also subject to uncertainties (13). Third, we did not model any particle-phase reactions, such as oligomerization. Reactive uptake is thought to be more important at larger particle sizes (28), again in part because of the Kelvin effect (29).

Particle-Phase Composition Measurements. The predictions by the aerosol growth model were supported by the measurement of the particle-phase composition using a filter inlet for gas and aerosols (FIGAERO) (24) attached to a O_2^- -CI-API-TOF-MS [FIGAERO-chemical ionization mass spectrometer (CIMS)] (*SI Appendix*). Fig. 4 shows the desorption profiles of three molecular ion signals corresponding to $\text{C}_{10}\text{H}_{16}\text{O}_4$, $\text{C}_{10}\text{H}_{16}\text{O}_6$, and $\text{C}_{10}\text{H}_{16}\text{O}_9$. We accumulated particles on the FIGAERO filter inlet at chamber temperature during the three experiments at -25°C , 5°C , and 25°C . The signal intensity was normalized to the accumulated mass on the filter inferred from the measured particle-size distributions and sample flow rate, which allowed for quantitative comparison of the three temperatures. We fit the desorption profiles with a bimodal distribution, where the first mode represented the monomer signal and the second mode was due to fragmentation products of less volatile dimers which therefore desorb at higher temperatures (*SI Appendix*). Desorption of the monomer clearly occurred earlier for the less-oxygenated products, which experimentally confirmed the volatility dependence on n_{O} used for the volatility estimates.

It was evident that the less-oxygenated monomers only appeared at lower temperature in the particle phase. $\text{C}_{10}\text{H}_{16}\text{O}_4$ contributed significantly only at -25°C , and $\text{C}_{10}\text{H}_{16}\text{O}_6$ appeared already at 5°C in the particle phase. For $\text{C}_{10}\text{H}_{16}\text{O}_9$, a subsequent reduction in the normalized particle-phase intensity was observed for decreasing temperatures. Although the volatility of this molecule is low enough to contribute significantly even at 25°C , its production in the gas phase was reduced at lower temperatures, and its contribution to the particle phase thus decreased with decreasing temperature.

These trends are supported by the comparison of gas- and particle-phase composition within the representative $\text{C}_{10}\text{H}_{16}\text{O}_{3-9}$ series, which contains the most dominant peaks of the particle-phase mass spectra. In Fig. 5, the fractional contributions of $\text{C}_{10}\text{H}_{16}\text{O}_{3-9}$ are shown for the gas and particle phase for the three investigated temperatures. Generally, the most abundant gas-phase product at all temperatures within this series is pinonic acid ($\text{C}_{10}\text{H}_{16}\text{O}_3$), having a similar yield to all HOM products together (7, 30). However, the fraction of the contribution of highly oxygenated products increased significantly at warmer temperatures (see also *SI Appendix*, Fig. S4), while at -25°C , less oxygenated products dominated the gas phase completely. In the particle phase, HOM products were mainly found at 25°C , while at lower temperatures, the particle phase contained a large contribution of less-oxygenated molecules with even a strong contribution of the modestly oxygenated pinonic

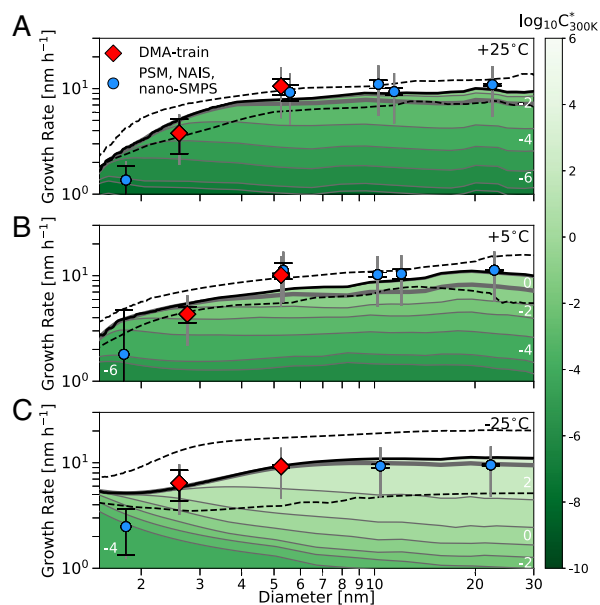


Fig. 3. Modeled and measured growth rate vs. particle diameter. (A) Shown is 25°C at increasing α -pinene ozonolysis reaction rates ($\sim 1.7 - 2.3 \cdot 10^6 \text{ cm}^{-3}\text{s}^{-1}$). (B) Shown is 5°C at increasing reaction rates ($\sim 1.2 - 1.8 \cdot 10^6 \text{ cm}^{-3}\text{s}^{-1}$). (C) Shown is -25°C at constant reaction rates ($\sim 1.9 \cdot 10^6 \text{ cm}^{-3}\text{s}^{-1}$). The thick black lines indicate the modeled total growth rate inferred from real-time oxidized organics measurements, and the dashed black lines indicate the associated uncertainty resulting from a ± 1 bin shift of the VBS distribution. The contribution of the different bins of the VBS distribution is illustrated by the colored areas, where white numbers and the color code represent the saturation mass concentration at 300 K for all three cases. The contribution below the thick gray line is from bins with $C^* > C^*$. For the measured growth rates, red diamonds show the DMA train (shown as well in Fig. 2) and blue circles show other instruments: the neutral cluster and air ion spectrometer (NAIS), the nanoscanning mobility particle sizer (nano-SMPS), and the particle-size magnifier (PSM) (*SI Appendix*). The capped black error bar shows the statistical uncertainty of the single measurements, while the gray error bar gives the 50% systematic uncertainty of the appearance time method.

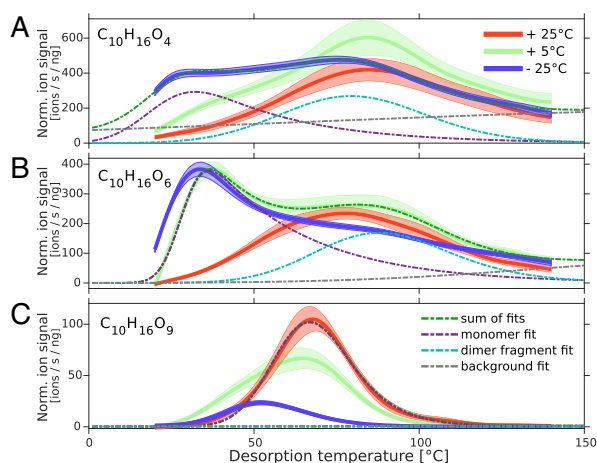


Fig. 4. Mean thermal desorption profile of three compounds found in particle-phase composition measurements with a FIGAERO-CIMS and the corresponding SE (shaded areas). The signal intensity normalized (Norm.) by primary ion signal and collected particle mass vs. the desorption temperature is compared for three representative experiments with red indicating 25 °C, green indicating 5 °C, and dark blue indicating –25 °C. For all three temperatures, the mean of the median mass diameters during sampling was between 40 and 50 nm, which should be representative for sizes $\gg D_{K10}$. A shows the desorption profiles of $C_{10}H_{16}O_4$, B of $C_{10}H_{16}O_6$, and C of $C_{10}H_{16}O_9$. Fits for the monomer, dimer fragment, and background signal are indicated for a single temperature on each profile.

acid. This is not only because of the decrease of the availability of gas-phase HOM products, but mainly due to a strong drop in volatility of all compounds, resulting in condensation of lower-oxygenated products. This is similar to the observations in ref. 15, where a significant decrease in O:C of the nucleating charged clusters was observed at colder temperatures.

Conclusion

Organics play a leading role in atmospheric new particle formation and growth and thus govern the global budget of CCN. VOC oxidation products in the atmosphere make up a substantial portion of condensing vapors causing growth of existing particles. Because oxidized organics span a wide range of volatilities, temperature is a crucial parameter. We use a combination of mass spectrometers, two using complementary ionization techniques for gas-phase measurements and one measuring particle-phase composition. Consideration of the volatility distribution of the measured gas-phase compounds, here with a volatility basis set, gives a sufficient constraint of the gas-phase products to comprehensively describe growth over a wide temperature range. The measured and modeled particle-phase compositions are self-consistent. The measurements are in good agreement with an aerosol growth model, and a direct estimate of the Kelvin diameter for organics of (4.8 ± 0.8) nm at 300 K could be inferred.

Temperature influences the growth by organics from dark α -pinene ozonolysis in several ways via competing processes. At higher temperatures, the increasing extent of autoxidation leads to high yields of highly oxygenated products in the gas phase. This is due to the temperature dependence of the unimolecular autoxidation reactions. It is highly likely that the intramolecular H-atom transfer reactions have significantly higher activation energies than radical–radical termination reactions, and so it is reasonable that the extent of autoxidation will increase with increasing temperature (31). On the other hand, the strong drop in volatility leads to significant condensation of less-oxygenated

molecules at lower temperatures. Our precision measurements of particle-growth rates across the critical size range from 2 to 30 nm reveals that organic condensation drives particle growth at a similar rate over a wide temperature range, when the precursor oxidation rate is held constant. The temperature-dependent effects illustrated in Fig. 5 are thus of the same order of magnitude: Less extensive oxygenation at lower temperature is counterbalanced by lower volatility. This suggests a crucial role of organics in aerosol growth across the wide temperature range of the troposphere. Not only due to higher emission and ozonolysis reaction rates, but also due to rapid autoxidation to highly oxygenated products, organics can influence aerosol growth dramatically in warm regions. However, due to the strong drop in volatility of modestly oxygenated organic products, such compounds can drive aerosol growth at low temperatures. This observation could be of special interest for regions with high biogenic emissions (e.g., the Amazon basin), where compounds like pinonic acid could dominate early aerosol growth at low temperatures after convective updraft (32). Global aerosol models therefore need to implement robust descriptions of these processes, not only considering the first-order rate constants of ozonolysis and OH reactivity, but, rather, a more detailed description of organic chemistry and its temperature dependence. Precision measurements with a complementary set of mass spectrometers and particle-size-distribution measurements in the crucial region of <10 nm provide important constraints for model predictions of the contribution of gas-to-particle conversion to the global budget of CCN.

Materials and Methods

The CERN, the European Organization for Nuclear Research, CLOUD chamber is a 26.1-m³ electropolished stainless-steel vessel, surrounded by a thermal housing capable of stabilizing temperature in a range from –65 °C to 100 °C with ± 0.1 K precision (33). The chamber is equipped with a gas-control system achieving extremely high purities by mixing boil-off nitrogen and boil-off oxygen at the atmospheric ratio of 79:21. Highly pure trace gases can be precisely added at the parts per trillion (ppt) level. Before the experiments, the chamber was heated to 100 °C and rinsed with ultrapure water. This assured operation at contaminant levels of $<5 \times 10^4$ cm^{–3} H₂SO₄ and total organics <150 ppt by volume (15, 20).

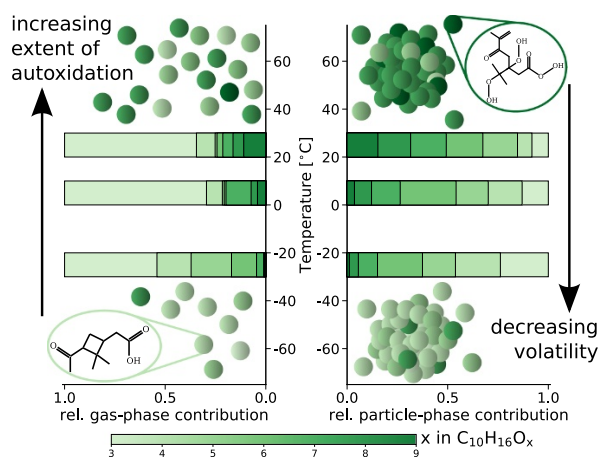


Fig. 5. Overview of the competing processes and their temperature dependence and comparison between the relative (rel.) gas- and particle-phase contribution of the ozonolysis product group $C_{10}H_{16}O_{3-9}$. *Left* shows the normalized relative contribution of the different oxygenated molecules within the gas phase, while *Right* shows the normalized relative contribution of the same compounds within the particle phase, inferred from monomer desorption fits.

Experiments were conducted as follows: At 38% relative humidity, with no SO₂ and no NO_x present in the chamber, stable ozone concentrations of 30–40 parts per billion were established. Under dark conditions (i.e., without any additional OH radical production mechanism except from the ozonolysis itself), a high-voltage field cage inside the chamber was switched on to perform neutral experiments first. Injection of α -pinene initiated the ozonolysis reaction and the subsequent formation of particles. After steady-state α -pinene concentrations were reached and particle growth was measured up to at least 10 nm, the high-voltage field was switched off. Ions now present in the chamber led to a significant increase in nucleation rate (7). Therefore, two growth rate measurements could eventually be performed, as the size distribution will show two growing particle populations. The second measurement was independent of changing gas concentrations, as steady-state was reached during the neutral stage. As no significant effect on growth due to different ionization levels was found, all measurements are treated equally.

The key particle-size distribution and growth-rate measurements of this study were performed with a DMA train (23). The sheath flows of the six DMAs were conditioned to chamber temperature to avoid possible particle evaporation during particle sizing. A 50% systematic uncertainty was assumed on the apparent particle-growth rates inferred by the appearance time method when comparing the values to growth rates from pure condensation. This also covered uncertainties of possible evaporation during the measurement procedure. Details can be found in *SI Appendix*. Gas-phase composition was measured by two complementary mass spectrometers using different ionization techniques (21, 22). For molecular ion signals observed in both instruments, the stronger signal was used to account for a reduced charging efficiency by any of the two ionization chemistries. For

more details, see *SI Appendix*. Particle-phase composition was measured with a FIGAERO-CIMS (24), which accumulated particles for 30 min on a filter inlet kept at chamber temperature. As all experiments were started with a particle-free chamber, all collected particles originated from new particle formation under similar experimental conditions. The accumulated particles were thermally desorbed by heating the filter, and their composition was analyzed by the connected mass spectrometer. Details can be found in *SI Appendix*.

ACKNOWLEDGMENTS. We thank T. Kurten and N. Hyttinen for providing helpful COSMOtherm volatility estimates. We also thank K. Ivanova, P. Carrie, L.-P. De Menezes, J. Dumollard, F. Josa, I. Krasin, R. Kristic, A. Laassiri, O. S. Maksumov, B. Marichy, H. Martinati, S. V. Mizin, R. Sitals, A. Wasem, and M. Wilhelmsson for their contributions to the experiment. We thank the European Organization for Nuclear Research (CERN) for supporting CLOUD with important technical and financial resources and for providing a particle beam from the CERN Proton Synchrotron. This research was supported by the European Commission Seventh Framework Programme (Marie Curie Initial Training Network "CLOUD-TRAIN" 316662); German Federal Ministry of Education and Research Grants 01LK1222 A and 01LK1601 A; Swiss National Science Foundation Projects 20FI20.159851, 200020.172602, and 20FI20.172622; Austrian Research Funding Association FFG Project 846050; Austrian Science Fund (FWF) Projects J3951-N36 and J-3900; European Research Council (ERC) Consolidator Grant NANODYNAMITE 616075; ERC-Advanced Grant DAMOCLES 692891; ERC Starting Grant COALA 638703; Horizon 2020 Marie Skłodowska-Curie Grant 656994 ("Nano-CAVa"); ERC Advanced Grant 742206 ATM-GP; Academy of Finland Center of Excellence Programme Grant 307331; US Department of Energy Grant DE-SC0014469; and the Presidium of the Russian Academy of Sciences Program "High Energy Physics and Neutrino Astrophysics" 2015.

- Gordon H, et al. (2017) Causes and importance of new particle formation in the present-day and preindustrial atmospheres. *J Geophys Res Atmos* 122:8739–8760.
- Lehtinen KE, Maso MD, Kulmala M, Kerminen VM (2007) Estimating nucleation rates from apparent particle formation rates and vice versa: Revised formulation of the Kerminen–Kulmala equation. *J Aerosol Sci* 38:988–994.
- Pierce JR, Adams PJ (2007) Efficiency of cloud condensation nuclei formation from ultrafine particles. *Atmos Chem Phys* 7:1367–1379.
- Riipinen I, et al. (2012) The contribution of organics to atmospheric nanoparticle growth. *Nat Geosci* 5:453–458.
- Guenther AB, et al. (2012) The model of emissions of gases and aerosols from nature version 2.1 (Megan2.1): An extended and updated framework for modeling biogenic emissions. *Geosci Model Dev* 5:1471–1492.
- Ehn M, et al. (2014) A large source of low-volatility secondary organic aerosol. *Nature* 506:476–479.
- Kirkby J, et al. (2016) Ion-induced nucleation of pure biogenic particles. *Nature* 533:521–526.
- Tröstl J, et al. (2016) The role of low-volatility organic compounds in initial particle growth in the atmosphere. *Nature* 533:527–531.
- Gordon H, et al. (2016) Reduced anthropogenic aerosol radiative forcing caused by biogenic new particle formation. *Proc Natl Acad Sci USA* 113:12053–12058.
- Kulmala M, et al. (2013) Direct observations of atmospheric aerosol nucleation. *Science* 339:943–946.
- Donahue NM, Trump ER, Pierce JR, Riipinen I (2011) Theoretical constraints on pure vapor-pressure driven condensation of organics to ultrafine particles. *Geophys Res Lett* 38:L16801.
- Kulmala M, Kerminen VM, Anttila T, Laaksonen A, O'Dowd CD (2004) Organic aerosol formation via sulphate cluster activation. *J Geophys Res Atmos* 109:D04205.
- Donahue NM, Epstein SA, Pandis SN, Robinson AL (2011) A two-dimensional volatility basis set: 1. Organic-aerosol mixing thermodynamics. *Atmos Chem Phys* 11:3303–3318.
- Lehtipalo K, et al. (2016) The effect of acid–base clustering and ions on the growth of atmospheric nano-particles. *Nat Commun* 7:11594.
- Frege C, et al. (2018) Influence of temperature on the molecular composition of ions and charged clusters during pure biogenic nucleation. *Atmos Chem Phys* 18: 65–79.
- Bianchi F, et al. (2016) New particle formation in the free troposphere: A question of chemistry and timing. *Science* 352:1109–1112.
- Murphy BN, Julin J, Riipinen I, Ekman AML (2015) Organic aerosol processing in tropical deep convective clouds: Development of a new model (CRM-ORG) and implications for sources of particle number. *J Geophys Res Atmos* 120:10,441–10,464.
- Wang J, et al. (2016) Amazon boundary layer aerosol concentration sustained by vertical transport during rainfall. *Nature* 539:416–419.
- Andreae MO, et al. (2018) Aerosol characteristics and particle production in the upper troposphere over the Amazon basin. *Atmos Chem Phys* 18:921–961.
- Kirkby J, et al. (2011) Role of sulphuric acid, ammonia and galactic cosmic rays in atmospheric aerosol nucleation. *Nature* 476:429–433.
- Jokinen T, et al. (2012) Atmospheric sulphuric acid and neutral cluster measurements using CI-API-TOF. *Atmos Chem Phys* 12:4117–4125.
- Breitenlechner M, et al. (2017) PTR3: An instrument for studying the lifecycle of reactive organic carbon in the atmosphere. *Anal Chem* 89:5824–5831.
- Stolzenburg D, Steiner G, Winkler PM (2017) A DMA-train for precision measurement of sub-10 nm aerosol dynamics. *Atmos Meas Tech* 10:1639–1651.
- Lopez-Hilfiker FD, et al. (2014) A novel method for online analysis of gas and particle composition: Description and evaluation of a filter inlet for gases and AEROSols (FIGAERO). *Atmos Meas Tech* 7:983–1001.
- Donahue NM, Robinson AL, Stanier CO, Pandis SN (2006) Coupled partitioning, dilution, and chemical aging of semivolatile organics. *Environ Sci Technol* 40:2635–2643.
- Nieminen T, Lehtinen KEJ, Kulmala M (2010) Sub-10 nm particle growth by vapor condensation—Effects of vapor molecule size and particle thermal speed. *Atmos Chem Phys* 10:9773–9779.
- Kurtén T, et al. (2016) Alpha-pinene autooxidation products may not have extremely low saturation vapor pressures despite high O: C ratios. *J Phys Chem A* 120:2569–2582.
- Apsokardu MJ, Johnston MV (2018) Nanoparticle growth by particle-phase chemistry. *Atmos Chem Phys* 18:1895–1907.
- Chuang WK, Donahue NM (2017) Dynamic consideration of smog chamber experiments. *Atmos Chem Phys* 17:10019–10036.
- Yu J, Cocker DR, Griffin RJ, Flagan RC, Seinfeld JH (1999) Gas-phase ozone oxidation of monoterpenes: Gaseous and particulate products. *J Atmos Chem* 34:207–258.
- Praske E, et al. (2018) Atmospheric autooxidation is increasingly important in urban and suburban North America. *Proc Natl Acad Sci USA* 115:64–69.
- Topping D, Connolly P, McFiggans G (2013) Cloud droplet number enhanced by co-condensation of organic vapours. *Nat Geosci* 6:443–446.
- Dias A, et al. (2017) Temperature uniformity in the CERN CLOUD chamber. *Atmos Meas Tech* 10:5075–5088.



Supplementary Information for

Rapid growth of organic aerosol nanoparticles over a wide tropospheric temperature range

Dominik Stolzenburg et al.

Paul Winkler

E-mail: paul.winkler@univie.ac.at

This PDF file includes:

Supplementary text

Figs. S1 to S6

Table S1

References for SI reference citations

Supporting Information Text

Measurement of particle growth with the appearance time method

Particle-size-distributions are measured by several sizing instruments optimized for a certain size range. Each instrument was thereby treated separately but we found comparable results in the overlapping regions for all presented experiments. Particle growth rate measurements were performed with the appearance time method, which can be used especially in chamber experiments, where a clear front of a growing particle population can be identified during most nucleation experiments.

Key part of this study is the precision measurement of particle-size-distributions in the size range between 1.8-8 nm by a newly developed instrument, a DMA-train (1). It uses six differential mobility analyzers in parallel with the classified size fixed for every device. Subsequent detection of the size-selected aerosol is done by the usage of six condensation particle counters. As no scanning is involved, high counting statistics at a single size is achieved, providing unprecedented high sensitivity to low number concentrations in the crucial sub 10-nm range. At diameters above 5 nm higher counting statistics allow one DMA to be set alternating every 10 seconds between 6.2 and 8 nm, hence providing in total seven measured sizes for the DMA-train: 1.8, 2.2, 2.5, 3.2, 4.3, 6.2, 8.0 nm (see Fig. S1 (B)).

The other size-ranges were covered by three additional instruments: Below 2.5 nm, a particle size magnifier in scanning mode was used (2). Above 8 nm a scanning mobility particle sizer system, TSI nano-SMPS model 3982, measured up to 65 nm (3). Additionally, a neutral cluster and air ion spectrometer (NAIS) measured between 3-42 nm (4). For the size distribution of particles >10 nm two additional SMPS systems were attached to the chamber, but were not used for detailed growth rate analysis.

Considering the evolution of particle size-distribution binned into different size-channels as given by most particle size-distribution measuring instruments, the signal in each size-channel is fitted individually with a four parameter sigmoid function using a least-square algorithm:

$$S_{dp}(t) = \frac{a - b}{1 + (t/t_{app})^d} + b, \quad [1]$$

where a and b represent the background and plateau value of the sigmoid function respectively, d is a parameter for the steepness of the rising signal and t_{app} is the time at which the 50 % value between plateau and background is reached.

A representative fit for a 3.2 nm size channel of the DMA-train is shown in Fig. S1 (A). All size-channels are cross-checked manually after the automated fitting and a statistical error of t_{app} is estimated from the covariance of the fit-result. The values obtained for t_{app} can be plotted against the corresponding diameter as shown in Fig. S1 (B). A linear fit with an orthogonal distance regression is used to take into account both the uncertainties of t_{app} and of the diameter of the size-channels. The resulting value of the slope and its associated error can be interpreted as an apparent particle growth rate and its statistical uncertainty.

For the DMA-train two size-intervals for the growth rate measurement were defined: One between 1.8-3.2 nm and one between 3.2-8 nm. The choice of the size-intervals is arbitrary but proofed to be representative to show differences between early and later growth. In (5) it was shown that growth driven by biogenic organics shows only a minor size-dependence above 5 nm, i.e. the upper growth rate size-interval of the DMA-train is representative for growth >5 nm.

However, this apparent growth rate of the particle size distribution does not necessarily represent the growth caused by pure condensation, as it omits coagulation and, in chamber experiments, wall losses, which both alter the particle size-distribution (6). Therefore, a systematic uncertainty of the method is estimated to be 50 % (7). On the other hand, methods accounting for coagulation and loss effects do need reliable absolute number concentration measurements and therefore good knowledge of overall detection efficiencies of the sizing instruments. In the presented experiments there might be high uncertainties due to possible evaporation effects of particles produced at e.g. cold temperatures and brought into warmer analyzing instruments. To ensure precise sizing at different chamber temperatures, the sheath-air of all six DMAs of the DMA-train was passed through an heat exchanger maintained at chamber temperature. All inlet lines and sheath flow lines as well as the DMAs were insulated to be maintained as close to chamber temperature as possible. Subsequent evaporation losses inside the detecting CPCs are unlikely to affect the appearance time method. This method does not depend on absolute particle concentrations as long as there is enough signal detected in a channel to get reliable results with the fit by Eq. 1. To further investigate possible effects of particle evaporation on the measured growth rates a custom-build SMPS was operated while being completely contained inside a refrigerator which was kept at chamber temperature for the experiments at +5°C and -25°C. A comparison of this cooled SMPS with the nano-SMPS used in this study is presented in Fig. S2. The differences in absolute concentrations are within a factor of 2 and the growth rate measurements inferred are generally agreeing within the measurement uncertainties. We therefore conclude that the results of the appearance time method should be generally robust with respect to possible evaporation of the sampled particles and the major uncertainties are covered within the 50 % systematic error given by (7).

Absolute HOM concentration measurements using nitrate-CI-API-ToF

The nitrate-CI-API-ToF (nitrate-CI) uses negative nitrate, $(\text{HNO}_3)_n(\text{NO}_3^-)$, as reagent ion (8), which shows high charging efficiencies towards H_2SO_4 and HOMs. This rather selective ionization technique is used obtain a very clean spectrum of HOMs (9). The concentration of a HOM species is estimated via

$$[\text{HOM}_i] = C \cdot T_i \cdot \text{SL}_{\text{HOM}_i} \cdot \ln \left(1 + \frac{[\text{HOM}_i \cdot \text{NO}_3^-]}{\sum_{j=0}^2 [\text{NO}_3^- \cdot (\text{HNO}_3)_j]} \right) \quad [2]$$

Here $[\text{HOM}_i \cdot \text{NO}_3^-]$ is the background corrected peak area which is normalized to the intensity of the main reagent ions. To obtain a quantitative concentration, three factors are applied: First, a calibration factor C , which is inferred from a calibration using sulfuric acid (10) and assuming that all detected HOMs have the same ionization efficiency (9). Second, a mass dependent transmission efficiency T_i of the API-ToF can be inferred in a separate experiment by depleting the reagent ions with several perfluorinated acids (11). Third, sampling line losses SL_{HOM_i} are estimated assuming laminar flow diffusional losses in the sampling lines (12) with a diffusion coefficient of HOMs scaling with the molecular mass M_i of the compound via $D[\text{cm}^2\text{s}^{-1}] = 0.31 \cdot M_i^{-1/3}$ at 278 K, determined from wall loss measurements in the CLOUD chamber. As the sampling lines of the nitrate-CI are thermally insulated, for other experiment temperatures $D \propto (T/278\text{K})^{1.75}$ is assumed. As the compounds detected by the nitrate-CI are mostly classified ELVOC or LVOC in the temperature range of this study, we can assume that they all get lost irreversibly to sampling line walls due to diffusion.

Absolute concentration measurements of oxidized organics using PTR3-ToF

The PTR3-ToF (PTR3) uses $(\text{H}_3\text{O}^+)(\text{H}_2\text{O})_n$ clusters as reagent ions, ionizing α -pinene as well as first and higher order oxidation products by proton transfer or ligand switch reactions (13). A contact minimized laminar flow inlet system with core sampling is used to transfer the sample air into the tripole reaction chamber operated at 80 mbar and reduces transmission losses. The $(\text{H}_3\text{O}^+)(\text{H}_2\text{O})_n$ cluster ion distribution can be regulated by a radio-frequency-amplitude applied to the tripole rods without influencing the reaction time. Increased pressure in the reaction region and longer reaction times compared to traditional PTR instruments yield a 500 fold increased sensitivity to a broad range of organics. At the operating conditions of the PTR3, secondary reactions of ionized species with the most abundant neutral VOCs in the sample gas are limited to less than one percent at the highest measurable concentrations. The new instrument bridges the gap between precursor measurements at ppbv level to HOM measurements at sub ppt level, complementing atmospheric pressure CIMS techniques.

A quadrupole interfaced Long-ToF mass spectrometer (TOFWERK AG, Thun, Switzerland) is providing the high mass resolving power needed to separate isobaric compounds. We obtained more than 1500 individual mass peaks, excluding isotopes, during α -pinene ozonolysis experiments. A multi-peak fitting algorithm is applied to separate the major compounds and assign chemical sum formulas. Extracting the relevant signals is done omitting all masses rising less than 3σ above chemical background noise during ozonolysis measurements and removing peaks with possible uncertainties caused by interference of higher neighboring peaks. $(\text{H}_3\text{O}^+)(\text{H}_2\text{O})_n$ clusters are known to be soft ionization reagent ions. Nevertheless we cannot exclude completely fragmentation of some ionized HOMs losing most likely H_2O especially when containing an (-OOH) group.

The PTR3 was calibrated with a gas standard containing 1 ppm of 3-hexanone, heptanone and α -pinene in nitrogen, which was dynamically diluted by a factor of 1000 in VOC-free air to contain 1 ppbv of each compound. Duty cycle corrected counts per second $dcps$ are used in order to compensate for the mass-dependent transmission of the TOF mass spectrometer ($dcps(i) = cps(i) \cdot (101/m_i)^{1/2}$) (13). For 3-hexanone and heptanone we obtained a sensitivity which is in agreement with the calculated sensitivity taking into account the duty cycle corrected $(\text{H}_3\text{O}^+)(\text{H}_2\text{O})_n$ reagent ion count rates, the pressure and the reaction time in the reaction chamber (80 mbar; 3 ms) and using $2 - 3 \cdot 10^{-9} \text{cm}^3\text{s}^{-1}$ as a fast reaction rate constant close to the collisional limit value. Consequently, only lower end product concentrations can be given.

In a previous α -pinene ozonolysis study PTR3 results showed quantitative agreement for several HOMs with the nitrate-CI (13). The authors estimated 80 % inlet losses for low volatility molecules with $n_{\text{O}} \geq 5$, bringing the two instruments into reasonable quantitative agreement for common molecular ion signals. However, the assumption for the nitrate-CI, that all detected molecules get lost on contact with sampling line walls, does not hold for all substances measured by the PTR3. In the transition from SVOC to LVOC the partitioning of substances between inlet line walls and sample gas is temperature dependent. We therefore extended the approach of (13) with our knowledge about an approximate volatility of the measured compounds. Assuming that all molecules in the LVOC and ELVOC range get lost by diffusion (the diffusion coefficient of a molecule is estimated similar to the nitrate-CI) according to (12), we can apply a temperature dependent loss-correction for the sampling line losses, which is split up into three sections:

$$\eta_{\text{tot}} = \eta_{\text{line,int}}(T) \cdot \eta_{\text{line,ext}}(298\text{K}) \cdot \eta_{\text{PTR3}}(310\text{K}) \quad [3]$$

We account for losses at the sampling line within the CLOUD chamber $\eta_{\text{line,int}}$ at chamber temperature T , as well as losses occurring at the sampling line outside the chamber at room temperature $\eta_{\text{line,ext}}$ (as it was not thermally insulated) and losses within the PTR3 instrument heated to 37°C η_{PTR3} . Therefore, for each sampling section other molecules might be subject to losses according to their temperature-dependent volatility classification.

Comparison of the used mass spectrometers

The considerations of the two previous sections result in the comparison for data obtained in three representative experiments at three different temperatures which is shown in Fig. S3, where $\eta_{\text{line,int}}$ and $\eta_{\text{line,ext}}$ are calculated assuming diffusional losses similar to the nitrate-CI and η_{PTR3} is estimated to correct for the 80% discrepancy found in (13).

For higher oxygenated molecules the agreement between both mass spectrometers is in a reasonable range including the additional loss term η_{PTR3} for losses within the PTR3 ion source and inlet. This indicates that the loss in measured concentration from $+25^\circ\text{C}$ to -25°C for the three experiments at similar initial precursor oxidation rates is caused by the reduced reaction rates of the auto-oxidation process. For lower temperatures and lower oxidized states ($n_{\text{O}} = 4/5/6$) a discrepancy between the instruments gets significant. However, even at elevated temperatures, the nitrate-CI is only detecting a small fraction of all

oxidation products with $n_O = 5/6$ observed by the PTR3. Therefore it is concluded that the increasing discrepancy is likely due to a lowered sensitivity of the nitrate-CI for such compounds. The ionization efficiency in the nitrate-CI depends on the relative binding energy of a $(\text{HNO}_3)(\text{NO}_3^-)$ cluster compared to a $(\text{Analyte})(\text{NO}_3^-)$ cluster (14). A relative shift in binding energies at lower temperatures that favors $(\text{HNO}_3)(\text{NO}_3^-)$ clustering instead of $(\text{Analyte})(\text{NO}_3^-)$ clustering, could explain the observed decrease of signal for the lower oxidation states for the nitrate-CI. The higher oxidation states however are unaffected because the $(\text{HOM})(\text{NO}_3^-)$ clustering is generally very strong and will always dominate the $(\text{HNO}_3)(\text{NO}_3^-)$ clustering, which explains the good agreement of the two instruments for higher oxidized states.

When combining the two mass spectrometers, for molecular ion signals observed in both instruments the higher signal is used. Both spectra are background subtracted and therefore a weaker signal in either of the mass spectrometers could point towards a lower ionisation efficiency.

Combined gas-phase mass defect plots

Fig. S4 shows mass defect plots from the nitrate-CI and the PTR3 during three representative experiments at three different temperatures. For all three cases the α -pinene ozonolysis rate is comparable.

The mass defect plots for all temperatures show the typical pattern of HOMs (5). Two bands can be identified, one representing monomers ($n_C=6-10$, 100-400 Th) and one representing dimers ($n_C=16-20$, 400-600 Th); molecules with increasing oxidation state are found towards the lower right of the panels. The reduction in temperature mainly reduces the signal of the higher oxygenated compounds towards the lower right of the panels. This is in agreement with (15) and the observation of reduced auto-oxidation rates at lower temperatures leading to less highly oxygenated molecules (16). This trend is as well shown in Fig. 5 for some representative molecules.

The symbol color for peaks with an identified composition in Fig. S4 corresponds to a broad temperature-dependent classification of their volatility, based on the carbon and oxygen numbers of the individual compounds. We place them in four general groups, according to their saturation mass concentration C^* : extremely low volatility compounds (ELVOC, $\log_{10} C^* \leq -4.5$), low volatility compounds (LVOC, $\log_{10} C^* = (-4.5, -0.5]$), semi-volatile compounds (SVOC, $\log_{10} C^* = (-0.5, 2.5]$) and intermediate volatility compounds (IVOC, $\log_{10} C^* > 2.5$) (17). Compounds in the ELVOC and LVOC ranges have been shown to contribute to nanoparticle growth (5). Comparing this classification for the three different temperatures clearly indicates the importance of the compounds observed by the PTR3. At -25°C , large quantities of LVOC compounds can be observed by the usage of this additional ionization technique.

FIGAERO-CIMS: Measurement procedure, data analysis, normalization on aerosol mass and thermogram fitting

Chemical composition of the bulk particle phase composition was measured by the Filter Inlet for Gases and Aerosols (FIGAERO) (18) coupled to a chemical ionization time-of-flight mass spectrometer (CI-ToF-MS) (Tofwerk, HTOF). Measurement cycles were set to 30 minutes particle sampling at 8 SLPM sampling flow rate, followed by a thermal desorption ramp (10 minutes, maximal heating rate). The particle phase sampling line outside of the thermal housing (~ 0.5 m) of the CLOUD chamber was insulated, and due to the high sampling flow rates we assume that $T_{\text{chamber}} \approx T_{\text{sampling}}$. Desorption temperature in the FIGAERO is measured by a thermocouple installed in front of the particle filter. The particle filter was exchanged approximately every 48 hours between the experiments (Zeffluor membrane, $2.0 \mu\text{m}$ pore size, 25 mm diameter, PALL, USA). The thermal desorption gas flow was 2 SLPM ultrapure synthetic air (from the CLOUD liquid nitrogen and oxygen reservoirs). O_2^- ions are formed by passing a 2.2 SLPM flow of synthetic air through a radioactive charger (^{210}Po , 370 MBq, Model P-2021, NRD Inc., USA) and into the ion molecule reaction (IMR) chamber, where the chemical ionization occurs. The body of the IMR was heated to approximately 50°C to avoid condensation of low volatility compounds and kept at 800 mbar using an active pressure control device (Aerodyne Inc., USA). The voltages of the transfer optics were tuned for maximum sensitivity and strong declustering in order to minimize cluster ions and maximize the signal of $[\text{M-H}]^-$ ions. Blank particle phase samples were obtained between the chamber experiments by continuous sampling or by manually switching a HEPA filter in front of the FIGAERO filter during the experiments. Gas phase concentrations of the majority of oxidation products were too low throughout all experiments to be monitored in real-time by the gas-phase sampling position of the FIGAERO.

Data analysis using Tofware (version 2.5.11 FIGAERO) gave 10 seconds average mass spectra. A post-acquisition mass calibration using the ions O_2^- , CO_3^- , NO_3^- , HCO_4^- and $\text{C}_{16}\text{H}_{31}\text{O}_2^-$ resulted in a mass accuracy < 10 ppm. High-resolution peak identification of the particle phase products was done with the constraints of n_C : 1-20, n_H : 2-50, n_O : 0-20. Shoulder peaks were fitted also when no ion was identified, in order to resolve background signal from varying analyte signal. The ion signal [ions/s] was normalized by the reagent ion signal $((\text{O}_2^- + \text{CO}_3^-) \cdot 10^{-6})$, where 10^6 is the reference value. Selected high-resolution ion traces ($\text{C}_{10}\text{H}_{15}\text{O}_{3-9}$) of the FIGAERO desorption ramps of three experimental runs at $T = -25, +5$ and $+25^\circ\text{C}$ were further processed: The aerosol mass collected (M_{coll}) per FIGAERO filter cycle was calculated by the product of FIGAERO sampling flowrate and integrated mass of the combined nanoSMPS and SMPS particle size distribution. Aerosol density was approximated with 1.5 g cm^{-3} . For sampling cycles during which $M_{\text{coll}} > 10 \text{ ng}$ (Fig. S5), the FIGAERO ion signal was normalized by the sampled mass, providing the thermograms shown in Fig. 4 and enabling quantitative comparison between results at different temperatures. The number of thermal desorptions (n_{Des}) are 31, 12 and 15 for the experiments at -25°C , $+5^\circ\text{C}$ and $+25^\circ\text{C}$, respectively. Mean and standard error of the mean are calculated from the results of a cubic smoothing spline fit (smoothparam=0.01) for each normalized thermogram, resulting in the thick lines and shaded areas in Fig. 4, respectively. During desorption, we observed a lower effective heating rate for the low temperature experiments, since

the tubing and the FIGAERO filter material cooled down during sampling. This observation explains different T_{\max} for the same molecular formulas in the thermograms. Thermograms of monomeric ion signals often exhibit a mode that originates from fragment ions of compounds that decompose at high temperatures (19). For most monomeric ion signals we observed bimodal thermograms, indicating that thermal decomposition during the temperature ramping is a significant phenomenon. Therefore, we fitted the thermograms with three modes (monomer mode, dimer (decomposition) mode and background mode) at different temperature boundaries using a fitting function used in chromatography (20). A non-linear least squares solver (lsqcurvefit, Matlab) was applied for fitting the thermograms and extracting the peak areas from the monomer mode.

Growth rate parametrization

Growth rates were parametrized in Fig. 2 (A) and (B) by the simple exponential relation $GR = m(T, d_p) \cdot [k(T) \cdot ap \cdot O_3]^q$, to express the correlation between growth rate and α -pinene ozonolysis reaction rate. While the coefficients $m(T, d_p)$ depend on temperature and size-range of the growth rate measurement, q is chosen to be independent of both. A minimum least-square regression yields the results presented in Table S1.

Volatility of HOMs

Direct measurements of volatilities of individual HOM are extremely challenging as they are difficult to synthesize and the vapour pressures are too low for current volatility measurement techniques. To overcome this problem, vapour pressures can be inferred by several model calculations, like so-called group contribution methods (21) or parametrizations according to the oxidation state (17). In this study a combined approach is applied.

We use a volatility parametrization according to the carbon n_C^i and oxygen n_O^i number of the specific molecule i . This is based on two general observed trends that increasing carbon and increasing oxygen number lower the volatility of oxidized organic molecules. Thus, these quantities are linked to volatility, expressed as the logarithm of the saturation mass concentration $\log_{10} C_i^*$ for compound i :

$$\log_{10} C_i^*(300K) = (n_C^0 - n_C^i) \cdot b_C - n_O^i \cdot (b_O - b_{\text{add}}) - 2 \frac{n_C^i n_O^i}{n_C^i + n_O^i} b_{CO} \quad [4]$$

where the parameter $n_C^0=25$ is the baseline carbon backbone for a volatility of $1 \mu\text{g m}^{-3}$ without the addition of any functional groups. $b_C=0.475$ is the roughly half decade decrease in volatility per carbon atom and $b_O=2.3$ is the more than two decade decrease in volatility per oxygen atom assuming an average of (=O) and (-OH) groups. b_{CO} is a non-linearity term. More details can be found in (17).

However, other functionalities e.g. hydroperoxides (-OOH) and covalently bound dimers are not included in b_O , but are both abundant in HOMs from α -pinene ozonolysis. To account for these specific attributes, a representative set of proposed products (5, 22) with known structure is analyzed with the group contribution method SIMPOL (21). The results are fitted with Eq. 4 including a free parameter b_{add} altering the effect of oxygen b_O . Monomer and dimer products are fitted separately allowing this parameter to include the covalent binding.

The resulting parametrization at 300 K is shown in Fig. S6. The free parameter yields $b_{\text{add}} = 0.90$ for monomers and $b_{\text{add}} = 1.13$ for dimers. Accordingly, for any α -pinene ozonolysis product with unambiguously identified composition, a volatility can be calculated.

However, computed volatilities from group-contribution methods generally tend to underestimate vapour pressures at low vapour pressures. A recent study investigating the volatility of α -pinene oxidation products with quantum-chemical based model calculations found large deviations due to intramolecular H-bonds (22). These deviations were significant especially for highly oxygenated monomers and dimers, while the agreement for the higher volatilities was much better.

This study focuses on the temperature dependence of the volatilities which is described by:

$$\log_{10} C^*(T) = \log_{10} C^*(300K) + \frac{\Delta H_{\text{vap}}}{R \ln(10)} \left(\frac{1}{300} - \frac{1}{T} \right) \quad [5]$$

The evaporation enthalpy ΔH_{vap} can be linked to the saturation mass concentration at 300 K $\log_{10} C^*(300K)$ according to (17) and combined with (23):

$$\Delta H_{\text{vap}} [\text{kJ mol}^{-1}] = -5.7 \cdot \log_{10} C^*(300K) + 129 \quad [6]$$

The correlation between volatility at 300 K and the evaporation enthalpy ΔH_{vap} is very comparable for approaches like (23), (17) and (22). Moreover, the shift in volatility due to temperature in this study is most important for oxygenated compounds with volatilities around $\log_{10} C^*(300K) \approx 0$, at the transition between LVOC and SVOC. For those molecules also the predictions of the volatility between the different methods don't differ drastically (22). Therefore, we assume an overall uncertainty of the volatility description of ± 1 bin (i.e. 1 decade in $C^*(300K)$) for volatility distributions within a volatility basis set). This uncertainty is shown Fig. 2 (E) and (F) and gives the method uncertainties in Fig. 3.

Aerosol growth model

The measured VBS-distributions can be used to model aerosol growth. The modeling framework is based on the one used in (5) but simplified for the input of direct VBS-distribution measurements. Starting from a VBS-distribution at $t = 0$ the growth of a monodisperse population of nucleated particles at an initial size of 1.2 nm mobility diameter is modeled. Every VBS bin is treated like a single surrogate molecule having the properties of the averaged mass and concentration of the bin. It is assumed that the measured gas-phase concentrations are in steady-state with losses to particles and chamber walls. The condensation flux $\phi_{i,p}$ of every VBS bin i should then follow:

$$\phi_{i,p} = N_p \cdot \sigma_{i,p} \cdot k_{i,p} \cdot F_{i,p} \quad [7]$$

N_p gives the number concentration of particles of a given size. $\sigma_{i,p} = \pi/4(d_p + d_i)^2$ is the particle-vapor collision cross-section including the diameter of the monodisperse particle population d_p and mass-diameter of the VBS bin d_i . $k_{i,p} = \alpha_{i,p} \nu_{i,p} \beta_{i,p}$ is the deposition rate of vapor molecules at surface, with $\alpha_{i,p}$ the mass accommodation coefficient, $\nu_{i,p} = (8RT/(\pi\mu_{i,p}))^{1/2}$ the center of mass velocity for particle and vapor (with the reduced mass $\mu_{i,p} = (M_i M_p)/(M_i + M_p)$) and $\beta_{i,p}$ the correction factor for non-continuum dynamics (24). $F_{i,p}$ is the driving force of condensation, closely related to the saturation ratio S_i of the VBS bin by $F_{i,p} = C_i^0 (S_i - X_{i,p} \gamma_{i,p} K_{i,p})$. This driving force of condensation for a VBS bin i gives the difference between gas phase activity S_i and particle phase activity ($X_{i,p} \gamma_{i,p} K_{i,p}$), which includes the Raoult term $X_{i,p} \gamma_{i,p}$ to account for the mixture effect of the particles and the Kelvin-term $K_{i,p} = \exp(4\sigma M/(RT\rho d_p))$ accounting for the curvature effect of the particle surface. The model assumes an ideal mass based solution, i.e. the condensed phase activity is the mass fraction $X_{i,p}$ and hence $\gamma_{i,p} = 1$. Therefore we use C^* as saturation mass concentration throughout this study, as $C^* = \gamma_{i,p} C_i^0$.

Solving the above condensation equations for the measured evolution of the VBS-distribution assuming this distribution always reflects a steady-state between production from α -pinene ozonolysis and wall losses and following the growing monodisperse aerosol population, yields a diameter versus time evolution which can be connected to a growth rate.

Besides from the different input VBS-distributions at different temperature, only the Kelvin-term and the collision-frequency include a temperature dependence.

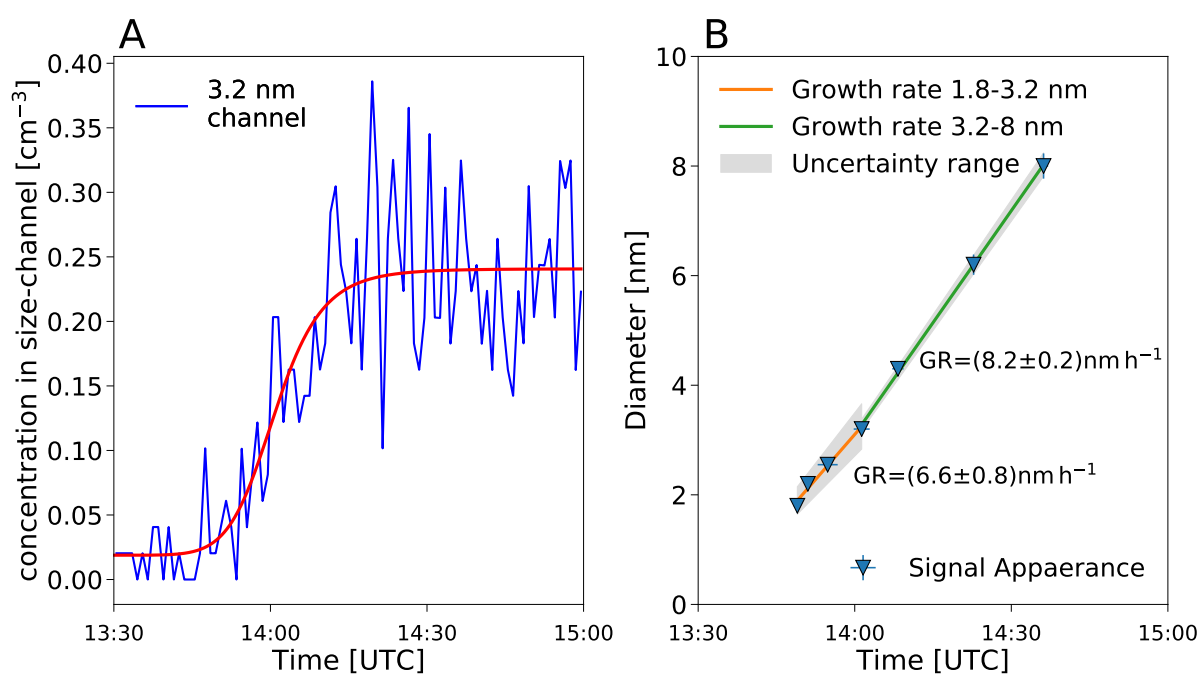


Fig. S1. Example for a representative determination of the particle growth rate with the appearance time method for data obtained by the DMA-train. (A) shows the sigmoid function fit to the measured concentration within the 3.2 nm channel. (B) shows the orthogonal distance regression for the growth rate determination in two intervals.

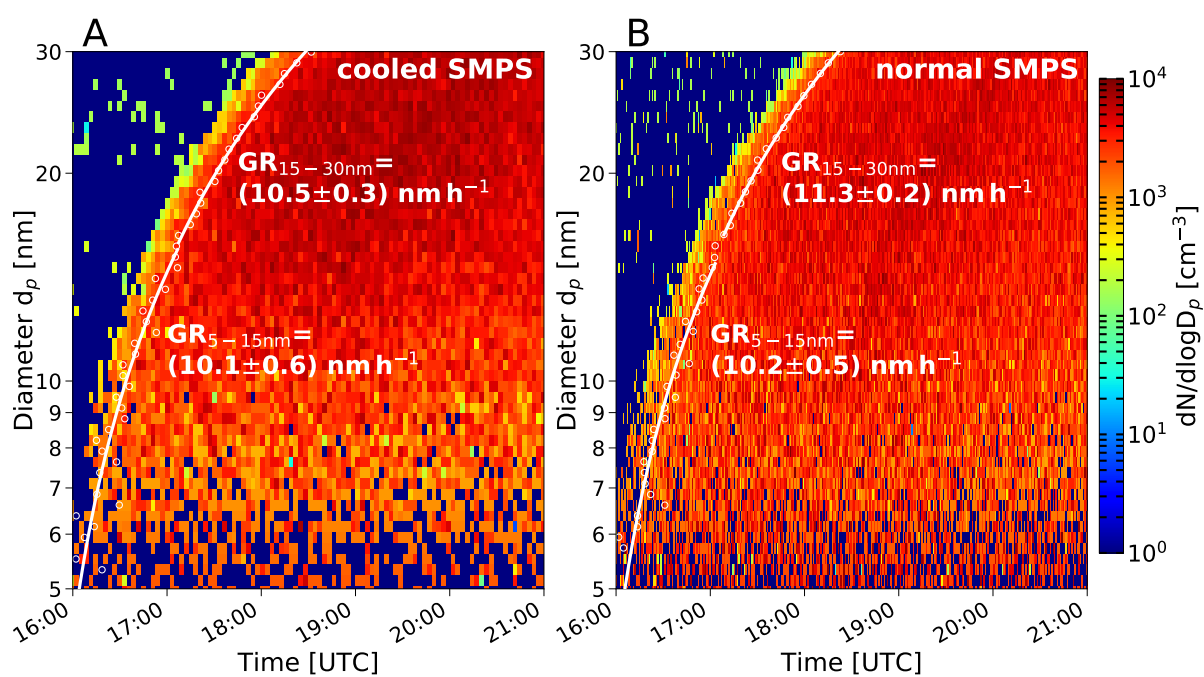


Fig. S2. Comparison of a completely cooled (kept at chamber temperature) and normal SMPS (operated at ambient temperature) during a dark α -pinene ozonolysis experiment at +5°C. White circles and lines show the appearance time growth rate estimation. Note that both instruments have slightly different time-resolution.

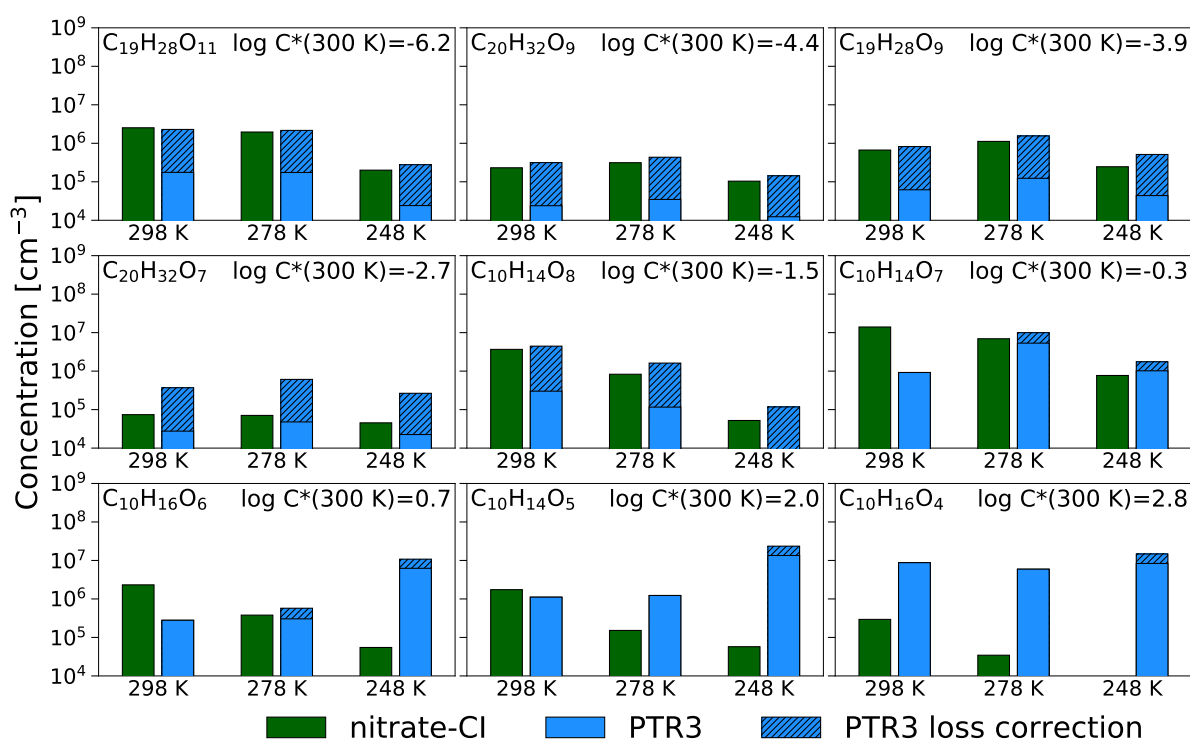


Fig. S3. Quantitative comparison of selected peaks observed in both mass spectrometers and its temperature dependence for three representative runs with similar α -pinene ozonolysis rate. The correction for PTR3 compounds to account for sampling line losses and the additional 80 % wall loss inside the PTR3 ion source are displayed by the hatched area.

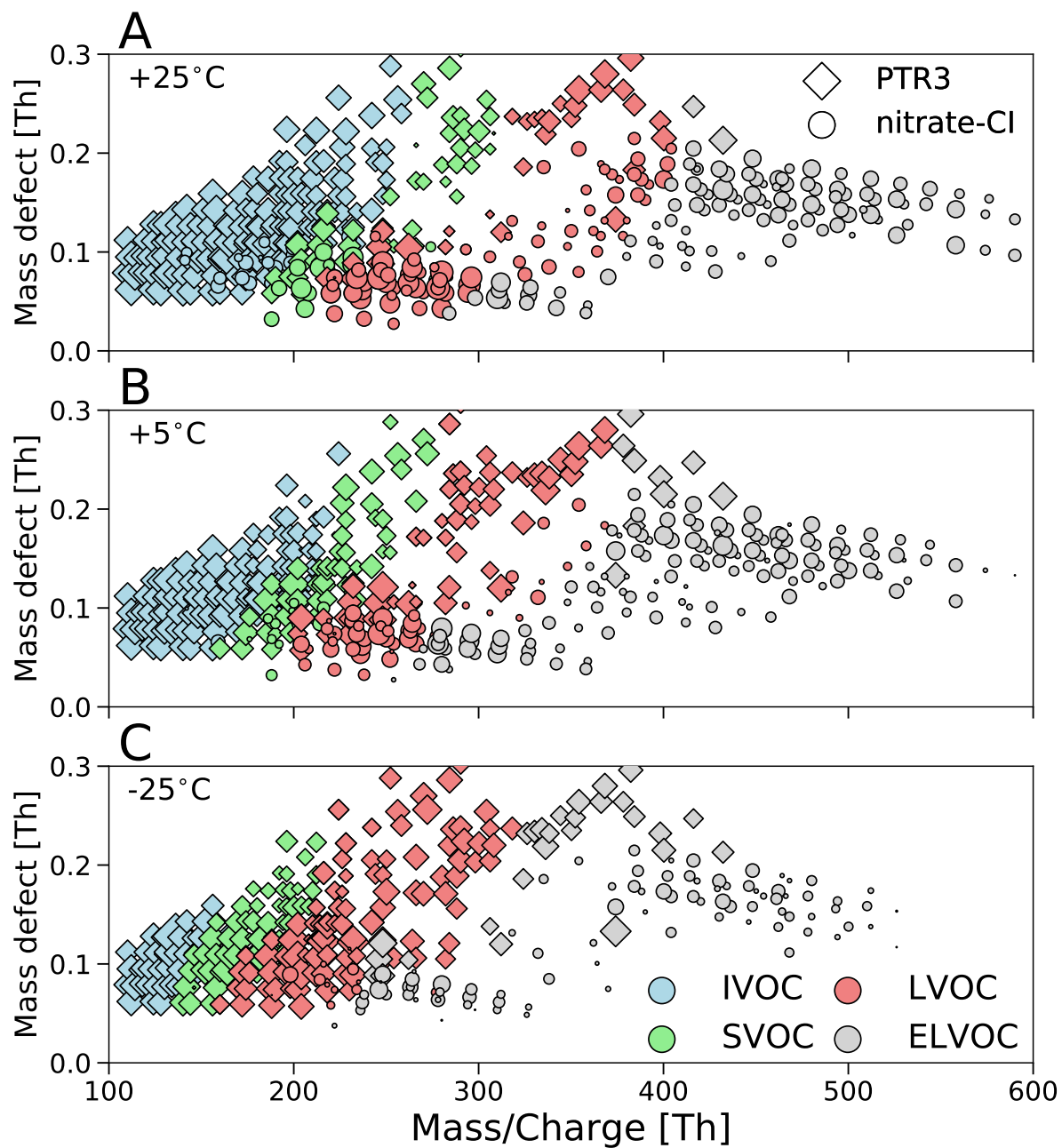


Fig. S4. Mass defect of all measured neutral oxidized organic compounds versus the nominal mass to charge ratio of three representative experiments, at +25°C (A), at +5°C (B) and at -25°C (C), all with a similar α -pinene ozonolysis reaction rate. Diamonds represent molecular ions measured by the PTR3 and circles compounds measured by the nitrate-Cl, both taking the different reagent ions into account. The size of the symbols is proportional to the logarithm of the measured concentration and the color is related to the volatility class as defined in Fig. S6.

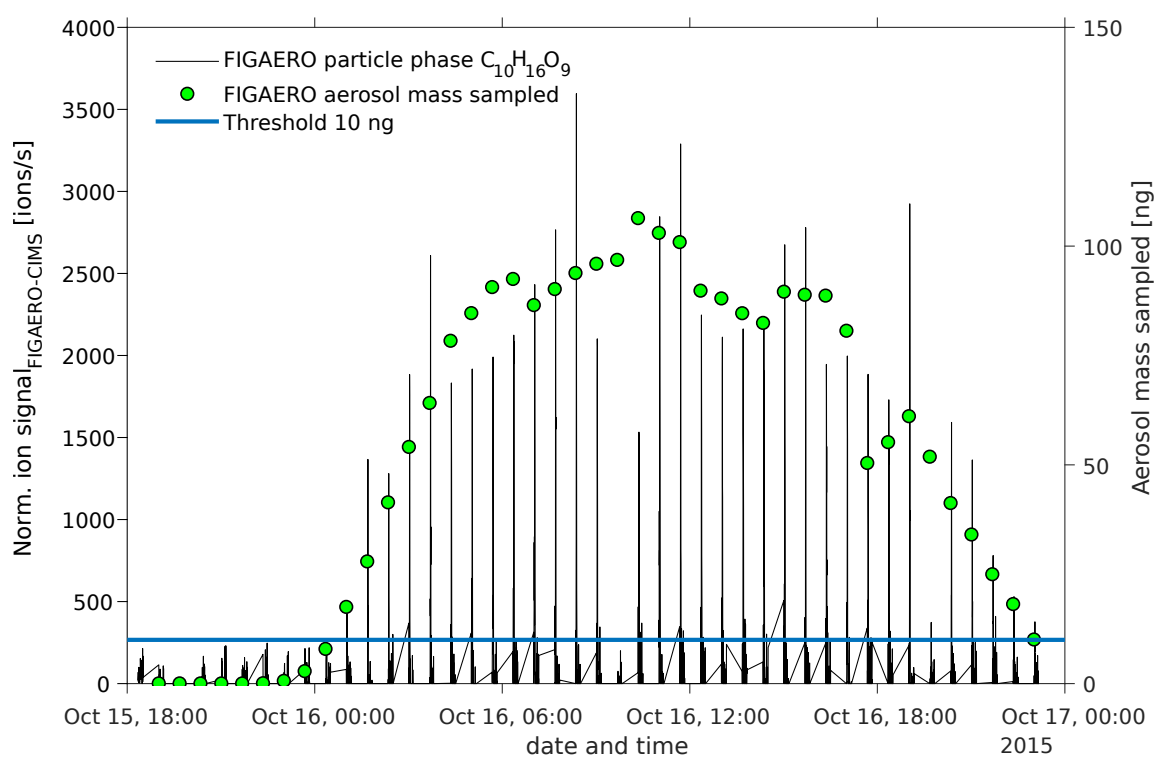


Fig. S5. Time series of $C_{10}H_{16}O_9$ from FIGAERO particle phase measurements showing consecutive thermal desorptions. The blue line indicates the threshold value above which thermograms were normalized on the sampled aerosol mass and used for further analysis.

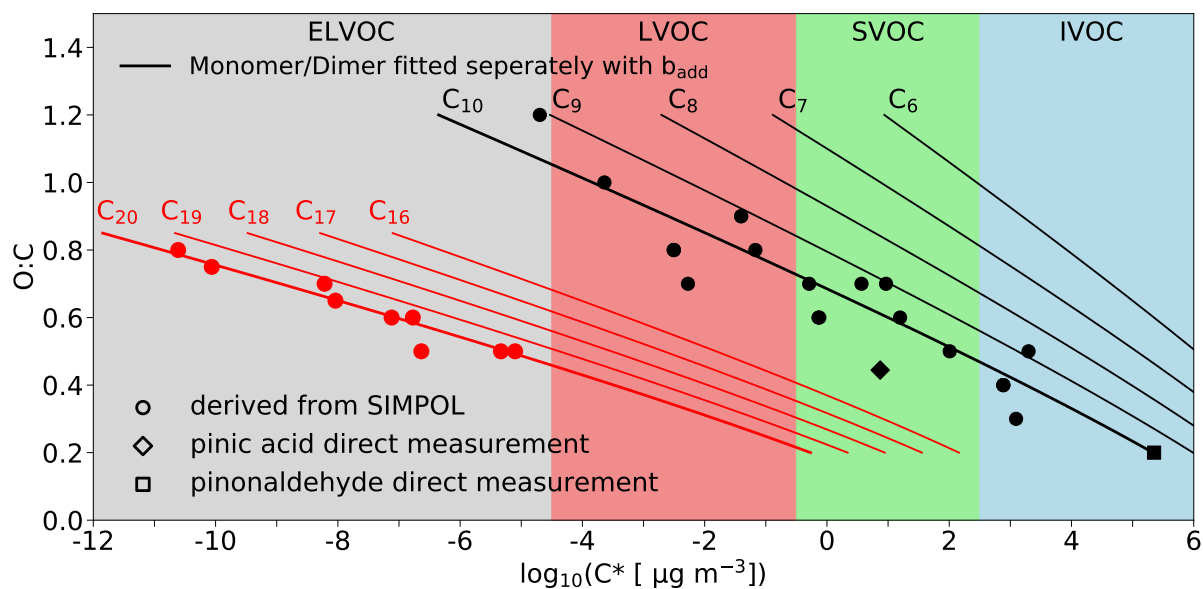


Fig. S6. Volatility model used in this study. For a representative set of proposed products from α -pinene ozonolysis the known structure is used to calculate the volatility by the group-contribution method SIMPOL or are directly measured by (25, 26). Results are fitted with the proposed relationship from (17) including a free parameter for the oxygen dependence.

Table S1. Resulting parameters from least-square regression for the growth rate parametrization of Fig. 2 (A) and (B) by the simple exponential relation $GR = m(T, d_p) \cdot [k(T) \cdot a_p \cdot O_3]^q$.

Size-Range	$m(+25^\circ\text{C})$	$m(+5^\circ\text{C})$	$m(-25^\circ\text{C})$	q
1.8-3.2 nm	$1.12 \cdot 10^{-7}$	$2.09 \cdot 10^{-7}$	$2.67 \cdot 10^{-7}$	1.21
3.2-8.0 nm	$2.66 \cdot 10^{-7}$	$3.12 \cdot 10^{-7}$	$3.57 \cdot 10^{-7}$	1.21

References

1. Stolzenburg D, Steiner G, Winkler PM (2017) A DMA-train for precision measurement of sub-10 nm aerosol dynamics. *Atmos. Meas. Tech.* 10(4):1639–1651.
2. Vanhanen J, et al. (2011) Particle size magnifier for nano-cn detection. *Aerosol Sci. Tech.* 45(4):533–542.
3. Tröstl J, et al. (2015) Fast and precise measurement in the sub-20 nm size range using a scanning mobility particle sizer. *J. Aerosol Sci.* 87:75–87.
4. Manninen HE, et al. (2009) Long-term field measurements of charged and neutral clusters using neutral cluster and air ion spectrometer (nais). *Boreal Environ. Res* 14:591–605.
5. Tröstl J, et al. (2016) The role of low-volatility organic compounds in initial particle growth in the atmosphere. *Nature* 533:527–531.
6. Pichelstorfer L, et al. (2018) Resolving nanoparticle growth mechanisms from size- and time-dependent growth rate analysis. *Atmos. Chem. Phys.* 18(2):1307–1323.
7. Lehtipalo K, et al. (2014) Methods for determining particle size distribution and growth rates between 1 and 3 nm using the particle size magnifier. *Boreal Environ. Res.* 19(suppl. B):215–236.
8. Kürten A, Rondo L, Ehrhart S, Curtius J (2011) Performance of a corona ion source for measurement of sulfuric acid by chemical ionization mass spectrometry. *Atmos. Meas. Tech.* 4(3):437–443.
9. Ehn M, et al. (2014) A large source of low-volatility secondary organic aerosol. *Nature* 506:476–479.
10. Kürten A, Rondo L, Ehrhart S, Curtius J (2012) Calibration of a chemical ionization mass spectrometer for the measurement of gaseous sulfuric acid. *J. Phys. Chem. A* 116(24):6375–6386. PMID: 22364556.
11. Heinritzi M, et al. (2016) Characterization of the mass-dependent transmission efficiency of a cims. *Atmos. Meas. Tech.* 9(4):1449–1460.
12. Gormley PG, Kennedy M (1948) Diffusion from a stream flowing through a cylindrical tube. *P. Roy. Irish Acad. A* 52:163–169.
13. Breitenlechner M, et al. (2017) PTR3: An instrument for studying the lifecycle of reactive organic carbon in the atmosphere. *Anal. Chem.* 89(11):5824–5831. PMID: 28436218.
14. Hyttinen N, Rissanen MP, Kurtén T (2017) Computational comparison of acetate and nitrate chemical ionization of highly oxidized cyclohexene ozonolysis intermediates and products. *J. Phys. Chem. A* 121(10):2172–2179. PMID: 28234483.
15. Frege C, et al. (2018) Influence of temperature on the molecular composition of ions and charged clusters during pure biogenic nucleation. *Atmos. Chem. Phys.* 18(1):65–79.
16. Praske E, et al. (2018) Atmospheric autoxidation is increasingly important in urban and suburban north america. *P. Nat. Acad. Sci. USA* 115(1):64–69.
17. Donahue NM, Epstein SA, Pandis SN, Robinson AL (2011) A two-dimensional volatility basis set: 1. organic-aerosol mixing thermodynamics. *Atmos. Chem. Phys.* 11(7):3303–3318.
18. Lopez-Hilfiker FD, et al. (2014) A novel method for online analysis of gas and particle composition: description and evaluation of a Filter Inlet for Gases and AEROSols (FIGAERO). *Atmos. Meas. Tech.* 7(4):983–1001.
19. Stark H, et al. (2017) Impact of thermal decomposition on thermal desorption instruments: Advantage of thermogram analysis for quantifying volatility distributions of organic species. *Environ. Sci. Technol.* 51(15):8491–8500. PMID: 28644613.
20. Goodman KJ, Brenna JT (1994) Curve fitting for restoration of accuracy for overlapping peaks in gas chromatography/combustion isotope ratio mass spectrometry. *Anal. Chem.* 66(8):1294–1301. PMID: 8210045.
21. Pankow J, Asher W (2008) SIMPOL.1: a simple group contribution method for predicting vapor pressures and enthalpies of vaporization of multifunctional organic compounds. *Atmos. Chem. Phys.* 8:2773–2796.
22. Kurtén T, et al. (2016) Alpha-pinene autoxidation products may not have extremely low saturation vapor pressures despite high O:C ratios. *J. Phys. Chem. A* 120(16):2569–2582. PMID: 27049168.
23. Epstein SA, Riipinen I, Donahue NM (2010) A semiempirical correlation between enthalpy of vaporization and saturation concentration for organic aerosol. *Environ. Sci. Technol.* 44(2):743–748. PMID: 20025284.
24. Fuchs N, Sutugin A (1965) Coagulation rate of highly dispersed aerosols. *J. Colloid Sci.* 20(6):492–500.
25. Hallquist M, Wängberg I, Ljungström E (1997) Atmospheric fate of carbonyl oxidation products originating from alpha-pinene and delta-3-carene: Determination of rate of reaction with OH and NO₃ radicals, UV absorption cross sections, and vapor pressures. *Environ. Sci. Technol.* 31(11):3166–3172.
26. Bilde M, Pandis SN (2001) Evaporation rates and vapor pressures of individual aerosol species formed in the atmospheric oxidation of alpha- and beta-pinene. *Environ. Sci. Technol.* 35(16):3344–3349. PMID: 11529575.

4.8 Molecular understanding of the suppression of new-particle formation by isoprene (Heinritzi et al. (2018))

1 **Molecular understanding of the suppression of new-particle formation by**
2 **isoprene**

3 Martin Heinritzi¹, Lubna Dada², Mario Simon¹, Dominik Stolzenburg³, Andrea C. Wagner¹, Lukas Fischer⁴,
4 Lauri R. Ahonen², Stavros Amanatidis⁵, Rima Baalbaki², Andrea Baccarini⁶, Paulus S. Bauer³, Bernhard
5 Baumgartner³, Federico Bianchi^{2,7}, Sophia Brilke³, Dexian Chen⁸, Antonio Dias^{9,10}, Josef Dommen⁶,
6 Jonathan Duplissy², Henning Finkenzeller¹¹, Carla Frege⁶, Claudia Fuchs⁶, Olga Garmash², Hamish
7 Gordon^{10,12}, Manuel Granzin¹, Imad El Haddad⁶, Xucheng He², Johanna Helm¹, Victoria Hofbauer⁸,
8 Christopher R. Hoyle¹³, Juha Kangasluoma^{2,7}, Timo Keber¹, Changhyuk Kim^{5,14}, Andreas Kürten¹, Houssni
9 Lamkaddam⁶, Janne Lampilahti², Tiia M. Laurila², Chuan Ping Lee⁶, Katrianne Lehtipalo², Markus
10 Leiminger⁴, Huajun Mai⁵, Vladimir Makhmutov¹⁵, Ruby Marten⁶, Serge Mathot¹⁰, Roy Lee Mauldin^{2,16,17},
11 Bernhard Mentler⁴, Ugo Molteni⁶, Tatjana Müller¹, Wei Nie¹⁸, Tuomo Nieminen¹⁹, Antti Onnela¹⁰, Eva
12 Partoll⁴, Monica Passananti², Tuukka Petäjä², Joschka Pfeifer^{1,10}, Veronika Pospisilova⁶, Lauriane L. J.
13 Quéléver², Matti P. Rissanen², Clémence Rose^{2,20}, Siegfried Schobesberger¹⁹, Wiebke Scholz⁴, Kay
14 Scholze³, Mikko Sipilä², Gerhard Steiner⁴, Yuri Stozhkov¹⁵, Christian Tauber³, Yee Jun Tham², Miguel
15 Vazquez-Pufleau³, Annele Virtanen¹⁹, Alexander L. Vogel^{1,10}, Rainer Volkamer¹¹, Robert Wagner², Mingyi
16 Wang⁸, Lena Weitz¹, Daniela Wimmer², Mao Xiao⁶, Chao Yan², Penglin Ye^{8,21}, Qiaozhi Zha², Xueqin
17 Zhou^{1,6}, Antonio Amorim⁹, Urs Baltensperger⁶, Armin Hansel⁴, Markku Kulmala^{2,7,22}, António Tomé²³, Paul
18 M. Winkler³, Douglas R. Worsnop^{2,21}, Neil M. Donahue⁸, Jasper Kirkby^{1,10} & Joachim Curtius¹

19

20 ¹Institute for Atmospheric and Environmental Sciences, Goethe University Frankfurt, 60438 Frankfurt am
21 Main, Germany

22 ²Institute for Atmospheric and Earth System Research (INAR) / Physics, Faculty of Science, University of
23 Helsinki, 00014 Helsinki, Finland

24 ³Faculty of Physics, University of Vienna, 1090 Vienna, Austria

25 ⁴Institute for Ion and Applied Physics, University of Innsbruck, 6020 Innsbruck, Austria

26 ⁵California Institute of Technology, Pasadena, CA 91125, USA

27 ⁶Laboratory of Atmospheric Chemistry, Paul Scherrer Institute, 5232 Villigen, Switzerland

28 ⁷Aerosol and Haze Laboratory, Beijing Advanced Innovation Center for Soft Matter Science and
29 Engineering, Beijing University of Chemical Technology, Beijing, 100029, P.R. China

30 ⁸Center for Atmospheric Particle Studies, Carnegie Mellon University, Pittsburgh, PA, 15213, USA

31 ⁹CENTRA and FCUL, University of Lisbon, 1749-016 Lisbon, Portugal

32 ¹⁰CERN, 1211 Geneva, Switzerland

33 ¹¹Department of Chemistry & CIRES, University of Colorado at Boulder, Boulder, CO, 80309-0215, USA

- 34 ¹²University of Leeds, Leeds LS2 9JT, United Kingdom
- 35 ¹³Institute for Atmospheric and Climate Science, ETH Zurich, Switzerland
- 36 ¹⁴Department of Environmental Engineering, Pusan National University, Busan 46241, Republic of Korea
- 37 ¹⁵Lebedev Physical Institute, Russian Academy of Sciences, 119991, Moscow, Russia
- 38 ¹⁶Department of Atmospheric and Oceanic Sciences, University of Colorado at Boulder, Boulder, CO
39 80309, USA
- 40 ¹⁷Department of Chemistry, Carnegie Mellon University, Pittsburgh, PA 15213, USA
- 41 ¹⁸Joint International Research Laboratory of Atmospheric and Earth System Sciences, School of
42 Atmospheric Sciences, Nanjing University, Nanjing, 210023, China
- 43 ¹⁹Department of Applied Physics, University of Eastern Finland, FI-70211 Kuopio, Finland
- 44 ²⁰Laboratory for physical meteorology, UMR6016, University Clermont Auvergne-CNRS, 63178, Aubière,
45 France
- 46 ²¹Aerodyne Research, Inc., Billerica, MA 01821, USA
- 47 ²²Helsinki Institute of Physics, University of Helsinki, 00014 Helsinki, Finland
- 48 ²³IDL-University of Beira Interior, Covilhã, Portugal

49 **Nucleation of atmospheric aerosols from gaseous precursors produces roughly half of the global cloud**
50 **condensation nuclei, thus strongly affecting cloud coverage and Earth's radiative balance¹. Recent**
51 **studies show that highly-oxygenated products of monoterpene (C₁₀H₁₆) oxidation² can nucleate on their**
52 **own³ or with the help of sulfuric acid⁴. Monoterpenes are emitted mainly from trees; however, many**
53 **plants also emit isoprene (C₅H₈), which has the highest global emissions of all biogenic organic vapors⁵.**
54 **Several field measurements and laboratory studies have shown that isoprene suppresses new-particle**
55 **formation, but the cause of this suppression is under debate⁶⁻¹¹. Here, in experiments performed under**
56 **atmospheric conditions at two different temperatures (+5 and +25 °C) in the CERN CLOUD chamber, we**
57 **show that isoprene reduces nucleation of monoterpene oxidation products by altering peroxy-radical**
58 **(RO₂) termination reactions and thus inhibiting the formation of highly-oxygenated dimers containing**
59 **19 to 20 carbon atoms. We observe an increase of dimers with 14 to 15 carbon atoms, which are,**
60 **however, not efficient nucleators on their own. This effect increases when the isoprene-to-**
61 **monoterpene ratio increases. Additionally, the altered oxidation chemistry reduces initial particle**
62 **growth in the size range from 1.3 to 3.2 nm by a factor of roughly two compared to monoterpene-only**
63 **conditions. Overall, this results in a suppression of new-particle formation, especially at warmer**
64 **temperatures. By identifying peroxy-radical termination as the critical mechanism responsible for**
65 **isoprene suppression of pure biogenic nucleation and initial growth, our findings can explain to a large**
66 **degree the hitherto puzzling absence of biogenic new-particle formation in the Amazon¹¹ and the**
67 **southeastern United States¹⁰.**

68 Nucleation of aerosol particles is observed in many environments, ranging from boreal forests to urban
69 and coastal areas, from polar to tropical regions and from the boundary layer to the free troposphere¹².
70 Gaseous sulfuric acid, ammonia¹³, amines¹⁴ and, in coastal regions, iodine¹⁵, were shown to contribute to
71 nucleation. Additionally, a small fraction of the large pool of organic molecules in the atmosphere, namely
72 highly-oxygenated organic molecules (HOMs), some of which possess extremely low vapor pressures,
73 nucleate together with other precursors as well as on their own^{3,4,16}. This means nature is nucleating
74 particles on a large scale without pollution, and this may have been especially pervasive in the pre-
75 industrial atmosphere¹⁷. HOMs are formed with molar yields in the single-digit percent range from the
76 oxidation of monoterpenes (C₁₀H₁₆) with endocyclic C=C double-bonds^{2,3}. Monoterpenes are emitted by a
77 variety of trees in regions ranging from the tropics to northern latitudes, often reaching mixing ratios of
78 tens to hundreds of parts per trillion by volume (pptv)^{5,18}. Isoprene is a hemiterpene (C₅H₈) emitted by
79 broad-leaf trees and has the highest emissions of any biogenic organic compound, with concentrations
80 reaching several parts per billion by volume (ppbv) in the Amazon rainforest and the southeastern United
81 States despite high reactivity^{5,10,11}. Numerous studies report suppression of nucleation in isoprene-rich
82 environments, even if sufficient monoterpenes are present^{6-10,19,20}. This isoprene suppression effect has
83 been demonstrated in carefully controlled chamber studies^{6,8} and observed in isoprene-rich ambient
84 locations^{7,9,10}. In addition to observing isoprene suppression, earlier studies have proposed mechanisms
85 to explain it. One possibility is OH· depletion by isoprene, which would reduce the oxidation rate of
86 monoterpenes and thus supersaturation driving nucleation^{6,8}. However, OH· is observed to remain high
87 and undisturbed in isoprene-rich environments due to atmospheric OH· recycling mechanisms triggered
88 by isoprene²¹⁻²³. Further, HOM formation from endocyclic monoterpenes is dominated by ozonolysis^{2,3}.
89 Another proposed possibility is the deactivation of sulfuric acid cluster growth due to addition of isoprene

90 oxidation products¹⁰. However, HOMs can nucleate without sulfuric acid³ and suppression of nucleation
91 by isoprene is observed in pristine environments such as the Amazon¹¹.

92 Isoprene oxidation by OH· triggers complex peroxy-radical chemistry with a variety of products such as
93 hydroxy-hydroperoxides (ISOPOOH), hydroperoxy-aldehydes (HPALD) as well as second-generation low-
94 volatility compounds^{24,25}. Isoprene oxidation products with low volatility such as dihydroxyepoxides
95 (IEPOX) contribute to secondary organic aerosol formation²⁶⁻³¹. However, the interaction of isoprene and
96 monoterpene oxidation chemistry and the consequent effect on nucleation and growth of new particles
97 remains unclear. One consequence of this is an over-prediction of cloud condensation nuclei (CCN) in the
98 Amazon by models that simulate pure biogenic nucleation, but neglect the role of isoprene in new-particle
99 formation¹⁷.

100 Here we show on a molecular level how isoprene affects the chemistry of monoterpene oxidation, thus
101 reducing nucleation rates. We conducted experiments at the CLOUD (Cosmics Leaving Outdoor Droplets)
102 chamber at CERN (European Center for Nuclear Research) in Geneva, Switzerland. The CLOUD chamber is
103 a 26.1 m³ stainless steel aerosol reactor with very controlled and clean conditions that span those found
104 in the atmosphere. It is equipped with a suite of state-of-the-art mass spectrometers and particle-counting
105 instruments. We measured isoprene and α -pinene with a newly developed proton transfer reaction mass
106 spectrometer and the resulting HOMs with a nitrate chemical ionization atmospheric pressure interface
107 time-of-flight mass spectrometer (CI-API-TOF). We detected the ultrafine particles with a suite of particle
108 size magnifiers (PSM) and counters, as well as a newly developed DMA-train (for further details on
109 instrumentation see Methods).

110 We performed several experiments at +5 and +25 °C and relative humidity (RH) ranging from 20 to 80 %
111 with most of the experiments being carried out at 38 % RH. Ozone levels ranged from 30 – 50 ppbv. We
112 directly compare experiments performed with α -pinene as the sole biogenic vapor to experiments with a
113 mixture of α -pinene and isoprene. α -Pinene levels ranged from 0.33 to 2.5 ppbv, while isoprene levels
114 ranged from 2.5 to 10 ppbv. We thus could recreate conditions similar to ref. 3, as well as to regions like
115 the Amazon and southeastern parts of the United States.

116 Ozone attack to the endocyclic α -pinene C=C double bond leads to the well-described formation of highly-
117 oxygenated RO₂· radicals via intramolecular H-shift and autoxidation (mainly C₁₀H₁₅O_{4,6,8,10}, from now on
118 referred to as RO₂(α p)) as well as a wide spectrum of closed-shell monomers (mainly C₁₀H_{14,16}O_{5,7,9,11}) and
119 covalently bound dimers (mainly C₂₀H₃₀O₈₋₁₆ and C₁₉H₂₈O₇₋₁₁, see Fig. 1a)^{2,3,32}. These highly-oxygenated
120 organic molecules (HOMs) nucleate at atmospherically relevant concentrations with the help of ions but
121 without other species (e.g. sulfuric acid or bases) required³. Here, we group the HOMs according to carbon
122 atom number and define C₅, C₁₀, C₁₅ and C₂₀ classes as sum of all HOMs with 2-5, 6-10, 11-15 and 16-20
123 carbon atoms, respectively. This resembles the basic building block unit of a C₅ isoprenoid skeleton.

124 An isoprene/ozone mixture in the CLOUD chamber produces C₅H₉O₅₋₉ RO₂· radicals (referred to as RO₂(ip))
125 which terminate to C₅H₈O₅₋₈ and C₅H₁₀O₅₋₉ monomers and also some C₁₀H₁₈O₈₋₁₀ dimers under UV-
126 illuminated conditions (see Extended Data Fig. 5 a, b). The C₅H₉O₅₋₉ radicals originate presumably from an
127 OH· addition to isoprene and subsequent autoxidation. Under dark conditions, when the only source of
128 OH· is isoprene ozonolysis at 26 % yield³³, we observe only C₅ monomers. None of these molecules are

129 able to nucleate under atmospherically relevant conditions despite having an oxygen to carbon ratio (O:C)
130 ≥ 1 , which agrees with earlier observations that products from isoprene ozonolysis do not drive significant
131 new-particle formation³⁴⁻³⁶.

132 When isoprene is present together with α -pinene and ozone, the HOM chemistry of α -pinene is altered.
133 We observe the appearance of C_{15} and an increase in C_5 class molecules compared to α -pinene only
134 conditions as well as a decrease in C_{20} and C_{10} class molecules (see Fig. 1 and Extended Data Fig. 3). Without
135 isoprene, $RO_2(\alpha p)$ can terminate with another $RO_2(\alpha p)$, thus forming either one C_{20} dimer or two C_{10}
136 monomers. Monomers can also be formed by termination with HO_2 or unimolecular termination³². The
137 presence of $RO_2(ip)$ offers additional termination channels (see Fig. 4) and acts as an additional loss term
138 for $RO_2(\alpha p)$. $RO_2(ip)$ reactions are expected to result in C_5 and C_{10} monomers as well as C_{15} dimers. Most
139 importantly, the reduced $RO_2(\alpha p)$ steady state concentrations lead to a reduction of C_{20} class dimers by
140 roughly 50 % (depending on detailed conditions) compared to their level in the absence of isoprene for all
141 studied α -pinene concentrations (see Extended Data Fig. 3).

142 We measured the particle formation rate directly at a 1.7 nm cut-off diameter with a scanning Particle Size
143 Magnifier (PSM) under neutral (high voltage field cage switched on, see Methods for details) and ion
144 conditions (high voltage field cage switched off, allowing for galactic cosmic ray (gcr) ionization in the
145 chamber), further referred to as J_n and J_{gcr} (see Methods for detail). Fig. 2a shows J_n and J_{gcr} plotted against
146 the total HOM concentration (the sum of the C_5 , C_{10} , C_{15} and C_{20} classes) for the α -pinene only case and α -
147 pinene + isoprene. For +5 °C we find good agreement with ref. 3. However, the presence of isoprene and
148 the consequent change in oxidation chemistry reduces J_{gcr} by a factor of two to four and J_n even more by
149 around one order of magnitude at 5 °C. The suppression is stronger for lower α -pinene concentrations and
150 thus higher values of R (the ratio of isoprene to monoterpene carbon).

151 The larger gap between J_{gcr} and J_n with isoprene present compared to α -pinene only conditions is direct
152 evidence that isoprene oxidation products destabilize the nucleating clusters, thus making cluster
153 stabilization through the presence of charge more efficient. This also confirms that C_{20} class molecules are
154 mainly responsible for pure biogenic nucleation³⁷. C_{15} class molecules, which tend to counteract the losses
155 of the C_{20} class, do not prevent a decrease in J . Earlier studies have already suggested that C_{10} class
156 molecules do not have low enough vapor pressure to qualify as Extremely Low Volatility Organic
157 Compounds^{16,38} and thus drive nucleation, leaving C_{20} class molecules as the most likely nucleator
158 molecules. At +25 °C and UV light illumination, we find that nucleation rates of the pure α -pinene system
159 are reduced by a factor of about 2-3 compared to +5 °C. This is a much smaller reduction in nucleation rate
160 compared to, e.g., the inorganic sulfuric acid water system, for which the same temperature increase
161 reduces nucleation rates by around two orders of magnitude¹³ due to an increase in vapor pressure at
162 warmer temperatures. In our organic system, however, accelerated oxidation chemistry counters the
163 effect of higher vapor pressures. This includes a higher rate of initial oxidation of α -pinene by ozone, as
164 well as a faster autoxidation process, which leads to HOMs with generally higher oxygen content. When
165 we add isoprene at +25 °C with a constant ratio of isoprene to monoterpene carbon ($R = 2$), we find a
166 reduction in J_{gcr} of around a factor of about 2. Similar to the data at +5 °C where R ranges from 1.6 to 6.5,
167 we expect a stronger decrease for higher values of R. This can be understood as higher isoprene
168 concentrations enhance $RO_2(ip)$ formation, which in turn reduces C_{20} production and subsequent

169 nucleation. R can reach levels around 15 in the Amazon³⁹ and around 26 in Michigan⁷, were we would thus
170 expect an even stronger isoprene effect on nucleation.

171 Comparing HOM formation and nucleation for three different α -pinene/isoprene settings, we observe that
172 the addition of 2.7 ppbv of isoprene to an α -pinene/ozone mixture (770 pptv and 49 ppbv, respectively)
173 mitigates C_{20} production and reduces $J_{1.7}$ from $3.2 \text{ cm}^{-3}\text{s}^{-1}$ to $0.81 \text{ cm}^{-3}\text{s}^{-1}$ (see Extended Data Figure 6). A
174 rough doubling of both the α -pinene and isoprene levels to 1326 pptv and 4.87 ppbv, respectively,
175 increases overall HOM production; however, C_{20} levels and consequently $J_{1.7}$ remain lower than in the
176 original pure α -pinene setting without isoprene. Thus even increasing monoterpene concentrations can
177 lead to lower J values when isoprene is added as well. A strong coupling of daily cycles of isoprene and
178 monoterpenes is frequently observed in the Amazon basin with overall isoprene mixing ratios reaching up
179 to 20 ppbv^{40,41}. We thus do not expect significant C_{20} formation in the Amazon and subsequent nucleation,
180 even if monoterpene concentrations are relatively high, which agrees with the lack of new-particle
181 formation events observed. Further evidence for the important role of C_{20} class molecules for nucleation
182 is that fits for $J_{1.7}$ vs C_{20} agree for both α -pinene only and α -pinene + isoprene conditions, while for $J_{1.7}$ vs
183 $C_{15}+C_{20}$, these fits are significantly different depending on isoprene presence (see Extended Data Figure 9
184 a). Additionally, regressing each individual HOM peak with J_{gcr} also gives high coefficients of determination
185 for C_{20} class molecules (see Extended Data Figure 9 b).

186 It has been argued that $\text{OH}\cdot$ depletion by isoprene is responsible for the absence of nucleation in isoprene-
187 rich environments^{6,8}; however, under atmospheric conditions, isoprene induced $\text{OH}\cdot$ recycling can lead to
188 undisturbed high $\text{OH}\cdot$ levels, which might not be true in chamber experiments²¹⁻²³. In our study we also
189 see an $\text{OH}\cdot$ depletion effect due to isoprene addition (see Extended Data Fig. 1 and Methods for detailed
190 discussion). However, if $\text{OH}\cdot$ depletion were the reason for suppression of nucleation, an increase of $\text{OH}\cdot$
191 would lead to an increase in the nucleation rate. When we increase $\text{OH}\cdot$ levels by switching on UV lights in
192 the presence of isoprene, this reduces $\text{RO}_2(\alpha\text{p})$ further, as well as the C_{20} and C_{10} class molecules, while
193 enhancing the C_5 and C_{15} classes (see Extended Data Fig. 1, 4 and 5c,d as well as Methods for details).
194 Accordingly, J is also reduced slightly instead of being increased. This $\text{OH}\cdot$ effect can be understood by
195 comparing the reactivity of α -pinene and isoprene towards $\text{OH}\cdot$ at our given concentrations. For 300 and
196 1200 pptv the reactivity of α -pinene towards $\text{OH}\cdot$ at +5 °C ($[\alpha\text{p}]\cdot k_{\alpha\text{pOH}}$) is 25.1 and 6.3 times lower than the
197 reactivity of 4 ppbv isoprene towards $\text{OH}\cdot$ ($[\text{ip}]\cdot k_{\text{ipOH}}$), respectively. At +25 °C these numbers are similar
198 (25.4 and 6.3, respectively). This implies that any additional $\text{OH}\cdot$ provided by e.g. UV illumination will favor
199 the formation of additional $\text{RO}_2(\text{ip})$ instead of $\text{RO}_2(\alpha\text{p})$, thus favoring the formation of C_{15} over C_{20} and
200 consequently reducing nucleation rates. $\text{OH}\cdot$ does not enhance nucleation in this chemical system; it
201 suppresses it.

202 We performed experiments at +25 °C with three different levels of relative humidity (20, 38 and 80 %) to
203 probe the effect of water on new-particle formation. Changes in humidity do not significantly affect HOM
204 formation and J_{gcr} (see Extended Data Fig. 7). J_n increased slightly with humidity, showing an increased
205 stabilization of nucleating clusters by water; however, in gcr conditions, this role is fulfilled more efficiently
206 by ions.

207 We further studied the effect of sulfuric acid on nucleation of an α -pinene/isoprene mixture (about 1300
208 pptv and 4.5 ppbv, respectively) in experiments with excess ammonia (0.4 - 2.5 ppbv) in order to reproduce

209 typical conditions in the eastern parts of the United States¹⁰. We find that sulfuric acid does not enhance
210 biogenic nucleation up to a concentration of $5 \cdot 10^6 \text{ cm}^{-3}$ (see Extended Data Fig. 8). This decoupling of
211 biogenic nucleation from low sulfuric acid levels is similar to the pure α -pinene system reported in ref. 3.
212 At sulfuric acid levels higher than $5 \cdot 10^6 \text{ cm}^{-3}$, nucleation rates depend strongly on sulfuric acid levels, which
213 agrees with a wide variety of atmospheric measurements³. In the Amazon, sulfuric acid levels are typically
214 in the range of $1 \cdot 5 \cdot 10^5 \text{ cm}^{-3}$ ⁷, well below the threshold value of $5 \cdot 10^6 \text{ cm}^{-3}$. In Alabama this threshold was
215 exceeded only three times in a 45-day measurement period due to transported sulfur plumes, which led
216 to two events of particles growing to larger sizes¹⁰. In Michigan, sulfuric acid concentrations are typically
217 in the range of $1 \cdot 10^6 \text{ cm}^{-3}$ ⁷. We thus conclude that isoprene can exert its suppression of biogenic nucleation
218 in the Amazon as well as in different regions of the eastern United States, despite the presence of small
219 amounts of sulfuric acid.

220 We measured the growth rates of freshly nucleated particles from 1.3 nm onwards with a scanning Particle
221 Size Magnifier, a DMA-train and a nanoSMPS (see Methods for details). The change in HOM chemistry
222 caused by concurrent isoprene oxidation reduces the growth rates of particles in the range of 1.3 – 1.9 nm
223 and 1.8 – 3.2 nm roughly by a factor of two (Fig. 2b). This confirms that C_{15} class molecules have a higher
224 vapor pressure than C_{20} class molecules and are thus less efficient than C_{20} class molecules at causing
225 growth of the smallest particles. Likewise, most C_{10} class molecules are too volatile to contribute
226 significantly to the early stages of growth¹⁶. For the size range from 3.2 – 8.0 nm and larger, we observed
227 no suppression effect due to isoprene, indicating that molecules smaller than C_{20} are capable of
228 condensing onto larger particles. We find a linear relationship of growth rate vs C_{20} for 1.3 - 1.9 and 1.8 -
229 3.2 nm, regardless of isoprene presence. For larger sizes the linear relationship is independent of isoprene
230 presence, when plotted against $C_{15} + C_{20}$; this again indicates that C_{15} contributes to growth at larger sizes
231 (Extended Data Fig. 10). Besides C_{15} and C_{20} , however even lighter and less oxygenated molecules can
232 contribute to particle growth at larger sizes⁴². Growth rates at +25 °C are typically halved compared to +5
233 °C due to higher vapor pressure of the HOMs⁴², which leads to a higher chance of particles being scavenged
234 while growing, even more so in the presence of isoprene.

235 Fig. 3 shows the formation rate of particles measured at diameters of 1.7, 2.2, 2.5 and 6 nm for gcr
236 conditions and six concentration values (low/mid/high α -pinene mixing ratios with and without isoprene)
237 at +25 °C. We find that due to the reduced growth rates in the presence of isoprene, a moderate reduction
238 of formation rates at 1.7 nm becomes much more pronounced, while the particles grow to larger sizes.
239 When we compare α -pinene only data (771 pptv α -pinene, 49 ppbv O_3) with a mixture (1320 pptv α -
240 pinene, 39 ppbv O_3 and 4.9 ppbv isoprene, orange data points in Fig. 3), $J_{1.7}$ is reduced by 45 %, while the
241 corresponding formation rate at 6 nm is reduced by an order of magnitude. The corresponding precursor
242 concentrations are similar to conditions found in e.g. Alabama¹⁰. Isoprene can thus drastically reduce the
243 formation of particles larger than 6 nm even at relatively warm temperatures like +25 °C. This growth-rate
244 driven effect becomes stronger when α -pinene concentrations are reduced. We conclude that the
245 suppression of early growth by isoprene can explain the presence of small clusters that are however not
246 able to grow further, as was observed in Alabama¹⁰ and the Amazon²⁰. Increased levels of preexisting
247 aerosols (i.e. condensation sink) can scavenge freshly nucleated particles; however, due to the reduced
248 initial growth rates, the likelihood for that process at a given condensation sink is increased when isoprene
249 is present compared to α -pinene only conditions.

250 In summary, we find that isoprene interferes with α -pinene HOM chemistry via $\text{RO}_2\cdot$ peroxy-radical
251 termination. When isoprene is present, fewer C_{20} class molecules are formed, which directly reduces the
252 nucleation rate. We could show that C_{20} class molecules act as “nucleator” species. The reduction of
253 nucleation rate becomes stronger with higher isoprene to monoterpene carbon ratio (R), consistent with
254 earlier observations⁶; however, in the monoterpene-isoprene chemical system, increased $\text{OH}\cdot$ does not
255 enhance nucleation, but, on the contrary, reduces it due to C_{20} class reduction. Biogenic nucleation in the
256 α -pinene isoprene system is not affected by typical concentrations of sulfuric acid found in the Amazon or
257 in eastern parts of the United States. The change in monoterpene HOM chemistry due to isoprene reduces
258 organic growth rates in the 1.3 – 3.2 nm range by around 50 %, which strongly reduces the probability that
259 the smallest, freshly-nucleated particles will survive scavenging as they grow to larger sizes. While other
260 factors can also inhibit nucleation (like NO_x ⁴³ or a high condensation sink), at atmospherically relevant
261 conditions, isoprene can make the difference between measurable new-particle formation events and
262 their absence even at relatively high monoterpene concentrations (> 1 ppbv). Our findings can thus explain
263 on a molecular level the lack of biogenic new-particle formation in isoprene-rich environments like the
264 Amazon basin or the eastern United States.

265 **References:**

- 266 1 Dunne, E. M. *et al.* Global atmospheric particle formation from CERN CLOUD measurements.
267 *Science* **354**, 1119 (2016).
- 268 2 Ehn, M. *et al.* A large source of low-volatility secondary organic aerosol. *Nature* **506**, 476-479,
269 doi:10.1038/nature13032 (2014).
- 270 3 Kirkby, J. *et al.* Ion-induced nucleation of pure biogenic particles. *Nature* **533**, 521-526,
271 doi:10.1038/nature17953 (2016).
- 272 4 Riccobono, F. *et al.* Oxidation Products of Biogenic Emissions Contribute to Nucleation of
273 Atmospheric Particles. *Science* **344**, 717 (2014).
- 274 5 Guenther, A. B. *et al.* The Model of Emissions of Gases and Aerosols from Nature version 2.1
275 (MEGAN2.1): an extended and updated framework for modeling biogenic emissions. *Geosci.*
276 *Model Dev.* **5**, 1471-1492, doi:10.5194/gmd-5-1471-2012 (2012).
- 277 6 Kiendler-Scharr, A. *et al.* New particle formation in forests inhibited by isoprene emissions.
278 *Nature* **461**, 381-384 (2009).
- 279 7 Kanawade, V. P. *et al.* Isoprene suppression of new particle formation in a mixed deciduous
280 forest. *Atmos. Chem. Phys.* **11**, 6013-6027, doi:10.5194/acp-11-6013-2011 (2011).
- 281 8 Kiendler-Scharr, A. *et al.* Isoprene in poplar emissions: effects on new particle formation and OH
282 concentrations. *Atmos. Chem. Phys.* **12**, 1021-1030, doi:10.5194/acp-12-1021-2012 (2012).
- 283 9 Yu, H. *et al.* New Particle Formation and Growth in an Isoprene-Dominated Ozark Forest: From
284 Sub-5 nm to CCN-Active Sizes. *Aerosol Science and Technology* **48**, 1285-1298,
285 doi:10.1080/02786826.2014.984801 (2014).
- 286 10 Lee, S.-H. *et al.* Isoprene suppression of new particle formation: Potential mechanisms and
287 implications. *Journal of Geophysical Research: Atmospheres* **121**, 14,621-614,635,
288 doi:10.1002/2016JD024844 (2016).
- 289 11 Martin, S. T. *et al.* Sources and properties of Amazonian aerosol particles. *Reviews of Geophysics*
290 **48**, n/a-n/a, doi:10.1029/2008RG000280 (2010).
- 291 12 Kulmala, M. *et al.* Formation and growth rates of ultrafine atmospheric particles: a review of
292 observations. *Journal of Aerosol Science* **35**, 143-176 (2004).
- 293 13 Kirkby, J. *et al.* Role of sulphuric acid, ammonia and galactic cosmic rays in atmospheric aerosol
294 nucleation. *Nature* **476**, 429, doi:10.1038/nature10343 (2011).
- 295 14 Almeida, J. *et al.* Molecular understanding of sulphuric acid-amine particle nucleation in the
296 atmosphere. *Nature* **502**, 359, doi:10.1038/nature12663 (2013).
- 297 15 Sipilä, M. *et al.* Molecular-scale evidence of aerosol particle formation via sequential addition of
298 HIO₃. *Nature* **537**, 532 (2016).
- 299 16 Tröstl, J. *et al.* The role of low-volatility organic compounds in initial particle growth in the
300 atmosphere. *Nature* **533**, 527, doi:10.1038/nature18271 (2016).
- 301 17 Gordon, H. *et al.* Reduced anthropogenic aerosol radiative forcing caused by biogenic new
302 particle formation. *Proceedings of the National Academy of Sciences* **113**, 12053-12058 (2016).
- 303 18 Jardine, A. B. *et al.* Highly reactive light-dependent monoterpenes in the Amazon. *Geophysical*
304 *Research Letters* **42**, 1576-1583, doi:10.1002/2014GL062573 (2015).
- 305 19 Varanda Rizzo, L. *et al.* Multi-year statistical and modeling analysis of submicrometer aerosol
306 number size distributions at a rain forest site in Amazonia. *Atmospheric Chemistry and Physics*
307 **18**, 10255-10274 (2018).
- 308 20 Wimmer, D. *et al.* Ground-based observation of clusters and nucleation-mode particles in the
309 Amazon. *Atmospheric Chemistry and Physics* **18**, 13245-13264 (2018).
- 310 21 Taraborrelli, D. *et al.* Hydroxyl radical buffered by isoprene oxidation over tropical forests.
311 *Nature Geoscience* **5**, 190, doi:10.1038/ngeo1405 (2012).

- 312 22 Martinez, M. *et al.* Hydroxyl radicals in the tropical troposphere over the Suriname rainforest:
313 airborne measurements. *Atmos. Chem. Phys.* **10**, 3759-3773, doi:10.5194/acp-10-3759-2010
314 (2010).
- 315 23 Fuchs, H. *et al.* Experimental evidence for efficient hydroxyl radical regeneration in isoprene
316 oxidation. *Nature Geoscience* **6**, 1023, doi:10.1038/ngeo1964 (2013).
- 317 24 Teng, A. P., Crounse, J. D. & Wennberg, P. O. Isoprene Peroxy Radical Dynamics. *Journal of the*
318 *American Chemical Society* **139**, 5367-5377, doi:10.1021/jacs.6b12838 (2017).
- 319 25 Berndt, T., Herrmann, H., Sipilä, M. & Kulmala, M. Highly Oxidized Second-Generation Products
320 from the Gas-Phase Reaction of OH Radicals with Isoprene. *The Journal of Physical Chemistry A*
321 **120**, 10150-10159, doi:10.1021/acs.jpca.6b10987 (2016).
- 322 26 Carlton, A. G., Wiedinmyer, C. & Kroll, J. H. A review of Secondary Organic Aerosol (SOA)
323 formation from isoprene. *Atmos. Chem. Phys.* **9**, 4987-5005, doi:10.5194/acp-9-4987-2009
324 (2009).
- 325 27 Krechmer, J. E. *et al.* Formation of Low Volatility Organic Compounds and Secondary Organic
326 Aerosol from Isoprene Hydroxyhydroperoxide Low-NO Oxidation. *Environmental Science &*
327 *Technology* **49**, 10330-10339, doi:10.1021/acs.est.5b02031 (2015).
- 328 28 Paulot, F. *et al.* Unexpected epoxide formation in the gas-phase photooxidation of isoprene.
329 *Science* **325**, 730-733 (2009).
- 330 29 Surratt, J. D. *et al.* Reactive intermediates revealed in secondary organic aerosol formation from
331 isoprene. *Proceedings of the National Academy of Sciences* **107**, 6640-6645 (2010).
- 332 30 Lin, Y.-H. *et al.* Isoprene epoxydiols as precursors to secondary organic aerosol formation: acid-
333 catalyzed reactive uptake studies with authentic compounds. *Environmental science &*
334 *technology* **46**, 250-258 (2011).
- 335 31 Budisulistiorini, S. H. *et al.* Real-time continuous characterization of secondary organic aerosol
336 derived from isoprene epoxydiols in downtown Atlanta, Georgia, using the Aerodyne Aerosol
337 Chemical Speciation Monitor. *Environmental science & technology* **47**, 5686-5694 (2013).
- 338 32 Rissanen, M. P. *et al.* Effects of Chemical Complexity on the Autoxidation Mechanisms of
339 Endocyclic Alkene Ozonolysis Products: From Methylcyclohexenes toward Understanding α -
340 Pinene. *The Journal of Physical Chemistry A* **119**, 4633-4650, doi:10.1021/jp510966g (2015).
- 341 33 Malkin, T. L., Goddard, A., Heard, D. E. & Seakins, P. W. Measurements of OH and HO₂ yields
342 from the gas phase ozonolysis of isoprene. *Atmos. Chem. Phys.* **10**, 1441-1459, doi:10.5194/acp-
343 10-1441-2010 (2010).
- 344 34 Kamens, R. M., Gery, M. W., Jeffries, H. E., Jackson, M. & Cole, E. I. Ozone-isoprene reactions:
345 Product formation and aerosol potential. *International Journal of Chemical Kinetics* **14**, 955-975
346 (1982).
- 347 35 Kleindienst, T. E., Lewandowski, M., Offenberg, J. H., Jaoui, M. & Edney, E. O. Ozone-isoprene
348 reaction: Re-examination of the formation of secondary organic aerosol. *Geophysical Research*
349 *Letters* **34** (2007).
- 350 36 Riva, M. *et al.* Multiphase reactivity of gaseous hydroperoxide oligomers produced from isoprene
351 ozonolysis in the presence of acidified aerosols. *Atmospheric Environment* **152**, 314-322 (2017).
- 352 37 Frege, C. *et al.* Influence of temperature on the molecular composition of ions and charged
353 clusters during pure biogenic nucleation. *Atmos. Chem. Phys.* **18**, 65-79, doi:10.5194/acp-18-65-
354 2018 (2018).
- 355 38 Kurtén, T. *et al.* α -Pinene Autoxidation Products May Not Have Extremely Low Saturation Vapor
356 Pressures Despite High O:C Ratios. *The Journal of Physical Chemistry A* **120**, 2569-2582,
357 doi:10.1021/acs.jpca.6b02196 (2016).
- 358 39 Greenberg, J. P. *et al.* Biogenic VOC emissions from forested Amazonian landscapes. *Global*
359 *Change Biology* **10**, 651-662 (2004).

- 360 40 Yáñez-Serrano, A. M. *et al.* Monoterpene chemical speciation in a tropical rainforest: variation
361 with season, height, and time of day at the Amazon Tall Tower Observatory (ATTO). *Atmospheric*
362 *Chemistry and Physics* **18**, 3403-3418 (2018).
- 363 41 Karl, T. *et al.* The tropical forest and fire emissions experiment: Emission, chemistry, and
364 transport of biogenic volatile organic compounds in the lower atmosphere over Amazonia.
365 *Journal of Geophysical Research: Atmospheres* **112** (2007).
- 366 42 Stolzenburg, D. *et al.* Rapid growth of organic aerosol nanoparticles over a wide tropospheric
367 temperature range. *Proceedings of the National Academy of Sciences*, 201807604 (2018).
- 368 43 Wildt, J. *et al.* Suppression of new particle formation from monoterpene oxidation by NO_x.
369 *Atmospheric chemistry and physics* **14**, 2789-2804 (2014).
- 370

371 **Acknowledgements:**

372 We thank CERN for supporting CLOUD with technical and financial resources, and for providing a particle
373 beam from the CERN Proton Synchrotron. We thank P. Carrie, L.-P. De Menezes, J. Dumollard, K. Ivanova,
374 F. Josa, I. Krasin, R. Kristic, A. Laassiri, O. S. Maksumov, B. Marichy, H. Martinati, S. V. Mizin, R. Sitals, A.
375 Wasem and M. Wilhelmsson for their contributions to the experiment. This research has received funding
376 from the EC Seventh Framework Programme and European Union's Horizon 2020 programme (Marie
377 Skłodowska Curie ITNs no. 316662 "CLOUD-TRAIN" and no. 764991 "CLOUD-MOTION", MSCA-IF no.
378 656994 "nano-CAVa", MC-COFUND grant no. 600377, ERC projects no. 692891 "DAMOCLES", no. 638703
379 "COALA", no. 616075 "NANODYNAMITE", no. 335478 "QAPPA", no. 742206 "ATM-GP", no. 714621
380 "GASPARCON"), the German Federal Ministry of Education and Research (projects no. 01LK0902A,
381 01LK1222A 01LK1601A), the Swiss National Science Foundation (projects no. 20020_152907,
382 200020_172602, 20FI20_159851, 200020_172602, 20FI20_172622), the Academy of Finland (Center of
383 Excellence no. 307331, projects 299574, 296628, 306853, 304013), the Finnish Funding Agency for
384 Technology and Innovation, the Väisälä Foundation, the Nessling Foundation, the Austrian Science Fund
385 (FWF; project no. J3951-N36, project no. P27295-N20), the Austrian research funding association (FFG,
386 project no. 846050), the Portuguese Foundation for Science and Technology (project no.
387 CERN/FP/116387/2010), the Swedish Research Council Formas (project number 2015-749),
388 Vetenskapsrådet (grant 2011-5120), the Presidium of the Russian Academy of Sciences and Russian
389 Foundation for Basic Research (grants 08-02-91006-CERN, 12-02-91522-CERN), the U.S. National Science
390 Foundation (grants AGS1136479, AGS1447056, AGS1439551, CHE1012293, AGS1649147, AGS1602086),
391 the Wallace Research Foundation, the US Department of Energy (grant DE-SC0014469), the NERC GASSP
392 project NE/J024252/1m, the Royal Society (Wolfson Merit Award), United Kingdom Natural Environment
393 Research Council grant NE/K015966/1, Dreyfus Award EP-11-117, the French National Research Agency
394 the Nord-Pas de Calais, European Funds for Regional Economic Development Labex-Cappa grant ANR-11-
395 LABX-0005-01).

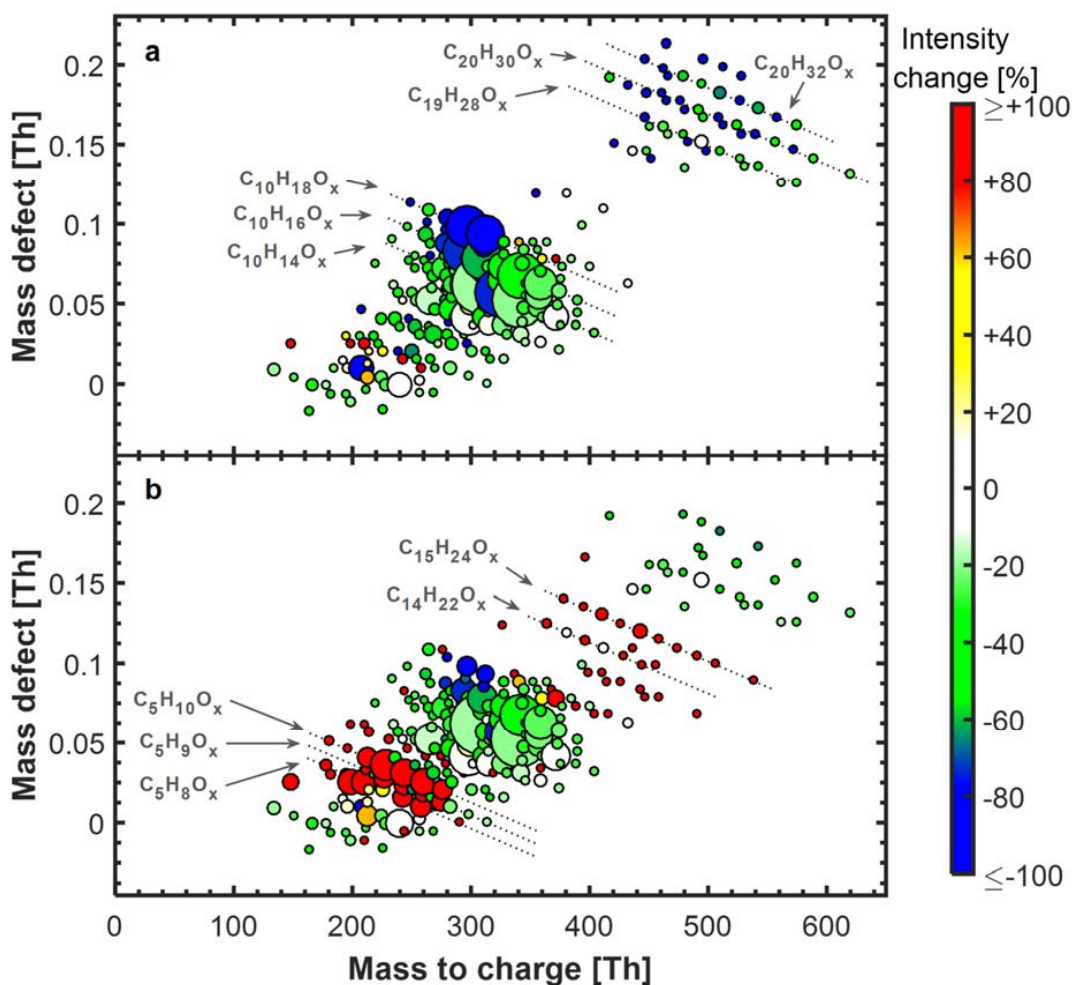
396 **Author contributions:**

397 M. H., L. D., M. Sim., D. S., A. C. W., L. F., L. R. A., S. A., F. B., S. B., R. B., A. D., J. Du., I. E.-H., H. F., C. Fr., C.
398 Fu., H. G., M. G., X. H., J. H., V. H., C. K., T. K., A. K., J. Ka., M. L., K. L., T. M. L., J. L., C. P. L., H. L., H. M., U.
399 M., S. M., V. M., B. M., R. L. M., T. M., R. M., W. N., A. O., T. P., V. P., J. P., L. L. J. Q., M. P. R., Y. S., W. S., S.
400 S., K. S., G. S., M. Sip., Y. J. T., R. V., A. L. V., A. V., M. V.-P., M. W., L. W., D. W., R. W., M. X., P. Y., C. Y., Q.
401 Z., X. Z., J. Kir. and A. T. prepared the CLOUD facility and measurement instruments. M. H., L. D., M. Sim.,
402 D. S., A. C. W., L. F., L. R. A., S. A., F. B., A. B., S. B., P. S. B., B. B., R. B., D. C., A. D., J. Du., I. E.-H., H. F., C.
403 Fu., H. G., O. G., M. G., X. H., J. H., C. R. H., V. H., C. K., T. K., K. L., J. L., C. P. L., H. L., U. M., V. M., B. M., R.
404 L. M., T. M., R. M., T. N., W. N., J. P., M. Pa., L. L. J. Q., M. P. R., C. R., Y. S., W. S., S. S., K. S., G. S., C. T., Y.
405 J. T., R. V., A. V., M. V.-P., L. W., D. W., M. X., P. Y., C. Y., Q. Z., X. Z., J. Kir., A. A. and A. T. collected the
406 data. M. H., L. D., M. Sim., D. S., L. F., H. F., V. H., J. Ka., B. M., T. N., E. P., G. S., R. V., M. X. and C. Y.
407 analyzed the data. M. H., L. D., M. Sim., D. S., A. C. W., L. F., J. Do., H. G., A. K., K. L., R. L. M., M. P. R., M.
408 Sip., A. L. V., P. Y., C. Y., N. M. D., J. Kir., U. B., P. M. W., J. Cu., D. R. W., A. H. and M. K. contributed to the
409 scientific discussion. M. H., L. D., M. Sim., D. S., A. C. W., A. K., N. M. D., J. Kir., U. B. and J. Cu. contributed
410 to writing the manuscript.

411

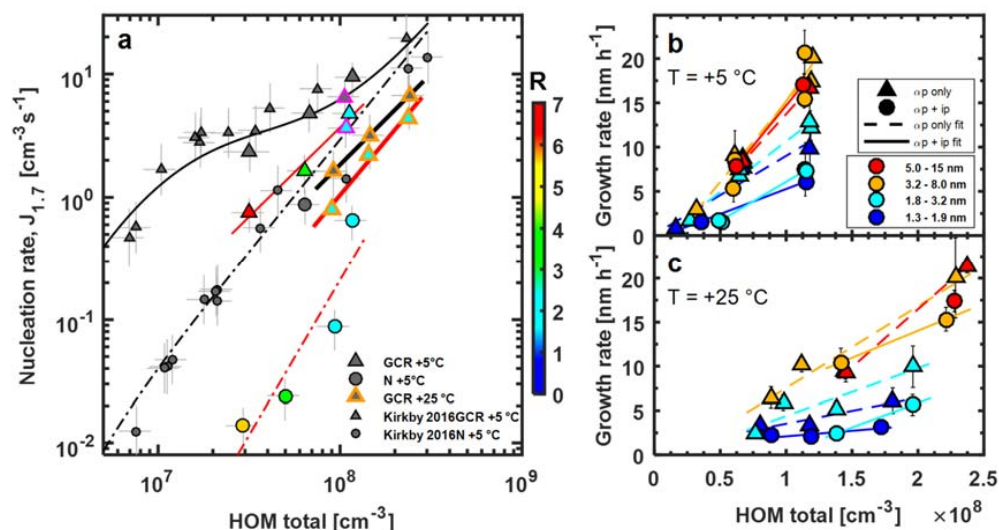
412 **Author Information:**

413 The authors declare no competing financial interests. Correspondence and requests for materials should
414 be addressed to J. Cu. (curtius@iau.uni-frankfurt.de).



415

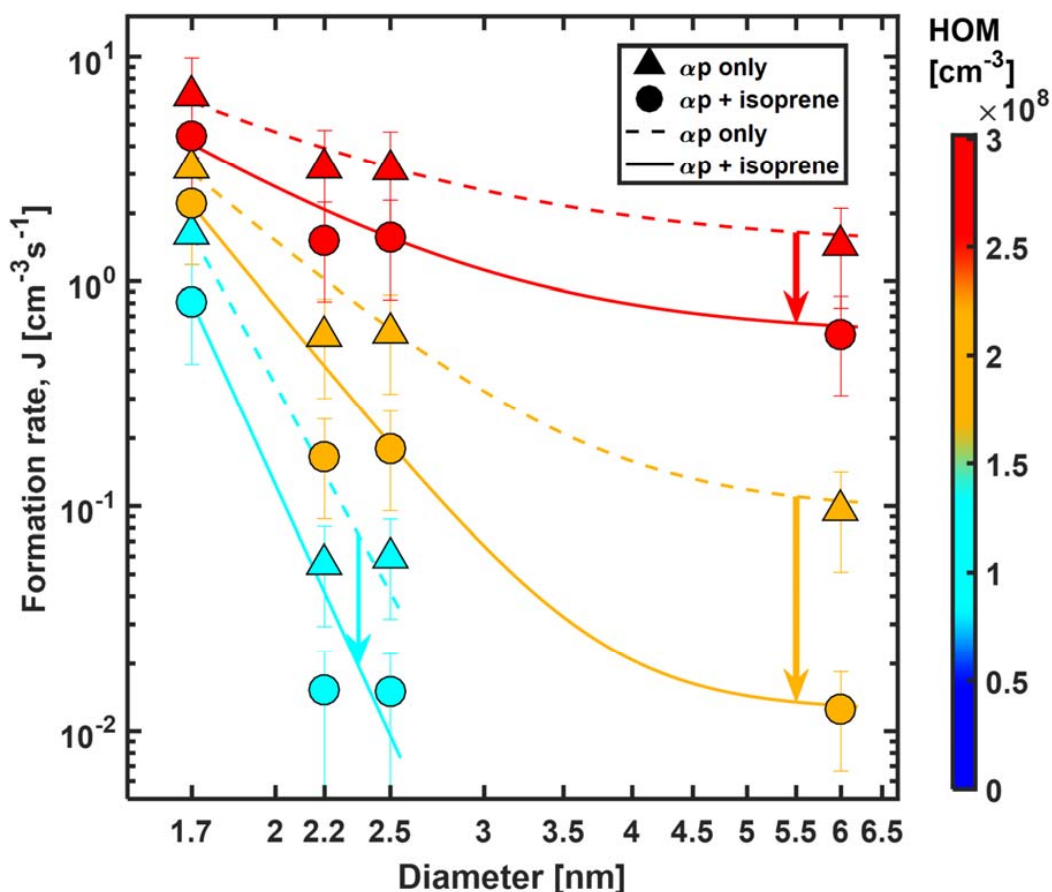
416 **Figure 1: Mass defect plots of neutral HOM molecules measured with nitrate CI-API-TOF without**
417 **isoprene (a) and with isoprene added (b) at +25 °C. α -pinene levels were 771 and 1326 pptv, respectively.**
418 **Ozone levels were 49 and 39 ppbv, respectively. Isoprene was 4.9 ppbv. in (b). Relative humidity was 38 %**
419 **in (a) and (b). The area of the marker points is linearly scaled with the intensity of the HOM signals. Color**
420 **code shows the relative intensity change for each HOM peak due to isoprene addition, i.e. the percentage**
421 **intensity change between (a) and (b). The color for each peak is thus the same in (a) and (b). HOM intensity**
422 **in (a) was scaled up linearly by 38 % to match $[\alpha\text{-pinene}] \cdot [\text{O}_3]$ levels present in (b) to calculate the intensity**
423 **change.**



424

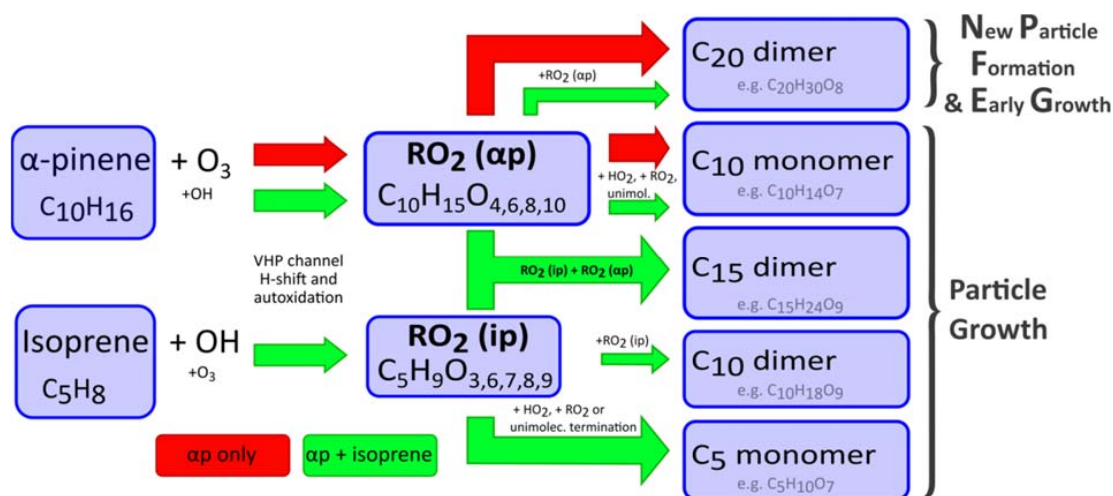
425 **Figure 2: Pure biogenic nucleation rates at 1.7 nm diameter and growth rates against total HOM**
 426 **concentration with and without isoprene added at +5 and +25 °C.** HOM total is defined as the sum of C₅,
 427 C₁₀, C₁₅ and C₂₀ carbon classes. Relative humidity is 38 % for all data points. **(a)** Triangles represent J_{gcr} and
 428 circles J_n . Small grey points were taken from ref. 3. Magenta edges indicate UV-illuminated conditions at
 429 +5 °C, at +25 °C all data points are with UV light on. Color shows isoprene to monoterpene carbon ratio
 430 (R). Black solid and dash-dotted lines are parametrizations of J_{gcr} and J_n from ref. 3. Red solid and dash-
 431 dotted lines are power law fits to J_{gcr} and J_n in the presence of isoprene at +5 °C. Thick solid black and red
 432 line represent power law fits to +25 °C data for α-pinene only and α-pinene + isoprene systems. Bars
 433 indicate 1σ run-to-run uncertainty. The overall systematic scale uncertainty of HOMs of +78 %/-68 % and
 434 of J for ±47 % is not shown. In **(b)** and **(c)**, triangles represent α-pinene only, circles α-pinene + isoprene
 435 conditions. Marker color indicates the size range in which growth rate was measured: dark blue 1.3 – 1.9
 436 nm (measured by scanning PSM), light blue 1.8 – 3.2 nm, orange 3.2 – 8.0 nm (both measured by DMA-
 437 train) and red 5.0 – 15 nm (measured by nanoSMPS). Bars indicate 1σ uncertainties in growth rate
 438 estimation. Dashed lines are linear fits to α-pinene only data points; solid lines are linear fits to α-pinene
 439 + isoprene conditions, respectively.

440



441

442 **Figure 3: Formation rate (gcr) vs diameter of particles at +25 °C and 38 % RH.** Triangles represent α -pinene
 443 only, circles α -pinene + isoprene conditions. α -Pinene levels were 456, 771 and 1442 pptv for triangles and
 444 677, 1326 and 2636 pptv for circles. Ozone levels were 49 ppbv for triangles and 38 to 40 ppbv for circles.
 445 Isoprene levels ranged from 2.7 to 9.8 ppbv for circles. Color code represents HOM concentration. Bars
 446 indicate overall scale uncertainty for formation rates of $\pm 47\%$. The uncertainty in the diameters is ± 0.3
 447 nm. Dashed and solid lines are lines to guide the eye. The steeper slope at lower diameter values is caused
 448 by the Kelvin effect, i.e. a smaller growth rate at small sizes that leads to higher losses of newly formed
 449 particles. The formation rate measurements at 2.2 and 2.5 nm for the lowest α -pinene/isoprene setting
 450 (cyan circles) are upper limits.



451

452 **Figure 4: Proposed mechanism for the interference of isoprene in α -pinene oxidation chemistry.** The
 453 pathway of HOM formation of an α -pinene/ozone mixture alone is indicated by red arrows. When isoprene
 454 is present, the green arrows indicate the additional interference of isoprene in α -pinene oxidation
 455 chemistry via RO_2 radicals. The oxidation of α -pinene at the conditions used in our experiments is
 456 dominated by ozonolysis. After the initial ozone attack a $C_{10}H_{15}O_4$ peroxy-radical forms via a
 457 vinylhydroperoxyde channel (VHP), which can undergo various intramolecular H-shifts and autoxidation
 458 steps^{2,3}. Thus the chain of $RO_2(\alpha)$ mostly consists of $C_{10}H_{15}O_{4,6,8,10}$. These radicals can terminate either via
 459 reaction with other RO_2 radicals, via reaction with HO_2 or via unimolecular processes³². The resulting
 460 closed shell products are then either covalently bound C_{20} class dimers, which are mostly responsible for
 461 nucleation or C_{10} class monomers. Possible fragmentation might also lead to a low amount of C_5 and C_{15}
 462 class molecules being formed even without isoprene present. Isoprene oxidation is dominated by reactions
 463 with OH in the CLOUD chamber, which produce a series of C_5 RO_2 radicals ($C_5H_9O_{3,6,7,8,9}$). These $RO_2(ip)$
 464 radicals can now interfere in the termination of $RO_2(\alpha)$. The reaction of $RO_2(ip)$ with $RO_2(\alpha)$ can lead to
 465 C_{15} class dimers, C_{10} class monomers or C_5 class monomers. The reaction of $RO_2(ip)$ with another $RO_2(ip)$
 466 can lead to C_{10} class dimers or C_5 class monomers. The presence of $RO_2(ip)$ reduces the steady state
 467 concentration of $RO_2(\alpha)$, as it acts as an additional sink for $RO_2(\alpha)$. This directly reduces the formation
 468 of C_{20} class dimers, as two $RO_2(\alpha)$ radicals are needed to form one C_{20} class dimer. We link this reduction
 469 of C_{20} class dimers to the reduction of biogenic nucleation and early growth rates in the presence of
 470 isoprene.

471

472 **Methods**473 **CLOUD Facility**

474 We conducted our measurements at the CLOUD (Cosmics Leaving OUtdoor Droplets) chamber at CERN
475 (European Center for Nuclear Research), Geneva, Switzerland. The CLOUD chamber is a 26.1 m³ electro-
476 polished stainless-steel tank used to recreate atmospheric condition in the laboratory (for more details on
477 the chamber see refs. 3,13,44). Data for this study are from the CLOUD 11 and 12 campaigns in autumn
478 2016 and 2017. Various measures are taken to reduce unwanted contaminants in the CLOUD chamber.
479 The air in the chamber is mixed from cryogenic nitrogen and oxygen, all lines are made of stainless steel
480 and intense cleaning cycles are performed prior to each campaign. Each cleaning cycle consists of at least
481 24 h of rinsing the chamber from the inside with ultrapure water, followed by a period of at least 24 h with
482 the chamber at 100°C and high ozone levels (several parts per million by volume). These measures result
483 in very low organic contamination below 150 pptv³ in total.

484 Ultrapure water is used to humidify the air in the chamber. Ozone is produced by a UV ozone generator.
485 Liquid α -pinene (Sigma Aldrich, purity >98 %) is stored in a temperature controlled water bath and
486 evaporated into a dry nitrogen flow and fed into the chamber. Isoprene from a gas bottle (Carbagas AG,
487 purity >99%) is additionally cleaned by a cryotrap. The cryotrap consists of a ~2 m long ¼" stainless steel
488 tube spiral placed in a cryogenic liquid held at 233 K. By using this trap, non-negligible monoterpene-like
489 contaminants in the isoprene gas bottle are effectively frozen out⁴⁵. Isoprene and α -pinene are diluted by
490 separate two stage dilution systems prior to being fed into the chamber. All gases are fed into the chamber
491 from the bottom and are mixed by two magnetically driven fans.

492 A unique feature of the CLOUD chamber is its control of ion concentrations. A high voltage electric field
493 cage (± 30 kV) can sweep ions that are constantly produced by naturally occurring galactic cosmic rays out
494 of the chamber in around 1 s. This enables us to study pure neutral nucleation. By switching the field cage
495 off, the naturally formed ions are allowed to stay in the chamber and affect nucleation processes. To
496 artificially enhance ion concentrations, CERN's Proton Synchrotron provides a 3.5 GeV π^+ beam that is
497 diverged to >1 m² beam profile and crosses the center region of the chamber.

498 The CLOUD chamber is equipped with four HgXe UV lamps (LightningCure LC8, Hamamatsu Photonics K.K.)
499 positioned at the top of the chamber and connected via fiber bundles. An additional UV source is provided
500 by a KrF excimer laser (ATLEX-1000, ATL Lasertechnik GmbH) at 248 nm wavelength and also connected
501 to the chamber via fiber bundles to enhance OH \cdot production via photolysis of O₃ further.

502

503 **Typical Run sequence and conditions**

504 Our experiments were performed at +5 and +25 °C and mostly 38 % relative humidity. A typical run
505 sequence can be seen in Extended Data Fig. 1 and 2. First, α -pinene is present with ozone under both
506 neutral and gcr conditions at three different atmospherically relevant concentrations. HOMs are forming
507 as seen by the CI-API-TOF and new-particle formation is induced. The purpose of this experiment was also
508 to ensure inter-campaign comparability to ref. 3. In the following run a stable isoprene concentration is

509 established in the chamber and ozone is added shortly afterwards. As ozone and isoprene only react very
510 slowly, effects on HOMs are minor. As UV light in the chamber is switched on, OH· production increases
511 and thus formation of OH· induced isoprene HOMs. However, only the subsequent addition of α -pinene
512 leads to formation of C₂₀ class HOMs and thus new-particle formation. UV effects were studied by
513 switching on the Hamamatsu lamp, as well as the KrF-excimer laser.

514

515 **Gas-phase measurements**

516 Ozone was measured by a calibrated ozone monitor (Thermo Environmental Instruments TEI 49C).
517 Isoprene and α -pinene were measured by the newly developed proton transfer reaction time-of-flight
518 mass spectrometer (PTR3⁴⁶). The instrument was frequently calibrated for both gases and has a limit of
519 detection of 2 pptv for isoprene and α -pinene for 1 s integration time. The accuracy of the instrument for
520 both gases is mainly determined by the uncertainty of the calibration gas standard (5 %) and accuracies of
521 mass flow controllers and is estimated to be 7 %.

522 The chemical ionization atmospheric pressure interface time-of-flight (CI-API-TOF) mass spectrometer
523 (Tofwerk AG) measured highly-oxygenated organic compounds with a limit of detection of $\sim 5 \cdot 10^4$ cm⁻³.
524 The instrument operates with a nitrate based ion source similar to the design in ref. 47. However, a corona
525 discharge was used instead of a radioactive source⁴⁸. The instrument was calibrated for sulfuric acid⁴⁹ and
526 the data corrected for mass dependent transmission efficiency⁵⁰. HOM quantification was performed as
527 described in ref. 3. The run-to-run uncertainty for HOMs is estimated to be 20 %. Due to technical reasons
528 at the start of CLOUD 11 the CI-API-TOF could only start measuring at 03 Oct 2016, 10:28 UTC (see
529 Extended Data Fig. 1). As HOMs depend linearly on the product [α -pinene]·[O₃]^{2,3}, HOM concentrations
530 measured during the mid α -pinene settings were used and scaled down according to this relation to obtain
531 HOM concentrations for the low α -pinene settings for the appropriate times where *J* and growth rates
532 were estimated. This also gave a higher uncertainty for this data point (28 %) as indicated in Fig. 2a. The
533 overall uncertainty in HOM quantification consists of contributions from sulfuric acid calibration (+50 %/
534 -33 %), charging efficiency of HOMs in the ion source (25 %), transmission correction (50 %) and sampling
535 line loss correction (20 %). This results in an overall scale uncertainty for HOMs of +78 %/-68 %. There are
536 however additional uncertainties in our HOM estimation that cannot be readily quantified. On the one
537 hand nitrate ionization of HOMs shows a drop in charging efficiency for HOMs with six or less oxygen
538 atoms⁵¹. This leads to an underestimation of these molecules. However, these molecules with comparably
539 low oxygen content are not expected to contribute significantly to nucleation and early growth.
540 Additionally, it was shown that nitrate ionization has a reduced charging efficiency towards HOMs formed
541 by OH· oxidation compared to HOMs formed by ozonolysis^{52,53}. This could affect also C₂₀ class molecules
542 that show OH· dependence, like C₂₀H₃₂O₇ (see Extended Data Figure 1). The real increase of these C₂₀ class
543 HOMs due to UV light could be larger than the measured one, thus dampening the overall decrease of C₂₀
544 when UV is switched on. The fact that *J* decreases when UV is switched on, however, confirms that the
545 total nucleating molecules in the chamber decrease. That effect is thus not strong enough to lead to a real
546 increase instead of a decrease in C₂₀ class molecules.

547 We group all HOMs within the m/z range from 235 to 625 Th in four groups according to their carbon
548 number. This m/z range was chosen to remain consistent with the definition of total HOM in ref. 3. We
549 sum up HOMs with 2-5, 6-10, 11-15 and 16-20 carbon atoms to get C_5 , C_{10} , C_{15} and C_{20} class HOMs,
550 respectively. The sum of these four classes represents HOM total as shown e.g. in Fig. 2.

551

552 **OH· estimation and comparison to ambient environments**

553 We estimate OH· levels in our chamber via a steady state approach (see Extended Data Figure 1). OH·
554 sources taken into account are ozonolysis of α -pinene and isoprene, with yields of 79 %⁵⁴ and 26 %^{33,55},
555 respectively, as well as photolysis of ozone with our UV laser. The OH· source strength of the UV laser was
556 characterized with a separate experiment (SO_2 to sulfuric acid conversion) and depends on laser settings,
557 ozone concentration and absolute water vapor concentration. Sink terms taken into account are reactions
558 of OH· with α -pinene and isoprene. Secondary reactions of OH· with further oxidation products of α -pinene
559 or isoprene are not taken into account, as their effect is expected to be minor (e.g. two orders of
560 magnitude smaller than the former sink terms in case of the pinonaldehyde-OH· reaction). OH· recycling
561 in our chamber is expected to be weak, as we do not have NO_x in the chamber and many runs are
562 performed under dark conditions. The recycling mechanism due to photolysis of hydroperoxy-aldehydes
563 (HPALDs)²¹ can in principal take place during UV runs, however, HPALDs may also decompose on our
564 stainless steel chamber walls without releasing OH· in a process similar to the one described in ref. 56,
565 thus further reducing recycling efficiency. However, the O_x recycling mechanisms (reaction of O_3 and HO_2
566 yielding OH·, as well as photolysis of H_2O_2 under UV conditions) might take place in our conditions⁵⁷. All
567 gas phase reaction rate constants are preferred values provided by IUPAC (International Union of Pure and
568 Applied Chemistry) and were evaluated at +5 °C ($k_{\alpha p O_3} = 8.1 \cdot 10^{-17} \text{ cm}^3 \text{ s}^{-1}$, $k_{\alpha p OH} = 5.8 \cdot 10^{-11} \text{ cm}^3 \text{ s}^{-1}$, $k_{i p O_3} =$
569 $7.9 \cdot 10^{-18} \text{ cm}^3 \text{ s}^{-1}$ and $k_{i p OH} = 1.1 \cdot 10^{-10} \text{ cm}^3 \text{ s}^{-1}$) and +25 °C ($k_{\alpha p O_3} = 9.4 \cdot 10^{-17} \text{ cm}^3 \text{ s}^{-1}$, $k_{\alpha p OH} = 5.2 \cdot 10^{-11} \text{ cm}^3 \text{ s}^{-1}$, $k_{i p O_3}$
570 $= 1.3 \cdot 10^{-17} \text{ cm}^3 \text{ s}^{-1}$ and $k_{i p OH} = 1.0 \cdot 10^{-10} \text{ cm}^3 \text{ s}^{-1}$).

571 We calculate OH· levels of around $1 \cdot 10^6 \text{ cm}^{-3}$ during dark α -pinene ozonolysis, with roughly a doubling to
572 $2 \cdot 10^6 \text{ cm}^{-3}$ when the UV laser is switched on. When isoprene is present together with α -pinene it foremost
573 acts as a sink for OH· and thus reduces its concentrations. The strength of this depletion depends on the
574 main OH· source strength, i.e., the α -pinene ozonolysis rate. We find OH· levels 5 to 20 times lower when
575 isoprene is present than under α -pinene only conditions. This depletion can also be recognized in the
576 traces of HOMs that originate from OH· oxidation, like $C_{10}H_{18}O_6$ (see Extended Data Figure 1).

577 In the atmosphere, OH· levels of 10^6 cm^{-3} and higher are reported even in the presence of isoprene, as
578 several OH· recycling mechanisms take place^{10,22,57}. However, given the reduction in C_{20} class molecules
579 when OH· is increased from $2 \cdot 10^5 \text{ cm}^{-3}$ to $4 \cdot 10^5 \text{ cm}^{-3}$ by switching on UV light, it is a reasonable assumption
580 that, if OH· would be fully replenished to $1 \cdot 10^6 \text{ cm}^{-3}$, we would see a further decrease of total C_{20} class
581 molecules and subsequently a reduction in J and early growth rates. This assumption is also valid when
582 the reduced charging efficiency of nitrate ionization towards OH· initiated HOMs is taken into account as
583 outlined above. The decrease of C_{20} class molecules and nucleation rate when OH· is increased is direct
584 evidence that the suppression effect of isoprene on nucleation is not due to depletion of OH·.

585

586 **Particle Measurements**

587 The total particle number concentration above 2.5 nm is measured by a TSI 3776 condensation particle
 588 counter (CPC) using butanol as working fluid. For smaller particles, an Airmodus A10 particle size magnifier
 589 (PSM), using diethylene glycol as working fluid, is used⁵⁸ in combination with an Airmodus A20 CPC. This
 590 setup achieves detection of airborne particles down to 1 nm. By varying the supersaturation inside the
 591 PSM, particle size distributions between 1 – 3 nm can be inferred⁵⁹.

592 A DMA-train⁶⁰ is used to measure the particle size distribution and growth rates between 1.8 – 8.0 nm. It
 593 uses a parallel design of six sampling channels each equipped with a differential mobility analyser (DMA)
 594 together with an ultrafine condensation particle counter (uCPC). For detection of sub-2.5 nm particles,
 595 two of the channels are equipped with either an Airmodus A10 particle size magnifier (PSM) or a TSI 3777
 596 nanoEnhancer as booster stage upstream of the CPC. The channels are operated at fixed sizes to increase
 597 time-resolution and counting-statistics leading to higher sensitivities for smaller sizes compared to
 598 standard scanning mobility devices.

599 The size distribution above 5 nm is measured with a TSI Scanning Mobility Particle Sizer (nanoSMPS,
 600 Model 3938) using a TSI 3082 nanoDMA and a water-based TSI 3788 CPC for detection of the size-
 601 selected particles. For particles larger than 65 nm a custom-built SMPS with a long column DMA was
 602 used.

603

604 **Determination of nucleation rates**

605 The nucleation rate J defines the number of particles formed within a volume per unit of time. It is
 606 calculated using the flux of the total concentration of particles growing past a specific diameter (here at
 607 1.7, 2.2, 2.5 and 6 nm). In the following, the method for calculating $J_{1.7}$ is presented, however the
 608 calculation for $J_{2.2}$, $J_{2.5}$ and J_6 follows the same procedure unless specified otherwise. The nucleation rate
 609 is the sum of the time derivative of the concentration of particles above a certain diameter, as well as
 610 correction terms accounting for aerosol losses due to dilution in the chamber, wall losses and coagulation.

$$611 \quad J_{1.7} = \frac{dN_{\geq 1.7 \text{ nm}}}{dt} + S_{dil} + S_{wall} + S_{coag} \quad (1)$$

612 N is the concentration of particles of diameter equal or larger than 1.7 nm. The term S_{dil} describes the size-
 613 independent losses of particles due to dilution of the gases in the chamber. The chamber is continuously
 614 flushed with a total flow of 230 liters per minute to replenish the sampling flow of the instruments. This
 615 results in the dilution factor $k_{dil} = 1.47 \cdot 10^{-4} \text{ s}^{-1}$ and

$$616 \quad S_{dil} = N_{\geq 1.7 \text{ nm}} \cdot k_{dil} \cdot \quad (2)$$

617 The term S_{wall} describes the size-dependent particle losses to the chamber walls and was calculated based
 618 on the decay rate of sulfuric acid monomer (of mobility diameter = 0.85 nm⁶¹) in the chamber (at
 619 temperature = 278 K). The wall loss rate k_{wall} is a function of particle diameter and temperature.

620 $S_{wall}(T) = \sum_{d_{p,i}=1.7nm}^{d_{p,max}} N(d_{p,i}) \cdot k_{wall}(d_{p,i}, T)$ (3)

621 At 278 K

622 $k_{wall}(d_{p,i}) = 1.7 \cdot 10^{-3} nm s^{-1} \cdot \frac{1}{d_{p,i}}$ (4)

623 The term S_{coag} represents the coagulation losses to the surface of pre-existing aerosol particles in the
624 chamber and was calculated using the full number size distribution present in the chamber⁶².

625 $S_{Coag}(d_p = 1.7 nm) = \sum_{d_{p,i}=d_p}^{d_{p,max}} \sum_{d_{p,j}=d_p}^{d_{p,max}} \delta_{i,j} \cdot K(d_{p,i}, d_{p,j}) \cdot N_i \cdot N_j$ (5)

626 where $K(d_{p,i}, d_{p,j})$ is the coagulation coefficient for particles of the size $d_{p,i}$ and $d_{p,j}$, N_i and N_j are the number
627 concentrations of particles in the size bins $d_{p,i}$ and $d_{p,j}$, and $\delta_{i,j} = 0.5$, if $i = j$ and $\delta_{i,j} = 1$, if $i \neq j$. $d_{p,i}$ is the
628 midpoint diameter for the size bin with index i .

629 The number size distribution of particles used for the calculation of formation rates were obtained from
630 the scanning PSM at cut-off diameters 1.7 nm and 2.2 nm for the determination of $J_{1.7}$ and $J_{2.2}$, and from a
631 butanol CPC (model CPC3776, TSI Inc.) of fixed cut-off (2.5 nm) for determining the formation rate of 2.5
632 nm particles. For determining J_6 the integrated size bins from the nanoSMPS were used. A correction factor
633 of +0.3 nm on the cut-off diameter of the PSM was included to account for the poorer detection efficiency
634 of neutral organic particles compared to calibration with tungsten oxide⁶³. The concentrations obtained
635 were corrected for sampling line losses. During each run, the value of J was determined after reaching a
636 steady state value. A median value of the formation rate was then obtained. The errors on the reported J
637 rates were obtained by considering an inter-campaign reproducibility error of 30 % as well as a series of
638 run-dependent systematic and statistical uncertainties which include errors on sampling (10 %), dilution
639 (10 %), wall loss (20 %) and coagulation sink (20 %). The resulting overall scale uncertainty for J is 47 %.

640

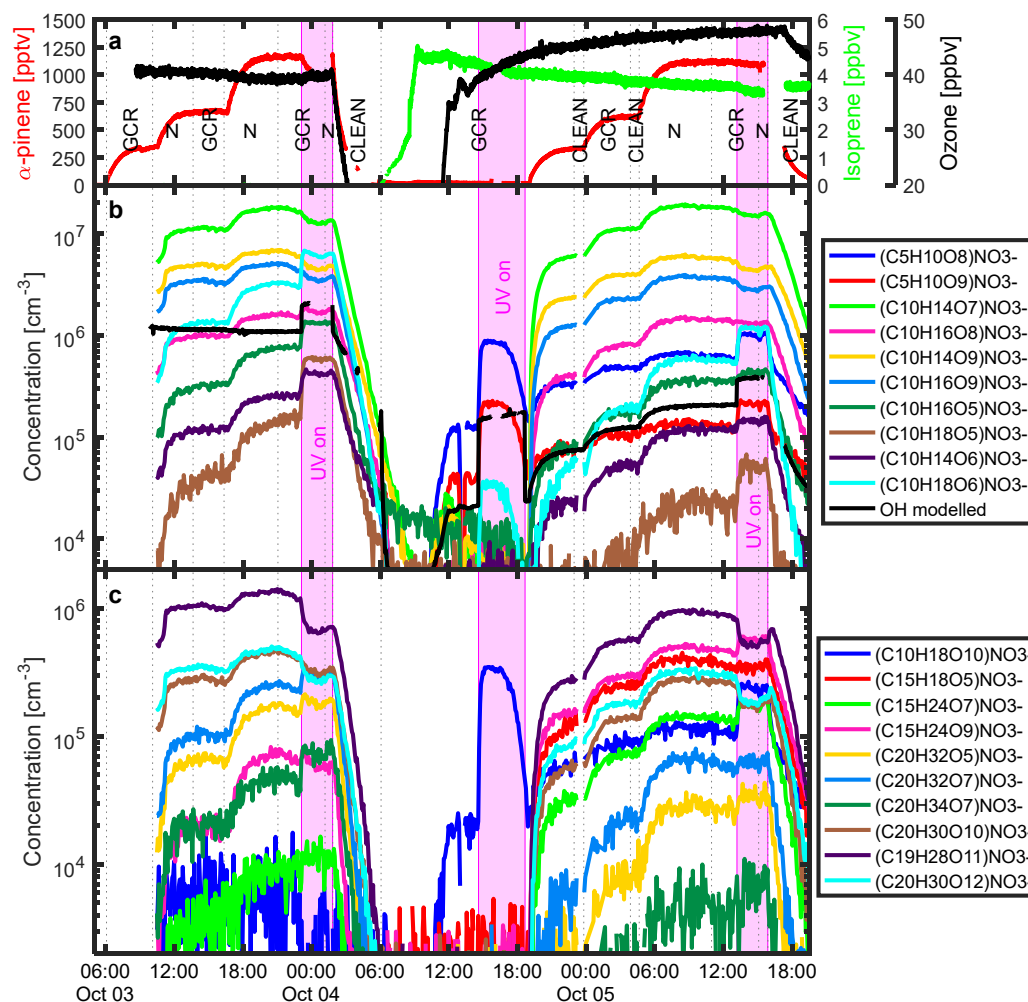
641 **Determination of growth rates**

642 Particle growth rates were derived from several instruments individually with the widely used appearance
643 time method⁵⁹. For this method the signal rise in a single size channel is fitted with a sigmoidal function
644 during the particle formation event. The fit determines the appearance time t_{app} at which the signal
645 intensity reaches 50 % between a potential background and the final value reached at steady-state
646 nucleation conditions. A linear fit of t_{app} and the corresponding diameters of several size channels yields
647 an average apparent growth rate of the size distribution for a diameter interval. To infer a size-dependence
648 of the measured growth rates, several instruments and size-intervals were used. Growth rates between
649 1.3 – 1.9 nm were measured with the scanning PSM, the DMA-train size channels were split up into two
650 intervals, one between 1.8 – 3.2 nm and one between 3.2 – 8.0 nm. For size-intervals above 8 nm the size
651 channels of the nanoSMPS was used. Uncertainties in the sigmoidal fit result are promoted to the linear
652 fit of the growth rate providing an estimate of the statistical uncertainties. However, at least a systematic
653 uncertainty of approximately 50 % has to be assumed if apparent growth rates are interpreted as
654 condensational growth values.

655 **Method references**

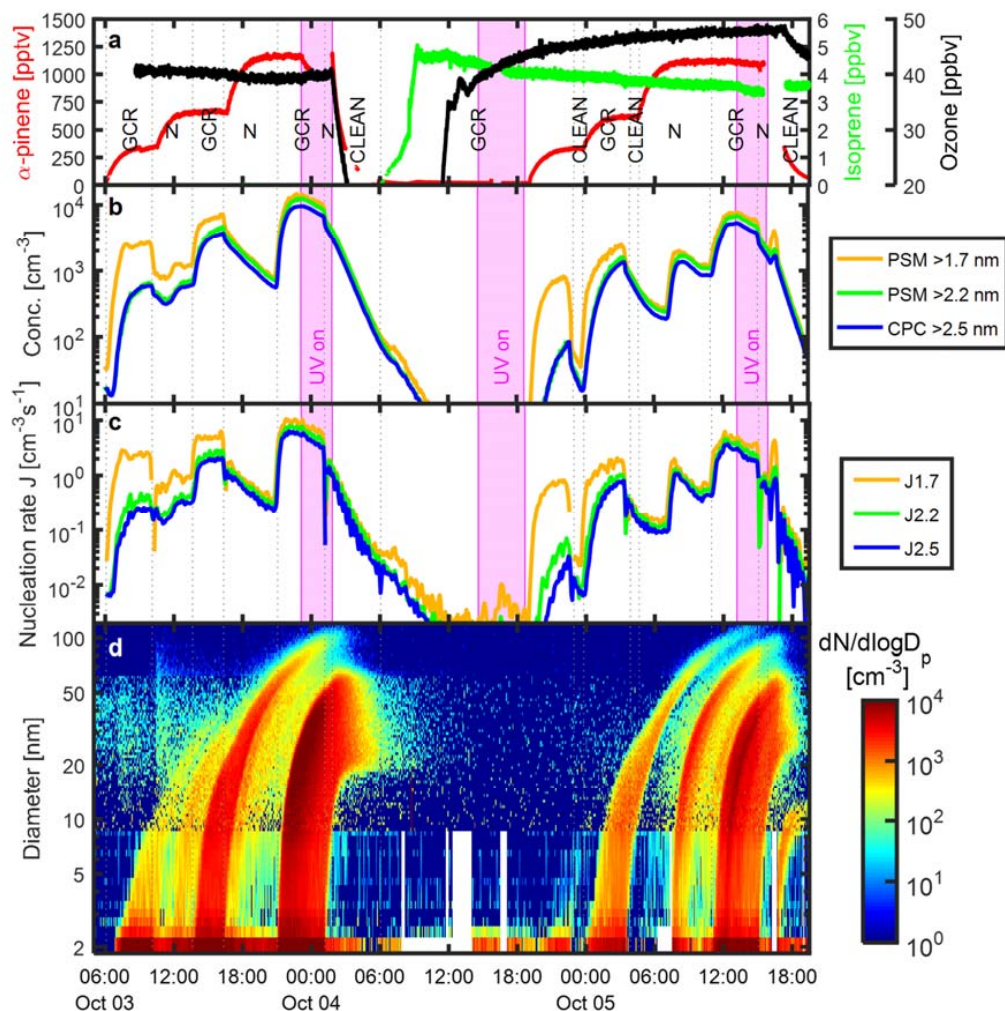
- 656 44 Duplissy, J. *et al.* Effect of ions on sulfuric acid-water binary particle formation: 2. Experimental
657 data and comparison with QC-normalized classical nucleation theory. *Journal of Geophysical*
658 *Research: Atmospheres* **121**, 1752-1775, doi:10.1002/2015JD023539 (2016).
- 659 45 Bernhammer, A.-K. *et al.* Production of highly oxygenated organic molecules (HOMs) from trace
660 contaminants during isoprene oxidation. *Atmospheric Measurement Techniques* **11**, 4763-4773
661 (2018).
- 662 46 Breitenlechner, M. *et al.* PTR3: An Instrument for Studying the Lifecycle of Reactive Organic
663 Carbon in the Atmosphere. *Analytical Chemistry* **89**, 5824-5831,
664 doi:10.1021/acs.analchem.6b05110 (2017).
- 665 47 Eisele, F. L. & Tanner, D. J. Measurement of the gas phase concentration of H₂SO₄ and methane
666 sulfonic acid and estimates of H₂SO₄ production and loss in the atmosphere. *Journal of*
667 *Geophysical Research: Atmospheres* **98**, 9001-9010, doi:10.1029/93JD00031 (1993).
- 668 48 Kürten, A., Rondo, L., Ehrhart, S. & Curtius, J. Performance of a corona ion source for
669 measurement of sulfuric acid by chemical ionization mass spectrometry. *Atmos. Meas. Tech.* **4**,
670 437-443, doi:10.5194/amt-4-437-2011 (2011).
- 671 49 Kürten, A., Rondo, L., Ehrhart, S. & Curtius, J. Calibration of a Chemical Ionization Mass
672 Spectrometer for the Measurement of Gaseous Sulfuric Acid. *The Journal of Physical Chemistry A*
673 **116**, 6375-6386, doi:10.1021/jp212123n (2012).
- 674 50 Heinritzi, M. *et al.* Characterization of the mass-dependent transmission efficiency of a CIMS.
675 *Atmos. Meas. Tech.* **9**, 1449-1460, doi:10.5194/amt-9-1449-2016 (2016).
- 676 51 Hyttinen, N., Rissanen, M. P. & Kurtén, T. Computational Comparison of Acetate and Nitrate
677 Chemical Ionization of Highly Oxidized Cyclohexene Ozonolysis Intermediates and Products. *The*
678 *Journal of Physical Chemistry A* **121**, 2172-2179, doi:10.1021/acs.jpca.6b12654 (2017).
- 679 52 Berndt, T. *et al.* Gas-Phase Ozonolysis of Cycloalkenes: Formation of Highly Oxidized RO₂
680 Radicals and Their Reactions with NO, NO₂, SO₂, and Other RO₂ Radicals. *The Journal of Physical*
681 *Chemistry A* **119**, 10336-10348, doi:10.1021/acs.jpca.5b07295 (2015).
- 682 53 Berndt, T. *et al.* Hydroxyl radical-induced formation of highly oxidized organic compounds.
683 *Nature Communications* **7**, 13677 (2016).
- 684 54 Tillmann, R. *et al.* Influence of relative humidity and temperature on the production of
685 pinonaldehyde and OH radicals from the ozonolysis of α -pinene. *Atmos. Chem. Phys.* **10**,
686 7057-7072, doi:10.5194/acp-10-7057-2010 (2010).
- 687 55 Kroll Jesse, H., Hanisco Thomas, F., Donahue Neil, M., Demerjian Kenneth, L. & Anderson James,
688 G. Accurate, direct measurements of OH yields from gas-phase ozone-alkene reactions using an
689 in situ LIF Instrument. *Geophysical Research Letters* **28**, 3863-3866, doi:10.1029/2001GL013406
690 (2001).
- 691 56 Bernhammer, A. K., Breitenlechner, M., Keutsch, F. N. & Hansel, A. Technical note: Conversion of
692 isoprene hydroxy hydroperoxides (ISOPROOHs) on metal environmental simulation chamber
693 walls. *Atmos. Chem. Phys.* **17**, 4053-4062, doi:10.5194/acp-17-4053-2017 (2017).
- 694 57 Lelieveld, J., Gromov, S., Pozzer, A. & Taraborrelli, D. Global tropospheric hydroxyl distribution,
695 budget and reactivity. *Atmos. Chem. Phys.* **16**, 12477-12493, doi:10.5194/acp-16-12477-2016
696 (2016).
- 697 58 Vanhanen, J. *et al.* Particle Size Magnifier for Nano-CN Detection. *Aerosol Science and*
698 *Technology* **45**, 533-542, doi:10.1080/02786826.2010.547889 (2011).
- 699 59 Lehtipalo, K. *et al.* Methods for determining particle size distribution and growth rates between
700 1 and 3 nm using the Particle Size Magnifier. *Boreal Env. Res.* **19 (suppl. B)**, 215-236 (2014).

- 701 60 Stolzenburg, D., Steiner, G. & Winkler, P. M. A DMA-train for precision measurement of sub-
702 10 nm aerosol dynamics. *Atmos. Meas. Tech.* **10**, 1639-1651, doi:10.5194/amt-10-1639-2017
703 (2017).
- 704 61 Kulmala, M. *et al.* Direct Observations of Atmospheric Aerosol Nucleation. *Science* **339**, 943-946,
705 doi:10.1126/science.1227385 (2013).
- 706 62 Seinfeld, J. H. & Pandis, S. N. *Atmospheric chemistry and physics: from air pollution to climate*
707 *change*. (John Wiley & Sons, 2016).
- 708 63 Kangasluoma, J. *et al.* Sub-3 nm particle size and composition dependent response of a nano-CPC
709 battery. *Atmos. Meas. Tech.* **7**, 689-700, doi:10.5194/amt-7-689-2014 (2014).



710

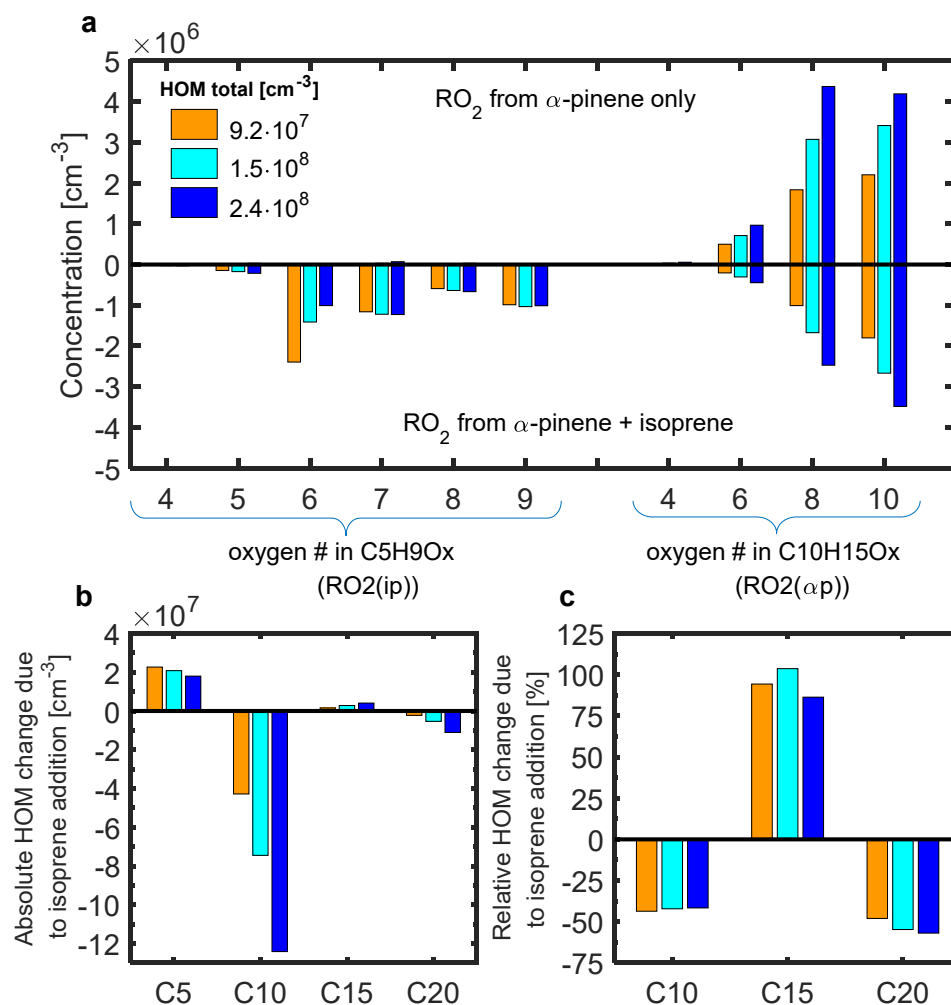
711 **Extended Data Figure 1: Time series of a nucleation experiment with example HOM traces.** (a) shows
 712 traces of α -pinene, isoprene and ozone. (b) and (c) show selected time traces of HOM monomers and
 713 dimers measured by the CI-API-TOF, respectively. The temperature in the chamber was +5 °C and rel.
 714 humidity was 38 %. N, GCR and CLEAN indicate neutral (high voltage cleaning field on), galactic cosmic ray
 715 (high voltage cleaning field off) and cleaning (neutral periods to clean the chamber of particles) conditions,
 716 respectively. In the first part until 04 Oct, 06:00 UTC, α -pinene was present in the chamber at three
 717 different concentrations to study pure biogenic nucleation under both neutral and gcr conditions with an
 718 additional UV stage at the end. Afterwards an isoprene/ozone mixture was studied under both dark and
 719 UV-illuminated conditions. Note that during the UV stage on 04 Oct the laser intensity deteriorated
 720 towards the end of the stage and thus corresponding HOM signals went down as well. At 04 Oct, starting
 721 at 18:40 UTC, α -pinene was added at three concentration levels similar to the first part of the experiment.



722

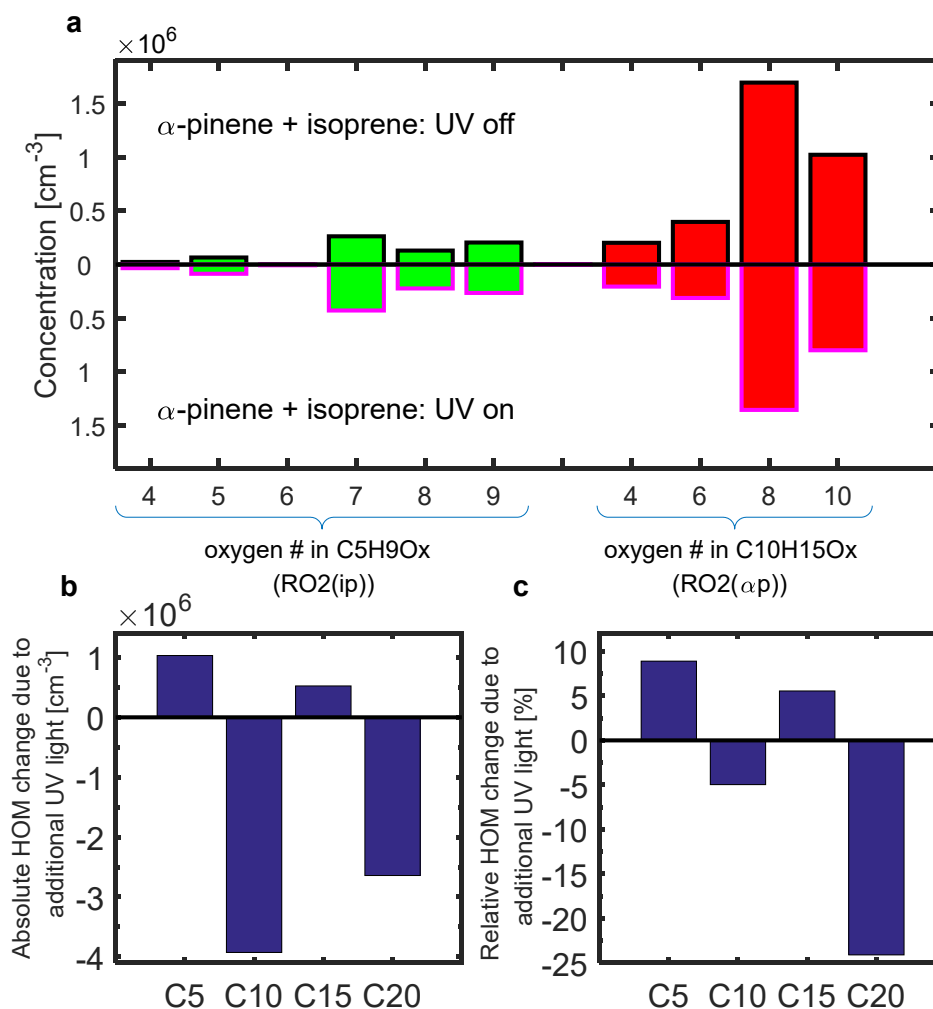
723 **Extended Data Figure 2: Time series of a nucleation experiment with particle counter data and J rates.**

724 The temperature in the chamber was +5 °C and rel. humidity was 38 %. The time window shown is the
725 same as in Extended Data Fig. 1. **(a)** shows traces of α -pinene, isoprene and ozone. N, GCR and CLEAN
726 indicate neutral (high voltage cleaning field on), galactic cosmic ray (high voltage cleaning field off) and
727 cleaning (neutral periods to clean the chamber of particles) conditions, respectively. **(b)** shows particle
728 concentration above 1.7, 2.2 and 2.5 nm, measured with a scanning PSM (1.7 nm and 2.2 nm) and a
729 butanol-based CPC (2.5 nm). **(c)** shows the nucleation rate J determined at 1.7, 2.2 and 2.5 nm using the
730 particle concentrations shown in **(b)**. **(d)** shows a combined size distribution of aerosol particles in the
731 CLOUD chamber. The DMA-train contributed the size range from 1.8 – 8 nm, the nanoSMPS from 8 – 65
732 nm and the long-SMPS for sizes >65 nm.



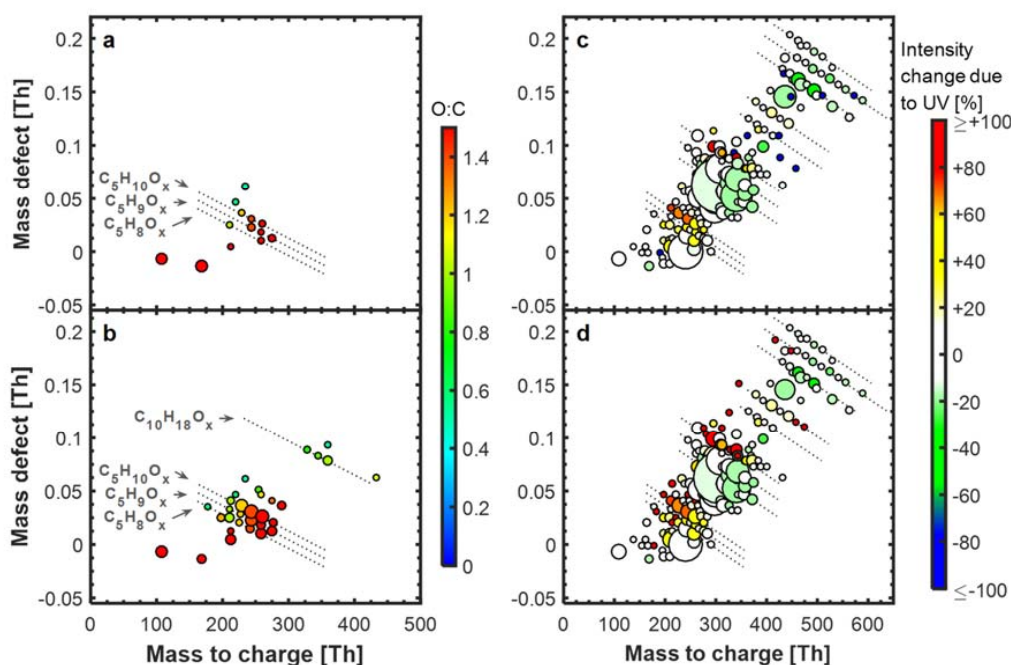
733

734 **Extended Data Figure 3: Effects of isoprene addition on RO₂· radical and HOM classes distribution.**
 735 Chamber conditions were +25 °C and 38 % RH. α -Pinene levels were 456, 771 and 1442 pptv for α -pinene
 736 only and 677, 1326 and 2636 pptv for α -pinene + isoprene conditions. Ozone levels were 49 ppbv for α -
 737 pinene only and 38 to 40 ppbv for α -pinene + isoprene conditions. Isoprene levels were 2.7, 4.9 and 9.8
 738 ppbv. All data from the α -pinene only runs was scaled up linearly (21, 38 and 45 % for low, mid and high
 739 α -pinene levels, respectively) to match the exact same [α -pinene] · [O₃] values as in the α -pinene + isoprene
 740 runs. **(a)** shows the distribution of the most prominent RO₂· radicals originating from isoprene and α -
 741 pinene oxidation. **(b)** shows the absolute and **(c)** the relative changes of the HOM class distribution due to
 742 isoprene addition.



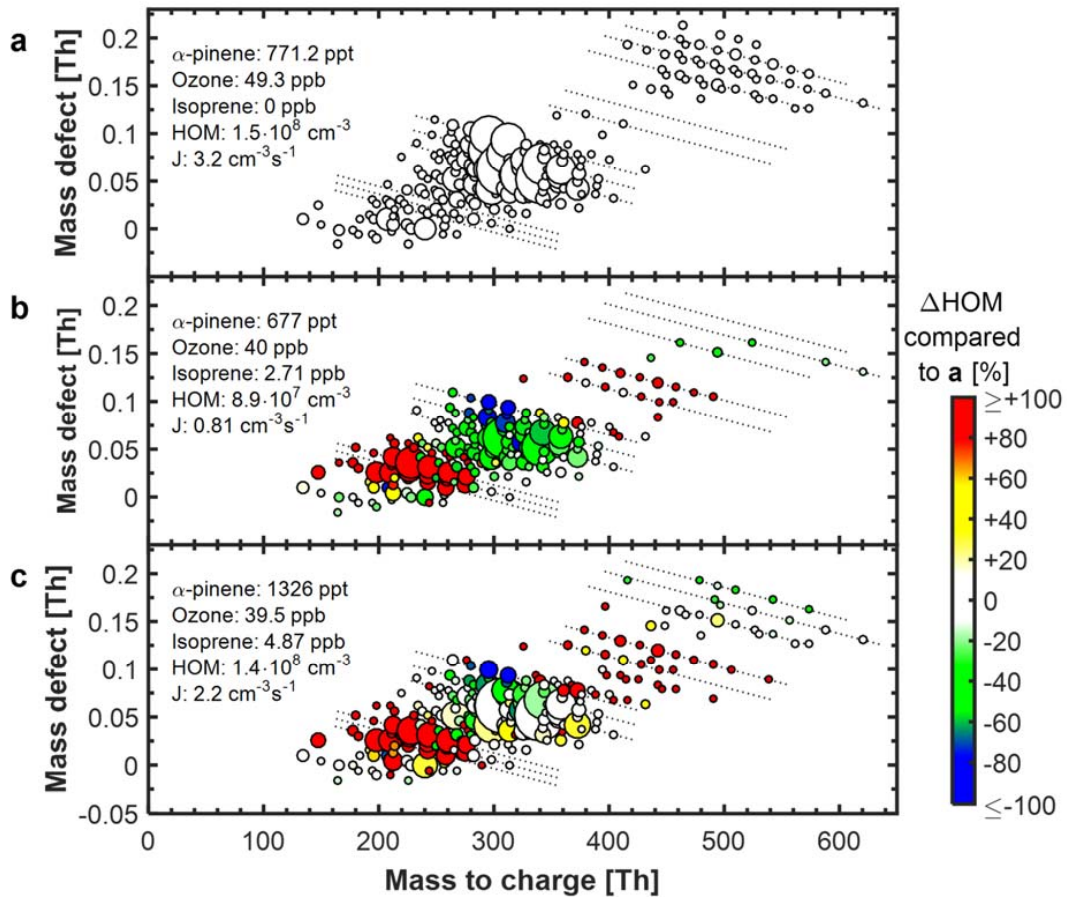
743

744 **Extended Data Figure 4: Changes of RO₂· radical and HOM classes distribution due to UV light in an α-**
 745 **pinene, isoprene and ozone mixture.** Chamber conditions were +5 °C and 38 % RH. α-pinene levels were
 746 1116 (dark) and 1096 pptv (UV illuminated). The ozone level was 48 ppbv, the isoprene level was 3.6 and
 747 3.4 ppbv in dark and UV illuminated conditions, respectively. Data from the dark run was slightly scaled
 748 down linearly (1.2 %) to match exact same [α-pinene]·[O₃] values as in the UV run. **(a)** shows the
 749 distribution of the most prominent RO₂· radicals originating from isoprene (green) and α-pinene (red)
 750 oxidation. **(b)** shows the absolute and **(c)** the relative changes of the HOM class distribution due to UV
 751 light.



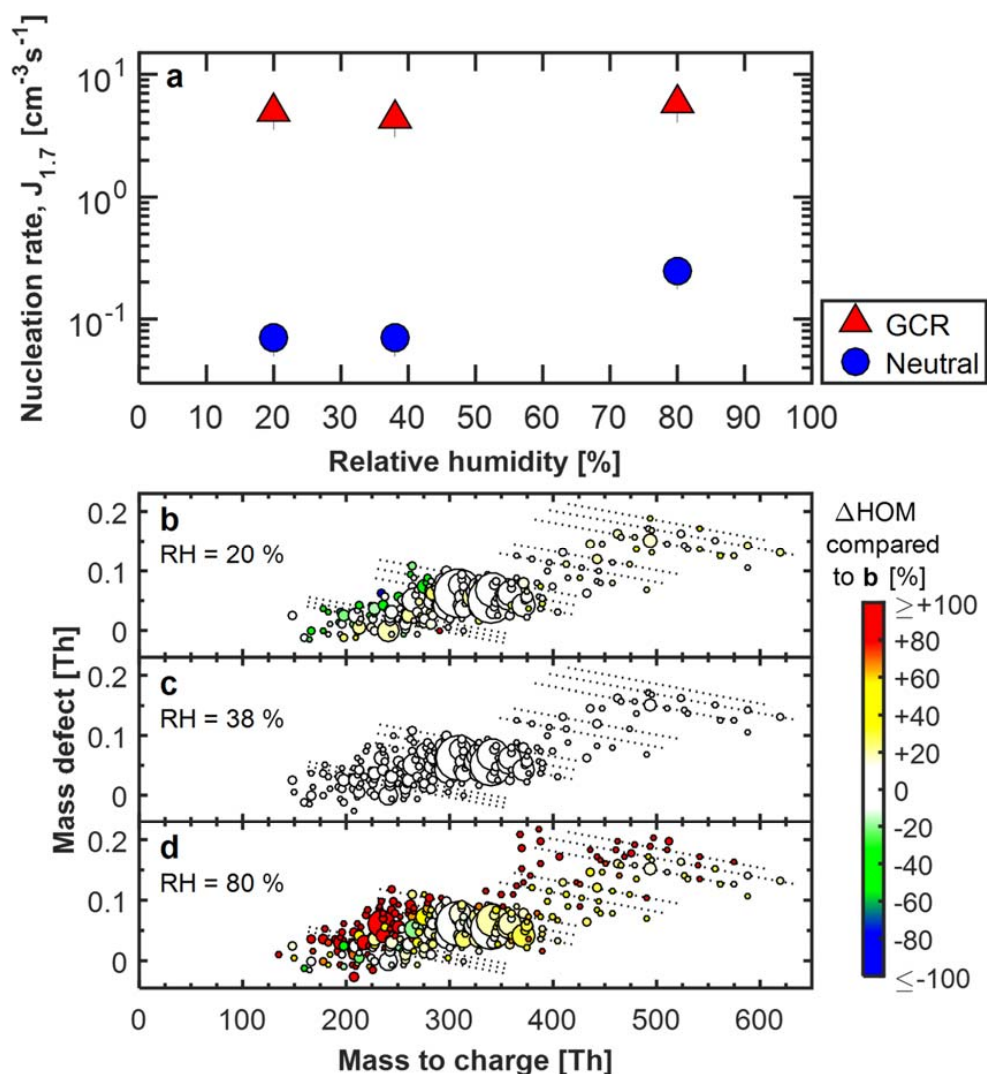
752

753 **Extended Data Figure 5: Mass defect plots showing HOM production from isoprene alone (a, b) and the**
 754 **effect of UV light on an α -pinene/isoprene mixture (c, d).** Chamber conditions were +5 °C and 38 % RH.
 755 HOM production from a mixture of isoprene (4.5 ppbv) and ozone (40 – 50 ppbv) under (a) dark conditions
 756 and (b) UV-illuminated conditions with higher OH \cdot levels. The area of the marker points is linearly scaled
 757 to intensity of the HOM signals. Color code represents oxygen-to-carbon ratio (O:C) of HOMs. UV light
 758 strongly enhances OH \cdot and thus HOM production. This even leads to the formation of some C₁₀ dimers
 759 resulting from the combination of two RO₂(ip). Mass defect plot of HOMs from a mixture of α -pinene,
 760 isoprene and ozone under (c) dark and (d) UV-illuminated conditions. α -pinene is 1116 and 1096 pptv,
 761 isoprene was 3.6 and 3.4 ppbv in (c), and (d), respectively. Ozone was 47 ppbv for both runs. The area of
 762 the marker points is linearly scaled to intensity of the HOM signals. Color code indicates the change in
 763 intensity for each HOM peak when switching from dark to UV light conditions, i.e. the percentage intensity
 764 change between (c) and (d). The color for each peak is thus the same in (c) and (d). Data from the dark run
 765 was slightly scaled down linearly (1.2 %) to match the same [α -pinene] \cdot [O₃] values as in the UV run for
 766 calculating the intensity change.

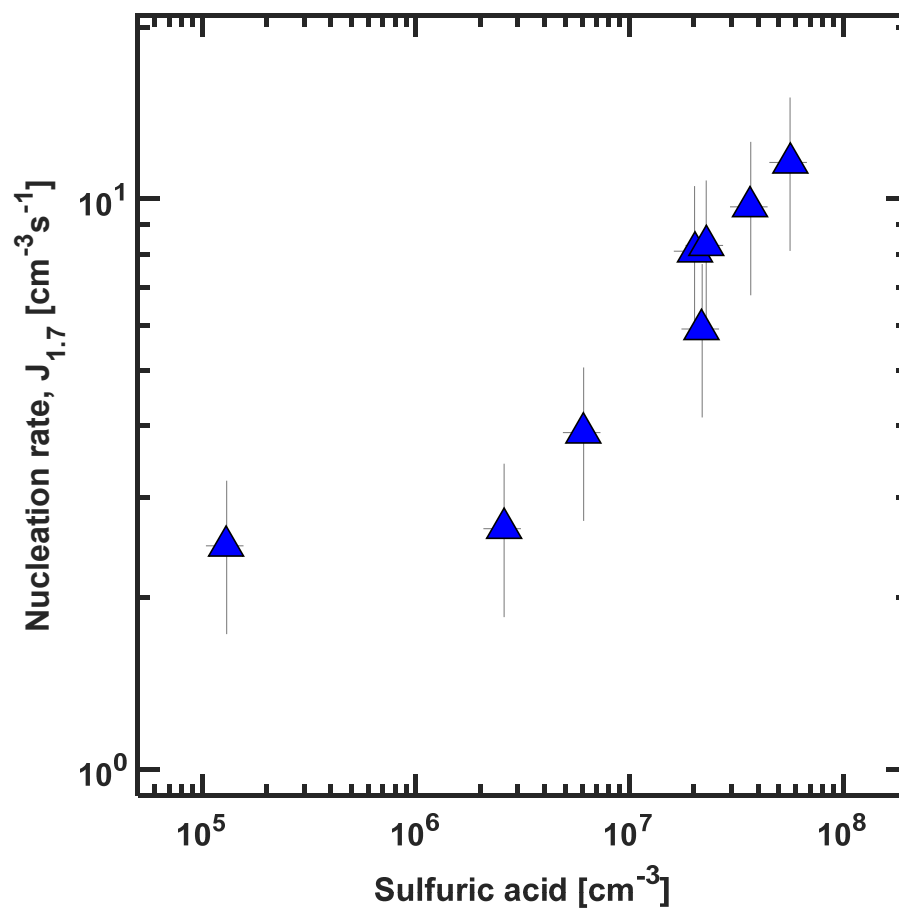


767

768 **Extended Data Figure 6: Mass Defect plots showing the effect of increased isoprene and monoterpene**
 769 **concentrations on HOM formation and nucleation rate $J_{1.7}$.** Chamber conditions were +25 °C and 38 %
 770 RH. **(a)** describes the base case without isoprene, **(b)** shows the effect of addition of isoprene. Color code
 771 in **(b)** and **(c)** shows the relative change in HOM intensity compared to **(a)**. **(c)** shows HOM spectra after α -
 772 pinene and isoprene concentrations have been roughly doubled compared to **(b)**.

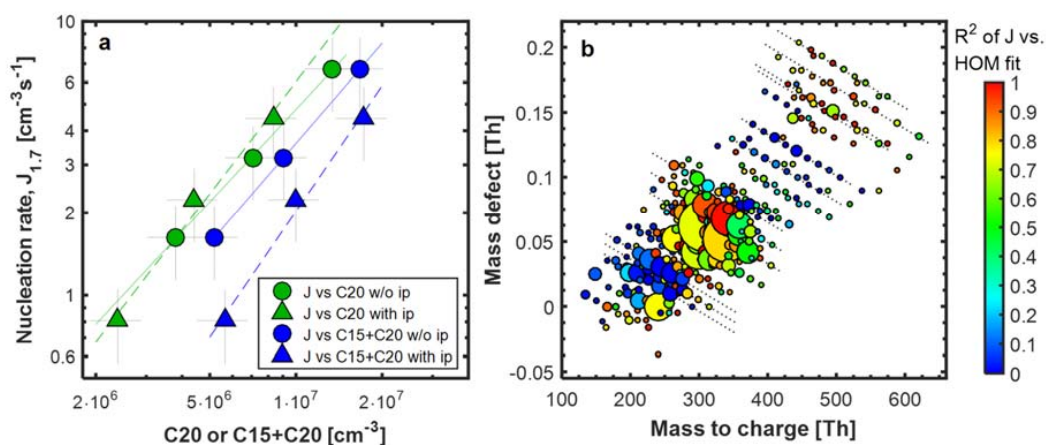


773
 774 **Extended Data Figure 7: Nucleation rate $J_{1,7}$ vs relative humidity at +25 °C (a) and corresponding HOM**
 775 **spectra (c-d).** All data shown was recorded with similar precursor concentrations (1.4 ppbv α -pinene, 5.1-
 776 6.2 ppbv isoprene, however, ozone decreased slightly from 46 to 40 ppbv as humidity was increased).
 777 HOM levels were fairly constant ranging from $1.3 \cdot 10^8$ to $1.6 \cdot 10^8$ cm^{-3} . Bars indicate 1σ run-to-run
 778 uncertainty. The overall systematic scale uncertainty of J for $\pm 47\%$ is not shown. The mass defect plots (b,
 779 c and d) show the HOM distribution measured by the nitrate CI-API-TOF under different humidity levels.
 780 The color code represents the relative change in HOM signal compared to the standard 38 % RH setting
 781 shown in (c). To calculate this change, HOM levels in (b) and (d) were scaled down by 11 % and scaled up
 782 by 10 %, respectively to match the same $[\alpha\text{p}] \cdot [\text{O}_3]$ levels as in (b). We attribute the strong increase of
 783 certain HOMs with low O:C ratios in (d) (red marker symbols) to a more efficient charging process with
 784 nitrate ions in our ion source due to assistance of water molecules rather than to an increased production
 785 inside the CLOUD chamber.



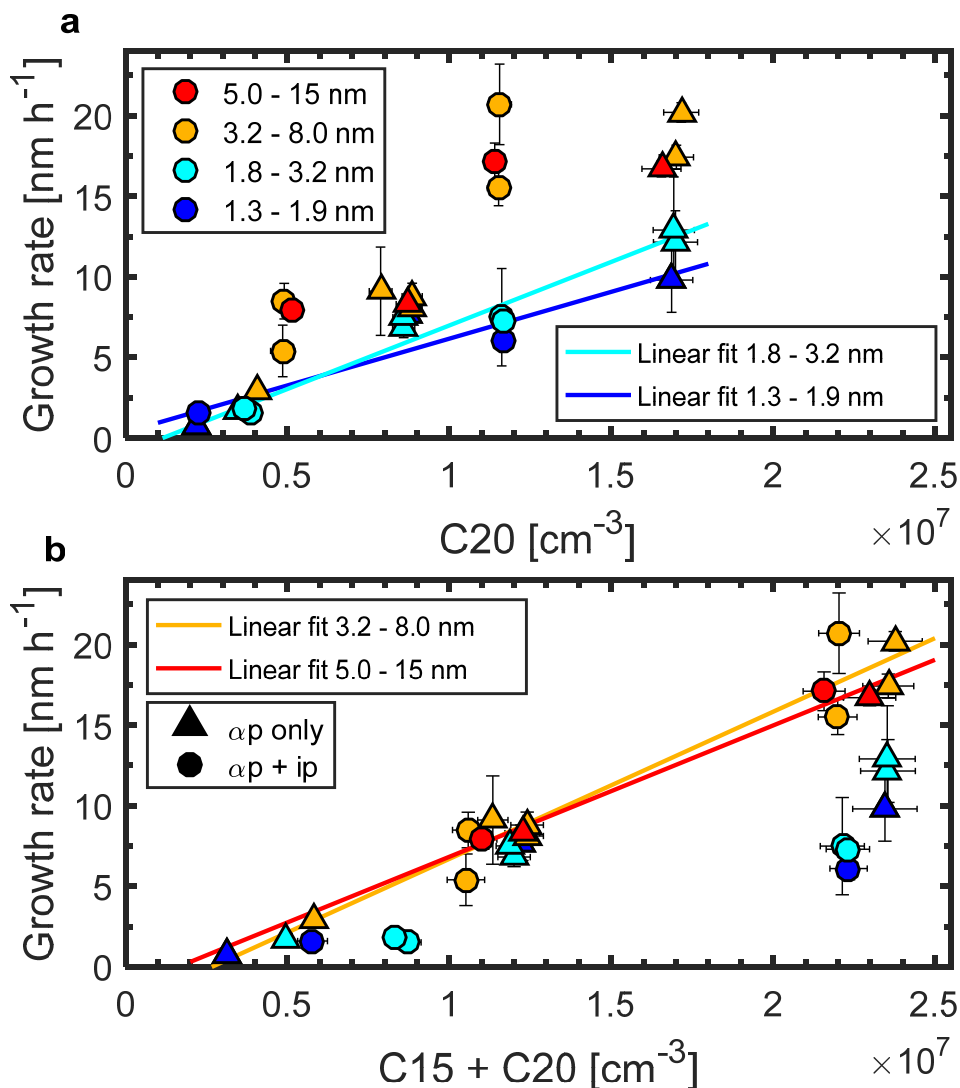
786

787 **Extended Data Figure 8: Nucleation rate $J_{1,7}$ (gr) vs sulfuric acid at +25 °C.** α -pinene and isoprene levels
788 were kept constant for all data points (around 1300 pptv and 4.5 ppbv, respectively), ozone levels ranged
789 from 35 to 39 ppbv. HOM levels were fairly constant for all data points, ranging from $1.2 \cdot 10^8$ to $1.5 \cdot 10^8 \text{ cm}^{-3}$.
790 ³. All data was taken with excess ammonia (0.4 -2.5 ppbv), relative humidity was 38 % for all runs. Bars
791 indicate 1σ run-to-run uncertainty. The overall systematic scale uncertainty of J for $\pm 47\%$ is not shown.



792

793 **Extended Data Figure 9: Role of HOM classes and individual HOMs in nucleation.** (a) Nucleation rate $J_{1.7}$
 794 with and without isoprene vs C_{20} and $C_{15}+C_{20}$ class molecules at +25 °C and 38 % RH. Green marker symbols
 795 represent $J_{1.7}$ vs C_{20} and blue marker symbols $J_{1.7}$ vs $C_{15}+C_{20}$. Circles show data taken without isoprene in
 796 the chamber (only α -pinene and ozone present); triangles show data taken with α -pinene and isoprene
 797 present at the same time. α -Pinene levels were 456, 771 and 1442 pptv for α -pinene only and 677, 1326
 798 and 2636 pptv for α -pinene + isoprene conditions. Ozone levels were 49 ppbv for α -pinene only and 38 to
 799 40 ppbv for α -pinene + isoprene conditions. Isoprene levels were 2.7, 4.9 and 9.8 ppbv. Bars indicate 1σ
 800 run-to-run uncertainty. The overall systematic scale uncertainty of HOMs of +78 %/-68 % and of $J_{1.7}$ for
 801 ± 47 % is not shown. Green and blue lines are power law fits to $J_{1.7}$ vs C_{20} and $J_{1.7}$ vs $C_{15} + C_{20}$, respectively.
 802 Here, solid lines represent fits under α -pinene only and dashed lines fits under α -pinene + isoprene
 803 conditions. (b) Mass defect plot of HOMs with coefficient of determination of J_{gr} vs individual HOM as
 804 color code. The data points displayed are taken from a run with 2.6 ppbv α -pinene, 9.8 ppbv isoprene and
 805 38 ppbv ozone under UV illuminated conditions. The area of the marker points is linearly scaled to the
 806 intensity of the HOM signals. The color code indicates coefficient of determination (R^2) of a power law fit
 807 of J vs every individual HOM peak. The dataset used for the fit contains the six J_{gr} data points taken under
 808 low/medium/high α -pinene levels with and without isoprene at +25 °C. High R^2 does not necessarily mean
 809 that the corresponding molecules contribute directly to nucleation, but that they are predominantly
 810 formed in a chemical setting that favors the production of nucleator molecules.



811

812 **Extended Data Figure 10: Growth rate vs (a) C_{20} class concentration and (b) $C_{15} + C_{20}$ class concentration**
 813 **at +5 °C and 38 % RH.** Growth rates were measured by scanning PSM (1.3 – 1.9 nm, dark blue), DMA-train
 814 (1.8 – 3.2 nm, light blue and 3.2 – 8.0 nm, orange) and nanoSMPS (5.0 – 15 nm, red). Triangles represent
 815 α -pinene only runs, circles represent α -pinene + isoprene runs. The growth rate between 1.8 nm and 3.2
 816 nm can be parametrized by a linear fit when plotted against C_{20} class molecules, for the size range from
 817 3.2 nm – 8.0 nm there is a linear relationship for growth rate when plotted against $C_{15} + C_{20}$ class molecules.

818

5 | Summary and Outlook

This work focused on the development and characterization of instruments for nanoaerosol analysis and their application for research on organic new particle formation. Laboratory, chamber and field measurements were conducted to assess nanoaerosols under different aspects.

The main project was the development of an instrument for the chemical analysis of sub-30-nm particles. The TD-DMA uses an online discontinuous principle. Particles are charged, a given size is selected and they are electrostatically sampled on a filament. Consecutively, the filament is moved into a mass spectrometers inlet line and the sample is desorbed in a carrier gas to be analyzed by a negative nitrate CI-APi-TOF. The characterization of the instrument shows reproducible results and in test measurements at an aerosol chamber it proved to be suitable for the measurement of freshly formed nanoparticles. In the second project, a broad spectrum of particle measurement instruments were deployed to characterize a particle population originating from a skyscraper blasting. A single mode of fine particles under 100 nm leads to a rise in particle mass by a factor of 30. As the dust cloud was pushed away by the wind, the particle strain was only elevated for 15 minutes at a fixed measurement point. Further analysis excluded an elevated appearance of heavy metals. The particles mainly consisted of the building's concrete and steel grinders and were not fibrous, like e.g. asbestos. Thus, the blasting led to an intense but short-timed particle burden without enhancement of particularly toxic compounds. The third project was also an ambient observation of nanoaerosols. New particle formation in a rural German area was observed and quantified. It was proven that the negative nitrate CI-APi-TOF is capable of sensitive ambient measurement for of many substances relevant for new particle formation. In the fourth project, this instrument was characterized for its mass dependent transmission efficiency. Therefore the measurements with this instrument, which is key for most of the projects, can be quantified better. The following projects were chamber experiments of new particle formation from biogenic organic precursors. It was discovered for the first time that organic substances can nucleate on their own without the presence of other substances like sulfuric acid under atmospherically relevant conditions. From the precursor alpha-pinene, highly

oxygenated molecules are formed, which cluster together and form particles. From the same experiments, the growth of these freshly nucleated particles at different particle sizes was assessed, showing the contribution of more and more volatile substances as the particles grow. The influence of temperature on this process was also examined. At higher temperatures, those molecules which can already contribute to particle growth at small sizes, are formed to an increasing degree. Conversely, at lower temperatures, the same molecules can condense more easily, so that the absolute growth rate is almost constant over temperature. In the following, the previous chemical system of alpha-pinene was extended by another precursor, isoprene. Isoprene suppresses the initial nucleation and early particle growth, as its reaction products combine with those from alpha-pinene to form substances that can only contribute to growth at larger diameters, but not to the very first steps of new particle formation.

Concluding, this work significantly contributed to the understanding of nano-aerosols: An instrument for the chemical analysis of nanoaerosol particles was successfully developed, tested and characterized. In chamber measurements, mechanisms for organic nucleation and growth were discovered and additionally, nanoaerosol populations of different origin were characterized in field measurements.

The newly developed TD-DMA proved its ability to successfully analyze nano-aerosol particles and operate stable for long measurement campaigns. However, in the future, further optimization can be implemented. There is currently a discrepancy between the TD-DMA's sample mass calibration and the gas-phase calibration of sulfuric acid, which indicates high losses in the transition of the sample from filament to mass spectrometer. Further possibilities for the coupling of TD-DMA to mass spectrometer are being investigated, as reducing these losses would greatly benefit the sensitivity of the system.

Up to now, the newly developed TD-DMA was deployed with a negative nitrate CI-APi-TOF. As chemical ionization is a selective technique, different primary ions can be chosen to target more substances. The TD-DMA has been used in chamber experiments with timed nucleation events, but it is also intended for field use in the future. Here, the size-selective mode is especially useful to make sure that newly formed particles are analyzed, as there can be larger background particles that would otherwise dominate the mass concentration.

It will be especially interesting to perform TD-DMA measurements at a flow tube with a continuous production of nanoparticles, so that measurements are not limited by time resolution or small number concentrations as it is often the case in the chamber measurements. Like this, one can analyze particles starting at small sizes with a high size resolution, and gain a very detailed picture of the growth process.

Although the knowledge about new particle formation has advanced tremendously in the past years, there are still many open research questions. To receive an understanding of the atmosphere which is as realistic as possible, chamber simulations need to approach the complexity of the Earth's atmosphere more and more. In practice, this means to include additional substances like nitrates and the simulation of additional systems like marine or urban environments, also while varying atmospheric parameters like temperature, relative humidity and UV light. With the CLOUD experiment, there is a suitable infrastructure to explore these topics.

6 | Zusammenfassung

Atmosphärische Nanoaerosole haben weitreichende Effekte auf Klima und Gesundheit. Diese kumulative Arbeit beschäftigt sich mit der Entwicklung und Charakterisierung von Instrumenten zur Analyse von Nanoaerosolen, und mit deren Einsatz zur Erforschung der Aerosolpartikelbildung aus biogenen Vorläuferstoffen. Die zentrale Forschungsfrage ist, wie die chemische Komposition kleinster Partikel gemessen werden kann und wie die Atmosphärenchemie Aerosolprozesse beeinflusst, insbesondere Partikelneubildung und Partikelwachstum. Hierzu wurden Nanoaerosole unter verschiedenen Aspekten untersucht, unter anderem wurde ein Instrument zur Partikelmessung entwickelt sowie Kammer- und Feldmessungen durchgeführt.

Um atmosphärische Partikelneubildung zu verstehen, ist es wichtig, die kondensierenden Substanzen zu analysieren, und zwar sowohl in der Gas- als auch in der Partikelphase. Für Gasphasenmoleküle und molekulare Cluster werden Chemische Ionisations-Massenspektrometer eingesetzt (CI-APi-TOFs, Kürten et al. (2014), Jokinen et al. (2012)), und für bereits angewachsene Partikel meist Aerosolmassenspektrometer (AMS, Jayne et al. (2000), Zhang et al. (2011)). Jedoch ist die chemische Analyse von Nanopartikeln unter 30 nm äußerst anspruchsvoll, da diese kleinen Partikel eine sehr geringe Masse haben. Das Hauptprojekt dieser Arbeit besteht in der Entwicklung des Gerätes “Thermal Desorption Differential Mobility Analyzer” (TD-DMA, Wagner et al. (2018)), das die massenspektrometrische Analyse (Maher et al. (2015)) kleinster Aerosolpartikel ermöglicht. Der TD-DMA funktioniert nach einem online diskontinuierlichen Prinzip. Die Partikel werden geladen, in einem Differenziellen Mobilitätsanalysator (Knutson and Whitby (1975)) nach ihrer Größe selektiert und auf einem Filament elektrostatisch gesammelt. Anschließend wird das Filament in die Einlassleitung eines Massenspektrometers bewegt. Durch Heizen des Filamentes desorbiert das gesammelte Material in ein Trägergas und wird dann massenspektrometrisch analysiert. Hierdurch wird die Partikelphase von der Gasphase getrennt und die Konzentration so erhöht, dass das Detektionslimit des Massenspektrometers erreicht wird. Die Vorteile dieses Messprinzips sind wie folgt: I) Da die Partikel größenselektiert analysiert werden

können, kann die chemische Komposition in verschiedenen Stadien des Wachstumsprozesses verglichen und der relative Beitrag von Substanzen abhängig von der Partikelgröße bestimmt werden. II) Ein integraler Messmodus erlaubt das Sammeln von Partikeln aller Größen, sodass die analysierte Partikelmasse maximiert wird und Messungen auch bei sehr schwachen Partikelkonzentrationen des Analytaerosols möglich sind. III) Der TD-DMA ist modular und kompakt. Bisher wurde er in Kombination mit einem NO_3^- -CI-API-TOF (Kürten et al. (2014), Jokinen et al. (2012)) eingesetzt, jedoch kann er im Prinzip auch mit anderen Gasphasen-Analysatoren kombiniert werden. IV) Während Partikel auf dem Filament gesammelt werden, kann das Massenspektrometer zur Analyse der Gasphase genutzt werden. Somit entfallen die Kosten für ein weiteres Massenspektrometer und beide Phasen können direkt verglichen werden. Alle Schritte des Messprozesses wurden im Labor charakterisiert, um die Messungen quantifizieren zu können. Die DMA-Einheit zur Größenselektion ist auf eine hohe Transmissionseffizienz bei eher niedriger Auflösung ausgelegt, damit genug Partikelmasse gesammelt werden kann. Sie wurde für sechs Durchmesser zwischen 7.5 und 30 nm getestet. Die Transmissionseffizienz (Stolzenburg and McMurry (2008)) in Abhängigkeit vom Partikeldurchmesser zeigt eine gute Übereinstimmung mit Gaußskurven, wobei die maximale Transmissionseffizienz für 15 nm bei über 50% liegt. Die Größenauflösung ist mit 1.19 recht grob, sodass trotz erfolgreicher Größenselektion viel Partikelmasse selektiert wird. Das elektrostatische Sammeln der Partikel auf dem Filament geschieht für kleine Partikel unter 15 nm zu 100%, für größere Partikel fällt aufgrund der sinkenden elektrischen Mobilität die Sammeleffizienz ab. Um die gesammelte Partikelmasse zu dem massenspektrometrisch gemessenen Signal in Verbindung zu setzen, werden während Kalibrationsmessungen definierte Mengen einer Substanz auf dem Filament platziert und anschließend desorbiert. Die Ergebnisse dieser Kalibrierung sind hochgradig vom verwendeten Massenspektrometer abhängig und von der Art und Weise, wie der TD-DMA mit diesem gekoppelt ist. Für das verwendete System beträgt der Kalibrationsfaktor $42.95 \text{ ng ncps}^{-1} \cdot \text{s}^{-1}$ für Schwefelsäure, bei anderen Substanzen muss zusätzlich deren Ionisierungseffizienz berücksichtigt werden. Durch Kombination der verschiedenen Charakterisierungen kann das Signal des Massenspektrometers quantitativ der analysierten Aerosolpartikelpopulation zugeordnet werden. Der TD-DMA ist sensitiv genug für Messungen bei Analytmassenkonzentrationen im Bereich Pikogramm pro Kubikmeter. In einer Testmessung konnten frisch gebildete Partikel von 15 nm chemisch analysiert wer-

den. Mit dem TD-DMA wurde somit ein Gerät entwickelt, das geeignet ist, Nanoaerosolpartikel unter 30 nm unter atmosphärisch relevanten Bedingungen chemisch zu analysieren.

Im zweiten Projekt wurde ein breites Spektrum von Aerosolmessgeräten eingesetzt, um die bei einer Turmsprengung entstandene Partikelpopulation zu charakterisieren (Wagner et al. (2017)). Die Sprengung produzierte eine einzelne Mode von Partikel mit Modendurchmesser 93 nm, die mit verschiedenen Instrumenten zur Messung der Anzahlgrößenverteilung beobachtet wurde (CPC, Hermann et al. (2007), SMPS, Wang and Flagan (1990), OPC, Hinds (1999) und APS, Peters et al. (2006)). Da die Anzahlkonzentration von noch kleineren Partikeln dominiert war, stieg diese nur um den Faktor 3.8 über den Hintergrund von $6.9 \cdot 10^4 \text{ cm}^{-3}$, während die Massenkonzentration um den Faktor 30.7 auf $844.9 \mu\text{g m}^{-3}$ anstieg. Die räumliche Verteilung wurde mittels Wiegen von sedimentiertem Material abgeschätzt und zeigte, dass die deutlich sichtbare Staubwolke vom Wind entlang der Straßenschlucht bewegt wurde und ihre Intensität mit der Distanz zum Turm abnahm. Am Hauptmesspunkt, 350 m von der Sprengung entfernt, war die erhöhte Nanopartikelbelastung bereits nach 15 Minuten vorüber. Somit wurde auch der von der EU festgelegte maximale Feinstaubwert, der im 24-Stunden-Mittel berechnet wird, nicht überschritten. Die Partikel bestanden laut Energiedispersiver Röntgenspektroskopie (EDX, Goldstein et al. (2012)) hauptsächlich aus dem Beton und den Stahlträgern des Gebäudes, mit 60% Kalziumkarbonaten, 19% Kalziumsulfaten, 19% Silikaten und 2% Stahl. Bei einer Metallfällung wurde kein erhöhter Schwermetallgehalt festgestellt. Die im Rasterelektronenmikroskop (SEM, Goldstein et al. (2012)) gewonnenen Bilder der Partikel zeigen, dass sie nicht faserartig wie beispielsweise Asbest waren. Insgesamt generierte die Turmsprengung eine intensive, aber zeitlich kurze Nanopartikelbelastung ohne erhöhte Konzentrationen von Schwermetallen oder faserartigen Partikeln. Im Hinblick auf die menschliche Gesundheit gibt es keinen Grenzwert, unterhalb dessen keine negativen Auswirkungen zu befürchten sind. Jedoch helfen Messungen wie diese, eine Abwägung zu treffen zwischen Sprengungen und herkömmlichen Abrissmaßnahmen, welche in der Regel deutlich länger andauern.

Das dritte Projekt (Kürten et al. (2016)) ist ebenfalls eine atmosphärische Messung von Aerosolen. Es wurde die Partikelneubildung in einer ländlichen Gegend in Deutschland beobachtet und quantifiziert. Ziel war es, einen möglichen Zusammenhang zwischen Partikelneubildung und Ammoniak- und Aminemis-

sionen von nahe gelegenen Rinderfarmen (Behera et al. (2013)), sowie organischen Emissionen des umgebenden Waldes zu beobachten. Die Mechanismen der einzelnen chemischen Systeme waren bereits in Kammerexperimenten untersucht worden (Kirkby et al. (2011), Almeida et al. (2013), Kürten et al. (2014), Kirkby et al. (2011), Tröstl et al. (2016)). Außerdem sollten unsere Instrumente auf ihre Anwendbarkeit im Feld getestet werden. Das NO_3^- -CI-APi-TOF zeigte seine Fähigkeit, auch im Feld sensitiv Schwefelsäure, hoch oxygenierte organische Substanzen (HOMs, Ehn et al. (2014)) und Amine (Simon et al. (2016)) zu messen, außerdem konnten erstmals Iodsäure, Nitrosamine und Ammoniak mit diesem Instrument detektiert werden. Somit zeigte sich das Instrument als noch vielseitiger als bislang angenommen. Mit einer Zusammenstellung von Partikelzählern wurden Partikelneubildungsraten bestimmt, die mit 5 bis $200 \text{ cm}^{-3}\text{s}^{-1}$ recht hoch für ein ländliches Gebiet waren. Aufgrund der Vielzahl der Parameter konnte die Partikelneubildung jedoch nicht einer einzelnen Quelle zugeordnet werden. Die Messungen liefern Beiträge zum Datensatz atmosphärischer Beobachtung und das unerwartete Vorkommen von Iodsäure wirft weitere Forschungsfragen auf.

Im vierten Projekt (Heinritzi et al. (2016)) wurde das NO_3^- -CI-APi-TOF, das zentral für fast alle Projekte war, bezüglich seiner massenabhängigen Transmissioneffizienz kalibriert, sodass die Messungen mit diesem Gerät besser quantifizierbar sind. Hierzu wurden zwei verschiedene Methoden getestet: In der ersten Methode wird mithilfe eines hochauflösenden DMAs (HR-DMA, Steiner et al. (2010), Fernández de la Mora and Kozłowski (2013)) eine bekannte Konzentration verschiedener Ionen in das Massenspektrometer gegeben, um dessen absolute Transmission zu erhalten. In der zweiten Methode wird jeweils ein Überschuss einer bestimmten Substanz verwendet, sodass die Primärionen weggesättigt werden. Die Ladung der Primärionen wird somit im Spektrum auf das Masse-zu-Ladungs-Verhältnis der eingegebenen Substanz verschoben. Aufgrund der Ladungserhaltung ergibt der Vergleich der Primärionensignale zu den Produktionensignalen die relative Transmissioneffizienz zwischen beiden. Die erste Methode hat den Vorteil, dass die absolute Transmissioneffizienz bestimmt wird, somit ist sie beispielsweise geeignet, um die Einstellungen des Massenspektrometers zu optimieren. In der zweiten Methode wird die Transmission relativ zu den Primärionen bestimmt. Jedoch ist die Methode unaufwändiger und benötigt keine weitere Instrumentierung. Wichtiger noch, es wird hierbei das Massenspektrometer mitsamt Ionenquelle in derselben Konfiguration genutzt wie es auch zur Analyse der Analyten verwendet

wird: Es werden neutrale Substanzen verwendet, welche erst in der Ionenquelle geladen werden. Tatsächlich zeigen beide Methoden leicht unterschiedliche Transmissionskurven, was bedeutet, dass der Einfluss der Ionenquelle auf die Transmissionseffizienz nicht zu vernachlässigen ist.

Die folgenden Projekte sind Kammermessungen zur Partikelneubildung aus biogenen organischen Vorläuferstoffen. Die Experimente hierzu fanden an der Cosmics Leaving Outdoor Droplet Kammer (Kirkby et al. (2011)) am CERN statt. Im fünften Projekt (Kirkby et al. (2016)) konnte erstmals gezeigt werden, dass biogene Organika ohne die Beteiligung von anderen Stoffen wie Schwefelsäure unter atmosphärischen Bedingungen Partikel bilden können. Dies war möglich, da die CLOUD-Kammer einerseits sehr rein war, andererseits mit dem NO_3^- -CI-API-TOF sehr sensitiv Schwefelsäure detektiert wurde, sodass Kontaminationen ausgeschlossen werden konnten. In dem betrachteten chemischen System werden aus dem Vorläuferstoff α -Pinen hochoxygenierte Stoffe gebildet, die dann aneinander haften und Partikel formen. Dies funktioniert besonders gut, wenn die anwachsenden molekularen Cluster durch Ladung stabilisiert werden. Da man zuvor angenommen hatte, dass Partikelneubildung nur unter dem Einfluss von Schwefelsäure passieren könnte, ist dies ein bedeutendes Ergebnis. Insbesondere die Modellierung der Aerosolpartikelkonzentration in naturbelassenen Gegenden und des vorindustriellen Klimas, wo wenig Schwefelsäure vorkommt, konnte durch den neu entdeckten Mechanismus verbessert werden. In Projekt 6 (Tröstl et al. (2016)) wurde anhand der gleichen Experimente das Wachstum dieser neugebildeten Nanoaerosolpartikel und die Beteiligung verschiedener Klassen an organischen Molekülen bei verschiedenen Partikelgrößen analysiert. Während bei kleinen Größen eher Substanzen mit einer sehr niedrigen Flüchtigkeit das Partikelwachstum verursachen (EL-VOCs, Ehn et al. (2014)), können bei steigendem Partikeldurchmesser auch flüchtigere Substanzen beitragen. Deshalb wird mit steigendem Durchmesser das Wachstum beschleunigt. Werden diese Prozesse in einem globalen Aerosolmodell berücksichtigt, hat das starke Auswirkungen auf die Konzentration der stark angewachsenen Partikeln, den Wolkenkondensationskeimen. Verglichen mit einem Szenario, indem der Einfluss von Organika auf das Partikelwachstum gänzlich vernachlässigt wird, ergibt der Prozess eine Steigerung der Wolkenkondensationskeime um bis zu 50%. Wird hingegen angenommen, alle Organika könnten von Anfang an zum Wachstum beitragen, wird die Konzentration um 50% überschätzt. Somit haben die in diesem Projekt gezeigten partikelgrößenabhängigen Beiträge verschiedener organischer Klassen eine si-

gnifikante Verbesserung der Modellierung von Wolkenkondensationskeimen zur Folge. Projekt 7 (Stolzenburg et al. (2018)) erweitert das vorherige Projekt um den Einfluss der Temperatur. In diesen Experimenten wurde ein erweitertes Set an Messgeräten und Analysemethoden eingesetzt. Unter anderem wurde im Bereich von 1.8 bis 8 nm, in der sich die Wachstumsrate der Partikel sehr stark ändert, der DMA-train (Stolzenburg et al. (2017)) eingesetzt, um das Wachstum in hoher Zeitaufösung verfolgen zu können. Zudem wurden Daten des NO_3^- -CI-APi-TOF mit Daten eines speziellen Protonentransfer-Massenspektrometers (PTR, Breitenlechner et al. (2017)) kombiniert, um die organischen Substanzen über einen sehr breiten Bereich an Flüchtigkeit detektieren zu können. Es stellte sich heraus, dass bei höheren Temperaturen vermehrt jene sehr hochoxygenierten organischen Stoffe gebildet werden, die bereits sehr kleine Partikel anwachsen lassen können. Jedoch können bei niedriger Temperatur die Stoffe leichter kondensieren und bereits weniger hochoxygenierte Substanzen zum Partikelwachstum beitragen. Somit ist das Wachstum der Partikel bei gleicher Konzentration des Vorläuferstoffes α -Pinen kaum temperaturabhängig. Im achten Projekt (Heinritzi et al. (2018)) wird das reine α -Pinen-System um den Vorläuferstoff Isopren erweitert. Isopren interferiert mit der α -Pinen Oxidationschemie über die Terminierung von Peroxyradikalen. Es werden weniger Verbindungen aus zwei α -Pinen-Grundeinheiten mit insgesamt 20 Kohlenstoffatomen gebildet. Gleichzeitig steigt die Bildungsrate von Mischprodukten aus α -Pinen und Isopren mit 15 Kohlenstoffatomen. Diese sind jedoch volatiler als die Produkte aus zwei α -Pinen-Grundeinheiten. Dies führt zu einer Reduktion der biogenen Nukleation durch Isopren, sowie einer Abschwächung des frühen Partikelwachstums. Die Kombination aus reduzierter Nukleation und Wachstumsrate kann die Abwesenheit typischer Nukleationsereignisse in isoprenreichen Regionen erklären.

Insgesamt hat diese Arbeit signifikant zum Verständnis von Nanoaerosolen beigetragen: Ein Instrument zur chemischen Analyse von neugebildeten Nanoaerosolpartikeln wurde erfolgreich entwickelt, getestet und charakterisiert. In Kammermessungen wurden Mechanismen zur rein biogenen organischen Partikelneubildung und zum Partikelwachstum entdeckt und ergänzend in atmosphärischen Feldmessungen Nanoaerosolpopulationen verschiedener Herkunft charakterisiert.

Bisher wurde der TD-DMA mit einem NO_3^- -CI-APi-TOF eingesetzt. Da chemische Ionisierungsmethoden jedoch immer selektiv auf bestimmte Analyten sind, könnte man das Gerät auch mit anderen Primärionen zu testen, um eine noch größere Bandbreite an Substanzen detektieren zu können. Ebenso ist der TD-DMA für Feldmessungen geeignet. Insbesondere ist hier der gröbenselektive Modus sehr hilfreich, um frisch gebildete Partikel zu messen, da bei nicht-gröbenselektiven Methoden größere Hintergrundpartikel die Messungen dominieren. Besonders interessant wäre es, den TD-DMA an einem Strömungsrohr einzusetzen, in dem Nanopartikel kontinuierlich gebildet werden. Somit entfällt die zeitliche Limitierung und oftmals geringe Anzahlkonzentration, die in den bisher durchgeführten Kammerstudien meist limitierend für den TD-DMA waren. So könnten Partikel bereits ab sehr kleinen Größen mit einer hohen Größenaufösung analysiert werden, um ein sehr detailliertes Verständnis der Partikelwachstumsprozesse zu erhalten.

Obwohl die Forschung zur Partikelneubildung und zum Partikelwachstum in den letzten Jahren sehr große Fortschritte gemacht hat, sind noch viele Forschungsfragen für die Zukunft offen. Um ein möglichst realistisches Bild der Atmosphäre zu erhalten, nähern sich Kammersimulationen immer mehr der Komplexität der Erdatmosphäre an. Konkret bedeutet das die Inklusion weiterer Substanzen wie zum Beispiel Nitratverbindungen und die Simulation weiterer Gegenden wie marinen oder urbanen Systemen, auch unter Variation atmosphärischer Grundparameter wie Temperatur, Feuchte und UV Licht. Mit dem CLOUD-Experiment besteht eine gut geeignete Infrastruktur, diese Themen zu erkunden.

Glossary

AMS	Aerosol Mass Spectrometer	Jayne et al. (2000), Zhang et al. (2011)
APi-TOF	Atmospheric Pressure Interface Time-Of-Flight Mass Spectrometer	Schobesberger et al. (2013)
APS	Aerodynamic Particle Sizer	Peters et al. (2006)
CCN	Cloud Condensation Nuclei	Lohmann and Feichter (2005)
CI-APi-TOF	Chemical Ionization Atmospheric Pressure Interface Time-Of-Flight Mass Spectrometer	Kürten et al. (2014), Jokinen et al. (2012)
CIMS	Chemical Ionization Mass Spectrometer	Maher et al. (2015)
CLOUD	Cosmics Leaving Outdoor Droplets experiment	Kirkby et al. (2011)
CPC	Condensation Particle Counter	Aitken (1890), Hermann et al. (2007)
DMA	Differential Mobility Analyzer	Knutson and Whitby (1975)
DMA-train	instrument with six DMAs for high-time-resolution particle-size-distribution measurements	Stolzenburg et al. (2017)
EDX	Energy Dispersive X-Ray Spectroscopy	Goldstein et al. (2012)

ELVOC	Extremely Low Volatile Organic Compound	Ehn et al. (2014)
GR	Growth Rate	
HOM	Highly Oxigenated Organic Molecule	Ehn et al. (2014)
HR-DMA	High Resolution Differential Mobility Analyzer	Steiner et al. (2010), Fernández de la Mora and Kozlowski (2013)
J_x	Nucleation Rate at a diameter of X nm	
LVOC	Low Volatile Organic Compound	
m/z	mass to charge ratio of an ion	
MS	Mass Spectrometer	Maher et al. (2015)
npf	New Particle Formation	
nSMPS	nano Scanning Mobility Particle Sizer (see SMPS)	
OPC	Optical Particle Counter	Hinds (1999)
PSM	Particle Size Magnifier	Vanhanen et al. (2011)
PTR-MS	Proton Transfer Reaction Mass Spectrometer	Hansel et al. (1995), Graus et al. (2010), Breitenlechner et al. (2017)
SEM	Scanning Electron Microscopy	Goldstein et al. (2012)
SHARP	Synchronized Hybrid Ambient Real Time Particulate Monitor	Thermo Fisher Scientific Inc. Air Quality Instruments (2007)

SIMPOL	simplified prediction method for predicting vapor pressures of organic compounds	Pankow and Asher (2008)
SMPS	Scanning Mobility Particle Sizer	Wang and Flagan (1990)
SOA	Secondary Organic Aerosol	Hallquist et al. (2009)
SVOC	Semi Volatile Organic Compound	
TD-DMA	Thermal Desorption Differential Mobility Analyzer	Wagner et al. (2018)

References

- Aitken, J. (1890). On a simple pocket dust-counter. *Proceedings of the Royal Society of Edinburgh*, 8:39–53.
- Allen, J. S. (1939). The detection of single positive ions, electrons and photons by a secondary electron multiplier. *Physical Review*, 55(10):966–971. <http://dx.doi.org/10.1103/PhysRev.55.966>.
- Almeida, J., Schobesberger, S., Kürten, A., Ortega, I. K., Kupiainen-Määttä, O., Praplan, A. P., Adamov, A., Amorim, A., Bianchi, F., Breitenlechner, M., David, A., Dommen, J., Donahue, N. M., Downard, A., Dunne, E., Duplissy, J., Ehrhart, S., Flagan, R. C., Franchin, A., Guida, R., Hakala, J., Hansel, A., Heinritzi, M., Henschel, H., Jokinen, T., Junninen, H., Kajos, M., Kangasluoma, J., Keskinen, H., Kupc, A., Kurtén, T., Kvashin, A. N., Laaksonen, A., Lehtipalo, K., Leiminger, M., Leppä, J., Loukonen, V., Makhmutov, V., Mathot, S., McGrath, M. J., Nieminen, T., Olenius, T., Onnela, A., Petäjä, T., Riccobono, F., Riipinen, I., Rissanen, M., Rondo, L., Ruuskanen, T., Santos, F. D., Sarnela, N., Schallhart, S., Schnitzhofer, R., Seinfeld, J. H., Simon, M., Sipilä, M., Stozhkov, Y., Stratmann, F., Tomé, A., Tröstl, J., Tsagkogeorgas, G., Vaattovaara, P., Viisanen, Y., Virtanen, A., Vrtala, A., Wagner, P. E., Weingartner, E., Wex, H., Williamson, C., Wimmer, D., Ye, P., Yli-Juuti, T., Carslaw, K. S., Kulmala, M., Curtius, J., Baltensperger, U., Worsnop, D. R., Vehkamäki, H., and Kirkby, J. (2013). Molecular understanding of sulphuric acid–amine particle nucleation in the atmosphere. *Nature*, 502:359. <http://dx.doi.org/10.1038/nature12663>.
- Anderson, J. O., Thundiyil, J. G., and Stolbach, A. (2012). Clearing the air: A review of the effects of particulate matter air pollution on human health. *Journal of Medical Toxicology*, 8(2):166–175. <http://dx.doi.org/10.1007/s13181-011-0203-1>.
- Atkinson, R. and Arey, J. (2003). Gas-phase tropospheric chemistry of biogenic volatile organic compounds: a review. *Atmospheric Environment*, 37:197–219. [http://dx.doi.org/10.1016/S1352-2310\(03\)00391-1](http://dx.doi.org/10.1016/S1352-2310(03)00391-1).

- Baron, P. A. and Willeke, K. (2001). *Aerosol Measurement –Principles, Techniques and Applications*. Wiley Interscience. <http://dx.doi.org/10.1002/9781118001684>.
- Behera, S. N., Sharma, M., Aneja, V. P., and Balasubramanian, R. (2013). Ammonia in the atmosphere: a review on emission sources, atmospheric chemistry and deposition on terrestrial bodies. *Environmental Science and Pollution Research*, 20(11):8092–8131. <http://dx.doi.org/10.1007/s11356-013-2051-9>.
- Bergen, A. (2016). *Entwicklung eines Thermal Desorption Differential Mobility Analyser (TD–DMA) mit Schwerpunkt auf der Sammel–und Verdampfungs-funktion*. Master thesis, Goethe University Frankfurt.
- Boucher, O., Randall, D., Artaxo, P., Bretherton, C., Feingold, G., Forster, P., Kerminen, V.-M., Kondo, Y., Liao, H., Lohmann, U., Rasch, P., Satheesh, S., Sherwood, S., Stevens, B., and Zhang, X. (2013). *Clouds and Aerosols. In: Climate Change 2013: The Physical Science Basis. Contribution of Working Group I to the Fifth Assessment Report of the Intergovernmental Panel on Climate Change*. Stocker, T.F., Qin, D., Plattner, G.-K., Tignor, M., Allen, S.K., Boschung, J., Nauels, A., Xia, Y., Bex, V. and Midgley, P.M. (Eds.) Cambridge University Press, Cambridge, United Kingdom and New York, NY, USA.
- Breitenlechner, M., Fischer, L., Hainer, M., Heinritzi, M., Curtius, J., and Hansel, A. (2017). Ptr3: An instrument for studying the lifecycle of reactive organic carbon in the atmosphere. *Analytical Chemistry*, 89(11):5824–5831. <http://dx.doi.org/10.1021/acs.analchem.6b05110>.
- Brilke, S. (2016). *Thermal Desorption –Differential Mobility Analysis: Instrument Development, Characterization & Measurements during CLOUD–10*. Master thesis, Goethe University Frankfurt.
- Brook, R. D., Rajagopalan, S., Pope, C. A., Brook, J. R., Bhatnagar, A., Diez-Roux, A. V., Holguin, F., Hong, Y., Luepker, R. V., and Mittleman, M. A. (2010). Particulate matter air pollution and cardiovascular disease an update to the scientific statement from the american heart association. *Circulation*, 121(21):2331–2378. <http://dx.doi.org/10.1161/CIR.0b013e3181d8bec1>.
- Bzdek, B. R., Pennington, M. R., and Johnston, M. V. (2012). Single particle

- chemical analysis of ambient ultrafine aerosol: A review. *Journal of Aerosol Science*, 52:109–120. <http://dx.doi.org/10.1016/j.jaerosci.2012.05.001>.
- Choi, H. S., Ashitate, Y., Lee, J. H., Kim, S. H., Matsui, A., Insin, N., Bawendi, M. G., Semmler-Behnke, M., Frangioni, J. V., and Tsuda, A. (2010). Rapid translocation of nanoparticles from the lung airspaces to the body. *Nature Biotechnology*, 28:1300. <http://dx.doi.org/10.1038/nbt.1696>.
- Curtius, J. (2006). Nucleation of atmospheric aerosol particles. *Comptes Rendus Physique*, 7(9):1027–1045. <http://dx.doi.org/10.1016/j.crhy.2006.10.018>.
- Donaldson, K., Murphy, F. A., Duffin, R., and Poland, C. A. (2010). Asbestos, carbon nanotubes and the pleural mesothelium: a review of the hypothesis regarding the role of long fibre retention in the parietal pleura, inflammation and mesothelioma. *Part Fibre Toxicol*, 7(5):5. <http://dx.doi.org/10.1186/1743-8977-7-5>.
- Dunne, E. M., Gordon, H., Kürten, A., Almeida, J., Duplissy, J., Williamson, C., Ortega, I. K., Pringle, K. J., Adamov, A., Baltensperger, U., Barmet, P., Benduhn, F., Bianchi, F., Breitenlechner, M., Clarke, A., Curtius, J., Dommen, J., Donahue, N. M., Ehrhart, S., Flagan, R. C., Franchin, A., Guida, R., Hakala, J., Hansel, A., Heinritzi, M., Jokinen, T., Kangasluoma, J., Kirkby, J., Kulmala, M., Kupc, A., Lawler, M. J., Lehtipalo, K., Makhmutov, V., Mann, G., Mathot, S., Merikanto, J., Miettinen, P., Nenes, A., Onnela, A., Rap, A., Reddington, C. L. S., Riccobono, F., Richards, N. A. D., Rissanen, M. P., Rondo, L., Sarnela, N., Schobesberger, S., Sengupta, K., Simon, M., Sipilä, M., Smith, J. N., Stozkhov, Y., Tomé, A., Tröstl, J., Wagner, P. E., Wimmer, D., Winkler, P. M., Worsnop, D. R., and Carslaw, K. S. (2016). Global atmospheric particle formation from cern cloud measurements. *Science*, 354(6316):1119. <http://dx.doi.org/10.1126/science.aaf2649>.
- Ehn, M., Thornton, J. A., Kleist, E., Sipilä, M., Junninen, H., Pullinen, I., Springer, M., Rubach, F., Tillmann, R., Lee, B., Lopez-Hilfiker, F., Andres, S., Acir, I. H., Rissanen, M., Jokinen, T., Schobesberger, S., Kangasluoma, J., Kontkanen, J., Nieminen, T., Kurtén, T., Nielsen, L. B., Järngensen, S., Kjaergaard, H. G., Canagaratna, M., Maso, M. D., Berndt, T., Petäjä, T., Wahner, A., Kerminen, V. M., Kulmala, M., Worsnop, D. R., Wildt, J., and Mentel, T. F. (2014). A large source of low-volatility secondary organic aerosol. *Nature*, 506:476. <http://dx.doi.org/10.1038/nature13032>.

- Eisele, F. L. and Tanner, D. J. (1993). Measurement of the gas phase concentration of H_2SO_4 and methanesulfonic acid and estimates of H_2SO_4 production and loss in the atmosphere. *Journal of Geophysical Research: Atmospheres*, 98(D5):9001–9010. <http://dx.doi.org/10.1029/93JD00031>.
- Fernández de la Mora, J. and Kozlowski, J. (2013). Hand-held differential mobility analyzers of high resolution for 1–30nm particles: Design and fabrication considerations. *Journal of Aerosol Science*, 57:45–53. <http://dx.doi.org/10.1016/j.jaerosci.2012.10.009>.
- Forster, P., Ramaswamy, V., Artaxo, P., Berntsen, T., Betts, R., Fahey, D., Haywood, J., Lean, J., Lowe, D., Myhre, G., Nganga, J., Prinn, R., Raga, G., Schulz, M., and Dorland, R. V. (2007). *Changes in Atmospheric Constituents and in Radiative Forcing. In: Climate Change 2007: The Physical Science Basis. Contribution of Working Group I to the Fourth Assessment Report of the Intergovernmental Panel on Climate Change.* Solomon, S., Qin, D., Manning, M., Chen, Z., Marquis, M., Averyt, K. B., Tignor, M. and Miller, H.L. (Eds.). Cambridge University Press, Cambridge, United Kingdom.
- Goldstein, J., Newbury, D., Echlin, P., Joy, D., Romig, A., Lyman, C., Fiori, C., and Lifshin, E. (2012). *Scanning Electron Microscopy and X-Ray Microanalysis: A Text for Biologists, Materials Scientists, and Geologists*, volume 2. Springer US.
- Gordon, H., Sengupta, K., Rap, A., Duplissy, J., Frege, C., Williamson, C., Heinritzi, M., Simon, M., Yan, C., Almeida, J., Tröstl, J., Nieminen, T., Ortega, I. K., Wagner, R., Dunne, E. M., Adamov, A., Amorim, A., Bernhammer, A. K., Bianchi, F., Breitenlechner, M., Brilke, S., Chen, X., Craven, J. S., Dias, A., Ehrhart, S., Fischer, L., Flagan, R. C., Franchin, A., Fuchs, C., Guida, R., Hakala, J., Hoyle, C. R., Jokinen, T., Junninen, H., Kangasluoma, J., Kim, J., Kirkby, J., Krapf, M., Kürten, A., Laaksonen, A., Lehtipalo, K., Makhmutov, V., Mathot, S., Molteni, U., Monks, S. A., Onnela, A., Peräkylä, O., Piel, F., Petäjä, T., Praplan, A. P., Pringle, K. J., Richards, N. A. D., Rissanen, M. P., Rondo, L., Sarnela, N., Schobesberger, S., Scott, C. E., Seinfeld, J. H., Sharma, S., Sipilä, M., Steiner, G., Stozhkov, Y., Stratmann, F., Tomé, A., Virtanen, A., Vogel, A. L., Wagner, A. C., Wagner, P. E., Weingartner, E., Wimmer, D., Winkler, P. M., Ye, P., Zhang, X., Hansel, A., Dommen, J., Donahue, N. M., Worsnop, D. R., Baltensperger, U., Kulmala, M., Curtius, J., and Carslaw, K. S.

- (2016). Reduced anthropogenic aerosol radiative forcing caused by biogenic new particle formation. *Proceedings of the National Academy of Sciences*, 113(43):12053–12058. <http://dx.doi.org/10.1073/pnas.1602360113>.
- Graus, M., Müller, M., and Hansel, A. (2010). High resolution PTR-TOF: Quantification and formula confirmation of VOC in real time. *Journal of the American Society for Mass Spectrometry*, 21(6):1037–1044. <http://dx.doi.org/10.1016/j.jasms.2010.02.006>.
- Guenther, A. B., Jiang, X., Heald, C. L., Sakulyanontvittaya, T., Duhl, T., Emmons, L. K., and Wang, X. (2012). The model of emissions of gases and aerosols from nature version 2.1 (MEGAN2.1): an extended and updated framework for modeling biogenic emissions. *Geosci. Model Dev.*, 5(6):1471–1492. <http://dx.doi.org/10.5194/gmd-5-1471-2012>.
- Hallquist, M., Wenger, J. C., Baltensperger, U., Rudich, Y., Simpson, D., Claeys, M., Dommen, J., Donahue, N. M., George, C., Goldstein, A. H., Hamilton, J. F., Herrmann, H., Hoffmann, T., Iinuma, Y., Jang, M., Jenkin, M. E., Jimenez, J. L., Kiendler-Scharr, A., Maenhaut, W., McFiggans, G., Mentel, T. F., Monod, A., Prévôt, A. S. H., Seinfeld, J. H., Surratt, J. D., Szmigielski, R., and Wildt, J. (2009). The formation, properties and impact of secondary organic aerosol: current and emerging issues. *Atmos. Chem. Phys.*, 9(14):5155–5236. <http://dx.doi.org/10.5194/acp-9-5155-2009>.
- Hansel, A., Jordan, A., Holzinger, R., Prazeller, P., Vogel, W., and Lindinger, W. (1995). Proton transfer reaction mass spectrometry: on-line trace gas analysis at the ppb level. *International Journal of Mass Spectrometry and Ion Processes*, 149-150(Supplement C):609–619. [http://dx.doi.org/10.1016/0168-1176\(95\)04294-U](http://dx.doi.org/10.1016/0168-1176(95)04294-U).
- Heinritzi, M., Dada, L., Simon, M., Stolzenburg, D., Wagner, A. C., Fischer, L., Ahonen, L. R., Amanatidis, S., Baalbaki, R., Baccarini, A., Bauer, P. S., Baumgartner, B., Bianchi, F., Brilke, S., Chen, D., Dias, A., Dommen, J., Duplissy, J., Finkenzeller, H., Frege, C., Fuchs, C., Garmash, O., Gordon, H., Granzin, M., Haddad, I. E., He, X., Helm, J., Hofbauer, V., Hoyle, C. R., Kangasluoma, J., Keber, T., Kim, C., Kürten, A., Lamkaddam, H., Lampilahti, J., Laurila, T. M., Lee, C. P., Lehtipalo, K., Leiminger, M., Mai, H., Makhmutov, V., Marten, R., Mathot, S., Mauldin, R. L., Mentler, B., Molteni, U., Müller, T., Nie, W., Nieminen, T., Onnela, A., Partoll, E.,

- Passananti, M., Petäjä, T., Pfeifer, J., Pospisilova, V., Quéléver, L., Rissanen, M. P., Rose, C., Schobesberger, S., Scholz, W., Scholze, K., Sipilä, M., Steiner, G., Stozhkov, Y., Tauber, C., Tham, Y. J., Vazquez-Pufleau, M., Virtanen, A., Vogel, A. L., Volkamer, R., Wagner, R., Wang, M., Weitz, L., Wimmer, D., Xiao, M., Yan, C., Ye, P., Zha, Q., Zhou, X., Amorim, A., Baltensperger, U., Hansel, A., Kulmala, M., Tomé, A., Winkler, P. M., Worsnop, D. R., Donahue, N. M., Kirkby, J., and Curtius, J. (2018). Molecular understanding of the suppression of new-particle formation by isoprene. *Nature (under review)*.
- Heinritzi, M., Simon, M., Steiner, G., Wagner, A. C., Kürten, A., Hansel, A., and Curtius, J. (2016). Characterization of the mass-dependent transmission efficiency of a cims. *Atmos. Meas. Tech.*, 9(4):1449–1460. <http://dx.doi.org/10.5194/amt-9-1449-2016>.
- Hermann, M., Wehner, B., Bischof, O., Han, H. S., Krinke, T., Liu, W., Zerrath, A., and Wiedensohler, A. (2007). Particle counting efficiencies of new tsi condensation particle counters. *Journal of Aerosol Science*, 38(6):674–682. <http://dx.doi.org/10.1016/j.jaerosci.2007.05.001>.
- Hinds, W. C. (1999). *Aerosol Technology*. Wiley Interscience, 2 edition. book.
- Iida, K., Stolzenburg, M. R., and McMurry, P. H. (2009). Effect of working fluid on sub-2 nm particle detection with a laminar flow ultrafine condensation particle counter. *Aerosol Science and Technology*, 43:81–96. <http://dx.doi.org/10.1080/02786820802488194>.
- Jayne, J. T., Leard, D. C., Zhang, X., Davidovits, P., Smith, K. A., Kolb, C. E., and Worsnop, D. R. (2000). Development of an aerosol mass spectrometer for size and composition analysis of submicron particles. *Aerosol Science and Technology*, 33(1-2):49–70. <http://dx.doi.org/10.1080/027868200410840>.
- Jiang, J., Zhao, J., Chen, M., Eisele, F. L., Scheckman, J., Williams, B. J., Kuang, C., and McMurry, P. H. (2011). First measurements of neutral atmospheric cluster and 1-2 nm particle number size distributions during nucleation events. *Aerosol Science and Technology*, 45(4):ii–v. <http://dx.doi.org/10.1080/02786826.2010.546817>.
- Jokinen, T., Sipilä, M., Junninen, H., Ehn, M., Lönn, G., Hakala, J., Petäjä, T., Mauldin Iii, R. L., Kulmala, M., and Worsnop, D. R. (2012). Atmospheric sulphuric acid and neutral cluster measurements using ci-api-tof.

Atmos. Chem. Phys., 12(9):4117–4125. <http://dx.doi.org/10.5194/acp-12-4117-2012>.

Kerminen, V.-M., Chen, X., Vakkari, V., Petäjä, T., Kulmala, M., and Bianchi, F. (2018). Atmospheric new particle formation and growth: review of field observations. *Environmental Research Letters*, 13(10):103003. <http://dx.doi.org/10.1088/1748-9326/aadf3c>.

Kirkby, J., Curtius, J., Almeida, J., Dunne, E., Duplissy, J., Ehrhart, S., Franchin, A., Gagne, S., Ickes, L., Kurten, A., Kupc, A., Metzger, A., Riccobono, F., Rondo, L., Schobesberger, S., Tsagkogeorgas, G., Wimmer, D., Amorim, A., Bianchi, F., Breitenlechner, M., David, A., Dommen, J., Downard, A., Ehn, M., Flagan, R. C., Haider, S., Hansel, A., Hauser, D., Jud, W., Junninen, H., Kreissl, F., Kvashin, A., Laaksonen, A., Lehtipalo, K., Lima, J., Lovejoy, E. R., Makhmutov, V., Mathot, S., Mikkila, J., Minginette, P., Mogo, S., Nieminen, T., Onnela, A., Pereira, P., Petaja, T., Schnitzhofer, R., Seinfeld, J. H., Sipila, M., Stozhkov, Y., Stratmann, F., Tome, A., Vanhanen, J., Viisanen, Y., Vrtala, A., Wagner, P. E., Walther, H., Weingartner, E., Wex, H., Winkler, P. M., Carslaw, K. S., Worsnop, D. R., Baltensperger, U., and Kulmala, M. (2011). Role of sulphuric acid, ammonia and galactic cosmic rays in atmospheric aerosol nucleation. *Nature*, 476(7361):429–433. <http://dx.doi.org/10.1038/nature10343>.

Kirkby, J., Duplissy, J., Sengupta, K., Frege, C., Gordon, H., Williamson, C., Heinritzi, M., Simon, M., Yan, C., Almeida, J., Tröstl, J., Nieminen, T., Ortega, I. K., Wagner, R., Adamov, A., Amorim, A., Bernhammer, A. K., Bianchi, F., Breitenlechner, M., Brilke, S., Chen, X., Craven, J., Dias, A., Ehrhart, S., Flagan, R. C., Franchin, A., Fuchs, C., Guida, R., Hakala, J., Hoyle, C. R., Jokinen, T., Junninen, H., Kangasluoma, J., Kim, J., Krapf, M., Kürten, A., Laaksonen, A., Lehtipalo, K., Makhmutov, V., Mathot, S., Molteni, U., Onnela, A., Peräkylä, O., Piel, F., Petäjä, T., Praplan, A. P., Pringle, K., Rap, A., Richards, N. A. D., Riipinen, I., Rissanen, M. P., Rondo, L., Sarnela, N., Schobesberger, S., Scott, C. E., Seinfeld, J. H., Sipilä, M., Steiner, G., Stozhkov, Y., Stratmann, F., Tomé, A., Virtanen, A., Vogel, A. L., Wagner, A. C., Wagner, P. E., Weingartner, E., Wimmer, D., Winkler, P. M., Ye, P., Zhang, X., Hansel, A., Dommen, J., Donahue, N. M., Worsnop, D. R., Baltensperger, U., Kulmala, M., Carslaw, K. S., and Curtius, J. (2016). Ion-induced nucleation of pure biogenic particles. *Nature*, 533:521. <http://dx.doi.org/10.1038/nature17953>.

- Knutson, E. O. and Whitby, K. T. (1975). Aerosol classification by electric mobility: apparatus, theory, and applications. *Journal of Aerosol Science*, 6(6):443–451. [http://dx.doi.org/10.1016/0021-8502\(75\)90060-9](http://dx.doi.org/10.1016/0021-8502(75)90060-9).
- Kuang, C., Chen, M., Zhao, J., Smith, J., McMurry, P. H., and Wang, J. (2012). Size and time-resolved growth rate measurements of 1 to 5 nm freshly formed atmospheric nuclei. *Atmos. Chem. Phys.*, 12(7):3573–3589. <http://dx.doi.org/10.5194/acp-12-3573-2012>.
- Kuang, C., McMurry, P. H., McCormick, A. V., and Eisele, F. L. (2008). Dependence of nucleation rates on sulfuric acid vapor concentration in diverse atmospheric locations. *Journal of Geophysical Research: Atmospheres*, 113(D10). <http://dx.doi.org/10.1029/2007JD009253>.
- Kulmala, M., Kontkanen, J., Junninen, H., Lehtipalo, K., Manninen, H. E., Nieminen, T., Petäjä, T., Sipilä, M., Schobesberger, S., Rantala, P., Franchin, A., Jokinen, T., Järvinen, E., äijälä, M., Kangasluoma, J., Hakala, J., Aalto, P. P., Paasonen, P., Mikkilä, J., Vanhanen, J., Aalto, J., Hakola, H., Makkonen, U., Ruuskanen, T., Mauldin, R. L., Duplissy, J., Vehkamäki, H., Bäck, J., Kortelainen, A., Riipinen, I., Kurtén, T., Johnston, M. V., Smith, J. N., Ehn, M., Mentel, T. F., Lehtinen, K. E. J., Laaksonen, A., Kerminen, V. M., and Worsnop, D. R. (2013). Direct observations of atmospheric aerosol nucleation. *Science*, 339(6122):943–946. <http://dx.doi.org/10.1126/science.1227385>.
- Kulmala, M., Vehkamäki, H., Petäjä, T., Dal Maso, M., Lauri, A., Kerminen, V. M., Birmili, W., and McMurry, P. H. (2004). Formation and growth rates of ultrafine atmospheric particles: a review of observations. *Journal of Aerosol Science*, 35(2):143–176. <http://dx.doi.org/10.1016/j.jaerosci.2003.10.003>.
- Kürten, A., Bergen, A., Heinritzi, M., Leiminger, M., Lorenz, V., Piel, F., Simon, M., Sitals, R., Wagner, A. C., and Curtius, J. (2016). Observation of new particle formation and measurement of sulfuric acid, ammonia, amines and highly oxidized organic molecules at a rural site in central Germany. *Atmos. Chem. Phys.*, 16(19):12793–12813. <http://dx.doi.org/10.5194/acp-16-12793-2016>.
- Kürten, A., Jokinen, T., Simon, M., Sipilä, M., Sarnela, N., Junninen, H., Adamov, A., Almeida, J., Amorim, A., Bianchi, F., Breitenlechner, M.,

- Dommen, J., Donahue, N. M., Duplissy, J., Ehrhart, S., Flagan, R. C., Franchin, A., Hakala, J., Hansel, A., Heinritzi, M., Hutterli, M., Kangasluoma, J., Kirkby, J., Laaksonen, A., Lehtipalo, K., Leiminger, M., Makhmutov, V., Mathot, S., Onnela, A., Petäjä, T., Praplan, A. P., Riccobono, F., Rissanen, M. P., Rondo, L., Schobesberger, S., Seinfeld, J. H., Steiner, G., Tomé, A., Tröstl, J., Winkler, P. M., Williamson, C., Wimmer, D., Ye, P., Baltensperger, U., Carslaw, K. S., Kulmala, M., Worsnop, D. R., and Curtius, J. (2014). Neutral molecular cluster formation of sulfuric acid-dimethylamine observed in real time under atmospheric conditions. *Proceedings of the National Academy of Sciences*, 111(42):15019–15024. <http://dx.doi.org/10.1073/pnas.1404853111>.
- Kürten, A., Rondo, L., Ehrhart, S., and Curtius, J. (2012). Calibration of a chemical ionization mass spectrometer for the measurement of gaseous sulfuric acid. *The Journal of Physical Chemistry A*, 116(24):6375–6386. <http://dx.doi.org/10.1021/jp212123n>.
- Laskin, J., Laskin, A., and Nizkorodov, S. A. (2018). Mass spectrometry analysis in atmospheric chemistry. *Analytical Chemistry*, 90(1):166–189. <http://dx.doi.org/10.1021/acs.analchem.7b04249>.
- Lehtinen, K. E. J., Dal Maso, M., Kulmala, M., and Kerminen, V. M. (2007). Estimating nucleation rates from apparent particle formation rates and vice versa: Revised formulation of the kerminen–kulmala equation. *Journal of Aerosol Science*, 38(9):988–994. <http://dx.doi.org/10.1016/j.jaerosci.2007.06.009>.
- Lelieveld, J., Evans, J. S., Fnais, M., Giannadaki, D., and Pozzer, A. (2015). The contribution of outdoor air pollution sources to premature mortality on a global scale. *Nature*, 525(7569):367–371. <http://dx.doi.org/10.1038/nature15371>.
- Li, N., Sioutas, C., Cho, A., Schmitz, D., Misra, C., Sempf, J., Wang, M., Oberley, T., Froines, J., and Nel, A. (2003). Ultrafine particulate pollutants induce oxidative stress and mitochondrial damage. *Environmental Health Perspectives*, 111(4):455. <http://dx.doi.org/10.1289/ehp.6000>.
- Lohmann, U. and Feichter, J. (2005). Global indirect aerosol effects: a review. *Atmos. Chem. Phys.*, 5(3):715–737. <http://dx.doi.org/10.5194/acp-5-715-2005>.

- Lopez-Hilfiker, F. D., Mohr, C., Ehn, M., Rubach, F., Kleist, E., Wildt, J., Mentel, T. F., Lutz, A., Hallquist, M., Worsnop, D., and Thornton, J. A. (2014). A novel method for online analysis of gas and particle composition: description and evaluation of a filter inlet for gases and aerosols (figaero). *Atmos. Meas. Tech.*, 7(4):983–1001. <http://dx.doi.org/10.5194/amt-7-983-2014>.
- Lovejoy, E. R., Curtius, J., and Froyd, K. D. (2004). Atmospheric ion-induced nucleation of sulfuric acid and water. *Journal of Geophysical Research: Atmospheres*, 109(D8). <http://dx.doi.org/10.1029/2003JD004460>.
- Maher, S., Jjunju, F. P. M., and Taylor, S. (2015). Colloquium: 100 years of mass spectrometry: Perspectives and future trends. *Reviews of Modern Physics*, 87(1):113–135. <http://dx.doi.org/10.1103/RevModPhys.87.113>.
- Mann, G. W., Carslaw, K. S., Spracklen, D. V., Ridley, D. A., Manktelow, P. T., Chipperfield, M. P., Pickering, S. J., and Johnson, C. E. (2010). Description and evaluation of glomap-mode: a modal global aerosol microphysics model for the ukca composition–climate model. *Geosci. Model Dev.*, 3(2):519–551. <http://dx.doi.org/10.5194/gmd-3-519-2010>.
- McMurry, P. (2000). The history of condensation nucleus counters. *Aerosol Science and Technology*, 33:297–322.
- Merikanto, J., Spracklen, D. V., Mann, G. W., Pickering, S. J., and Carslaw, K. S. (2009). Impact of nucleation on global ccn. *Atmos. Chem. Phys.*, 9(21):8601–8616. <http://dx.doi.org/10.5194/acp-9-8601-2009>.
- Noble, C. A. and Prather, K. A. (2000). Real-time single particle mass spectrometry: A historical review of a quarter century of the chemical analysis of aerosols. *Mass Spectrometry Reviews*, 19(4). [http://dx.doi.org/10.1002/1098-2787\(200007\)19:4<248::AID-MAS3>3.0.CO;2-I](http://dx.doi.org/10.1002/1098-2787(200007)19:4<248::AID-MAS3>3.0.CO;2-I).
- Pankow, J. F. and Asher, W. E. (2008). Simpol.1: a simple group contribution method for predicting vapor pressures and enthalpies of vaporization of multifunctional organic compounds. *Atmos. Chem. Phys.*, 8(10):2773–2796. <http://dx.doi.org/10.5194/acp-8-2773-2008>.
- Peters, T. M., Ott, D., and OShaughnessy, P. T. (2006). Comparison of the grimm 1.108 and 1.109 portable aerosol spectrometer to the tsi 3321 aero-

- dynamic particle sizer for dry particles. *Annals of Occupational Hygiene*, 50(8):843–850. <http://dx.doi.org/10.1093/annhyg/mel067>.
- Schobesberger, S., Junninen, H., Bianchi, F., Lönn, G., Ehn, M., Lehtipalo, K., Dommen, J., Ehrhart, S., Ortega, I. K., Franchin, A., Nieminen, T., Riccobono, F., Hutterli, M., Duplissy, J., Almeida, J., Amorim, A., Breitenlechner, M., Downard, A. J., Dunne, E. M., Flagan, R. C., Kajos, M., Keskinen, H., Kirkby, J., Kupc, A., Kürten, A., Kurtén, T., Laaksonen, A., Mathot, S., Onnela, A., Praplan, A. P., Rondo, L., Santos, F. D., Schallhart, S., Schnitzhofer, R., Sipilä, M., Tomé, A., Tsagkogeorgas, G., Vehkamäki, H., Wimmer, D., Baltensperger, U., Carslaw, K. S., Curtius, J., Hansel, A., Petäjä, T., Kulmala, M., Donahue, N. M., and Worsnop, D. R. (2013). Molecular understanding of atmospheric particle formation from sulfuric acid and large oxidized organic molecules. *Proceedings of the National Academy of Sciences*, 110(43):17223. <http://dx.doi.org/10.1073/pnas.1306973110>.
- Seinfeld, J. H. and Pandis, S. N. (2006). *Atmospheric Chemistry and Physics - From Air Pollution to Climate Change*. Wiley Interscience.
- Simon, M., Heinritzi, M., Herzog, S., Leiminger, M., Bianchi, F., Praplan, A., Dommen, J., Curtius, J., and Kürten, A. (2016). Detection of dimethylamine in the low pptv range using nitrate chemical ionization atmospheric pressure interface time-of-flight (ci-api-tof) mass spectrometry. *Atmos. Meas. Tech.*, 9(5):2135–2145. <http://dx.doi.org/10.5194/amt-9-2135-2016>.
- Steiner, G., Attoui, M., Wimmer, D., and Reischl, G. P. (2010). A medium flow, high-resolution vienna dma running in recirculating mode. *Aerosol Science and Technology*, 44(4):308–315. <http://dx.doi.org/10.1080/02786821003636763>.
- Stolzenburg, D., Fischer, L., Vogel, A. L., Heinritzi, M., Schervish, M., Simon, M., Wagner, A. C., Dada, L., Ahonen, L. R., Amorim, A., Baccarini, A., Bauer, P. S., Baumgartner, B., Bergen, A., Bianchi, F., Breitenlechner, M., Brilke, S., Buenrostro Mazon, S., Chen, D., Dias, A., Draper, D. C., Duplissy, J., El Haddad, I., Finkenzeller, H., Frege, C., Fuchs, C., Garmash, O., Gordon, H., He, X., Helm, J., Hofbauer, V., Hoyle, C. R., Kim, C., Kirkby, J., Kontkanen, J., Kürten, A., Lampilahti, J., Lawler, M., Lehtipalo, K., Leiminger, M., Mai, H., Mathot, S., Mentler, B., Molteni, U., Nie, W., Nieminen, T., Nowak, J. B., Ojdanic, A., Onnela, A., Passananti, M., Petäjä, T.,

- Quéléver, L. L. J., Rissanen, M. P., Sarnela, N., Schallhart, S., Tauber, C., Tomé, A., Wagner, R., Wang, M., Weitz, L., Wimmer, D., Xiao, M., Yan, C., Ye, P., Zha, Q., Baltensperger, U., Curtius, J., Dommen, J., Flagan, R. C., Kulmala, M., Smith, J. N., Worsnop, D. R., Hansel, A., Donahue, N. M., and Winkler, P. M. (2018). Rapid growth of organic aerosol nanoparticles over a wide tropospheric temperature range. *Proceedings of the National Academy of Sciences*, 115(37):9122. <http://dx.doi.org/10.1073/pnas.1807604115>.
- Stolzenburg, D., Steiner, G., and Winkler, P. M. (2017). A dma-train for precision measurement of sub-10nm aerosol dynamics. *Atmos. Meas. Tech.*, 10:1639–1651. <http://dx.doi.org/10.5194/amt-10-1639-2017>.
- Stolzenburg, M. R. and McMurry, P. H. (2008). Equations governing single and tandem dma configurations and a new lognormal approximation to the transfer function. *Aerosol Science and Technology*, 42(6):421–432. <http://dx.doi.org/10.1080/02786820802157823>.
- Thermo Fisher Scientific Inc. Air Quality Instruments (2007). Model 5030 synchronized hybrid ambient real-time particulate monitor. Instruction Manual.
- Tröstl, J., Chuang, W. K., Gordon, H., Heinritzi, M., Yan, C., Molteni, U., Ahlm, L., Frege, C., Bianchi, F., Wagner, R., Simon, M., Lehtipalo, K., Williamson, C., Craven, J. S., Duplissy, J., Adamov, A., Almeida, J., Bernhammer, A. K., Breitenlechner, M., Brilke, S., Dias, A., Ehrhart, S., Flagan, R. C., Franchin, A., Fuchs, C., Guida, R., Gysel, M., Hansel, A., Hoyle, C. R., Jokinen, T., Junninen, H., Kangasluoma, J., Keskinen, H., Kim, J., Krapf, M., Kürten, A., Laaksonen, A., Lawler, M., Leiminger, M., Mathot, S., Möhler, O., Nieminen, T., Onnela, A., Petäjä, T., Piel, F. M., Miettinen, P., Rissanen, M. P., Rondo, L., Sarnela, N., Schobesberger, S., Sengupta, K., Sipilä, M., Smith, J. N., Steiner, G., Tomè, A., Virtanen, A., Wagner, A. C., Weingartner, E., Wimmer, D., Winkler, P. M., Ye, P., Carslaw, K. S., Curtius, J., Dommen, J., Kirkby, J., Kulmala, M., Riipinen, I., Worsnop, D. R., Donahue, N. M., and Baltensperger, U. (2016). The role of low-volatility organic compounds in initial particle growth in the atmosphere. *Nature*, 533:527. <http://dx.doi.org/10.1038/nature18271>.
- TSI Incorporated (2001). Model 3080-series electrostatic classifiers. Instruction Manual.

-
- TSI Incorporated (2007). Ultrafine condensation particle counter model 3776. Instruction Manual.
- TSI Incorporated (2012a). Aerodynamic particle sizer model 3321. Instruction Manual.
- TSI Incorporated (2012b). Optical particle sizer model 3330. Instruction Manual.
- Vanhanen, J., Mikkilä, J., Lehtipalo, K., Sipilä, M., Manninen, H. E., Siivola, E., Petäjä, T., and Kulmala, M. (2011). Particle size magnifier for nano-cn detection. *Aerosol Science and Technology*, 45:533–542. <http://dx.doi.org/10.1080/02786826.2010.547889>.
- Wagner, A. C., Bergen, A., Brilke, S., Bühner, B., Ebert, M., Haunold, W., Heinritzi, M., Herzog, S., Jacobi, S., Kürten, A., Piel, F., Ramme, A., Weber, D., Weinbruch, S., and Curtius, J. (2017). Characterization of aerosol particles produced by a skyscraper demolition by blasting. *Journal of Aerosol Science*, 112(Supplement C):11–18. <https://doi.org/10.1016/j.jaerosci.2017.06.007>.
- Wagner, A. C., Bergen, A., Brilke, S., Fuchs, C., Ernst, M., Hoker, J., Heinritzi, M., Simon, M., Bühner, B., Curtius, J., and Kürten, A. (2018). Size-resolved online chemical analysis of nanoaerosol particles: a thermal desorption differential mobility analyzer coupled to a chemical ionization time-of-flight mass spectrometer. *Atmos. Meas. Tech.*, 11(10):5489–5506. <http://dx.doi.org/10.5194/amt-11-5489-2018>.
- Wang, S. C. and Flagan, R. C. (1990). Scanning electrical mobility spectrometer. *Aerosol Science and Technology*, 13:2:230–240. <http://dx.doi.org/10.1080/02786829008959441>.
- Weber, R. J., Marti, J. J., McMurry, P. H., Eisele, F. L., Tanner, D. J., and Jefferson, A. (1996). Measured atmospheric new particle formation rates: Implications for nucleation mechanisms. *Chemical Engineering Communications*, 151(1):53–64. <http://dx.doi.org/10.1080/00986449608936541>.
- Wellenius, G. A., Burger, M. R., Coull, B. A., Schwartz, J., Suh, H. H., Koutrakis, P., Schlaug, G., Gold, D. R., and Mittleman, M. A. (2012). Ambient air pollution and the risk of acute ischemic stroke. *Archives of internal medicine*, 172(3):229–234. <http://dx.doi.org/10.1001/archinternmed.2011.732>.

- Wiza, J. L. (1979). Microchannel plate detectors. *Nuclear Instruments and Methods*, 162:587 – 601.
- Zhang, Q., Jimenez, J. L., Canagaratna, M. R., Ulbrich, I. M., Ng, N. L., Worsnop, D. R., and Sun, Y. (2011). Understanding atmospheric organic aerosols via factor analysis of aerosol mass spectrometry: a review. *Analytical and Bioanalytical Chemistry*, 401(10):3045–3067. <http://dx.doi.org/10.1007/s00216-011-5355-y>.